IMPERIAL COLLEGE OF SCIENCE AND TECHNOLOGY

DEPARTMENT OF ELECTRICAL ENGINEERING

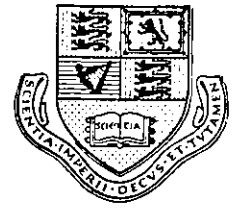

TWO-PHASE AUTO-PILOTED SYNCHRONOUS MOTORS AND ACTUATORS

☆

Thesis submitted for the degree
of Doctor of Philosophy of the
University of London.

☆

by

Amadeu Leão Santos Rodrigues, M.Sc.(D.I.C.)

July 1983

ABSTRACT

The thesis is concerned with certain aspects of the design and performance of drives based on variable speed synchronous motors fed from variable frequency sources, controlled by means of rotor-position sensors. This auto-piloted or self-synchronised form of control enables the machine to operate either with an adjustable load angle or an adjustable torque angle depending on whether a voltage or a current source feed is used. D.c. machine-type characteristics can thus be obtained from the system.

The thesis commences with an outline of some fundamental design aspects and a summary of torque production mechanisms in electrical machines. The influence of configuration and physical size on machine performance is discussed and the advantages of the use for servo applications of direct-drive as opposed to step-down transmissions are explained.

Developments in permanent magnet materials have opened the way to permanent magnet motors of improved performance, and a brief review of the properties of the various materials presently available is given. A finite-difference method using magnetic scalar potential for calculating the magnetic field of permanent magnets in the presence of iron cores and macroscopic currents is described. A comparison with the load line method is made for some typical cases.

Analogies between the mechanical commutator of a d.c. machine and the electronic commutator of the system studied are drawn and a theory valid for damper-less motors operating under both steady and dynamic

conditions is presented.

The design, manufacture and testing of a 1000 lb.ft, limited motion, rare-earth permanent-magnet-excited rotary actuator, begun in an earlier project, is described. Computer solutions for the numerical calculation of air gap flux density distribution, air gap inductance and demagnetisation current limit are given and correlated with test results.

D.c. disc motors with printed circuit armatures are now widely used in servo applications. The design, construction and testing of a permanent-magnet-excited, rotating-armature, auto-piloted synchronous disc motor is described. Two types of rotor construction were investigated.

Finally, experimental results serve to supplement a theoretical comparison between disc and equivalent drum motors. Both coil excitation and permanent magnet field excitation are considered.

ACKNOWLEDGEMENTS

The work described in this thesis was carried out under the supervision of Dr H.Bolton, B.Sc.(Eng.), Ph.D., Reader in Electrical Machines at the Department of Electrical Engineering, Imperial College of Science and Technology, London. For the invaluable help, advice, constant encouragement and stimulating discussions during the course of this work, the author would like to express his extreme gratitude to his supervisor.

The bulk of the manufacturing work of the prototypes and test rigs was carried out in the Electrical Engineering Workshop at Imperial College, under the supervision of Mr. R. Moore to whom, along with his staff, the author is grateful. Thanks are also due to Mr. R.B. Owen for his practical assistance and advice during the work. Considerable assistance was received from Dr. D. Pedder and Mr N. Mallinson on problems associated with the electronic portions.

The author is deeply indebted to the "Universidade Nova de Lisboa" for all the facilities provided and to the "Instituto Nacional de Investigação Científica" for generous financial support received during his studies in England, without which this work would not have been possible.

Thanks are finally due to many colleagues and friends at Imperial College who have helped to make the research enjoyable.

CONTENTS

☆ ☆ ☆

INTRODUCTION

The idea of phase locking a variable frequency polyphase feed to a synchronous motor via the use of a shaft position sensor can probably be traced back to the early 19th century. Of course when the sensor and the (mechanical) switching system are combined a machine is obtained that is very close to an inverted d.c. machine (field on the rotor, armature on stator). If one elects to locate the field of such a system on the stator and the armature on the rotor the resulting structure is in fact identical in operation to the d.c. machine.

However it is believed that the first occasion on which an "electronic" as opposed to a mechanical or synchro-derived variable frequency feed system was envisaged, occurred in the nineteen thirties, when a patent was filed describing the use of a thyratron-based inverter to feed a synchronous motor. For obvious reasons, few developments took place until the advent of the thyristor and even then the efforts of most groups in the inverter-fed variable-speed-drives field were orientated in the direction of induction motor and "open-loop" reluctance and synchronous motor schemes where the inverter is essentially unaware of the rotor shaft position.

The merits of the "phase-locked" or "auto-piloted" or "brushless d.c." scheme for synchronous motor variable speed drives (briefly: no speed hunting; no pole slippling; operation at optimum load or torque angles, even if these are normally unstable in open-loop schemes; little need for rotor dampers) become more widely recognized in the nineteen seventies particularly in the U.S.A., Canada, France, Germany, UK and

Japan. Medium/high power drives were brought onto the market by Siemens, ASEA and latterly by most of the other principal western electrical manufacturers. A certain amount of theoretical work has been done mainly by university groups in Germany, France, Japan and U.S.A. In the U.K. the author is aware of papers by A.C. Williamson [1] and by B.J. Chalmers et al [2] (both at UMIST) and by Macpherson and Shepherd [3] at John D. Wood Ltd of Aberdeen and Edinburgh University.

In parallel with this work has been a considerable effort into the development of phase-locked linear synchronous motor drives for unconventional guided-traction applications. Projects have been conducted primarily in Canada, U.S.A., Germany, U.K. (Bath and Manchester Universities) and Japan, and in some of these, inductor-type machines and combined maglev/drive systems have been involved. In a few cases, (notably Slemon et al [4] in Canada), a number of general operating characteristics for phase-locked schemes have been delineated.

Finally, and perhaps most relevant in the context of this thesis, a widespread and somewhat diverse variety of developments have occurred in the small power and servo drives area. In most cases, permanent magnet field systems and power transistor-based feeds have been involved. The pace of development of both permanent magnets and power transistors has rapidly accelerated over the last decade and this has led to an ever increasing activity in these drive areas. At the beginning of the nineteen seventies, the use of the "brushless d.c." motors (as the permanent magnet excited version commonly termed) was restricted to certain sub-100 W aerospace, defence and hi-fi applications where its long life (limited in principle only by bearing wear), low losses (compared with the two-phase induction servo motor - the traditional type of brushless servo) and absence of brush hazards (for hazardous, hi-fi, fluid and some space environments) compensated for its extra cost per power rating.

However, recently, brushless d.c. motors have made their appearance

in virtually standard applications as sub-kW fan drives (mainly for electronic equipment cooling both in the military and the industrial fields) and, this year, as sub-kW and low-integral kW machine-tool servo-drives. In some cases the companies concerned (Walter Jones and Papst for fans and Bosch for machine tools) are believed to be marketing the drives for prices that are competitive with equivalent, transistor-fed d.c. drives. Usage in such "standard" areas is likely to increase markedly in future as inverter and magnet costs fall further. The Printed Motor Co Ltd announced in 1980 a rotating-field, brushless disc motor employing semi-standard, twin, punched-copper disc armatures, but this motor is not believed to be yet available.

There has been only a limited amount of learned-society literature dealing with small-power and servo brushless d.c. drives. The main papers known to the author have appeared in I.E.E. Conference Publications (Small Machines 1976, 81, Electrical Variable-Speed Drives 1979, Power Electronics 1977) and Electromechanics Quarterly (Weh et al, Braunschweig, Germany) though some others are referenced in Chapter 3 and in Ashen's Ph.D. thesis [5]. A few papers, mostly dealing with small, wound-field machines appeared in "Electrical Engineering in Japan" in the early seventies, and other papers can be found in the I.C.E.M. Conference Proceedings of 1981 and 1982, and also in the 1980 Conumel Conference Proceedings. Where any of these are thought to bear directly on the contents of the thesis, they are referenced at the relevant point.

It should finally be mentioned, as it has been an important area of activity in the U.K., that considerable development, mostly accompanied by easily accessible (I.E.E. Proceedings) publications, has taken place in the field of permanent-magnet-excited synchronous motors designed primarily for use on fixed frequency mains supply. As is the case with the equivalent type of reluctance motor, these can certainly be operated "closed-loop" with a position sensor in the a brushless d.c. mode and in

some cases their performance levels (and/or performance per cost) exceed those obtainable from motors designed solely for "brushless d.c." operation. However, much of the design process for such motors, and many of the design features particularly on their rotors is dominated by the need for good starting performance, and rotor conductorwork is hence much in evidence. The virtual absence of conductorwork on permanent magnet and reluctance rotors designed specifically for brushless d.c. operation is allowable because of the inherently synchronised nature of the scheme (though some damping is occasionally useful with rotors employing metal pole shoes and/or alloy magnets to cope with rapid "transformer" e.m.f.'s following sudden armature current changes) and this is thought to mean that such rotors are cheaper to manufacture and give better performance than rotors with conductorwork where design compromises are necessary.

In order to put small-power and servo brushless d.c. drives in perspective, it is interesting to make a brief and necessarily somewhat oversimplified list of their merits alongside competing types of drive.

In comparison with small-power and servo d.c. variable speed drives, brushless d.c. drives have the following advantages: no brushes or commutator; loss-free rotor; no risk of air gap seizure due to armature heating; no speed limit due to commutation "or volts per segment" limit; reduced no-load losses, maintenance and radio-frequency interference; extended lifetime. However some disadvantages occur: a multi-phase feed is required (power per phase is smaller but component count is inevitably higher); a shaft position sensor is required; significant torque ripple occurs unless a "sine" feed basis is used (see section 1.5).

Compared to fixed frequency two-phase induction servo drives, the brushless d.c. drive is much less lossy (hence better output per size) and has no inherent synchronous speed limit, but the variable frequency feed, shaft position sensing and a more expensive and less robust

permanent magnet rotor is needed.

Compared to the variable frequency, polyphase conduction drive, the brushless d.c. drive can be said to be more efficient (no rotor losses), to give a higher output per inverter V.A., and to allow load commutation of thyristor inverters (over some parts of the load and speed range). In control terms, a brushless d.c. motor (whether voltage-fed at fixed load angle or current-fed at fixed torque angle) behaves very much like a (voltage-fed or current-fed) d.c. motor. Hence the complexities of "flux vector orientation" systems necessary to obtain good control bandwidths from inverter-fed induction servos are avoided. With the sine current-fed brushless d.c. system discussed later, the behaviour is virtually that of an ideal, controllable, ripple-free torque source. Mutual e.m.f.'s can be minimized by using a two-phase basis, and the use of a two-phase approach is a common thread running through much of the hardware-oriented portions of the thesis.

Against these advantages must again be set the disadvantages of a more costly and less robust rotor, and the difficulty of controlling flux (only possible with auxiliary rotor windings or d-axis current control on the armature).

In practice, it is thought that the brushless d.c. drive's merits are most significant for small power drives (magnetising current, stator losses and rotor R/X of the equivalent induction motor are all relatively high) and for servo drives (simpler control concept and implementation). If wound-field synchronous machines are included in the comparison, a further area where induction drives are at something of a disadvantage is at large power levels (say above 200 kW) where the inverter cost savings accruing from the higher efficiency and power factor of the synchronous machine and the elimination of high-voltage artificial commutation circuits, stemming from the inverter thyristor-commutation capabilities

of the synchronous machine at reasonable speeds, more than compensate for its extra cost.

Outside these areas, d.c. and induction motor drives dominate and will probably continue to do so, though it is likely that d.c. brushless drives will continue to make inroads as suitable motors get developed and as power electronics costs fall.

This thesis makes its principal contributions in the electromagnetic and electromechanical aspects as opposed to the power electronics aspects of brushless d.c. drives technology. However, important portions of the work deal with entire brushless d.c. drive systems, and with the design, construction and operation of a complete system incorporating novel forms of motor and position sensor. For a full introduction to the topics covered, the reader is referred to the individual chapters, but in brief it can be said that the first three chapters deal primarily with fundamentals (respectively: general factors relating to brushless d.c. machine design; analysis and design of permanent magnet field systems for brushless d.c. motors; brushless d.c. motor operation and analysis). The next two chapters deal with investigations into two specific types of brushless d.c. drive (high torque, limited rotation positioning drive with arcuate geometry, where a novel form of brushless tachometer for limited rotation duties is included; low power rotating armature drive with disc geometry). Finally, the last chapter deals with some comparisons between a variety of synchronous motor types for brushless d.c. drive usage.

☆ ☆ ☆

CHAPTER 1

SOME FUNDAMENTAL ASPECTS OF ELECTRICAL MACHINES

1.1 - GENERALITIES

This chapter deals with some of the fundamentals of machine analysis. The material included is reasonably well known, but is presented in order to establish a good foundation for later portions of the work.

1.2 - ELECTROMAGNETIC TORQUE IN INDUCTIVELY COUPLED CIRCUITS

The magnetic energy stored in the magnetic field produced by m inductively coupled circuits confined to a medium of uniform and constant permeability is expressed, in terms of inductances and currents, by

$$W_{mag} = \sum_{j=1}^{m} \sum_{k=1}^{m} \frac{1}{2} L_{jk} i_j i_k \qquad (1.1)$$

assuming that there is no change in the configuration of the circuits relatively to each other [6]. In the particular case of the rotary electromagnet shown in fig. 1.1 the stator winding is coupled with the rotor winding and due to the saliency both self-inductances L_{11} and L_{22} are function of rotor postion θ. The mutual inductance between both windings, defined as the flux linkage of one winding when a unit current flows in the other, is independent of the coil selected to carry the current and so $L_{12} = L_{21} = M$, being also a function of the rotor position θ even without saliency. Hence, for a fixed rotor position and both coils excited, the energy stored in the component magnetic fields of

both coils and in the mutual field is, according to Eq. (1.1), given by

$$W_{mag} = \frac{1}{2} L_{11} i_1^2 + \frac{1}{2} L_{22} i_2^2 + M i_1 i_2 \qquad (1.2)$$

When there is a small movement $d\theta$ of the rotor in clockwise direction a small amount of mechanical work $dW_{mech} = T_{em} d\theta$ will be done by the movement. At the same time the flux will slightly increase and more

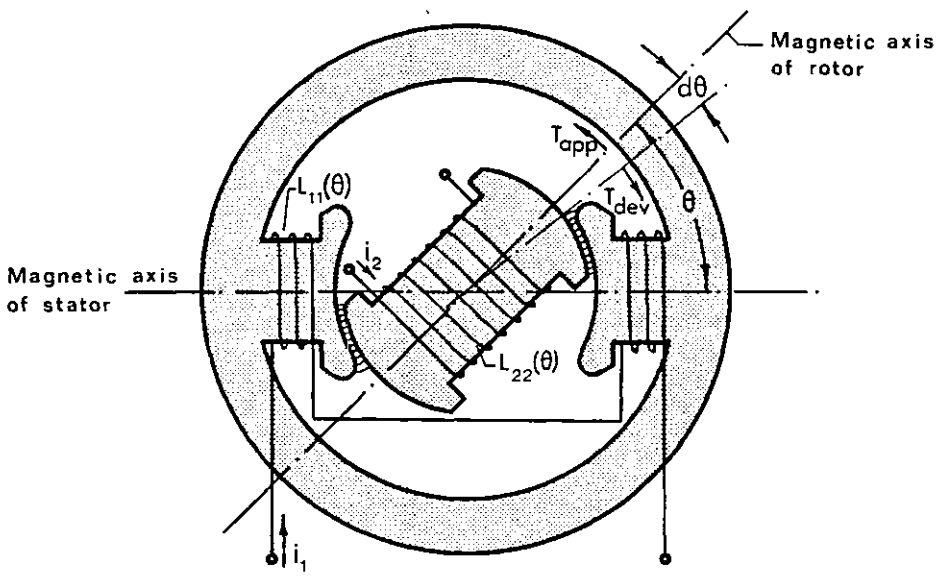

Fig. 1.1 - Rotating electromagnet with variable self and mutual inductance

magnetic energy will be stored in the magnetic field. The increase in the stored energy is found by differentiating Eq. (1.2), which gives:

$$dW_{mag} = L_{11} i_1 di_1 + M(i_1 di_2 + i_2 di_1) + L_{22} i_2 di_2 + \\ + \frac{1}{2} i_1^2 dL_{11} + \frac{1}{2} i_2^2 dL_{22} + i_1 i_2 dM \qquad (1.3)$$

As the two windings move near to the alignment position, the mutual flux will be increased, resulting in the electromagnetic energy input from the electrical sources expressed by:

$$dW_{em} = i_1 d(L_{11} i_1 + M i_2) + i_2 d(L_{22} i_2 + M i_1)$$

or

$$dW_{em} = L_{11}i_1di_1 + M(i_1di_2 + i_2di_1) + L_{22}i_2di_2 + \\ + i_1^2 dL_{11} + i_2^2 dL_{22} + 2i_1i_2dM \qquad (1.4)$$

which must satisfy the equation

$$dW_{em} = dW_{mag} + dW_{mech} \qquad (1.5)$$

Hence, according to Eq. (1.5), subtracting Eq. (1.3) from Eq. (1.4) the differential mechanical output becomes

$$dW_{mech} = \frac{1}{2} i_1^2 dL_{11} + \frac{1}{2} i_2^2 dL_{22} + i_1i_2dM \qquad (1.6)$$

and the electromagnetic torque or developed torque is

$$T_{em} = \frac{dW_{mech}}{d\theta} = \frac{1}{2} i_1^2 \frac{dL_{11}}{d\theta} + \frac{1}{2} i_2^2 \frac{dL_{22}}{d\theta} + i_1i_2 \frac{dM}{d\theta} \qquad (1.7)$$

The torque developed in a rotary machine having m-coupled circuits may be expressed as:

$$T_{em} = \sum_{j=1}^{m} \sum_{k=1}^{m} \frac{1}{2} i_j i_k \frac{dL_{jk}}{d\theta} \qquad (1.8)$$

Similarly, the electromagnetic force for a linear displacement x in the corresponding linear device is

$$F_{em} = \sum_{j=1}^{m} \sum_{k=1}^{m} \frac{1}{2} i_j i_k \frac{dL_{jk}}{dx} \qquad (1.9)$$

Comparison of Eq. (1.3) and Eq. (1.4) shows that, if the currents in the coils are kept constant, the input of electrical energy is equally

divided, half going out in the form of mechanical work and half going into the magnetic field store. However, this equal division is only true for linear magnetic circuits and does not apply when saturation is present [7].

1.2.1 - Particular cases

As can be seen from Eq. (1.7), the total developed torque of a doubly excited rotary electromagnet has three components. The first two components depend on the current in the coil with rotor position. The third component depends on the rate of change of mutual inductance and both currents. In order to analyse each component, four possible combinations of rotor and stator members of both salient and cylindrical forms are now considered.

a) - Reluctance torque

When only the stator winding is excited ($i_2 = 0$) and, in addition, one (or both) of the members is of the salient type as shown in fig. 1.2(a), Eq. (1.7) reduces to

$$T_{em} = T_{R1} = \frac{1}{2} i_1^2 \frac{dL_{11}}{d\theta} \tag{1.10}$$

Similarly, if only the rotor winding is excited ($i_1 = 0$), as shown in fig. 1.2(b), is:

$$T_{em} = T_{R2} = \frac{1}{2} i_2^2 \frac{dL_{22}}{d\theta} \tag{1.11}$$

Both Eq. (1.10) and Eq. (1.11) have the general form

$$T_R = \frac{1}{2} i^2 . \frac{dL(\theta)}{d\theta} \tag{1.12}$$

Since $L(\theta) = n^2/R(\theta)$, where n is the number of coil turns and $R(\theta)$ the magnetic circuit reluctance for the rotor position θ, Eq. (1.12) becomes

$$T_R = -\frac{1}{2}\left(\frac{ni}{R}\right)^2 \frac{dR(\theta)}{d\theta} = -\frac{1}{2}\phi^2 \frac{dR(\theta)}{d\theta} \qquad (1.13)$$

where ϕ is the flux in the magnetic circuit considered.

Eq. (1.13) shows that, if saliency exists, there is torque developed with only one member excited. This is called "reluctance torque",

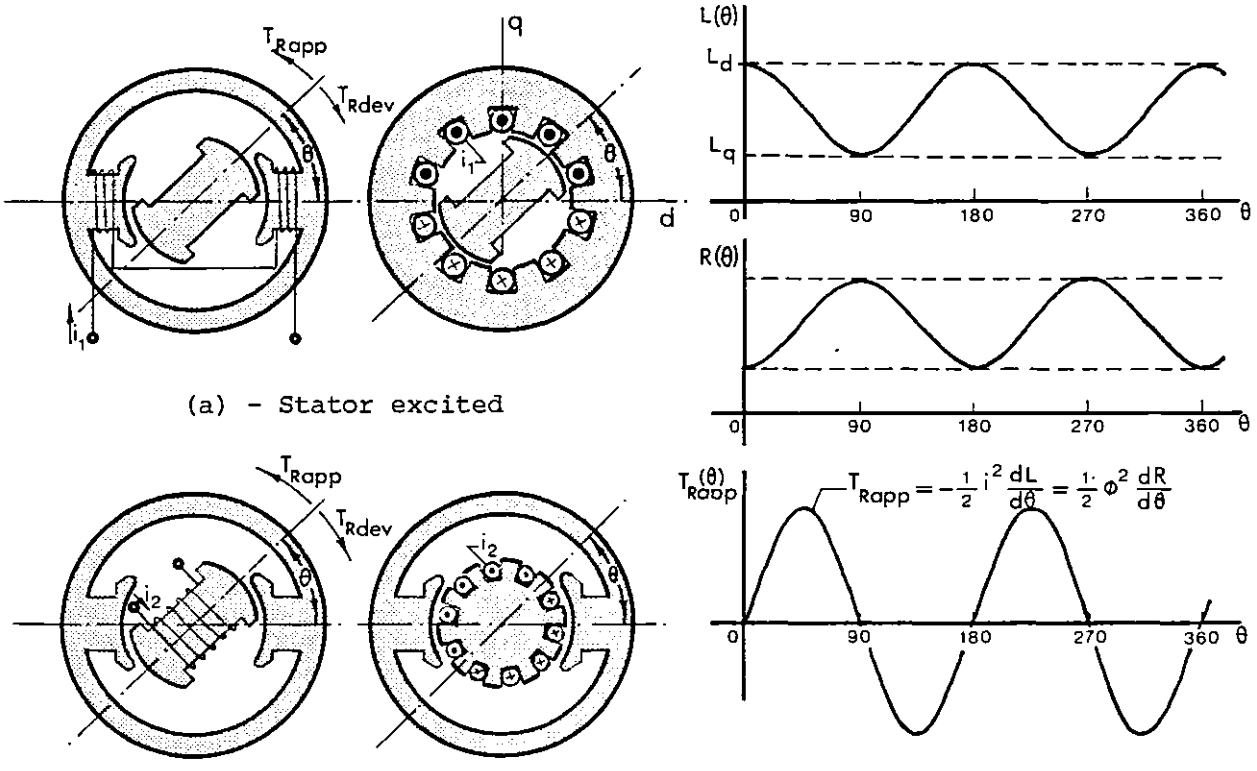

(a) - Stator excited

(b) - Rotor excited

(c) - Variation of inductance, reluctance and reluctance torque

Fig. 1.2 - Single excited rotating electromagnet

because of its origin in the reluctance variation of the magnetic circuit with rotor position. The applied reluctance torque variation versus rotor position is represented in fig. 1.2(c), which shows two complete

cycles per revolution of the rotor. If a sinusoidal variation for $L(\theta)$ is assumed, then peak reluctance torque is achieved for odd multiples of 45°E.

b) - Excitation torque

When both rotor and stator are of the cylindrical type as shown in fig. 1.3(a), the self-inductance of both windings is constant for any rotor position. Therefore, the reluctance torque will be constantly

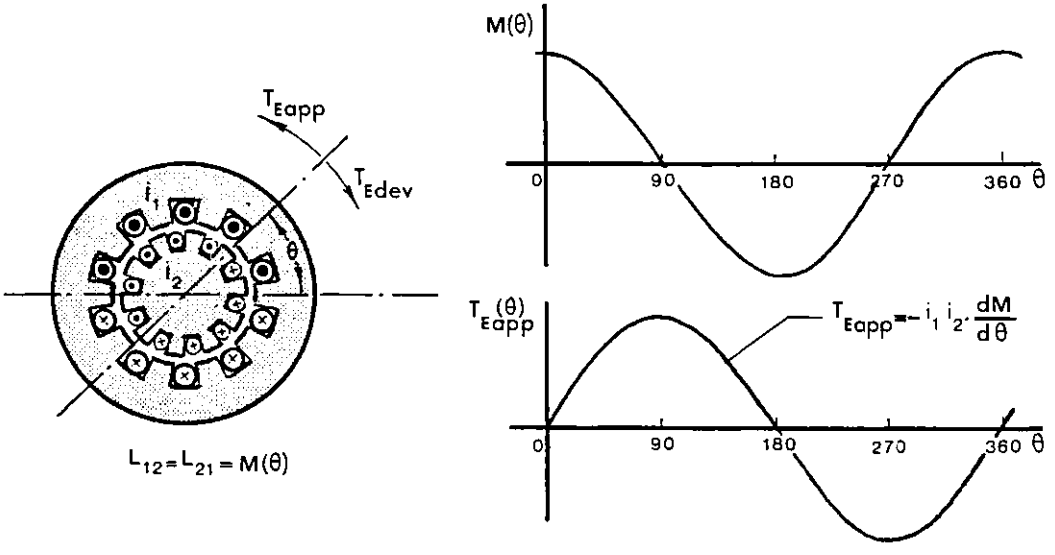

(a) - Cylindrical electromagnet (b) - Excitation torque variation

Fig. 1.3 - Double excited cylindrical electromagnet

zero. However, the mutual inductance will now vary in one complete cycle per revolution of the rotor. With both members excited, Eq. (1.7) then reduces to

$$T_{em} = T_E = i_1 i_2 \cdot \frac{dM}{d\theta} \qquad (1.14)$$

The torque considered, which is the result of exciting both windings, is called "excitation torque" T_E, and its variation versus rotor position is shown in fig. 1.3(b). The angle between the magnetic axes of the members will be designated by "torque angle" θ.

c) - Total torque

When one (or both) of the members is of the salient type and if both members are excited as shown in fig. 1.4(a) then, by superposition, the resulting torque is given by the summation of excitation torque and reluctance torque(s). The total torque/torque angle characteristic

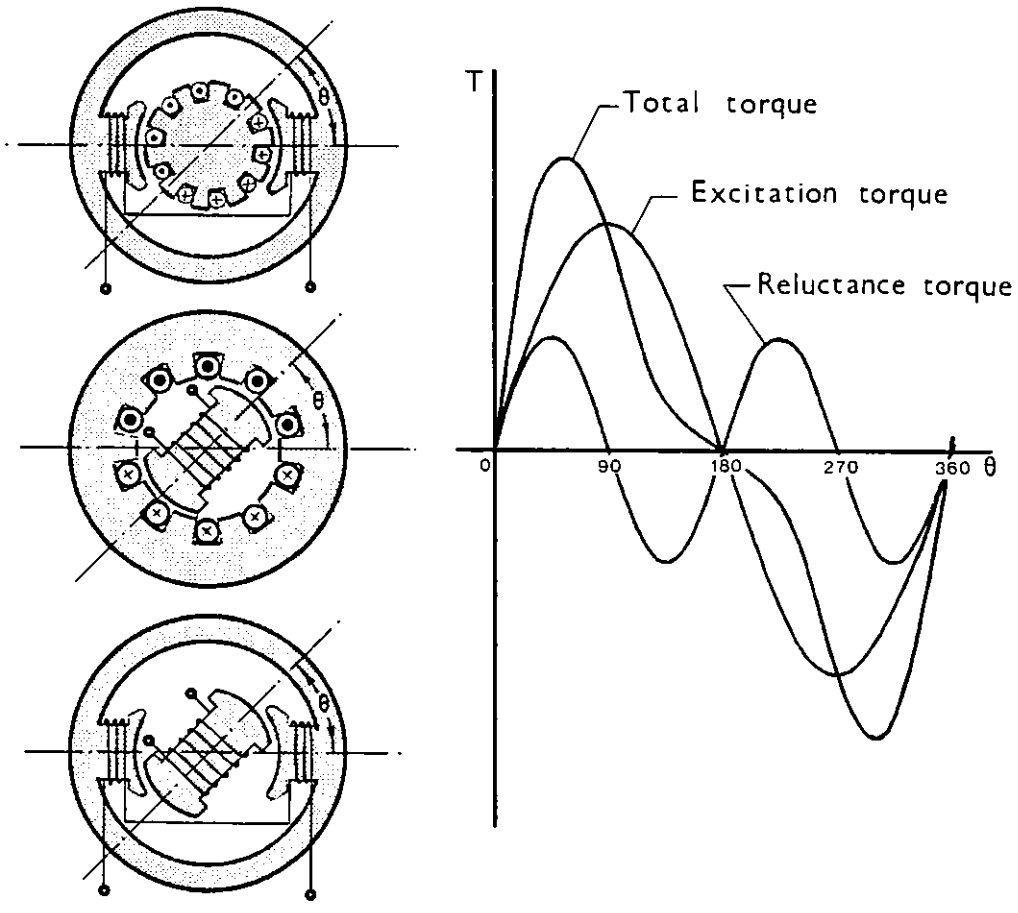

(a) - Double excited electromagnets (b) - Torque components

Fig. 1.4 - Total torque variation of doubly excited saliency electromagnets

rises more quickly and reaches a peak at a smaller torque angle than if no reluctance torque component is present, as shown in fig. 1.4(b).

However, it should be noted that for 90°E torque angle only excitation torque exists.

1.3 - MAGNETIC AND ELECTROMAGNETIC MACHINES

The force (or torque) in an electrical machine may be due to an "electromagnetic" or a "magnetic" effect or simultaneously to both effects. Electric machines may hence be classified as primarily "electromagnetic" or "magnetic" machines [8].

1.3.1 - Electromagnetic machines

In an electromagnetic machine the torque (or force) $T = i_1 i_2 \, dM/d\theta$ results from the interaction between two electric circuits carrying the current i_1 and i_2. For a system with linear motion, as shown in fig. 1.5, Eq. (1.14) reduces to

$$F_{em} = i_2 \cdot \frac{d\phi_{12}(x)}{dx} \tag{1.15}$$

where $\phi_{12}(x) = i_1 M(x)$ is the flux linked with the circuit 2 produced by the current i_1. With the direction for currents shown in the diagram

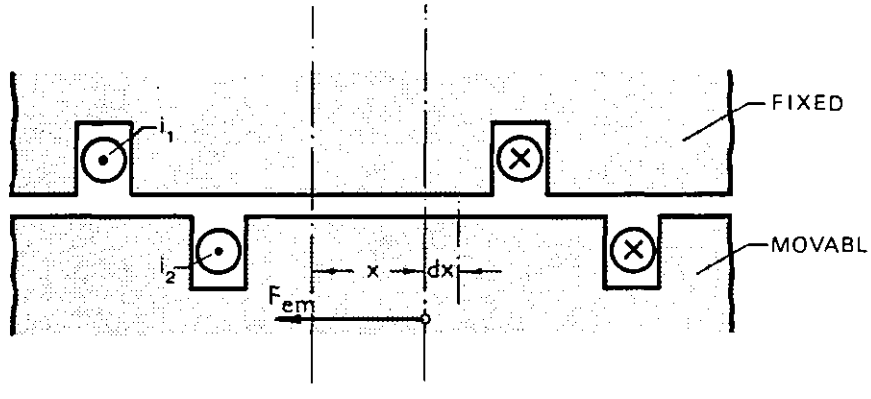

Fig. 1.5 - Electromagnetic force

the direction of force is such that it tends to decrease x, i.e. the system tends to a position of maximum magnetic energy.

In a real machine the winding is distributed over several slots, as shown in fig. 1.6. If $A = \Sigma ni$ is the ampère-conductors per unit tangential length of the air gap surface, often referred to as the "electric loading", then the force per unit area of stator surface may be derived

from Eq. (1.15) as

$$F_u = AB \quad N/m^2 \tag{1.16}$$

where B is the normal component of flux density produced by the primary

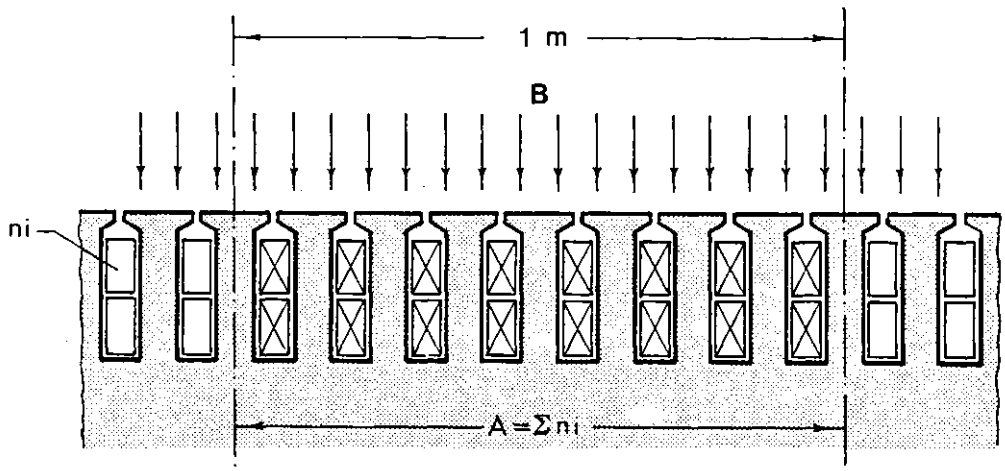

Fig. 1.6 - Definition of electric loading

member. Electrical machines such as synchronous, induction and d.c. motors which use this effect to produce force, may be called "electromagnetic machines".

1.3.2 - Magnetic machines

Not all electrical machines however are seen to have such interlinking circuits as the electromagnetic machines. Force may be also obtained using directly the air gap flux produced by one member interacting with the ferromagnetic material of the other member. Such machines may be called "magnetic machines" and they include reluctance motors, hysteresis motors and relay-type electromagnets.

In the relay electromagnet shown in fig. 1.7, the reluctance of the air gap is $R = x/\mu_o S$ and neglecting the reluctance of the iron circuit, the magnetic force becomes

$$F_R = -\frac{1}{2}\phi^2 \cdot \frac{dR}{dx} = -\frac{B^2}{2\mu_o} \cdot S$$

where the (-) sign indicates that the force decreases as x increases. Hence, the magnetic force per unit area is

$$F_{mag} = \frac{F_R}{S} = \frac{B^2}{2\mu_o} = \frac{1}{2}BH \quad N/m^2 \tag{1.17}$$

rather than AB, and it is equal to the magnetic energy stored per unit volume of the air gap.

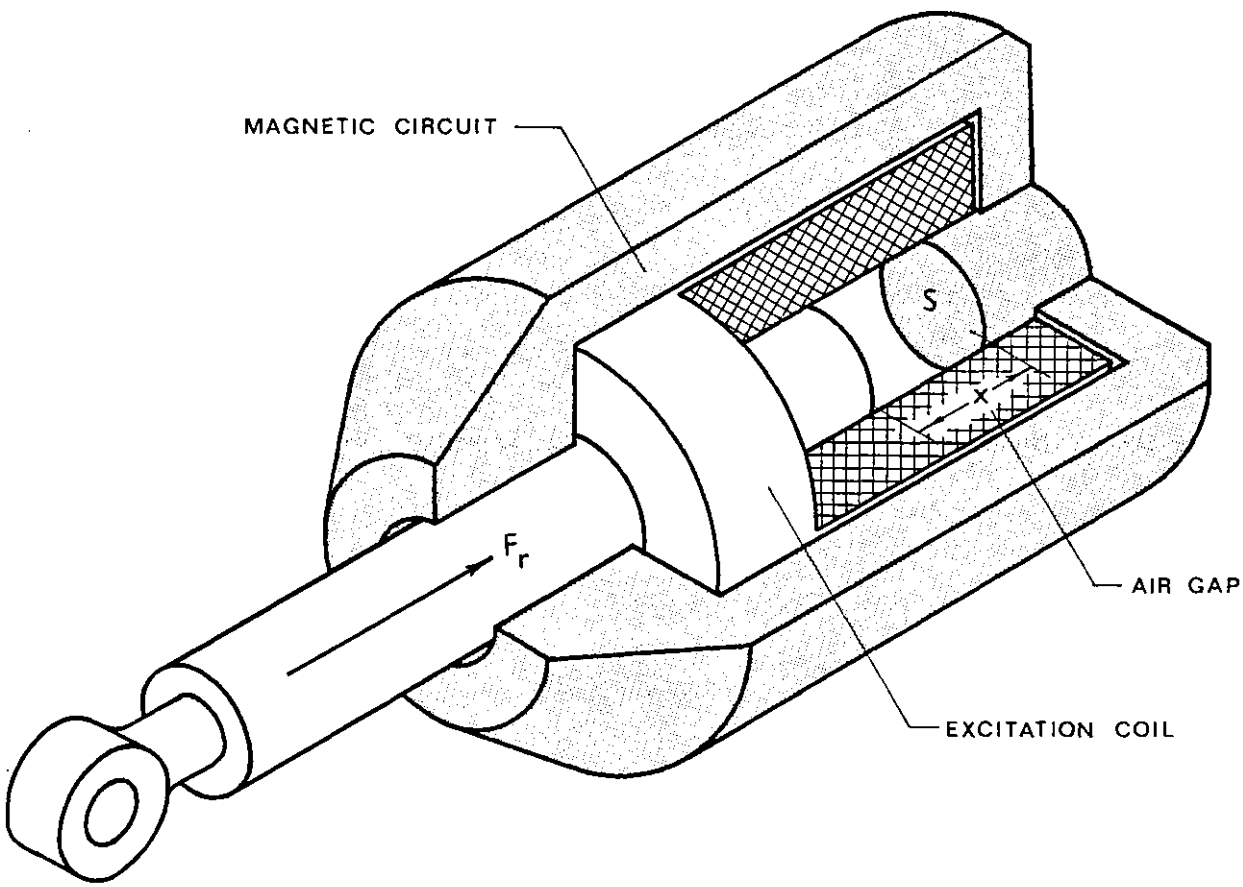

Fig. 1.7 - Relay electromagnet

It is interesting to compare the practical maximum force values per unit area for electromagnetic and magnetic machines. A rotary electromagnetic machine can ususally be designed with a maximum value of electric loading about 30 x 10^3 A/m and due to the magnetic circuit saturation with an air gap flux density of 1.0 T. Hence, Eq. (1.16) becomes

$$F_u = AB = 30 \times 10^3 \quad N/m^2 \tag{1.18}$$

while for the magnetic pull Eq. (1.17) gives:

$$F_{mag} = \frac{B^2}{2\mu_o} = \frac{10^7}{8\pi} \simeq 400 \times 10^3 \quad N/m^2$$

Thus the radial magnetic pull of a conventional rotary machine is seen to be an order of 13 times the useful or tangential force. Unfortunately, for a conventional rotary magnetic machine, the tangential useful component of a distorted air gap flux is only a fraction of the magnetic pull, giving a value to the same order as that of the tangential force of an electromagnetic machine.

In a reluctance motor, the inductance is a function of the angular position of the rotor and assuming sinusoidal variation it may by described by

$$L(\theta) = \frac{1}{2}(L_d + L_q) + \frac{1}{2}(L_d - L_q)\cos 2\theta \qquad (1.19)$$

as illustrated graphically in fig. 1.2(c). Substitution of Eq. (1.19) into Eq. (1.12) gives the reluctance torque as

$$T_R = \frac{1}{2} I^2(L_q - L_d)\sin 2\theta \qquad (1.20)$$

and the maximum possible torque, with a torque angle of 45°E, would be

$$\hat{T}_R = \frac{1}{2} I^2(L_q - L_d) \qquad (1.21)$$

For maximum torque, $(L_q - L_d)$ should thus be made as high as possible. For an n_p pole machine with a stator inside diameter D_g and axial length ℓ, the difference between the inductances becomes

$$L_q - L_d = n^2 n_p \mu_o \frac{\pi D_g \ell}{n_p}\left(\frac{1}{g_{max}} - \frac{1}{g_{min}}\right) = n^2 \mu_o D_g \left(\frac{K_1}{D_g} - \frac{K_2}{D_g}\right)\ell = K\ell \qquad (1.22)$$

where K_1, K_2 and K are constants. Therefore, from Eq. (1.21) and Eq. (1.22) the specific tangential force

$$F_u = \frac{\hat{T}_R}{\pi D_g \ell \frac{D_g}{2}} = \pi K \left(\frac{I}{\pi D_g}\right)^2$$

and from the definition for electric loading

$$F_u = \pi K A^2 \tag{1.23}$$

The flux density on the d-axis is

$$B_d = n_p \frac{\phi_d}{\pi D_g \ell} = n_p \frac{L_d I}{\pi D_g \ell} = n_p K_2 A$$

Hence, for a magnetic machine of given pole number, the electric loading is limited by the B_d value. For a fixed B_d, Eq. (1.23) reduces to

$$F_u = \text{Const.} \tag{1.24}$$

As will be shown later, this result contrasts with the specific tangential force obtained for an electromagnetic machine which tends to increase with $\sqrt{D_g}$.

1.4 - ELECTRICAL MACHINES TOPOLOGY

When electrical machines are seen from a topological point of view, a large number of possible shapes exist such as planar, cylindrical, disc, tubular, spherical, conical, helicoidal, etc. It is well known that in an electrical machine, the electric and magnetic circuits must both be linked. A planar type is shown in fig. 1.8(a). If three planes α, β, γ intersecting mutually at right angles are considered, the magnetic circuit

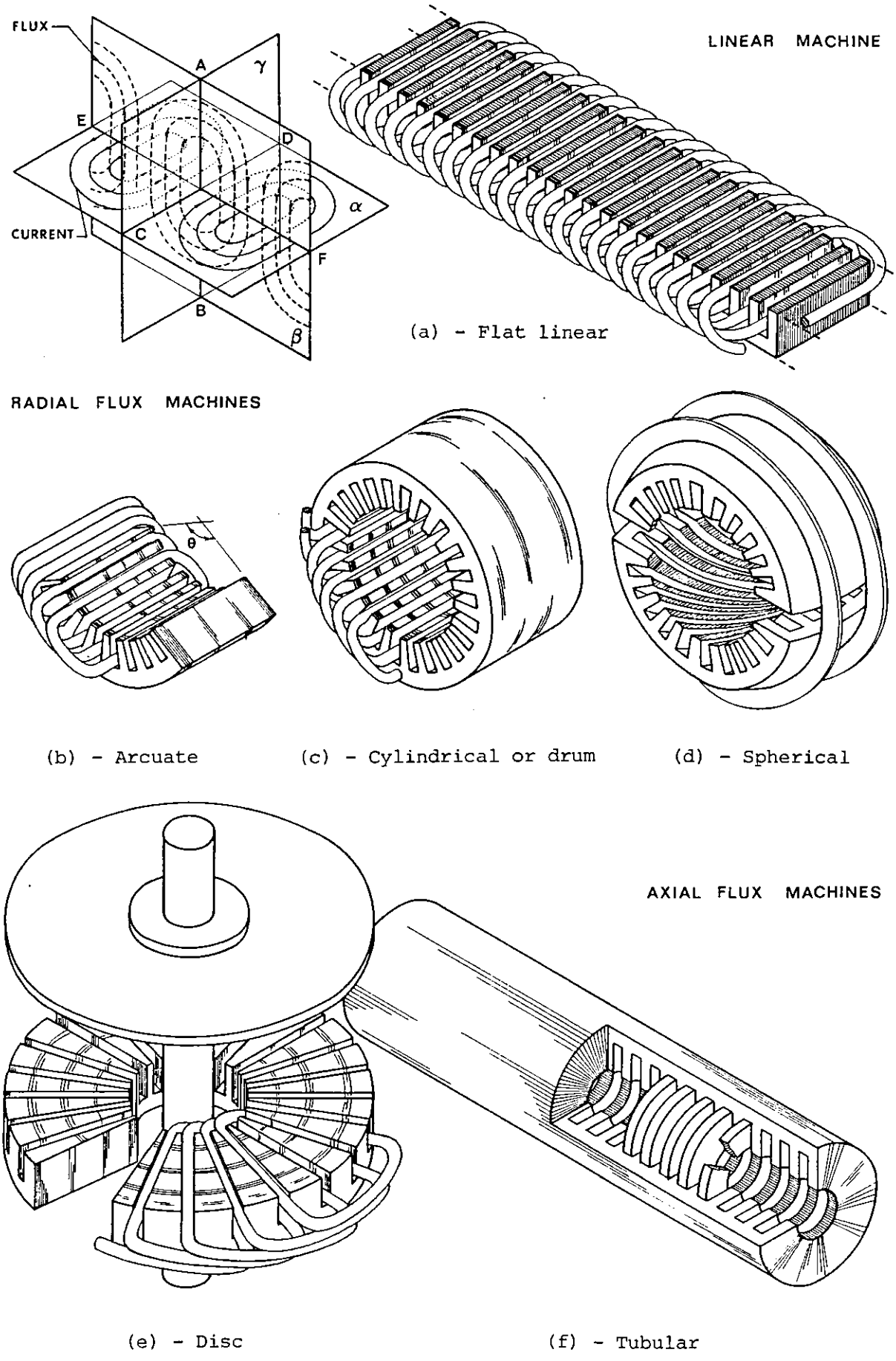

Fig. 1.8 - Electrical machine configurations

lies in the β plane while the electric circuits lie fundamentally in the α plane [9]. Electromagnetic action takes place between the flux components parallel to AB and current components parallel to CD, resulting in a direction of force parallel to EF. All machine configurations can, if desired, be derived from the planar or flat linear type.

The arcuate type shown in fig. 1.8(b) can be obtained by rolling the plane α along the line EF through an angle θ. If $\theta = 2\pi$ a cylindrical or drum type machine (c) is obtained. In addition, by turning the plane γ through a small angle δ, a skewed stator results. The spherical version (d) is achieved by rolling the last type along the line CD [8]. These three configurations are classified as radial flux machines, because of the radial direction of the main components of flux.

The disc type (e) is obtained by rolling the plane β along the line EF and the tubular machine by rolling the plane α along the line CD. Again, skewing can be obtained by acting in plane γ, and the tubular type resulting in a helicoidal machine. Both disc and tubular configurations are designated as axial flux machines.

This thesis is essentially devoted to certain machines having arcuate, disc and cylindrical configurations and most of the machines considered are two phase-wound.

1.5 - TORQUE EXPRESSION FOR A TWO PHASE MULTI-POLE SYNCHRONOUS MOTOR

A general expression for the torque of an electric machine, valid under both transient and steady-state conditions, may be derived from energy considerations. Combination of Eq. (1.1) and Eq. (1.8) gives

$$T_{em} = \frac{\partial W_{mag}}{\partial \theta}\bigg|_{\text{all currents constant}} \tag{1.25}$$

which means that the torque acting on the rotor is equal to the rate of

change, with respect to rotor position $\theta = \omega t$, of the total stored magnetic energy in the machine.

The energy stored in the magnetic field of a magnetically-linear two-phase cylindrical rotor synchronous motor shown in fig. 1.9(a) is from Eq. (1.1) given by:

$$W_{mag} = \frac{1}{2} L_{aa} i_a^2 + \frac{1}{2} L_{bb} i_b^2 + L_{ab} i_a i_b + i_f L_{af} i_a + i_f L_{bf} i_b + \frac{1}{2} L_{ff} i_f^2$$

The inductances $L_{aa} = L_{bb}$ and L_{ff} can be taken independently of angular position in a cylindrical rotor machine and therefore constant.

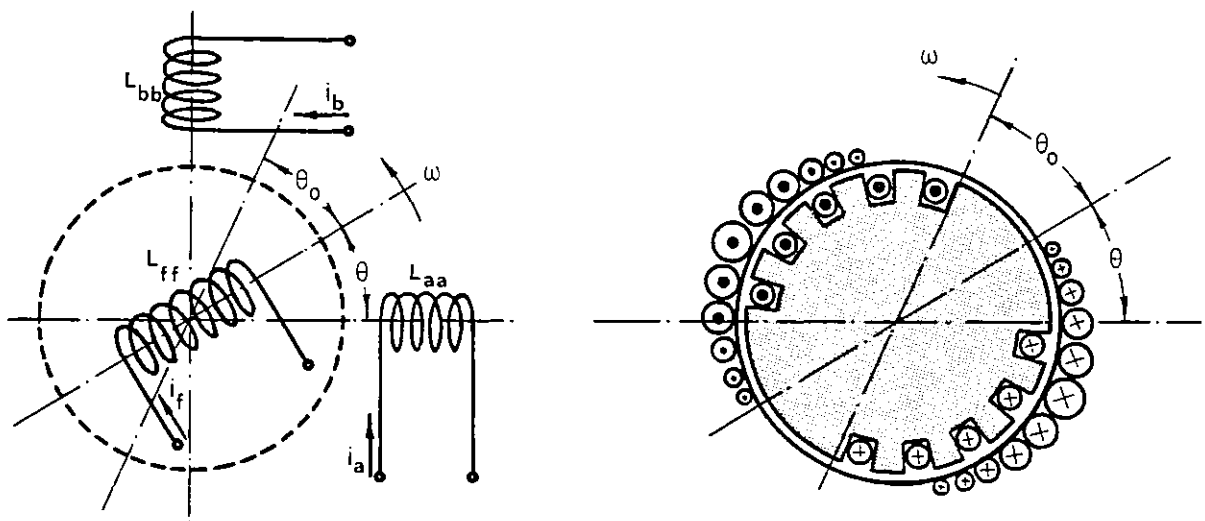

(a) - Schematic diagram

(b) - Space m.m.f. distribution

Fig. 1.9 - Two-phase cylindrical rotor synchronous motor

In addition for a two-phase winding $L_{ab} = 0$. Hence, for a two-pole machine

$$T_{em} = \frac{\partial W_{mag}}{\partial \theta} = i_f \left[i_a \frac{dL_{af}}{d\theta} + i_b \frac{dL_{bf}}{d\theta} \right] \tag{1.26}$$

If the mutual inductances are assumed to vary sinusoidally:

$$\begin{aligned} L_{af} &= L_{afm} \cos \theta \\ L_{bf} &= L_{afm} \sin \theta \end{aligned} \tag{1.27}$$

and if the phase currents are sinusoidal and balanced such that

$$\begin{aligned} i_a &= \hat{I} \cos(\theta + \theta_o) \\ i_b &= \hat{I} \sin(\theta + \theta_o) \end{aligned} \tag{1.28}$$

a space m.m.f. distribution is produced along the air gap whose axis is displaced from an angle θ_o relative to the rotor's magnetic axis, as shown in fig. 1.9(b). For a machine with n_p poles, substitution of Eqs. (1.27) and (1.28) into Eq. (1.26) gives the excitation torque as:

$$T = \frac{n_p}{2} \cdot i_f L_{afm} \hat{I} \sin \theta_o \tag{1.29}$$

Eq. (1.29) shows that for a constant field current i_f and constant balanced two-phase stator current, the instantaneous torque is constant and a function of torque angle θ_o.

Another method which may be used to calculate the machine torque for a general field flux distribution and stator current waveform in terms of the machine's physical dimensions is now presented. The interaction between the air gap field flux density distribution $B(\theta, t)$ and the stator current space distribution $\mathcal{J}(\theta, t)$ is considered.

Fig. 1.10 shows a salient multi-pole synchronous motor operating at 90°E torque angle. Under this condition, the fundamental space current distribution and excitation air gap flux density are in phase and so the reluctance torque component is absent. If ℓ represents the effective air gap axial length, the elementary force on the rotor at the air gap is, according to Eq. (1.16), given by:

$$dF = B(\theta, t).\mathcal{J}(\theta, t)\ell \, d\theta$$

With n_p poles, the total excitation torque developed becomes

$$T = n_p R_g \ell \cdot \int_0^{\pi} B(\theta, t) \mathcal{J}(\theta, t)\, d\theta \qquad (1.30)$$

where R_g is the stator inside radius.

In a synchronous motor ideally both $B(\theta, t)$ and $\mathcal{J}(\theta, t)$, have a time invariant shape and rotate at synchronous speed ω around the air gap in the same direction.

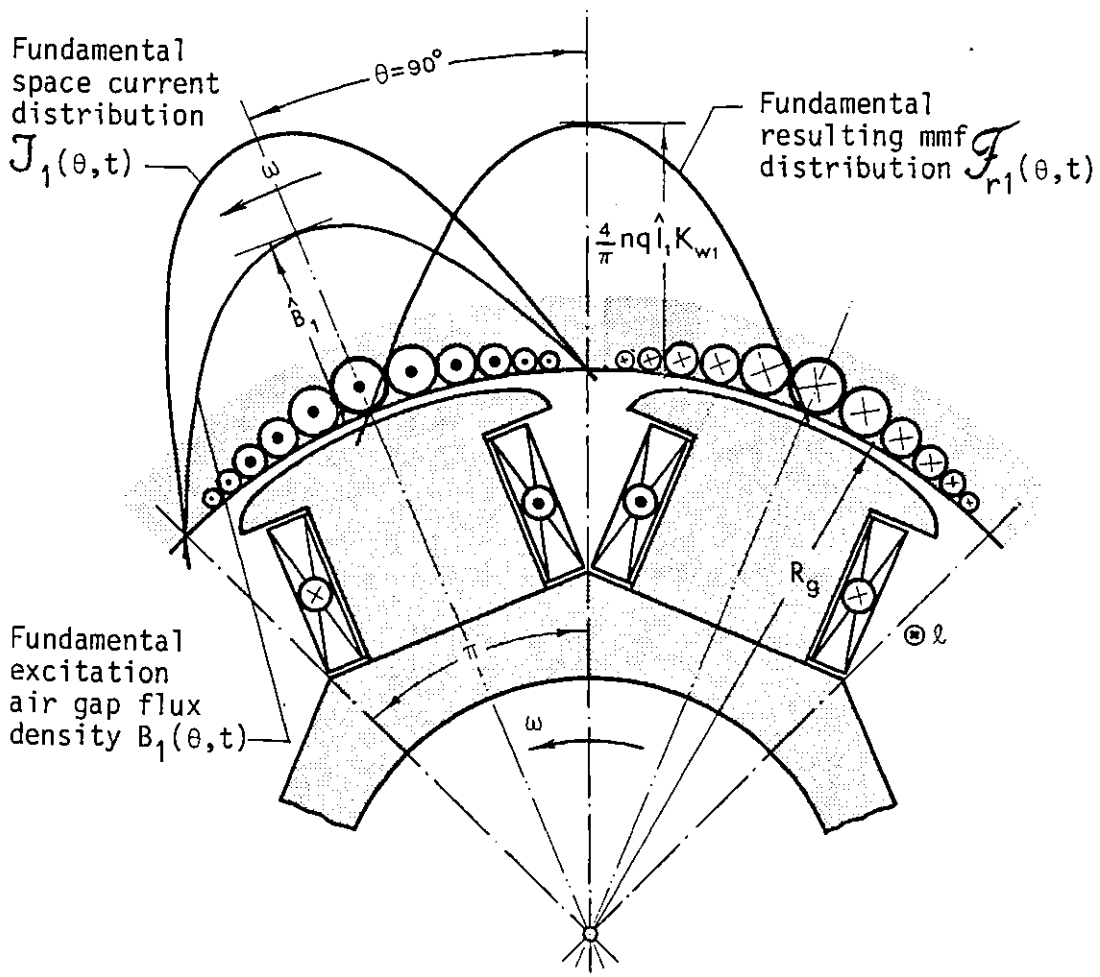

Fig. 1.10 - Torque acting on a multi-pole rotor

In general however the waveform $B(\theta, t)$ is non-sinusoidal and may be represented by the series:

$$B(\theta, t) = \hat{B}_1 \sin(\omega t - \theta) + \hat{B}_3 \sin 3(\omega t - \theta) + \ldots + \hat{B}_h \sin h(\omega t - \theta) + \ldots$$

$$= \hat{B}_1 \cdot \sum_{h=1}^{2n+1} K_{Bh} \sin h(\omega t - \theta) \qquad (1.31)$$

where

$$K_{Bh} = \frac{\hat{B}_h}{\hat{B}_1} \tag{1.32}$$

are the excitation field harmonic factors, usually much less than unity.

The space current distribution $\mathcal{J}(\theta, t)$ is by definition

$$\mathcal{J}(\theta, t) = \frac{\partial \mathcal{F}_r(\theta, t)}{\partial \theta} \tag{1.33}$$

where $\mathcal{F}_r(\theta, t)$ is the resultant rotating m.m.f., which waveform depends on the stator winding arrangement and current waveform. As is well known in a practical winding arrangement the harmonics in the m.m.f. wave are supressed by using q coils/pole/phase distributed over q slots/pole/phase with a slot pitch angle α, as shown in fig. 1.11(a). The pitch of each

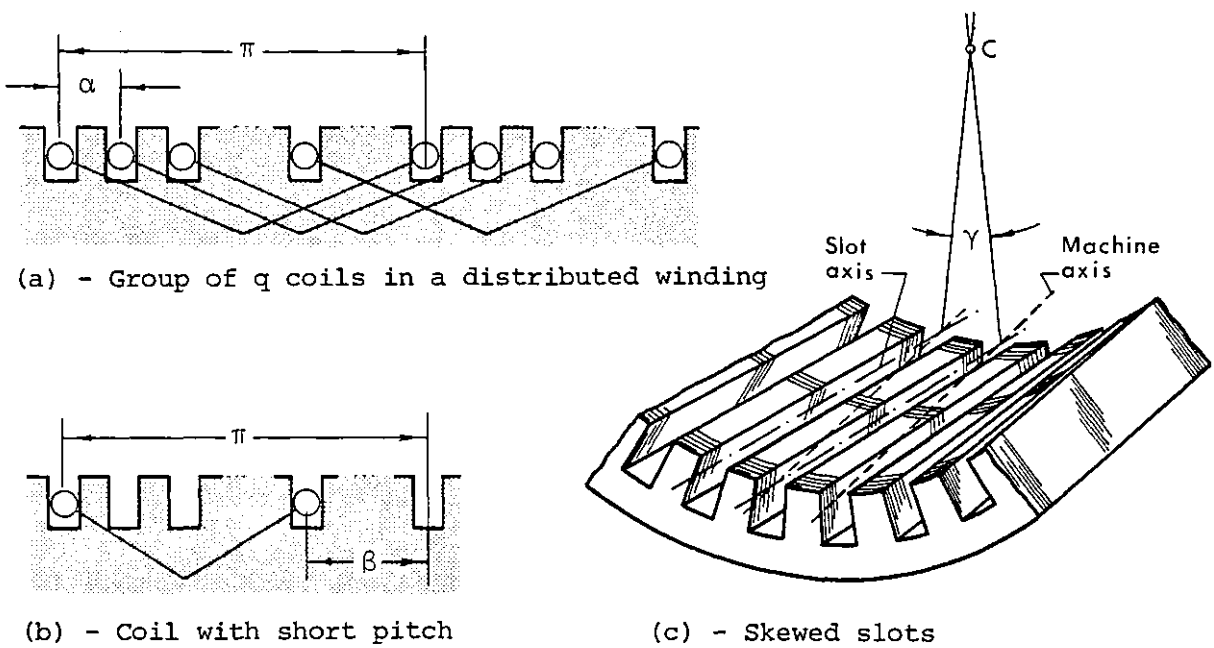

Fig. 1.11 - Practical winding arrangement in an a.c. machine

coil is usually less than a pole pitch, in which case it is described as short-pitched or chorded by an angle β, as shown in fig. 1.11(b). The slots also distort the m.m.f. waveform by creating so-called tooth ripples,

which may be eliminated by skewing the slots of an appropriate centre skew angle γ, as shown in fig. 1.11(c).

Such arrangements respectively introduce a factor for the h^{th} harmonic on the m.m.f. wave [10] given by:

$$K_{dh} = \frac{\sin(q\frac{h\alpha}{2})}{q\sin(\frac{h\alpha}{2})} \quad , \quad K_{ph} = \cos(h\frac{\beta}{2}) \quad , \quad K_{skh} = \frac{\sin(h\frac{\gamma}{2})}{h\frac{\gamma}{2}} \qquad (1.34)$$

called distribution, pitch and skew factor. When all the arrangements are simultaneously present, the h^{th} harmonic amplitude on the m.m.f. wave must be multiplied by

$$K_{wh} = K_{dh}K_{ph}K_{skh} \qquad (1.35)$$

where K_{wh} is the harmonic winding factor.

The various coil groups of a phase may be connected in series, in parallel, or, in series-parallel, depending on the number of poles and the general winding arrangement. If the q coils/pole/phase are all in series carrying the current i arranged in a two-phase double-layer winding, as shown in fig. 1.12, the m.m.f. per phase can be represented [11] by the Fourier series

$$F = \frac{4}{\pi}nqi\,(K_{w1}\sin\theta + \frac{K_{w3}}{3}\sin 3\theta + \ldots + \frac{K_{wh}}{h}\sin h\theta + \ldots)$$

$$= \frac{4}{\pi}nqi\sum_{h=1}^{2n+1}\sin h\theta \qquad (1.36)$$

where n is the number of turns of each coil. Considering for generality the current i non-sinusoidal

$$i = \hat{I}_1\sum_{s=1}^{2n+1}K_{Is}\sin s\omega t \qquad (1.37)$$

where

$$K_{Is} = \frac{\hat{I}_s}{\hat{I}_1} < 1 \qquad (1.38)$$

are the stator current harmonic factors, then Eq. (1.36) takes the form

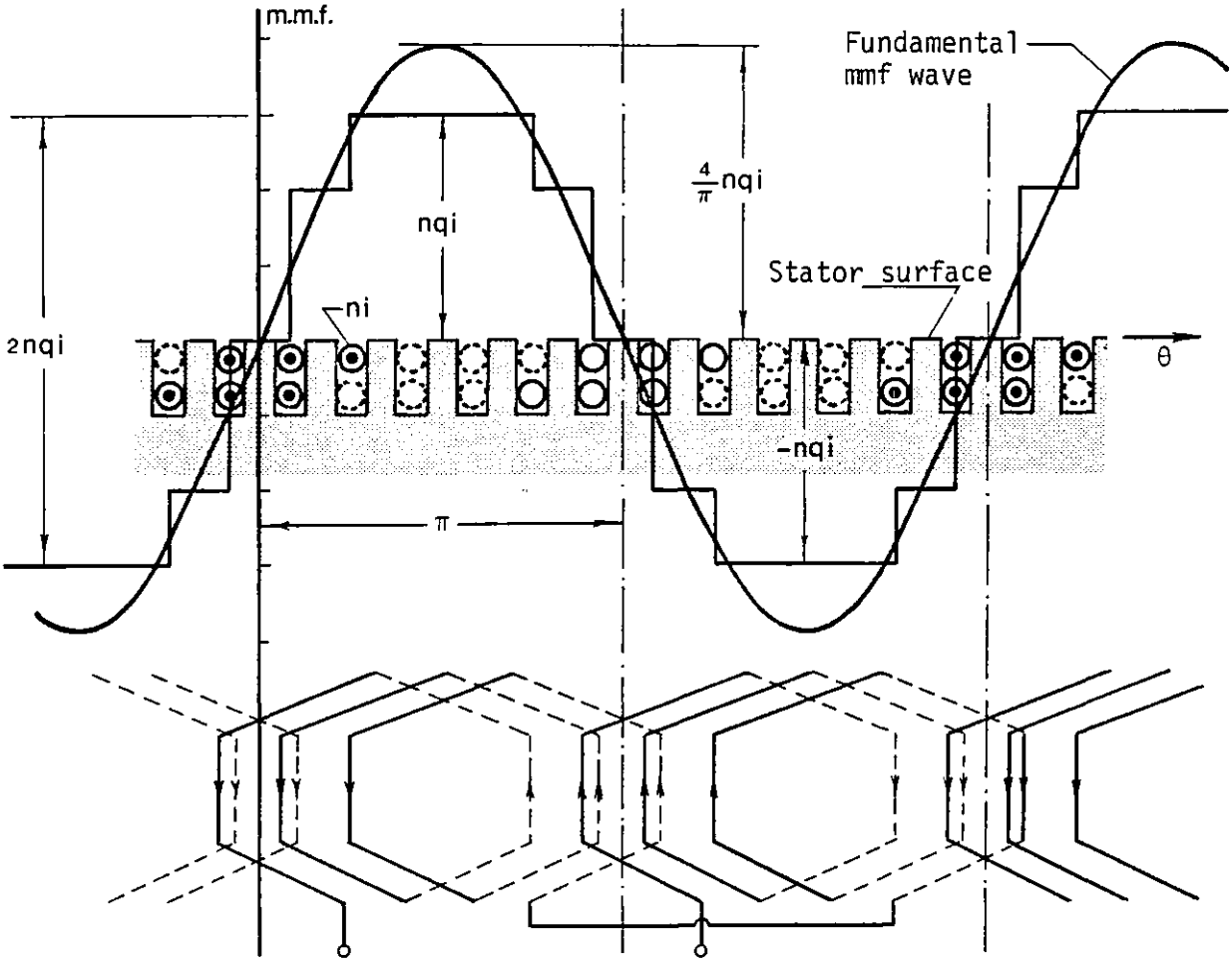

Fig. 1.12 - M.m.f. distribution of one phase of a two-phase double-layer winding with q = 3 coils/pole/phase

$$F = \frac{4}{\pi} nq\hat{I}_1 \sum_{h,s=1}^{2n+1} K_{Is} \sin s\omega t \frac{K_{wh}}{h} \sin h\theta \qquad (1.39)$$

which is a pulsating stationary wave.

For a two-phase winding the current harmonic s gives for each phase

$$s,hF_a = A_{h,s} \sin s\omega t \sin h\theta$$

$$s,hF_b = A_{h,s} \sin s(\omega t - \tfrac{\pi}{2}) \sin h(\theta - \tfrac{\pi}{2})$$

where

$$A_{h,s} = \frac{4}{\pi} nq\hat{I}_1 K_{Is} \frac{K_{wh}}{h} \tag{1.40}$$

Since h and s are odd, the resulting m.m.f. for any space harmonic h produced by a time harmonic s will be

$$s,h\mathcal{F}_r = s,hF_a + s,hF_b$$

$$= \frac{1}{2} A_{h,s}\left[(1+\cos(s-h)\tfrac{\pi}{2}) \cos(s\omega t-h\theta)-(1+\cos(s+h)\tfrac{\pi}{2}) \cos(s\omega t+h\theta)\right] \tag{1.41}$$

When s = h, Eq. (1.41) reduces to

$$h,h\mathcal{F}_r = A_{h,h} \cos h(\omega t - \theta) \tag{1.42}$$

which is a rotating wave of constant magnitude with an angular speed ω in anti-clockwise direction relative to the stator.

When $s \neq h$, a rotating wave is also obtained as

$$s,h\mathcal{F}_r = \mp A_{h,s} \cos(s\omega t \pm \theta) \tag{1.43}$$

but with an angular speed $\omega_{h,s} = \pm \frac{s}{h}\omega$ relative to the stator. The negative sign indicates that the respective wave is travelling in clockwise direction. Hence, for a two-phase synchronous machine there are all odd space harmonics associated with all current harmonics. Only the harmonics which satisfy the condition s = h are stationary relative to the rotor. Harmonics for $s \neq h$ rotate with an angular speed $(1 \pm \frac{s}{h})\omega$

relative to the rotor. However, these harmonics are attenuated in practice if the machine is provided with a damper winding or if the stator winding is designed to minimise $A_{h,s}$.

Adding all rotating waves of the type of Eq. (1.42) and Eq. (1.43), the total m.m.f. rotating wave is

$$\mathcal{F}_r(\theta,t)=\sum_{s,h=1}^{2n+1} {}_{s,h}\mathcal{F}_r = A_{11}\cos(\omega t-\theta)-A_{31}\cos(\omega t+3\theta)+A_{51}\cos(\omega t-5\theta)- \ldots$$
$$- A_{13}\cos(3\omega t+\theta)+A_{33}\cos(3\omega t-3\theta)-A_{53}\cos(3\omega t+5\theta)+ \ldots$$
$$+ A_{15}\cos(5\omega t-\theta)-A_{35}\cos(5\omega t+3\theta)+A_{55}\cos(5\omega t-5\theta)- \ldots$$

Alternatively, from Eq. (1.40) and Eq. (1.38), the resultant m.m.f. expression for a two-phase machine becomes:

$$\mathcal{F}_r(\theta,t) = \frac{4}{\pi} nq\hat{I}_1 \left[K_{W1}\cos(\omega t-\theta) - \frac{K_{W3}}{3}\cos(\omega t+3\theta) + \frac{K_{W5}}{5}\cos(\omega t-5\theta)- \ldots \right.$$
$$-K_{I3}K_{W1}\cos(3\omega t+\theta) + K_{I3}\frac{K_{W3}}{3}\cos(3\omega t-3\theta) - K_{I3}\frac{K_{W5}}{5}\cos(3\omega t+5\theta)+ \ldots$$
$$\left. +K_{I5}K_{WI}\cos(5\omega t-\theta) - K_{I5}\frac{K_{W3}}{3}\cos(5\omega t+3\theta) + K_{I5}\frac{K_{W5}}{5}\cos(5\omega t-5\theta)- \ldots \right]$$

From Eq. (1.33), the stator current distribution $\mathcal{J}(\theta, t)$ correspondent to this rotating m.m.f. is given by

$$\mathcal{J}(\theta,t) = \frac{4}{\pi} nq\hat{I}_1 \left[K_{W1}\sin(\omega t-\theta) + K_{W3}\sin(\omega t+3\theta) + K_{W5}\sin(\omega t-5\theta+ \ldots \right.$$
$$+K_{I3}K_{W1}\sin(3\omega t+\theta) + K_{I3}K_{W3}\sin(3\omega t-3\theta) + K_{I3}K_{W5}\sin(3\omega+5\theta)+ \ldots$$
$$\left. +K_{I5}K_{W1}\sin(5\omega t-\theta) + K_{I5}K_{W3}\sin(5\omega t+3\theta) + K_{I5}K_{W5}\sin(5\omega t-5\theta)+ \ldots \right] \quad (1.44)$$

Since $B(\theta, t)$ is given by Eq. (1.31) and $\mathcal{J}(\theta, t)$ by Eq. 1.44 the integrand in Eq. (1.30) can be evaluated. After performing the product $B(\theta, t).\mathcal{J}(\theta, t)$ all the terms of the form $\cos(\pm \sigma\omega t \pm \upsilon\theta)$, where σ and

υ are even numbers, may be ignored because they integrate to zero over the interval $\theta = 0$ to $\theta = \pi$. Thus, including harmonics up to order 11, the expression for output torque [5] reduces to:

$$T = n_p R_g \ell \frac{4}{\pi} nq \hat{I}_1 \hat{B}_1 \frac{1}{2} \int_0^{\pi} \Big[K_{W1} + K_{B3}K_{I3}K_{W3} + K_{B5}K_{I5}K_{W5} + \cdots$$

$$+(K_{B5}K_{W5} + K_{I5}K_{W1} - K_{B3}K_{W3} - K_{I3}K_{W1} + K_{B3}K_{I7}K_{W3} + K_{B7}K_{I3}K_{W7} + \ldots)\cos 4\omega t +$$

$$+(K_{B9}K_{W9} + K_{I9}K_{W1} - K_{B7}K_{W7} - K_{I7}K_{W1} - K_{B3}K_{I5}K_{W3} + K_{B3}K_{I11}K_{W3} + \ldots)\cos 8\omega t + \ldots \Big] d\theta$$

If triple multiples are neglected, this equation becomes

$$T = T_1(1 + A \cos 4\omega t + B \cos 8\omega t + \ldots) \tag{1.45}$$

where

$$T_1 = n_p R_g \ell N \hat{I}_1 B_1 K_{W1} \tag{1.46}$$

is the fundamental excitation torque and

$$N = 2nq \tag{1.47}$$

is the total number of conductors per pole per phase.

Eq. (1.46) shows that for a constant field flux excitation and constant balanced two-phase stator current the fundamental excitation torque is constant. However, the total output torque includes ripple torques with frequencies which are integral multiples of four times fundamental frequency. For low speed servo applications this torque pulsation can be very undesirable. In Eq. (1.45) the per unit magnitude of the first two ripple torques is:

$$A = \frac{K_{B5}K_{W5}}{K_{W1}} + K_{I5} - \frac{K_{B3}K_{W3}}{K_{W1}} - K_{I3} \qquad (1.48)$$

$$B = \frac{K_{B9}K_{W9}}{K_{W1}} + K_{I9} - \frac{K_{B7}K_{W7}}{K_{W1}} - K_{I7} \qquad (1.49)$$

These equations show that for a sinusoidal input current ($K_{I3} = K_{I5} = \ldots = 0$) the output torque is free of ripple torque if the air gap field flux density is sinusoidal, as already shown in Eq. (1.29). If the air gap field flux density distribution is non-sinusoidal, ripple torque may be reduced to negligible values by controlling the winding factors such that $K_{B5}K_{W5} = K_{B3}K_{W3}$ and $K_{B9}K_{W9} = K_{B7}K_{W7}$. As seen in Eq. (1.35) the winding factor is restricted by stator slotting and therefore an air gap field flux density excitation with a near-sinusoidal distribution around the stator surface is most desirable if a ripple-free torque is to be obtained.

1.6 - POLE PROFILE FOR A SINUSOIDAL AIR GAP FLUX DENSITY DISTRIBUTION

The air gap flux density distribution depends essentially on the air gap reluctance and consequently on the pole profile. Assuming infinity permeability for iron, both surfaces of stator and pole face are magnetic scalar equipotential surfaces. Hence, for a constant gap between both surfaces the air gap flux density set up by the rotor has a constant magnitude over a wide range of the pole pitch, as shown in fig. 1.13(a). A theoretical sinusoidal distribution of air gap flux density may be obtained by increasing the gap progressively, and therefore the reluctance, in a convenient manner from the pole centre to the edges, as shown in fig. 1.13(b).

The problem of the pole profile required to produce a sinusoidal distribution of air gap flux density in a salient pole synchronous machine has been treated by Hague [12]. Fig. 1.14 shows a cylindrical equipotential surface of radius R_g with an arc $2\pi/n_p$ which may represent one pole pitch

of a synchronous machine with n_p poles. The equation for the magnetic equipotential surface derived by Hague, passing through any point of coordinates (r, θ_{mec}) to produce a sinusoidal air gap flux density around

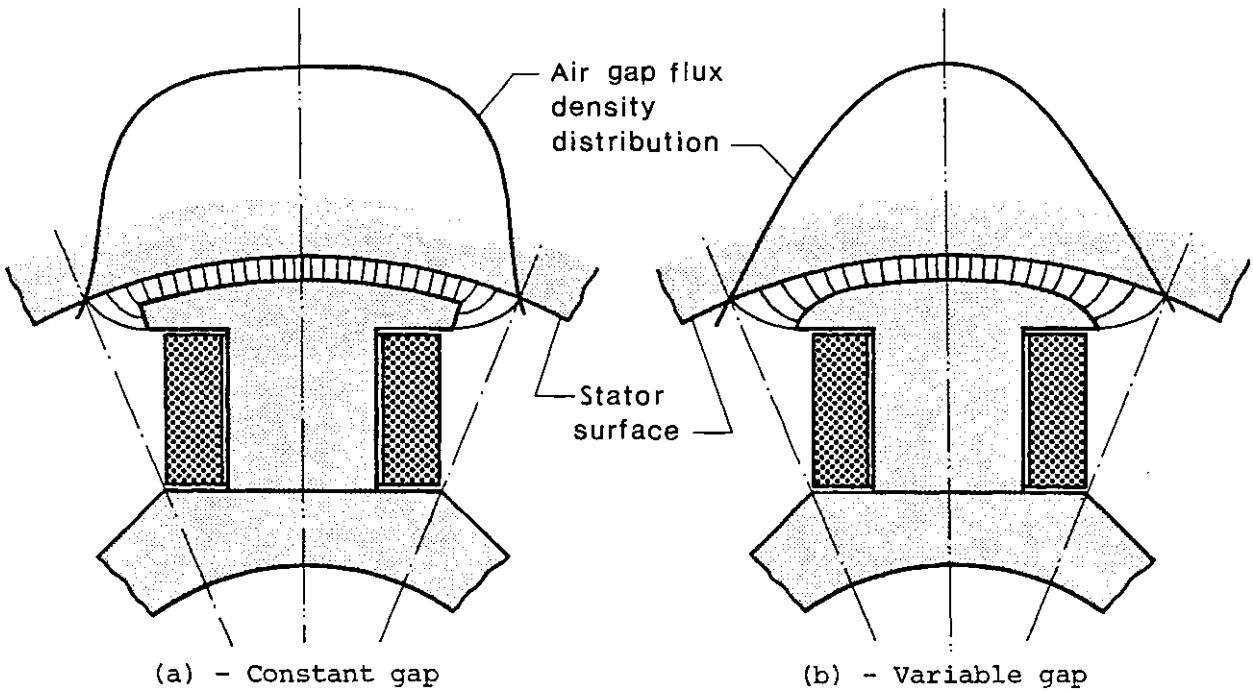

Fig. 1.13 - Effect of pole profile on air gap flux density distribution

the surface, is

$$r^{\frac{n_p}{2}} = \left[\frac{C_1}{\sin \frac{n_p}{2} \theta_{mec}} + \sqrt{\left(\frac{C_1}{\sin \frac{n_p}{2} \theta_{mec}} \right)^2 + \frac{4}{R_g^{n_p}}} \right] \cdot \frac{R_g^{n_p}}{2} \qquad (1.50)$$

and the equation for the flux line passing through the same point is

$$r^{\frac{n_p}{2}} = \left[\frac{C_2}{\cos \frac{n_p}{2} \theta_{mec}} - \sqrt{\left(\frac{C_2}{\cos \frac{n_p}{2} \theta_{mec}} \right)^2 - \frac{4}{R_g^{n_p}}} \right] \cdot \frac{R_g^{n_p}}{2} \qquad (1.51)$$

Also, the air gap permeance between an equipotential surface of centre radius r_c and the cylindrical surface of radius R_g is derived as

$$P_g = 4\mu_o \ell \left(\frac{r_c}{R_g} \right)^{\frac{n_p}{2}} \cdot \frac{1}{1 - \left(\frac{r_c}{R_g} \right)^{n_p}} \qquad (1.52)$$

where ℓ is the effective stator axial length. In Eq. (1.50) and Eq. (1.51) C_1 and C_2 are constants which depend on boundary conditions. As will be

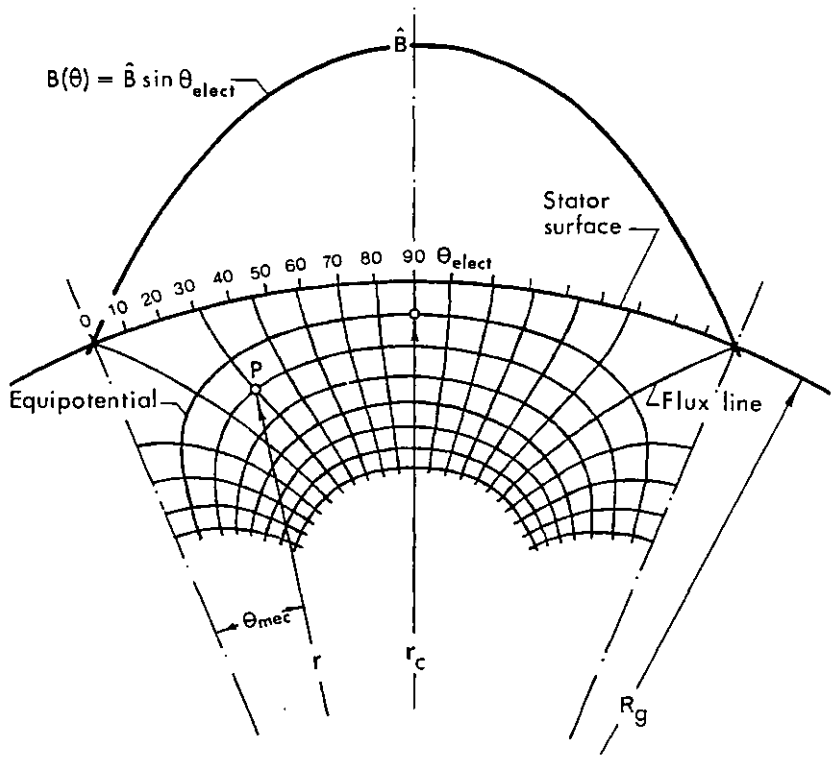

Fig. 1.14 - Equipotential and flux lines for a sinusoidal stator flux density distribution

shown later in Chapter 6, these equations allow one to determine the pole profile in order to obtain a sinusoidal air gap flux density distribution along a smooth iron surface for any minimum gap $R_g - r_c$.

1.7 - SPECIFIC TANGENTIAL FORCE DEVELOPED BY AN ELECTROMAGNETIC MACHINE

In an electromagnetic machine the current interacts with the excitation flux to produce torque and Eq. (1.46) may be generally applied to a cylindrical type machine. The specific tangential force acting on the rotor at the air gap becomes

$$F_u = \frac{T}{R_g \pi D_g \ell} = \frac{n_p N \hat{I}}{\pi D_g} \hat{B}_g K_{W1} \qquad (1.53)$$

where D_g is the stator inside diameter.

By definition, the electric loading A is given by

$$A = \frac{n_p N \hat{I}}{\pi D_g} K_{W1}$$

and therefore Eq. (1.53) reduces to

$$F_u = A\hat{B}_g \tag{1.54}$$

Since $\hat{B}_g$ is inherently limited by saturation in the iron circuit and for the sake of argument may be assumed constant, the value of specific tangential force is determined by permissible values of electric loading. The electrical loading tends to set the level of copper loss in the armature.

For a cylindrical machine, resistance is proportional to ℓ/D_g^2 and assuming fixed K_2 copper loss dissipation per $\pi D_g \ell$ (the area through which the heat flows being taken as proportional to the area of the rotor's curved surface),

$$K_1 \frac{\ell}{D_\ell^2} (AD_g)^2 = K_2 \pi D_g \ell$$

whence

$$A = K\sqrt{D_g} \tag{1.55}$$

Substitution of Eq. (1.55) into Eq. (1.54) and an assumption of constant $\hat{B}_g$ gives

$$F_u = \sigma\sqrt{D_g} \tag{1.56}$$

where σ is a constant numerically equal to the mean specific tangential

force developed by an electromagnetic machine of unit air gap diameter. As seen in Eq. (1.18), σ is of the order of 3×10^4 N/m$^{2.5}$. Eq. (1.56) is in good agreement with practical designs [13, 14], especially for machines with diameters less than one meter of fixed pole number (i.e. pole pitch increasing proportionally with D_g).

1.8 - VARIATION OF STATOR INSIDE RADIUS WITH STATOR OUTSIDE RADIUS

In a drum machine the outer diameter D_o is related to the stator inside diameter D_g by the relationship

$$D_o = D_g + 2(h + b) \tag{1.57}$$

where h is the slot depth and b the backing iron width, as shown in fig. 1.15. Both h and b are a function of D_g, the latter being also a function of the pole number n_p.

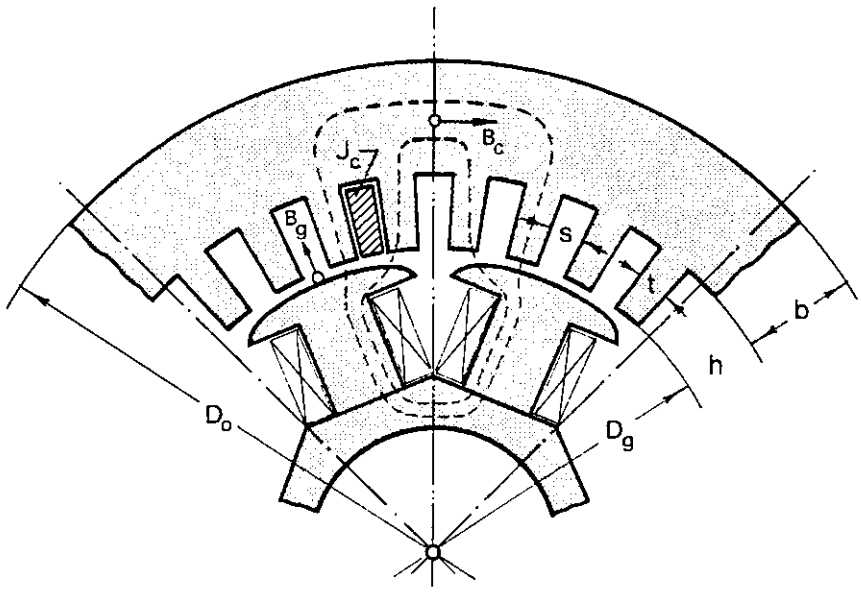

Fig. 1.15 - Relation between D_g and D_o in a drum machine

For an electric loading A, the current density J_c in stator conductors is

$$J_c = \frac{A\pi D_g}{h\pi D_g} \cdot \frac{s+t}{s}$$

where s and t are the slot and tooth widths respectively. The electric loading is given by Eq. (1.55) and so the slot depth h on thermal grounds is

$$h = \frac{K}{J_c}\left(1 + \frac{t}{s}\right)\sqrt{D_g} = \varepsilon\sqrt{D_g} \tag{1.58}$$

If the tooth per slot ratio t/s and current density J_c are assumed constant for all values of D_g, then ε is a constant. If it is assumed typically that h = 0.03 m when D_g = 1 m, from Eq. (1.58) is $\varepsilon = 0.03\ m^{\frac{1}{2}}$.

On the other hand, if B_g is the average air gap flux density, assuming sinusoidal distribution, the peak core flux density is

$$\hat{B}_c = \frac{\tau}{2} B_g \frac{1}{b} = \frac{\pi D_g}{2n_p} \frac{B_g}{b}$$

For typical values B_g = 0.5 T and $\hat{B}_c$ = 1.5 T, the backing iron width b becomes:

$$b = \frac{\pi D_g}{6n_p} \tag{1.59}$$

Substitution of Eq. (1.59) and Eq. (1.58) into Eq. (1.57), gives:

$$D_o = \left(1 + \frac{\pi}{3n_p}\right) D_g + 2\varepsilon\sqrt{D_g} \tag{1.60}$$

Solution of this quadratic equation for $\varepsilon = 0.03\ m^{\frac{1}{2}}$ and putting $\gamma = 1 + \frac{\pi}{3n_p}$ yields:

$$D_g = \left[-\frac{0.03}{\gamma} + \left(\frac{0.03}{\gamma}\right)^2 + \frac{D_o}{\gamma} \right]^2 \tag{1.61}$$

Then, D_g may be evaluated for any value of stator outside diameter D_o and number of poles n_p. Typical results are shown in fig. 1.16 and

these show that when the pole number is sufficiently high, the characteristics become very close. This is a consequence of Eq. (1.59), since for

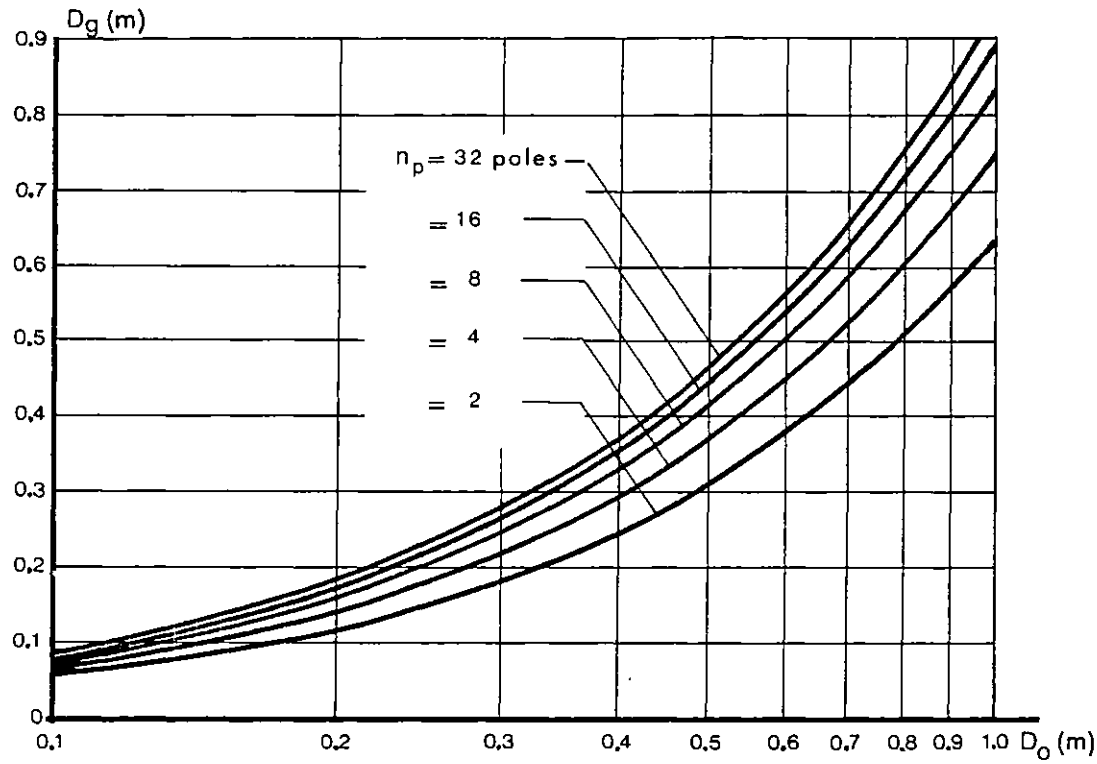

Fig. 1.16 - Variation of stator inside diameter versus outer diameter with pole number

a high pole number, the backing iron width b increases only slightly with D_g.

1.9 - DYNAMIC FACTORS OF A MOTOR

From the servo point of view it is important to obtain in the motor-gear-load combination the highest possible torque to inertia ratio, or initial angular acceleration, so that the servo can have as rapid a response as possible. Unfortunately other requirements often conflict with this, and in this section a choice of gear ratio and factors affecting the motor design are discussed.

1.9.1 - Optimal gear ratio

Fig. 1.17 shows a motor with inertia J_m and torque T_m driving a load of intertia J_ℓ geared down through a gear of ratio G, i.e., $G = \omega_m/\omega_\ell = \theta_m/\theta_\ell$ where θ_m and θ_ℓ are the input and output shaft angle respectively.

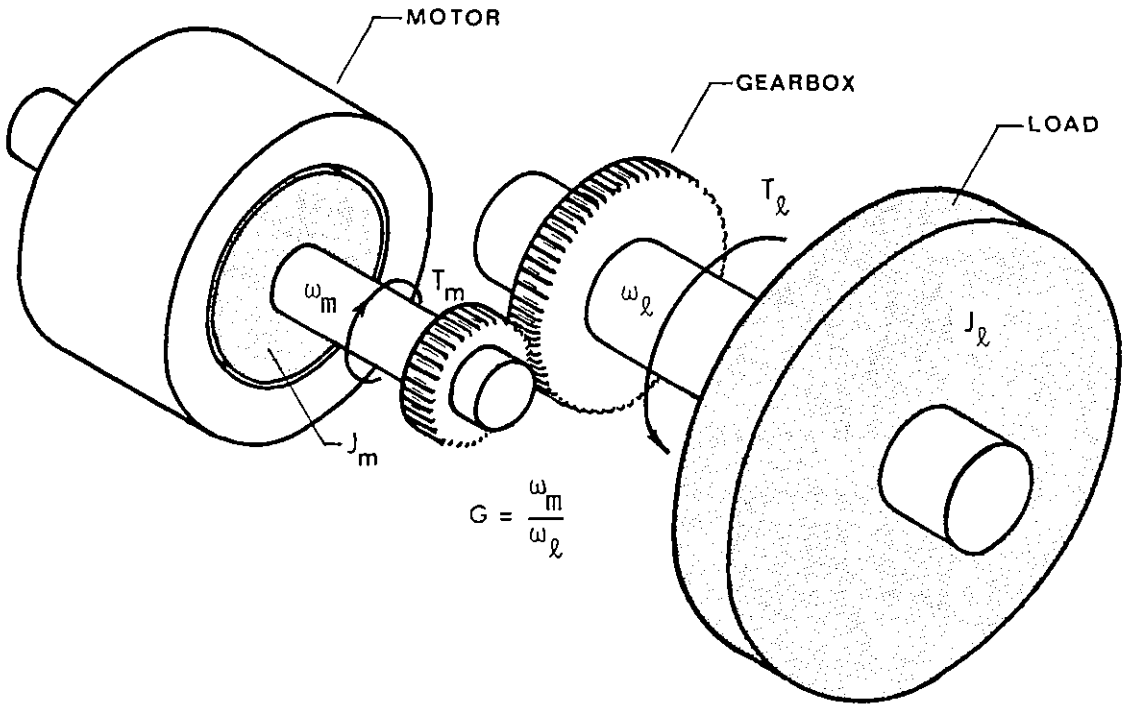

Fig. 1.17 - Motor driving a load through a G:1 step down gearbox

Assuming that there is no power losses in the gearing,

$$T_\ell = \frac{\omega_m}{\omega_\ell} T_m = G\,T_m \tag{1.62}$$

where T_ℓ and T_m represent the load and motor torque respectively. The equation of motion of the load is

$$J_\ell \frac{d^2\theta}{dt^2} + D_\ell \frac{d\theta_\ell}{dt} + K_\ell\theta_\ell = T_\ell = G\,T_m$$

where D_ℓ is the viscous damping and K_ℓ is the column friction or stiffness coefficient. Substituting $\theta_\ell = \theta_m/G$ and then dividing by G, gives:

$$\frac{J_\ell}{G^2} \frac{d^2\theta_m}{dt^2} + \frac{D_\ell}{G^2} \frac{d\theta_m}{dt} + \frac{K_\ell}{G^2} \theta_m = T_m \tag{1.63}$$

If instead of being geared to a load shaft, the driving shaft actually had inertia J_r, damping D_r and stiffness K_r, then

$$J_r \frac{d^2\theta_m}{dt^2} + D_r \frac{d\theta_m}{dt} + K_r\theta_m = T_m \tag{1.64}$$

Comparing Eq. (1.63) and Eq. (1.64), the effect of the gearing is to transfer or reflect the actual load to the driving shaft as a reflected inertia $J_r = J_\ell/G^2$, damping $D_r = D_\ell/G^2$ and stiffness $K_r = K_\ell/G^2$. The result is analogous to a transformer of turns ratio $m = n_1/n_2$ with reflection of load inductance, resistance and capacitance respectively to the primary winding.

The total effective inertia on the load side is

$$J_\ell'' = J_\ell + G^2 J_m$$

and the initial angular acceleration of load shaft becomes:

$$\ddot{\theta}_\ell = \frac{T_\ell}{J_\ell''} = \frac{GT_m}{J_\ell + G^2 J_m} \tag{1.65}$$

For varying G and a given motor and load, Eq. (1.65) is a maximum when

$$G = G_o = \sqrt{\frac{J_\ell}{J_m}} \tag{1.66}$$

and this optimal gear ratio G_o is said to match the inertias. Under these conditions, Eq. (1.65) becomes

$$\ddot{\theta}_{\ell(max)} = \frac{T_m}{\sqrt{J_m}} \cdot \frac{1}{2\sqrt{J_\ell}} = \frac{1}{2}\sqrt{\frac{P_R}{J_\ell}} \tag{1.67}$$

where

$$P_R = \frac{T_m^2}{J_m} \tag{1.68}$$

is a factor inherent to the motor, and since it has units of power/time is called "power rate". Hence for matched gearing and inertia loading, a motor's power rate sets the level of load acceleration.

If the load is driven directly (G = 1), Eq. (1.65) reduces to

$$\ddot{\theta}_\ell = \frac{T_m}{J_\ell + J_m} \tag{1.69}$$

The factor T_m/J_m then determines the initial angular acceleration of an unloaded motor and like the power rate is an important dynamic characteristic in servo applications.

1.9.2 - Variation of dynamic factors with motor proportions

Both power rate and torque/inertia are severely affected by the motor proportions, and the influence of motor D_g/ℓ ratio on these factors may be examined. A cylindrical solid rotor of constant volume represented by $D_g^2\ell = 1$ product in fig. 1.18 is assumed. Under this condition the ratio

$$r = \frac{D_g}{\ell} = \frac{D_g^3}{D_g^2\ell} = D_g^3 \tag{1.70}$$

From Eq. (1.56), the motor torque may be expressed in terms of ratio r as

$$T_m = F_u \pi D_g \ell \frac{D_g}{2} = \frac{\pi\sigma}{2} D_g^2 \ell \sqrt{D_g} = \frac{\pi\sigma}{2} \cdot \sqrt[6]{r} \tag{1.71}$$

For a solid rotor of uniform density ρ and mass distribution, the inertia is given by

$$J_m = \frac{\pi}{64} \rho D_g^4 \ell = \frac{\pi}{64} \rho \cdot \left(\sqrt[3]{r}\right)^2 \tag{1.72}$$

Hence,

$$P_R = \frac{T_m^2}{J_m} = \frac{16\pi\sigma^2}{\rho} \frac{1}{\sqrt[3]{r}} \tag{1.73}$$

and

$$\ddot{\theta}_m = \frac{T_m}{J_m} = \frac{32\sigma}{\rho} \frac{1}{\sqrt{r}} \tag{1.74}$$

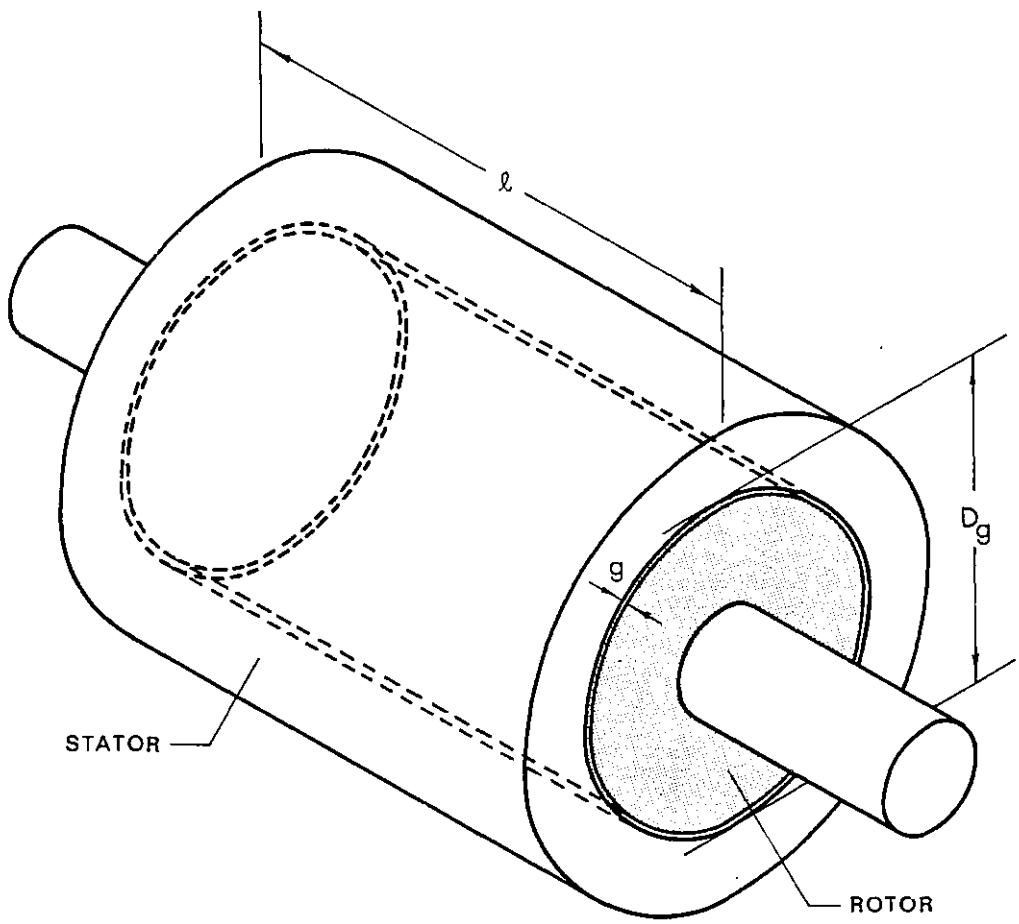

Fig. 1.18 - $D_g^2 \ell$ product

Normalised curves for Eq. (1.71) to Eq. (1.74) are shown in fig. 1.19. As far as dynamic response characteristics are concerned, it is clear from these results that for a motor of given power, a thin and long rotor is preferable to a short one of larger diameter. However, for "torque"

applications, where the dynamic characterisitics are not so important, machines of large diameter and short axial lengths can be considered. It is certainly true that the inertia for a solid rotor increases with D_g^4, but for larger diameters an annular rather than a solid rotor may be used, giving a substantial reduction in motor inertia.

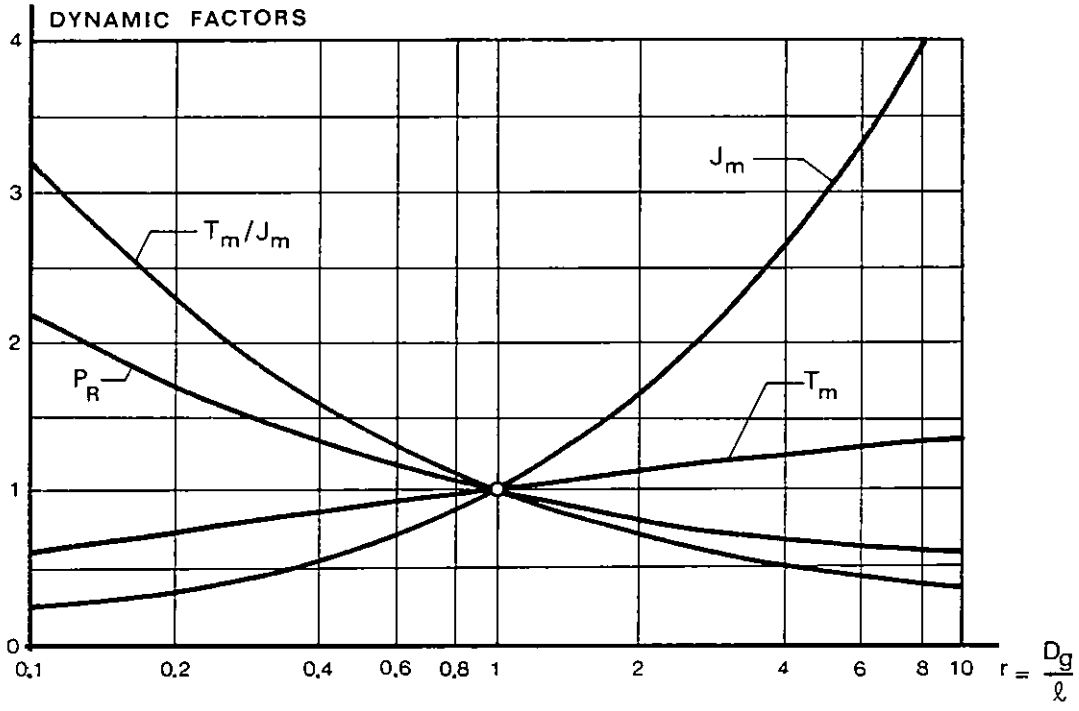

Fig. 1.19 - Variation of dynamic factors versus D_g/ℓ ratio

Hence, it can be concluded that machines with relatively low D_g/ℓ ratio make good servo-motors, while machines with high D_g/ℓ make good "torque-motors".

1.9.3 - Comparison between a direct and an optimal gearing drive

It is usually economic to design servo-motors which run at a much higher speed than that required for the output shaft. As seen a reduction gear is then used to connect the motor to the load shaft.

Direct drives are rarely used, although they find some applications where ultra-high positioning performance is required, for example in inertial-navigation platform, aerial control, etc. A comparison between

a direct drive and an optimal gearing drive for both motors with solid and annular rotors is now presented [15]. It is assumed that both rotors have a fixed $r = D_g/\ell$ ratio and drive a fixed load inertia J_ℓ.

Combining Eq. (1.66) and Eq. (1.67) the maximum initial acceleration for an optimal gearing system becomes:

$$\ddot{\theta}_\ell = \frac{1}{2G_o} \frac{T_m}{J_m} \tag{1.75}$$

From Eq. (1.71) the torque for both rotors of diameter $D_g = r\ell$ with fixed r is

$$T_m = \frac{\pi\sigma}{2} r^{2.5} \ell^{3.5} \tag{1.76}$$

and the inertia for solid rotor

$$J_{ms} = \frac{\pi}{64} \rho r^4 \ell^5 \tag{1.77}$$

For annular rotors, the inertia vary approximately with $D_g^3\ell$ and so

$$J_{mA} \simeq \frac{\pi}{64} \rho r^3 \ell^4 \tag{1.78}$$

For matched inertias

$$G_{os} = \sqrt{\frac{J_\ell}{J_{ms}}} = \sqrt{\frac{64J_\ell}{\pi\rho r^4}} \frac{1}{\ell^{2.5}} \quad \text{and} \quad G_{oA} = \sqrt{\frac{J_\ell}{J_{mA}}} = \sqrt{\frac{64J_\ell}{\pi\rho r^3}} \frac{1}{\ell^2} \tag{1.79}$$

Torque/inertia for both rotors is

$$\frac{T_m}{J_{ms}} = \frac{32\sigma}{\rho r^{1.5}} \frac{1}{\ell^{1.5}} \quad \text{and} \quad \frac{T_m}{J_{mA}} = \frac{32\sigma}{\rho r^{0.5}} \frac{1}{\ell^{0.5}} \tag{1.80}$$

Eliminating ℓ in Eq. (1.80) using Eq. (1.79) and substitution into

Eq. (1.75) gives

$$\ddot{\theta}_{\ell s} = \frac{K_s}{G_o^{0.4}} \qquad \text{and} \qquad \ddot{\theta}_{\ell A} = \frac{K_A}{G_o^{0.75}} \tag{1.81}$$

where K_s and K_A are constants. Normalised curves of $\ddot{\theta}_\ell$ and ℓ for both solid and annular rotor drives of different size are shown in fig. 1.20(a). As an example, these results show that a motor with a solid rotor for a 10:1 optimally geared system will be accelerated 0.40 times less than a load driven directly ($G_o = 1$) by a rotor of appropriate size, i.e., the direct drive being 1/0.40 = 2.5 times longer. The advantage of direct drive is still better if an annular rotor is considered.

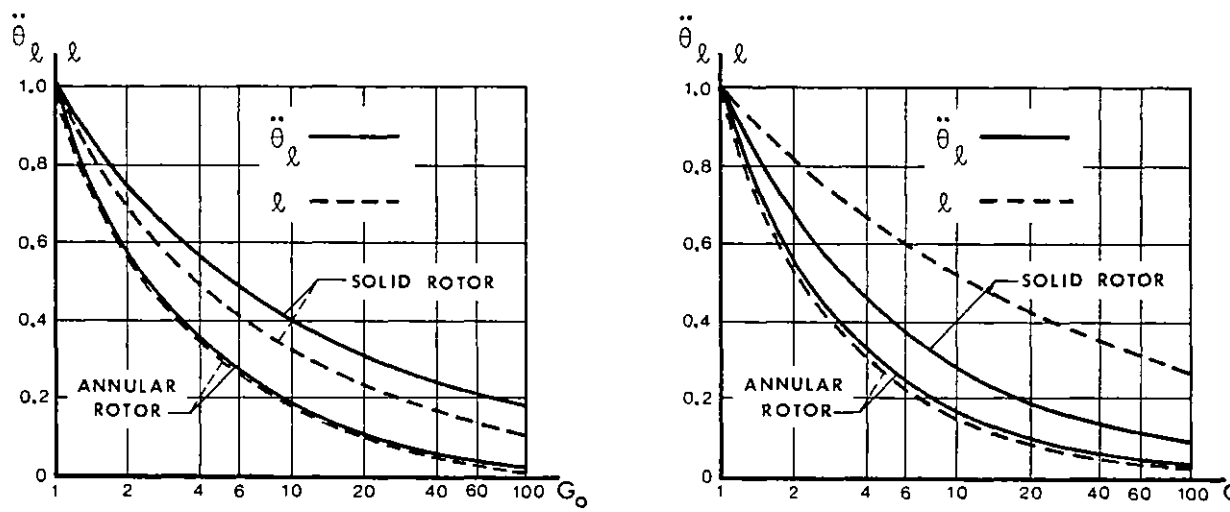

(a) - Constant load inertia and optimal gear

(b) - Constant load torque and small load inertia

Fig. 1.20 - Normalised load response and drive motor size versus gear ratio for both solid and annular rotors

A comparison between this case and the motor operating as a servo of some type where the load is negligible may be also analysed. In this situation $J_\ell << G^2 J_m$ and the load torque, friction for instance, is assumed to be some fixed fraction α of the drive torque at the load shaft, i.e., $T_\ell = \alpha G T_m$.

Hence, from Eq. (1.65), the load acceleration becomes

$$\ddot{\theta}_\ell \simeq \frac{GT_m - T_\ell}{G^2 J_m} = \frac{T_m}{J_m}\,\frac{1-\alpha}{G} \tag{1.82}$$

where G is now a general rather than optimal gear ratio. From Eq. (1.76) the drive size for both solid and annular types with constant D_g/ℓ, becomes

$$\ell = \left[\frac{2T_m}{\pi\sigma r^{2.5}}\right]^{1/3.5} = \left[\frac{2T_\ell}{\pi\sigma r^{2.5}\alpha}\right]^{1/3.5} \cdot \frac{1}{G^{0.29}} \tag{1.83}$$

Eliminating ℓ in Eq. (1.80) using Eq. (1.83) and substituting in Eq. (1.82) gives the load acceleration as

$$\ddot{\theta}_{\ell s} = \frac{K_S'}{G^{0.57}} \quad \text{and} \quad \ddot{\theta}_{\ell A} = \frac{K_A'}{G^{0.86}} \tag{1.84}$$

respectively for solid and annular types. Normalised curves for Eq. (1.83) and Eq. (1.84) versus gear ratio G are shown in fig. 1.20(b).

From these results it can be seen that the direct drive in place of a geared drive is more advantageous for the motor driving a small load inertia than for the motor driving a high inertia. For the specific example of a 10:1 geared drive replaced by a solid rotor direct drive with size ℓ = 1.95 times as big, acceleration will be improved by a factor of 1/0.27 or 3.72. If instead an annular rotor with the same length was used, acceleration would be improved by a factor 7.24.

It should be noted that both motor weight/torque and cost/torque generally decrease with motor size. Hence the weight and cost of the larger machine necessary for a direct drive will usually be considerably less than G times that of the motor in geared system. The weight and cost of the gearbox are of course absent.

Hence, from Eq. (1.65), the load acceleration becomes

$$\ddot{\theta}_{\ell} \simeq \frac{GT_m - T_{\ell}}{G^2 J_m} = \frac{T_m}{J_m} \frac{1 - \alpha}{G} \tag{1.82}$$

where G is now a general rather than optimal gear ratio. From Eq. (1.76) the drive size for both solid and annular types with constant D_g/ℓ, becomes

$$\ell = \left[\frac{2T_m}{\pi \sigma r^{2.5}} \right]^{1/3.5} = \left[\frac{2T_{\ell}}{\pi \sigma r^{2.5} \alpha} \right]^{1/3.5} \cdot \frac{1}{G^{0.29}} \tag{1.83}$$

Eliminating ℓ in Eq. (1.80) using Eq. (1.83) and substituting in Eq. (1.82) gives the load acceleration as

$$\ddot{\theta}_{\ell s} = \frac{K_S'}{G^{0.57}} \quad \text{and} \quad \ddot{\theta}_{\ell A} = \frac{K_A'}{G^{0.86}} \tag{1.84}$$

respectively for solid and annular types. Normalised curves for Eq. (1.83) and Eq. (1.84) versus gear ratio G are shown in fig. 1.20(b).

From these results it can be seen that the direct drive in place of a geared drive is more advantageous for the motor driving a small load inertia than for the motor driving a high inertia. For the specific example of a 10:1 geared drive replaced by a solid rotor direct drive with size ℓ = 1.95 times as big, acceleration will be improved by a factor of 1/0.27 or 3.72. If instead an annular rotor with the same length was used, acceleration would be improved by a factor 7.24.

It should be noted that both motor weight/torque and cost/torque generally decrease with motor size. Hence the weight and cost of the larger machine necessary for a direct drive will usually be considerably less than G times that of the motor in geared system. The weight and cost of the gearbox are of course absent.

1.10 - HYDRAULIC MOTOR VERSUS ELECTRIC TORQUE MOTOR

When high torque per size is required, the electric motor has very strong competitors in the form of hydraulic and pneumatic drives [16]. By the use of high pressures on fluid operated pistons, very large forces are developed and fluid devices are very common for producing slow motion with large forces. With hydraulic or pneumatic drives, torque can be much improved, mainly because the normal stress level in fluid devices can exceed 3×10^7 N/m^2, being essentially limited only by metal and seal strengths. In comparison with this, for a well designed electric motor, the value of sheer stress at stator/rotor interface, limited by current and flux density, rarely reaches 5×10^4 N/m^2.

The simplest form of hydraulic motor is the gear motor represented in fig. 1.21(a). This design is suitable for pressures up to about 2×10^6 N/m^2, since for higher pressures it is difficult to machine the gears [17] and so for higher pressures piston motors tend to be used instead. However, due to its simple geometry a comparison on a torque basis with an electric motor shown in fig. 1.21(b), can be easily made. It is assumed that both machines have the same height D_o, axial length ℓ amd constant D_o/ℓ ratio.

In a rotary hydraulic motor, the work done during a displacement $Rd\theta$ is $dW = dD_p(p_1 - p_2)$ where $dD_p = Rh\ell d\theta$ is the flow displacement and $p_1 - p_2$ the pressure difference. Hence, the total torque produced

$$T_h = 2\pi Rh\ell(p_1 - p_2) \tag{1.85}$$

where for typical designs $h = 0.4R$ and $D_o = 4R$. Since $r = D_o/\ell$ is fixed, Eq. (1.85) becomes:

$$T_h = \frac{\pi}{20r} D_o^3 (p_1 - p_2) \tag{1.86}$$

For the electric motor, from Eq. (1.71) the torque equation is

$$T_e = \frac{\pi\sigma}{2r} D_g^{2.5} D_o \tag{1.87}$$

Combining Eq. (1.87) and Eq. (1.86) gives:

$$\frac{T_e}{T_h} = 10 \frac{\sigma}{p_1 - p_2} \frac{D_g^{2.5}}{D_o^2} \tag{1.88}$$

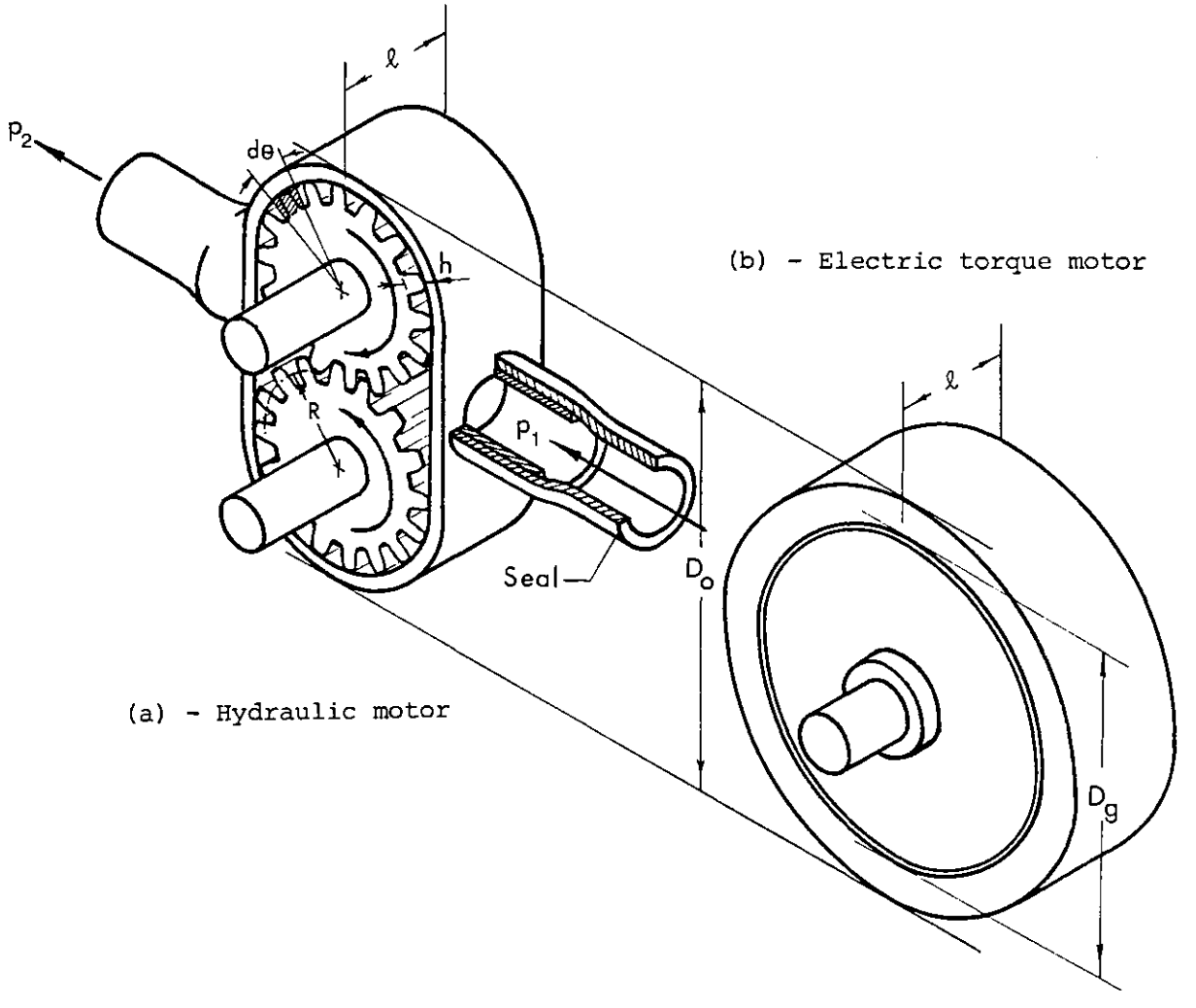

Fig. 1.21 - Geometry for hydraulic and electric torque motor

For a given D_o and number of poles n_p of the electric motor, the air gap diameter may be calculated from Eq. (1.61). Hence, Eq. (1.88) may be evaluated as a function of D_o for differing values of n_p. Taking $\sigma = 5 \times 10^4$ N/m$^{2.5}$ and $p_1 - p_2 = 2 \times 10^6$ N/m^2, typical characteristics

are shown in fig. 1.22.

In a torque ratio basis it is evident that hydraulic motors have inherent advantages over electric motors. However, electric torque becomes comparatively better as outer diameter and pole number increases. This can be an advantage of the electric torque motor when used in high sizes.

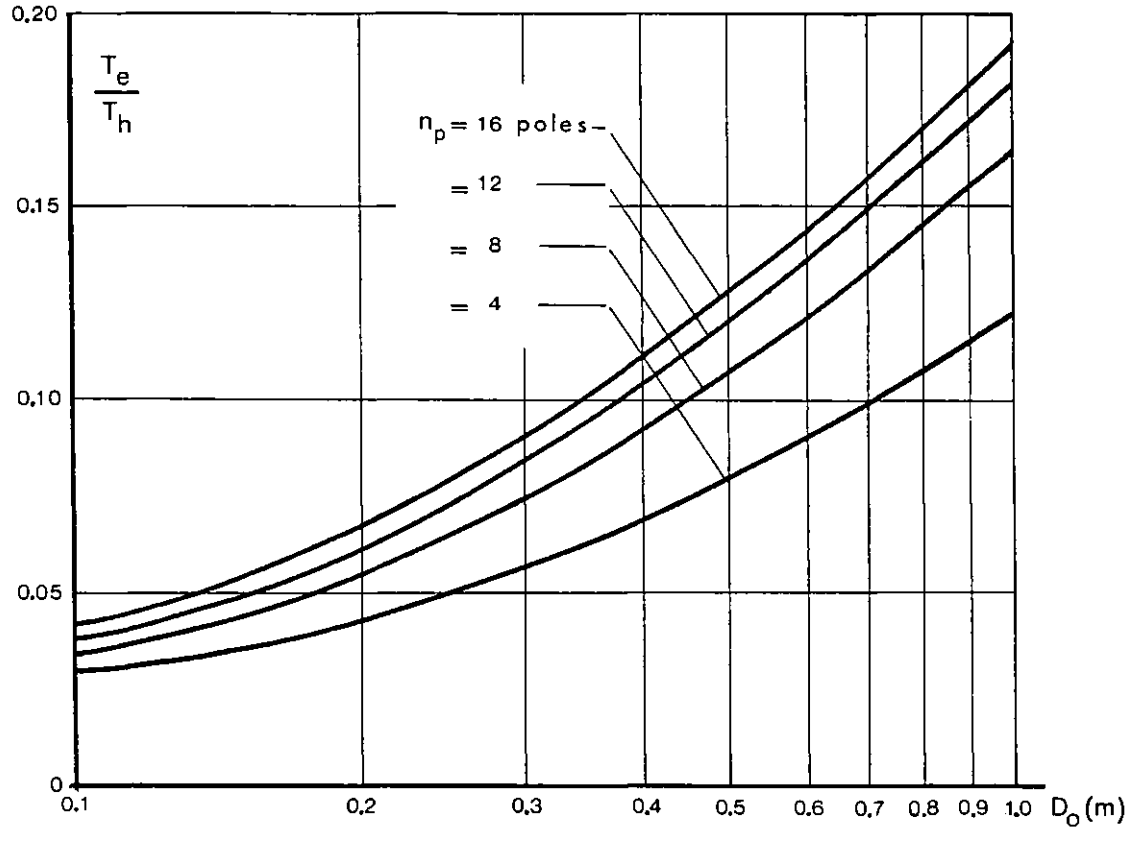

Fig. 1.22 - Electric to hydraulic torque ratio variation versus outer diameter

Nevertheless there are some other reasons why electric motors are still preferred to hydraulic systems in many applications and they can be summarised as follows:

a) - Facility of supply

Hydraulic systems need their own source to be installed with consequent difficulty to handle hydraulic pipes. Long piping presents problems if remote supply needed, while wiring is generally easily mounted.

b) - Initial costs

Hydraulic systems require very accurate manufacture (sometimes even to otpical limits) of the moving parts. Due to high pressure, seals must be made with great care. Additionally, installation of pump, reservoir, control device and piping implies much higher initial costs than electric systems.

c) - Reliability

Pump, reservoir and piping need frequent maintenance as well as the hydraulic motor. Comparatively, electric systems are reliable for years without attention.

d) - Cleanliness

Electric systems are clean and have less noise pollution than hydraulic systems, where there is possibility of fluid leakage with consequent mess of oil.

1.11 - COMPARISON BETWEEN ARCUATE AND CYLINDRICAL CONFIGURATIONS

In the arcuate type motor (or actuator) the rotor subtends some angle ε less than 2π, while the stator has a centre angle $\varepsilon + \theta$ where θ is the required rotor angular displacement. Fig. 1.23 shows an arcuate machine and a conventional 2π machine. Assuming that both machines have the same height D_o and axial length ℓ, a comparison in terms of torque/inertia, power rate, torque/volume and torque/rotor air gap area can be made.

From Eq. (1.56), the torque developed by the arcuate machine is

$$T_A = F_u \varepsilon D_g \ell D_g = \sigma \varepsilon \ell \sqrt{2D_g}\, D_g^2 \qquad (1.89)$$

while for the conventional cylindrical machine:

$$T_C = F_u \pi D_g \ell \frac{D_g}{2} = \frac{\sigma \pi \ell}{2} \sqrt{D_g}\, D_g^2 \qquad (1.90)$$

Combination of Eq. (1.89) and Eq. (1.90) gives

$$T_A = 2\sqrt{2}\ \frac{\varepsilon}{\pi}\ T_C \tag{1.91}$$

Similar relations for rotor inertia, overall volume and rotor air gap area can be found respectively as:

$$J_A = \frac{8\varepsilon}{\pi}\ J_C \qquad V_A = 2\ \frac{\varepsilon+\theta}{\pi}\ V_C \qquad A_A = \frac{\varepsilon}{\pi}\ A_C \tag{1.92}$$

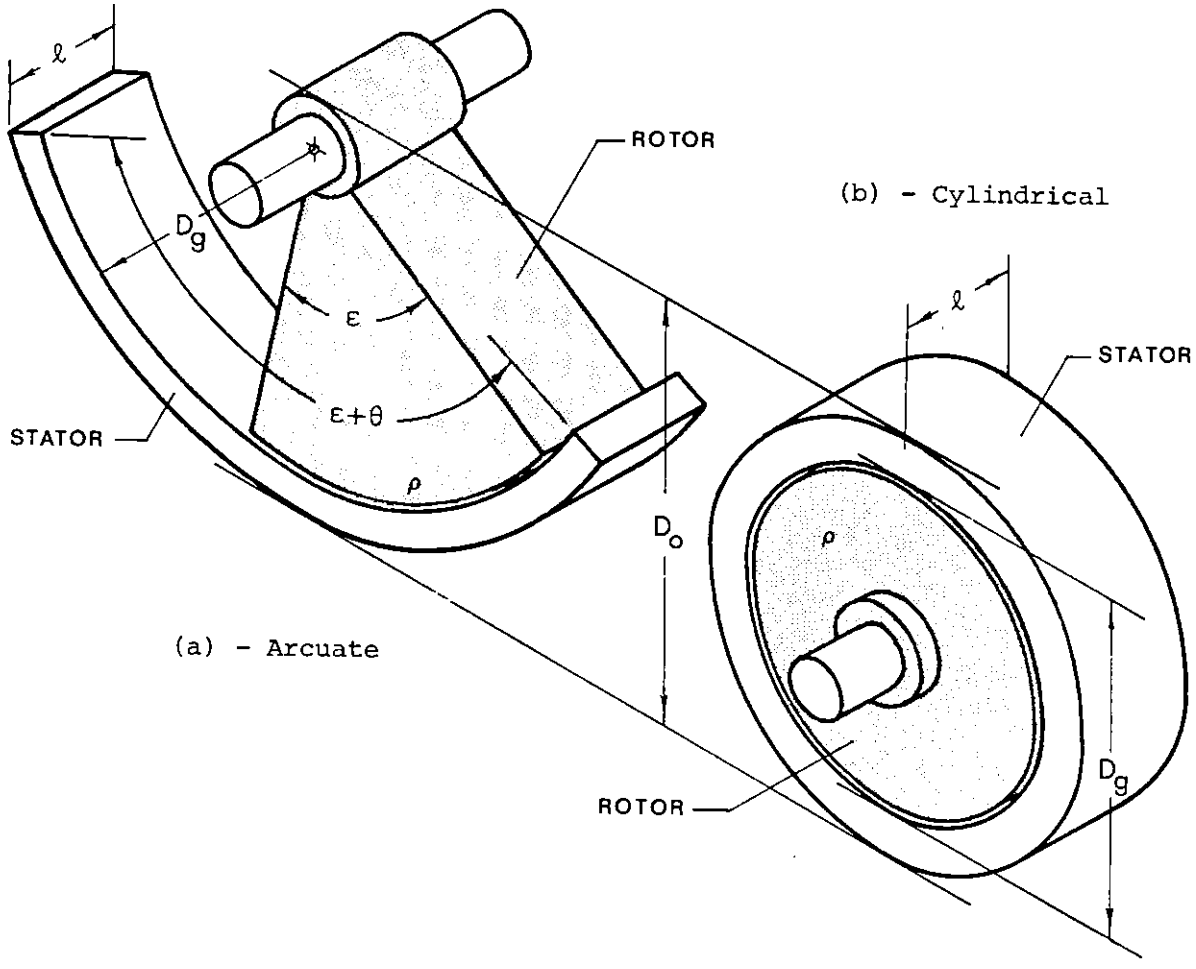

Fig. 1.23 - Arcuate and conventional configurations

Hence, using Eq. (1.91) and Eq. (1.92) the following relationships yield:

$$\frac{T_A}{J_A} = \frac{\sqrt{2}}{4}\ \frac{T_C}{J_C} \qquad \frac{T_A^2}{J_A} = \frac{\varepsilon}{\pi}\ \frac{T_C^2}{J_C}$$

$$\frac{T_A}{V_A} = \sqrt{2}\ \frac{\varepsilon}{\varepsilon+\theta}\ \frac{T_C}{V_C} \qquad \frac{T_A}{A_A} = 2\sqrt{2}\ \frac{T_C}{A_C}$$

These results show that in terms of initial angular acceleration the conventional machine has a better response increased by a factor 2.83 with respect to the arcuate machine, whatever ε and θ. Again, in terms of power rate, the conventional machine is still better being equal when $\varepsilon = \pi$, but this is an impractical design. However torque per overall volume becomes the same if $\varepsilon = 90°$ and $\varepsilon + \theta = 127°$ are chosen and a design using these parameters is described in Chapter 4. Additionally, torque per rotor air gap area is improved by a factor of $2\sqrt{2}$ (and not a factor of 2 as in reference [15]), independent of ε and θ used. When rotor weight and/or rotor cost are likely to be critical factors, this improvement is sometimes sufficient to justify the use of the arcuate configuration in certain applications, particularly where it fits in well with the mechanical layout of the load.

1.12 - COMPARISON BETWEEN DISC AND CYLINDRICAL CONFIGURATIONS

Due to high torque to inertia ratio, disc motors have been used over recent years in a wide variety of high performance servo applications [18, 19, 20]. Chapter 5 is devoted to such a machine and a comparison in full detail between disc and drum machines using both permanent and coil excitation is developed in Chapter 6. In this section, a basic comparison between disc and cylindrical configuration in terms of torque, inertia and torque per inertia ratios to both machines is briefly discussed.

Fig. 1.24 shows a single-sided disc machine and a conventional cylindrical machine both with the same rotor thickness d. The comparison is made assuming that both machines have the same diameters D_o as defined in the diagram and identical active conductor lengths such that giving maximum torque in the disc machine.

From fig. 1.25, the elementary force dF for the disc machine at distance x from the centre due to the elementary current $2A_i \frac{D_i}{2} d\theta$ (go and return conductors) is

$$dF = B(x)A_i D_i d\theta dx$$

where $A_i = \frac{ni}{\pi D_i}$ is the current loading on the inner disc periphery and B(x) the flux density at position x.

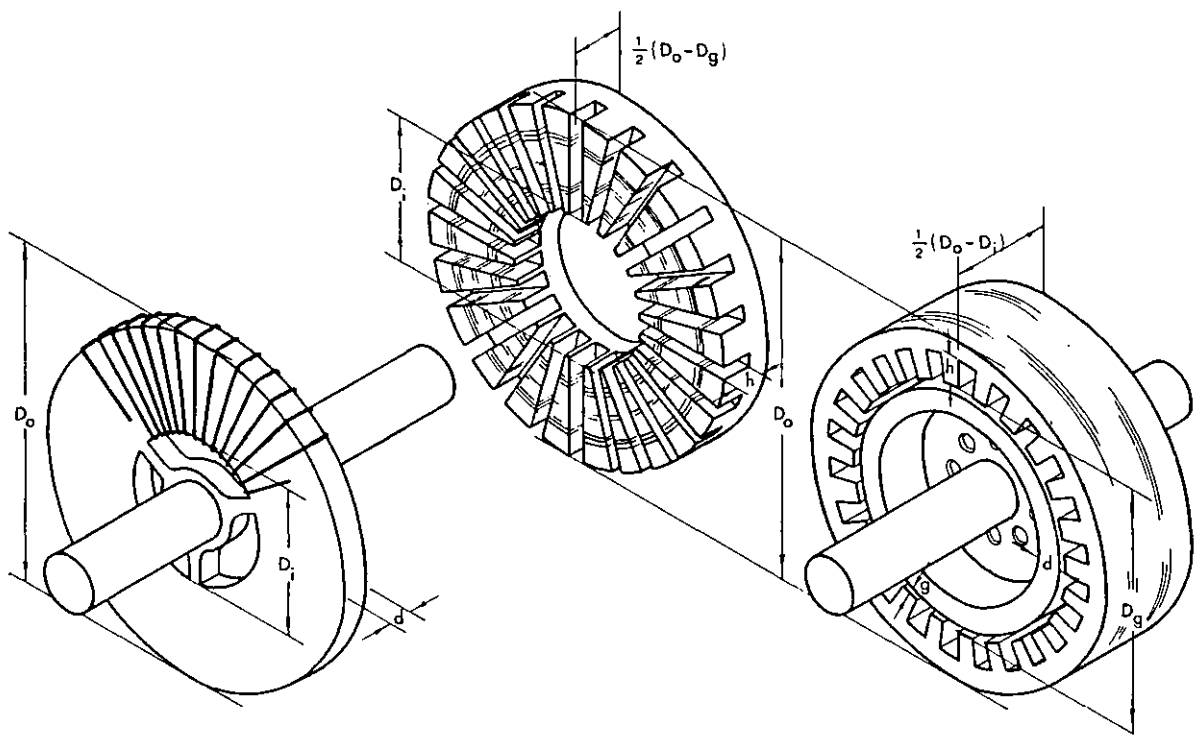

(a) - Disc machine (b) - Cylindrical machine

Fig. 1.24 - Single-sided disc and conventional cylindrical machines

Hence, assuming B(x) is maintained constant with x, the output torque is:

$$T_d = BA_i D_i \int_{\frac{D_i}{2}}^{\frac{D_o}{2}} x\,dx \cdot \int_0^{2\pi} d\theta = \frac{\pi}{4} BA_i D_i (D_o^2 - D_i^2) \qquad (1.93)$$

On thermal considerations, the electric loading for the disc machine may be also assumed to be of the form of Eq. (1.55), i.e., $A_i = K\sqrt{D_i}$. Thus,

for a fixed D_o, the particular value of D_i which maximises Eq. (1.93) is given by

$$D_i = \sqrt{\frac{3}{7}}\, D_o \tag{1.94}$$

Noting that BA_i is the specific tangential force F_u at radius $D_i/2$ given by Eq. (1.56), from Eq. (1.94) one obtains:

$$F_u = BA_i = \sigma\sqrt{D_i} = \sigma \left(\frac{3}{7}\right)^{\frac{1}{4}} \sqrt{D_o} \tag{1.95}$$

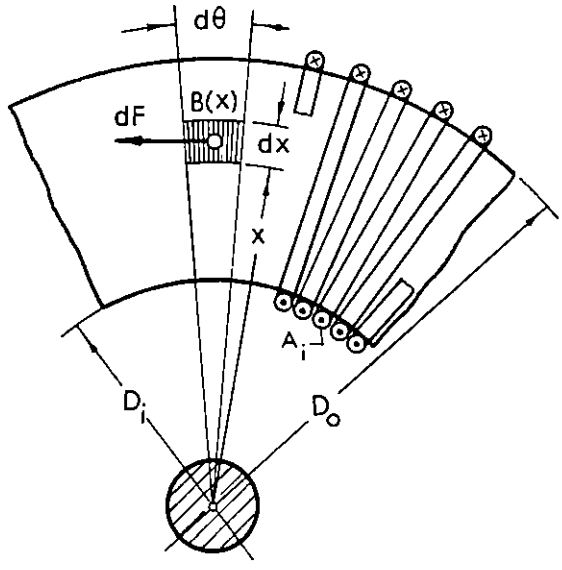

Fig. 1.25 - Elementary force for the disc machine

Substitution of Eq. (1.94) and Eq. (1.95) into Eq. (1.93) gives the peak torque of the disc motor as

$$\hat{T}_d = 0.08\, \pi\, \sigma \sqrt{D_o}\; D_o^3 \tag{1.96}$$

The torque for the cylindrical motor is given by

$$T_c = F_u\, \pi\, D_g\, \frac{1}{2}\, (D_o - D_i)\, \frac{D_g}{2}$$

Hence from Eq. (1.56) and Eq. (1.94),

$$T_c = 0.09\,\pi\,\sigma\,D_o.\sqrt{D_g}\;D_g^2 \tag{1.97}$$

Combining Eq. (1.96) and Eq. (1.97) gives

$$\frac{\hat{T}_d}{T_c} = 0.89\left(\frac{D_o}{D_g}\right)^{2.5} \tag{1.98}$$

and since D_g can be derived from D_o using Eq. (1.61), Eq. (1.98) may be evaluated for any outer diameter D_o and any number of poles n_p.

For the rotor inertia calculation, both rotors are assumed to have the same density ρ and uniform mass distributions. The inertia of the disc rotor is then:

$$J_d = 2\pi\rho d\int_{\frac{D_i}{2}}^{\frac{D_o}{2}} x^3 dx = \frac{1}{32}\,\pi\rho d(D_o^4 - D_i^4) \tag{1.99}$$

and the cylindrical rotor

$$J_c = 2\pi\rho\,\frac{1}{2}(D_o - D_i)\int_{\frac{D_g}{2}-d}^{\frac{D_g}{2}} x^3 dx = \frac{1}{64}\,\pi\rho(D_o - D_i)\left[D_g^4 - (D_g - 2d)^4\right] \tag{1.100}$$

Comparison of Eq. (1.99) and Eq. (1.100) and substituting from Eq. (1.94) gives:

$$\frac{J_d}{J_c} = 4.8\,d\;\frac{D_o^3}{D_g^4 - (D_g - 2d)^4} \tag{1.101}$$

Hence, using Eq. (1.98) and Eq. (1.101), the initial angular acceleration ratio becomes:

$$\frac{\ddot{\theta}_d}{\ddot{\theta}_c} = 0.185\;\frac{D_g^4 - (d_g - 2d)^4}{d\sqrt{D_o}.\,D_g^{2.5}} \tag{1.102}$$

Eq. (1.98) has been calculated for outer diameters up to 1 m and numbers of poles n_p = 2, 4, 8. For n_p = 8 poles, Eq. (1.101) and Eq. (1.102) were then calculated for rotor thickness d = 0.05 D_o, d = 0.10 D_o and d = 0.20 D_o and the results obtained for torque, inertia and torque per inertia ratios of the two designs are shown in fig. 1.26.

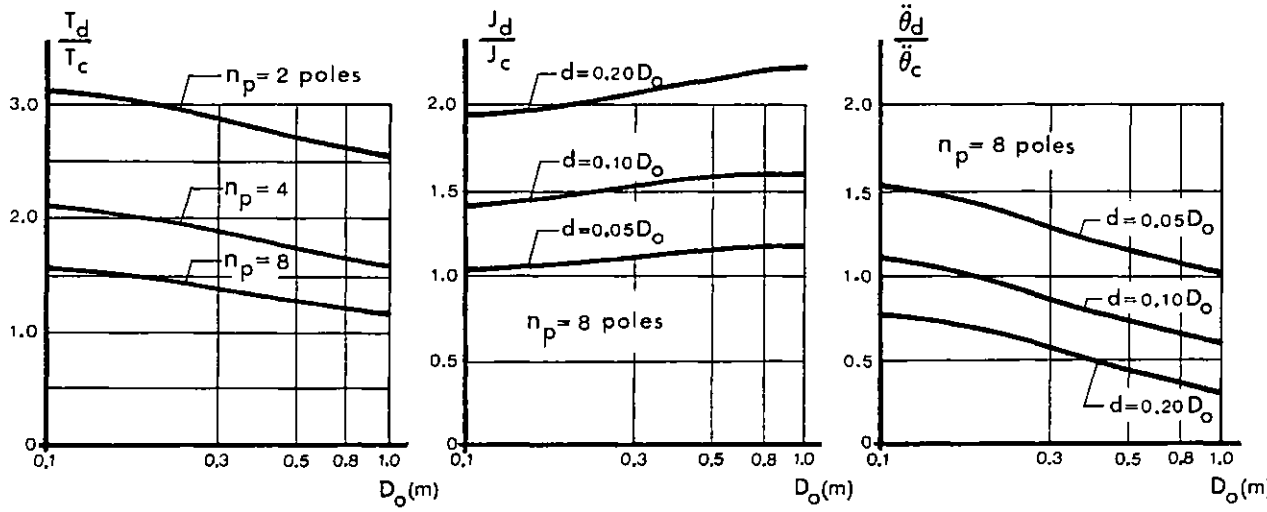

Fig. 1.26 - Comparative characteristics of disc and cylindrical machines

From these results it can be concluded that for the assumptions made the disc motor always produces higher torque, but the cylindrical version results improve as outer diameter and number of poles increase due to the reduction in backing iron and consequent increasing in air gap diameter.

The cylindrical motor rotors have lower inertias, becoming of the same order when d is less than 5% of the outer diameter. For rotor thickness of this order and n_p = 8 poles the initial angular acceleration of the disc motor becomes greater than that for cylindrical version, which is an advantage of the disc motor in servo applications. This shows the importance of keeping d as small as possible because of its direct proportionality to the disc rotor inertia. The prototype of the disc motor described in Chapter 5 uses a wound rotor of thickness d = 0.05 D_o and subsequently an "ironless" printed rotor of d = 0.02 D_o. The respective responses are compared.

1.13 - EQUIVALENT CIRCUIT AND PHASOR DIAGRAM OF A SYNCHRONOUS MOTOR

The single phase equivalent circuit of a cylindrical rotor synchronous motor is shown in fig. 1.27, in which the current flows in the conventionally positive direction for motor-mode operation [21]. The fundamental travelling-wave m.m.f.'s F_f and F_a produce flux linkages with the armature which induce corresponding components $E = K\phi_{af}\omega$ and $\omega L_a I$ of armature voltage. The resultant m.m.f. $\bar{F}_r$ produces the net air gap flux which

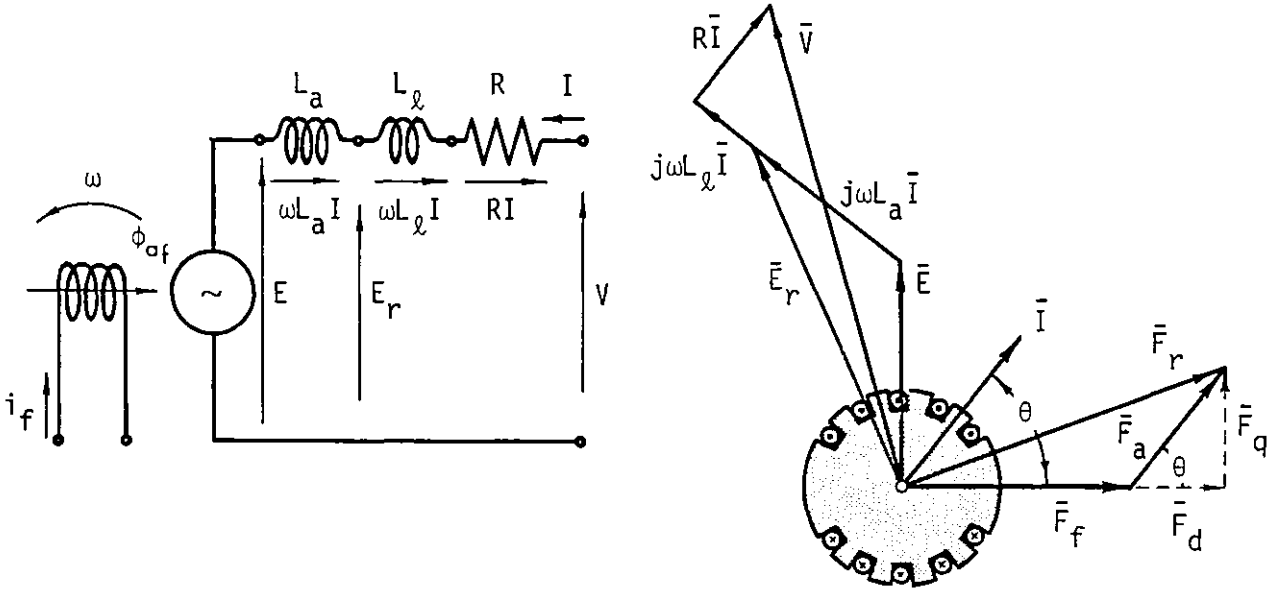

(a) - Equivalent circuit (b) - Phasor diagram

Fig. 1.27 - Equivalent circuit and phasor diagram for a cylindrical rotor synchronous motor

generates the corresponding resultant e.m.f. $\bar{E}_r = \bar{E} + j\omega L_a \bar{I}$. In addition, an actual machine winding will have resistance R and leakage inductance L_ℓ. It is evident, that the vector equation

$$\bar{V} = \bar{E} + R\bar{I} + j\omega(L_a + L_\ell)\bar{I} \qquad (1.103)$$

applies to this network and fig. 1.27(b) shows the corresponding phasor diagram. For a fixed value of separate excitation and constant rotor speed, the back e.m.f. E will be constant, but any change of load alters the resultant e.m.f. E_r.

In a salient pole machine, the m.m.f. diagram indicated in fig. 1.27(b) remains unchanged, but the flux density no longer takes the same ratio to the m.m.f. at every point. Hence, the flux density must be determined by resolving the armature m.m.f. into two sinusoidal components F_d and F_q along the two axes, giving the corresponding distorted waves B_{ad} and B_{aq} as shown in fig. 1.28. Cylindrical rotor theory when modified to take waveform into account could be applied to the salient pole machine

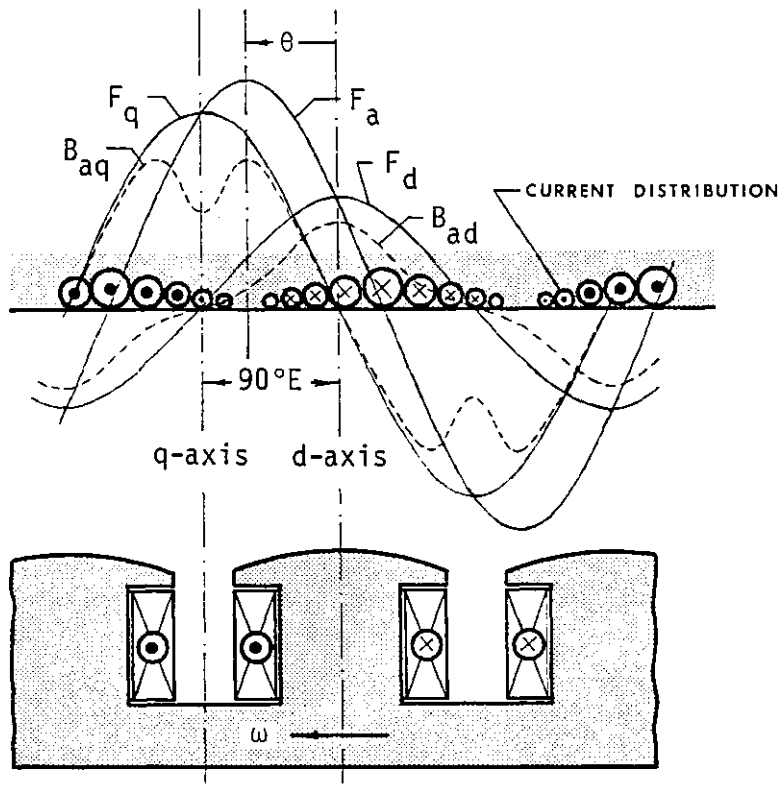

Fig. 1.28 - Sinusoidal armature m.m.f. wave and d and q-axis components

if the armature current were 90°E out of phase with the back e.m.f. $\bar{E}$ (current designated as I_d) or if it were in phase with $\bar{E}$ (current designated as I_q). In the first case the armature m.m.f. would react along the direct-axis and the direct axis inductance $L_d = L_{ad} + L_\ell$ would apply and the respective phasor diagram is shown in fig. 1.29(a). In the second case the armature m.m.f. reacts along the quadrature-axis and the quadrature-axis inductance $L_q = L_{aq} + L_\ell$ is used as shown in fig. 1.29(b).

Since only the air gap permeance is taken into account, the magnetic circuit is linear and the principle of superposition may be applied. Then, for a given current $\bar{I} = \bar{I}_d + \bar{I}_q$ displaced from the d-axis by an angle θ, the voltage applied to the motor must be

$$\bar{V} = \bar{E} + R\bar{I}_d + R\bar{I}_q + j\omega L_d \bar{I}_d + j\omega L_q \bar{I}_q \tag{1.104}$$

or

$$\bar{V} = \bar{E} + R\bar{I} + j\omega L_d \bar{I} - j\omega L_d(1 - \alpha)\bar{I}_q \tag{1.105}$$

where $\alpha = \frac{L_q}{L_d}$ is the saliency factor. If $\alpha = 1$ (cylindrical rotor), Eq. (1.105) reduces to Eq. (1.103). In Eq. (1.104) the vector $\bar{I}_d$ is

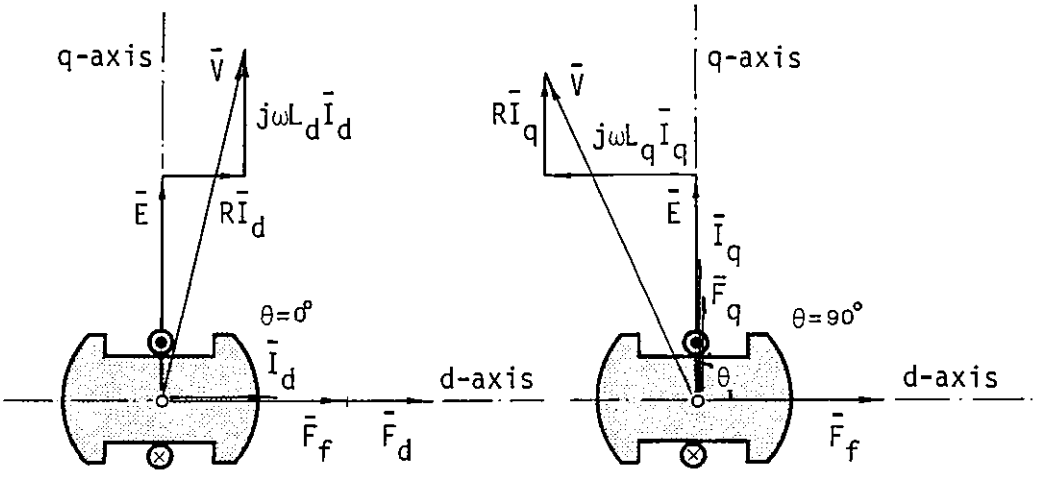

(a) - Current on d-axis (b) - Current on q-axis

Fig. 1.29 - Phasor diagram for salient pole motor with the armature m.m.f. (a) d-axis and (b) q-axis

called the direct-axis component of the current, and $\bar{I}_q$ is called the quadrature-axis component because they correspond to the components F_d and F_q of the m.m.f. along the two axes.

1.14 - INDUCTANCE CALCULATION

In a distributed winding of a synchronous machine, the total leakage inductance L_ℓ may be considered as the sum of the slot leakage inductance

$L_{s\ell}$ and end-winding inductance $L_{e\ell}$ and both are independent of rotor position, as can be seen in fig. 1.30.

In a salient pole machine, however, the air gap inductance L_a depends on the rotor position and varies between two extreme values for the d and q axis position. This variation depends also on the rotor excitation type used as will be shown in some detail in this section.

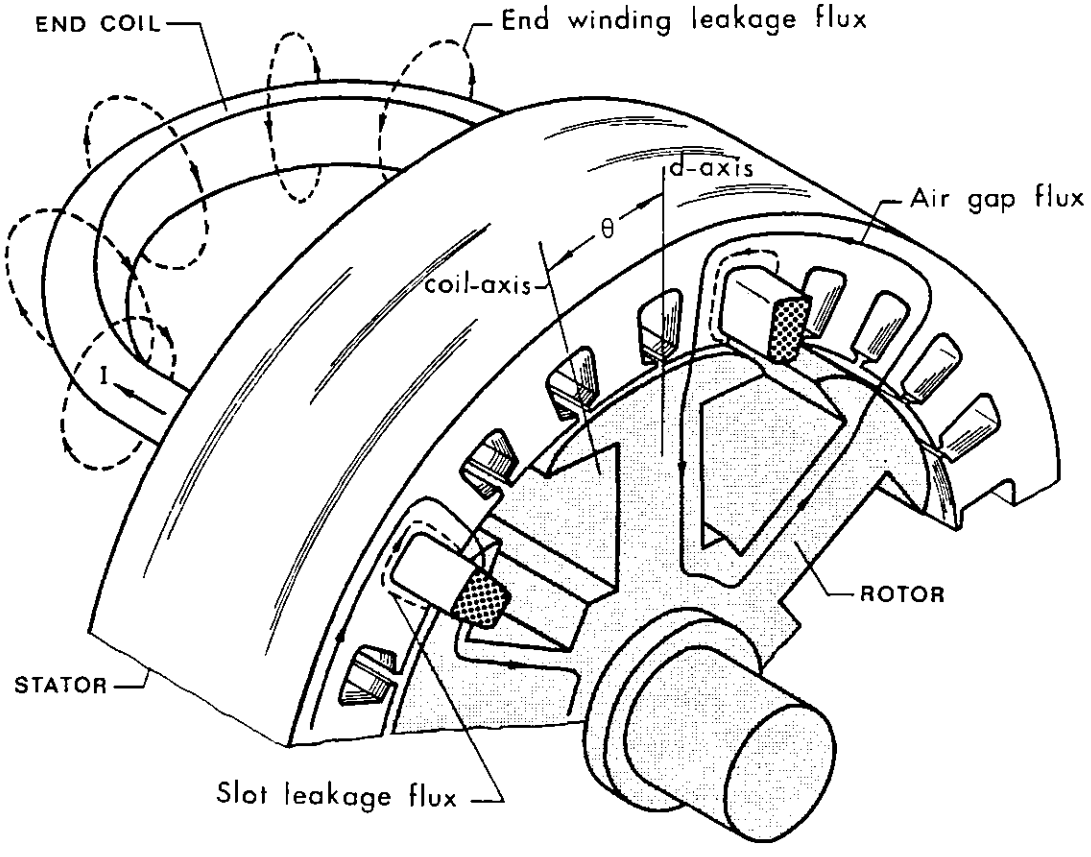

Fig. 1.30 - Leakage and air gap flux in a salient pole machine

Both L_ℓ and L_a are fundamental parameters for using in the equivalent circuit of the machine, and brief formulae for their evaluation are now presented.

1.14.1 - Expressions for leakage inductance

For the slot leakage inductance it is assumed that the machine has semi-closed slots and the flux paths in the slot are straight lines,

as shown in fig. 1.31. If the coil has n turns and an air gap axial length ℓ, calculation of the energy stored gives for the leakage inductance [22] the following expression:

$$L_{s\ell} = \mu_o n^2 \left[\frac{h_1}{3s} + \frac{h_2}{s} + \frac{2h_3}{a+s} + \frac{h_4}{a} \right] \ell = n^2 P_s \qquad (1.106)$$

where P_s is called the slot permeance. The slot leakage inductance may be also calculated using a numerical method and in Chapter 4 an example is given.

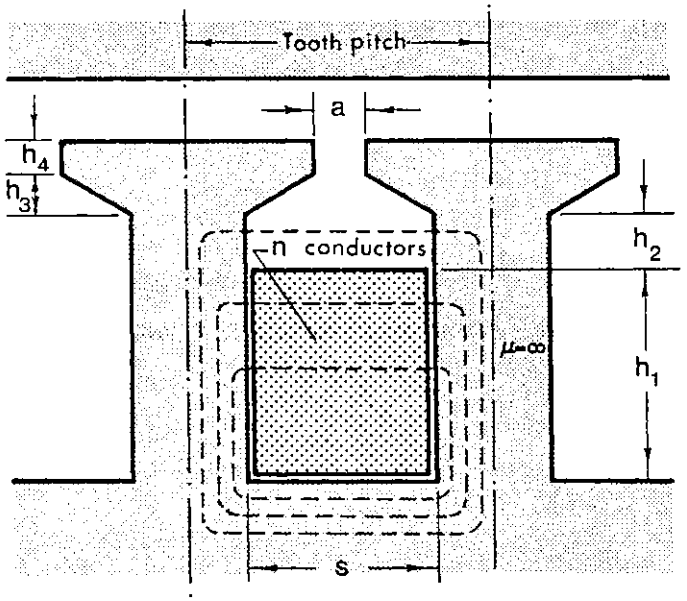

Fig. 1.31 - Slot leakage flux

The end-winding, or overhang, leakage inductance may be calculated approximately by Alger's formula [23] suitable for use with basket windings and it is given by:

$$L_{e\ell} = 0.3\, \mu_o m N^2 (3y_r - 1) D_g \qquad (1.107)$$

where D_g is the stator inside diameter in meters, $y_r = 1 - \beta/\pi$ the fractional winding pitch, m the number of phases and N the number of conductors per pole per phase given by Eq. (1.47).

Alternatively, assuming round end coils as shown in fig. 1.32(a), the overhang inductance may be worked out using the expression for the inductance of a single turn of mean radius R and cross sectional area πr^2 shown in fig. 1.32(b). Using first principles Rayleigh and Niven [24]

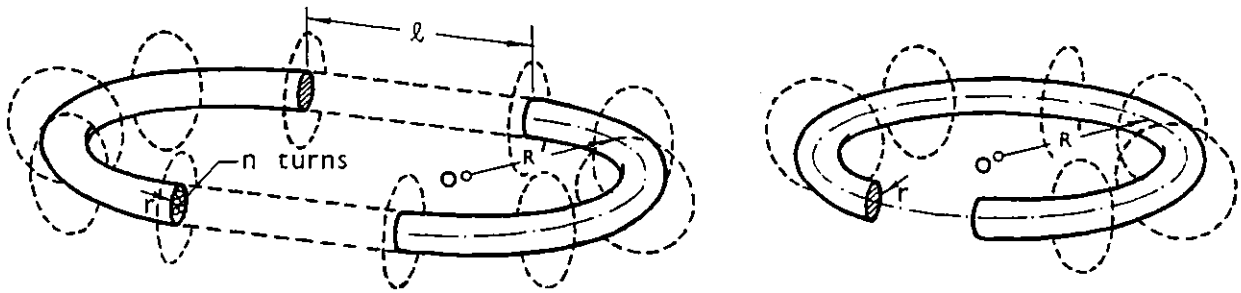

(a) - Round coil (b) - Single circular turn

Fig. 1.32 - Overhang leakage for a round coil

derived the following expression for the inductance:

$$L = \mu_o R \left[\left(1 + \frac{r^2}{8R^2} \right) \log_e \frac{8R}{r} + \frac{r^2}{24R^2} - 1.75 \right] \qquad (1.108)$$

For a coil with n turns in which the bundle of the conductors has a radius r, assuming that the q coils/pole/phase are linked n_p times in one phase the total end-winding leakage inductance is given by:

$$L'_{el} = n_p (qn)^2 L \qquad (1.109)$$

The overhang inductance per phase of the machine may be then obtained by averaging the results given by Eq. (1.107) and Eq. (1.109).

1.14.2 - Air gap inductance of q coils linked

Fig. 1.33 illustrates a distributed winding with q coils per pole per phase spanned β degrees and assumed all in series carrying a current I. A salient pole machine with variable air gap and the rotor pole axis displaced by an angle θ from the m.m.f. axis is considered. The air

gap inductance for the group of q coils and rotor position θ is now determined, and the general expression obtained is thought to be new.

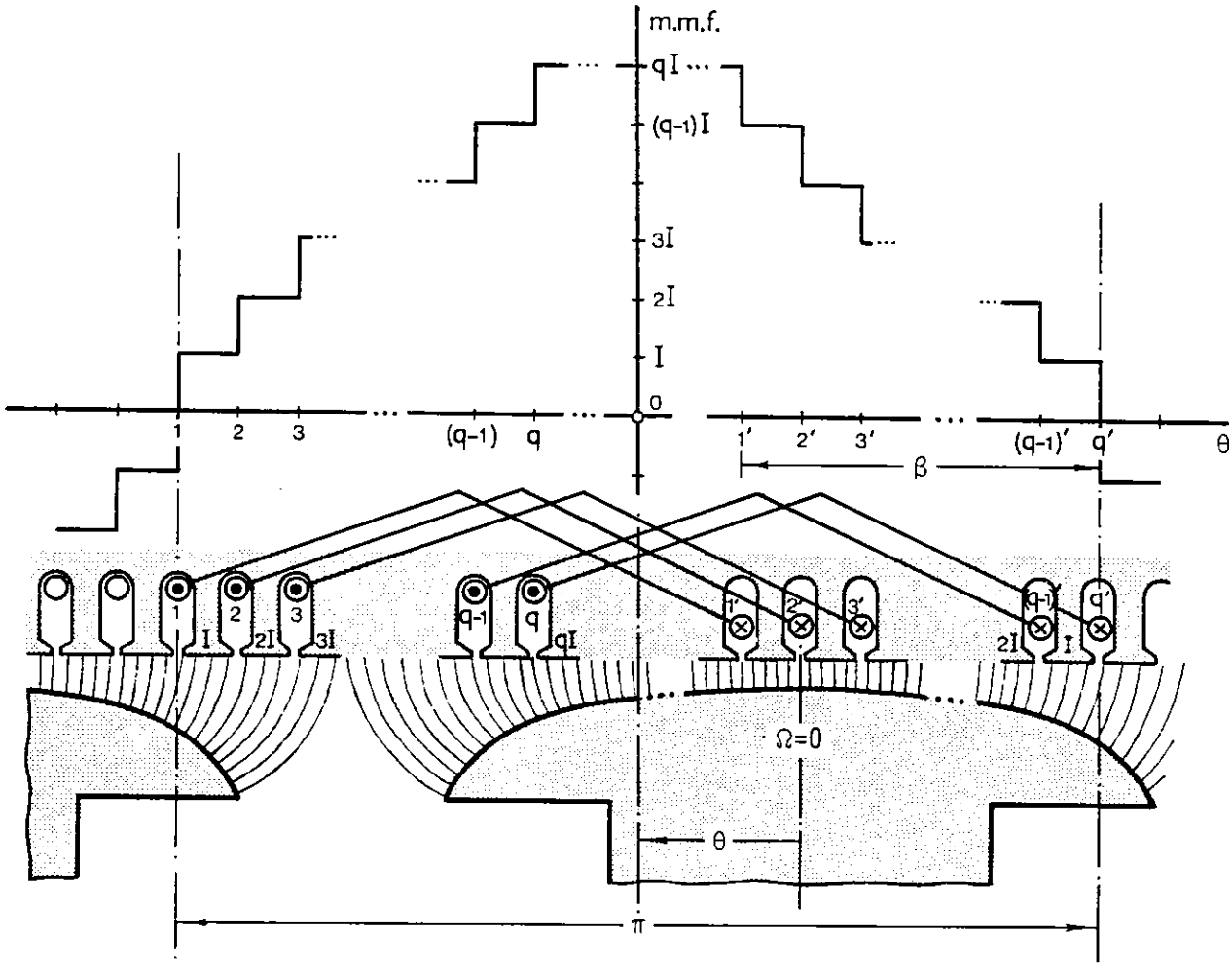

Fig. 1.33 - M.m.f. distribution for q coils in series

If ϕ_{ij} is the air gap flux between the typical conductors i and j, then the air gap flux linked with each coil is

$$\phi_1 = \phi_{12} + \phi_{21'} = \phi_{12} + \phi_{2q} = \phi_{q1'}$$

$$\phi_2 = \phi_{23} + \phi_{32'} = \phi_{23} + \phi_{3q} + \phi_{q1'} + \phi_{1'2'}$$

$$\phi_3 = \phi_{34} + \phi_{43'} = \phi_{34} + \phi_{4q} + \phi_{q1'} + \phi_{1'3'}$$

$$\vdots$$

$$\phi_{q-1} = \phi_{(q-1)q} + \phi_{q(q-1)'} = \phi_{(q-1)q} + 0 + \phi_{q1'} + \phi_{1'(q-1)'}$$

$$\phi_q = \phi_{q1'} + \phi_{1'q'} = \phi_{q1'} + \phi_{1'q'}$$

Hence, the total flux linked with the q coils in series becomes:

$$\phi = \sum_{i=1}^{q} \phi_i = \phi_{12} + \phi_{23} + \phi_{34} + \ldots + \phi_{(q-1)q} + \phi_{2q} + \phi_{3q} + \phi_{4q} + \ldots + \phi_{(q-1)q} +$$

$$+ q\phi_{q1'} + \phi_{1'2'} + \phi_{1'3'} + \ldots + \phi_{1'(q-1)'} + \phi_{1'q'}$$

But

$$\phi_{1q} = \phi_{12} + \phi_{23} + \phi_{34} + \ldots + \phi_{(q-1)q}$$

and so,

$$\phi = \phi_{1q} + \phi_{2q} + \phi_{3q} + \ldots + \phi_{(q-1)q} + q\phi_{q1'} + \phi_{1'2'} + \phi_{1'3'} + \ldots + \phi_{1'(q-1)'} + \phi_{1'q'}$$

If each individual coil has n turns carrying a current i per conductor the total flux linkage is $\psi = n\phi$ and $I = ni$. The total air gap inductance per pole is by definition:

$$L = \frac{\psi}{i} = n^2 \frac{\phi}{I}$$

Hence, for a rotor position θ:

$$L(\theta) = n^2 \frac{1}{I} (\phi_{1q} + \ldots + \phi_{(q-1)q} + q\phi_{q1'} + \phi_{1'2'} + \ldots + \phi_{1'q'}) \qquad (1.110)$$

This expression can be also written in terms of air gap permeance. Since ϕ = m.m.f.P, assigning to the stator surface the m.m.f. distribution and assuming zero magnetic potential on the rotor pole surface:

$$\phi_{1q} = \left[P_{12} + 2P_{23} + \ldots + (q-1)P_{(q-1)q}\right] I \qquad \phi_{1'2'} = (q-1)P_{1'2'} I$$

$$\phi_{2q} = \left[2P_{23} + \ldots + (q-1)P_{(q-1)q}\right] I \qquad \phi_{1'3'} = \left[(q-1)P_{1'2'} + (q-2)P_{2'3'}\right] I$$

$$\phi_{(q-1)q} = (q-1)P_{(q-1)q} I \qquad \phi_{1'q'} = \left[(q-1)P_{1'2'} + \ldots + P_{(q-1)'q'}\right] I$$

where P_{ij} is the air gap permeance of the flux tube between conductor i and j (see fig. 1.33). Hence, substitution of these values into Eq. (1.110) gives:

$$L(\theta) = n^2\Big[P_{12} + 2^2P_{23} +\ldots+ (q-1)^2P_{(q-1)q} + q^2P_{q1'} + (q-1)^2P_{1'2'} + \\ + (q-2)^2P_{2'3'} +\ldots+ P_{(q-1)'q'}\Big] \quad (1.111)$$

This is the general equation for the air gap inductance of q coils linked. Eq. (1.111) shows that the air gap inductance depends on the permeance under the stator surface and therefore of the type of pole used. Two situations, one with coil-excited poles and another with permanent magnet excitation, are now compared.

a) - Coil-excited poles

A two phase distributed-winding and an unsaturated iron salient rotor is considered. For the particular case of q = 2 coils/pole/phase Eq. (1.111) reduces to

$$L(\theta) = n^2\Big[P_{12} + 4P_{21'} + P_{1'2'}\Big] \quad (1.112)$$

and the air gap inductance is calculated for the rotor at the d and q-axis positions, as shown in fig. 1.34.

For the d-axis rotor position, and using the notation of the diagram, the air gap permeances are

$$P_{12} = P_{1'2'} = P_1 = \mu_o \frac{S}{g_1}$$

$$P_{21'} = 2P_2 = 2\mu_o \frac{S}{g_2}$$

where S is the mean tooth surface above the pole and g_1, g_2 the mean air

gap length. Assuming, for example, $g_1 = 2g_2$ is $P_2 = 2P_1$, and from Eq. (1.112) the d-axis inductance becomes:

$$L_d = n^2\left[P_1 + 4 \times 2 \times 2P_1 + P_1\right] = n^2 18P_1 \qquad (1.113)$$

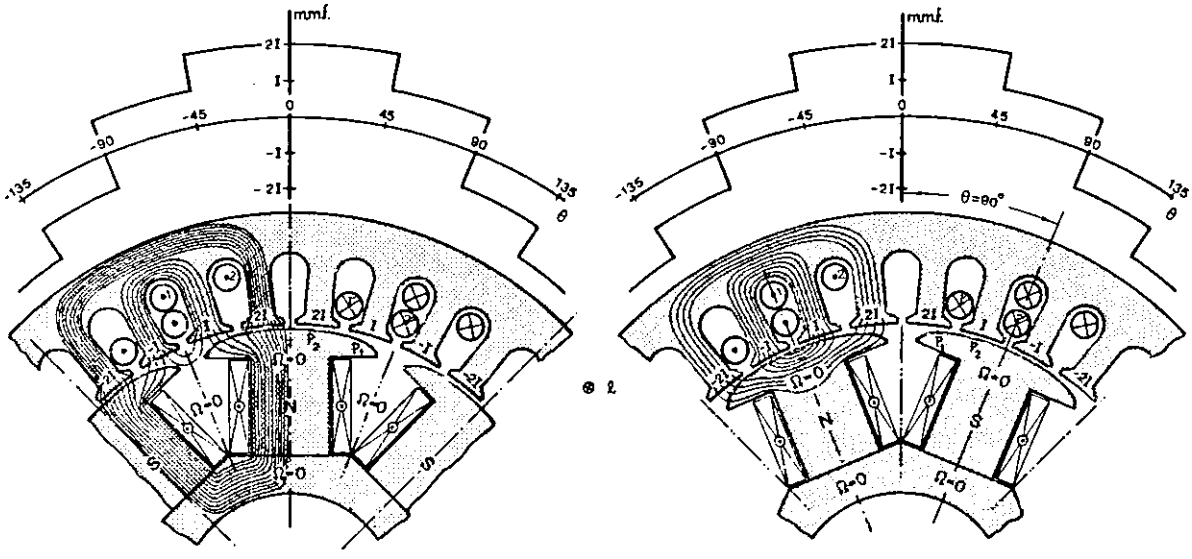

(a) - Current on d-axis (b) - Current on q-axis

Fig. 1.34 - Path of flux on the direct and quadrature-axis for coil excited poles

For the q-axis rotor position the tooth permeances are now related by:

$$P_{12} = P_{1'2'} = P_2 = 2P_1$$

$$P_{21'} = 2P_1$$

and substitution in Eq. (1.112) gives:

$$L_q = n^2\left[2P_1 + 4 \times 2P_1 + 2P_1\right] = n^2 12P_1 \qquad (1.114)$$

Comparison of Eq. (1.113) and Eq. (1.114) shows that

$$L_d = 1.5\,L_q \qquad (1.115)$$

and therefore for coil-excited poles $L_d > L_q$ as expected.

b) - Poles with permanent magnet excitation

It will be shown in the next chapter that when metallic magnets are used to produce the motor field excitation, they tend to require iron pole-piece protection against armature reaction. Such a rotor is shown in fig. 1.35 and again the d and q-axis positions are considered.

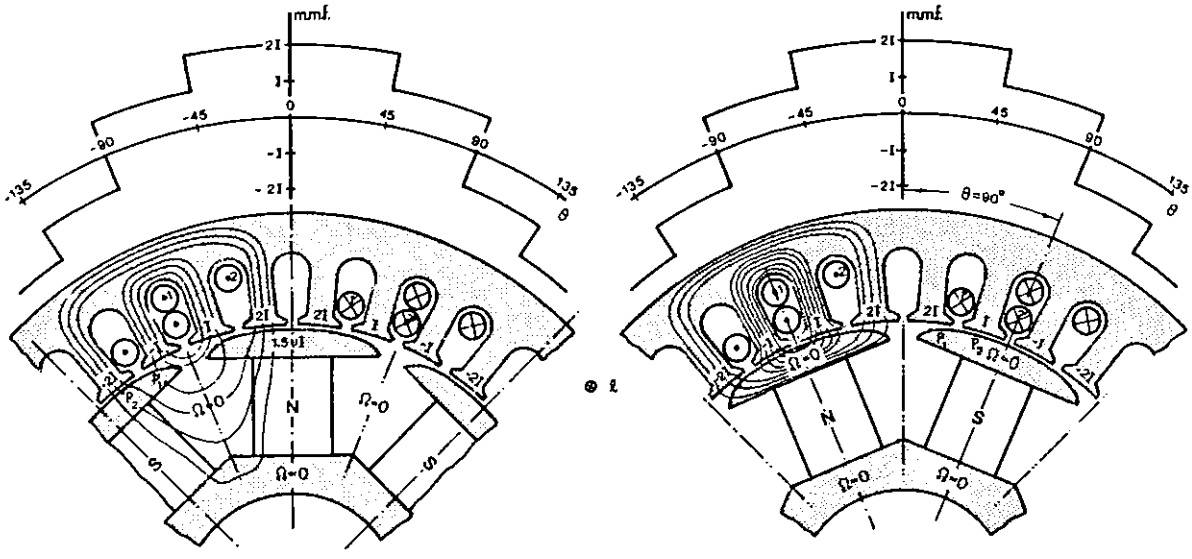

(a) - Current on d-axis (b) - Current on q-axis

Fig. 1.35 - Path of flux on the direct and quadrature-axis for permanent magnet excitation

With q-axis current, the radial plane through the centre of the permanent magnet and pole piece must be, by symmetry, at zero magnetic potential with respect to the stator m.m.f. Consequently, the pole itself must also be at zero potential. With d-axis current the interpolar bi-sector is also, by symmetry, at zero magnetic potential and hence so is the rotor backing iron. Since the permanent magnet permeability is much less than iron pole piece permeability, it follows that, with d-axis current, the pole piece must be at non-zero magnetic potential $1.5\nu I$ with respect to the stator m.m.f. [5]. The coefficient $\nu = 1/(1 + P_m/P_o)$ depends, of course, on the relative permeance values of the regions below the pole piece P_m and above P_o. For poles in iron $(P_m/P_o) = \infty$ and $\nu = 0$, as seen before.

Eq. (1.110) for q = 2 coils/pole/phase reduces to

$$L(\theta) = n^2 \frac{1}{I} (\phi_{12} + 2\phi_{21'} + \phi_{1'2'}) \tag{1.116}$$

where the fluxes for the d-axis position are now:

$$\phi_{12} = P_{12}(I - 1.5\nu I) = P_1(1 - 1.5\nu)I = \phi_{1'2'}$$

$$\phi_{21'} = P_{21'}(2I - 1.5\nu I) = 2P_2(2 - 1.5\nu)I$$

Substitution into Eq. (1.116) and putting that $P_2 = 2P_1$, gives

$$L_d = n^2(18 - 15\nu)P_1 \tag{1.117}$$

which is much less than the respective value given by Eq. (1.113). For a typical $(P_m/P_o) = 0.25$ ratio is $\nu = 0.8$ and then Eq. (1.117) gives $L_d = n^2 6P_1$.

Comparison of fig. 1.34 and fig. 1.35 shows that the q-axis inductance for permanent magnet excitation is roughly equal to the q-axis inductance with coil excitation, i.e., $L_q = n^2 12P_1$. It follows therefore that, on the assumptions made, for permanent magnet excitation

$$L_d = 0.5L_q \tag{1.118}$$

Assuming sinusoidal variation for $L(\theta)$, and from Eq. (1.115) and Eq. (1.118), a typical plot of the air gap inductance for permanent magnet and coil-excited salient pole synchronous machine is shown in fig. 1.36.

Eq. (1.12) shows that the reluctance torque of a salient pole synchronous motor depends critically on the air gap inductance variation.

Hence, as will be shown later, different total torque versus rotor angle

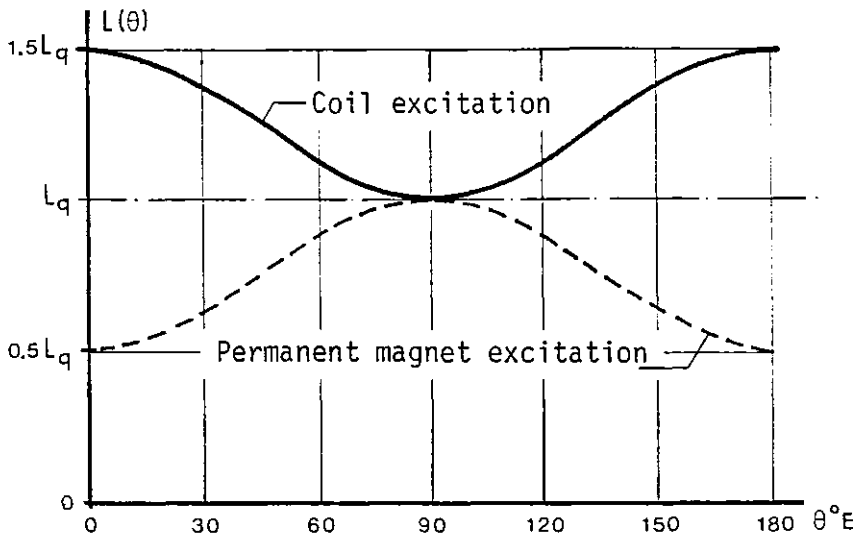

Fig. 1.36 - Air gap inductance variation for permanent magnet and coil excitation

characteristics are expected depending on whether coil or permanent magnet excitation is used.

1.15 - STATOR FLUX DENSITY ON LOAD

For the purposes of stator design, a knowledge of field flux density on load in critical regions of the magnetic circuit is necessary. A two-phase double-layer winding with q = 2 coils/pole/phase and a rotor excitation field flux density with a sinusoidal distribution around the stator surface with a peak magnitude $\hat{B}$ is assumed. The synchronous motor is also assumed current-fed at 90° torque angle with a sinusoidal current of peak value $\hat{I}$ per coil. Under these conditions, the regions of the magnetic circuit where maximum flux density may occur are the roots of some stator teeth and in the stator core in the interpolar region due to the rotor excitation flux. For semi-closed slots, high flux density may also be expected in tooth tips due to slot leakage flux. Two extreme situations, one for the instant of peak current in one phase and another

for equal currents in both phases, as shown in fig. 1.37, are examined. Expressions for flux density at the roots of tooth 1 and tooth 2 for both conditions are now derived. This extends Ashen's work [5], giving a general useful formulation rather than using specific numerical terms.

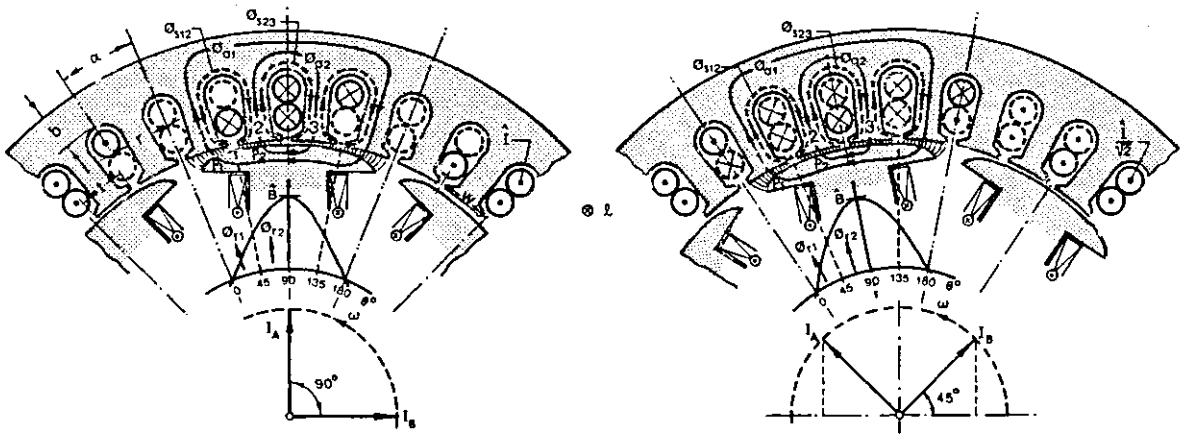

(a) - Instant $i_a = \hat{I}$, $i_b = 0$ (b) - Instant $i_a = i_b = \frac{\hat{I}}{\sqrt{2}}$

Fig. 1.37 - Flux components under load condition

Denoting by ϕ_{a1} and ϕ_{a2} the stator driven fluxes crossing the air gap into tooth 1 and tooth 2, ϕ_{r1} and ϕ_{r2} the excitation rotor fluxes entering tootn 1 and tooth 2 respectively and ϕ_{s12} and ϕ_{s23} the slot flux leakage, then the flux ϕ_1 at root of tooth 1 is

$$\phi_1 = \phi_{s12} + \phi_{a1} + \phi_{r1} \tag{1.119}$$

Similarly, at the root of tooth 2

$$\phi_2 = \phi_{s23} - \phi_{s12} + \phi_{a2} + \phi_{r2} \tag{1.120}$$

and the flux components are calculated as follows:

a) - Stator driven fluxes

Assuming infinite permeability for iron and denoting by P_1 and P_2 the air gap permeances for teeth 1 and 2, the stator driven fluxes

for the condition of peak current in one phase are:

$$\phi_{a1} = 4\hat{I}\,\frac{P_1}{2} = 2\hat{I}\,\mu_o\,\frac{t\ell}{g_{av1}} \tag{1.121}$$

$$\phi_{a2} = 2\hat{I}\,\frac{P_2}{2} = \hat{I}\,\mu_o\,\frac{t\ell}{g_{av2}} \tag{1.122}$$

and for the condition of equal currents,

$$\phi_{a1} = 6\,\frac{\hat{I}}{\sqrt{2}}\,\frac{P_1}{2} = \frac{3}{2}\sqrt{2}\,\hat{I}\,\mu_o\,\frac{t\ell}{g_{av1}} \tag{1.123}$$

$$\phi_{a2} = 2\,\frac{\hat{I}}{\sqrt{2}}\,\frac{P_2}{2} = \frac{1}{2}\sqrt{2}\,\hat{I}\,\mu_o\,\frac{t\ell}{g_{av2}} \tag{1.124}$$

where $t\ell$ represents the air gap tooth surface and g_{av} the average air gap length.

b) - Slot leakage fluxes

In order to calculate the slot leakage fluxes an equivalent rectangular slot fully filled with copper is assumed, as illustrated in fig. 1.38 for the condition of peak current in one phase. Then,using

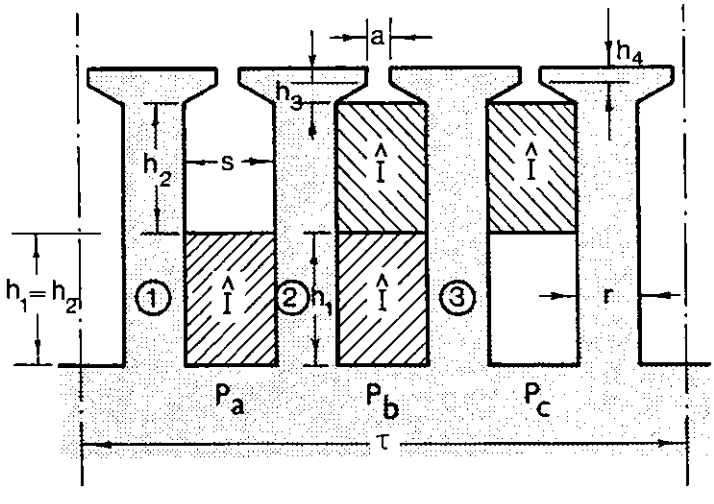

Fig. 1.38 - Coil distribution for one phase

the dimensions shown in the diagram and according to Eq. (1.106), the slot permeance of each slot of the group is:

$$P_a = \mu_o \left[\frac{h_1}{3s} + \frac{h_2}{s} + \frac{2h_3}{a+s} + \frac{h_4}{a} \right] \ell \tag{1.125}$$

$$P_b = \mu_o \left[\frac{2h_1}{3s} + \frac{2h_3}{a+s} + \frac{h_4}{a} \right] \ell \tag{1.126}$$

$$P_c = \mu_o \left[\frac{h_1}{3s} + \frac{2h_s}{a+s} + \frac{h_4}{a} \right] \ell \tag{1.127}$$

Hence, the leakage fluxes for the condition of peak current in one phase are given by:

$$\phi_{s12} = \hat{I} P_a = \mu_o \hat{I} \left[\frac{4h_1}{3s} + \frac{2h_3}{a+s} + \frac{h_4}{a} \right] \ell \tag{1.128}$$

$$\phi_{s23} = 2\hat{I} P_b = 2\mu_o \hat{I} \left[\frac{2h_1}{3s} + \frac{2h_3}{a+3} + \frac{h_4}{a} \right] \ell \tag{1.129}$$

Similarly, with equal currents in each phase

$$\phi_{s12} = \phi_{s23} = 2 \frac{\hat{I}}{\sqrt{2}} P_b = \sqrt{2}\, \mu_o \hat{I} \left[\frac{2h_1}{3s} + \frac{2h_3}{a+s} + \frac{h_4}{a} \right] \ell \tag{1.130}$$

c) - Excitation fluxes

If α_{elect} is the slot pitch angle in electrical degrees corresponding to a slot pitch w at stator surface, then the excitation fluxes entering tooth 1 and tooth 2 are respectively

$$\phi_{r1} = \frac{w\ell}{\alpha_{elect}} \int_{\theta=0}^{\theta=\alpha_{elect}} \hat{B} \sin\theta \, d\theta = \frac{w\ell}{\alpha_{elect}} \hat{B} \left[\cos\theta \right]_{\alpha_{elect}}^{0} \tag{1.131}$$

$$\theta_{r2} = \frac{w\ell}{\alpha_{elect}} \int_{\theta=\alpha_{elect}}^{\theta=2\alpha_{elect}} \hat{B} \sin\theta \, d\theta = \frac{w\ell}{\alpha_{elect}} \hat{B} \left[\cos\theta \right]_{2\alpha_{elect}}^{\alpha_{elect}} \tag{1.132}$$

Usually the slots are skewed by a centre angle $\gamma = \alpha_{elect}$, and so the flux excitation should take into account the skewing. Using Simpson's

rule for three stator positions, as shown in fig. 1.39, Eq. (1.131) and Eq. (1.132) for the particular case $\gamma = \alpha_{elect} = \pi/4$ becomes

$$\phi_{r1} = \frac{4}{\pi} w\ell\hat{B}\,\frac{1}{6}\Big[\,(\cos(-22.5)-\cos\,22.5) + 4(\cos\,0 - \cos\,45) + (\cos\,22.5 - \cos 67.5)\,\Big]$$

$$= 0.37\, w\ell\hat{B} \qquad (1.133)$$

and

$$\phi_{r2} = \frac{4}{\pi} w\ell\hat{B}\,\frac{1}{6}\Big[(\cos\,22.5 - \cos\,67.5) + 4(\cos\,45 - \cos\,90) + (\cos\,67.5 - \cos\,112.5)\Big]$$

$$= 0.88\, w\ell\hat{B} \qquad (1.134)$$

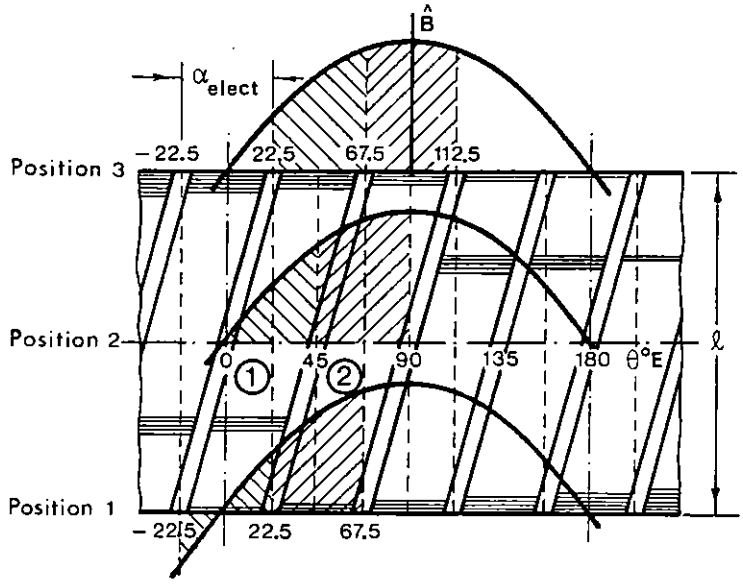

Fig. 1.39 - Average of excitation flux for $\gamma = \alpha_{elect} = \pi/4$

Substitution of flux components into Eq. (1.119) and Eq. (1.120) and with a tooth width r at the root, the root flux densities for the instant of peak current in one phase are given by:

$$B_1 = \frac{\phi_1}{r\ell} = \frac{\mu_0}{r}\left[\frac{4h_1}{3s} + \frac{2h_3}{a+s} + \frac{h_4}{a} + 2\,\frac{t}{g_{av1}}\right]\hat{I} + 0.37\,\frac{w}{r}\,\hat{B} \qquad (1.135)$$

$$B_2 = \frac{\phi_2}{r\ell} = \frac{\mu_r}{r}\left[\frac{2h_3}{a+s} + \frac{h_4}{a} + \frac{t}{g_{av2}}\right]\hat{I} + 0.88\,\frac{w}{r}\,\hat{B} \qquad (1.136)$$

and for the instant of equal currents in each phase

$$B_1' = 2\frac{\mu_o}{r}\left[\frac{2h_1}{3s} + \frac{2h_3}{a+s} + \frac{h_4}{a} + \frac{3}{2}\frac{t}{g_{av1}}\right]\hat{I} + 0.37\frac{w}{r}\hat{B} \qquad (1.137)$$

$$B_2' = \frac{2}{2}\frac{\mu_o}{r}\frac{t}{g_{av2}}\hat{I} + 0.88\frac{w}{r}\hat{B} \qquad (1.138)$$

Since $\hat{I} = sh_1\hat{J}_c$ where $\hat{J}_c$ is the peak current density and $w/r = 1 + s/r$, the above expressions show that the root flux density depends critically on the slot width/tooth width s/r ratio, slot depth $2h_1$ and t/g_{av} ratio. It is difficult to generalise which tooth is more affected, but for usual values of $\hat{J}_c$, $\hat{B}_c$, slot depth $2h_1$ and a fixed value of s/r, it is certainly true that Eq. (1.136) gives the highest value. Fixing B_2 to iron saturation level, it is most important to note that for small t/g_{av} ratio the ratio s/r can be substantially increased, giving more room for copper. This design is possible if permanent magnets with high coercivity are used for rotor excitation, as will be shown in Chapters 4 and 6.

To minimise tooth ripple it is desirable to make the slot opening a as small as possible, but this dimension is limited also by saturation. The maximum tooth tip flux density, occurring between tooth 2 and tooth 3 with peak current in one phase, is

$$B_t = \mu_o\frac{2\hat{I}}{a} \qquad (1.139)$$

Finally, the flux density in the backing iron with thickness b, due to the excitation flux, is

$$B_c = \frac{4}{\pi}\frac{w}{b}\hat{B} \qquad (1.140)$$

since half pole pitch is 2w. For a given $\hat{J}_c$ and $\hat{B}$ the above relationships help to establish suitable stator proportions.

In this chapter some basic treatments of a number of topics have been presented. They serve to support the following work and many of the formulae stated will be used later.

☆ ☆ ☆

CHAPTER 2

PERMANENT MAGNET FIELD ANALYSIS

2.1 - GENERALITIES

Permanent magnets have been used for many years to provide the excitation for some types of rotating electrical machines. Permanent magnet excited machines do not require field supply systems, sliprings or brush gear, and hence the possibility exists of reductions in weight, bulk and complexity [25]. Since no energy is expended in maintaining the field it should be also possible to obtain an improvement in the machine efficiency compared with an equivalent wound field.

The revolutionary improvements made in permanent magnet materials in recent years and the ingenious use of these materials in machine applications has initiated a succession of important developments. In brief, one can say that the risk of demagnetisation is greatly reduced in modern design of permanent magnet machines, and the cost of a permanent magnet field system relative to a wound field system has in some cases changed dramatically.

Permanent magnet cost factors are still however significant, particularly when designs of medium and large machines are attempted, and any design technique must be accurate and flexible enough to ensure reasonably efficient use of the minimum quantity of permanent magnet material. Most of the basic analytical and numerical methods used to calculate the performance of a permanent magnet have been known for a long time [26, 27]. The scalar potential method of computing permanent magnetic fields gives an accurate prediction of performance and it will be described in some

detail after a discussion of the characteristics of the current permanent magnets available.

2.2 - FUNDAMENTAL PARAMETERS OF A PERMANENT MAGNET MATERIAL

Permanent magnet materials are differentiated from softer substances fundamentally by their large magnetic hysteresis loop. A comparison of magnetic hysteresis loops of a "soft" magnetic material and a "hard" material is shown in fig. 2.1(a).

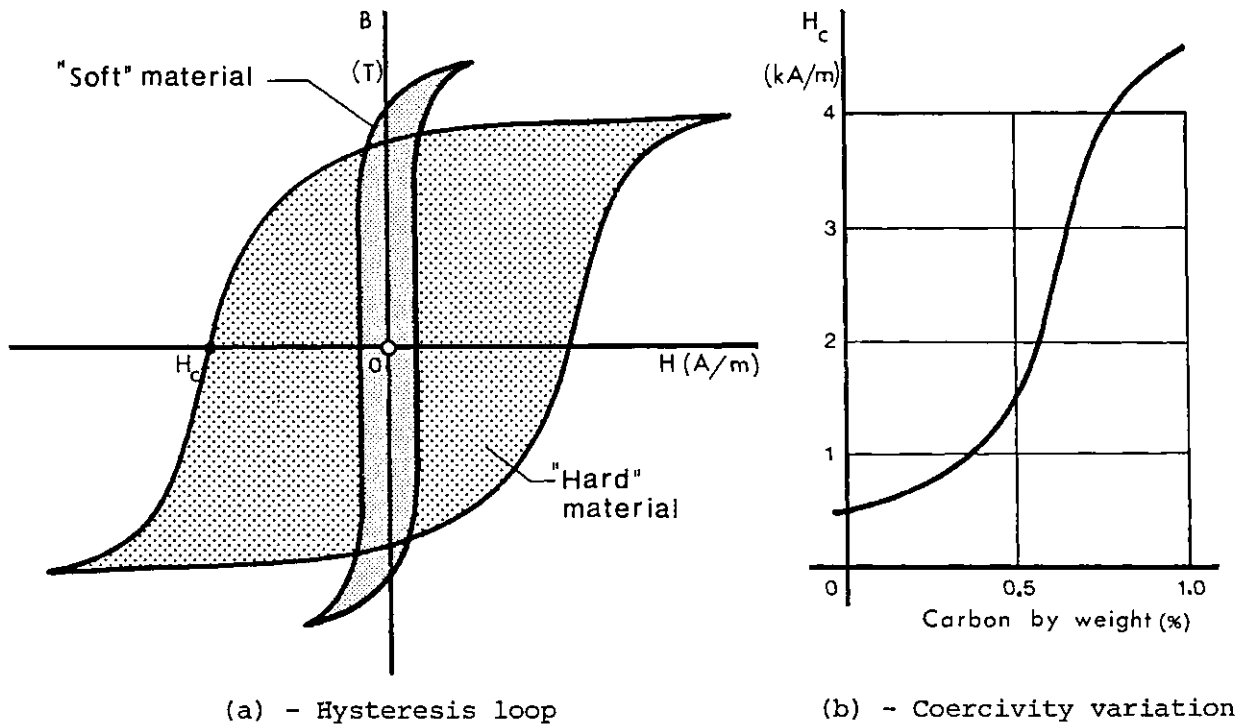

(a) - Hysteresis loop

(b) - Coercivity variation

Fig. 2.1 - Comparison of magnetic hysteresis loop of soft and hard materials

Two important parameters that are measures of the usefulness of the material for making permanent magnets can be immediately identified. The remanence, B_r, is the flux density that remains in the material after it has been fully magnetised and the magnetising force has been reduced to zero. The coercivity, H_c, is the negative magnetising force that must be applied to reduce the flux density in the material to zero, after it

has been fully magnetised. Modern metallurgic developments have provided materials in which both B_r and H_c are very large. Originally, the earliest materials used for permanent magnets, were iron to which carbon had been deliberately added. The presence of the carbon finely dispersed throughout the iron increases the hysteresis losses and therefore enlarges the area of the loop, but at the same time the material becomes mechanically glass hard. Fig. 2.1(b) shows approximately the coercivities attainable with different amounts of carbon in the iron [28].

For a permanent magnet, the region of the hysteresis loop in the second quadrant is the most important and this portion is designated by "demagnetisation characteristic". In this condition the magnet provides a source of both m.m.f. and magnetic flux which can be guided to the required location by means of a special shaping of the magnet or the addition of soft-iron pole pieces.

It should be pointed out that a permanent magnet is not a store of energy to be made available as required, otherwise the energy content would fall every time the magnet was used and would finally become exhausted. The energy of a permanent magnet is only so much potential energy and acts as a conservative system [29]. A magnet really does work each time it attracts a piece of iron, but an equal amount of work must be done to pull the iron away from the magnet.

2.2.1 - Intrinsic magnetisation or polarisation

If a ferromagnetic rod of cross-sectional S is magnetised with a single coil wound on its surface as shown in fig. 2.2, the flux ϕ in the rod consists of two components [30]: a component $\phi_1 = \mu_0 HS$ due to the coil and another component ϕ_2 due to the ferromagnetism. The field H in the material is uniform, and is the same as that in the coil without any material present, if the rod is sufficiently long. The flux appears from one end of the rod and re-enters the other, so that, viewed from

outside, each end appears as if it were a point source, or magnetic pole, of magnitude

$$m = \phi = \phi_1 + \phi_2$$

The rod is thus the magnetic analogue of an electric dipole, and if it is cut into shorter lengths, each will have the same effective pole strength. But the dipole moment of a short length ℓ is $m_2\ell$, where m_2 represents the contribution from the material alone, i.e.,

$$m_2 = \phi - \phi_1$$

and the dipole moment of the material, per unit volume, is

$$\frac{m_2\ell}{\ell S} = \frac{\phi\ell}{\ell S} - \frac{\phi_1\ell}{\ell S}$$

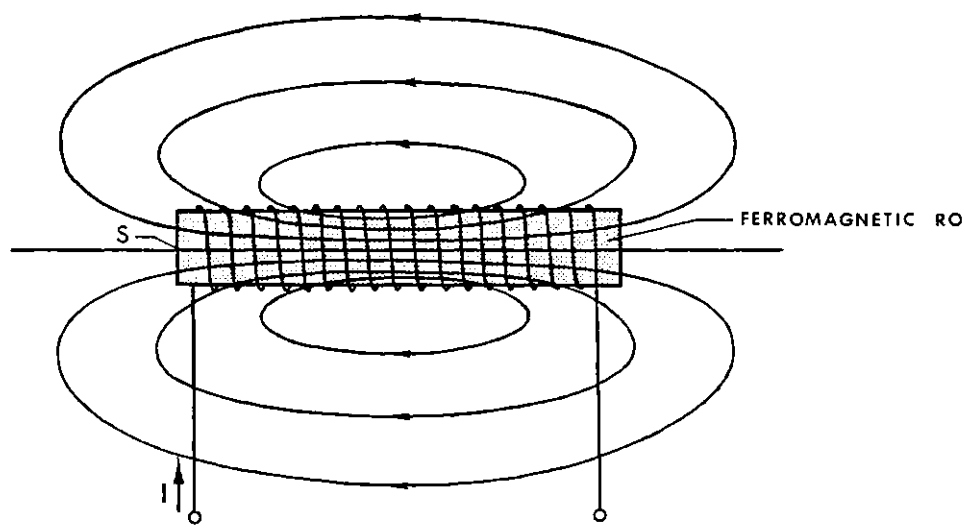

Fig. 2.2 - Magnetisation of a ferromagnetic rod

Denoting this quantity by the vector $\bar{M}$, measured in the direction of magnetisation, then

$$\bar{M} = \bar{B} - \mu_0\bar{H}$$

or

$$\bar{B} = \bar{M} + \mu_0\bar{H} \qquad (2.1)$$

Thus, subtracting from the normal flux density B the component $\mu_0 H$, which would be present if there were no magnetic material, the contribution

from the magnetic dipoles is obtained. This quantity $\bar{M}$ is numerically equal to the dipole moment per unit volume and is termed "intrinsic magnetisation or polarisation", since it represents the portion of flux density which is intrinsic to the material itself.

Eq. (2.1) is plotted in fig. 2.3 versus magnetising force for the virgin material. The flux density increases linearly with magnetising force in the case of air, but the normal flux density at first rises steeply and then may be increased without limit. The intrinsic magnetisation M, shown as the broken line, may be derived from both these curves. This gives that part of the flux density provided by the iron alone and the point where this curve becomes horizontal is the intrinsic saturation B_{is} with a value characterisitc of the material.

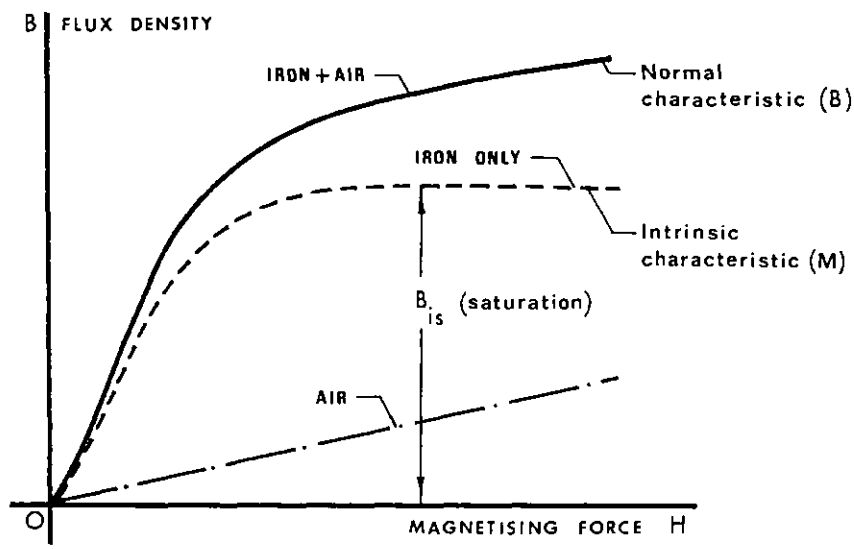

Fig. 2.3 - Magnetising characteristics for Iron and Air

If the magnetising force is steadily reduced to zero, the flux density will not follow the virgin magentisation curve due to the hysteresis (Greek hystereo = delay) of the material. Describing a complete cycle by application of a steadily increasing field of opposite polarity a closed major hysteresis loop is obtained as shown in fig. 2.4.

In the second and fourth quadrants the magnetising force and normal

flux density are opposite in sign and therefore, according to Eq. (2.1), the intrinsic characteristic lies outside of normal hysteresis loop. For a permanent magnet the two demagnetisation characteristics are shown in fig. 2.5, where the remanence B_r is the same for both curves. However the intrinsic coercive force H_{ci} is always greater than normal coercive force H_c. For many metallic magnets with low coercivity force these two values are nearly coincident. Nevertheless for high coercivity materials, such as ceramic and rare-earth type, the two curves are widely divergent and the difference between both coercivity values may be of the order of two or more.

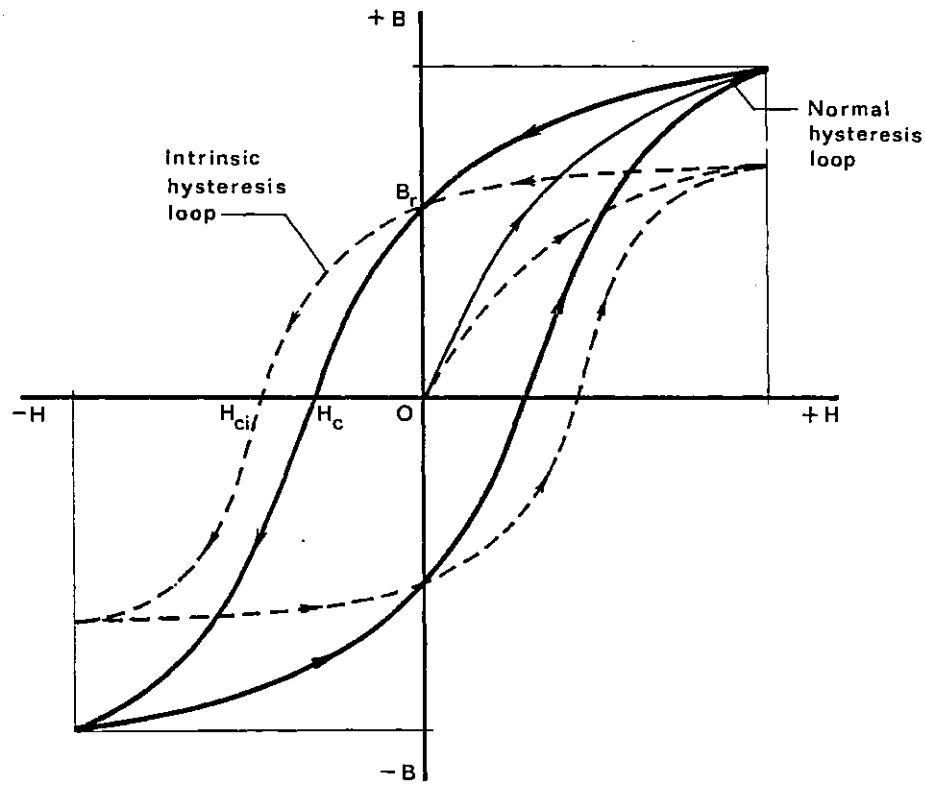

Fig. 2.4 - Major hysteresis loops for normal and instrinsic magnetisation

Although the normal demagnetisation characteristic is usually given by the manufacturer, it should be emphasized that it is the intrinsic characteristic which should be used as a basis for the calculation of a permanent magnet's performance. However, for most engineering applications of permanent magnets the normal characteristic may be employed [26], at least if metallic magnets are used where the difference

between the normal and instrinsic characteristics is negligible.

Several authors, such as Ireland [31], Gollhart and Beaudoin [32], have argued that, because of the comparatively large difference between B/H and M/H characteristics of the ferrite and rare-earth magnets, the

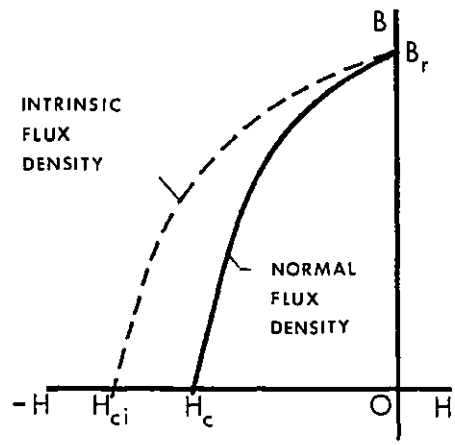

Fig. 2.5 - The second quadrant demagnetisation characteristics

treatment of these materials under dynamic conditions must be based on the intrinsic characteristic. However, Burnett and Overshott [33] have shown that the analysis of all permanent magnet types may be based on the normal characteristic, irrespective of the coercivity of the material.

2.2.2 - The various permeabilities

In simple terms, permeability is defined as the ratio of flux density to magnetising force and is an important parameter of a magnetic material and in particular of a permanent magnet. On the magnetisation curve shown in fig. 2.6 three such ratios are usually defined [26] as follows:

a) - Initial permeability

The initial permeability μ_i is the initial slope of the virgin magnetisation curve of the material and given by

$$\mu_i = \lim_{H \to 0} \frac{B}{H} = \tan \theta$$

It is found by extrapolating to zero measurements made at finite magnetising

force. The initial permeability is the same order as the gradient of the demagnetisation curve at the point of residual remanence B_r.

b) - Differential permeability

Differential permeability is defined by the gradient of the virgin magnetisation curve as

$$\mu_d = \frac{\Delta B}{\Delta H}$$

At inflection point I the permeability attains the maximum value for a magnetisation force approximate numerically equal to the intrinsic coercive force. If the flux density and the magnetising force are vectors with different directions, the permeability is a tensor.

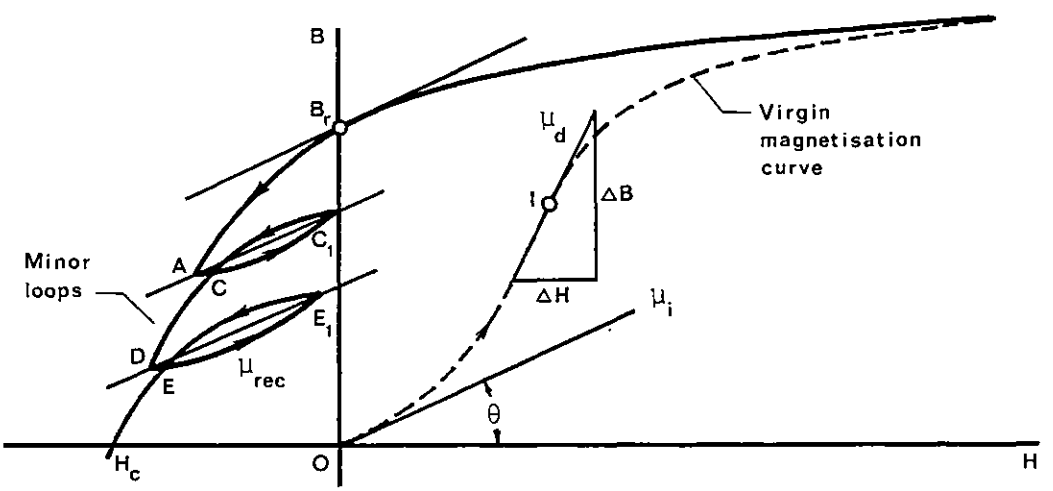

Fig. 2.6 - Definition of various permeabilities

c) - Recoil permeability

A permanent magnet is normally unstable, which means that the original working point is liable to shift due to changes in the magnetic circuit, external fields, temperature variations and mechanical vibrations. If the magnet is operating at point A (see fig. 2.6) and the demagnetising field is reduced, the flux density generally does not follow the major loop but a curve AC_1 is traced out. Increasing the magnetising force to the previous value a subsidiary hysteresis loop CC_1 is obtained. The

area enclosed by this minor loop is proportional to the energy dissipated as heat in the material, which is negligible in a permanent magnet. Then a straight line drawn through the points CC_1 may be used to represent the loop and is termed "recoil line". The slope of the recoil line is called the recoil permeability μ_{rec}.

When the permanent magnet is operating on the recoil line it is said to be stabilised. The stable condition can be reached by applying an external magnetising force which is switched ON and OFF several times (magnetic ageing) or assemble and disassemble the magnet. According to Heck [29], stabilisation can also be effected by taking the magnet some 20-30 times through a temperature interval from -20°C to +150°C.

An infinity of other minor loops may be traced such as EE_1, depending on the operating point considered. However, all the straight lines drawn through its tips have approximately the same slope and therefore the recoil permeability is nearly constant for any point on the demagnetisation characteristic. Then, the recoil permeability is also given by the slope at point of remanence B_r, which is itself of the same order of the initial permeability.

2.2.3 - The Energy Product

The energy product of a permanent magnet is defined as the quantity numerically equal to the area BH of the rectangle which can be fitted below the normal demagnetisation characteristic. It should be emphasized, however, that the energy product represented by (B, H) point on the demagnetisation curve is actually twice the true energy density, and also actually not the energy in the magnet but that in the air gap supplied by the magnet.

Usually the manufacturer supplies the energy product figure together with demagnetisation characteristic of the magnet and this can be done in two ways [29], as shown in fig. 2.7.

i) - The product of corresponding coordinates for all values of B and H is formed and plotted as a function of B in the first quadrant adjacent to the demagnetisation curve. The point P of maximum BH product may be readily determined.

ii) - When many demagnetisation characteristics are displayed in the same graph, a given BH energy product value is more simply found by plotting together a family of hyperbolae BH = Const. The particular hyperbola just touching the demagnetisation curve will quickly determine the $(BH)_{max}$ of the magnet.

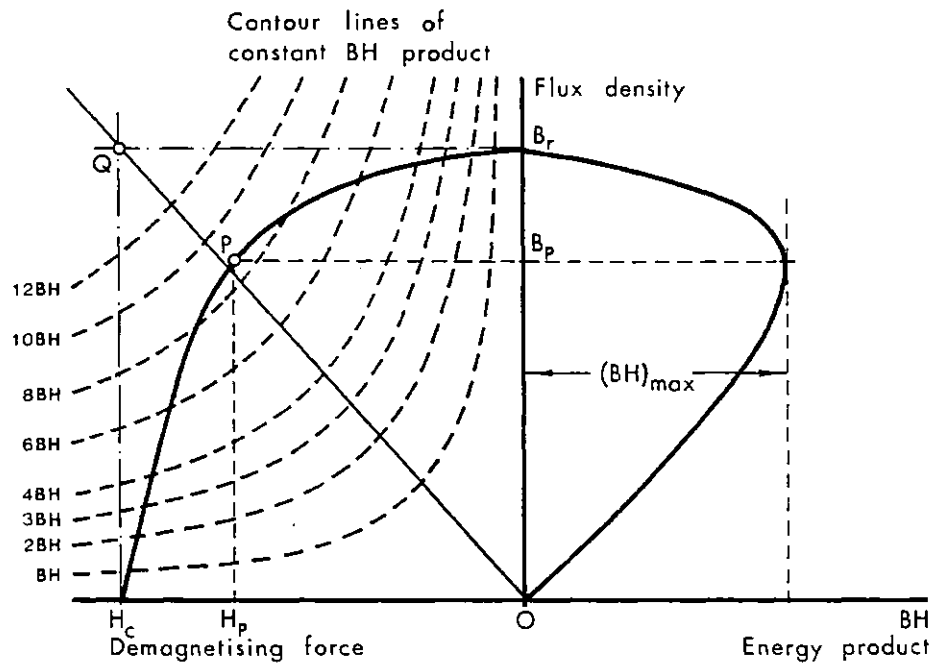

Fig. 2.7 - Energy product and family of hyperbolae BH = Const.

Both methods provide an easy reading of maximum energy product $(BH)_{max}$. Incidentally, the point of maximum BH product can be quickly approximated by drawing lines parallel to the axes through B_r and H_c points to intercept at Q forming a rectangle QB_rOH_c. The diagonal line OQ of this rectangle cuts approximately the demagnetisation curve at point P of the $(BH)_{max}$ product. This construction based on Lamont's law [26] is not quite accurate but it is often used as a starting point in dimensioning a permanent magnet.

The quantity $(BH)_{max}$ has the dimensions of energy per unit volume (J/m^3) and it is an important parameter of the material in comparing capabilities of permanent magnet properties. The higher the value of this energy product the greater is the external value of the field which can be produced by a given volume of material. The ultimate value of $(BH)_{max}$ attainable for any material may be derived from Eq. (2.1).

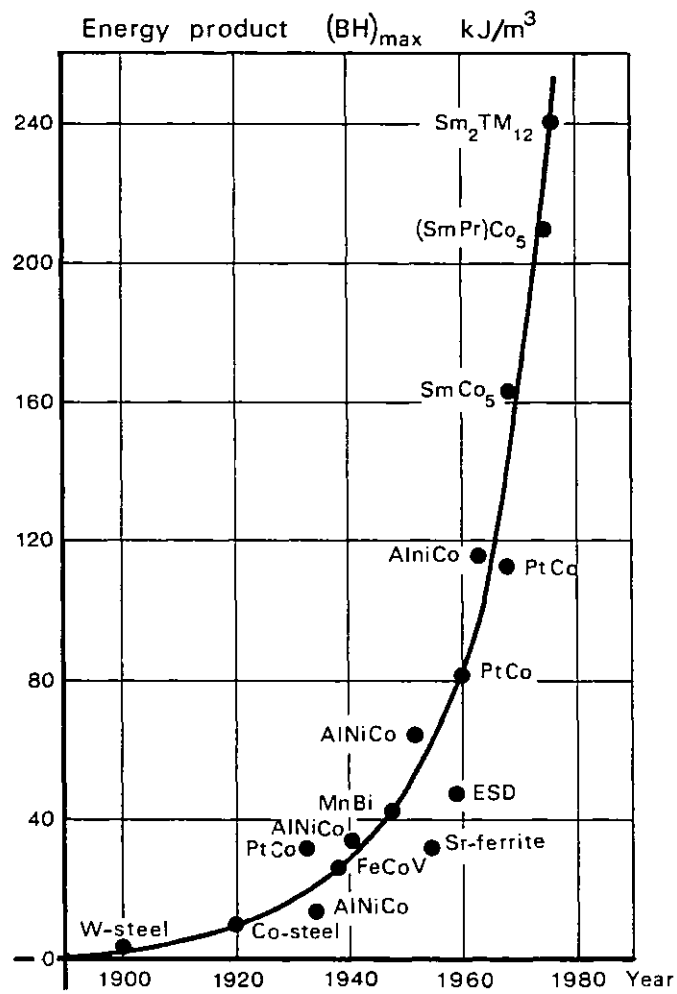

Fig. 2. 8 - Improvements in the energy product of permanent magnets

A permanent magnet operates in the demagnetising quadrant for which B and H are antiparallel. Thus

$$B = -\mu_o H + M$$

and so

$$BH = -\mu_o H^2 + MH \qquad (2.2)$$

The product $(BH)_{max}$ is found by setting d(BH)/dH = 0 in Eq. (2.2) which gives:

$$(BH)_{max} = \frac{M^2}{4\mu_o} \tag{2.3}$$

Since M can, at most, equal the intrinsic saturation B_{is}, Eq. (2.3) becomes:

$$(BH)_{max} = \frac{B_{is}^2}{4\mu_o} \tag{2.4}$$

Eq. (2.4) is a very important guide in the development of permanent magnet materials. Fig. 2.8 shows the improvements achieved in terms of the energy product, since the search for better materials began [34].

Rare-earth magnets have $B_{is} \simeq 1.05$ T and peak values of energy product achieved in the laboratory are around 220 kJ/m^3. Prospects of improving the energy product are still being made.

2.2.4 - The shape factor

In order to have an idea of the demagnetising curve shape, the relation

$$f = \frac{(BH)_{max}}{B_r H_c} \tag{2.5}$$

is defined and is called "shape factor". This quantity is a dimensionless number which approaches the value of unity with increasing rectangularity of the demagnetisation characteristic.

2.3 - CLASSIFICATION OF PERMANENT MAGNET MATERIALS

According to the above exposition, a good material for permanent magnet construction will have a high remanence B_r and coercivity H_c, a large maximum energy product $(BH)_{max}$ and shape factor, low recoil permeability and a high Curie point. The Curie temperature is that at which a ferromagnetic material becomes virtually non-magnetic.

High remanence B_r is simply a matter of composition, although the remanence value can be significantly increased if magnetic anisotropy can be proudced. Anisotropy can be generated by cooling the magnet from a high temperature in a magnetic field, followed by a prolonged temperature treatment. In this way the magnetic domains are aligned in a preferred direction. Magnets without a preferred direction of magnetisation, having similar magnetic properties in all directions, are known as isotropic.

High coercivity H_c is achieved by introducing irregularities in the crystal lattice. An inlcusion of non-magnetic impurities also increases coercivity [28].

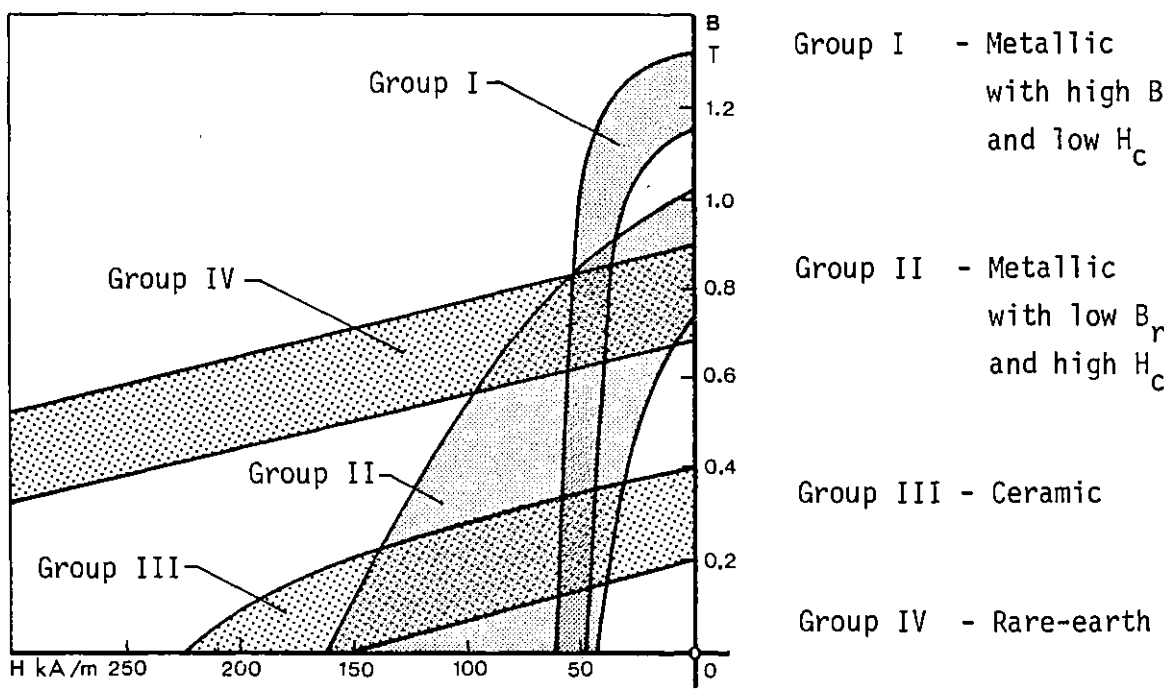

Fig. 2.9 - Demagnetisation characteristics for typical permanent magnet materials

Hence, in the classification of the various permanent magnet materials, the type of composition used, together with the values of B_r and H_c, will serve as a guideline [29]. In this way, the permanent magnetic materials may fall into three main groups such as METALLIC, CERAMIC and RARE-EARTH COBALT alloys. Lynch [35] subdivided the metallic group into

two sub-groups as metallic magnets of high B_r and low H_c and metallic magnets of low B_r and high H_c and a comparison of their demagnetisation characteristics is shown in fig. 2.9. They will now be considered individually:

Group I - Metallic magnets with high B_r and low H_c.

The Alnico (Fe-Co-Ni-Al) series has been the most important metallic magnets used for the last half century. According to its chemical composition it is variously called Alcomax 2, 3, 4, Magloy 1, 2, NL 2, 3, 4, Ticonal 440, 600, each being anisotropic. The composition of this alloy is roughly 25% Co, 8% Al, 14% Ni with the balance iron. It is produced either by melting or sintering the component metals together [36].

The demagnetisation characteristic of these magnets is non-linear and due to their low coercivity ($H_c \simeq 60$ kA/m) the magnet must be long and may require protective pole-shoes against external fields.

Group II - Metallic magnets with low B_r and high H_c.

By adding niobium and titanium to the Alnico, magnets such as Hycomax 2, 3, Magloy 8 and Columax are obtained with coercivities around 150 kA/m. Their demagnetisation characteristic is again non-linear, but the recoil permeability is less than that of previous group, giving greater reduction of flux density with demagnetising fields.

Group III - Ceramic magnets

A ceramic magnet consists of mixed oxides with the general formula $MO\ 6Fe_2O_3$ where for a good magnet M is either barium or strontium. This is known as a ferrite magnet and accordingly the composition is called Ferroba, Magnadur, Magnal and Neoperm.

Ferrite magnets are usually made by firing iron oxide (Fe_2O_2) with barium carbonate ($BaCO_3$) or strontium carbonate ($SrCO_3$) in a stoichiometric proportion. The resulting compound is powdered to a particle

size of about 1 micron and then pre-sintered (calcinated) at 1150 to 1400°C, pressed into shape, and finally sintered at 1100 to 1300°C. The sintering atmosphere is air [37]. To produce anisotropic material the powder is pressed in a strong magnetic field to align the ferrite particles and so produce a perferred magnetic orientation.

The ferrite powder can also be mixed with rigid or flexible bonding agents to produce other types of magnets, such as bonded Ferroba.

Compared with metallic magnet materials, ferrites have high stability, low density ($\sim 5\,g/cm^3$), high electrical resistance ($\rho \simeq 1 M\Omega m$) and may thus be regarded as insulators. They are mechancially hard and brittle and can only be machined using special techniques. The anisotropic ferrite has relatively high coercivity ($\sim 200\,kA/m$), moderate values of remanence and relative linear demagnetisation characteristics, which can be changed within wide limits by varying the production routines. Due to the low cost, ferrites are widely used in many applications.

Group IV - Rare-earth magnets

The rare-earth cobalt alloys have the general formula RCo_5, where R is one of the rare-earth elements samarium, praseodymium of the alloy mishmetal. These magnets are produced by powder metallurgical techniques, pressing to the required shape in a strong magnetic field ($\sim 2400\,kA/m$), and finally sintering in an inert atmosphere [38]. Although many different combinations of rare-earth have been tried, the most important type is based on samarium and cobalt ($SmCo_5$), known as Supermagloy.

The advantages of rare-earth cobalt magnets are its high energy product which is about three times greater than other types (see fig. 2.8), and its high coercivity which is about four times greater than metallic magnets. The remanence value lies between metallic and ceramic magnets but its demagnetisation characteristic is perfectly linear over all range of the demagnetisation force and the magnet is very stable.

The main disadvantage is the cost per unit weight is inevitably

greater than that of conventional materials, because of the high raw material cost. However, due to its high energy product and coercivity these magnets allow the use of short magnet lengths without the need of pole-shoes protection. Hence, for the same application, $SmCo_5$ has the smallest volume as will be shown in section 2.5.1, and rare-earth magnets may become cheaper.

Magnets may also be produced by bonding RCo_5 powder with polymer or epoxy and pressing in a magnetic field to the required shape, of which the Hera magnet is an example. Bonded polymer rare earth (B.P.R.E.) magnets are cheaper than $SmCo_5$ and are easily machinable. Due to the bonding agent, however, both B_r and H_c are reduced by about one third as compared with $SmCo_5$ and therefore about twice of the volume is required to replace the unbonded material. A further disadvantage is its maximum operating temperature limited to about 60°C for B.P.R.E. (set by the polymer), and to about 150°C for epoxy bonded magnets.

Finally, R_2T_{17} compounds especially those in which T is a mixture of iron and cobalt are now being investigated. The 2-17 compounds offer the prospect of improved $(BH)_{max}$ and higher B_r and H_c than $SmCo_5$.

2.4 - MAGNET ARRANGEMENTS IN ROTATING ELECTRICAL MACHINES

Three basic configurations are possible for setting up permanent magnet field system for rotating electrical machines, with the magnet axis radial, circumferential or axial. This arrangement can be used either in the rotor or in the stator, as illustrated in fig. 2.10 for a four-pole machine.

In the radial configuration each magnet must drive the total flux per pole across the air gap, while in the circumferential configuration each magnet drives half of the flux per pole across double air gap. Thus, for identical magnets and the same air gap the flux per pole in both arrangements is the same. As already said, when metallic magnets with

low coercivity are used, soft iron pole pieces protection are needed in order to shield the flux set up by the stator and avoid magnet demagnetisation. Fig. 2.11 illustrates this action for stator current on the q-axis.

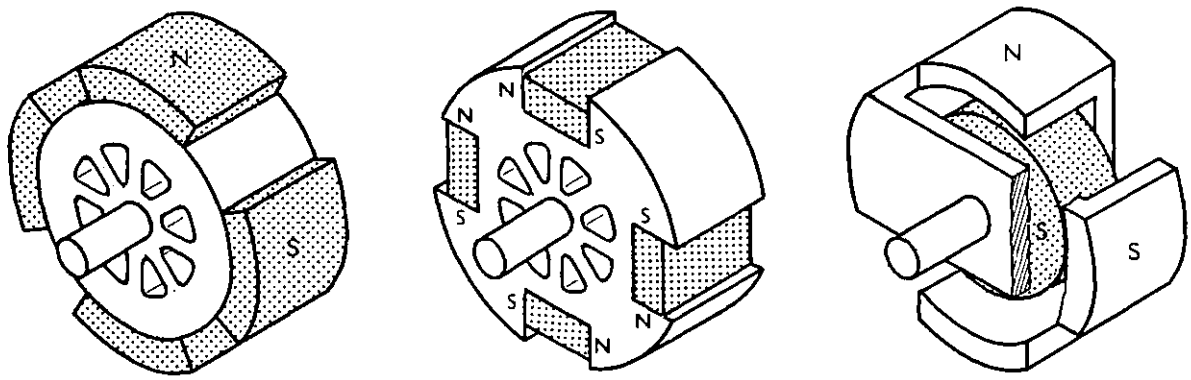

i) - Radial ii) - Circumferential iii) - Axial

(a) - Arrangement for rotors

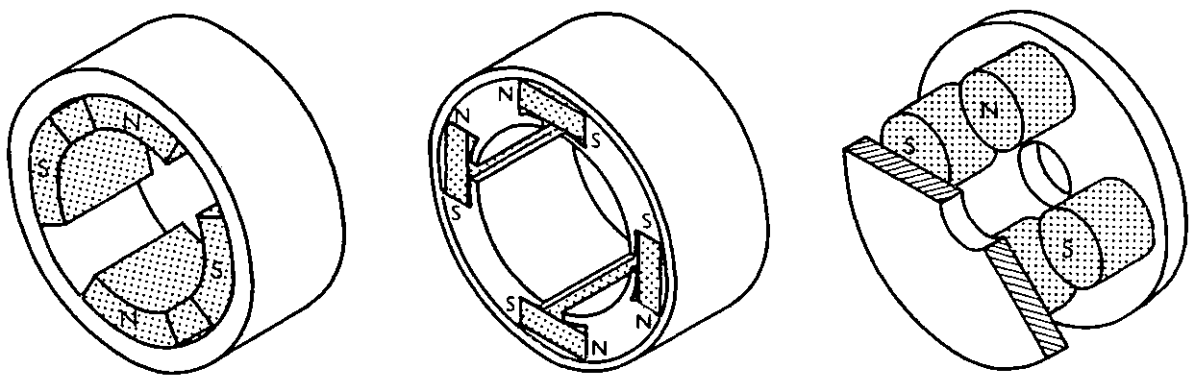

i) - Radial ii) - Circumferential iii) - Axial

(b) - Arrangement for stators

Fig. 2.10 - Permanent magnet arrangements in rotors and stators

In the circumferential arrangement, however, this protection is inherent, although some regions of the magnet are still prone to demagnetisation. As can be seen in fig. 2.12, in the circumferential arrangement used as a stator of a d.c. machine, the design may be susceptible to demagnetisation due to armature reaction, mainly near the edges of the

magnets. To over-come this effect, metallic magnets with low remanence and high coercivity, such as Hycomax, should be employed. The circumferential layout has been widely used in synchronous motors [39, 40],

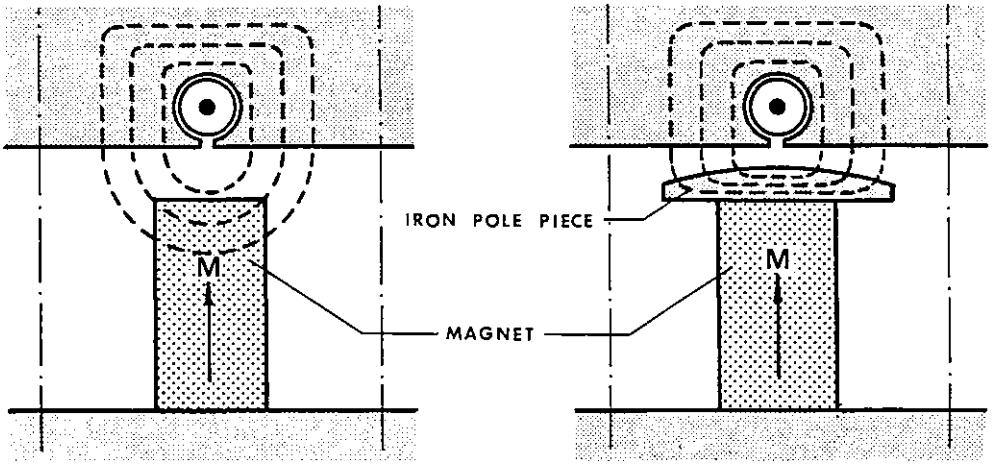

(a) - Without pole-shoe (b) - With pole-shoe protection

Fig. 2.11 - Effect of the soft pole-piece on magnet demagnetisation

but when rare-earth magnets are employed the radial configuration seems to be better [40], because of the lower constructional cost and because the absence of ironwork near the gap reduces armature reaction fluxes

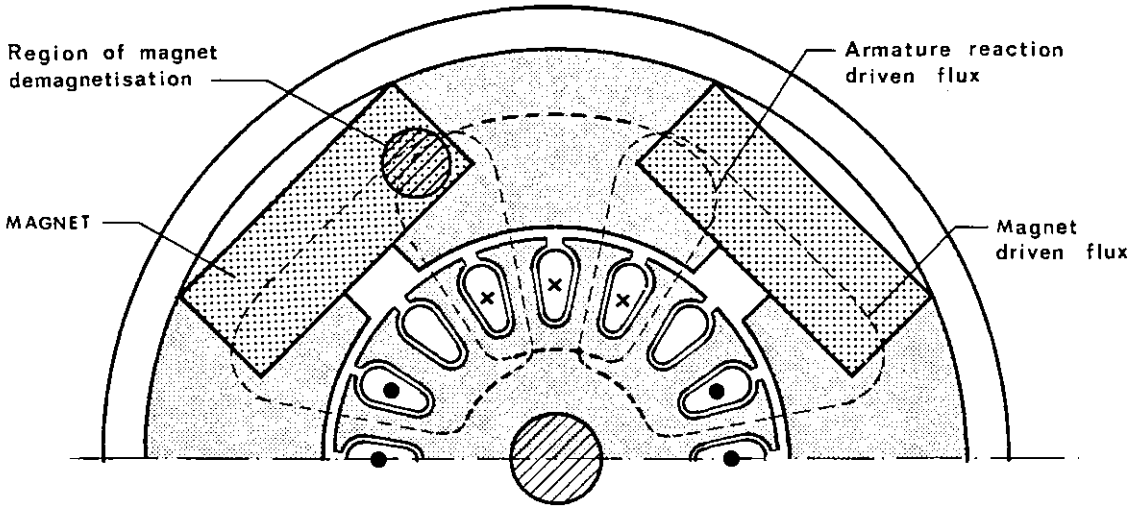

Fig. 2.12 - Circumferential arrangement for a d.c. machine

and enables higher peak torques to be achieved. Binns, in reference [41], describes a high performance permanent magnet synchronous motor using a rather unconventional circumferential configuration. Performances

for both ferrite and rare-earth magnets are compared and the paper discusses the importance of an optimal design in order to achieve maximum torque.

In the axial rotor configuration, a central axially magnetised permanent magnet is fixed on the shaft between two flanges. The pole pieces are imbricated so as to present alternating magnetic poles at the surface of the rotor. In spite of the high leakage flux involved, this design is widely used in alternators for cars due to its robust construction. The disadvantage of the high leakage flux may be overcome in this design by using a multi-stacked rotor built up from axially magnetised annular ceramic magnets interlinked with steel plates, to which pole-shoes are attached [42]. A typical application of the axially magnetised stator is in the disc configuration and in Chapter 5 a machine which employs this design is presented.

2.5 - THE CALCULATION OF A PERMANENT MAGNET UNDER STATIC CONDITIONS

A permanent magnet is operating under static conditions when, once magnetised the magnetic circuit, the air gap dimensions are fixed and the permanent magnet is not influenced by external magnetic fields. In the magnetic circuit represented in fig. 2.13, where a permanent magnet of cross-sectional area A_m and length ℓ_m is inserted, the air gap g in the soft iron is responsible for the self-demagnetisation. The static gap design problem then reduces simply to establish the relationships between the properties of the material and magnet dimensions with the useful flux in the air gap set up by the permanent magnet.

From Ampère's circuital law:

$$H_m\ell_m + H_{Fe}\ell_{Fe} + H_g g = 0 \qquad (2.6)$$

where $H_m\ell_m$ is the m.m.f. produced by the magnet, $H_{Fe}\ell_{Fe}$ is the m.m.f. drop in the iron of length ℓ_{Fe} and $H_g g$ the m.m.f. drop in the air gap.

From flux continuity considerations, the total flux $B_m A_m$ produced by the magnet must satisfy the equation

$$B_m A_m = B_g A_g + \phi_{leak} \tag{2.7}$$

where $B_g A_g = \phi_g$ is the useful flux in the air gap and ϕ_{leak} denotes the leakage flux wasted in all magnetic circuit.

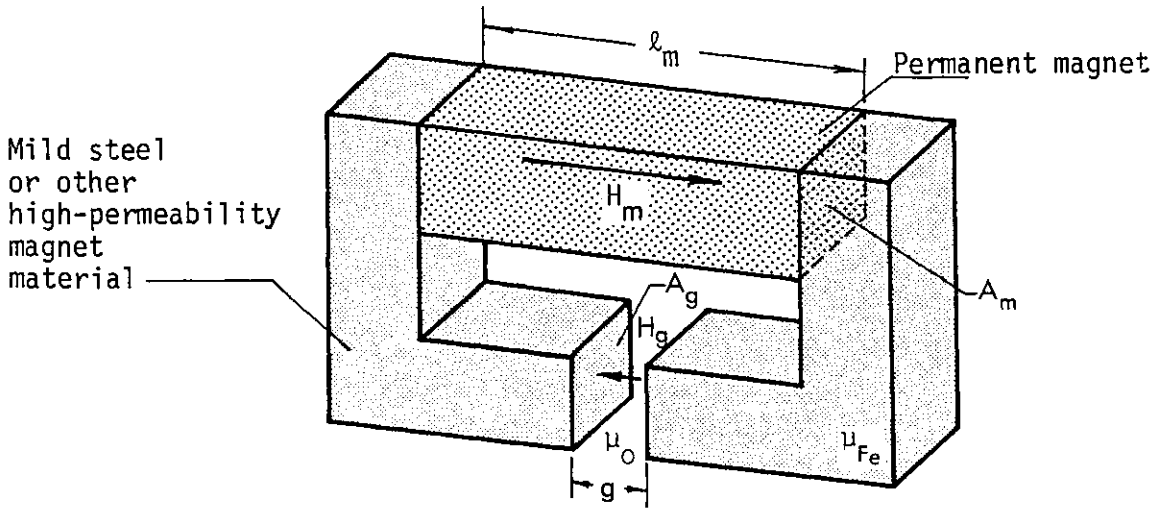

Fig. 2.13 - Static magnetic circuit

Eq. (2.7) and Eq. (2.6) can be written in the form

$$B_m A_m = B_g A_g \left(1 + \frac{\phi_{leak}}{B_g A_g}\right) = K_1 B_g A_g \tag{2.8}$$

$$H_m \ell_m = -H_g g \left(1 + \frac{H_{Fe} \ell_{Fe}}{H_g g}\right) = -K_2 H_g g \tag{2.9}$$

where

$$K_1 = 1 + \frac{\phi_{leak}}{\phi_g} = 1 + \frac{P_\ell}{P_g} \tag{2.10}$$

is the LEAKAGE FACTOR and

$$K_2 = 1 + \frac{H_{Fe} \ell_{Fe}}{H_g g} \tag{2.11}$$

is the RELUCTANCE FACTOR, responsible for the m.m.f. drop in the system in driving flux through pole pieces. The leakage factor K_1 depends on the magnetic circuit geometry and may be calculated from the knowledge of the total leakage permeance P_ℓ and air gap permeance P_g. In practice

K_1 is much greater than K_2. Normally K_2 varies from 1.05 to 1.45 approximately depending on the pole pieces permeability, but K_1 could be of the order of 20 in larger magnets.

Dividing both members of Eq. (2.8) and Eq. (2.9) and taking into account that the air gap flux density is related by $B_g = \mu_o H_g$, gives:

$$\frac{B_m}{H_m} = -\mu_o \frac{K_1 A_g \ell_m}{K_2 A_m g} \tag{2.12}$$

where, according to Eq. (2.8) and Eq. (2.9)

$$A_m = K_1 \frac{B_g}{B_m} A_g \tag{2.13}$$

$$\ell_m = -K_2 \frac{H_g}{H_m} g \tag{2.14}$$

It should be pointed out that length ℓ_m is essentially a positive quantity, since $H_m < 0$ in the second quadrant.

The quantity B_m/H_m is called the "unity permeance" and gives the slope of the load-line OP in the second quadrant of the demagnetisation curve, as shown in fig. 2.14. If any point P in the demagnetisation curve

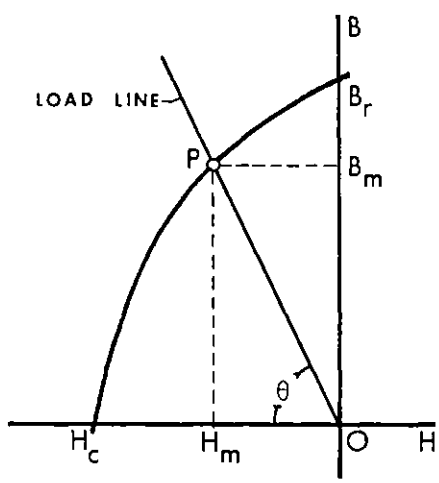

Fig. 2.14 - Working point for static condition

is selected as the working point, so that B_m and H_m are known, then Eq. (2.13) and Eq. (2.14) enable the cross-section and length of magnet to be determined for a given air gap flux density, air gap area and gap length.

2.5.1 - Working point for the minimum volume of the magnet material.

There is a particular position of the working point which will make the volume of the magnet a minimum. If $V_m = A_m \ell_m$ is the volume of the magnet material, then using Eq. (2.13) and Eq. (2.14) results

$$V_m = \frac{K_1 K_2 B_g^2}{\mu_o (B_m H_m)} V_g \qquad (2.15)$$

where $V_g = A_g g$ is the air gap volume. The volume V_m of the magnet is therefore a minimum for a given air gap volume when the energy product $B_m H_m$ is a maximum. A construction to find the point of $(B_m H_m)_{max}$ has already been shown in fig. 2.7. Thus, diagonal OQ of the rectangle $QB_r OH_c$ is approximately the unit permeance line given by Eq. (2.12) for the condition of minimum volume of the magnet.

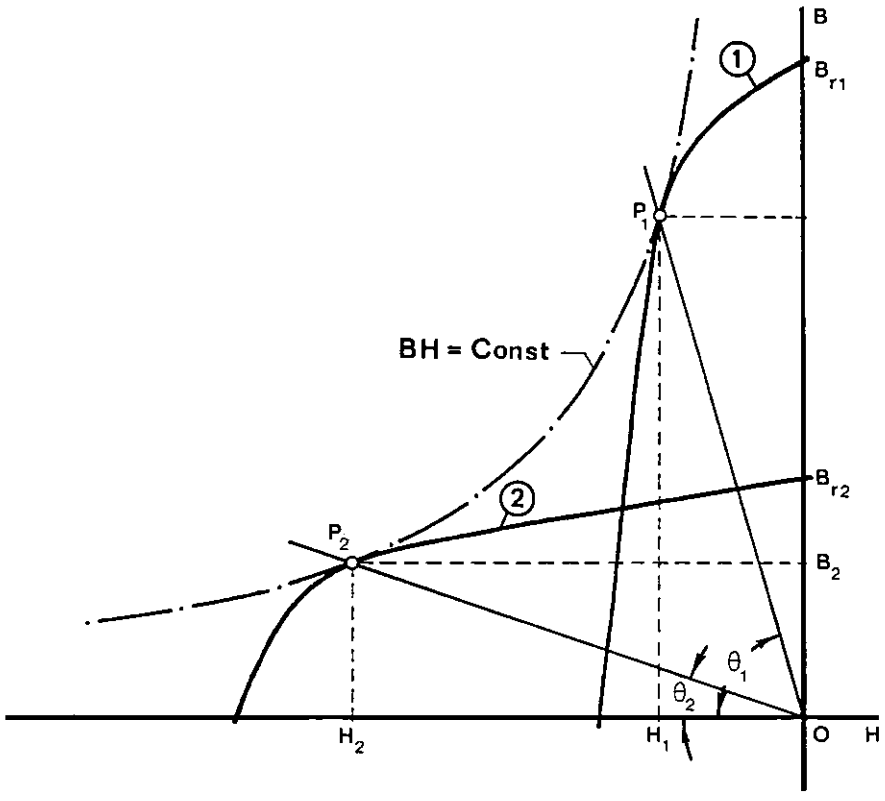

Fig. 2.15 - Different demagnetisation curves for the same $(BH)_{max}$ value

However for a fixed V_g Eq. (2.15) gives no indication of the ratio length to cross-section ℓ_m/A_m of the magnet, so in this respect it is ambiguous. This means that the same BH hyperbola may be tangential either

to a demagnetisation curve having high B_r and low H_c or to one with low B_r and high H_c, as shown in fig. 2.15. The slope of the load-lines OP_1 and OP_2 correspond to different ratios B_m/H_m, whereas the products B_1H_1 and B_2H_2 are identical. Therefore, for a fixed air gap flux, Eq. (2.13) shows that the cross-section of a magnet must be made greater the smaller values of B_m and B_r; and the length given by Eq. (2.14) can be made smaller the larger the values of H_m. Consequently, for the optimum working point, characteristic 1 gives thin and long magnets and characteristic 2 gives fat and short magnets in the magnetising direction.

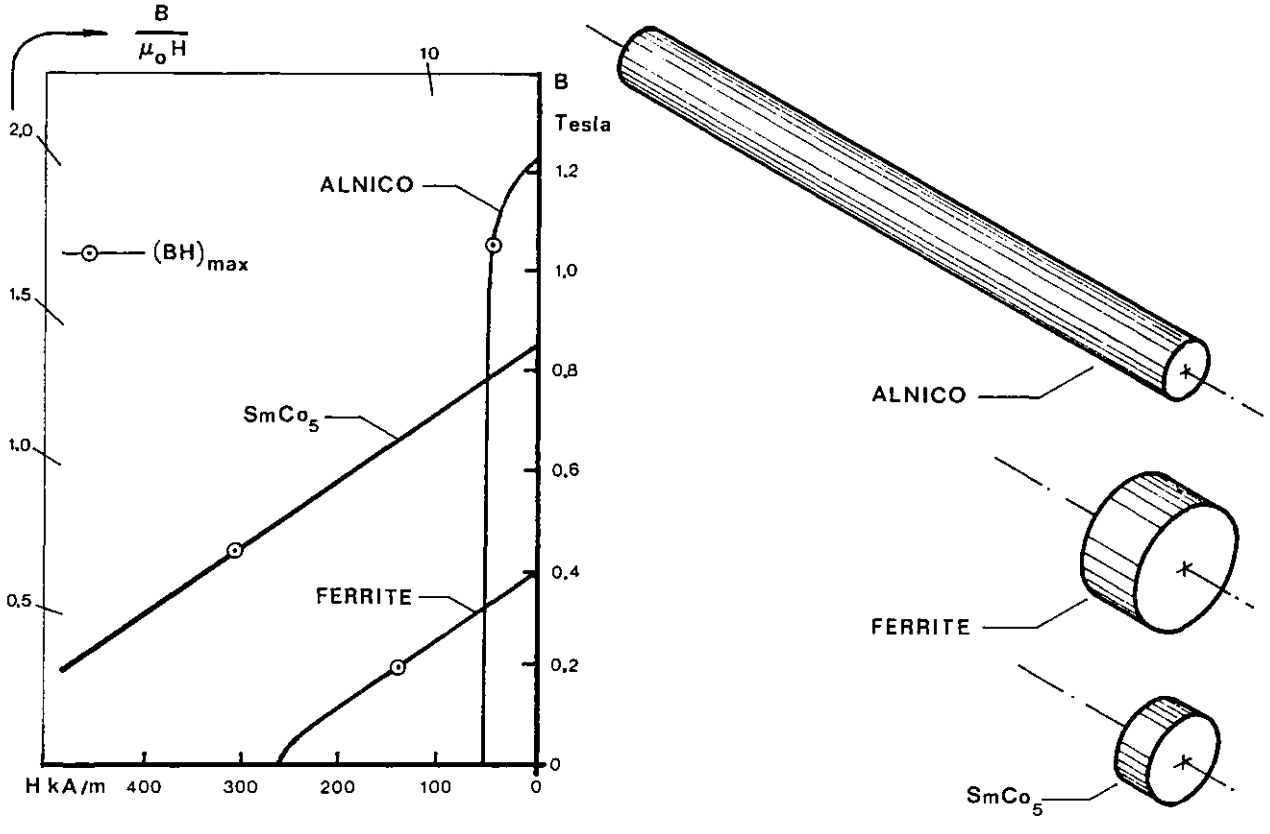

(a) - Demagnetisation characteristics (b) - Magnet proportions

Fig. 2.16 - Demagnetisation characteristics and comparison of the shape and size of three permanent magnets producing identical air gap flux

A comparison of the shape and size for three different types of permanent magnet material whose demagnetisation characteristics are shown in fig. 2.16(a) may be established. It is assumed that the bar magnets made from the three materials are working in the $(BH)_{max}$ point on its

characteristic and produce identical air gap flux in a fixed gap length. Neglecting leakage, fig. 2.16(b) shows the comparative sizes and proportions of bar magnets for each material used. The volume of metallic magnet, with a small cross section area and long length, needs to be about 6.5 times, and one of ceramic about 2.5 times as great as that of a rare-earth magnet. This result is not exclusively due to the high energy product of rare-earth magnets. It is also due to its high insensitivity to self-demagnetisation.

It should be emphasized that it is not always the case that the $(BH)_{max}$ point is the most desirable. In rotating electrical machines design different design criteria apply to different magnets. For example, metallic magnets must be stabilised on recoil lines, ceramic magnets should operate close to remanence for higher flux, whereas rare-earth magnets must ideally operate at $(BH)_{max}$ to minimise cost.

2.5.2 - Leakage factor formulae for specific permanent magnet configurations

To estimate K_1 given by Eq. (2.10) for a particular device it is necessary to have knowledge of the field geometry in order to determine the leakage and useful permeances. Analogue methods involving the use of field plotting paper or electrolytic tanks are sometimes useful. Approximate formulae to calculate leakage permeance have been suggested by Roters [43], and the problem is also discussed in Parker and Studders [26]. However, various empirical formulae for leakage factor calculation have been given to handle specific permanent magnet configurations. The most ambitious formula has been developed by Maynard and Tenzer [44], applicable to the configurations shown in fig. 2.17.

For each magnet arrangement the leakage factor K_1 is given respectively by

$$K_{1A} = 1 + \frac{g}{Ag}\left(1.1 L_a \frac{0.67a}{0.67a + g}\right)\left(1 + \frac{g}{a}\right) \qquad (2.16)$$

$$K_{1B} = 1 + \frac{g}{Ag}\left(1.7 L_a \frac{a}{a+g} + 1.4d + 0.94d\sqrt{\frac{L_b}{c} + 0.25}\right) \qquad (2.17)$$

$$K_{1C} = 1 + \frac{g}{Ag}\left(1.7 L_a \frac{a}{a+g} + 1.4b\sqrt{\frac{L_b}{c} + 0.25} + 0.33 L_c\right) \qquad (2.18)$$

where L_a, L_b, L_c are the perimeterlengths of the sections represented by the dimensions a, b, c respectively.

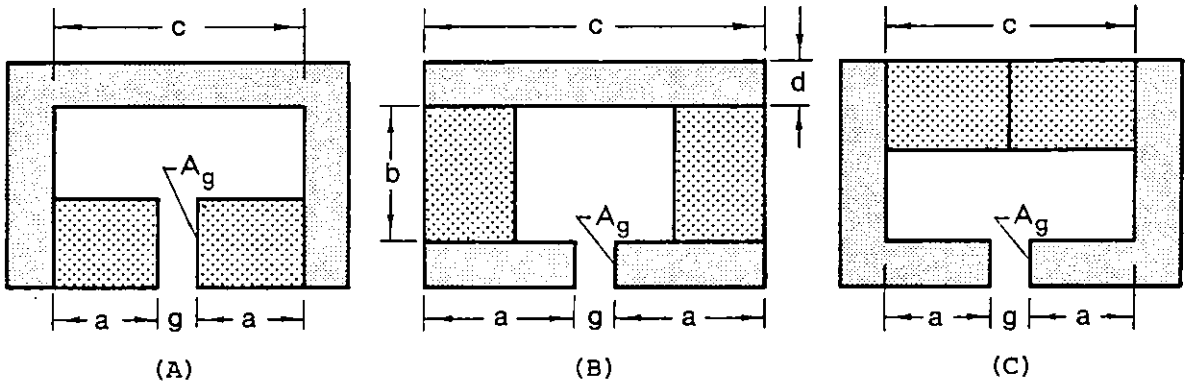

Fig. 2.17 - Location of permanent magnet material for three configurations (A) Good design, low leakage, (C) poor design, high leakage.

Maynard has made flux density measurements with a constant air gap and volume of magnet material in those three configurations. The formulae above are reputed to give errors about 10% with measurements for leakage factor.

In configuration (A) leakage flux is low since the magnetic potential is only that of the H drop in the soft iron. In configuration (C), however, the leakage is considerabley greater. Configuration (B) is an intermediate situation. Although configuration (A) is the most efficient magnetically it requires two magnets, and it may be seen that (C) could be accomplished with a single magnet.

The calculation of the leakage factor by using a numerical method for configuration (A) is worked out in section 2.7.7.a and compared with Maynard's formula.

2.6 - THE CALCULATION OF A PERMANENT MAGNET UNDER DYNAMIC CONDITIONS

A permanent magnet is operating under dynamic conditions when changes in the length of the air gap occur or externally applied m.m.f.'s are involved. In this situation the working point of the magnet moves inside the demagnetisation curve of the permanent magnet on the recoil line [7].

The magnetic circuit and demagnetisation curve of a permanent magnet machine are considered in fig. 2.18. The permeance of the air gap is a minimum when the permanent magnet rotor is in position (a) and maximum when it is in position (b). The load-line OA corresponds to position (a) and load-line OK to position (b) with the corresponding flux densities B_2 and B_1 respectively. However, when the rotor rotates the locus of

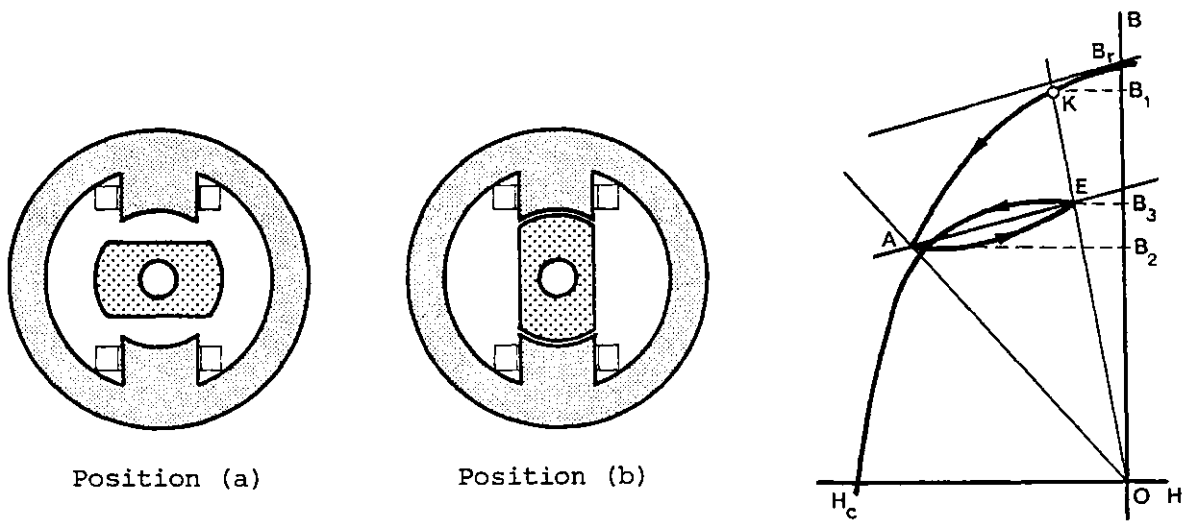

Fig. 2.18 - Flux density variation of a permanent magnet due to changes in the air gap

operation on the demagnetising curve is the minor hysteresis loop AE with the flux density oscillating between the values B_2 and B_3 twice for each revolution of the rotor. In practice, this minor loop may be replaced by the recoil line AD as seen before.

Fig. 2.19 illustrates the case of a permanent magnet rotor of a synchronous motor operating with a constant torque angle θ, subject to a demagnetising force produced by the stator m.m.f. The effect of the d-axis m.m.f. component H_d causes the load line OK to shift to the left parallel

to itself and interesecting the demagnetisation curve at point A. The result is a further reduction in the flux density to B_2. Removal of the demagnetising force H_d does not restore the flux density to its previous value B_1, but to a lower value B_3. Point A follows along the lower portion of the minor hysteresis loop to point E. Repeated application and

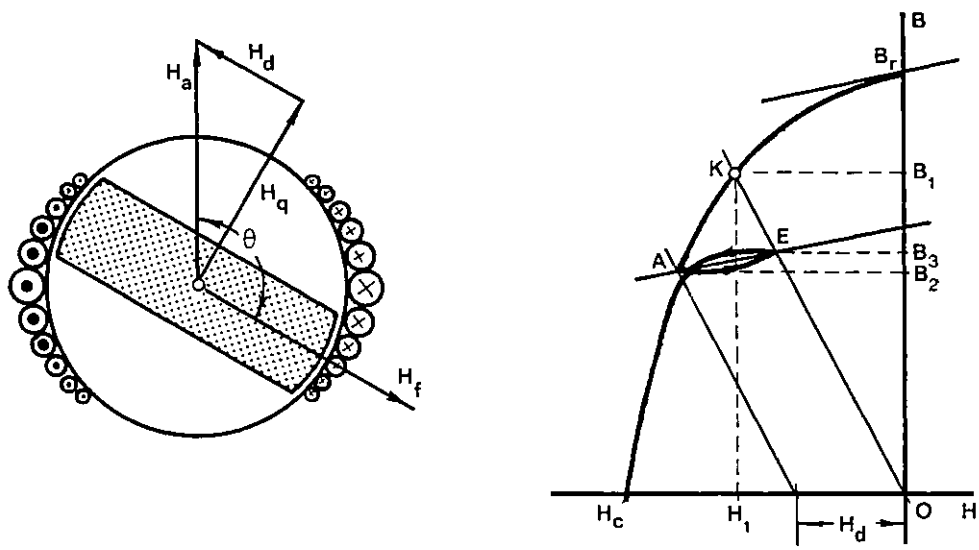

Fig. 2.19 - Effect of demagnetising m.m.f. on magnetising field of a permanent magnet

removal of H_d results in a relatively small flux density variation of B_3 to B_2, the locus of operation being practically the recoil line AD, with a slope to be about equal to that of the tangent to the demagnetisation curve through B_r. In both examples described, the magnet is said to be operating under dynamic conditions.

2.6.1 - Recoil constant energy contours

When the magnet is operating under dynamic conditions in the recoil line of slope μ_{rec}, the unit permeance varies over a fixed cycle. In fig. 2.20, points A and E correspond to the minimum and maximum permeance of the magnetic circuit of the permanent magnet rotor operating under dynamic conditions [26]. In position (a) all the flux produced by the magnet is leakage, with no useful flux passing through the stator winding.

Assuming that the leakage permeance line OA remains constant, a useful flux density EF passing through the gap in position (b) exists, since the flux FG is wasted. As a consequence of this flux variation, a corresponding change in the magnetic energy stored in the gap takes place and the area EFJI is a measure of the useful recoil energy. To maximise this area it is necessary to arrange that E bisects AD, since in a given triangle OAD the inscribed rectangle EFJI is a maximum when AE = ED and AF = FO. This analysis shows that for economy of permanent magnet material in the dynamic design problem, when the unit leakage permeance is situated at point A, the useful permenace must be controlled to operate in the recoil line of slope μ_{rec} at point E midway between A and D.

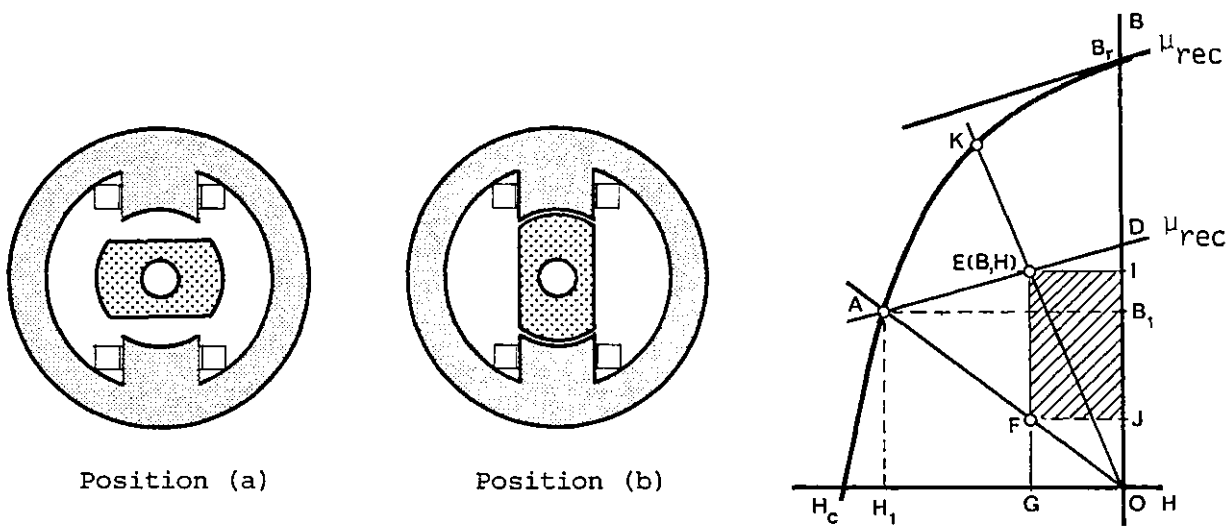

Fig. 2.20 - Permanent magnet operating under dynamic load conditions

For the particular unit leakage permeance B_1/H_1 situated at point A of the demagnetisation characteristic, other points of equal recoil energy may be obtained. In fact, the equation for the recoil line through H_1, B_1 with a slope μ_{rec} may be written as

$$B' = B_1 + \mu_{rec}(H - H_1)$$

and for the unit leakage permeance

$$B'' = \frac{B_1}{H_1} H$$

The useful recoil energy W_u available by operation at any point (H, B) on the recoil line through H_1, B_1 is given by

$$W_u = \frac{1}{2}(B' - B'')H = \frac{1}{2}\left[H^2(\mu_{rec} - \frac{B_1}{H_1}) + H(B_1 - \mu_{rec}H_1) \right] \qquad (2.19)$$

For a given value of W_u, Eq. (2.19) gives two values of H which are the abcissas of two points on the recoil line considered. For varying A other points may be obtained. The locus of all such points forms a closed curve termed "constant energy contour". Typical contours for the ALNICO permanent magnet are shown in fig. 2.21. If a given recoil energy

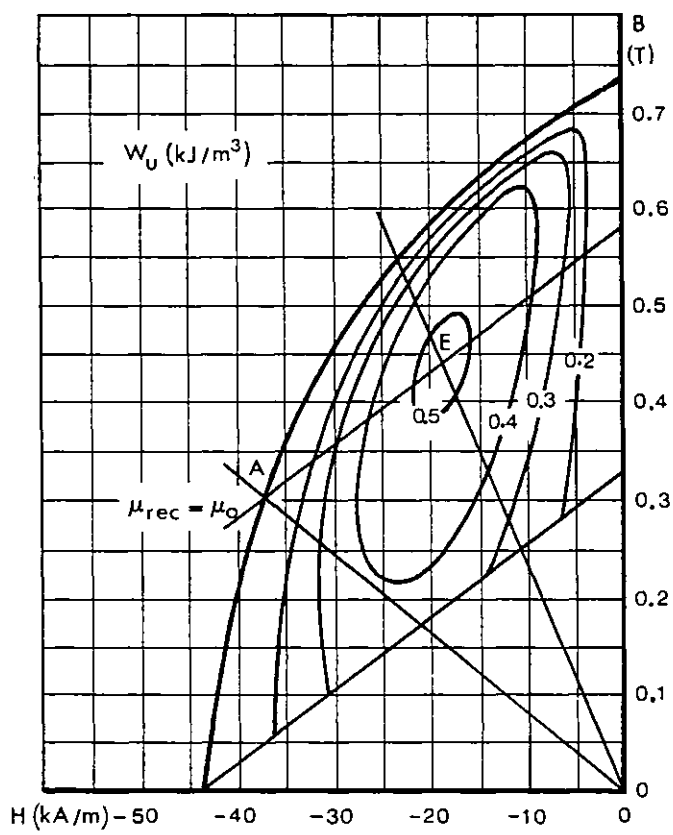

Fig. 2.21 - Useful recoil energy contours

is selected, these curves estimate the total and leakage permeances to be used and therefore the leakage factor of the device operating under dynamic conditions. Hence, points A and E should be chosen for an optimal design, giving the minimum volume of material under dynamic conditions.

2.7 - COMPUTATION OF THE FIELD DISTRIBUTION IN A PERMANENT MAGNET MACHINE

Two dimensional analytical techniques using load-line or unit permeance concepts for calculation of a permanent magnet have been descibed in the previous section. In permanent magnet circuits with simple geometry and short, well-defined air gaps, the load-line technique gives acceptable solutions since the assumption of uniform flux density for overall flux distribution within the permanent magnet and air gap is reasonably valid. However, when complex magnet shapes or relatively long air gaps are involved, appreciable leakage flux emanating from the sides of the magnet exists and therefore the assumption of uniform flux density within the permanent magnet is no longer acceptable. Due to the flux leakage, a reduction in the flux density within the magnet in the magnetised direction with distance towards the air gap takes place. In order to calculate this reduction and hence the flux density distribution, the axial and transversal permeability of the permanent magnet material must be taken into account. This is only possible by modelling the magnetic field problem and solving it using a digital computer.

A great number of papers have been published recently on digital computer techniques to permanent magnet problems. Vector potential finite-element [45, 46] and finite-difference [47, 48] solutions have been described, when non-linear permanent magnet characteristics and saturable iron are involved. A scalar potential formulation using a finite-difference method has also been given [49, 50].

The permanent magnet modelling technique described in this thesis was developed to calculate field-flux density distribution and current-loading effects in a permanent magnet rotary actuator and in a disc machine which will be examined later. A finite difference scalar potential formuation using polar and cylindrical coordinates is presented. This formulation [51], applied to magnets is thought to be new.

2.7.1 - Modelling the magnetic field problem

in permanent magnet devices

The static magnetic field in a system with air, iron currents and permanent magnets is described [52] by the following equations:

$$\text{curl}\,\bar{H} = \bar{J} + \frac{\partial \bar{D}}{\partial t} \tag{2.20}$$

$$\text{div}\,\bar{B} = 0 \tag{2.21}$$

$$\bar{B} = \mu_o \bar{H} + \bar{M} \tag{2.22}$$

where $\bar{H}$ is the magnetic field, $\bar{J}$ the current density, $\partial\bar{D}/\partial t$ the displacement current density, $\bar{B}$ the flux density and $\bar{M}$ the intrinsic magnetisation which is a function of the magnetic field as seen in section 2.2.1.

When dealing with iterative methods of field solution, it is not so convenient to use Eq. (2.22) directly, and it can be written as

$$\bar{B} = \mu_o \bar{H} + \bar{M}' + \bar{M}_o$$

where

$$\bar{M}' = \mu_o \chi \bar{H}$$

is a function of $\bar{H}$ and susceptibility χ and

$$M_o = B_r$$

is the remanent intrinsic magnetisation. Thus, Eq. (2.22) becomes

$$\bar{B} = \mu \bar{H} + \bar{M}_o \tag{2.23}$$

where

$$\mu = \mu_o(1 + \chi) \tag{2.24}$$

is the "apparent" permeability, since it has the dimensions of permeability but differs from the true permeability as normally defined.

The magnetic field distribution in a permanent magnet device can

now be obtained from Eq. (2.23). Taking the divergence of both sides and substituting Eq. (2.21) gives:

$$\text{div}\,\mu\bar{H} + \text{div}\,\bar{M}_o = 0 \tag{2.25}$$

Maxwell's first equation at low freqnecies ($\frac{\partial \bar{D}}{\partial t} = 0$), in a region free of macroscopic currents ($\bar{J} = 0$) reduces to

$$\text{curl}\,\bar{H} = 0 \tag{2.26}$$

Then, $\bar{H}$ can be readily defined by a magnetic scalar potential Ω such that

$$\bar{H} = -\text{grad}\,\Omega \tag{2.27}$$

and Eq. (2.25) becomes:

$$\text{div}\,\mu\,\text{grad}\,\Omega = \text{div}\,\bar{M}_o \tag{2.28}$$

Eq. (2.28) is the Scalar Poisson Equation for the three-dimensional field problem in terms of the magnetic potential function Ω, the remanent intrinsic magnetisation $\bar{M}_o$ and the permeability μ of the permanent magnet material or ferromagnetic parts. This equation can be particularised for the different regions of the device as follows:

$\text{div grad}\,\Omega = 0$	in air and copper region
$\text{div}\,\mu\,\text{grad}\,\Omega = 0$	in soft iron
$\text{div}\,\mu\,\text{grad}\,\Omega = \text{div}\,\bar{M}_o$	in permanent magnet material

Hence, a Poissonian field exists inside the magnet and outside a Laplacian field.

2.7.2 - Linear Representation of demagnetisation characteristics

In modelling the magnetic field problem the demagnetisation characteristic of the permanent magnets used are assumed to be linear. As seen in

section 2.3 the normal demagnetisation characteristics of the various permanment magnet materials may be broadly classified, according to their shape, into two groups, as shown in fig. 2.22. Metallic magnets have a non-linear demagnetisation characteristic over the greater part of their length, while for ferrites and rare-earth magnets it is essentially linear.

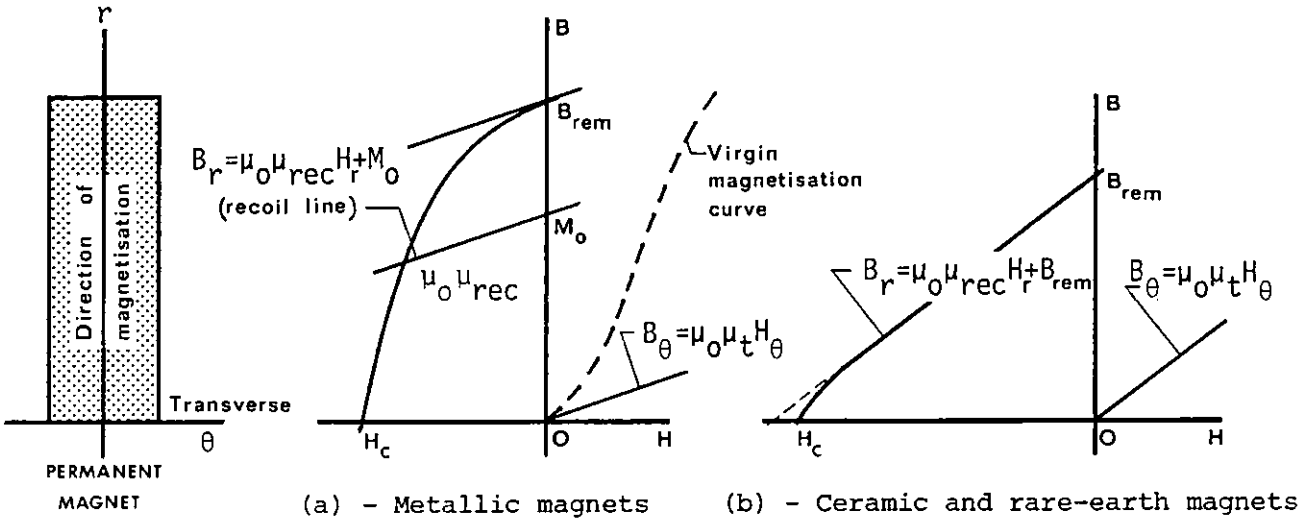

Fig. 2.22 - Typical permanent magnet demagnetisation characteristics

No problem is associated with modelling ceramic and rare-earth magnets, because such materials are normally operating on the linear portion of their characteristic. For metallic magnets it is assumed that the material is operating on the recoil line where it was stabilised, as indicated in fig. 2.22(a). Under these conditions, both characteristics in the magnetised direction may be represented by the linear equation

$$B_r = \mu_o\mu_{rec}H_r + M_o \qquad (2.29)$$

where $M_o = B_{rem}$ for ceramic and rare-earth magnets and μ_{rec} is the relative recoil permeability of the magnet.

When considering the transverse permeability of the magnet, problems arise because very little experimental data is available. However, it is assumed that the transverse magnetisation curve is identical to the virgin magnetisation curve in the magnetised direction and the transverse perm-

eability is equal to the initial permeability [26]. This implies therefore that transverse permeability is of the same order as the recoil permeability, as seen in section 2.2.2. Consequently, the transverse characteristic may be represented by the linear equation

$$B_\theta = \mu_o \mu_t H_\theta \tag{2.30}$$

where μ_t is the relative transverse permeability.

Eq. (2.29) and Eq. (2.30) are effectively the two orthogonal components of the general vector Eq. (2.23).

2.7.3 - Derivation of finite-difference equations for magnetic scalar potential in polar coordinates

The basic formulation is established for a permanent magnet machine with the magnets magnetised in the radial direction, as shown in fig. 2.23. Assuming infinite permeability for iron (unsaturated), the flux lines are normal to the iron surface, which is then a magnetic equipotential. By symmetry, the interpolar planes are also magnetic equipotentials. Hence, the boundary magnet/air region may be taken as an equipotential surface.

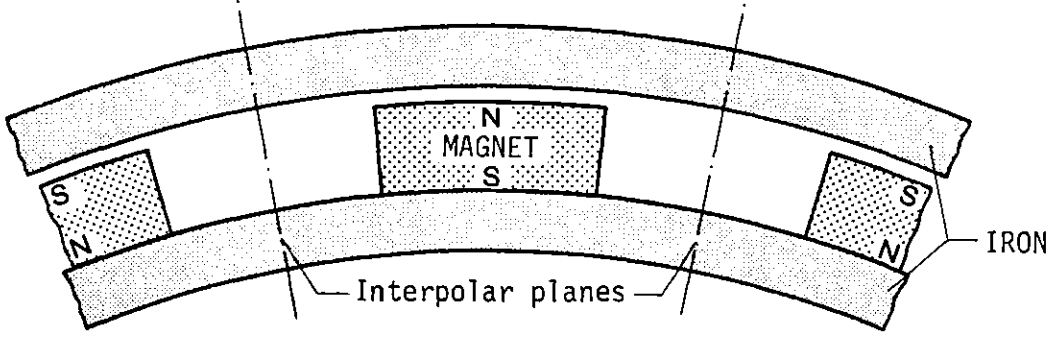

Fig. 2.23 - Permanent magnet machine

To develop the equivalent network for the permanent magnet and surrounding air region in the absence of macroscopic currents, the magnet may then be considered to be situated in an iron window, as shown in fig. 2.24.

A two-dimensional field is assumed, therefore a unit thickness of ma-

terial in the machine axial direction is considered. The region is divided up by a polar mesh and a node is inserted at each intersection of the sub-divided mesh. The solution consists in finding a node potential distribu-

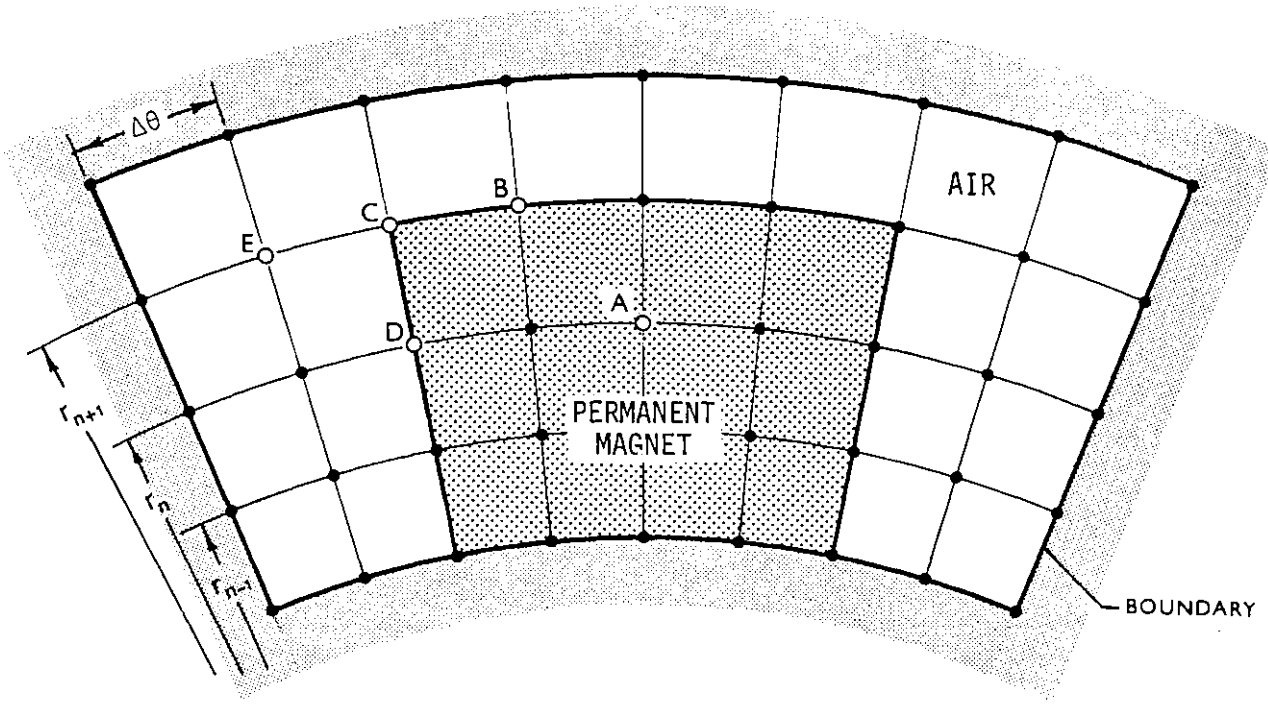

Fig. 2.24 - Permanent magnet in iron window

tion which satisfies Eq. (2.29) and Eq. (2.30) within the permanent magnet, and $B = \mu_0 H$ in the air region. To find the appropriate operator for each node, typical nodes A to E are considered individually.

NODE A - Within the permanent magnet

Node A and its four neighbours are shown in fig. 2.25 together with the associated scalar potential values.

Since the nodes are all within the permanent magnet material, from Eq. (2.29) and Eq. (2.27) the flux densities in the r direction are:

$$B_{02} = \mu_{rec}\mu_o \frac{\Omega_2 - \Omega_0}{r_{n+1} - r_n} + M_o$$

$$B_{40} = -\mu_{rec}\mu_o \frac{\Omega_0 - \Omega_4}{r_n - r_{n-1}} + M_o$$

Similarly, from Eq. (2.30) the flux densities in θ direction

$$B_{01} = -\mu_t \mu_o \frac{\Omega_1 - \Omega_0}{r_n \Delta\theta}$$

$$B_{30} = -\mu_t \mu_o \frac{\Omega_0 - \Omega_3}{r_n \Delta\theta}$$

where B_{02} is the component of the flux density in a radial direction directed from node 0 to node 2 and similarly for the other notation.

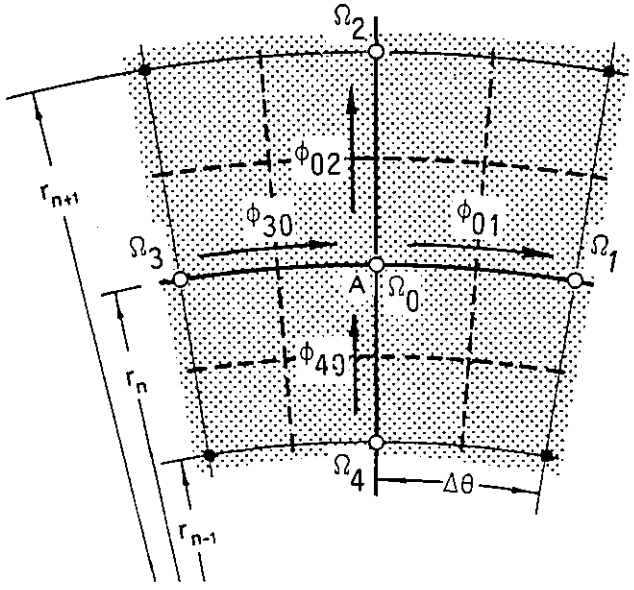

Fig. 2.25 - Generic node within the magnet

Hence, the flux in a tube of radial and transversal mesh per unit axial length is respectively:

$$\Phi_{02} = B_{02} \frac{r_{n+1} + r_n}{2} \Delta\theta = -\mu_{rec}\mu_o \frac{r_{n+1}+r_n}{2(r_{n+1}-r_n)} \Delta\theta (\Omega_2 - \Omega_0) + M_o \frac{r_{n+1}+r_n}{2} \Delta\theta$$

$$\Phi_{40} = B_{40} \frac{r_n + r_{n-1}}{2} \Delta\theta = -\mu_{rec}\mu_o \frac{r_n + r_{n-1}}{2(r_n - r_{n-1})} \Delta\theta (\Omega_0 - \Omega_4) + M_o \frac{r_n + r_{n-1}}{2} \Delta\theta$$

$$\Phi_{01} = B_{01} \frac{r_{n+1} - r_{n-1}}{2} \Delta\theta = -\mu_t \mu_o \frac{r_{n+1} - r_{n-1}}{2 r_n \Delta\theta} (\Omega_1 - \Omega_0)$$

$$\Phi_{30} = B_{30} \frac{r_{n+1} - r_{n-1}}{2} \Delta\theta = -\mu_t \mu_o \frac{r_{n+1} - r_{n-1}}{2 r_n \Delta\theta} (\Omega_0 - \Omega_3)$$

By defining the factor

$$K = \frac{r_{n+1}}{r_n} = \frac{r_n}{r_{n-1}} > 1 \qquad (2.31)$$

the above equations can be written in the form:

$$\phi_{02} = P_{2A}(\Omega_0 - \Omega_2) + M_o r_n \Delta\theta \frac{K+1}{2} \tag{2.32}$$

$$\phi_{40} = P_{4A}(\Omega_4 - \Omega_0) + M_o r_n \Delta\theta \frac{K+1}{2K} \tag{2.33}$$

$$\phi_{01} = P_{1A}(\Omega_0 - \Omega_1) \tag{2.34}$$

$$\phi_{30} = P_{3A}(\Omega_3 - \Omega_0) \tag{2.35}$$

where

$$P_{2A} = P_{4A} = \mu_{rec}\mu_o \frac{K+1}{2(K-1)}\Delta\theta$$

$$P_{1A} = P_{3A} = \mu_t\mu_o \frac{K^2-1}{2K\Delta\theta}$$

are the permeances inserted between reference node 0 and its neighbours.

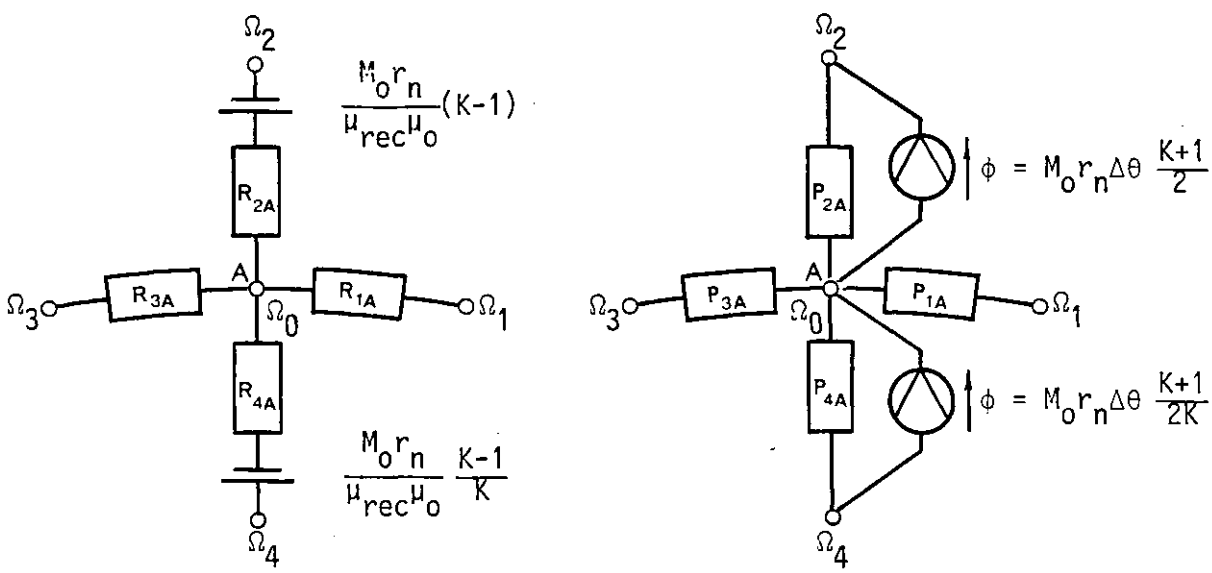

(a) - Equivalent circuit in terms of reluctance and m.m.f. generators

(b) - Equivalent circuit in terms of permeance and flux generators

Fig. 2.26 - Equivalent circuits for node within magnet

From the magnetic Ohm's law it can be readily demonstrated that Eq. (2.32) to Eq. (2.35) may be represented in terms of reluctance $R = P^{-1}$ shown in fig. 2.26(a) or in terms of permeance shown in fig. 2.26(b).

From the flux continuity considerations, the total flux into node 0 must be

$$-\phi_{01} - \phi_{02} + \phi_{30} + \phi_{40} = 0 \tag{2.36}$$

Substitution of Eq. (2.32) to Eq. (2.35) into Eq. (2.36) gives:

$$(\Omega_1+\Omega_3)P_{3A} + (\Omega_2+\Omega_4)P_{4A} - 2\Omega_0(P_{1A}+P_{2A}) + M_o r_n \Delta\theta \frac{K^2-1}{2K} = 0 \tag{2.37}$$

For a fine mesh, K is very close to unity and Eq. (2.37) may be written approximately as:

$$(\Omega_1+\Omega_3)P_{3A} + (\Omega_2+\Omega_4)P_{4A} - 2\Omega_0(P_{1A}+P_{2A}) = 0 \tag{2.38}$$

Eq. (2.38) is the finite-difference equation applicable for calculating the magnetic scalar potential Ω within the magnet. Fig. 2.27 shows the final simplified equivalent circuit in terms of permeance for such nodes.

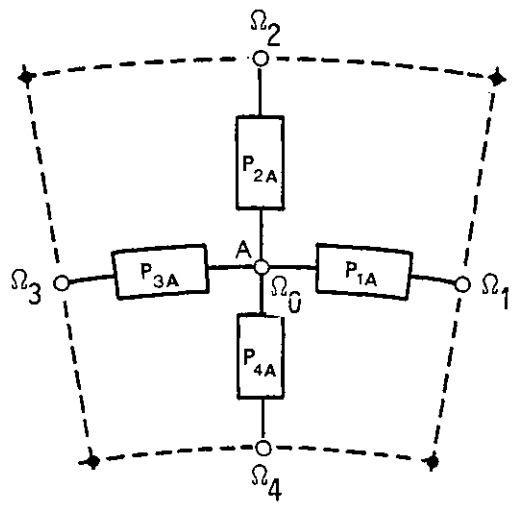

Fig. 2.27 - Simplified equivalent circuit for node within magnet

No flux generators appear since the net flux injected at node A is almost zero. It should be pointed out that for calculating the scalar potential field, and hence H_r and H_θ within the magnet, the flux generators are ignored. However, when calculating B_r, the flux generators shown in fig. 2.26(b) must be replaced.

NODE B - Top of the magnet surface

Node B is situated on the air/magnet top surface and the conditions are shown in fig. 2.28(a), the fluxes being given by

$$\phi_{01} = P_{1B}(\Omega_0 - \Omega_1)$$

$$\phi_{02} = P_{2B}(\Omega_0 - \Omega_2)$$

$$\phi_{30} = P_{3B}(\Omega_3 - \Omega_0)$$

$$\phi_{40} = P_{4B}(\Omega_4 - \Omega_0) + M_o\, r_{mag}\, \Delta\theta\, \frac{K+1}{2K}$$

where

$$P_{2B} = \mu_o \frac{K+1}{2(K-1)}\, \Delta\theta$$

and

$$P_{4B} = \mu_{rec}\mu_o \frac{K+1}{2(K-1)}\, \Delta\theta$$

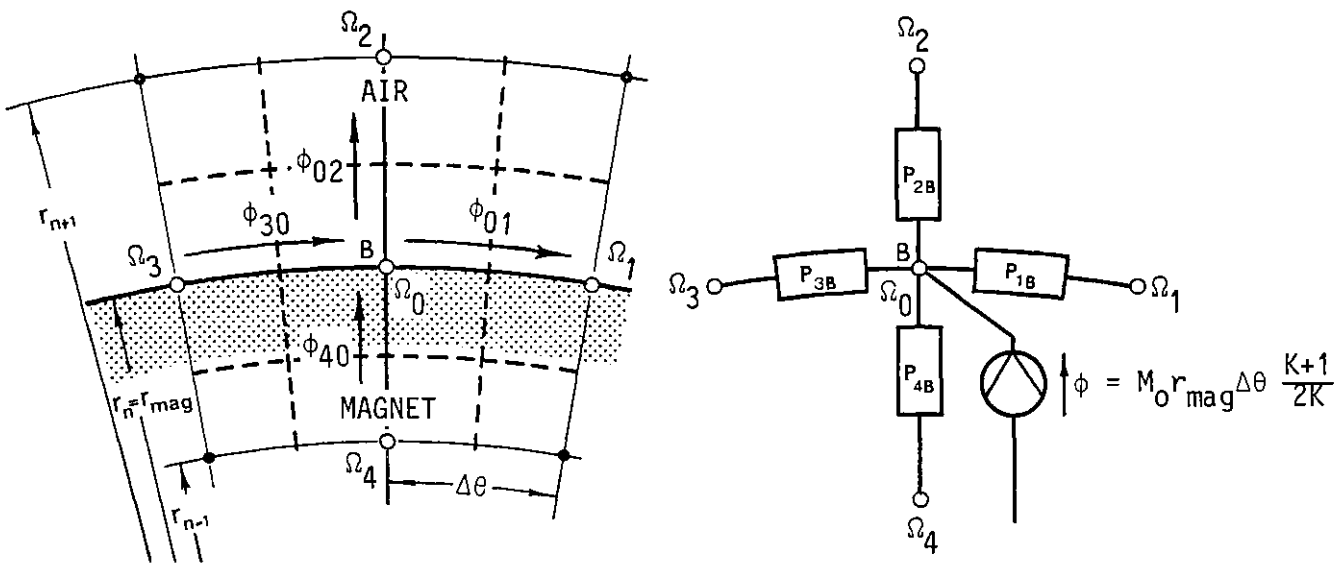

Fig. 2.28 - Conditions for node on top of the magnet surface

The transverse permeances P_{1B} and P_{3B} may be considered as the addition of two parallel permeances, one in air and one in the permanent magnets. Thus:

$$P_{1B} = P_{3B} = (1 + \mu_t)\mu_o \frac{K^2-1}{4K\Delta\theta}$$

By the summation of the total flux entering node 0 to zero, the following equation is obtained

$$(\Omega_1+\Omega_3)P_{1B} + \Omega_2 P_{2B} + \Omega_4 P_{4B} - \Omega_0(2P_{1B}+P_{2B}+P_{4B}) + M_o r_{mag}\Delta\theta \frac{K+1}{2K} = 0 \qquad (2.39)$$

and fig. 2.28(b) shows the corresponding equivalent circuit for this node.

NODE C - Corner of the magnet

The conditions at node C on the magnet corner are illustrated in fig. 2.29, where the permeances inserted are now given by:

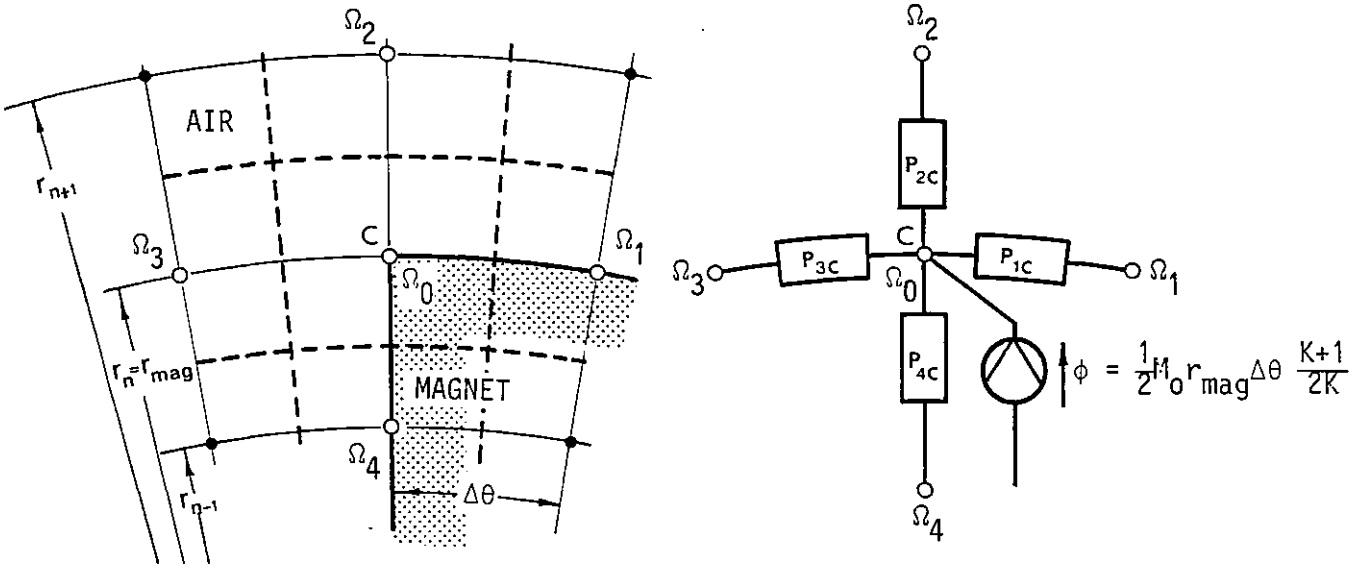

(a) - Node on magnet corner (b) - Equivalent circuit

Fig. 2.29 - Conditions for node on corner of the magnet

$$P_{1C} = (1 + \mu_t)\mu_o \frac{K^2-1}{4K\Delta\theta}$$

$$P_{2C} = \mu_o \frac{K+1}{2(K-1)} \Delta\theta$$

$$P_{3C} = \mu_o \frac{K^2-1}{2K\Delta\theta}$$

$$P_{4C} = (1 + \mu_{rec})\mu_o \frac{K+1}{4(K-1)} \Delta\theta$$

The flux continuity condition gives:

$$\Omega_1 P_{1C} + \Omega_2 P_{2C} + \Omega_3 P_{3C} + \Omega_4 P_{4C} - \Omega_0 \sum_1^4 P_{iC} + \frac{1}{2} M_o r_{mag} \Delta\theta \frac{K+1}{2K} = 0 \qquad (2.40)$$

It should be noted that the flux generator is only half the previous value, since it operates on only half the cross-sectional area of the mesh.

NODE D - Magnet /air side boundary

The physical configuration and the corresponding equivalent circuit for this node is represented in fig. 2.30. Here, as with node A, the flux generators need only be included in the final calculation of B_r. However,

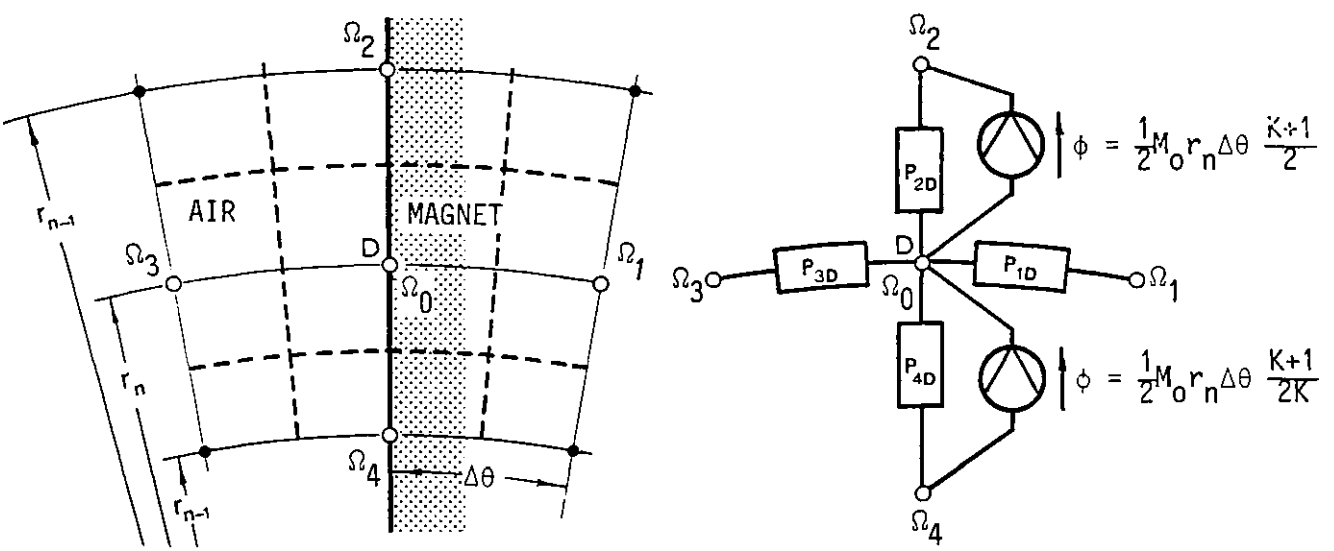

(a) - Node on magnet/air side boundary (b) - Equivalent circuit

Fig. 2.30 - Conditions for node on magnet/air side boundary

for calculating Ω and hence H, the flux generators should be ignored. The permeances inserted are given by

$$P_{1D} = \mu_t \mu_o \frac{K^2-1}{2K\Delta\theta}$$

$$P_{2D} = P_{4D} = (1 + \mu_{rec})\mu_o \frac{K+1}{4(K-1)} \Delta\theta$$

$$P_{3D} = \mu_o \frac{K^2-1}{2K\Delta\theta}$$

and the flux continuity conditions give:

$$\Omega_1 P_{1D} + (\Omega_2+\Omega_4)P_{2D} + \Omega_3 P_{3D} - \Omega_0(P_{1D} + 2P_{2D} + P_{3D}) = 0 \qquad (2.41)$$

NODE E - Air region

The characteristics for node E are illustrated in fig. 2.31 where the permeances inserted are given by

$$P_{1E} = P_{3E} = \mu_o \frac{K^2-1}{2K\Delta\theta}$$

$$P_{2E} = P_{4E} = \mu_o \frac{K+1}{2(K-1)} \Delta\theta$$

and the general operator is

$$(\Omega_1+\Omega_3)P_{1E} + (\Omega_2+\Omega_4)P_{2E} - 2\Omega_0(P_{1E}+P_{2E}) = 0 \qquad (2.42)$$

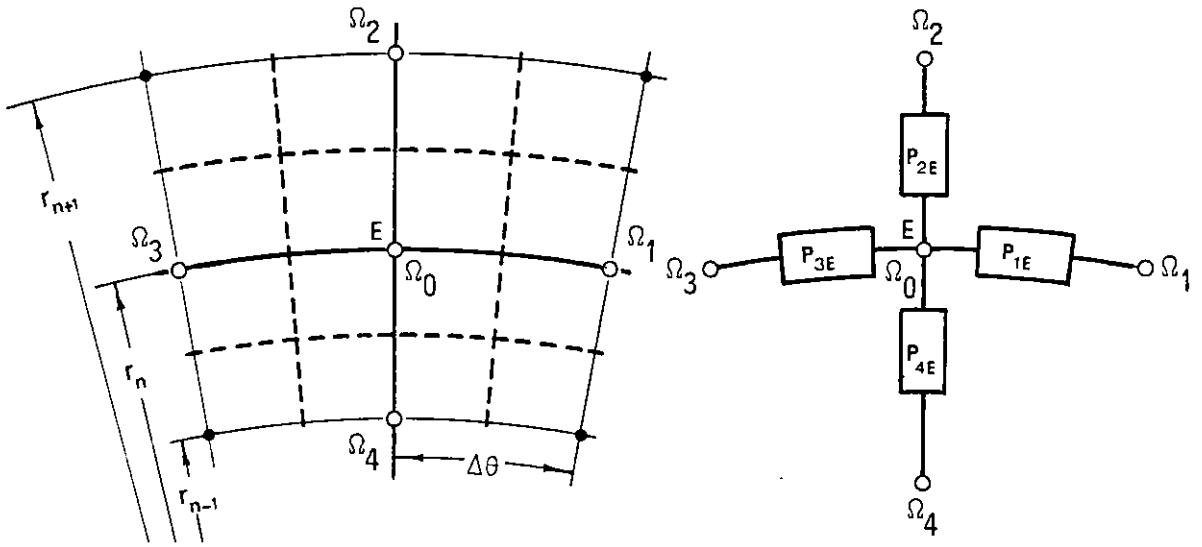

(a) - Node on air region (b) - Equivalent circuit

Fig. 2.31 - Conditions for node on air region

In order to make the relaxation operator independent of the mesh radius it must be

$$\mu_o \frac{K^2-1}{2K\Delta\theta} = \mu_o \frac{K+1}{2(K-1)} \Delta\theta$$

from where

$$(K-1)^2 - K\Delta\theta^2 = 0 \qquad (2.43)$$

For fixed $\Delta\theta$, Eq. (2.43) gives K and from the largest radius, which corres-

ponds to the stator surface, all the other radii are defined by Eq.(2.31) and a logarithmic mesh can be generated. Eq. (2.42) then reduces to

$$\Omega_1 + \Omega_2 + \Omega_3 + \Omega_4 - 4\Omega_0 = 0 \qquad (2.44)$$

an operator commonly found associated with Laplacian fields.

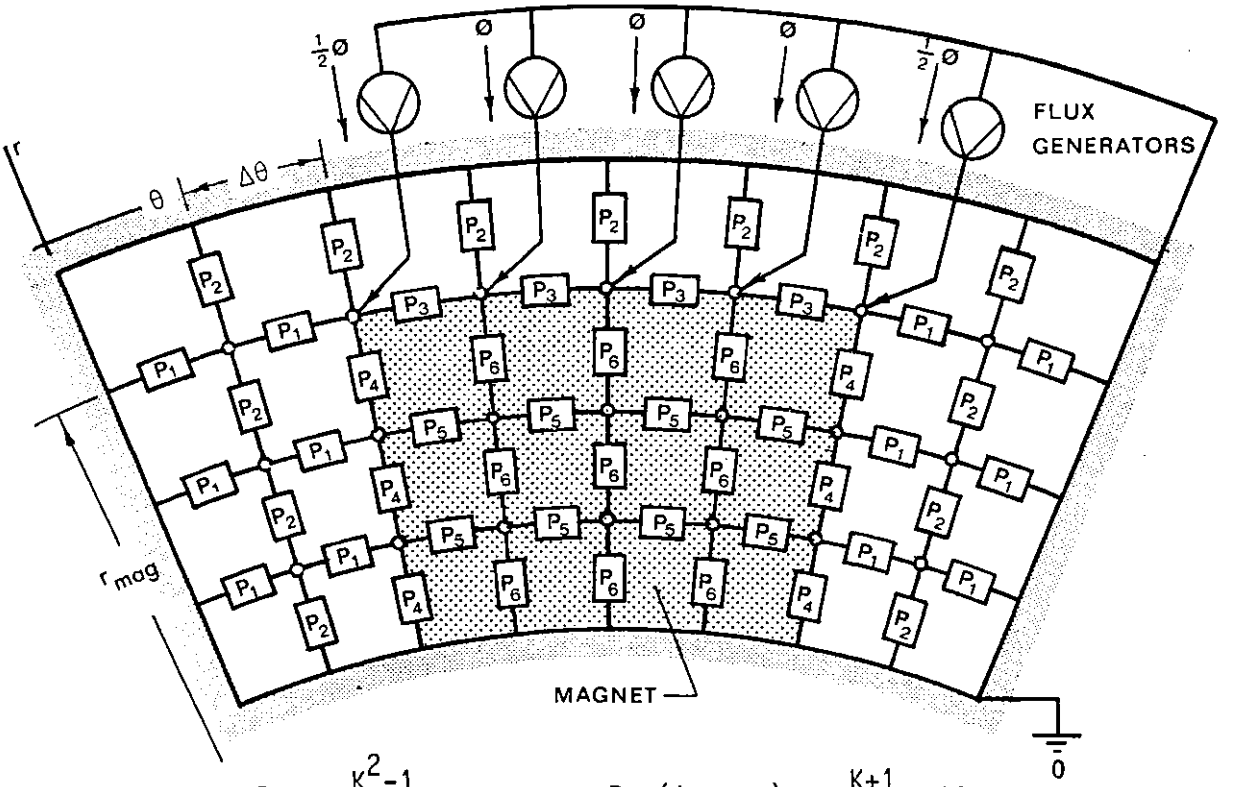

$$P_1 = \mu_o \frac{K^2-1}{2K\Delta\theta} \qquad P_4 = (1+\mu_{rec})\mu_o \frac{K+1}{4(K-1)}\Delta\theta$$

$$P_2 = \mu_o \frac{K+1}{2(K-1)}\Delta\theta \qquad P_5 = \mu_t\mu_o \frac{K^2-1}{2K\Delta\theta}$$

$$P_3 = (1+\mu_t)\mu_o \frac{K^2-1}{4K\Delta\theta} \qquad P_6 = \mu_{rec}\mu_o \frac{K+1}{2(K-1)}\Delta\theta$$

Fig. 2.32 - Complete equivalent circuit of one pole pitch

Finally, fig. 2.32 shows the resulting equivalent circuit for the complete magnet/air region of one pole pitch, where six different permeances can be considered. The flux generators with a value

$$\phi = M_o r_{mag} \Delta\theta \frac{K+1}{2K}$$

are only injected on magnet top surface nodes.

2.7.4 - Field solution at no-load

Having established the equivalent-circuit for the complete magnet/air region, the problem may be analysed as a simple electrical network. The permeance is analogous to conductance and the permanent magnet flux generators analogous to current generators in the electrical equivalent network. Thus, the node potentials may be found analogically using an equivalent electrical network model or numerically using a matrix method

$$[\phi] = [P]\cdot[\Omega] \tag{2.45}$$

where [P] is the matrix permeance. When few nodes are considered, solution of Eq. (2.45) may be obtained by manual matrix inversion and an example will be presented later. If the number of nodes are substantially increased, the matrix inversion may be carried out by a digital computer.

However, for a very fine mesh with a very large number of nodes it is convenient to use an iterative process, since in this case solution by matrix inversion becomes too expensive in terms of computing time. The iterative process is based on the concept of residuals [53]. When the potentials Ω_0, Ω_1,..., Ω_4 are so chosen as to satisfy a difference equation, say Eq. (2.44), the left-hand side is zero. When, however, the potentials do not satisfy the equation the right-hand side is not equal to zero but to some quantity R_0, given by

$$R_0 = \Omega(I+1,J) + \Omega(I,J-1) + \Omega(I-1,J) + \Omega(I,J+1) - 4.*\Omega(I,J) \tag{2.46}$$

where R_0 is known as the residual of the difference equation at point 0. When the residuals of all the difference equations are zero, the values of potential correspond to an exact solution. In practice, Eq. (2.46) is considered to be solved when $R_0 \leq$ RESMAX where RESMAX is a sufficiently low value to obtain a good approximation to the exact solution. At the node under consideration with a potential $\Omega(I, J)_{old}$ the residual is calculated using Eq. (2.46) and then the residual is reduced to zero by

a change in $\Omega(I, J)_{old}$ of $R_o/4$. Thus, in the next iteration cycle the new value of potential is given by

$$\Omega(I, J)_{new} = \Omega(I, J)_{old} + \left(\frac{\alpha}{4}\right)R_o \qquad (2.47)$$

where α is the acceleration factor to improve the rate of convergence of the solution. When the potential at a node is changed in such a way that the sign of the residual reverses, the operation is called over-relaxation.

Appendix A describes a computer program for solution of the magnetic potential distribution in the basic problem considered in fig. 2.23. Due to the symmetry of the problem, only half of the network needs to be solved. A mesh with 30 circumferential nodes and 20 radial nodes was used and the result is shown in fig. 2.33. The potentials in the right half-pole pitch are stored in the two dimensional array and a mirror image is obtained for the left half pole pitch. The complete field solution and a three-dimensional equipotential surface is shown in fig. 2.34.

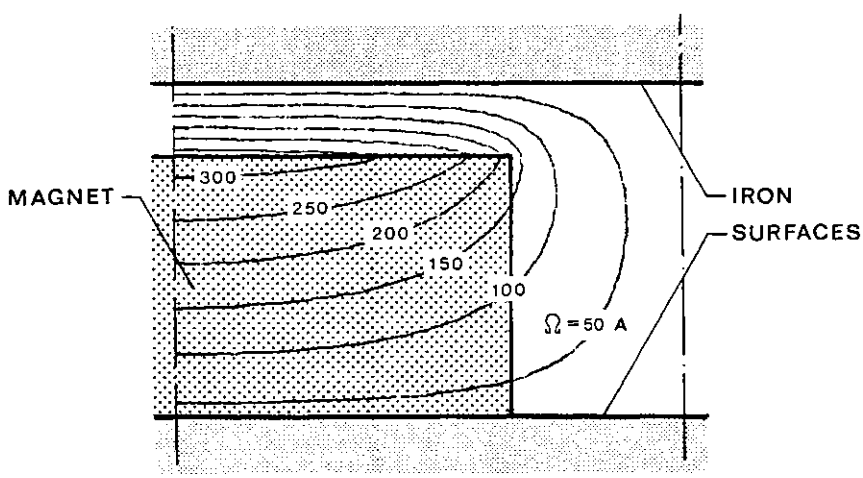

Fig. 2.33 - Equipotential contours for half pole-pitch

From the knowledge of the magnetic potential distribution, flux per pole, flux leakage, leakage factor and the air gap flux density distribution may readily be obtained.

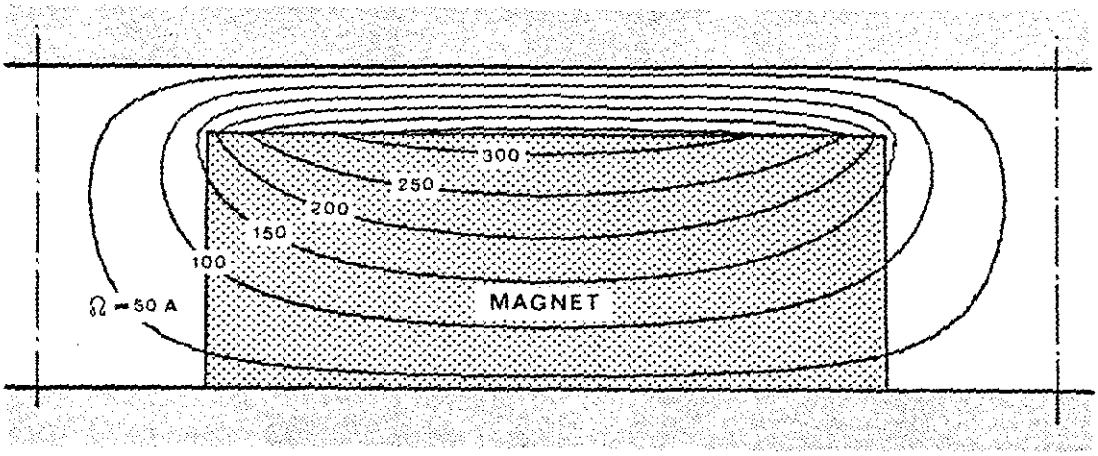

(a) - Equipotential contours for one pole-pitch

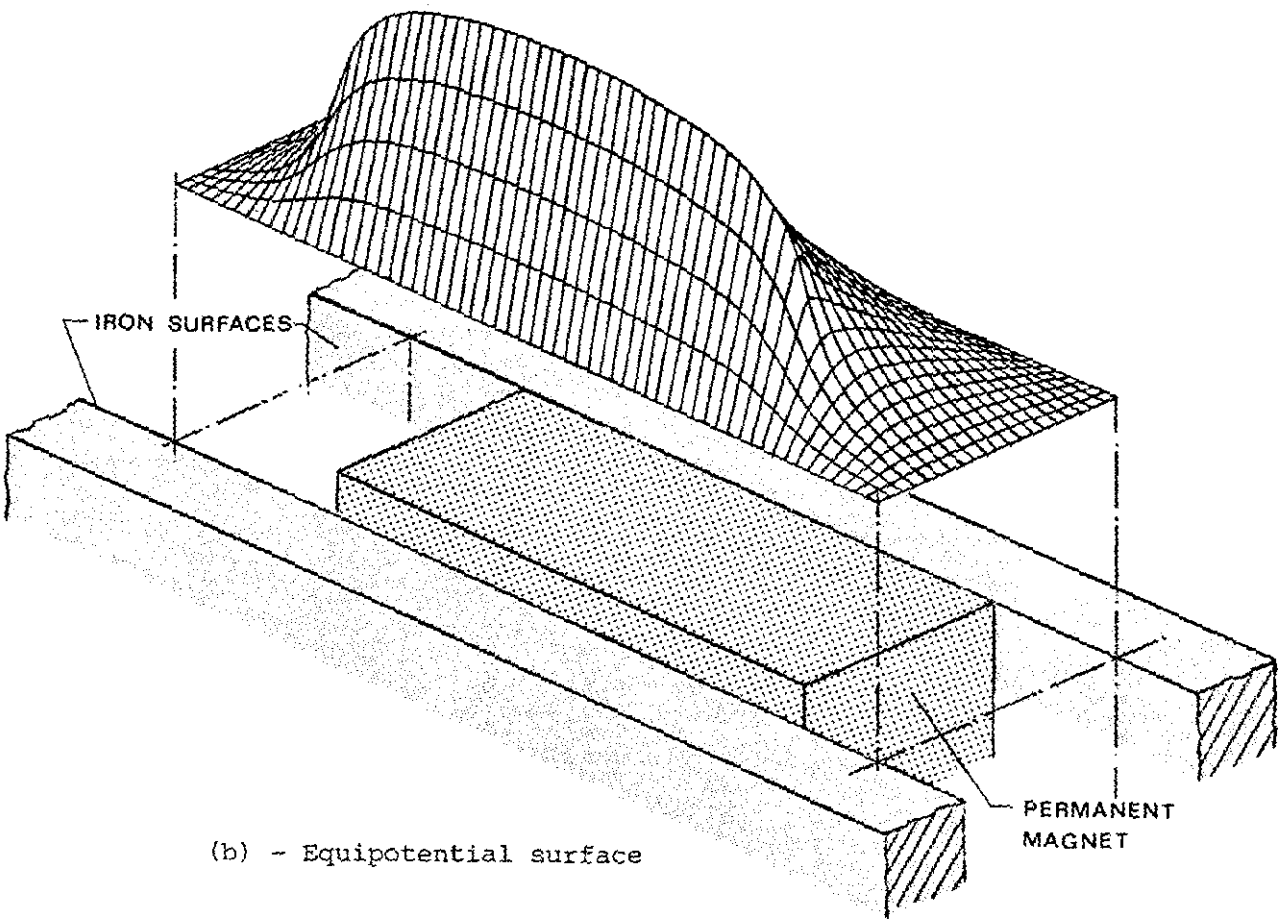

(b) - Equipotential surface

Fig. 2.34 - Complete field solution on no-load

a) - Flux per pole and leakage factor

Having obtained the magnetic potentials at the nodes adjacent to the stator surface (J = 2), the air gap flux density at the circumferential node I may be obtained from the relationship

$$B(I, 1) = \mu_o \frac{\Omega(I,2)-\Omega(I,1)}{r_1 - r_2} = \mu_o \frac{\Omega(I,2)}{r_1 - r_2} \tag{2.48}$$

and consequently the flux per pole and flux leakage set up by the magnet are given by

$$\phi_{pole} = \mu_o \sum_{I=1}^{I=n} \Omega(I, 2) \frac{K+1}{2(K-1)} \Delta\theta \ell \tag{2.49}$$

$$\phi_{leak} = 2\mu_o \sum_{J=1}^{J=m} \Omega(2, J) \frac{K^2-1}{2J\Delta\theta} \ell \tag{2.50}$$

where ℓ is the effective magnet axial length. From Eq. (2.49) and Eq. (2.50) the leakage factor defined by Eq. (2.10) may be obtained.

b) - Air gap flux density distribution

A Fourier analysis of the calculated values of B(I, 1) given by Eq. (2.48) from $\theta = 0$ to $\theta = 2\pi$ can be done by using Simpson's rule to evaluate numerically the harmonic coefficients

$$b_h = \frac{1}{\pi} \int_0^{2\pi} B(\theta).\sin h\theta \, d\theta \tag{2.51}$$

since the wave has only odd harmonics. From the harmonic coefficients, the resultant waveform of the air gap flux density distribution is given by

$$B(\theta) = \sum_{h=1}^{2n+1} b_h.\sin h\theta \tag{2.52}$$

and may be printed out together with harmonic components, as shown in fig. 2.35.

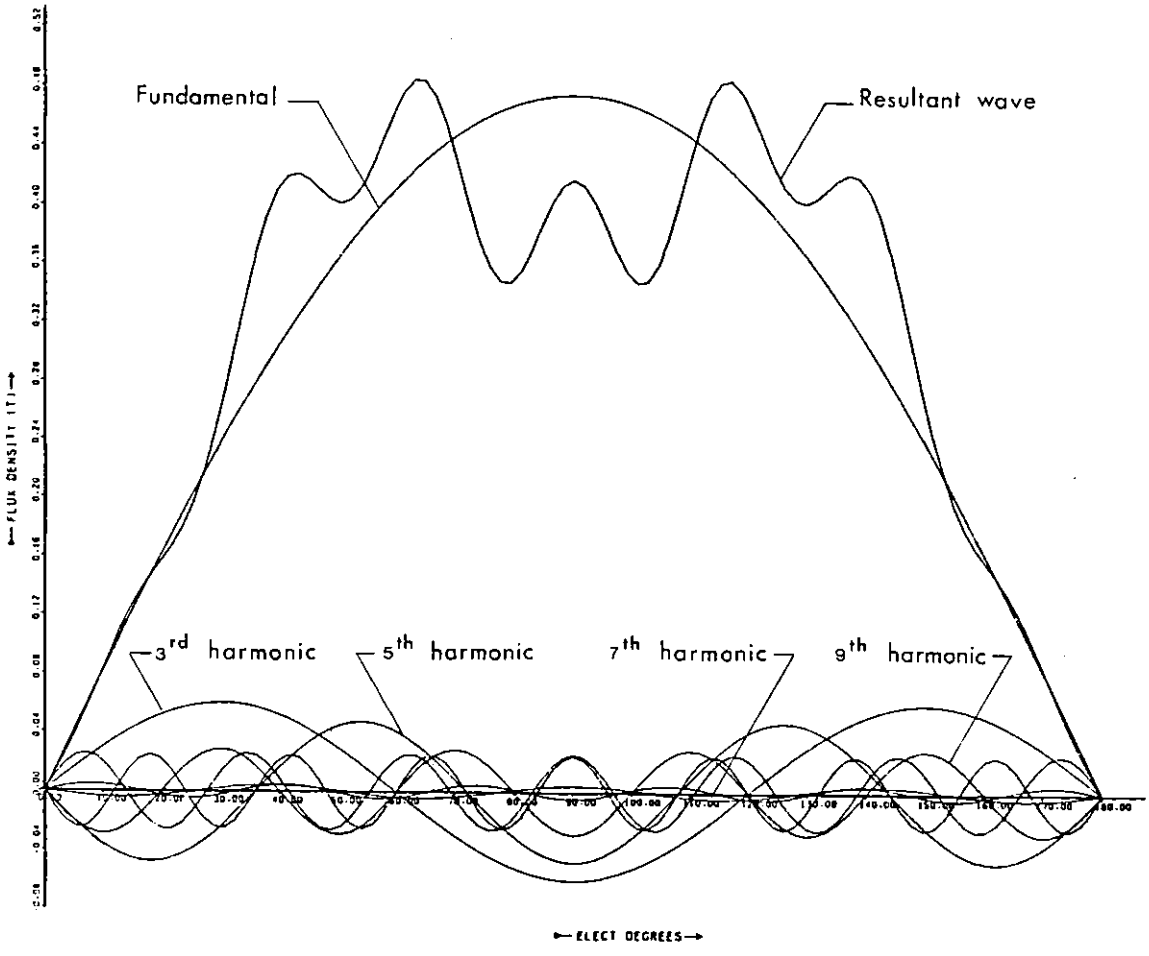

Fig. 2.35 - Resulting air gap flux density wave and harmonic components

2.7.5 - Field solution on load

When current is injected on the stator, Eq. (2.26) is invalid and, hence, H may be no longer represented by the gradient of a scalar potential field Ω. To overcome this problem, it has been suggested [54] to replace the stator current by a scalar potential distribution along the stator surface representing the resulting m.m.f. pattern. Assuming linearity, the field solution on load is then obtained using the superposition principle.

The technique may be applied to the permanent magnet machine illustrated in fig. 2.36(a), where for simplicity the stator current is considered on the q-axis. As already shown the resulting m.m.f. wave depends on the winding arrangement and in this example a triangular wave is considered, but the theory applies to any other shape.

The magnetic potential distribution in one pole-pitch only due to the stator current is then obtained by assigning a triangular scalar potential distribution to the top surface boundary nodes. In order to ignore the effect of the permanent magnet, the magnet polarisation M and hence flux generators must be set to zero, but the transverse and radial permeances of the magnet material and air region is considered.

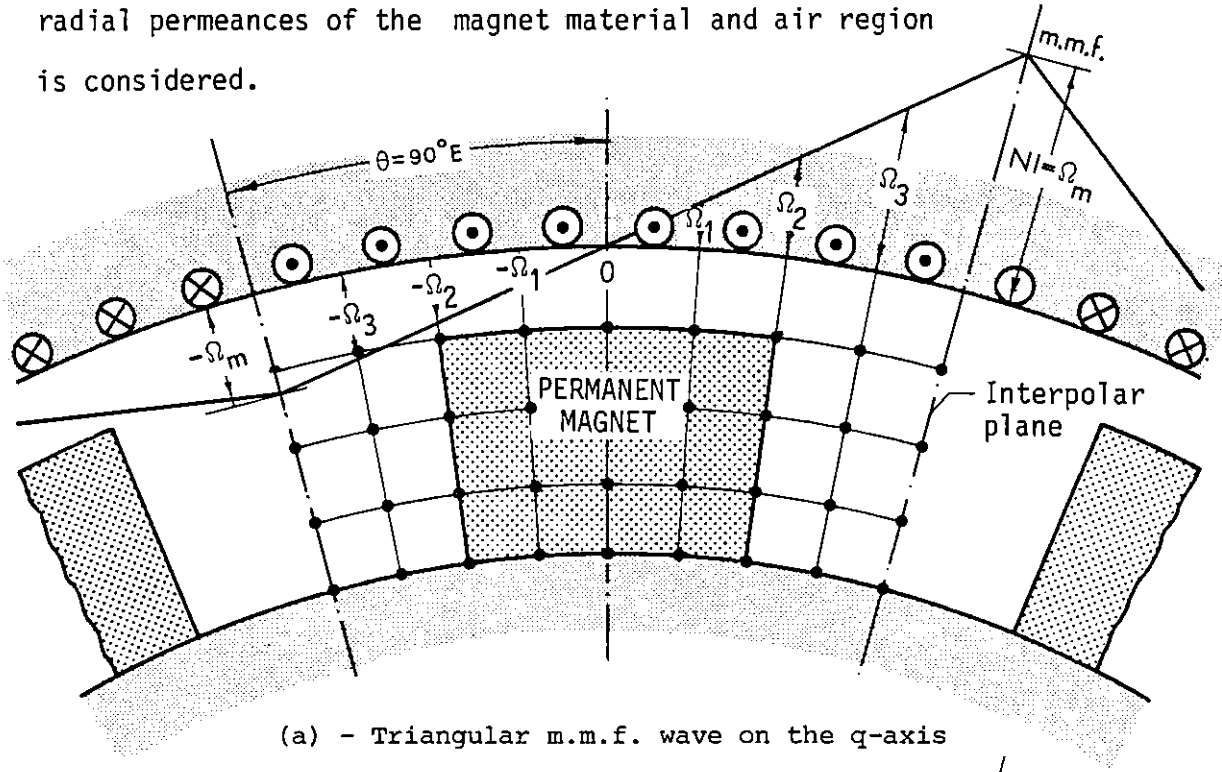

(a) - Triangular m.m.f. wave on the q-axis

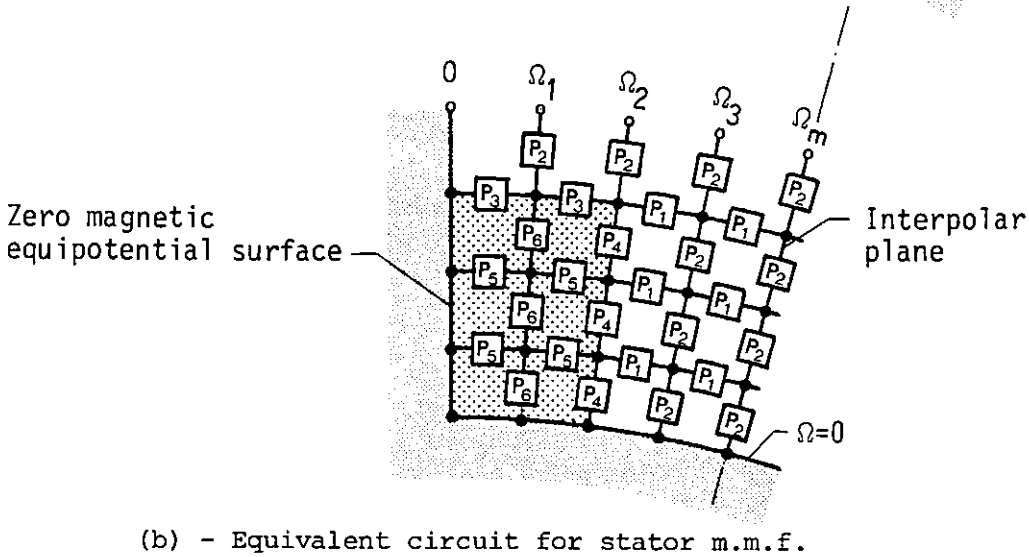

(b) - Equivalent circuit for stator m.m.f.

Fig. 2.36 - Equivalent circuit for stator m.m.f. on the q-axis

Thus the new equivalent network to be solved is shown in fig. 2.36(b), where the magnet centre plane becomes now a zero magnetic equipotential surface.

The new equivalent network may be solved using the same technique as before, and a typical solution is shown in fig. 2.37.

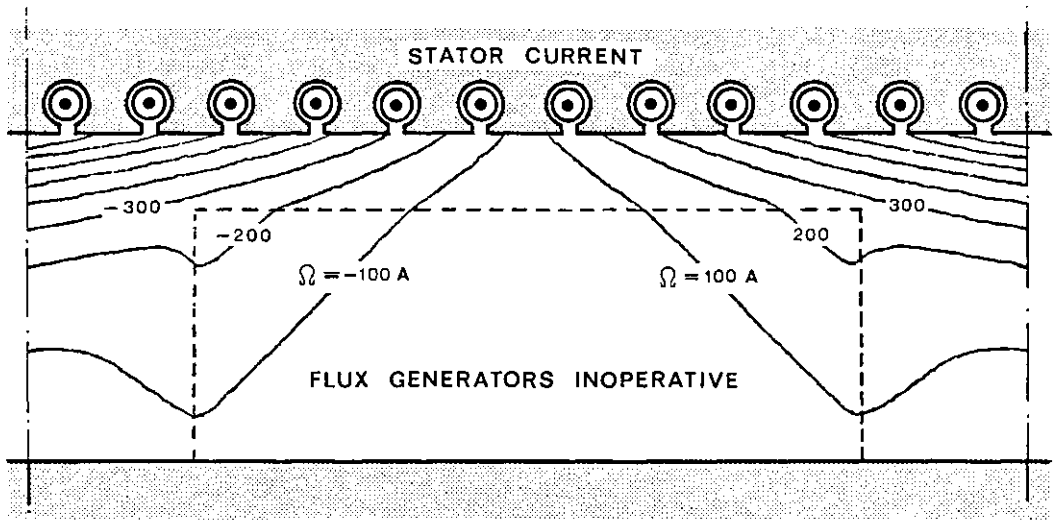

Fig. 2.37 - Equipotential contours in one pole pitch only due to the stator current

Now, invoking the superposition principle, the magnetic equipotential distribution on load is given by the addition of the two solutions obtained with magnet polarisation and stator current acting separately, as shown in fig. 2.34(a) and fig. 2.37 respectively. The resulting magnet potential distribution on load in one pole pitch is then shown in fig. 2.38.

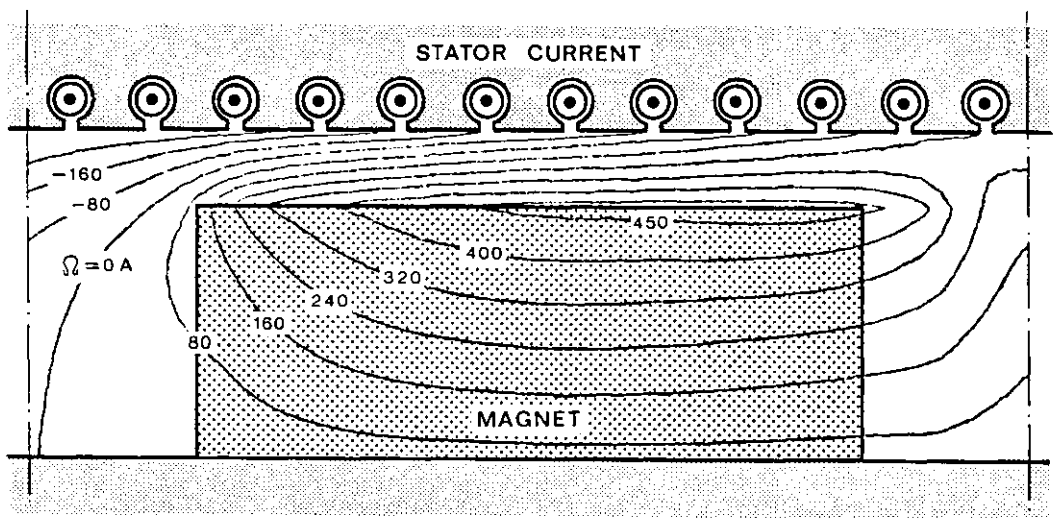

Fig. 2.38 - Equipotential contours in one pole pitch on load

From both solutions, the influence of stator current on the permanent magnet's operation may be examined. Also machine air gap inductance may be evaluated.

a) - Stator current limit for magnet demagnetisation

For permanent magnet demagnetisation the most severe condition occurs when stator current is on the q-axis. Fig. 2.39 illustrates diagrammatically the flux lines set up by the stator current and by the permanent magnet in the basic synchronous motor operating at 90°E torque angle.

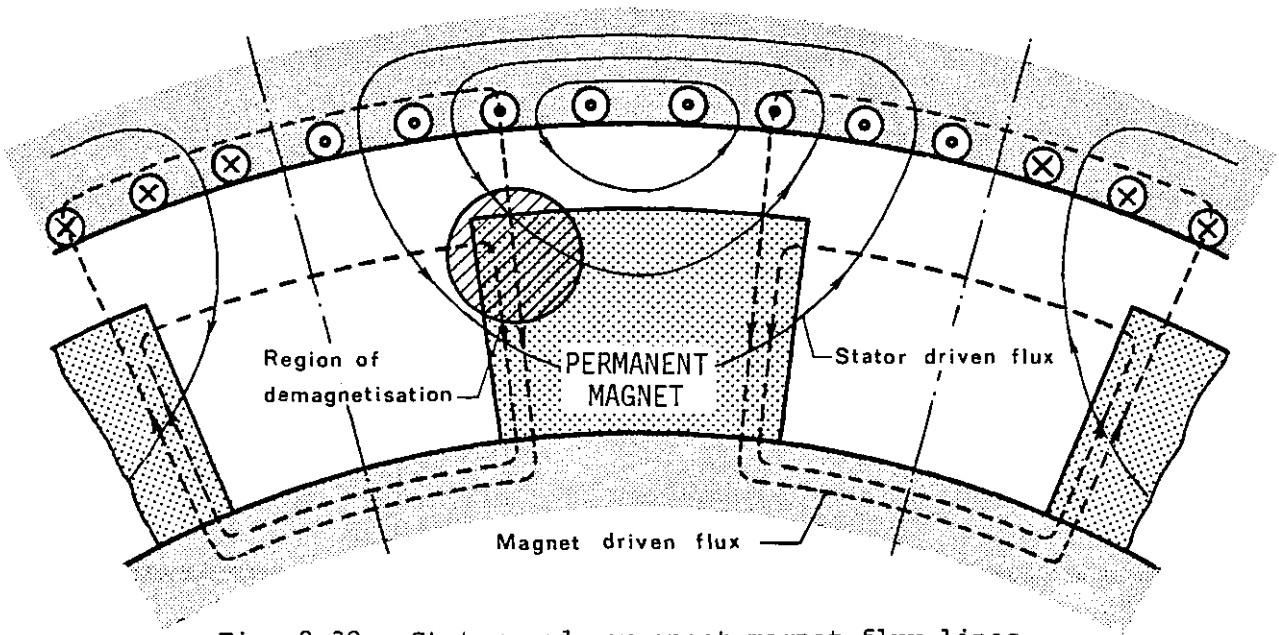

Fig. 2.39 - Stator and permanent magnet flux lines for 90°E torque angle

The magnetising force on load at any particular point of the magnet may be calculated as the sum of the no-load magnetising force H_o of the magnet and the magnetising force H_{Io} due to the stator m.m.f. NI_o acting alone with the permanent flux generators removed. If unsaturated iron is assumed, the magnetising force H_I for any value of stator m.m.f. NI is $H_{Io}I/I_o$. Then the magnetising force on load H_L is given by

$$H_L = H_o + H_{Io}\frac{I}{I_o} \qquad (2.53)$$

and so, two field solutions, the no-load and one load run, are sufficient to obtain H_L for any stator current I of a synchronous motor with fixed torque angle [50].

From the load field solution, the magnet region where H_L attains the maximum value may be found. For this particular region, if H_L is replaced

by the coercive force H_c of the magnet in Eq. (2.53), the current limit I to avoid magnet demagnetisation is:

$$I = I_o \frac{H_c - H_o}{H_{Io}} \tag{2.54}$$

Normally, the region most prone to demagnetisation is the top corner of the magnet, because in this region the stator surface potential attains its maximum value.

b) - Air gap inductance

The air gap inductance is by definition the flux linkage with stator coils per unit conductor current. The flux linkage for a given stator current may be obtained from a load run with magnet polarisation set to zero. As an example, fig. 2.40 illustrates a permanent magnet two-phase

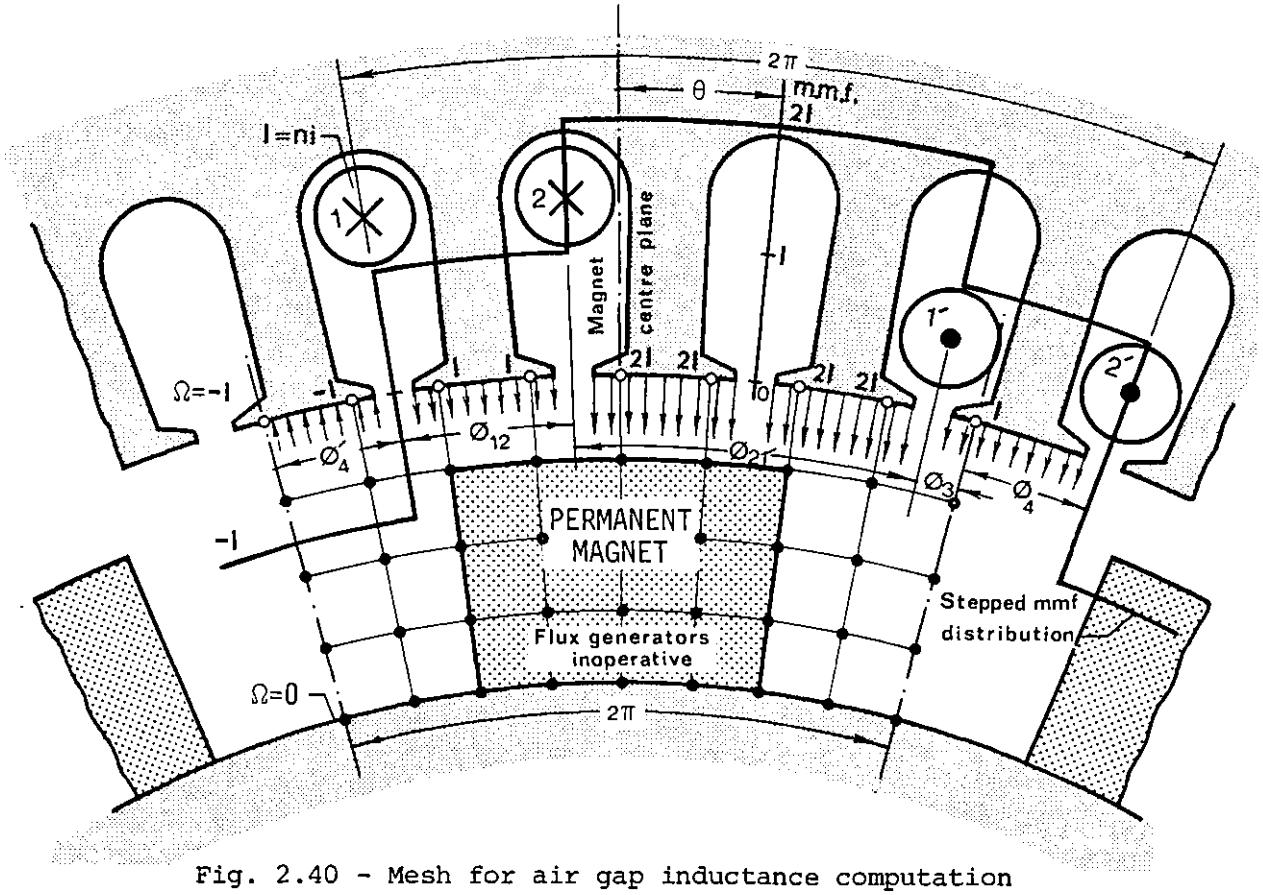

Fig. 2.40 - Mesh for air gap inductance computation at θ torque angle

synchronous motor with q = 2 coils/pole/phase operating at a generic θ torque angle. From Eq. (1.110), the air gap inductance per phase for

an n_p pole machine when the m.m.f. is in a particular position θ is given by

$$L_a(\theta) = n_p n^2 \frac{1}{I} (\phi_{12} + \phi_{21'} + \phi_3 + \phi_4') \tag{2.55}$$

where $I = ni$ and $\phi_3 - \phi_4' = \phi_{1'2'}$, since by symmetry $-\phi_4' = \phi_4$. Hence for any given torque angle the air gap inductance may be calculated using the equivalent circuit of one pole pitch only. By assigning the stepped m.m.f. distribution produced by the coils to the top boundary nodes, the flux components of Eq. (2.55) are then calculated from the magnetic potential distribution along the stator surface and $L_a(\theta)$ evaluated. An example is given in section 4.8.

2.7.6 - Flux plot

Although the potential scalar model provides a complete description of the field, a plot of flux lines would also be desirable in some cases. Just as for the scalar potential shown before, a similar formulation in terms of vector potential $\bar{A}$ can be derived.

As stated by Eq. (2.21) the divergence of $\bar{B}$ is identically zero, and from vector analysis it is known that the divergence of the curl of any vector is zero. Thus a vector potential $\bar{A}$ can be defined as

$$\bar{B} = \text{curl}\, \bar{A} \tag{2.56}$$

If Eq. (2.56) is integrated over a surface or radius r and Stoke's theorem is applied, it gives:

$$\oint_c \bar{A}\, \overline{d\ell} = \int_S (\text{curl}\ \bar{A}\ \bar{dS}) = \int_S (\bar{B}\ \bar{dS}) = \phi$$

or

$$2\pi r\, A(r, \theta) = \phi$$

Hence, the total flux enclosed by a circle of radius r is equal to $2\pi r\, A(r, \theta)$, and the locus of all circles of which $rA(r, \theta)$ is constant is coincident with a flux line. Equipotential lines of the vector potential $\bar{A}$ are coincident with flux lines [51].

Eq. (2.23) can be written as

$$\bar{H} = \frac{\bar{B}}{\mu} - \frac{\bar{M}_o}{\mu} \tag{2.57}$$

Since no macroscopic currents are present, Eq. (2.26) applies and Eq. (2.57) becomes:

$$\text{curl } \left(\frac{\bar{B}}{\mu} \right) = \text{curl } \left(\frac{\bar{M}_o}{\mu} \right) \tag{2.58}$$

Comparing Eq. (2.58) with Eq. (2.20), curl $\left(\frac{\bar{M}_o}{\mu} \right)$ can be visualised as a macroscopic current sheet $\bar{J}_r$ surrounding a body of permeability $\mu = \mu_o(1 + \chi)$. Hence, substitution of Eq. (2.56) into Eq. (2.58) gives

$$\frac{1}{\mu} \text{ curl curl } \bar{A} = \bar{J}_r$$

which can be written as

$$\text{grad div } \bar{A} - \text{lap } \bar{A} = \mu \bar{J}_r \tag{2.59}$$

In a two-dimensional field the vector potential $\bar{A}$ is parallel to current density $\bar{J}_r$ and so div $\bar{A} = 0$. Eq. (2.59) hence simplifies to:

$$\text{lap } A = -\mu J_r \tag{2.60}$$

which can be treated as a scalar equation, because $\bar{A}$ and $\bar{J}_r$ have only components normal to the field plane. Eq. (2.60) is the Scalar Poisson Equation for the two-dimensional field in terms of the vector potential $\bar{A}$ having the same basic form as Eq. (2.28).

a) - Finite-difference equation for vector potential

Eq. (2.60), the differential equation for $\bar{A}$, can be transformed into a finite-difference equation by the same procedure used to derive the

finite-difference equations for magnetic scalar potential when the magnet is situated in an iron window. Just as the scalar magnetic potential is analogous to node voltage in a network, the vector potential is analogous to node flux source [49]. Then for a general node the finite-difference equation for the vector potential $\bar{A}$ corresponds to a mesh current equation for the reluctance network analog illustrated in fig. 2.41. Thus, the mesh currents are:

$$i_{01} = (A_0 - A_1)R_1 \tag{2.61}$$

$$i_{02} = (A_0 - A_2)R_2 \tag{2.62}$$

$$i_{30} = (A_3 - A_0)R_3 \tag{2.63}$$

$$i_{40} = (A_4 - A_0)R_4 \tag{2.64}$$

where R_1, ..., R_4 are the reluctances inserted between the general node and its neighbours. By current continuity considerations, the total

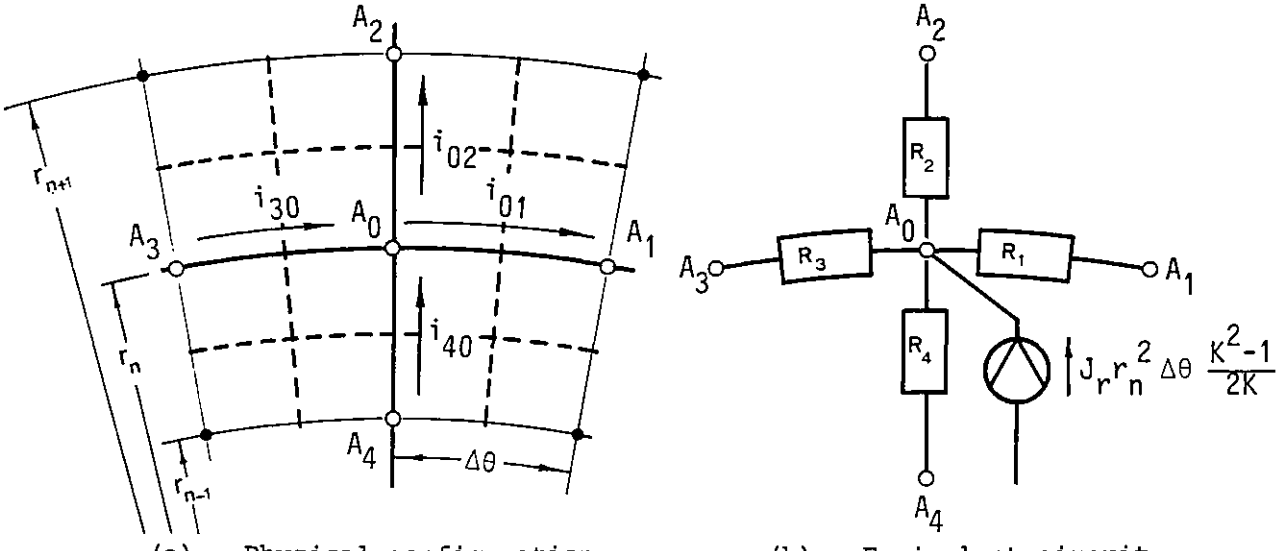

(a) - Physical configuration (b) - Equivalent circuit

Fig. 2.41 - Conditions for a general node in terms of vector potential

current into node 0 must be

$$-i_{01} - i_{02} + i_{30} + i_{40} + J_r r_n \Delta\theta \frac{r_{n+1} - r_{n-1}}{2} = 0 \tag{2.65}$$

Substitution of Eq. (2.61) to Eq. (2.64) into Eq. (2.65) gives the general

equation

$$A_1R_1 + A_2R_2 + A_3R_3 + A_4R_4 - A_0 \sum_{i=1}^{4} R_i + J_r r_n^2 \Delta\theta \frac{K^2-1}{2K} = 0$$

This is the approximate equation of the differential Eq. (2.60). Within the magnet and air region J_r is set to zero. On the magnet/air side boundaries $J_r = |\text{curl}(\frac{\bar{M}_0}{\mu_0\mu_{rec}})|$. For the complete magnet and air region the reluctances correspond to the reciprocal of the appropriate permeances shown in fig. 2.32. To specify the problem completely,

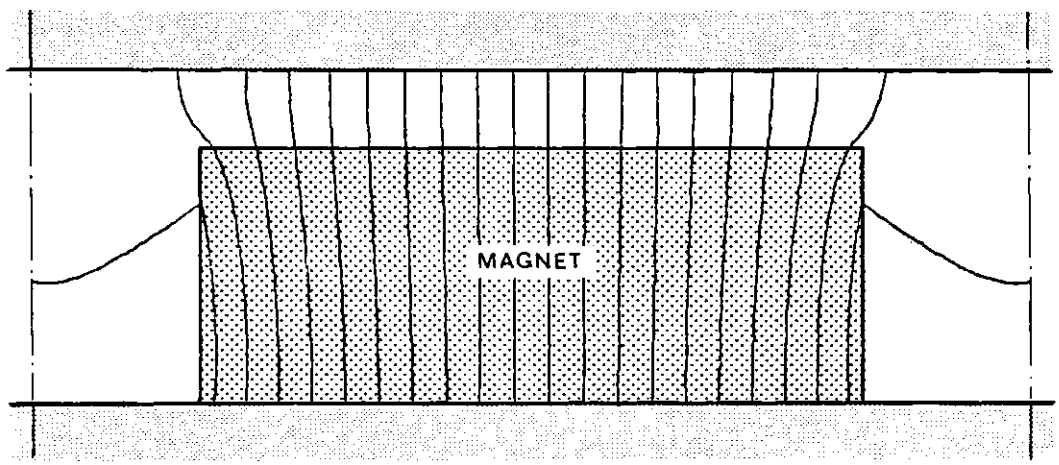

Fig. 2.42 - Flux lines plot

boundary conditions are required. For unsaturated iron flux lines must cross at right angles, which implies $\frac{\partial A}{\partial n} = 0$ at iron surfaces, where n represents distance measured orthogonally to the iron surfaces. Fig. 2.42 shows a plot of the flux lines set up by the magnet placed in an iron window obtained by the method described.

2.7.7 - Derivation of finite-difference equations for magnetic scalar potential in cylindrical coordinates

In some configurations the permanent magnet possesses rotational symmetry rather than polar or cartesian, so that the problem must be solved in a cylindrical coordinate system. The magnet is assumed to be magnetised in the axial direction and the region subdivided in a square

mesh, as shown in fig. 2.43.

With rotational symmetry, div $\bar{H}$ is represented in cylindrical coordinates [55] by the equation

$$\text{div } \bar{H} = \frac{\partial H_r}{\partial r} + \frac{1}{r} H_r + \frac{\partial H_z}{\partial z} \tag{2.66}$$

and so from Eq. (2.27) and Eq. (2.66), Eq. (2.28) becomes:

$$\mu \left(\frac{\partial^2 \Omega}{\partial r^2} + \frac{1}{r} \frac{\partial \Omega}{\partial r} + \frac{\partial^2 \Omega}{\partial z^2} \right) = \text{div } \bar{M}_o \tag{2.67}$$

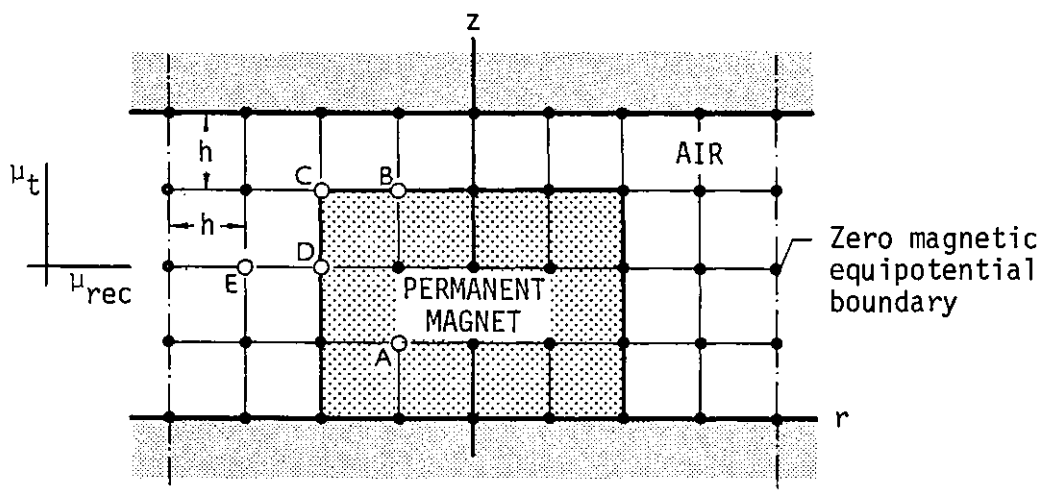

Fig. 2.43 - Permanent magnet problem with rotational symmetry

Using Eq. (2.67), the operator for typical nodes A to E can now be derived.

NODE A - Within the magnet

Fig. 2.44 shows the node A and its neighbours where the magnet potential was assigned.

In the r direction, the second derivative term in Eq. (2.67) may be approximated by

$$\mu \frac{\partial^2 \Omega}{\partial r^2} \simeq \mu_t \mu_o \frac{\frac{\Omega_3 - \Omega_0}{h} - \frac{\Omega_0 - \Omega_1}{h}}{h} = \mu_t \mu_o \frac{\Omega_1 + \Omega_3 - 2\Omega_0}{h^2}$$

Similarly, in the z direction

$$\mu \frac{\partial^2 \Omega}{\partial z^2} \simeq \mu_{rec}\mu_o \frac{\Omega_2+\Omega_4-2\Omega_0}{h^2}$$

and the first derivative term

$$\mu \frac{1}{r} \frac{\partial \Omega}{\partial r} \simeq \mu_t \mu_o \frac{\Omega_3-\Omega_1}{2h}$$

Since inside the magnet div $\bar{M}_o = 0$, a finite-difference approximation to the Eq. (2.67) becomes:

$$\mu_{rec}(\Omega_2 + \Omega_4) + \mu_t(1 - \frac{h}{2r})\Omega_1 + \mu_t(1 + \frac{h}{2r})\Omega_3 - 2\Omega_0(\mu_{rec} + \mu_t) = 0 \qquad (2.68)$$

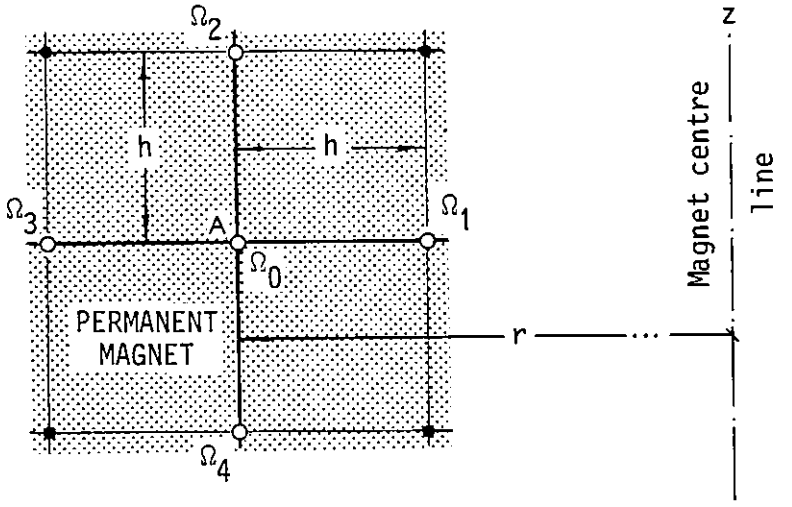

Fig. 2.44 - Node within the magnet

However, for small radii, Ω_1 and Ω_3 approach each other and their difference tends to zero, while the radius also tends to zero, yielding the indeterminate form 0/0. By L'Hospital's rule

$$\lim_{r\to 0}\left(\frac{1}{r}\frac{\partial \Omega_r}{\partial r}\right) = \lim_{r\to 0}\frac{\frac{\partial^2 \Omega}{\partial r^2}}{1} = \frac{\partial^2 \Omega}{\partial r^2}$$

and so Eq. (2.67) reduces to

$$\mu \left(2 \frac{\partial^2 \Omega}{\partial r^2} + \frac{\partial^2 \Omega}{\partial z^2} \right) = 0 \qquad (2.69)$$

So that along the line r = 0 within the magnet the operator may be defined by the equation:

$$2\mu_t \frac{\Omega_1+\Omega_3-2\Omega_0}{h^2} + \mu_{rec} \frac{\Omega_2+\Omega_4-2\Omega_0}{h^2} = 0$$

Because of rotational symmetry $\Omega_1 = \Omega_3$ at all points 0 along the centre line, and this equation becomes:

$$\mu_{rec}(\Omega_2 + \Omega_4) + 4\mu_t\Omega_1 - 2\Omega_0(2\mu_t + \mu_{rec}) = 0 \qquad (2.70)$$

Eq. (2.68) and Eq. (2.70) are then the general operators within the magnet the latter valid along the magnet axis.

NODE B - Top of the magnet surface

Four nodes situated on the air/magnet top suface boundary, as shown in fig. 2.45, the terms in Eq. (2.67) are approximately given by

$$\mu \frac{\partial^2 \Omega}{\partial r^2} \simeq \frac{1}{2}(1 + \mu_t)\mu_o \frac{\Omega_1+\Omega_3-2\Omega_0}{h^2}$$

$$\mu \frac{\partial^2 \Omega}{\partial z^2} \simeq \mu_o \frac{\Omega_2-\Omega_0}{h^2} - \mu_{rec}\mu_o \frac{\Omega_0-\Omega_4}{h^2}$$

$$\mu \frac{1}{r} \frac{\partial \Omega}{\partial r} \simeq \frac{1}{r} \mu_o(1 + \mu_t)\mu_o \frac{\Omega_3-\Omega_1}{2h}$$

$$\text{div } \bar{M}_o \simeq \frac{0 - M_o}{h} = - \frac{M_o}{h}$$

and after substitution and rearranging, gives:

$$\Omega_2+\mu_{rec}\Omega_4+\frac{1}{2}(1+\mu_t)(1-\frac{h}{2r})\Omega_1+\frac{1}{2}(1+\mu_t)(1+\frac{h}{2r})\Omega_3-\Omega_0(2+\mu_r+\mu_t)+\frac{M_o h}{\mu_o}=0 \qquad (2.71)$$

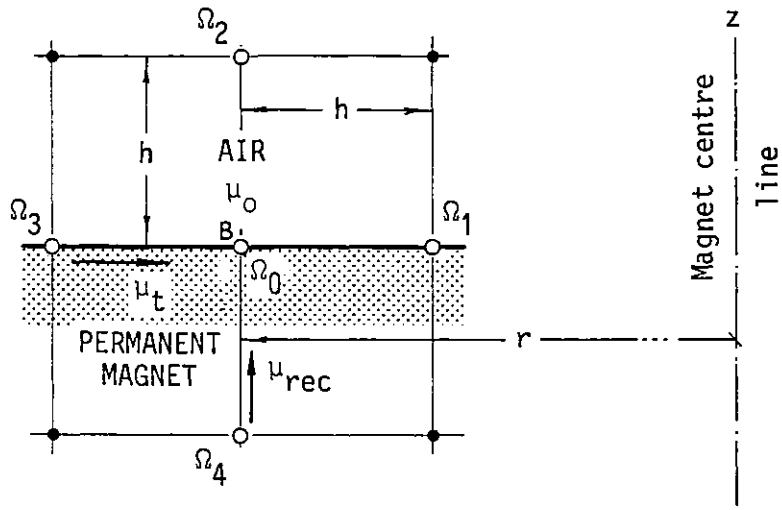

Fig. 2.45 - Node on top of the magnet surface

Again, for r = 0 Eq. (2.71) is indeterminate. Thus, for magnet top centre point where $\Omega_1 = \Omega_3$, from Eq. (2.69) the following equation yields:

$$\Omega_2 + \mu_{rec}\Omega_4 + 2(1+\mu_t)\Omega_1 - \Omega_0(3+2\mu_t+\mu_{rec}) + \frac{M_o h}{\mu_o} = 0 \qquad (2.72)$$

NODE C - Corner of the magnet

For node C on corner of the magnet shown in fig. 2.46, the following approximate differential equations yield

$$\mu\frac{\partial^2\Omega}{\partial r^2} \simeq \mu_o\frac{\Omega_3-\Omega_0}{h^2} - \frac{1}{2}(1+\mu)\mu_o\frac{\Omega_0-\Omega_1}{h^2}$$

$$\mu\frac{\partial 2\Omega}{\partial z^2} \simeq \mu_o\frac{\Omega_2-\Omega_0}{h^2} - \frac{1}{2}(1+\mu_{rec})\mu_o\frac{\Omega_0-\Omega_4}{h^2}$$

$$\mu\frac{1}{r}\frac{\partial\Omega}{\partial r} \simeq \frac{1}{r}\mu_o\frac{\Omega_3-\frac{1}{2}(1+\mu_t)\Omega_1}{2h}$$

and since the flux generator operates on only half the cross-sectional area:

$$\text{div } \bar{M}_o = - \frac{M_o}{2h}$$

Substitution into Eq. (2.67), gives:

$$\Omega_2 + \frac{1}{2}(1+\mu_{rec})\Omega_4 + \frac{1}{2}(1+\mu_t)(1- \frac{h}{2r})\Omega_1 + (1+ \frac{h}{2r})\Omega_3 - \Omega_0\left[3+ \frac{1}{2}(\mu_{rec}+\mu_t)\right] + \frac{Mh_o}{2\mu_o} = 0 \quad (2.73)$$

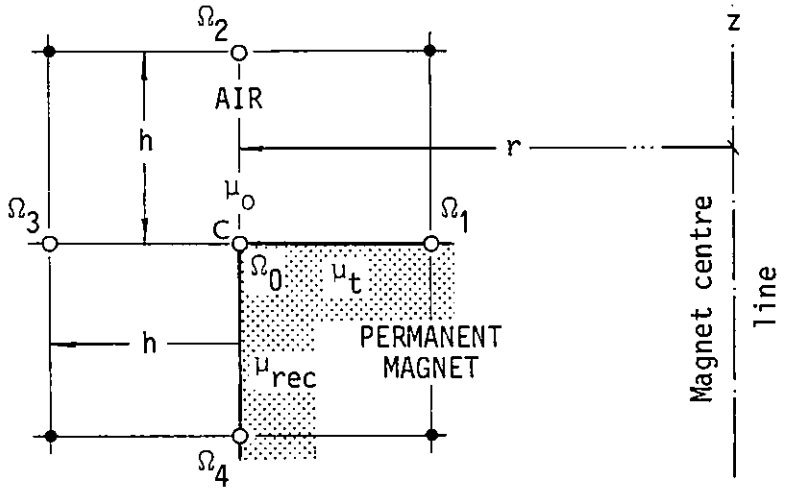

Fig. 2.46 - Node on corner of the magnet

which is the general operator for the corner of the magnet.

NODE D - Magnet/air side boundary

For nodes situated on magnet/air side boundary as shown in fig. 2.47, the following approximate differential equations may be written as:

$$\mu \frac{\partial^2 \Omega}{\partial r^2} \simeq \mu_o \frac{\Omega_3 - \Omega_0}{h^2} - \mu_t \mu_o \frac{\Omega_0 - \Omega_1}{h^2}$$

$$\mu \frac{\partial^2 \Omega}{\partial z^2} \simeq \frac{1}{2}(1 + \mu_{rec})\mu_o \frac{\Omega_2 + \Omega_4 - 2\Omega_0}{h^2}$$

$$\mu \frac{1}{r} \frac{\partial \Omega}{\partial r} \simeq \frac{1}{r} \mu_o \frac{\Omega_3 - \mu_t \Omega_1}{2h}$$

Since div $\bar{M}_o$ = 0, substitution into Eq. (2.67) gives:

$$\frac{1}{2}(1+\mu_{rec})(\Omega_2+\Omega_4)+\mu_t(1-\frac{h}{2r})\Omega_1+(1+\frac{h}{2r})\Omega_3-(2+\mu_{rec}+\mu_t)\Omega_0=0 \qquad (2.74)$$

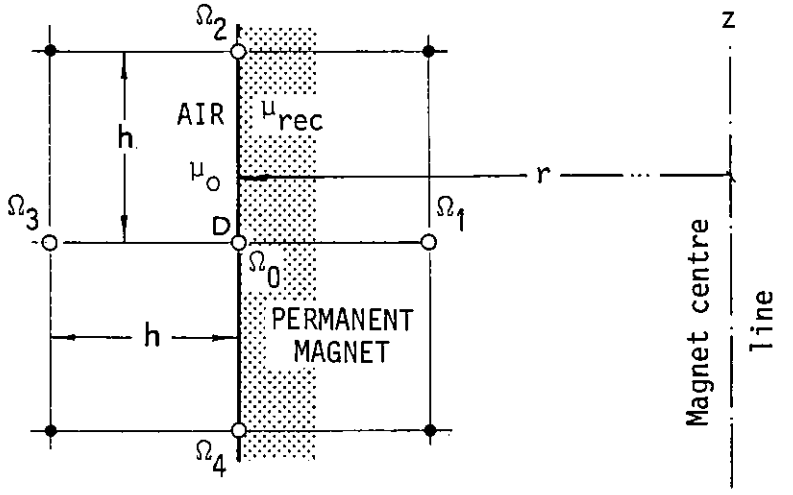

Fig. 2.47 - Node on magnet/air side boundary

which is the general operator on the magnet/air side boundary.

NODE E - Air region

The operator for the air region can be readily derived from Eq. (2.68) putting $\mu_{rec} = \mu_t = 1$, which gives

$$\Omega_2 + \Omega_4 + (1 - \frac{h}{2r})\Omega_1 + (1+\frac{h}{2r})\Omega_3 - 4\Omega_0 = 0 \qquad (2.75)$$

and from Eq. (2.70) for the centre line

$$\Omega_2 + \Omega_4 + 4\Omega_1 - 6\Omega_0 = 0 \qquad (2.76)$$

From the general operators derived for each typical node, a field solution in cylindrical coordinates is easily obtained by an iterative process.

a) - Example of a computer solution in cylindrical coordinates

To illustrate the method, the problem of two cylindrical magnets placed between soft iron pole pieces is considered. The air gap flux

density is computed for three different types of magnet materials, such as metallic, ceramic and rare-earth, whose characteristics are indicated in fig. 2.48. Between the cylindrical magnets of $\ell_m/D = 0.6$ ratio a gap $g = 8$ mm is left with a pole face area $A_g = 960\ mm^2$. From the field distribution the leakage factor for each magnet material is obtained and compared with that calculated using the Maynard and Tenzer formula (Eq. (2.16)), which gives for this particular configuration and proportions $K_1 = 1.88$.

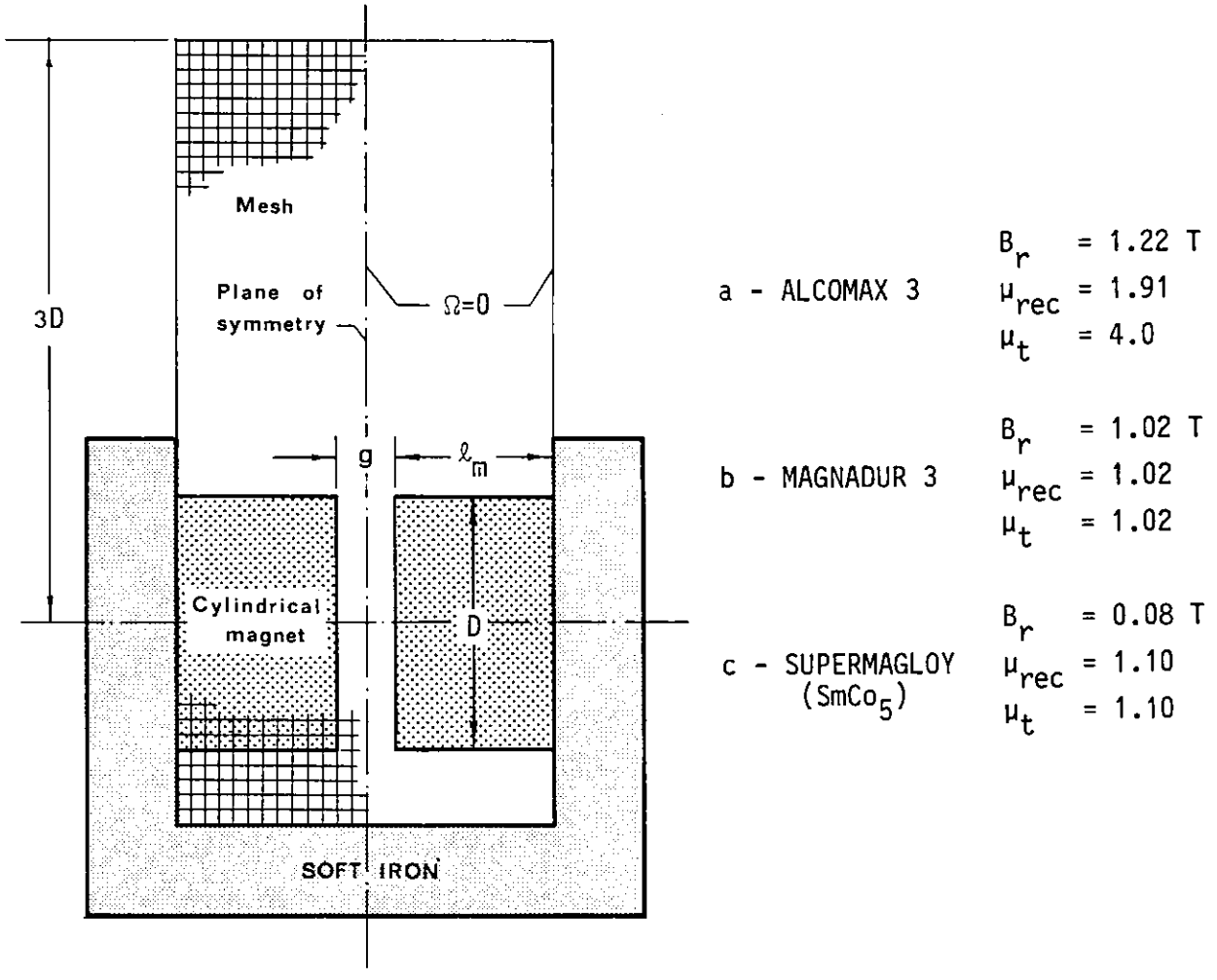

Fig. 2.48 - Basic configuration with cylindrical magnets

The program outline is very similar to that given in Appendix A, with some alterations. To represent the open iron boundary, the mesh was limited outside by a zero equipotential boundary, extended radially to a sufficient distance from the magnet centre axis to have negligible influence on the potential distribution. A mesh extended to a distance

five times the diameter D of the magnets was initially used. However, a mesh extended to a distance 3D showed no appreciable difference in the values of the potential distribution, and consequently this mesh was taken to represent the boundary at infinity. This reduces substantially the computing time, though even so the time is greater than that for the same problem in polar coordinates, because the operators in cylindrical coordinates require more operations to be performed for each residual.

The non-linear characteristic of Alcomax 3 has been approximated to the recoil line equation

$$B = \mu_0 1.91 H + 0.70 \quad T \tag{2.77}$$

and the other materials are considered to be stabilised on their demagnetisation characteristic.

The magnetic equipotential contours at 50 A intervals and flux density distribution along the centre plan of symmetry for the three materials considered, together with the respective leakage factor are shown in fig. 2.49.

For this configuration the ratio $\ell_m/g = 2.5$. As expected, for ratios of this order, the flux density produced by the $SmCo_5$ magnet is the highest value. The flux density is practically constant in the middle region of the air gap, falling abruptly near the magnet's side where about half of the maximum value is attainable.

The leakage factor K_1 obtained by Maynard and Tenzer formula appears to err on the high side about 20% to that obtained numerically for $SmCo_5$. However, this error is reduced as the transverse permeability of the magnet increases and it would appear that leakage factor is a function of magnet permeability. In fact, the transverse permeability has the effect of increasing the transverse potential gradient at the sides of the magnet, giving higher leakage flux. This explains why the metallic magnets present higher leakage factor than ceramic and rare-earth magnets for the same configuration.

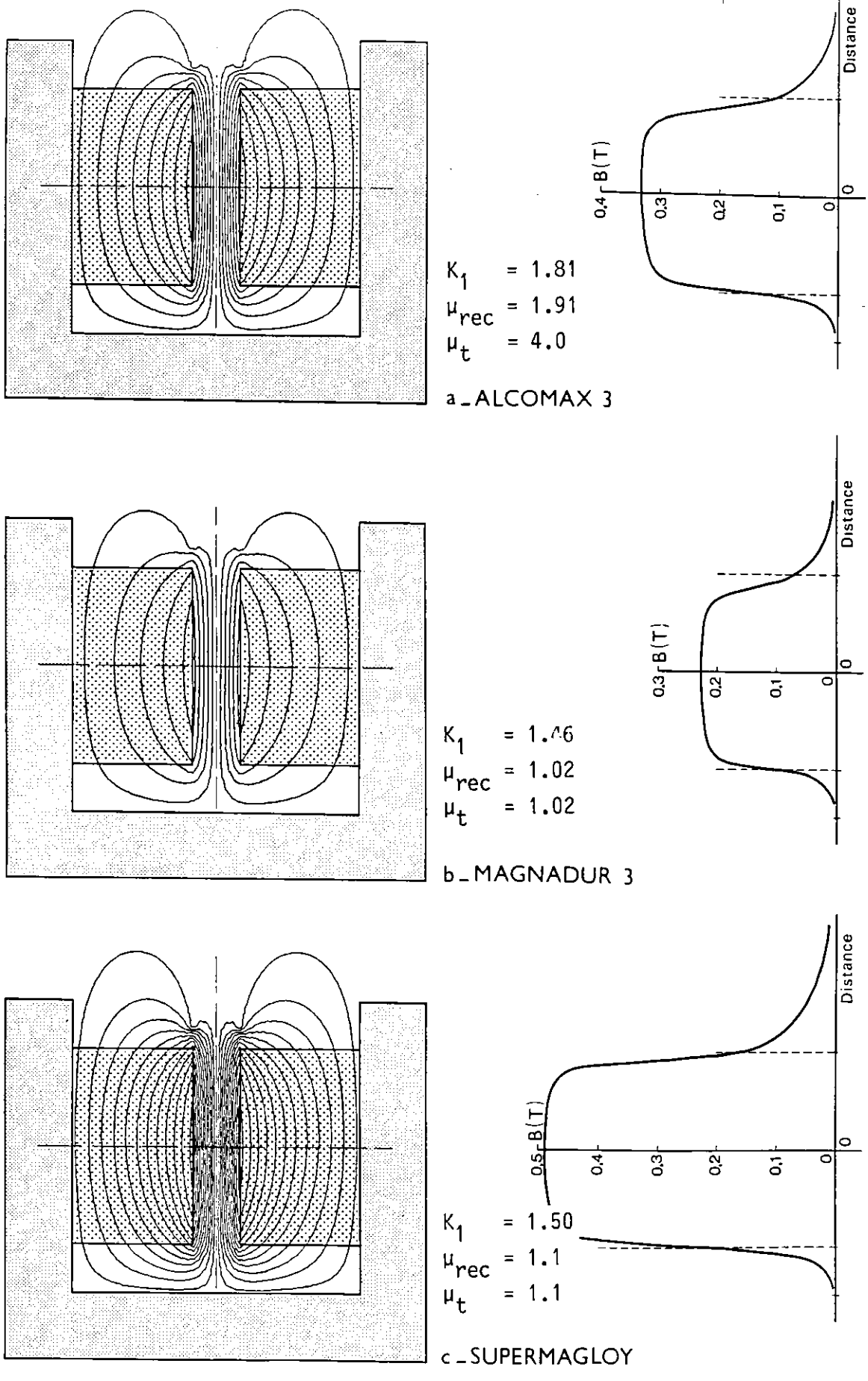

Fig. 2.49 - Magnetic equipotential contours at 50 A intervals and flux density distribution for three different types of material

2.8 - COMPARISON OF LOAD LINE AND MESH ANALYSIS METHODS

In order to compare the degree of accuracy between the load-line and mesh analysis methods, a permanent magnet static air gap problem is considered. For this investigation, the layout shown in fig. 2.50 is used, which represents one pole pitch of a permanent magnet machine with linear dimensions included. A constant pole arc to pole pitch ratio $\sigma = m/\tau$ is considered. Unit depth of material is assumed and Cartesian coordinates are used.

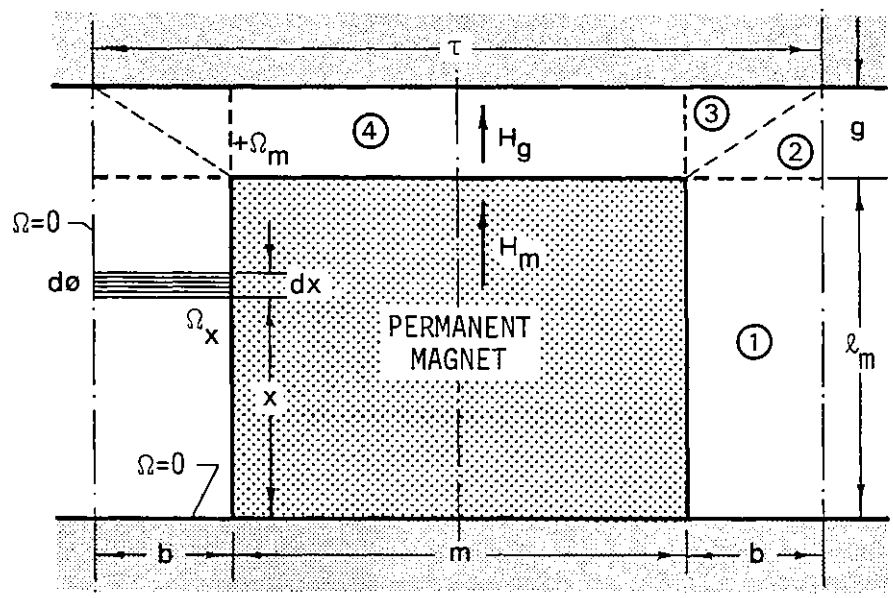

Fig. 2.50 - Geometry for permanent magnet static air gap problem

The interpolar planes between consecutive north and south poles are equipotential zero planes and again the magnet may be considered placed in an iron window. Calculations of air gap flux density for various magnetic circuit proportions using both methods are now presented.

2.81 - Calculation of the air gap flux density using the load-line method

Assuming unsaturated iron ($K_2 \simeq 1$), Eq. (2.12) applied to this geometry becomes:

$$B_m = -\mu_o H_m K_1 \frac{\tau}{m} \frac{\ell_m}{g} \qquad (2.78)$$

For stabilised magnets Eq. (2.23) applies, which combined with Eq. (2.78) gives:

$$H_m = - \frac{M_o}{\mu_o (K_1 \frac{1}{\sigma} \frac{\ell_m}{g} + \mu_{rec})} \tag{2.79}$$

But, from Eq. (2.9)

$$B_g = -\mu_o \frac{H_m \ell_m}{g} \tag{2.80}$$

and substitution of Eq. (2.79) into Eq. (2.80) gives:

$$B_g = \frac{M_o}{\frac{K_1}{\sigma} + \mu_{rec} \frac{g}{\ell_m}} \tag{2.81}$$

For a fixed magnetisation M_o, the air gap flux density thus depends on the ratio g/ℓ_m and leakage factor K_1.

Leakage factor is now calculated by Roters' method [18] and for the calculation of the permeances to be used in Eq. (2.10) the region is subdivided into four sections, as shown in fig. 2.50.

Section 1 - Side leakage permeance

Assuming that the magnet potential varies linearly along the magnetising direction, the potential at point x is given by

$$\Omega_x = \Omega_m \frac{x}{\ell_m}$$

where Ω_m is the constant potential at the magnet top surface.

Hence, the elementary flux in width dx is

$$d\phi = \Omega_x dP_x = \Omega_m \frac{x}{\ell_m} \mu_o \frac{dx \cdot 1}{b}$$

and the total flux leakage in section 1 is hence:

$$\phi = \mu_o \frac{\Omega_m}{b \ell_m} \int_0^{\ell_m} x \, dx = \frac{1}{2} \mu_o \Omega_m \frac{\ell_m}{b}$$

For both sides of the magnet the total leakage permeance is therefore

$$P_1 = \frac{2\phi}{\Omega_m} = \mu_o \frac{\ell_m}{b} \tag{2.82}$$

Section 2 - Leakage triangle

From fig. 2.50 the volume of the pyramidal triangle per unit depth is $V = \frac{1}{2} gb$ and the mean length of the flux path is given by $\ell_{mean} = \sqrt{b^2+(\frac{g}{2})^2}$. Hence, the mean area of the flux path is

$$S_{mean} = \frac{\frac{1}{2}gb}{\sqrt{b^2 + (\frac{g}{2})^2}}$$

and the permeance

$$P = \mu_o \frac{S_{mean}}{\ell_{mean}} = \frac{1}{2} \mu_o \frac{gb}{b^2 + (\frac{g}{2})^2}$$

Hence, the total leakage permeance for two triangles

$$P_2 = 2P = \mu_o \frac{4gb}{4b^2 + g^2} \tag{2.83}$$

Section 3 - Useful flux triangle

Similarly as for section 2

$$P_3 = \mu_o \frac{4gb}{b^2 + 4g^2} \tag{2.84}$$

Section 4 - Useful flux in main gap

Since the magnet top surface is an equipotential surface, the permeance of section 4 is readily obtained as

$$P = \mu_o \frac{m}{g} \tag{2.85}$$

From Eq. (2.10) the leakage factor is given by

$$K_1 = 1 + \frac{P_1 + P_2}{P_3 + P_4} \tag{2.86}$$

Substitution of Eq. (2.83) to Eq. (2.85) into Eq. (2.86) gives:

$$K_1 = 1 + \left[\frac{1}{(1-\sigma)r} + \frac{1}{(1-\sigma)\frac{r}{x} + \frac{1}{1-\sigma}\frac{x}{r}} \right] \cdot \left[\frac{\sigma}{2}\frac{r}{x} + \frac{1}{\frac{1-\sigma}{4}\frac{r}{x} + \frac{4}{1-\sigma}\frac{r}{x}} \right]^{-1} \tag{2.87}$$

where

$$\sigma = \frac{m}{\tau} \qquad x = \frac{g}{\ell_m} \quad \text{and} \quad r = \frac{\tau}{\ell_m} = \frac{m}{\sigma \ell_m}$$

For a typical value $\sigma = 0.75$, Eq. (2.87) is plotted in fig. 2.51 for several ratios of m/ℓ_m (magnet width/magnet length) versus g/ℓ_m (air gap length/magnet length).

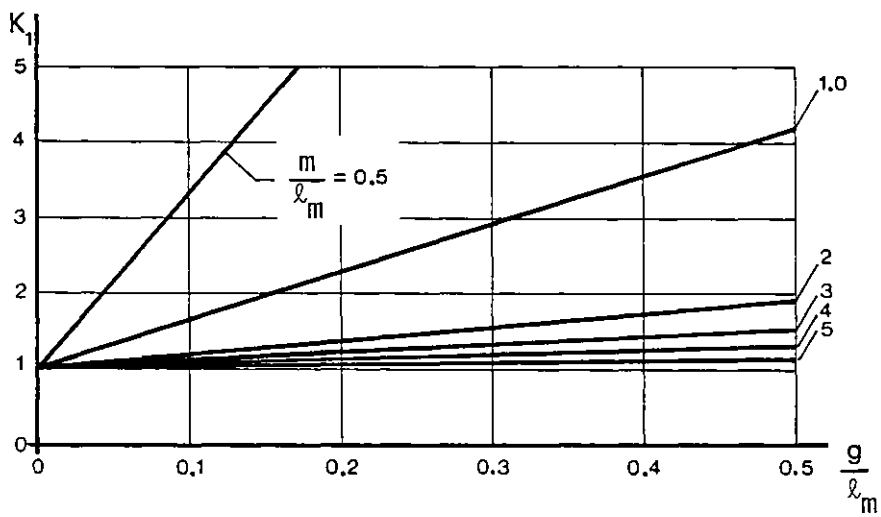

Fig. 2.51 - Leakage factor versus g/ℓ_m for $\sigma = 0.75$

Fig. 2.51 shows that the leakage factor calculated by Roters' method depends strongly on the ratio m/ℓ_m as expected, since the flux leakage is mainly due to the side leakage path which increases in importance with ℓ_m. Practically, for a magnet length ℓ_m less than 20% of magnet width m, the leakage factor becomes close to unity for any value g/ℓ_m.

Substitution of Eq. (2.87) into Eq. (2.81) allows calculation of air gap flux density versus g/ℓ_m for a fixed magnetisation M_o.

2.8.2 - Calculation of the air gap flux density using the mesh analysis method

The previous problem can also be solved using a simplified mesh suitable for manual solution. By symmetry only half of pole pitch is considered and the region subdivided as shown in fig. 2.52, where only four nodes are considered. Applying a similar technique developed in section 2.7.3 and assuming equal permeabilities in both axial and transverse directions ($\mu_{rec} = \mu_t = \mu_r$) the corresponding equivalent circuit in Cartesian coordinates is as shown in fig. 2.53.

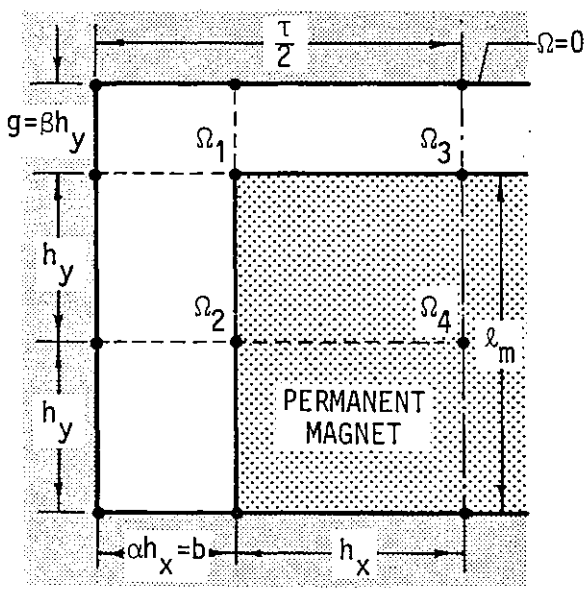

$$\sigma = \frac{m}{\tau}$$
$$h_y = \frac{1}{2}\ell_m$$
$$h_x = \frac{1}{2}m$$
$$\beta = 2\frac{g}{\ell_m} = 2x$$
$$\alpha = 2\frac{b}{m} = \frac{1-\sigma}{\sigma}$$
$$k = \frac{h_y}{h_x} = \frac{\ell_m}{m}$$

Fig. 2.52 - Mesh arrangement for manual solution

From mesh analysis theory, and by inspection of the equivalent circuit, the following matrix equation can be written

$$h_y \cdot \begin{bmatrix} \frac{1}{2}M_o \\ 0 \\ M_o \\ 0 \end{bmatrix} = \mu_o \cdot \begin{bmatrix} \frac{1}{2}\left[\left(\frac{1+\beta}{\alpha}\right)+\beta+\mu_r\right)k^2+\left(\frac{1+\alpha}{\beta}+\alpha+\mu_r\right)\right] & -\frac{1}{2}(\alpha+\mu_r) & -\frac{1}{2}(\beta+\mu_r)k^2 & 0 \\ -\frac{1}{2}(\alpha+\mu_r) & \left(\frac{1}{\alpha}+\mu_r\right)k^2+\alpha+\mu_r & 0 & -\mu_r k^2 \\ -(\beta+\mu_r)k^2 & 0 & (\beta+\mu_r)k^2+\frac{1}{\beta}+\mu_r & -\mu_r \\ 0 & -2\mu_r k^2 & -\mu_r & 2\mu_r(k^2+1) \end{bmatrix} \cdot \begin{bmatrix} \Omega_1 \\ \Omega_2 \\ \Omega_3 \\ \Omega_4 \end{bmatrix} \quad (2.88)$$

where $k = h_y/h_x$.

The air gap flux density for the position of nodes 1 and 3 is respectively

$$B_1 = \mu_o H_{10} = \mu_o \frac{\Omega_1}{g} = \mu_o \frac{\Omega_1}{\beta h_y}$$

$$B_3 = \mu_o \frac{\Omega_3}{\beta h_y}$$

and the mean air gap flux density

$$B_g = \frac{1}{2}(B_1 + B_3) = \frac{\mu_o}{2\beta h_y}(\Omega_1 + \Omega_3) \qquad (2.89)$$

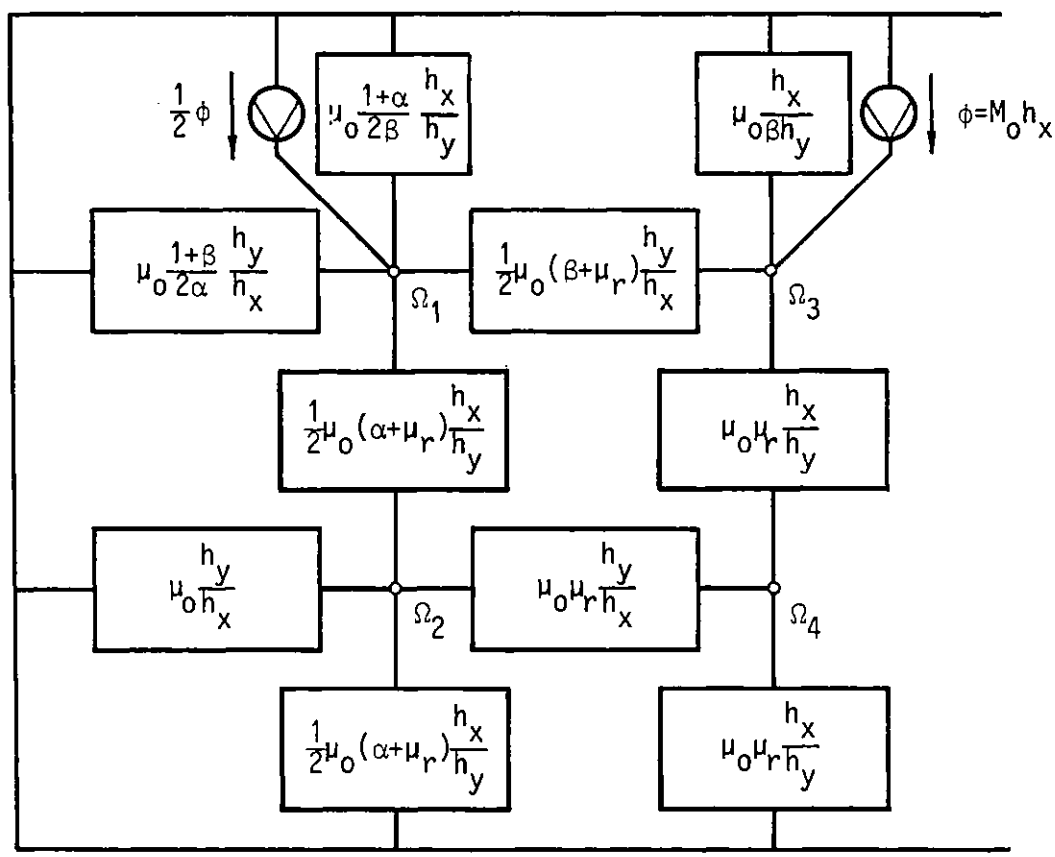

Fig. 2.53 - Equivalent circuit for a four node mesh

Solution for the Ω values can be found from matrix equation (2.88) using standard techniques and they are of the form

$$\Omega = CM_o \frac{h_y}{\mu_o}$$

where C is a dimensionless quantity which is a function of α, β, k and μ_r. Thus Eq. (2.89) becomes:

$$B_g = \frac{1}{2\beta}(C_1 + C_3)M_o \qquad (2.90)$$

Similarly, from the Ω values, the magnetising force between nodes 1 and 2 on the magnet corner may be obtained from the relationship:

$$H'_{12} = \frac{\Omega_1 - \Omega_2}{h_y} = \frac{C_1 - C_2}{\mu_o} M_o \qquad (2.91)$$

In order to compare the results obtained for the air gap flux density using the load-line and mesh analysis approach, the $SmCo_5$ material ($\mu_r = 1.1$ and $M_o = 0.8$ T) was taken as an example. For several ratios $k^{-1} = m/\ell_m$ and $\sigma = m/\tau = 0.75$, Eq. (2.90) is plotted in fig. 2.54 versus $\beta/2 = g/\ell_m$ together with the results obtained by Eq. (2.81) represented by heavy type.

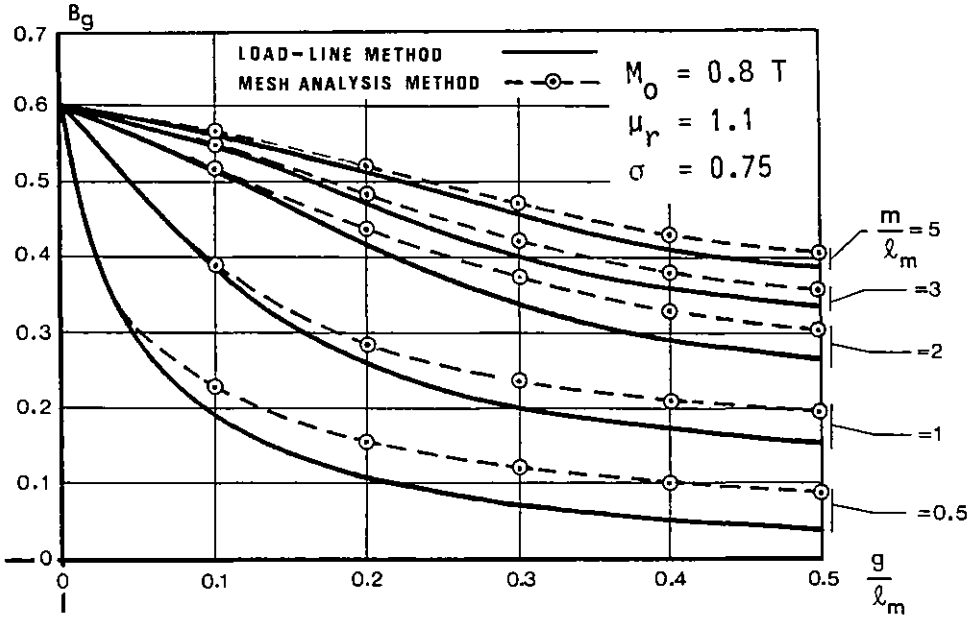

Fig. 2.54 - Air gap flux density versus g/ℓ_m

From these results some important conclusions arise:

i) - The air gap flux density decreases with g/ℓ_m, as expected.

ii) - For a fixed g/ℓ_m ratio the air gap flux density increases as magnet width m increases, because the flux leakage becomes less significant.

iii) - As the ratio g/ℓ_m decreases and the ratio m/ℓ_m increases both methods give close results. Thus, load-line method is only accurate for small gaps and small magnet lengths, and the degree of accuracy is better for relatively high ratios of m/ℓ_m.

2.9 - MANUAL SOLUTION FOR THE MAXIMUM PERMISSIBLE STATOR CURRENT CALCULATION

A stator winding may be added to the layout shown in fig. 2.50 to represent one pole of a permanent magnet machine on load, and a synchronous motor with current fed at 90°E torque angle with 2 coils per pole per phase and 4 slots per pole is shown in fig. 2.55.

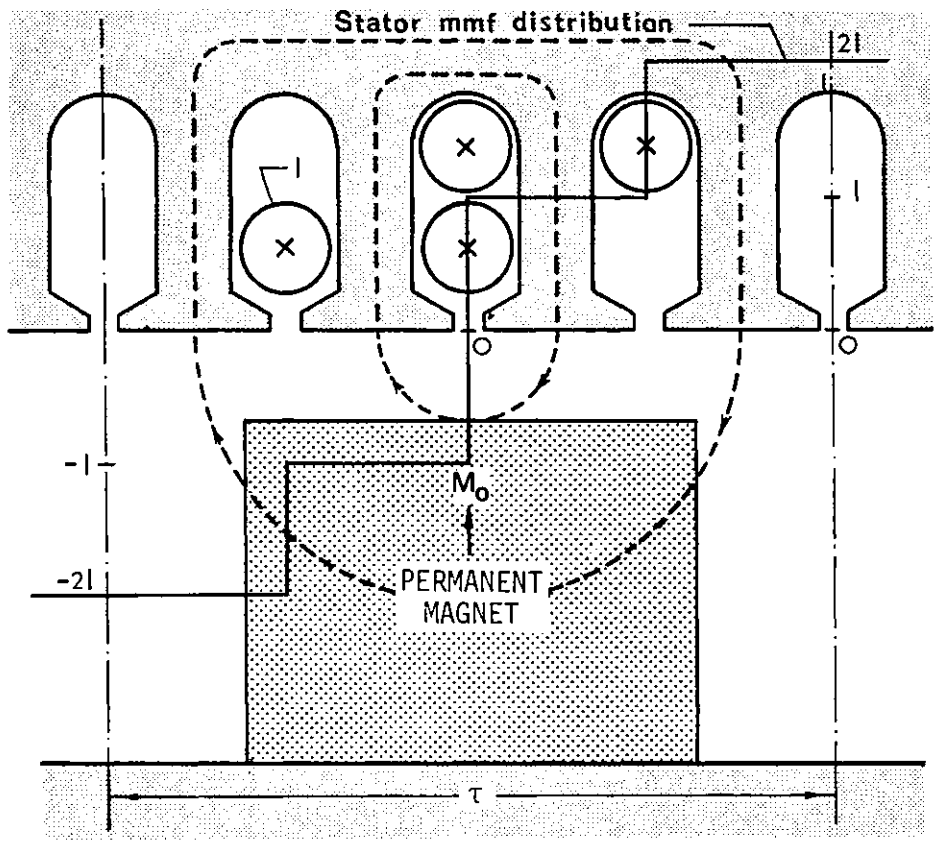

Fig. 2.55 - Permanent magnet synchronous motor at 90°E torque angle

The problem consists in determining the maximum permissible stator current to avoid magnet demagnetisation, using a simple mesh suitable for manual solution. As already explained in section 2.7.5.a, the problem may be solved by the superposition principle. The magnetising force on magnet edge in absence of stator currents may be obtained from Eq. (2.91) in the preceding section. The magnetising force due to the stator current in the same region, may be obtained from the potential distribution with the permanent magnet flux generators inoperative.

For the stator m.m.f. distribution considered, the magnet centre plane becomes a zero magnet equipotential surface short-circuiting potentials Ω_3 and Ω_4, and the interpolar plane becomes a plane of symmetry. Then two more nodes with magnet potentials Ω_5 and Ω_6 need to be inserted as shown in fig. 2.56. With this large mesh the m.m.f. to be assigned at interpolar planes is 2I and at magnet sides the average m.m.f. 1.5I is considered. Hence, the respective equivalent circuit is shown in fig. 2.57, where the flux generators ϕ_1 and ϕ_5 are related with m.m.f. sources by the expression ϕ = m.m.f. P.

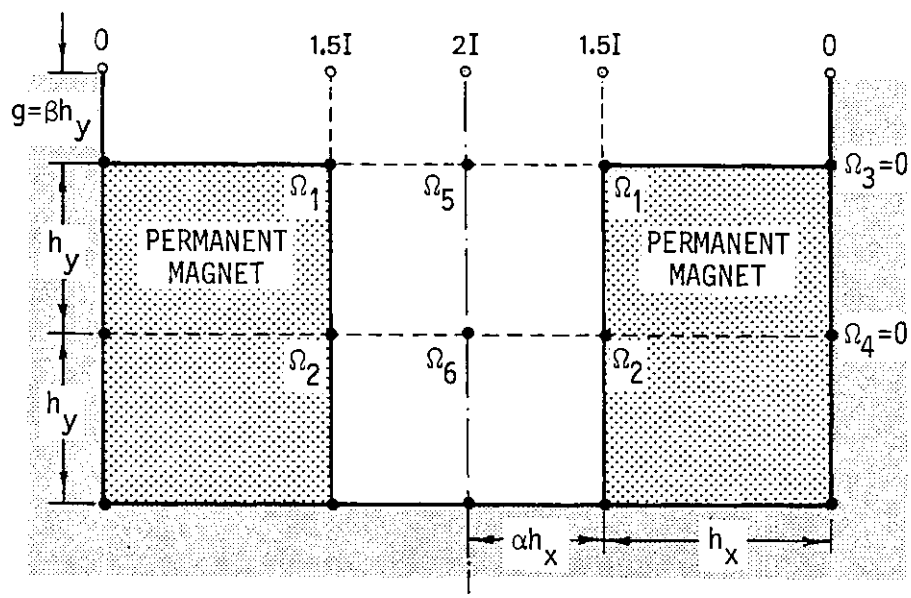

Fig. 2.56 - Mesh arrangement for stator m.m.f.

By inspection of the equivalent cicuit and putting again $k = h_y/h_x$, the equations for the network can be readily written in the following matrix form:

$$I\cdot\begin{bmatrix} \frac{3}{4}\frac{1+\alpha}{\beta} \\ 0 \\ 2\frac{\alpha}{\beta} \\ 0 \end{bmatrix} = \begin{bmatrix} \frac{1}{2}\left[\left(\frac{1+\beta}{\alpha}+\beta+\mu_r\right)k^2+\left(\frac{1+\alpha}{\beta}+\alpha+\mu_r\right)\right] & -\frac{1}{2}(\alpha+\mu_r) & -\frac{1+\beta}{2\alpha}k^2 & 0 \\ -\frac{1}{2}(\alpha+\mu_r) & \left(\frac{1}{\alpha}+\mu_r\right)k^2+\alpha+\mu_r & 0 & -\frac{1}{\alpha}k^2 \\ -\frac{1+\beta}{\alpha}k^2 & 0 & \frac{1+\beta}{\alpha}k^2+\alpha\left(1+\frac{1}{\beta}\right) & -\alpha \\ 0 & -\frac{2}{\alpha}k^2 & -\alpha & 2\left(\frac{k^2}{\alpha}+\alpha\right) \end{bmatrix}\cdot\begin{bmatrix} \Omega_1 \\ \Omega_2 \\ \Omega_3 \\ \Omega_4 \end{bmatrix} \qquad (2.92)$$

These equations may be solved for Ω with any value of I and they are of the form

$$\Omega = D \frac{I}{\beta}$$

where D is a dimensionless quantity which is a function of α, β, k and μ_r. For the model considered, the largest demagnetisation force occurs midway between nodes 1 and 2. For this region, the demagnetisation force only due to stator current is then

$$H_{12}^{''} = \frac{\Omega_1 - \Omega_2}{h_y} = \frac{D_1 - D_2}{\beta h_y} I = \frac{D_1 - D_2}{(g/\ell_m)} \frac{I}{\ell_m} \qquad (2.93)$$

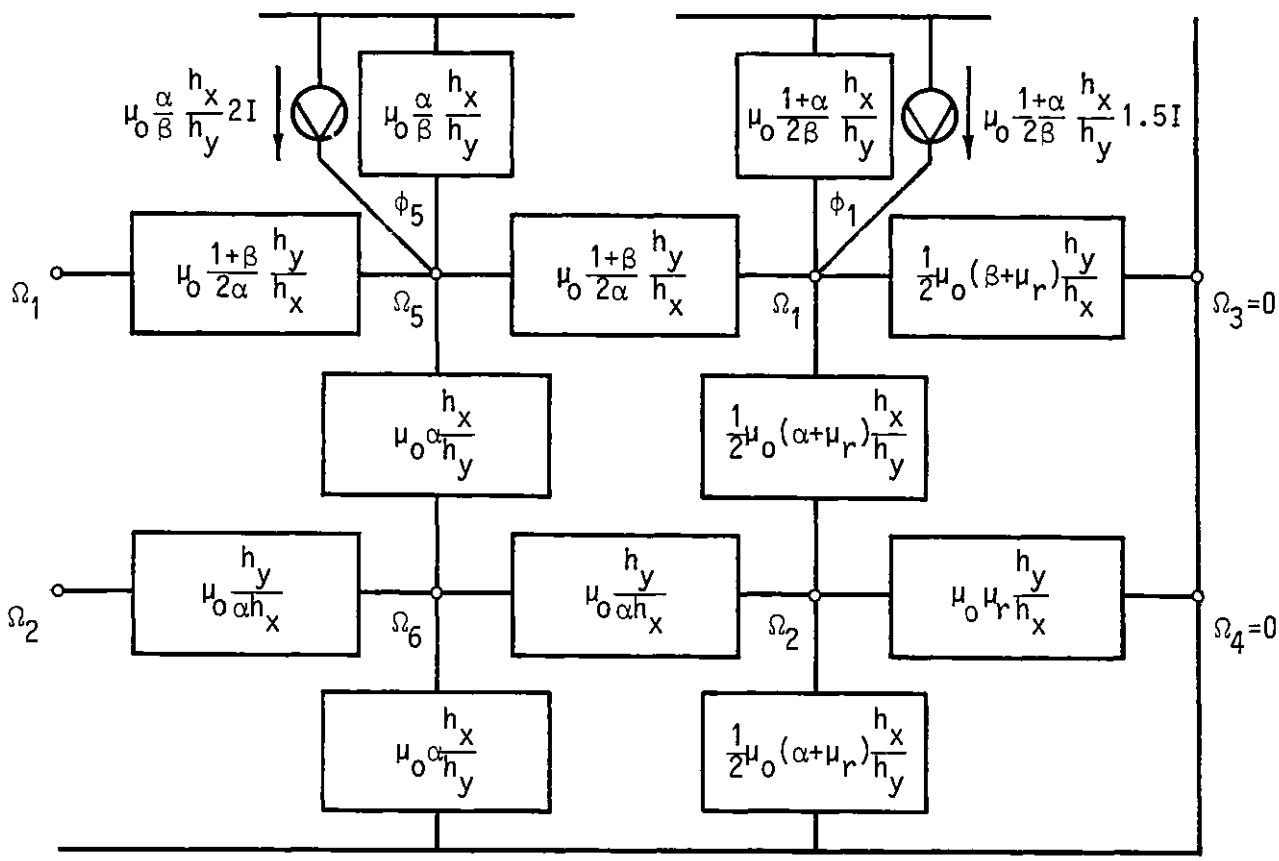

Fig. 2.57 - Equivalent circuit for stator m.m.f.

Hence, by superposition, the total magnetising force on the edge of the magnet for any load condition is given by adding Eq. (2.91) and Eq. (2.93), which gives:

$$H_{12} = \frac{C_1 - C_2}{\mu_o} M_o + \frac{D_1 - D_2}{(g/\ell_m)} \frac{I}{\ell_m} \qquad (2.94)$$

Obviously, demagnetisation starts when H_{12} is equal to magnet coercive force H_c. Taking H_c = 550 kA/m for $SmCo_5$ magnet material, the ratio maximum permissible current to magnet length I/ℓ_m is calculated from Eq. (2.94) and plotted versus g/ℓ_m in fig. 2.58 for several ratios $k^{-1} = m/\ell_g$ and $\sigma = 0.75$.

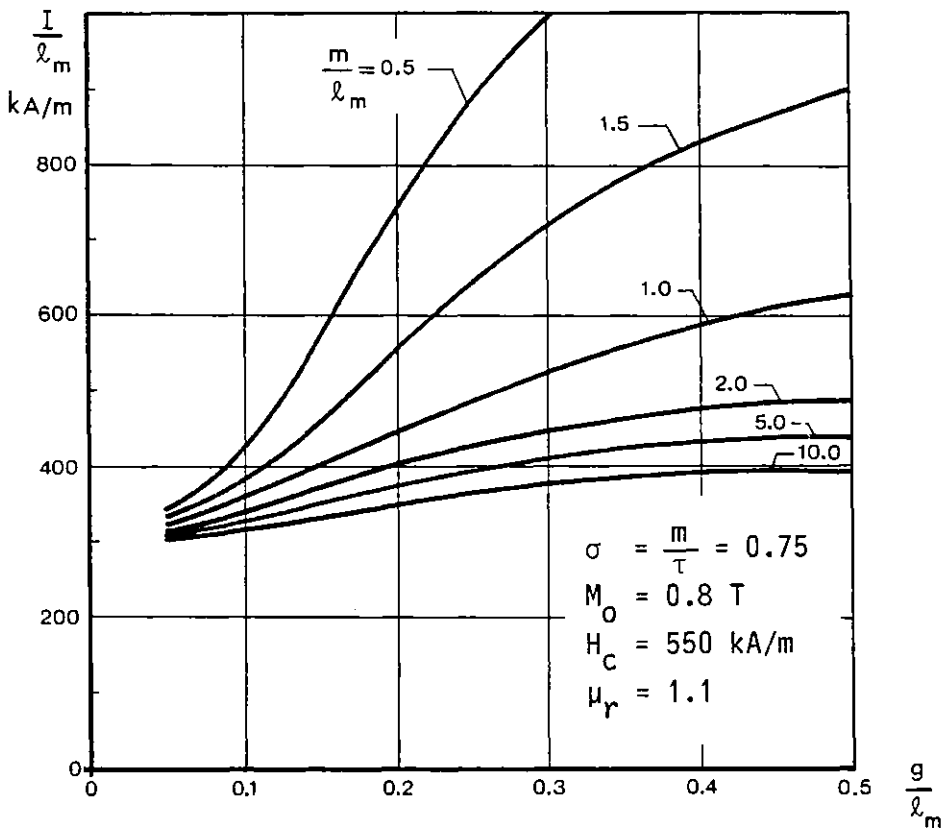

Fig. 2.58 - Maximum permissible current versus gap

Some interesting points emerge from fig. 2.58.

i) - For a fixed magnet length, the maximum permissible current increases with increasing air gap length.

ii) - Magnets with small ratios m/ℓ_m are more resistant to demagnetisation than fat magnets with short lengths.

iii) - The maximum permissible current for magnets with high ratios m/ℓ_m practically does not vary with air gap length.

These results will be used later for the design of a permanent magnet machine in Chapter 6.

☆ ☆ ☆

CHAPTER 3

AUTO-PILOTED SYNCHRONOUS MOTOR THEORY

3.1 - GENERALITIES

The excellent torque-speed characteristics of d.c. machines, inherently stable at all speeds, and the capacity for easy speed control account for their wide industrial usage. Their one major disadvantage is the use of the mechanical commutator, a relatively delicate part of the machine and perhaps the most expensive. The commutator and associated brushes are prone to sparking, which does not allow the d.c. motor's usage in hazardous atmospheres without special protection. Dirt and moisture attack the commutator, necessitating periodic maintenance and brush replacement. Additionally, the commutator restricts the machine design, since it adds appreciably to the motor's length which is undesirable when space is limited.

On the other hand, a.c. machines, such as induction, synchronous and reluctance motors, do not of course need commutators. However, they are inherently virtually constant speed machines when operated from the constant frequency mains.

Over recent years, with the advent of compact, low cost, high power, solid-state switching devices, there has been increasing development of variable frequency converters that enable one to avoid the shortcomings of the d.c. machines. Two important groups of drives are those in which:

i) - Induction, reluctance and synchronous motors of conventional design are supplied "open-loop" by variable frequency polyphase inverters, usually of the d.c. link type.

ii) - Synchronous and reluctance motors supplied from inverters whose output switching stages are controlled largely by signals derived from shaft-angle sensors. The designs of motors used in this group may differ in some respects from convention; for example, there is less need for rotor damping or induction conductorwork and this is hence often omitted.

The machines used in these two groups above have quite individual modes of operation and require different control schemes. However, in group ii) it will be shown that the operation in many ways is analogous to a d.c. motor where the mechanical commutator is replaced by an electronic one and essentially similar torque-speed characteristics are obtained [56].

Some of the important applications of these motors are to be found in the aerospace and defence industries, where great reliability and exceptional long life without maintenance is very important. In Chapter 4, a two-phase synchronous actuator for such application is described.

Other typical applications for motors of group ii) are drives for stereo record player turntables, high reliability tape records, gyro spin motors and cryogenic coolers, where saving in weight and energy is required. These are all "high-value" applications. The merits of this category of drive are becoming better recognised and each year sees the development by both industrial and academic groups of new examples of group ii) drives.

3.2 - MECHANICAL COMMUTATOR REPLACEMENT

The commutator of a conventional d.c. motor may be regarded as a system of controlled mechanical switches which reverses the voltage across the armature coils at certain angle positions. As an example and without loss of generality, fig. 3.1 shows a two-pole Gramme-ring winding d.c. machine

where the brushes on the twelve segment commutator are shifted by an angle θ from the d-axis. When a current I is injected in the rotating armature, the orientation of the current pattern remains almost unaltered with respect to the fixed poles, since the currents in some of the conductors have been reversed or "commutated" when those conductors have passed to the other side of the brush-axis. The action of the commutator is then to render the armature m.m.f.axis stationary in space and in line with the brush-axis. This action ensures that the motor torque is always unidirectional.

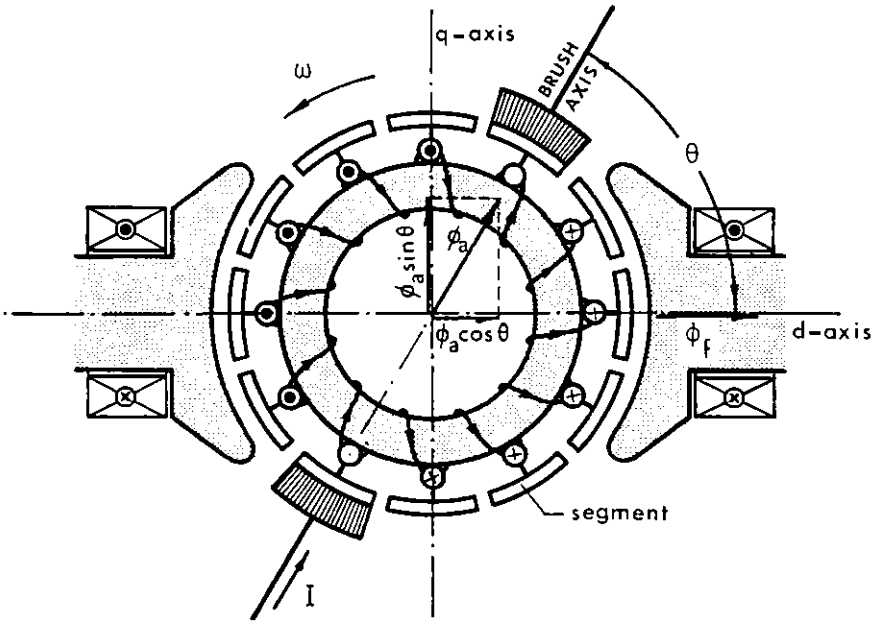

Fig. 3.1 - Gramme-ring winding d.c. machine

Hence, if a sinusoidal armature m.m.f. is assumed (this is of course not really a valid assumption for a d.c. machine, but is nevertheless made for the sake of the analogy), the motor excitation torque is given by

$$T = K\phi_f I \sin\theta = \hat{T} \sin\theta \qquad (3.1)$$

where ϕ_f is the field flux per pole and I is the current absorbed by the armature. Eq. (3.1) shows that torque can be varied by varying field excitation, armature current or brush-axis angle θ. Torque is then maximum when $\theta = 90°E$ and this is the reason why the brushes are commonly placed on the q-axis position.

The same result is obtained if instead of mechanical switches, electrical swithces are used. Replacement of the commutator with static switches was first proposed [57] in 1938, when thyratrons were the switching elements, but little progress was made until the introduction of solid-state devices twenty years later. The existence of power transistors and thyristors means that in principle, small, reliable and relatively easily controlled switches are available. Each commutator segment may in principle be replaced by a semiconductor switch, so that the motor coil current can be individually switched. However, this may lead to an expensive machine, as some d.c. motors have a large number of commutator segments. Hence the number required is reduced by interconnecting some of the armature coils in series. In the conventional d.c. machine this is equivalent to reducing the number of commutator segments. Ripple torque tends to increase but this may not matter in a larger number of applications. In fig. 3.2(a) a four segment commutator machine is considered.

When replacing the mechanical commutator, it is not desirable to have the switching elements rotating themselves and this may be avoided by placing the armature winding on the stator and the field poles on the rotor. The four segments may now be replaced by four equivalent fixed taps, as shown in fig. 3.2(b). Fig 3.2(c) and fig. 3.2(d) show the equivalent d and q-axis stator windings respectively, corresponding to those four taps. Consequently, the conventional d.c. machine becomes reduced to a two-phase synchronous machine, as shown in fig. 3.2(e). The transistors or thyristors which make up the electronic commutator need signals or firing pulses, which are dependent on the rotor position, to enable them to conduct at the correct time. As seen, this is done automatically with a conventional commutator, but with an electronic commutator an auxiliary mechanism, in effect a "rotor position sensor", is required. Several different rotor position sensors are available and a brief review is described later in the section 3.5.

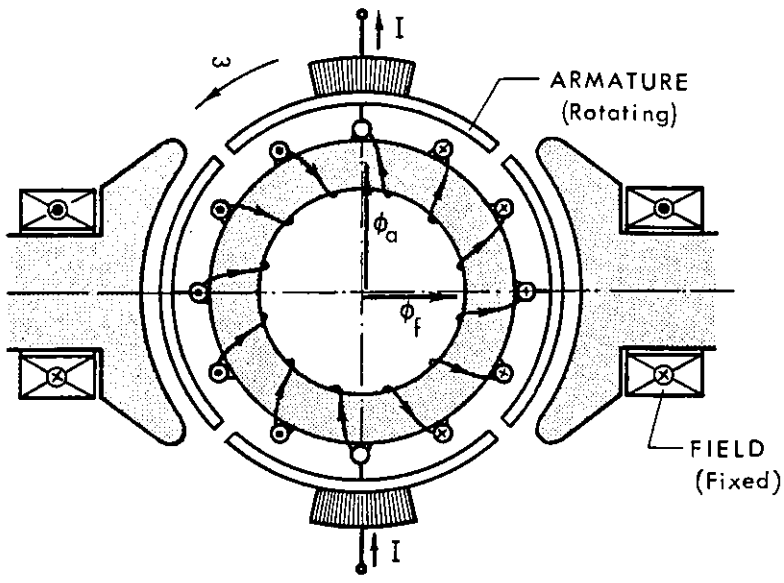

(a) - Conventional four segment d.c. motor

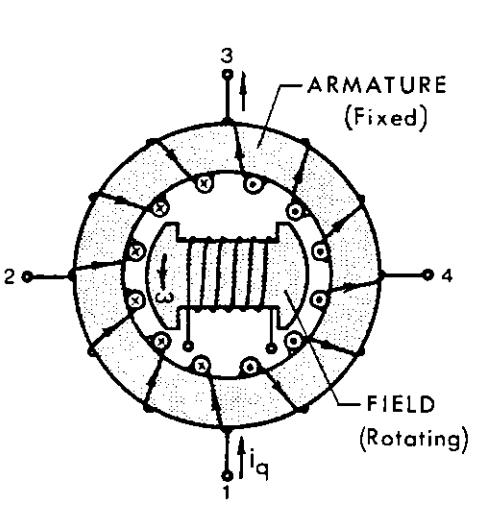

(b) - Inverted d.c. motor

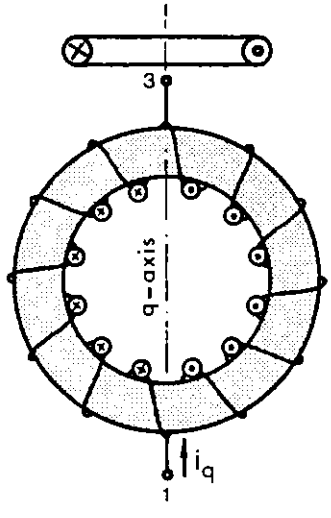

(c) - q-axis winding

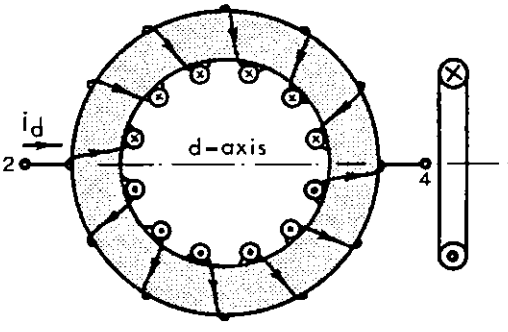

(d) - d-axis winding

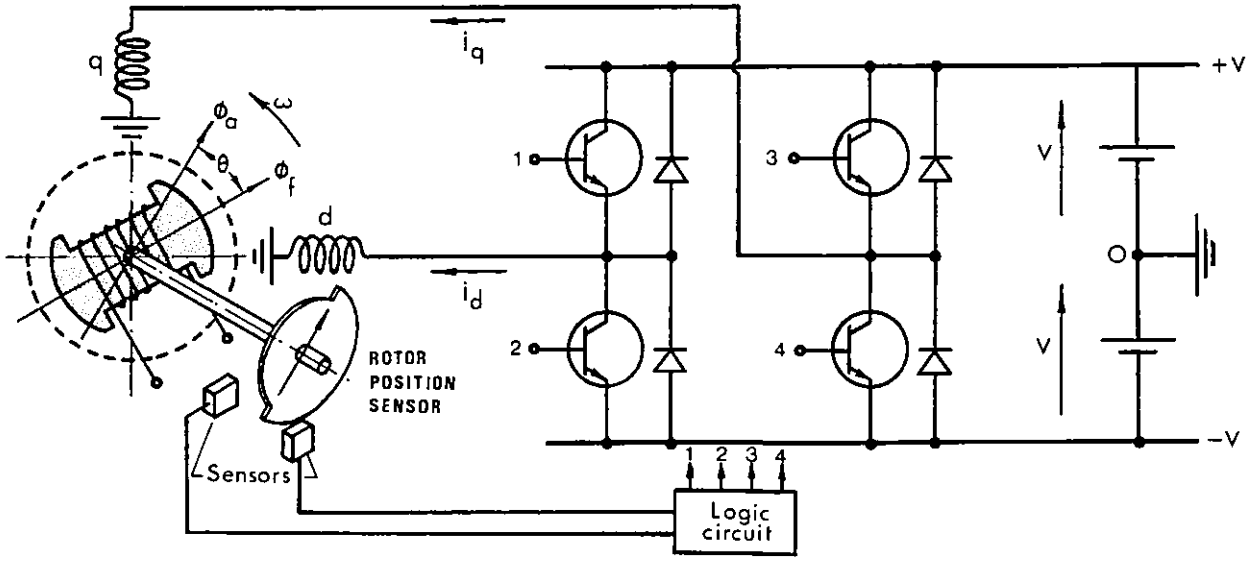

(e) - Two-phase statically commutated motor

Fig. 3.2 - Synthesis of a two-phase commutatorless motor from a d.c. machine

3.3 - "TRANSISTOR-SWITCHED" TWO-PHASE SYNCHRONOUS MOTOR PRINCIPLE

The angular position of the rotor should be made to control the armature supply switches in order to maintain the axis of armature field constantly at a given angle θ relative to the rotor pole axis. In fig. 3.2(e), the signals derived from the position sensor mounted on motor shaft are sent to a logic circuit which controls in a proper sequence and with appropriate timing the transistor base drives. The voltage waveform applied to the armature coils as a function of rotor position (neglecting freewheeling periods), is shown in fig. 3.3, where the sequence of firing pulses is indicated. The transistor switches in many ways are behaving exactly like their mechanical counterparts. In fig. 3.2(e) the diodes across each transistor enable inductive currents to be switched without damaging the transistors. Inductive current can flow through the diodes when the transistors turn OFF.

For a sinusoidally distributed winding and a current forced basis, Eq. (3.1) shows that the instantaneous torque for each phase varies sinusoidally according to rotor position. For a two-phase machine the torque waveforms for the two phases differ in phase by 90°E. Thus, switching the phase current four times per revolution the resulting torque variation with a current source feed is as shown in fig. 3.4. A similar torque pattern can be obtained with voltage feeds of the type shown in the case of low speed operation or with small motors where the winding resistance term dominates the loop equation and where the current waveform hence follows the supply voltage waveform very closely.

With the rotor position set at a switching angle θ_o, the average resulting torque with the assumption made is given by

$$T_{av} = \frac{2}{\pi} \int_{\theta_o}^{\theta_o + \frac{\pi}{2}} \hat{T} \sin \theta \, d\theta = \frac{2}{\pi} K\phi_f I(\sin \theta_o + \cos \theta_o) \qquad (3.2)$$

Eq. (3.2) shows that the average torque can be varied by varying

field excitation, armature current or choosing the instant of switching angle θ_o. The motor is then self-starting except for switching angles $\theta_o = 135°E$ or $\theta_o = -45°E$. Reversing rotation can be obtained by changing the sequence of the position sensors.

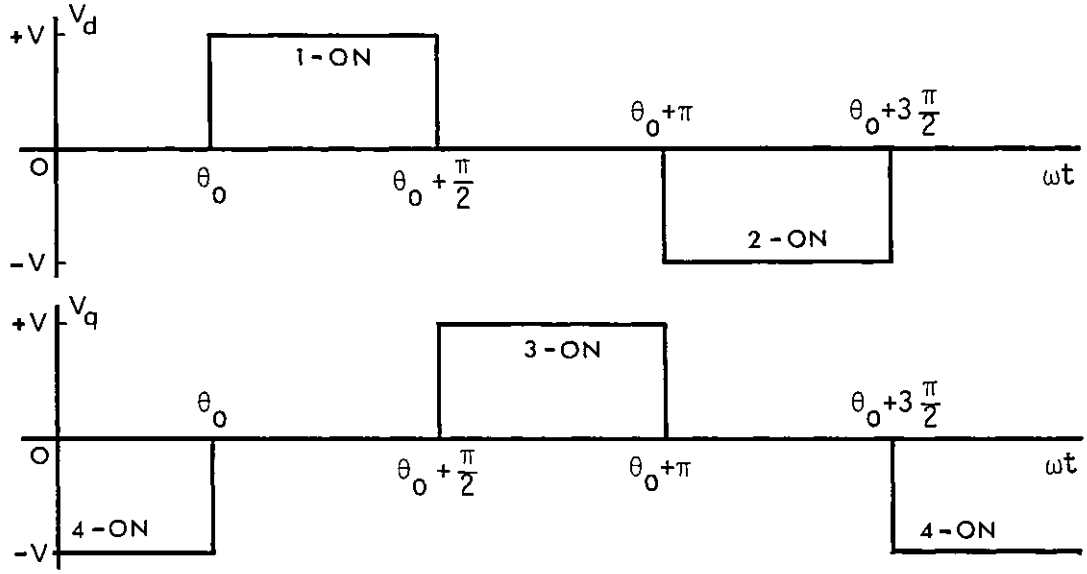

Fig. 3.3 - Voltage waveform

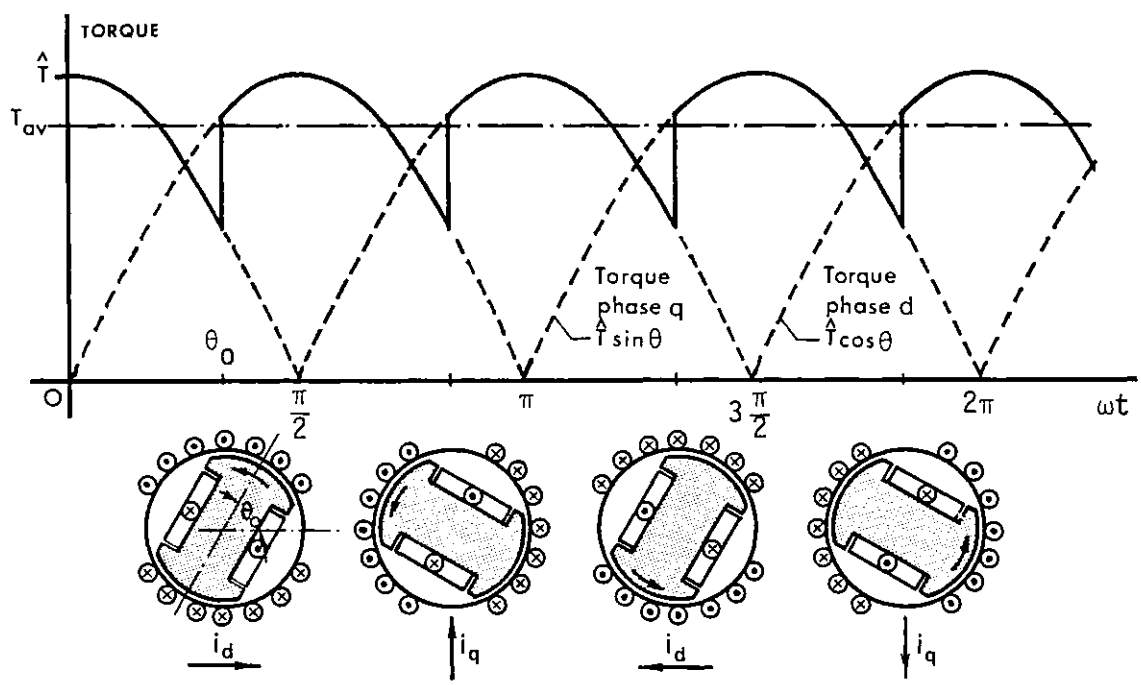

Fig. 3.4 - Resulting instantaneous torque

The method of controlling output torque by varying the switching angle can be achieved if desired by adjusting the position sensor orientation with respect to motor shaft and/or by employing electronic means.

This method of control corresponds to "brush shifting" in a conventional d.c. machine. Clearly, from Eq. (3.2) the switching angle to obtain the maximum average torque for a two-phase synchronous motor in switching mode is θ_o = 45°E, which gives:

$$T_{av} = \frac{2\sqrt{2}}{\pi} K \phi_f I \qquad (3.3)$$

The average torque is now 90% of peak value and consequently much smoother operation is achieved.

Drives employing the basic principle of shaft position sensor-control of the inverter switches are now dealt with in an extensive literature. In relatively few papers [58, 59] however is a two-phase system used, and in many papers, particularly those orientated towards large power schemes, aspects specific to thyristorised inverters are highlighted [2, 60, 61, 62]. Two-phase systems as opposed to those containing three or more phases tend to give higher levels of torque ripple, and the rating of each arm of the bridge in a two-phase system is of course higher. In the two-phase system's favour are however the following:

a) - For low power systems where the arm rating of a two-phase bridge can be handled by devices of reasonable cost, the inverter is simpler, cheaper and likely to be more reliable. It may be noted that low cost Darlington transistors are now produced with ratings in the 550 V, 20 A ranges. Even when paralleling is employed, the inverter may still be cheaper due to the smaller number of base drive (and sometimes sensor) channels involved.

b) - For applications requiring very low torque ripple, sinusoidal, current-forced operation is usually desirable. With a two-phase system, only two signal-shaping channels are required. Sine/cosine resolvers are cheaper than the three phase equivalent.

c) - There is no mutual inductance between the stator phases. Conditions at the inverter are hence likely to be correspondingly easier.

A similar scheme has been developed by Radziwill [63]. It consists of a two-pole, permanent magnet cylindrical rotor and a salient stator using four coils. The motor can be regarded as a four-phase machine and eight switches are employed. An overall drive efficiency of 80% is claimed.

3.4 - SINE WAVE OPERATION

As can be seen from Eq. (1.45) and as mentioned above, the ripple torque of even a two-phase synchronous motor can be ideally eliminated by using a pure sine wave current source supply. Fig. 3.5 shows one scheme for achieving this in a two-phase two-pole motor. Two current source amplifiers and a rotor position sensor mounted rigidly on the shaft are used. An early report dealing with this type of scheme has been presented by Manteuffel [39].

The principle of operation is basically the same as that described in the previous section and as can be seen in fig. 3.5 special position sensors outputting sine signals are indicated. If the position sensor is adjusted for an angle $\alpha_a = \theta + \alpha_f$ where α_f is the rotor pole axis angle, both angles with respect to the "d" stator winding, then the sensor signals will be of the form:

$$v_d = V_{in} \cos(\omega t + \alpha_a)$$

$$v_q = V_{in} \sin(\omega t + \alpha_a)$$

where ω is the common shaft angular speed. These signals are injected in each of the current souce power controllers (i.e., output current pro-

portional to input signal) and so two-phase currents are obtained as:

$$i_d = \hat{I} \cos(\omega t + \alpha_a)$$

$$i_q = \hat{I} \sin(\omega t + \alpha_a)$$

These two-phase currents, throughout a two-phase winding sinusoidally distributed, set up an armature m.m.f. whose position in space at instant t is given by

$$\omega t + \alpha_a = \text{atan}\left(\frac{i_q}{i_d}\right)$$

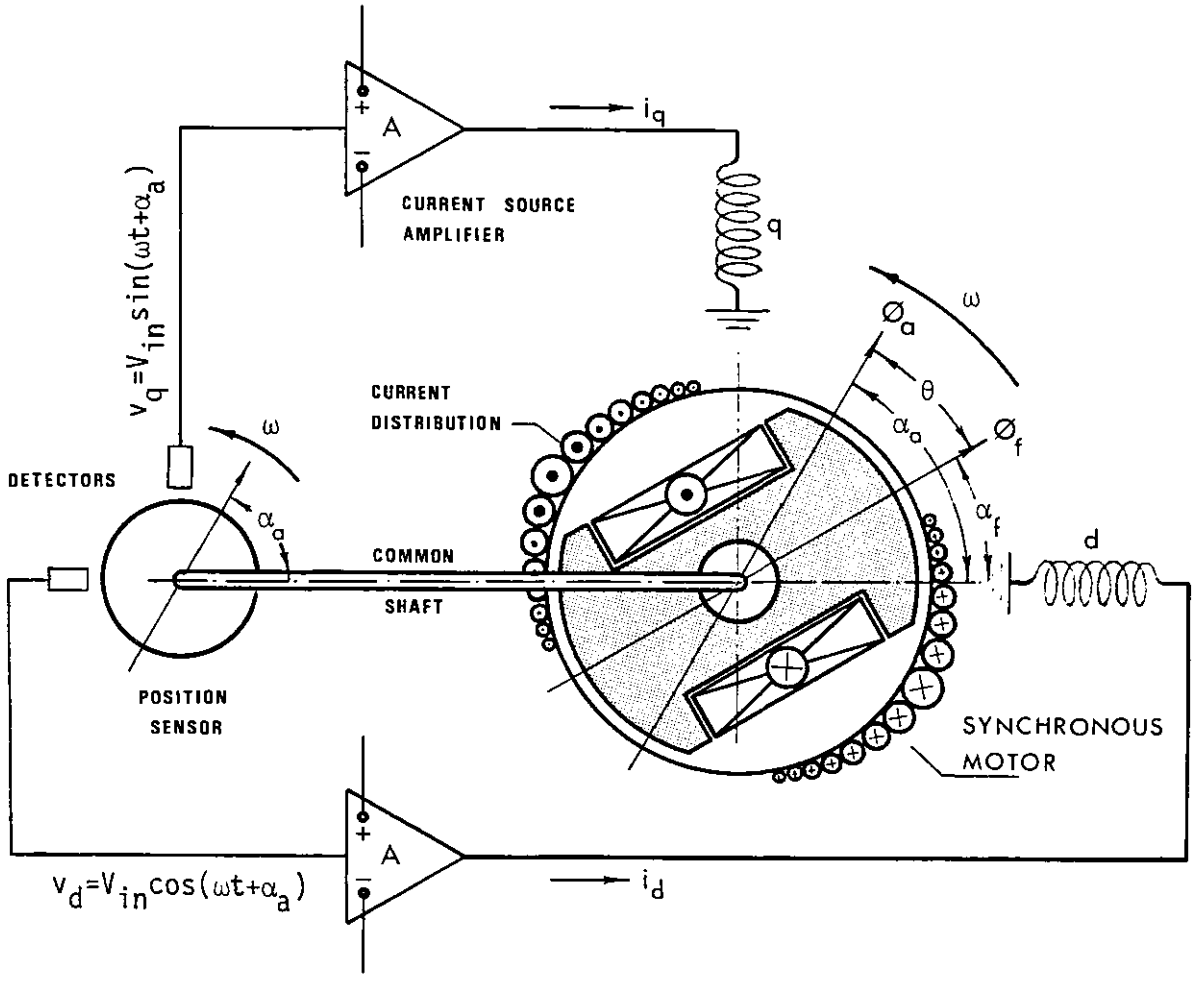

Fig. 3.5 - Two-phase auto-piloted synchronous motor

and rotates according to the rotor position sensor speed. The position sensor, locked with the motor shaft, senses instantaneously the rotor position $\omega t + \alpha_f$. Thus the angle $\theta = \alpha_a - \alpha_f$ between the rotor pole axis

and the stator m.m.f. is constant at any motor speed, including standstill and can be adjusted by setting α_a in the position sensor with respect to the motor shaft. With a moderate magnitude of the stator current and with sufficiently large field current, the motor may start without any auxiliary equipment.

The machine never loses synchronism, since the supply frequency ω is controlled or "piloted" by the information (rotor position) received from the machine itself, hence the term "auto-piloted". Since the angle θ is fixed, the operation is similar to a conventional d.c. motor, only here the locked stator and rotor m.m.f.'s rotate. This is why the auto-piloted synchronous motor with a permanent magnet field excitation is also known as a "brushless d.c. machine". The term is vague and misleading, since the machine is not a d.c. motor; thus the term "auto-piloted" is used here instead.

A comparison between "four-step" square wave operation and sine wave operation for an eight-pole disc synchronous motor is presented in Chapter 5.

3.5 - TYPES OF ROTOR POSITION SENSORS

The position sensor detects the rotor position and activates the inverter switching instants or the sine current source feed, when square wave or sine wave operation is used respectively. This device is in some ways the heart of the motor system and should have an output even at standstill. A controllable signal magnitude independent of rotor speed is desirable especially in the sine scheme. For sine wave operation a sine output is obviously convenient, while for square wave operation a pulsed or square wave output can be desirable in order to define precisely the instant of switching.

Many different types of sensing systems have been used [58, 64, 65],

but the most common position sensors employed are optical, magneto-sensitive, reluctance and electromagnetic. Brief descriptions of these are given below:

a) - Optical position sensor

One method for determining the rotor position which has gained favour, for small motors, in the last few years, is the use of photo-sensitive elements associated with some form of disc encoder. Fig. 3.6 shows the basic principles involved in shaft position sensing by optical means. A rugged, miniature light source, generated by a lamp

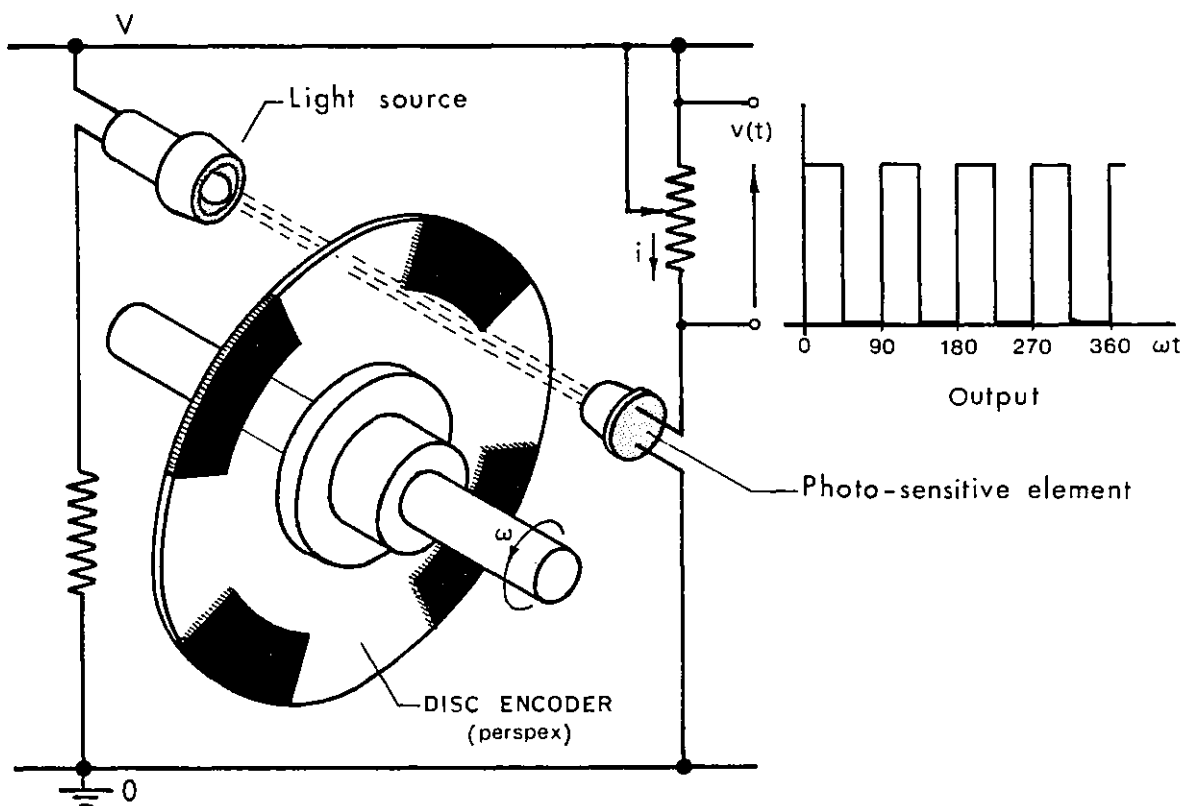

Fig. 3.6 - Optical position sensor

or light emitting diode (L.E.D.), is used to produce a narrow light beam, which activates a photo-sensitive device as a photo-diode or photo-transistor. The light source and the photo-sensitive element are both rigidly mounted on the stator of the machine. The disc encoder between these two elements is permanently fixed to the motor shaft. Thus, during

rotation, the disc periodically interrupts the light beam switching ON and OFF the photo-sensitive element accordingly. This allows a ring counter to be formed and with the precise switching instant, this system is particularly suitable for square wave operation.

A sine wave output is also possible with an optical system. Using a coded disc and several photo-sensitive elements a digital version of a sine wave may be obtained, which is filtered afterwards to give the fundamental component. However, in order to save electronic components, a sine wave output may be also obtained by using a variable opacity screen between the light source and the photo-sensitive element. There are commercially available discs with various forms of opacity variation made by photographic means. An optical position sensor using polaroid effect was developed for use with the eight pole disc synchronous motor, and it is described in section 5.7.

The optical position sensor is not affected by stray magnetic fields, needs relatively simple electronics and has a low inertia, which is an advantage when used associated with small motors. Two disadvantages of this system are its vulnerability to contamination by dirt and the limited lifetime of even solid state light sources. The second disadvantage has been almost removed with the greatly improved lifetimes of recently developed L.E.D.'s.

b) - Magnetosensitive sensor

Fig. 3.7 shows the layout of a basic position sensor of this type. A permanent magnet rotor produces a similar flux density distribution to the main rotor and some form of magnetosensitive element fixed on the stator converts the flux density variation into a voltage. Recent advances in semiconductor techniques have made available a number of magnetosensitive materials in which the Hall effect is particularly pronounced, and low cost, robust and compact units are now available [66].

Hall elements are made in the form of thin plates. When a field flux density B is applied normally to the plate surface, the e.m.f. induced in the element is $e = K_H \frac{i}{w} B$ where i is the excitation current, w the element thickness and K_H the Hall coefficient. If two Hall elements are arranged at right angles, then for a rotor position θ the outputs

$$e_1 = K_H \frac{i}{w} B \cos \theta$$

$$e_2 = K_H \frac{i}{w} B \sin \theta$$

will be obtained. A magneto-resistive device giving a corresponding variation in resistance is another option. However, Hall elements are preferable, since they have faster response.

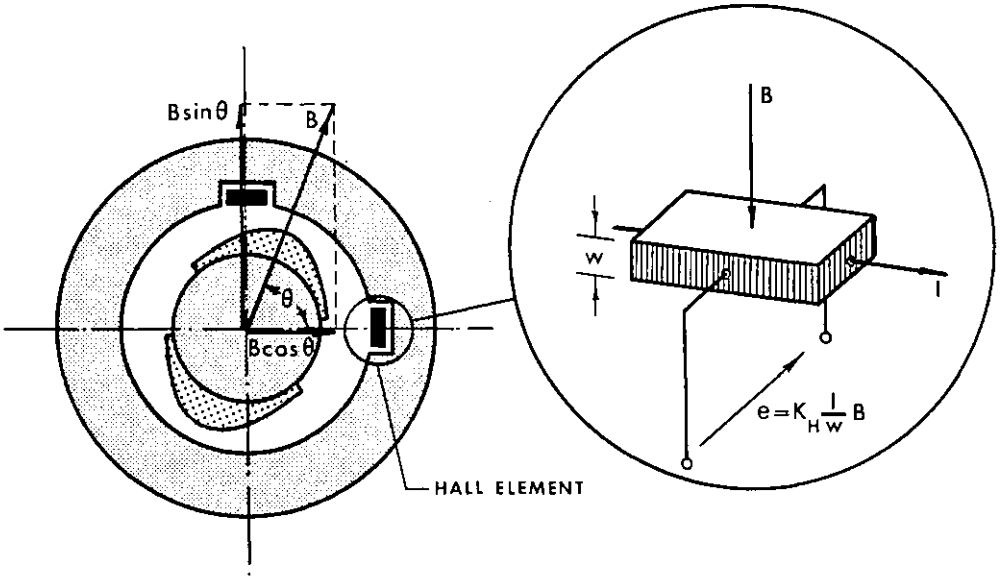

Fig. 3.7 - Magnetosensitive position sensor

The magnetosensitive elements can even be placed in the main air gap of the machine, dispensing therefore with the auxiliary rotor. Nevertheless, its correct operation there may be affected by the stator reaction flux and temperature dependence.

The magnetosensitive sensor is especially suitable for sine wave operation and as with optical systems electronic circuitry is required though this can usually be fairly simple. Attention must be given when setting up the elements on the stator, otherwise the Hall voltage may differ greatly.

c) - Reluctance position sensor

Reluctance position sensors are widely used in industrial motors and can take several forms. Fig. 3.8 shows a typical system. It consists of a high frequency oscillator which excites a primary coil mounted statically adjacent to the end of the motor shaft. A rotating segment on the

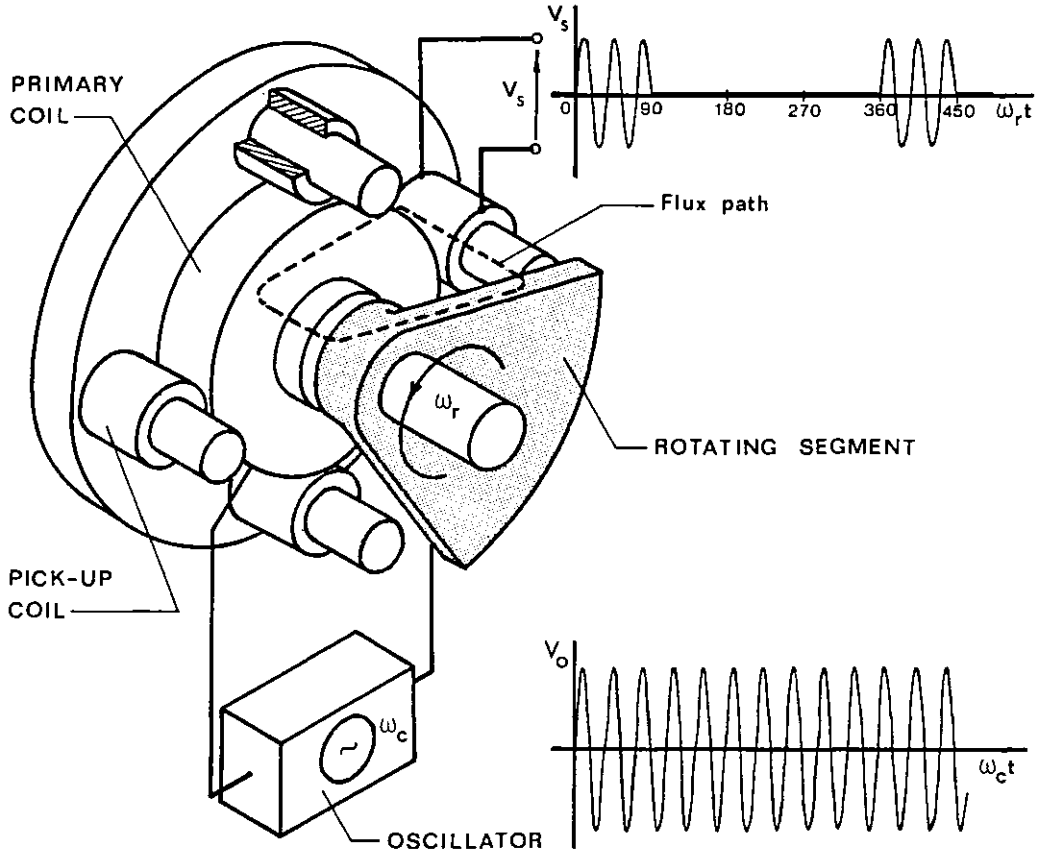

Fig. 3.8 - Reluctance position sensor

shaft closes the magnetic circuit through each fixed secondary coil. The reluctance for the flux path of the secondary coil coupled with the rotating segment is low as compared with the reluctance for the other coils. During rotation, e.m.f. with oscillator frequency is induced in each pick-up coil in succession as the rotating segment moves into position to couple the flux from the central coil. No e.m.f. is induced as the control segment moves away and therefore a sequence of pulses is obtained. Eddy-currents will be negligible if a ferrite core is used.

The output signal must be rectified and filtered, and the waveform obtained is suitable for square wave operation. The signal obtained is capable of directly driving the switching circuitry, thus dispensing the need for amplifying circuits. This direct driving capability enables the switching circuitry to be considerably simplified and hence more cheaply constructed. This device is robust, reliable and not affected by dirt. Similar devices based on the same principle have been developed [5, 58] for sine wave operation.

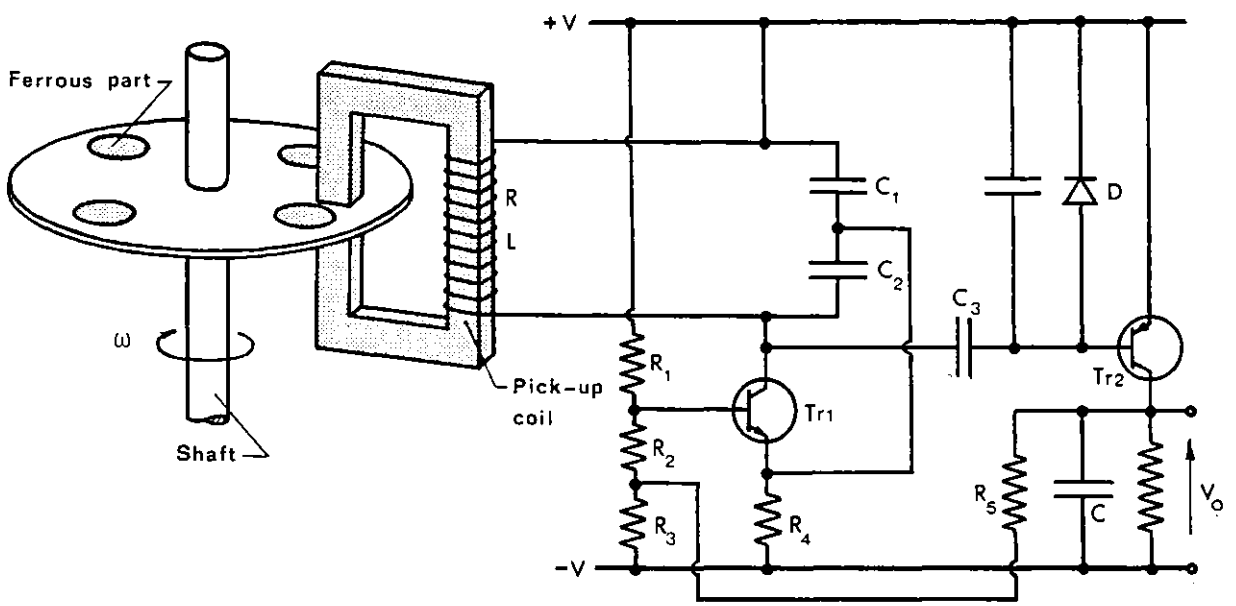

Fig. 3.9 - Proximity switch position sensor

Another position sensor of closely related mode of operation is the proximity switch using the reluctance effect. A non-magnetic disc provided with pieces of iron equally spaced from each other is rigidly attached to the motor shaft and rotates in the air gap of a wound C-core. The reluctance and hence the coil inductance varies periodically with shaft position and a switch is operated ON and OFF according to the value of the detector element. Fig. 3.9 shows the circuit diagram of a typical proximity switch position sensor [64]. The coil with variable inductance L according to the rotor position is connected in parallel with capacitors C_1 and C_2 constitutingan oscillator of Colpitz type. As the coil inductance

increases, the oscillation output voltage drops. Through the action of the positive feedback circuit R_5 the oscillation suddenly ceases to have a zero output. Thus, the rotor position is sensed and a sharp ON-OFF output signal can be obtained.

It may be noted that similar systems capable of sensing presence of non-conducting materials such as wood, P.V.C., glass, etc, as well as ferrous and non-ferrous metals are feasible [67].

d) - Synchro-resolver position sensor

This device is somewhat similar in basic construction to a conventional synchronous machine and exploits the sinusoidal relation between shaft angle and output voltage. For a direct drive the resolver should have

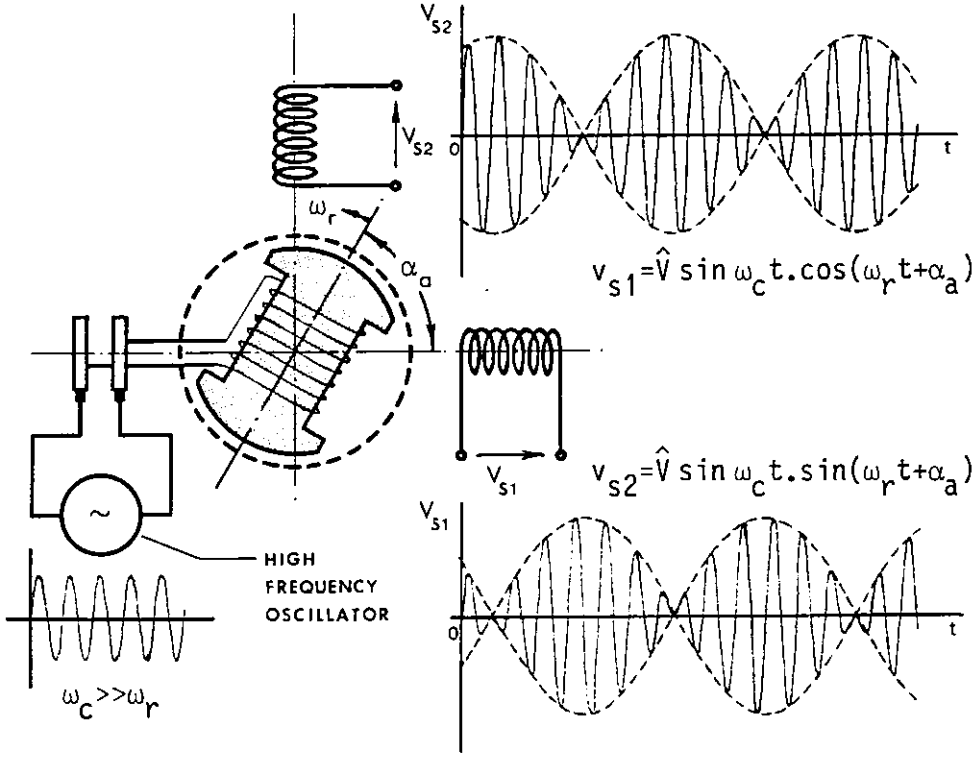

Fig. 3.10 - Synchro-resolver position sensor

the same number of poles and phases as the main motor. A basic two-pole two-phase synchro-resolver suitable for sine wave operation is shown in fig. 3.10.

The rotor winding is supplied from a high frequency oscillator via sliprings , although a brushless synchro construction is also possible. The pulsating rotor flux then induces a voltage in each stator phase whose magnitude depends on the mutual inductance between the rotor and the respective phase winding. The rotation of the synchro shaft thus modulates the e.m.f.'s induced in each phase. It is the envelope of these waveforms which indicates the shaft position. A system to demodulate those e.m.f.'s is described in some detail in the following section.

3.6 - OVERALL SYNCHRO-RESOLVER SYSTEM

For the two-phase 1000 lb.ft. rotary actuator described in Chapter 4, a synchro-resolver position sensor was used and the electronic system built is shown in the photograph of fig. 3.11.

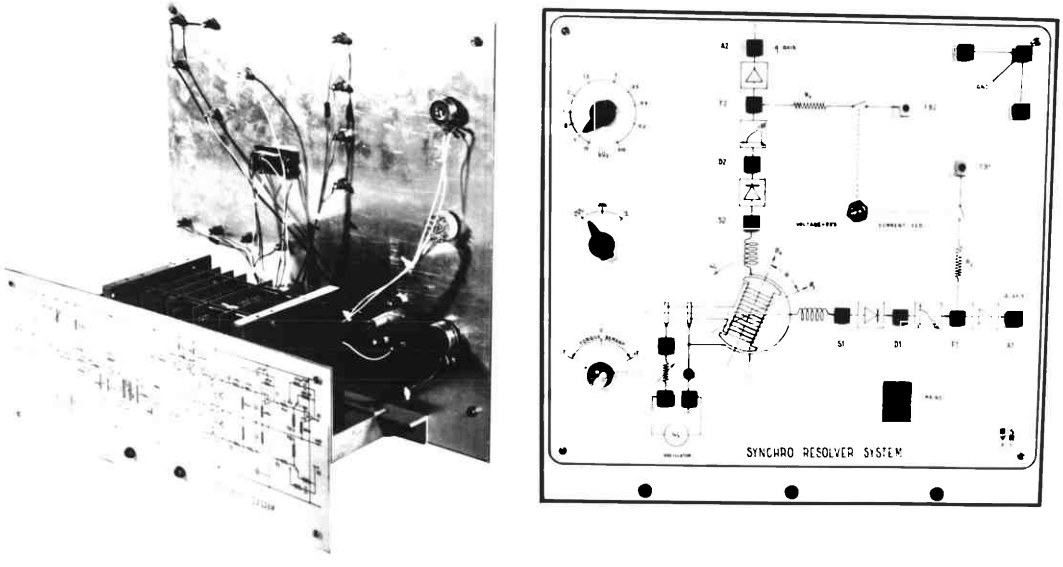

Fig. 3.11 - Electronic system for synchro-resolver position sensor

The block diagram of one phase of the system, using a two-pole, two-phase synchro-resolver, is shown in fig. 3.12. The working principle which is fairly standard is described below:

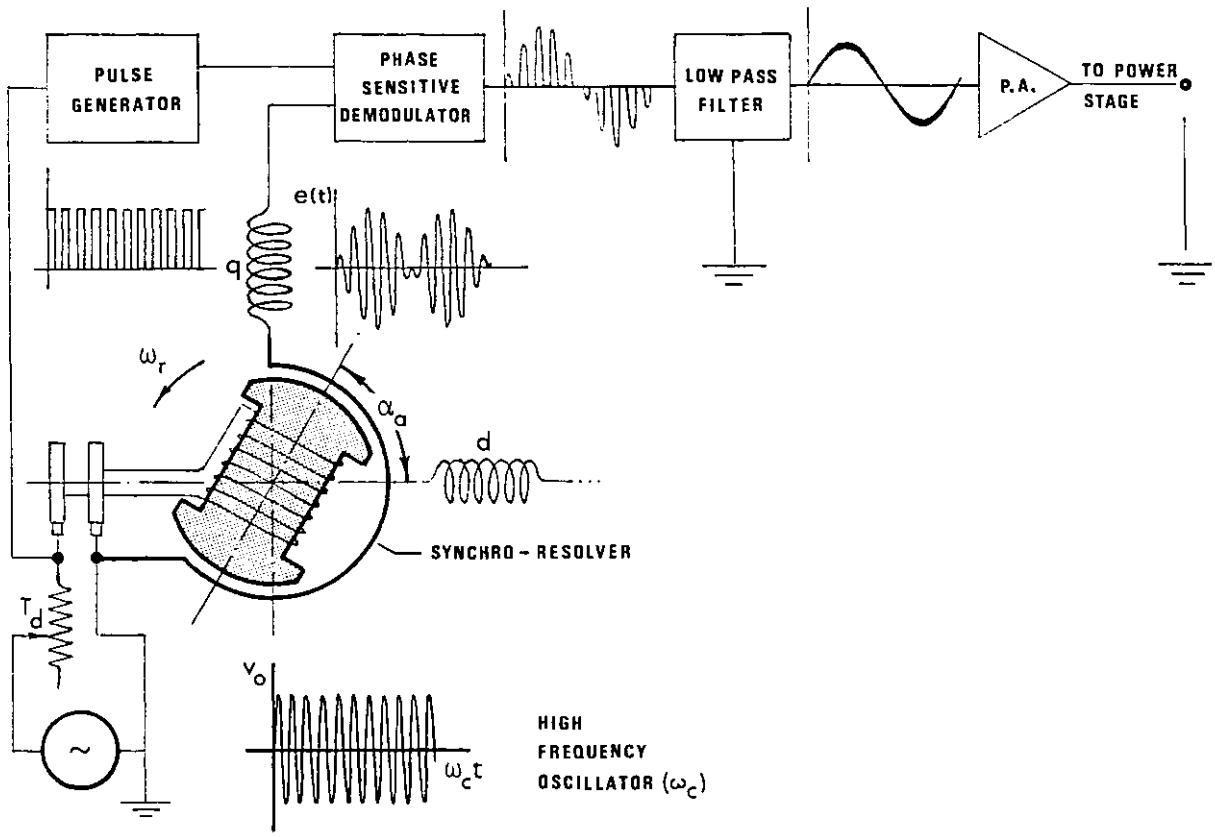

Fig. 3.12 - Block diagram of the basic synchro-resolver system

The magnitude of the sinusiodal excitation current from the high fre-frequency oscillator with a fixed frequency ω_c may be controlled by the potentiometer T_d. For an angular rotor speed ω_r the e.m.f. induced in the phase shown in the diagram is:

$$e(t) = \left[\hat{E} \sin(\omega_r t + \alpha_a) \right] . \sin \omega_c t \qquad (3.4)$$

where α_a is the initial rotor angle position and $\hat{E} \sin(\omega_r t + \alpha_a)$ is the e.m.f. induced for that particular rotor position depending on the mutual inductance between rotor and stator windings.

The phase sensitive demodulator is arranged to give an output signal of the form

$$e_s(t) = \left[\hat{E} \sin(\omega_r t + \alpha_a) \right] . |\sin \omega_c t| \qquad (3.5)$$

and so only alternate halves of the modulated wave, the positive and negative, are transmitted.

The carrier frequency ω_c is eliminated by low pass filtering giving:

$$e_f(t) = \hat{E}' \sin(\omega_r t + \alpha_a) \qquad (3.6)$$

which is the desired signal. Usually, the magnitude $\hat{E}'$ of this signal is too small to be applied directly to the power amplifier, and intermediate pre-amplification is needed.

If the rotor is at standstill, Eq. (3.6) gives:

$$e_{f1} = \hat{E}' \sin \alpha_a$$

and similarly for the other phase

$$e_{f2} = \hat{E}' \cos \alpha_a$$

Hence, even at standstill, signals proportional to sine and cosine of synchro rotor position are obtained.

Each section of the block diagram shown in fig. 3.12 is now explained.

a) - High frequency oscillator for synchro rotor supply.

The high frequency oscillator used was a monolithic integrated circuit capable of producing SINE, TRIANGULAR and SQUARE waveforms of high accuracy. The frequency can be selected externally over a range from less than 150 Hz to over 10 kHz, and is highly stable over a wide range of temperature and supply voltage [68]. The components of the synchro rotor supply system are shown in fig. 3.13, where the resitance R selects the frequency. The oscillator was operated from a dual power source of ±15 V giving an output magnitude of the triangle and sine-wave exactly one-half of the supply voltage. To prevent overload and to provide maximum amplitude an output buffer was required.

The motor rotation was reversed by phase inverting the input signal v_o. This was easily achieved with the transformer T, whose secondary centre tap was earthed. A pot ferrite core transformer RM7, suitable for high frequency operation, followed by another buffer stage was used.

With the 1 MΩ potentiometer in the central position there is no input to synchro-rotor and therefore no torque demand is achieved. Variation of this potentiometer for positions A or B allows the input magnitude $\hat{V}_o$ to vary from zero to $\hat{V}_R$ and in phase or anti-phase with the reference signal

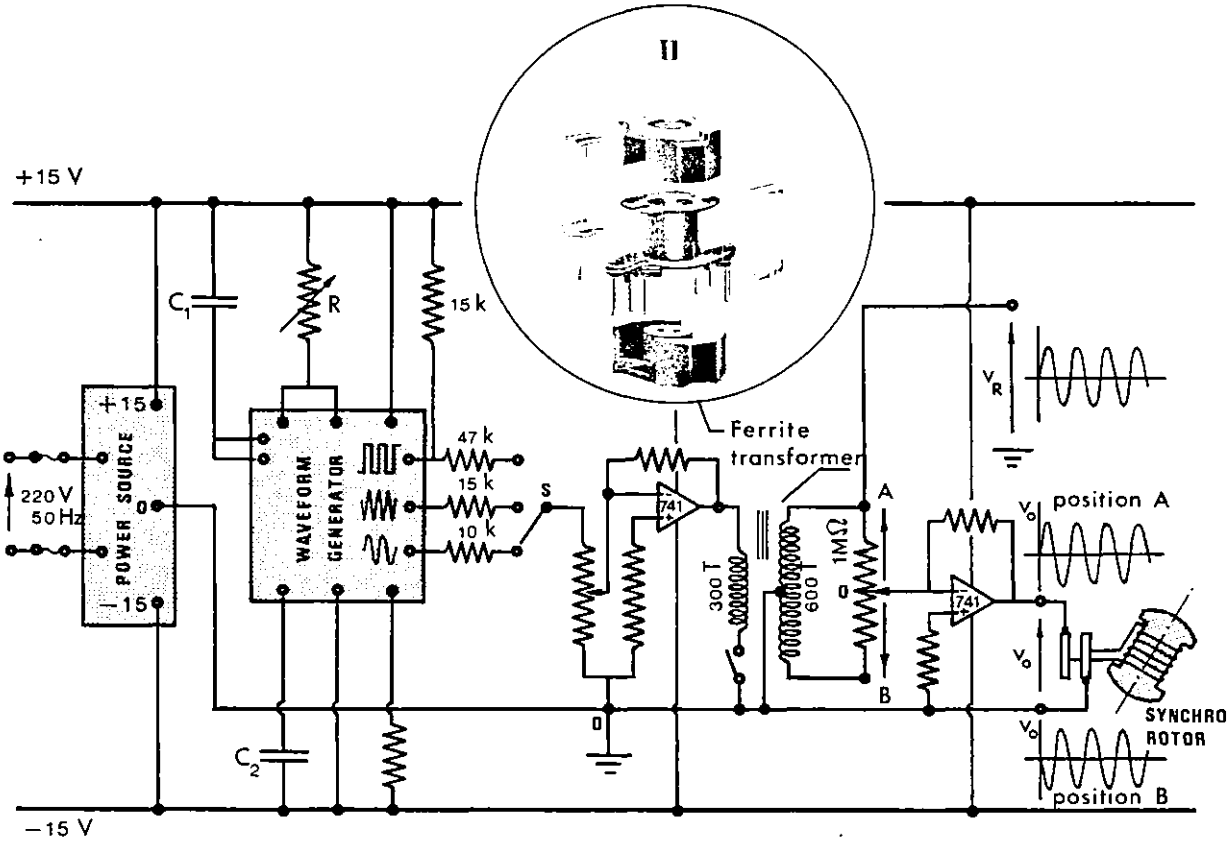

Fig. 3.13 - Synchro-rotor supply system

v_R respectively, hence controlling torque demand bi-directionally. This way of controlling torque demand may be also achieved by electrical means rather than mechanical means. In the section 4.13 some modifications are suggested for a practical application.

b) - Phase sensitive demodulator

The function of the phase sensitive demodulator is to recover from the modulated voltage given by Eq. (3.4) and shown plotted in fig. 3.14(a), the voltage given by Eq. (3.5) and shown in fig.3.14(c), which carries the information of shaft angular position. A simple rectifier is unsuitable because a change of sign of $\hat{E}\sin(\omega_r t + \alpha_a)$ appears as a change of phase

in the waveform e(t). It must be supplied with a reference voltage $v_R = \hat{V}_R \sin \omega_c t$ with which to compare the phase of e(t), and must produce an output voltage of correct polarity depending on that comparison.

Phase sensitive demodulators may be divided into two classes: additive and multiplicative. The first adds the reference and signal voltages, and subjects the sum waveform to rectification in a normal rectifying circuit [5]. The second acts by multiplying e(t) by a "switching function" derived from the reference voltage.

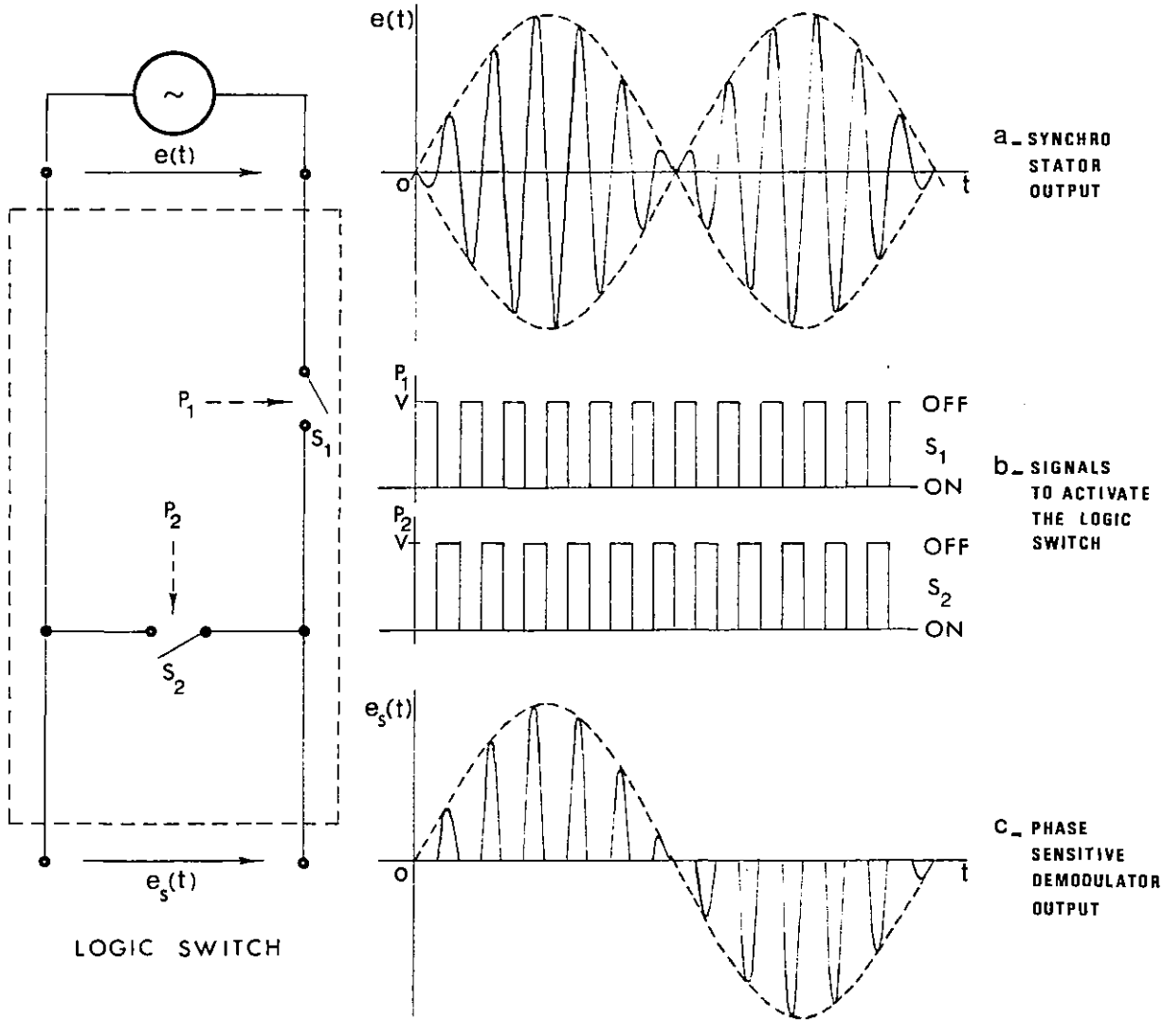

Fig. 3.14 - Phase sensitive demodulator principle

The phase sensitive demodulator developed belongs to the latter type and was fairly easily carried out using a logic switch DGM111AL monolithic integrated. The working principle is simply explained with the aid of the diagram shown in fig. 3.14. The signal e(t) to be demodulated is

applied to the input of the logic switch, where the switches S_1 and S_2 are controlled alternatively by square pulses derived from the reference voltage. The switch S_1 is OFF when excited by the pulse P_1 and S_2 is ON because it is not excited and vice-versa. The result is that the output voltage is made equal to the input voltage on the alternative half-cycles when S_1 is ON (and S_2 OFF), and zero at other times because of the short-circuit across output terminals by switch S_2.

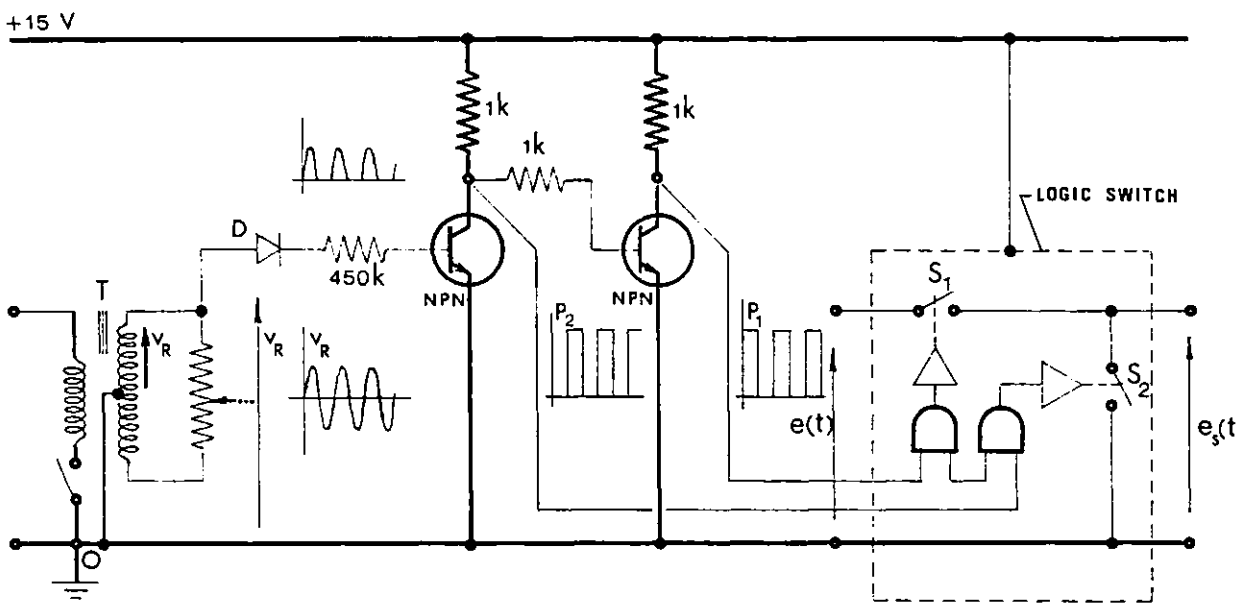

Fig. 3.15 - Square pulses generation for logic circuit operation

The circuit diagram suitable for generating the square pulses P_1 and P_2 is shown in fig. 3.15. The reference signal from the secondary side of the transformer is first rectified by the diode D. These pulses then activate two NPN TO5 transistors which generate the required signals to operate both switches.

c) - Filtering

Fourier analysis of the phase sensitive demodulator output signal $e_s(t)$ given by Eq. (3.5) is [69]:

$$e_s(t) = \frac{\hat{E}}{\pi}\sin(\omega_r t + \alpha_a) + \frac{\hat{E}}{4}\sin\omega_c t\,\sin(\omega_r t + \alpha_a) - \\ - \frac{2\hat{E}}{\pi}\sin(\omega_r t + \alpha_a)\left[\frac{1}{3}\cos 2\omega_c t + \frac{1}{15}\cos 4\omega_c t + \ldots\right] \qquad (3.7)$$

Neglecting high harmonics, Eq. (3.7) may be re-written as:

$$e_s(t) = \frac{\hat{E}}{\pi}\sin(\omega_r t + \alpha_a) + \frac{\hat{E}}{8}\left\{\cos\left[(\omega_c-\omega_r)t-\alpha_a\right]-\cos\left[(\omega_c+\omega_r)t+\alpha_a\right]\right\} \qquad (3.8)$$

The first term of Eq. (3.8) represents the required output signal to be applied to the d.c. linear amplifier. The second term with two sidebands of frequency $\omega_c \pm \omega_r$ can be removed by a low pass filter. The simplest filter consists of a series resistance R followed by a shunt capacitor C, the filtered signal appearing across the capacitor [70]. This passive filter was tried, but was unsuitable, since it did not discriminate sharply enough between the lowest signal frequency and the highest unwanted frequency. An active low pass filter of the Sallen and Key type [71] having a sharp cut-off was designed and its circuit diagram together with the components values is shown in fig. 3.16.

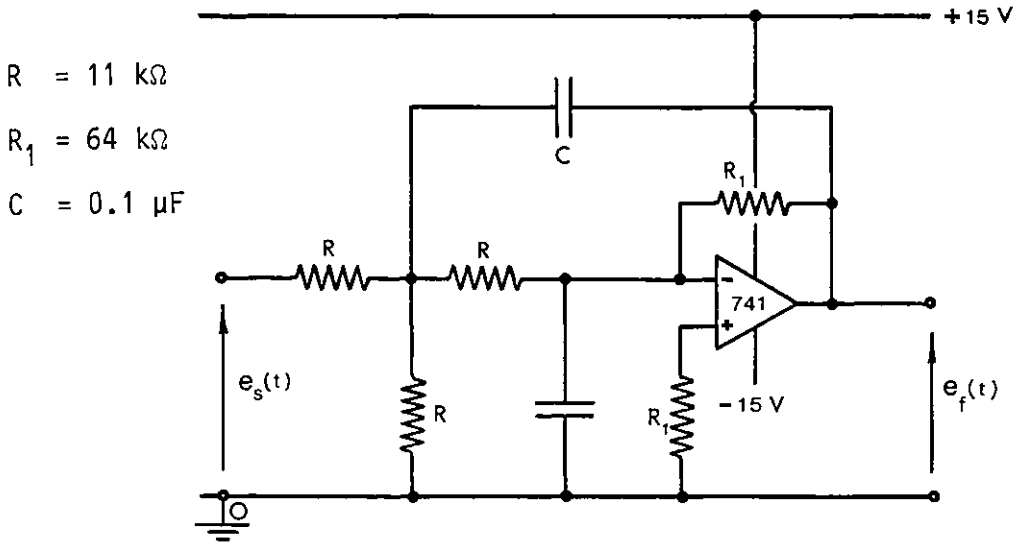

Fig. 3.16 - Sellen and Key active low pass filter

The transfer function of this filter is given by:

$$\bar{T}(\omega) = \frac{\bar{E}_f}{\bar{E}_s} = \frac{1}{1 - (\omega CR)^2 + j2\omega CR} \qquad (3.9)$$

Combining Eq. (3.8) and Eq. (3.9), the maximum p.u. ripple filter output becomes

$$\frac{\hat{E}_f - \hat{E}_{f1}}{\hat{E}_{f1}} = \frac{\pi}{8} \left| \frac{\bar{T}(\omega_c - \omega_r) + \bar{T}(\omega_c + \omega_r)}{\bar{T}(\omega_r)} \right| \qquad (3.10)$$

where $\hat{E}_{f1}$ is the peak value of the filter output fundamental component.

Assuming a maximum speed of N_r = 15 rev/min for the actuator, the frequency for the 72-poles synchro-resolver at that speed is f = 9 Hz or ω_r = 56.52 rad/s. In order to keep iron losses and heating effects to a minimum in the synchro-resolver, the oscillator was set for 5 Hz or 31.4 10^3 rad/s. For these angular frequencies and the component values used in filter design, Eq. (3.10) gives the maximum ripple level output as

$$\frac{\hat{E}_f - E_{f1}}{\hat{E}_{f1}} = \frac{\pi}{8} \left| \frac{0.001\angle -177° + 0.001\angle -177°}{0.996\angle -7.1°} \right| \simeq 0.08\%$$

which was judged to be quite acceptable.

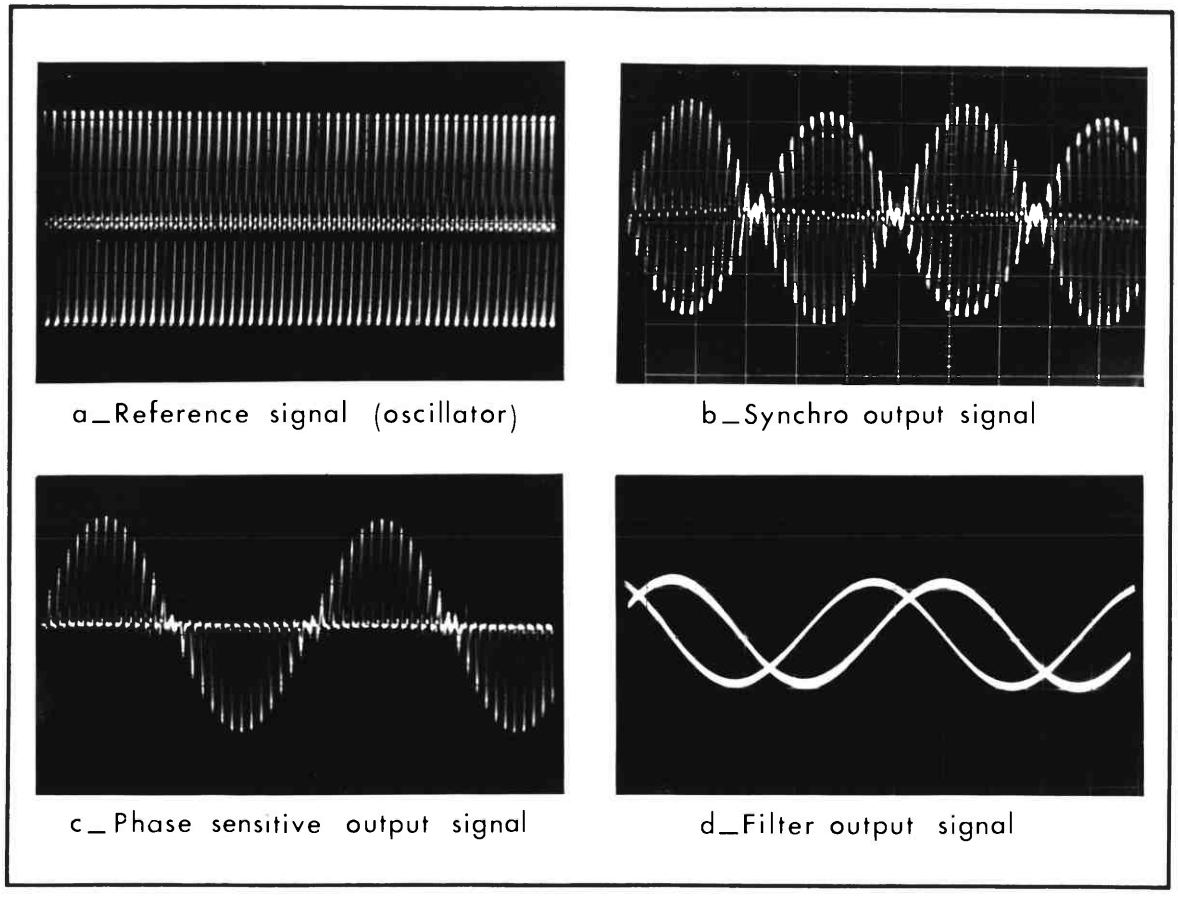

Fig. 3.17 - Oscillograms of the synchro-resolver system

Finally, fig. 3.17 shows oscillograms obtained in various stages of the synchro-resolver system developed and as can be seen the filter output signal is a very clean sine-wave indeed.

3.6.1 - Influence of the ratio ω_r/ω_c in synchro-resolver system

This section shows that the ratio of synchro shaft speed to synchro rotor supply frequency ω_r/ω_c should be limited to a reasonable value, otherwise the synchro-resolver system operation can be affected. To examine the effect of this ratio in the overall system, a brief analysis of the synchro-resolver is carried out using two-axis theory [22, 72]. Similar treatment is made in reference [5] where the phase sensitive demodulator is of the additive type. The analysis is carried out here, however, in order to see how the operation of the phase sensitive demodulator using a logic switch is affected.

Fig. 3.18(a) shows the synchro-resolver circuit diagram assuming the rotor to be fixed at the d-axis position and the stator rotating with angular speed ω_r, which is inverted but electrically equivalent to the actual machine. Fig. 3.18(b) shows its equivalent "pseudo-stationary"

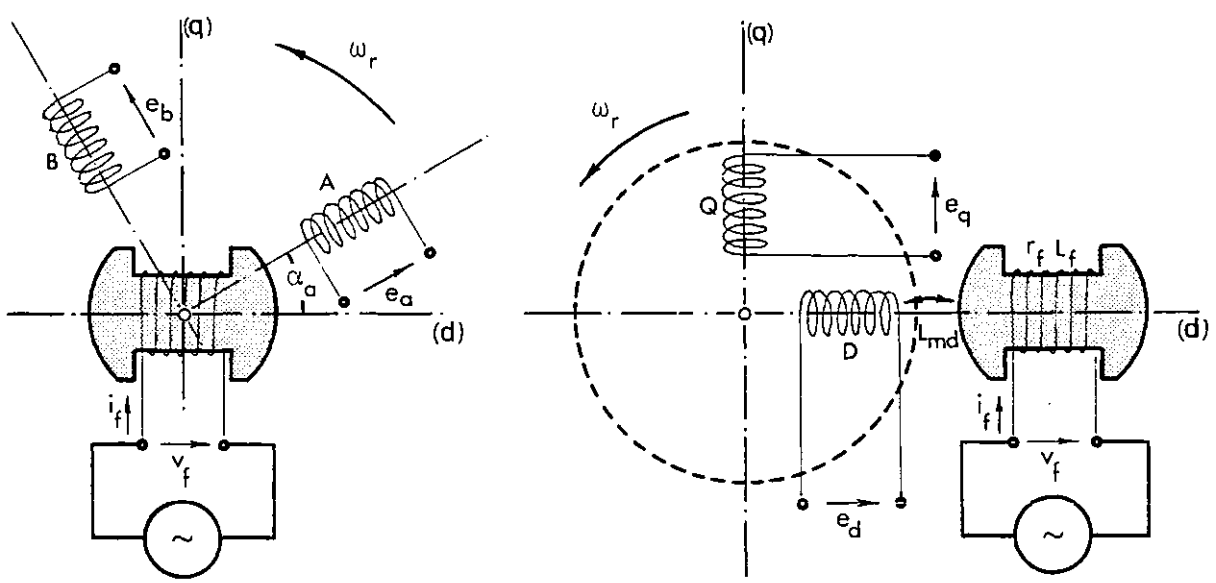

(a) - Rotating machine (b) - Pseudo-stationary

Fig. 3.18 - The rotating machine and the equivalent pseudo-stationary system

system. The voltages between both systems are related by the voltage transformation such that

$$\begin{bmatrix} e_a \\ \\ e_b \end{bmatrix} = \begin{bmatrix} \cos(\omega_r t + \alpha_a) & \sin(\omega_r t + \alpha_a) \\ \\ -\sin(\omega_r t + \alpha_a) & \cos(\omega_r t + \alpha_a) \end{bmatrix} \cdot \begin{bmatrix} e_d \\ \\ e_q \end{bmatrix} \tag{3.11}$$

Assuming that the two phases supply infinite impedence loads, the voltages for the pseudo-stationary system are

$$e_d = L_{md}\, p\, i_f \tag{3.12}$$

$$e_q = -L_{md}\, \omega_r\, i_f \tag{3.13}$$

$$v_f = (r_f + L_f\, p) i_f \tag{3.14}$$

where p is the Laplace operator and L_{md} is the mutual p.u. inductance between rotor and d-axis coil. Therefore, according to voltage transformation given by Eq. (3.11) and taking into account Eq. (3.12) and Eq. (3.13) the voltages across phases A and B in the synchro-resolver at any instant are respectively:

$$e_a = L_{md}\, p\, i_f \cos(\omega_r t+\alpha_a) - L_{md}\, \omega_r\, i_f \sin(\omega_r t+\alpha_a) \tag{3.15}$$

$$e_b = -L_{md}\, p\, i_f \sin(\omega_r t+\alpha_a) - L_{md}\, \omega_r\, i_f \cos(\omega_r t+\alpha_a) \tag{3.16}$$

Since v_f is sinusoidal of frequency ω_c, the operator p may be replaced by $j\omega_c$ in Eq. (3.14). Thus, substitution of i_f into Eq. (3.15) and Eq. (3.16) gives:

$$\bar{E}_a = L_{md}\, \frac{j\omega_c \cos(\omega_r t+\alpha_a) - \omega_r \sin(\omega_r t+\alpha_a)}{r_f + j\omega_c L_f}\, \bar{V}_f \tag{3.17}$$

$$\bar{E}_b = -L_{md}\, \frac{j\omega_c \sin(\omega_r t+\alpha_a) + \omega_r \sin(\omega_r t+\alpha_a)}{r_f + j\omega_c L_f}\, \bar{V}_f \tag{3.18}$$

If the oscillator frequency ω_c is high enough to make $r_f \ll \omega_c L_f$, Eq. (3.17) and Eq. (3.18) reduces to

$$\bar{E}_a = \frac{L_{md}}{L_f} \cos(\omega_r t+\alpha_a) \cdot \left[1 - j \frac{\omega_r}{\omega_c} \tan(\omega_r t+\alpha_a)\right] \bar{V}_f \tag{3.19}$$

$$\bar{E}_b = -\frac{L_{md}}{L_f} \sin(\omega_r t+\alpha_a) \cdot \left[1 + j \frac{\omega_r}{\omega_c} \operatorname{cotan}(\omega_r t+\alpha_a)\right] \bar{V}_f \tag{3.20}$$

As can be seen from these equations, the zeros of the oscillator signal v_f do not occur at the same instant as the zeros of the phase voltages, except for the particular case when the synchro is stationary ($\omega_r = 0$). This delay or phase angle introduced varies with rotor position $\omega_r t + \alpha_a$ and depends on the ratio ω_r/ω_c. Signal e_a is retarded in phase relative to v_f by an angle

$$\phi_a = \operatorname{atan}\left(\frac{\omega_r}{\omega_c}\right) \tan(\omega_r t + \alpha_a) \tag{3.21}$$

and signal e_b is advanced in phase by an angle

$$\phi_b = \operatorname{atan}\left(\frac{\omega_r}{\omega_c}\right) \operatorname{cotan}(\omega_r t + \alpha_a) \tag{3.22}$$

Clearly, this phase shift affects the correct operation of the phase sensitive demodulator. In fact, the logic switch, controlled by the reference signal v_f, will be operated out of phase relative to stator voltages given by Eq. (3.19) and Eq. (3.20). Then, the filter output d.c. component is also affected according to the phase introduced by the rotor position, which is not desirable. From Eq. (3.21) and Eq. (3.22) it is now evident that this effect is minimised by keeping ω_r/ω_c as small as possible. However, the oscillator supply frequency ω_c is limited by iron losses in the synchro-resolver magnetic circuit and so frequencies greater than 5 kHz are undesirable. The synchro-resolver speed ω_r must then be limited to a low level and so the system is not suitable for very high speed operation.

For the actuator studied within the project with an envisaged speed of N_r = 15 rev/min, the maximum value of ω_r/ω_c to be expected is 9/5000

or 1.8×10^{-3}. Substitution of this result into Eq. (3.21) and Eq. (3.22) shows that phase angles ϕ_a and ϕ_b are negligible for most angular positions, except for rotor positions close to $\omega_r t + \alpha_a = 90°E$ and $\omega_r t + \alpha_a = 0°$ respectively, where its value is appreciable. For an intermediate rotor position $\omega_r t + \alpha_a = 45°E$ is $\phi_a = \phi_b = 0.1°E$. Therefore, by keeping ω_r/ω_c to a minimum, the influence of phase shift in the overall synchro-resolver system is not very important.

3.7 - ANALYSIS OF THE SYNCHRONOUS MOTOR WITH ROTOR POSITION CONTROL

The basic system to be investigated is illustrated schematically in fig. 3.19, in which a two-phase synchronous motor receives its supply from power stages controlled by the signals received from the rotor position sensor. As seen previously the sensor may take several different

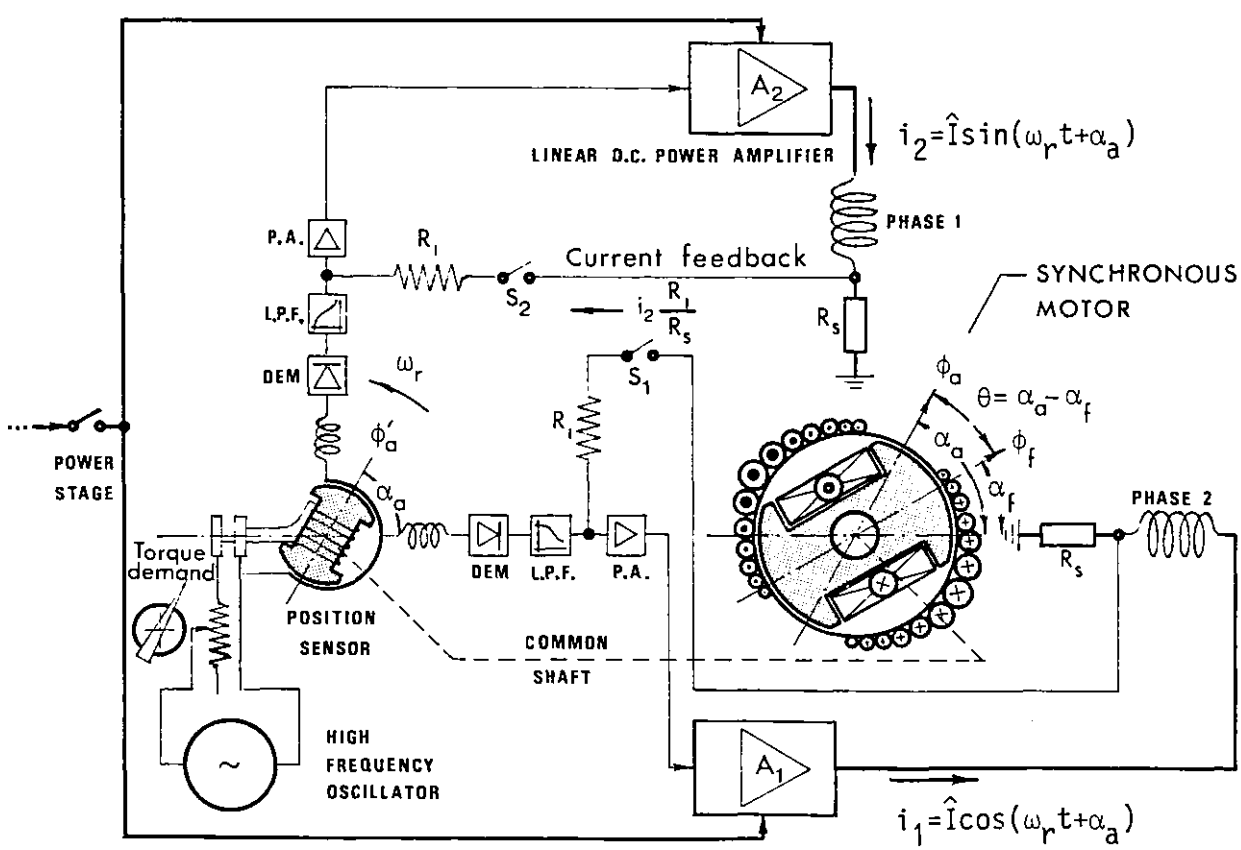

Fig. 3.19 - Auto-piloted synchronous motor for voltage or current forced operation

forms, but as an example a synchro-resolver position sensor is used. The power stage of this supply system may also consist of an inverter, cycloconverter [73, 74] or a power amplifier operating in class B [56], Pulse Width Modulation (P.W.M.) [75] or Pulse Frequency Modulation (P.F.M.) [76], depending on the particular application. In the diagram a linear d.c. power amplifier, which can be made to operate either as a constant voltage source or as a constant current source is shown, in either case controlled in magnitude by the level of signal injected into the rotor of the synchro-resolver. For constant current source operation, a current feedback signal is required (switches S_1 and S_2 ON) and the effect of this inner loop will be described in one application in Chapter 5. Other arrangements for producing current source operation are possible and current source feeding of synchronous motors and servo motors are detailed in references [77, 78] and [79] respectively.

Since with fig. 3.19 arrangement the motor operates in a synchronous mode at variable frequency and under sinusoidal conditions, the analysis of the motor can be carried out using standard two-axis theory.

The time phase diagram of a salient pole synchronous motor, under sinusoidal conditions, is represented according to Eq. (1.104) in fig. 3.20(a). Fig. 3.20(b) shows the respective space m.m.f. phasor diagram.

As already seen, the torque angle θ corresponds physically to the angle of misalignment between the fundamental rotor m.m.f. $\bar{F}_f$ and the resulting stator m.m.f. $\bar{F}_a$ and it appears in the time phasor diagram as the angle between the stator current and its direct-axis component.

The phase angle δ between the input voltage $\bar{V}$ and the back e.m.f. $\bar{E}$ on no-load is called load angle and it is taken conventionally positive when voltage is leading. When the synchronous motor is supplied by a fixed voltage and fixed frequency, operating in an open-loop under conventional a.c. conditions, the load angle δ varies according to the load torque applied to the shaft. Under steady conditions, and for a round

rotor, the maximum motor torque is achieved at δ = 90°E. If δ becomes larger than 90°E due to an attempt to obtain more than peak torque, increase in δ results in less torque output and the machine loses synchronism.

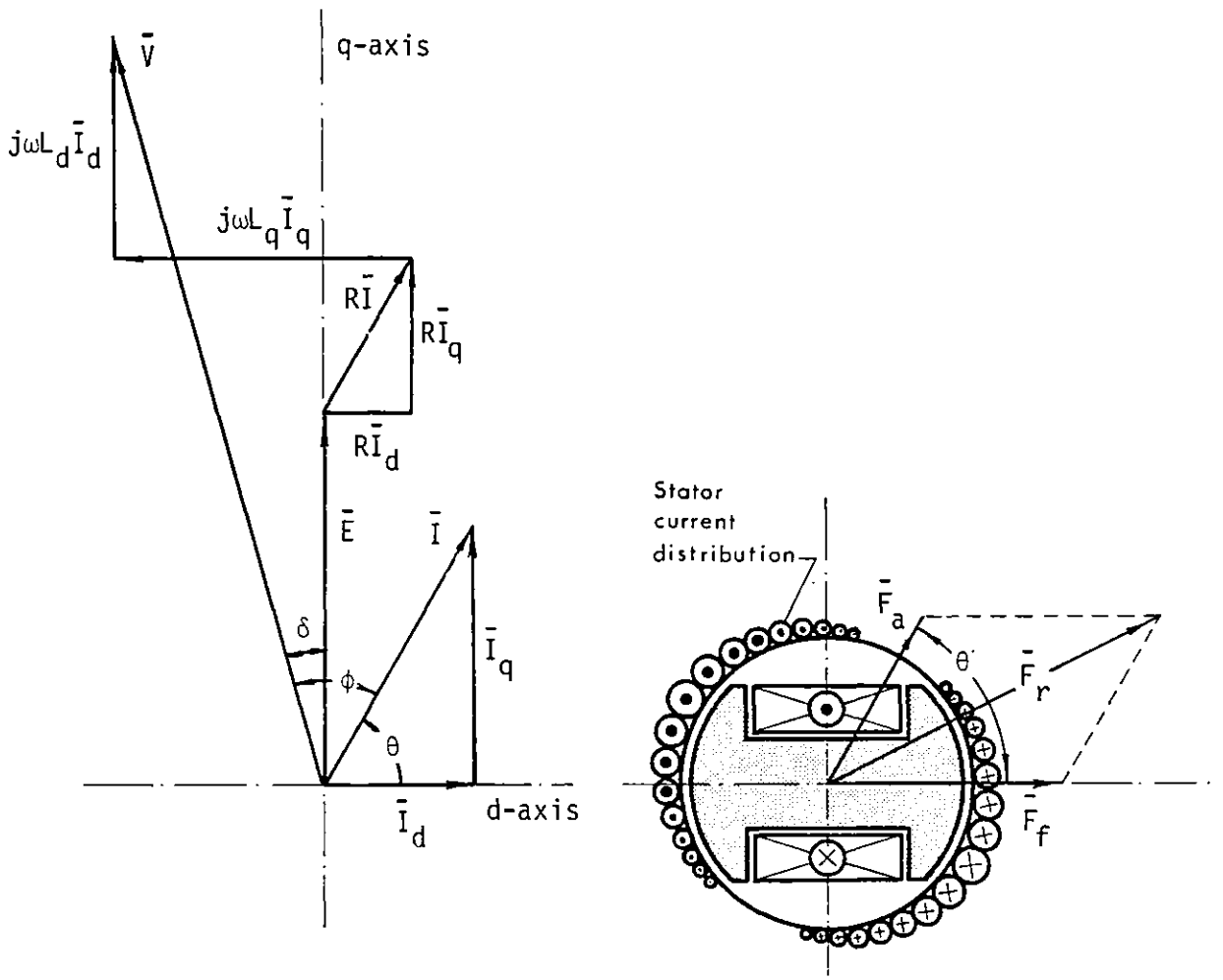

(a) - Phasor diagram (b) - Space m.m.f. phasor diagram

Fig. 3.20 - Phasor diagram for a salient pole synchronous motor

However, this is not the case in the auto-piloted mode, where the motor is operating in a closed-loop system. Due to the position sensor, voltage $\bar{V}$ or current $\bar{I}$ depending on the feed arrangements have a fixed relationship to the back e.m.f. $\bar{E}$. Since in the phasor diagram the phasor of machine back e.m.f. $\bar{E}$ is represented along the quadrature-axis, then the load angle δ between $\bar{E}$ and $\bar{V}$ or torque angle θ between $\bar{I}$ and d-axis are fixed for any given load torque at any rotor speed, when forced-voltage or forced-current are used respectively.

These two modes of machine operation with a fixed load angle and controlled voltage or a fixed torque angle and controlled current are quite different and their analysis is considered separately. Steady-state speed characteristics for both modes of operation are now described for the general case of a salient pole synchronous motor with adjustable d.c. rotor excitation. Aspects of the operating characteristics of auto-piloted synchronous machines, particularly of the non-salient type, have received a certain amount of attention in the recent literature, but steady-state relation of the degree of generality and variety presented in the following sections, and the presentation of corresponding performance characteristics, are matters that seem not to have been published so far as the author is aware.

3.7.1 - Steady state theory of a synchronous motor operating at variable-frequency and fixed load angle.

In this case the load angle δ is fixed by the position sensor and the voltage $\bar{V}$ is controlled only in magnitude by the torque demand signal applied to the sensor. In the steady-state, the motor is then operating from a constant voltage source and variable frequency.

a) - Stator supply current

Since the back e.m.f. $E = K\phi_f\omega$ is proportional to rotor speed and the direct $X_d = \omega L_d$ and quadrature $X_q = \omega L_q$ axes reactances vary with frequency, from the phasor diagram shown in fig. 3.20(a), it is evident that for a fixed voltage the stator current $\bar{I}$ varies in magnitude and phase with frequency or motor speed. In fact, projecting the voltage components on the d and q-axes gives:

$$V \sin \delta = \omega L_q I_q - R I_d \tag{3.23}$$

$$V \cos \delta = E + R I_q + \omega L_d I_d \tag{3.24}$$

Letting

$$\alpha = \frac{L_q}{L_d} \text{ (saliency factor)} \quad , \quad \beta = \frac{R}{\omega L_d} \quad , \quad \varepsilon = \frac{E}{V} \tag{3.25}$$

from solution of Eq. (3.23) and Eq. (3.24) the following expressions for I_d and I_q components are obtained as:

$$I_d = \frac{V}{X_d}\left[\frac{\alpha \cos\delta - \beta \sin\delta - \alpha\varepsilon}{\alpha + \beta^2}\right] \tag{3.26}$$

$$I_q = \frac{V}{X_d}\left[\frac{\sin\delta + \beta \cos\delta - \beta\varepsilon}{\alpha + \beta^2}\right] \tag{3.27}$$

Normally the parameters of an a.c. machine are determined for the nominal frequency ω_o. Assuming no saturation, the machine parameters can be calculated for any frequency ω with the aid of the following relationships [80]:

$$\begin{aligned} X_d &= \frac{\omega}{\omega_o} X_{do} = \lambda X_{do} \quad ; \qquad X_q = \lambda X_{qo} \\ \beta &= \frac{\beta_o}{\lambda} \quad ; \qquad \varepsilon = \lambda \varepsilon_o \end{aligned} \tag{3.28}$$

where $\lambda = \frac{f}{f_o}$ and X_{do}, X_{qo}, β_o and ε_o are the parameters at the nominal frequency f_o. Substitution of Eqs. (3.28) into Eq. (3.26) and Eq. (3.27) yields:

$$I_d = \frac{V}{\lambda X_{do}\left(\alpha + \frac{\beta_o^2}{\lambda^2}\right)}\left(\alpha\cos\delta - \frac{\beta_o}{\lambda}\sin\delta - \lambda\alpha\varepsilon_o\right) \tag{3.29}$$

$$I_q = \frac{V}{\lambda X_{do}\left(\alpha + \frac{\beta_o^2}{\lambda^2}\right)}\left(\sin\delta + \frac{\beta_o}{\lambda}\cos\delta - \beta_o\varepsilon_o\right) \tag{3.30}$$

From the phasor diagram, the stator current is given by

$$I = \left[I_d^2 + I_q^2\right]^{\frac{1}{2}} \tag{3.31}$$

and substitution of Eq. (3.29) and Eq. (3.39) into Eq. (3.31) and simplifying gives:

$$I = \frac{V}{\lambda X_{do}\left(\alpha + \frac{\beta_o^2}{\lambda_2}\right)}\left[\left(\alpha^2 + \frac{\beta_o^2}{\lambda^2}\right)\left(\lambda^2\varepsilon_o^2 + 1\right) + \frac{(1-\alpha)^2}{2} + \frac{2\varepsilon_o\beta_o}{\lambda}(\alpha-1)\sin\delta + \right.$$

$$\left. + \frac{\beta_o(1-\alpha)}{\lambda}\sin 2\delta - 2\lambda\varepsilon_o\left(\alpha^2 + \frac{\beta_o^2}{\lambda^2}\right)\cos\delta - \frac{1-\alpha^2}{2}\cos 2\delta\right] \quad (3.32)$$

Therefore, for a fixed load angle δ and fixed voltage V, Eq. (3.32) gives the variation of the stator current in magnitude with frequency or rotor speed. The starting current I_s, i.e., the current at zero speed, is the limit of Eq. (3.32) as λ tends to zero. Hence,

$$I_s = \lim_{\lambda \to 0} I = \frac{V}{X_{do}\beta_o} = \frac{V}{R} \quad (3.35)$$

and at starting, as with a d.c. motor, the voltage applied is equal to the voltage drop in winding resistance. As speed increases, back e.m.f

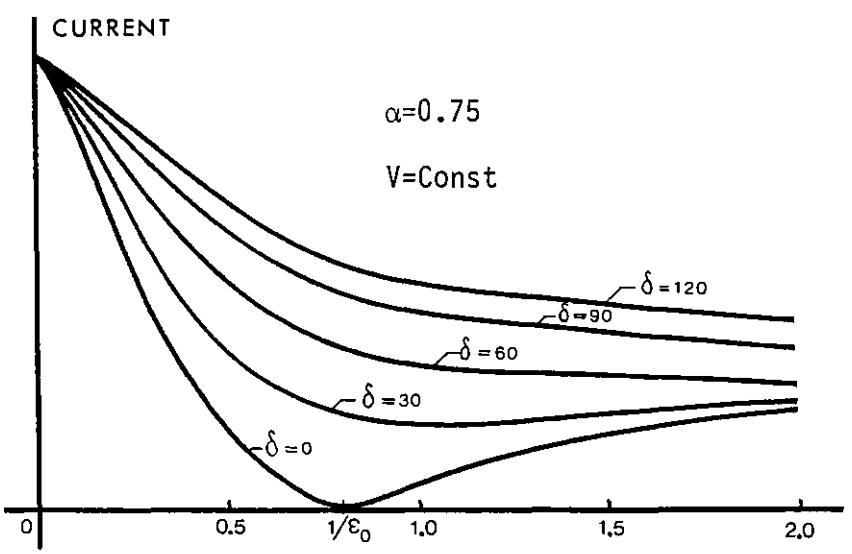

Fig. 3.21 - Stator current versus normalised speed for several load angles and fixed supply voltage

increases and stator current becomes less than starting current. Fig. 3.21 shows typical stator current/speed characteristics for several load angles

and fixed supply voltage. For $\delta = 0°$ the motor draws the minimum current and it will be zero when $V = E$ which corresponds to a normalised frequency $\lambda = 1/\varepsilon_o$.

b) - Motor torque

When the n_p pole machine is rotating with an angular speed ω_r, the electromagnetic torque developed is given by

$$T = \frac{P}{\omega_r} = \frac{n_p}{2} \frac{P}{\omega} \tag{3.34}$$

where P is the electromagnetic power and ω is the supply frequency. The power developed in the stator comprises two terms, each formed by the product of a rotational voltage and the component of stator current in phase with that rotational voltage or e.m.f. [72], as shown in fig. 3.22. Thus,

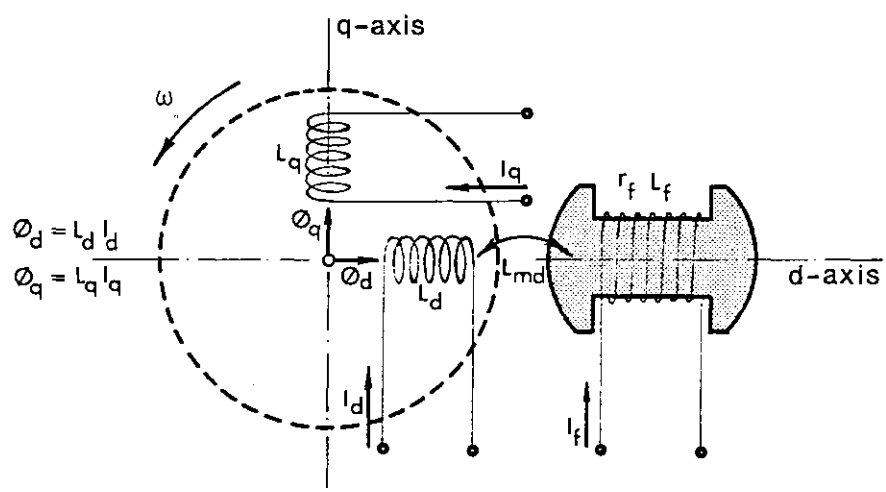

Fig. 3.22 - Basic synchronous machine

on the quadrature-axis

$$P_q = (L_d I_d \omega) I_q + E I_q$$

and on the direct-axis

$$P_d = -(L_q I_q \omega) I_d$$

where P_q and P_d are in units of power per phase. Hence, for a m-phase machine, total electromagnetic power developed becomes:

$$P = m(P_d + P_q) = m\left[I_d I_q(\omega L_d - \omega L_q) + E I_q\right] \tag{3.35}$$

Substitution of Eq. (3.35) into Eq. (3.34) gives the electromagnetic torque developed for a m-phase n_p-pole machine as:

$$T = \frac{m n_p}{2\omega}\left[I_d I_q (X_d - X_q) + E I_q \right] \tag{3.36}$$

Neglecting iron losses and windage, substitution of Eq. (3.29) and Eq. (3.30) into Eq. (3.36) gives the general expression for output torque as:

$$T = \frac{m n_p V^2}{4\pi f_o \lambda^2 (\alpha + \frac{\beta_o^2}{\lambda^2}) X_{do}} \left[-\varepsilon_o^2 \beta_o \lambda (\alpha^2 + \frac{\beta_o^2}{\lambda^2}) - \frac{\beta_o}{2\lambda}(1-\alpha)^2 + \right.$$

$$+ \varepsilon_o \lambda (\alpha(\alpha - \frac{\beta_o^2}{\lambda^2}) + \frac{2\beta_o^2}{\lambda^2}) \sin\delta +$$

$$+ \frac{1}{2}(1-\alpha)(\alpha - \frac{\beta_o^2}{\lambda^2}) \sin 2\delta + \varepsilon_o \beta_o (\alpha(2\alpha - 1) + \frac{\beta_o^2}{\lambda^2}) \cos\delta +$$

$$\left. + \frac{\beta_o}{2\lambda}(1-\alpha^2) \cos 2\delta \right] \tag{3.37}$$

Motor torque is then proportional to voltage squared, number of phases and number of poles, and varies with speed.

In particular, putting $\varepsilon_o = 0$ in Eq. (3.32) and Eq. (3.37) gives the variable current and torque/speed characteristics of a reluctance motor, while setting $\alpha = 1$ gives the characteristics of a cylindrical rotor machine.

From Eq. (3.37) the starting torque is given by:

$$T_s = \lim_{\lambda \to 0} T = \frac{m n_p \varepsilon_o V^2}{4\pi f_o X_{do} \beta_o} \cos\delta - \frac{m n_p V^2 (1-\alpha)}{8\pi f_o X_{do} \beta_o^2} \sin 2\delta \tag{3.38}$$

Starting torque can also be exprssed in terms of stator current and field excitation current I_f. The nominal back e.m.f. E_o is given by

$$E_o = X_{mdo} I_f' \tag{3.39}$$

where $I_f' = K I_f$ is the rotor excitation current referred to the m-phase stator and

$$X_{mdo} = X_{do} - X_{\ell o} \tag{3.40}$$

is the direct magnetising reactance and $X_{\ell o}$ the stator leakage reactance per phase at nominal frequency f_o. Substitution of Eq. (3.33) and Eq. (3.39) into Eq. (3.38) gives:

$$T_s = \frac{mn_p}{2} I'_f I_s L_{md} \cos\delta - \frac{mn_p}{4} I_s^2 (L_d - L_q) \sin 2\delta \qquad (3.41)$$

where

$$L_{md} = \frac{X_{mdo}}{2\pi f_o} \quad ; \quad L_d = \frac{X_{do}}{2\pi f_o} \quad ; \quad L_q = \frac{X_{qo}}{2\pi f_o}$$

Eq. (3.41) shows that no starting torque exists when $\delta = 90°E$.

As can be seen from Eq. (3.37) and Eq. (3.41) a sin 2δ term is introduced in the torque expression when saliency is present, except when the position sensor is set at $\delta = 0°$. Eq. (3.41) shows that for a given load angle $0 < \delta < 90°E$ the starting torque becomes less than the excitation starting torque for saliency $\alpha < 1$. Then, for the same conditions, when permanent magnet field excitation is used (see fig. 1.36) the starting torque is improved.

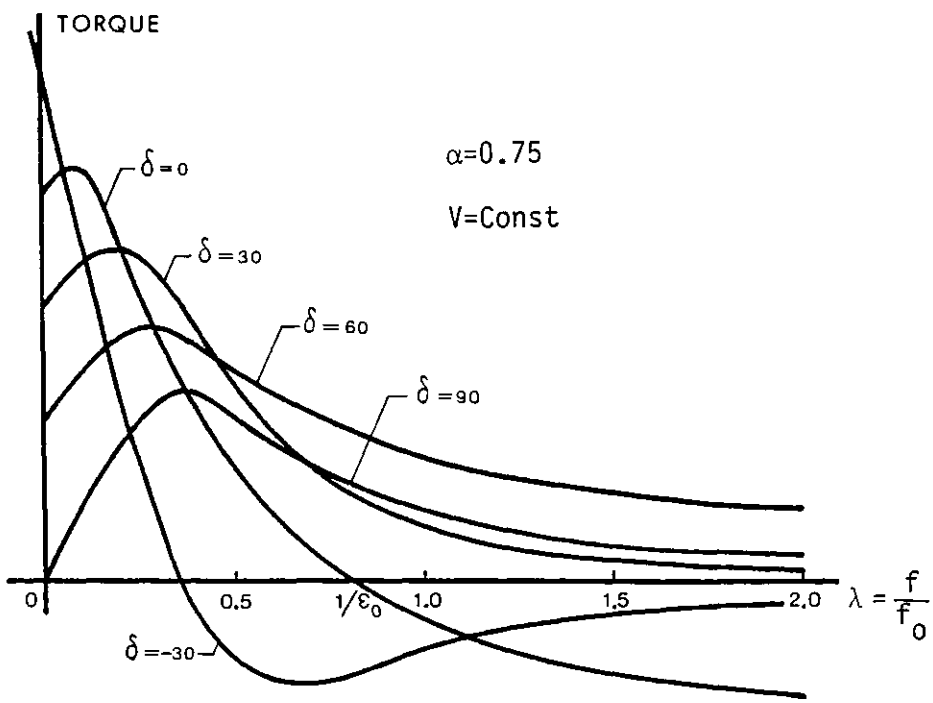

Fig. 3.23 - Output torque versus normalised speed for several load angles and fixed supply voltage

Fig. 3.23 shows the typical torque/speed characteristics with a saliency factor $\alpha = 0.75$ for several load angles and fixed voltage. It should be

pointed out that these characteristics are quite similar to the torque/speed characteristics of a conventional d.c. motor. In fact, when the operating speed is sufficiently low for the reactive volt drops to be swamped by resistive volt drops ($X \ll R$ or $\beta \to \infty$), Eq. (3.37) reduces to the form

$$T = \frac{mn_p}{2\omega R} (V \cos \delta - E) \tag{3.42}$$

With a fixed excitation $E = K_B\omega$ and setting the position sensor to operate at $\delta = 0°$, Eq. (3.42) gives

$$T = \frac{mn_p}{2\omega_o R\lambda} (V - \lambda K_B \omega_o) \tag{3.43}$$

which is characteristic of a d.c. SHUNT MOTOR. As speed is increased, winding inductance has porportionally more influence on the motor operation ($X \gg R$ or $\beta \to 0$) and resistance may be neglected, so that Eq. (3.37) may then be expressed as:

$$T = \frac{m n_p VE}{2\omega^2 L_d} \sin \delta + \frac{1}{2} \frac{m n_p V^2}{2\omega^2 L_d} \left(\frac{1}{L_q} - \frac{1}{L_d} \right) \sin 2\delta \tag{3.44}$$

Under this condition, setting the position sensor at $\delta = 90°E$, Eq. (3.44) becomes:

$$T = \frac{m n_p K_B}{2X_{do}} \frac{V}{\lambda} \tag{3.45}$$

Torque is proportional to supply voltage and inversely proportional to speed, which is the type characteristic of a d.c. SERIES MOTOR.

Fig. 3.24 shows the torque/speed characteristics of a synchronous motor obtained from the general equation (3.37) with the position sensor set at $\delta = 0°$ and $\delta = 90°E$ as well as the ideal characteristics of a d.c. shunt and series motor obtained from Eq. (3.43) and Eq. (3.45) respectively, which quite agree in a wide range of speed. By setting the position sensor in an intermediate position, the characteristics of a COMPOUND MOTOR may be obtained. Due to this extraordinary similarity with the torque/speed

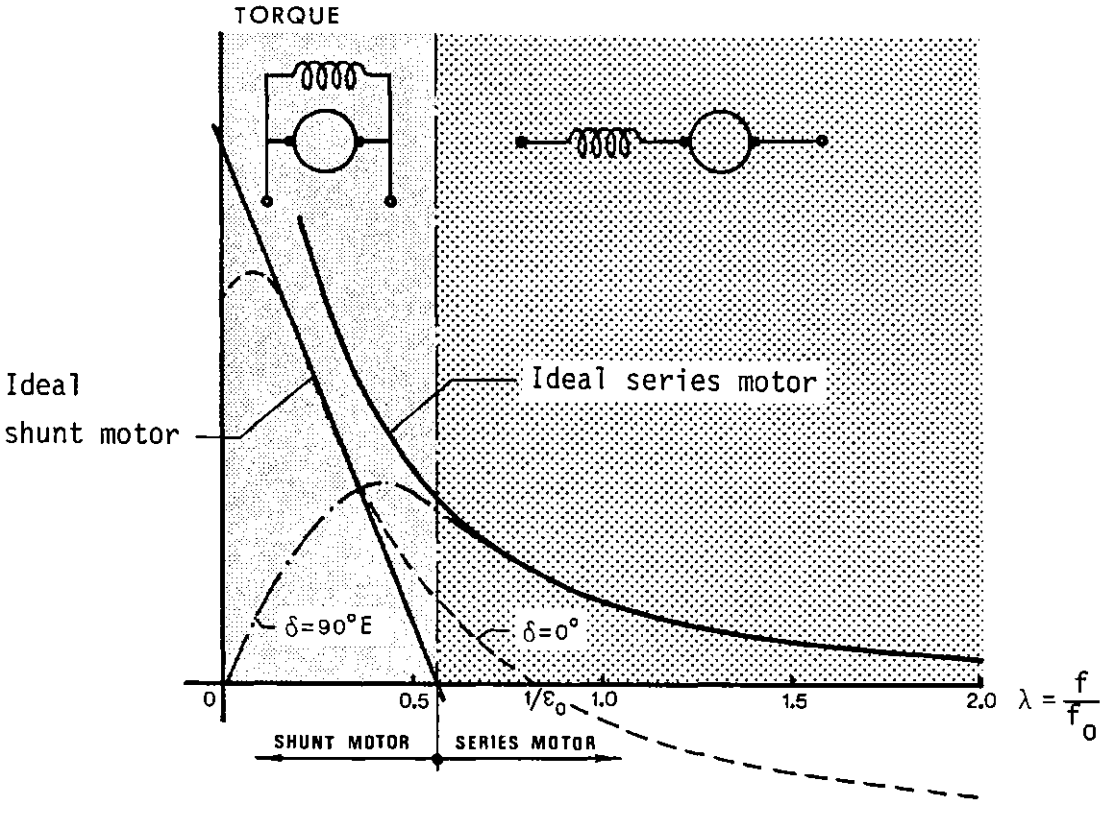

Fig. 3.24 - Comparison of a shunt and series d.c. motor with auto-piloted synchronous motor characteristics

characteristics of d.c. machines, the auto-piloted synchronous motor with this simple control scheme would fulfil some of the requirements for a traction drive.

c) - The required load angle variation with speed to maintain peak torque operation

As can be seen from the torque/speed characteristics shown in fig. 3.23, the maximum torque for a given load angle is only attainable for a certain rotor speed. Hence, if peak torque is to be maintained with rotor speed, the position sensor must be varied accordingly. For the particular case of a cylindrical rotor machine ($\alpha = 1$), Eq. (3.37) simplifies and the condition for maximum torque ($\frac{dT}{d\delta} = 0$) gives

$$\delta_{\hat{T}} = \text{atan} \left(\frac{\lambda}{\beta_0} \right) \qquad (3.46)$$

and the peak starting torque is achieved for $\delta = 0°$.

For the general case of saliency, the condition for maximum starting torque applied to Eq. (3.41) gives

$$\delta_{\hat{T}_s} = \text{asin}\left[\frac{\sigma}{4(1-\alpha)}\cdot\frac{I_f'}{I_s} \pm \sqrt{\left(\frac{\sigma}{4(1-\alpha)}\cdot\frac{I_f'}{I_s}\right)^2 + \frac{1}{2}}\right] \qquad (3.47)$$

where $\sigma = 1 - L_\ell/L_d$ is the machine leakage coefficient and the (+) sign is taken for $\alpha > 1$ and the (-) sign for $\alpha < 1$. Eq. (3.47) shows that the maximum starting torque is achieved for a load angle which depends on the ratio of current excitation to starting current. In particular, for a reluctance motor ($I_f' = 0$), $\delta_{\hat{T}_s} = -45°E$.

The condition for peak torque at any speed applied to Eq. (3.37) gives a transcendental equation, which can be solved by Newton-Raphson method for each speed. The result is plotted for $\alpha = 0.5$ and $\alpha = 1.5$ and fixed $\sigma\frac{I_f'}{I_s} = 0.2$ in fig. 3.25, together with Eq. (3.46).

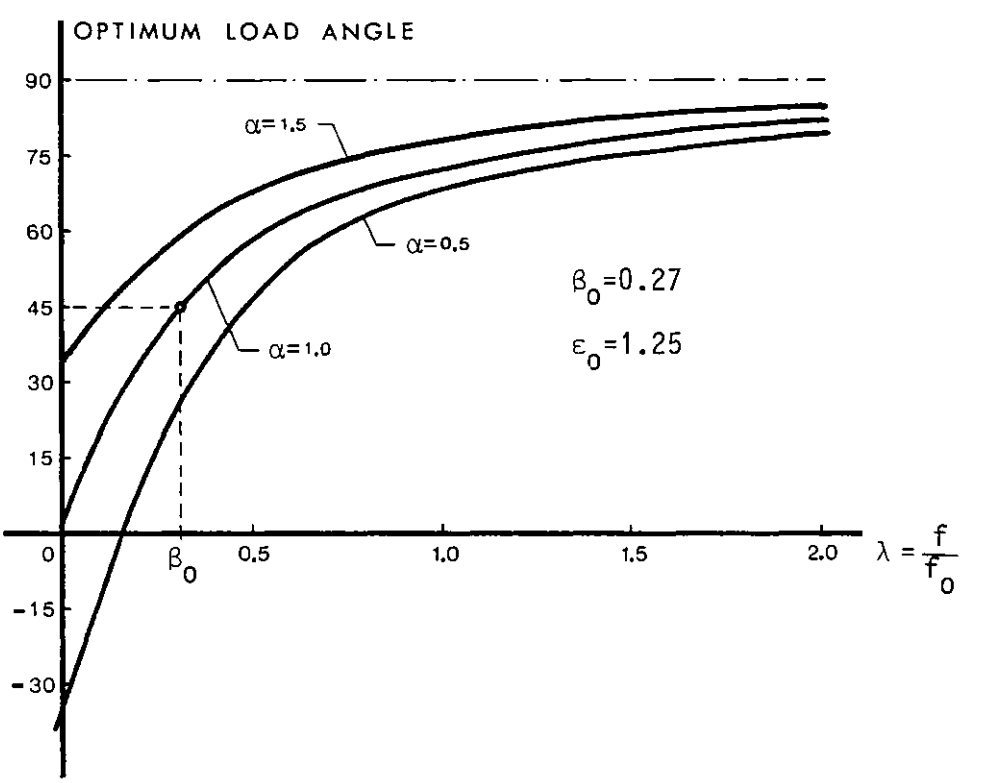

Fig. 3.25 - Load angle variation to achieve peak torque

These results illustrate how the load angle should be varied in order to achieve peak torque operation over a wide range of rotor speeds. At low speeds the load angle should be increased reasonably quickly as the

speed increases in order to maintain maximum torque. At high speeds, however, the required load angle hardly changes as the speed changes. As the speed tends to infinity the load angle settles at a maximum value of $\delta = 90°E$ for any level of rotor saliency.

d) - Torque angle variation with speed for a fixed load angle

Since the current $\bar{I}$ varies in magnitude (as already seen in fig. 3.21) and phase with speed, the torque angle θ and the phase angle ϕ also vary for a fixed load angle. In fact, from the phasor diagram, the torque angle is given by:

$$\theta = \text{atan}\left(\frac{I_q}{I_d}\right) \tag{3.48}$$

Hence, substitution of Eq. (3.29) and Eq. (3.30) into Eq. (3.48) and simplification gives:

$$\theta = \text{atan}\,\frac{\lambda \sin\delta + \beta_o \cos\delta - \lambda\beta_o\varepsilon_o}{\lambda\alpha\cos\delta - \beta_o \sin\delta - \lambda^2\alpha\varepsilon_o} \tag{3.49}$$

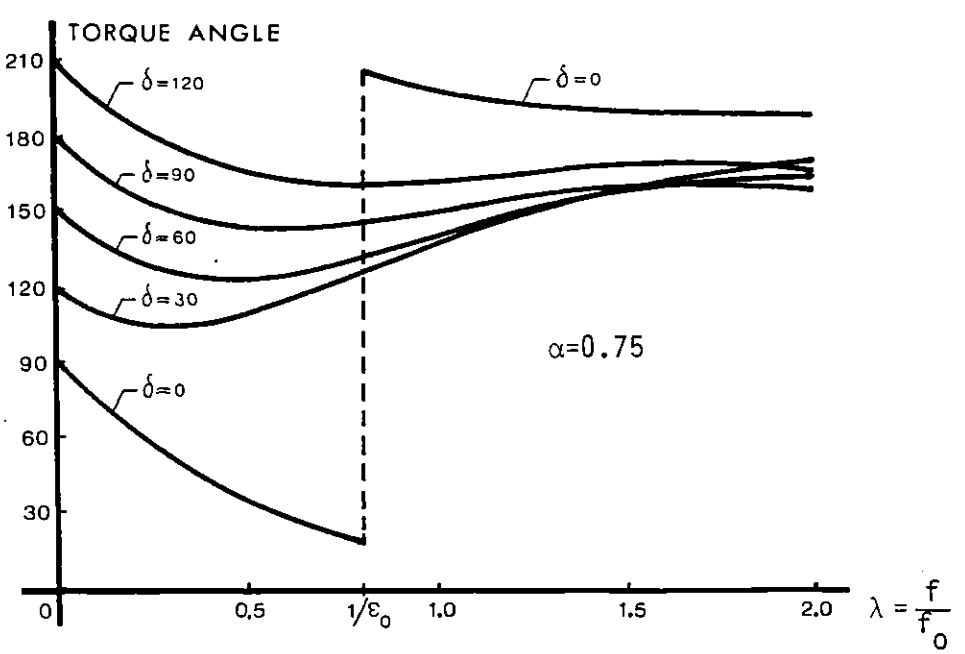

Fig. 3.26 - Torque angle versus speed for several fixed load angles

For a fixed load angle, the torque angle thus depends on voltage supply, rotor excitation and saliency, varying with speed. Fig. 3.26 shows typical curves of torque angle variation versus speed for several fixed load angles.

Since the phase angle $\phi = 90 + \delta - \theta$, the results show that the starting current has always zero phase angle, hence unity power factor, and is therefore in phase with applied voltage. This should be expected, since at starting, no back e.m.f. and no reactances are present and the voltage drop is purely resistive. For $\delta = 0°$, as speed increases, the torque angle decreases to a speed which makes the back e.m.f. equal to supply voltage for a speed ratio $\lambda = 1/\varepsilon_0$. Above this speed the machine operates as a generator.

e) - Unity power factor operation

From the phasor diagram the following relationship may be written:

$$\cos \phi = \frac{1}{I} (I_q \cos \delta - I_d \sin \delta) \qquad (3.50)$$

Substitution of Eq. (3.31), Eq. (3.29) and Eq. (3.30) into Eq. (3.50) enables computation of machine power factor at any speed. In fig. 3.27 is represented the power factor variation with speed for several load angles.

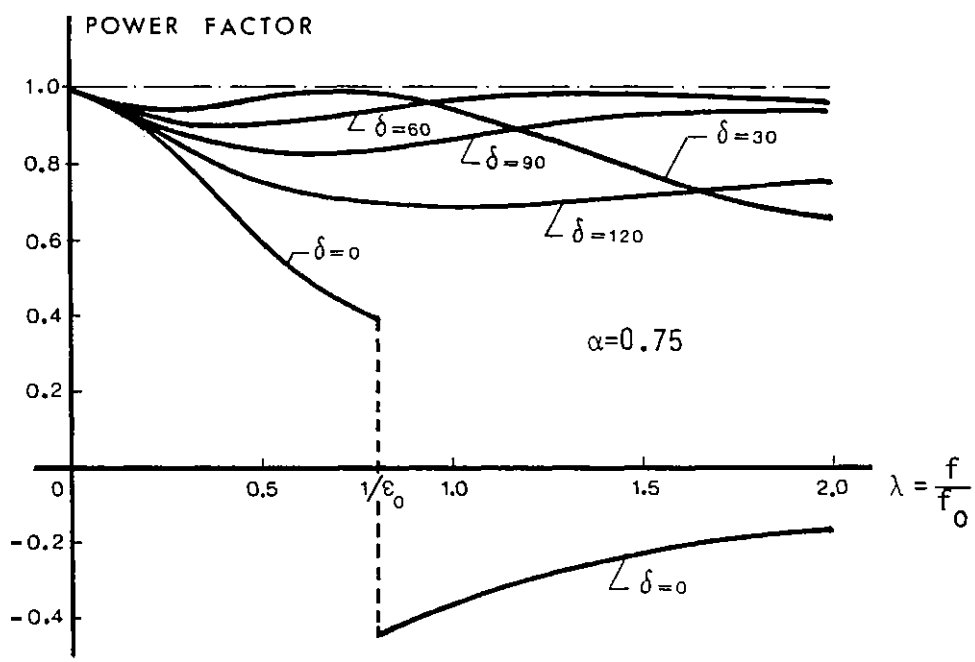

Fig. 3.27 - Power factor versus speed for several fixed load angles

Again, for $\delta = 0°$ the power factor at $\lambda = 1/\varepsilon_0$ reverses sign showing that the input power $P_e = mVI\cos\phi$ flowing into the machine is reversed, the machine becoming a generator. At low speeds, where the load presented

to the supply is predominantly resistive, the power factor is close to unity for any load angle. However, as speed increases power factor variation occurs depending on the load angle used.

For unity power factor operation, substitution of cos ϕ = 1 and Eq. (3.31) into Eq. (3.50) gives the relationship

$$I_q \sin\delta + I_d \cos\delta = 0 \tag{3.51}$$

Elimination of I_q and I_d using Eq. (3.29) and Eq. (3.30) gives:

$$\varepsilon_o = \frac{\alpha + (1-\alpha)\sin^2\delta}{\beta_o \sin\delta + \lambda\alpha\cos\delta} \tag{3.52}$$

But

$$\varepsilon_o = \frac{E_o}{V} = \frac{X_{mdo}}{V} \; I_f'$$

and so Eq. (3.52) can be written in the form

$$I_f' = \frac{V}{X_{mdo}} \left[\frac{\alpha + (1-\alpha)\sin^2\delta}{\beta_o \sin\delta + \lambda\alpha\cos\delta} \right] \tag{3.53}$$

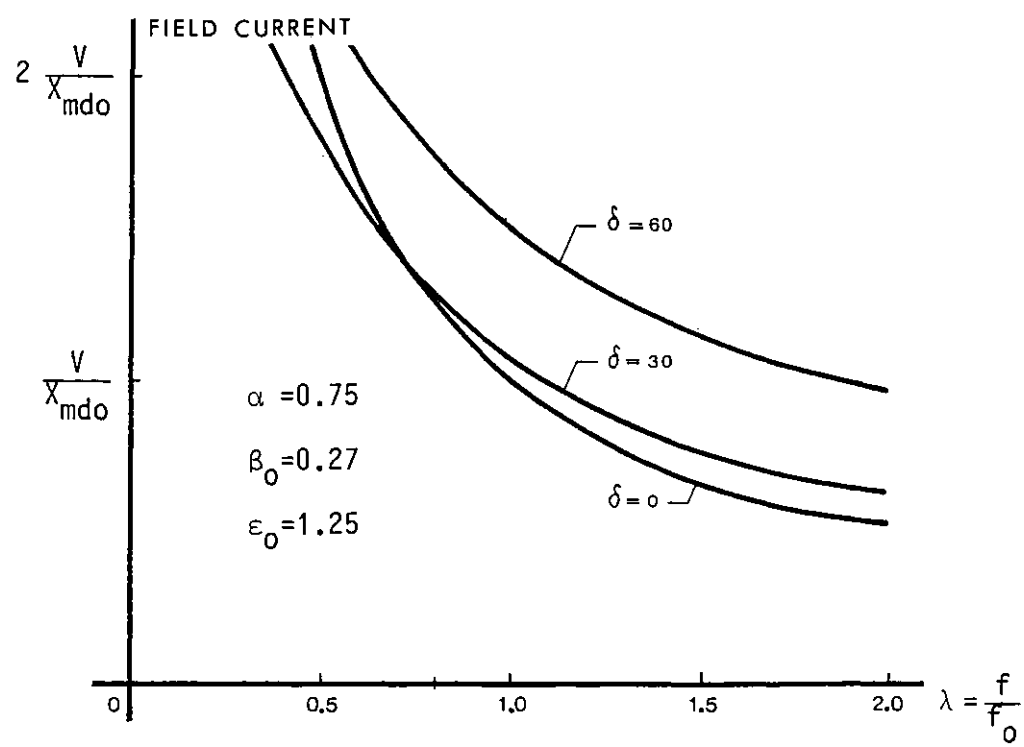

Fig. 3.28 - Field current variation to achieve unity power factor

This result shows that a unity power factor operation may be achieved at any given speed by adjusting the load angle or rotor field excitation.

In fact, a well known property of the synchronous motor is its ability to present a unit power factor to its supply if the current excitation is correctly controlled. With a permanent magnet excitation this, of course, is not possible and with fixed supply voltage, adjustment in load angle is required. With controlled excitation, at any speed, Eq. (3.53) sets the range of load angles at which unity power factor is possible. Fig. 3.28 shows typical plots of I_f' versus normalised speed for several values of fixed load angles to achieve unity power factor operation.

f) - Motor efficiency

The ratio output mechanical power to input electric power, may be written in the form

$$\frac{T\omega_r}{m\,VI\cos\phi} = \frac{2T\omega}{m\,n_p\,VI\cos\phi} \tag{3.54}$$

Neglecting iron losses and windage, substitution of Eq. (3.36) and Eq. (3.50) into Eq. (3.54) gives the motor efficiency as

$$\eta = \lambda\,\frac{\frac{X_{do}}{V}\,I_d I_q(1-\alpha) + \varepsilon_o I_q}{I_q\cos\delta - I_d\sin\delta} \tag{3.55}$$

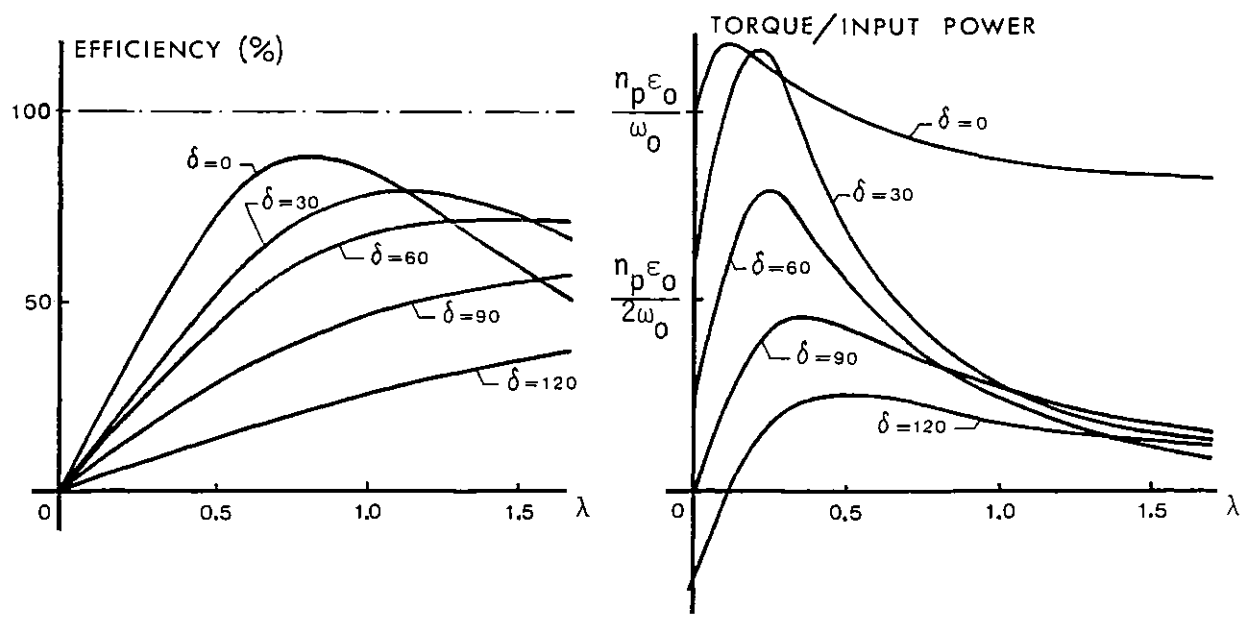

Fig. 3.29 - Efficiency and torque/input power versus normalised speed for several fixed load angles

Taking into account Eq. (3.29) and Eq. (3.30), Eq. (3.55) allows computation of efficiency characteristics, as shown in fig. 3.29. For $\delta = 0°$, peak efficiency and torque per input power is achieved.

3.7.2 - Steady-state theory of a synchronous motor operating at variable-frequency and fixed torque angle

In this case the torque angle θ is fixed by the position sensor and the current $\bar{I}$ is controlled only in magnitude by the torque demand signal applied to the sensor. In the steady-state the motor is then operating from a constant current source and variable frequency.

a) - Stator supply voltage

With a fixed current and variable frequency, the voltage $\bar{V}$ varies in magnitude and phase, since the back e.m.f. and the machine impedance also vary. From the phasor diagram, the voltage magnitude becomes

$$V = \left[(E + R\,I_q + \omega L_d I_d)^2 + (\omega L_q I_q - R\,I_d)^2 \right]^{\frac{1}{2}} \tag{3.56}$$

where the current components in terms of torque angle are:

$$I_d = I \cos\theta \tag{3.57}$$

$$I_q = I \sin\theta \tag{3.58}$$

Substitution of Eq. (3.57) and Eq. (3.58) into Eq. (3.56) and taking Eqs. (3.25), Eqs. (3.28) and Eq. (3.39) into account, yields:

$$V = \left[\lambda^2 X_{mdo}^2 I_f'^2 + R^2 I^2 + 2\lambda X_{mdo} X_{do} I_f' I(\beta_o \sin\theta + \lambda \cos\theta) + \right.$$

$$\left. + \lambda^2 X_{do}^2 I^2 (\alpha + (1-\alpha^2)\cos^2\theta) + \lambda X_{do} R\, I^2 (1-\alpha) \sin 2\theta \right]^{\frac{1}{2}} \tag{3.59}$$

For a fixed torque angle θ and fixed current $\bar{I}$, the supply voltage increases in magnitude with motor speed. The starting voltage ($\lambda = 0$) is

the minimum value attainable, which is from Eq. (3.59) $V_s = RI$ equal to the voltage drop in the winding resistance.

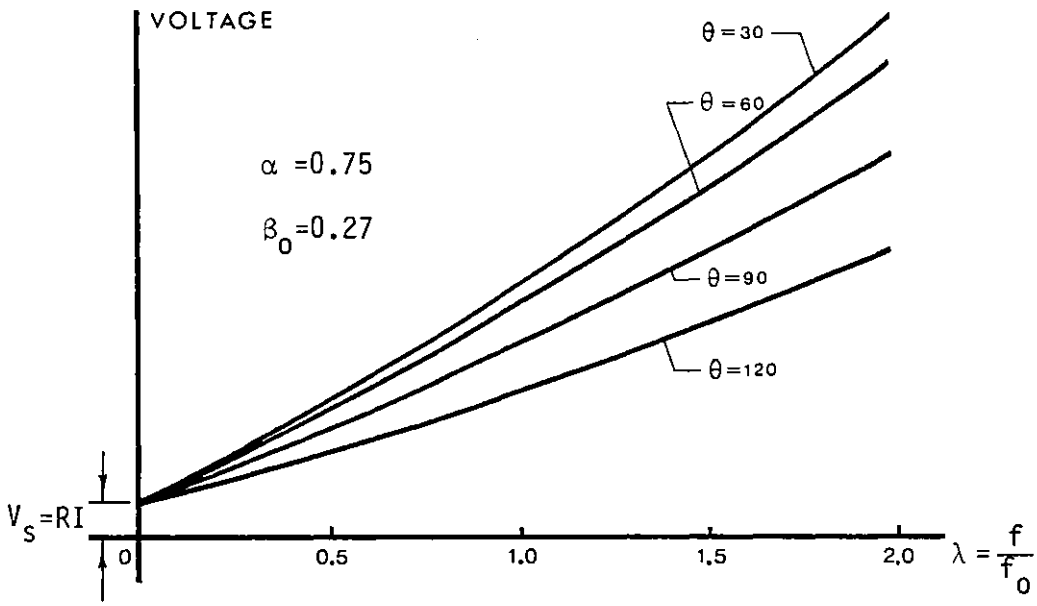

Fig. 3.30 - Supply voltage versus normalised speed for several torque angles and fixed current

For a fixed rotor excitation and several fixed torque angles, fig. 3.30 shows the variation of supply voltage in magnitude versus speed, for a saliency factor $\alpha = 0.75$. The voltage increases always with speed and its magnitude becomes lower as torque angle approaches to 90°E for a given speed.

b) - Motor torque

Substitution of Eq. (3.57) and Eq. (3.58) into Eq. (3.36) gives the electromagnetic torque as a function of the supply current and torque angle as:

$$T = \frac{m\,n_p}{2\omega} E\,I \sin\theta + \frac{1}{2}\frac{m\,n_p}{2\omega} I^2 (X_d - X_q)\sin 2\theta \qquad (3.60)$$

Since $E = \omega L_{md} I_f'$, Eq. (3.60) then gives

$$T = \frac{m\,n_p}{2} L_{md} I_f' I \sin\theta + \frac{1}{2}\frac{m\,n_p}{2} I^2 L_d (1-\alpha)\sin 2\theta \qquad (3.61)$$

The first term represents the excitation torque and is proportional to the quadrature-axis current component. The second term is the reluct-

ance torque, which reduces to zero for a cylindrical rotor machine ($\alpha = 1$). Eq. (3.61) is independent of winding resistance and rotor speed. With a fixed rotor excitation, torque is constant over all range of speeds giving constant ohmic losses. Fig. 3.31 shows the torque/speed characteristics for several fixed torque angles and fixed excitation.

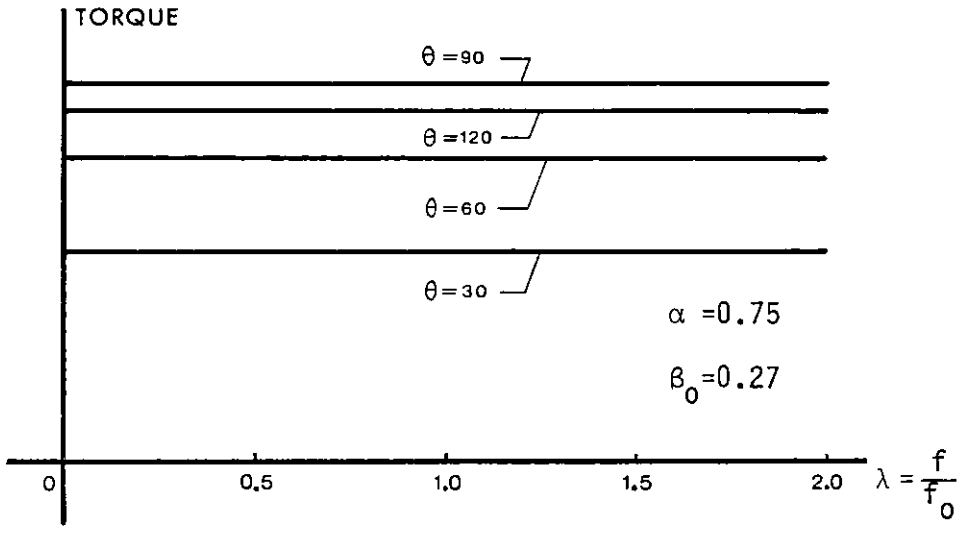

Fig. 3.31 - Torque/speed characteristics for several fixed torque angles

In particular, setting the position sensor at $\theta = 90°E$, Eq. (3.61) reduces to

$$T = \frac{m\, n_p}{2} L_{md}\, I_f' I \tag{3.62}$$

Torque is then directly proportional to supply current, which is ideal for low speed control applications. For a two-phase motor ($m = 2$) with fixed excitation ($E = K_B\omega$), Eq. (3.62) may be written in the form

$$T = n_p \frac{E}{\omega} I = n_p K_B I = K_T I \tag{3.63}$$

where $K_B = L_{md} I_f'$ is the back e.m.f. constant and $K_T = n_p K_B$ is called "motor torque constant".

c) - Optimum Torque angle for peak torque operation

Obviously, for a cylindrical rotor machine, the maximum torque attainable is when $\theta = 90°E$ and its value is given by Eq. (3.62). However, when saliency is presented the optimum torque angle for peak torque is no longer

constant with supply current, depending on the type of saliency (permanent magnet or coil-excitation) and current excitation.

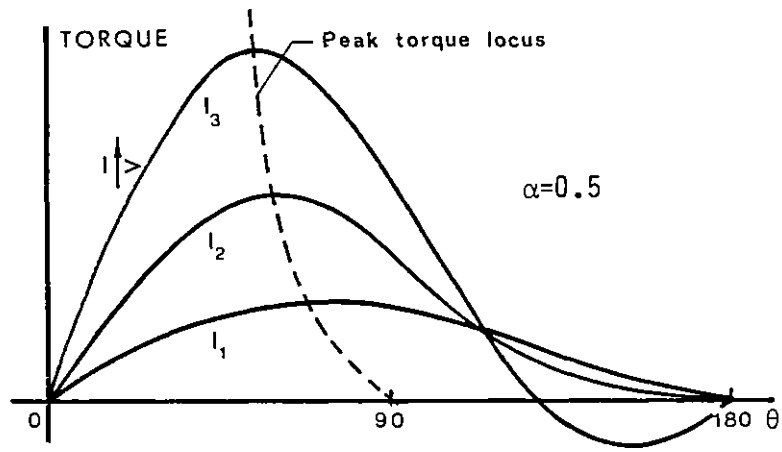

(a) - Rotor coil excitation

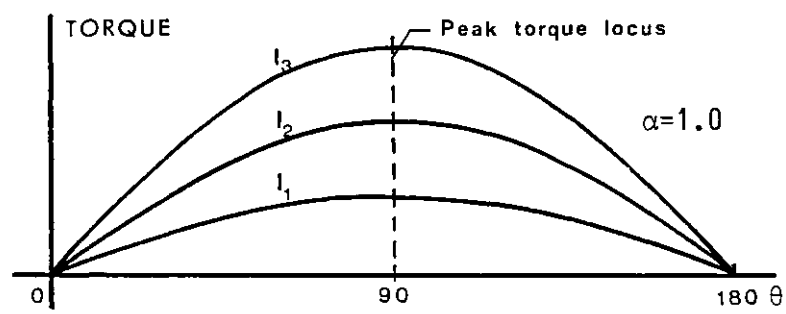

(b) - Cylindrical machine

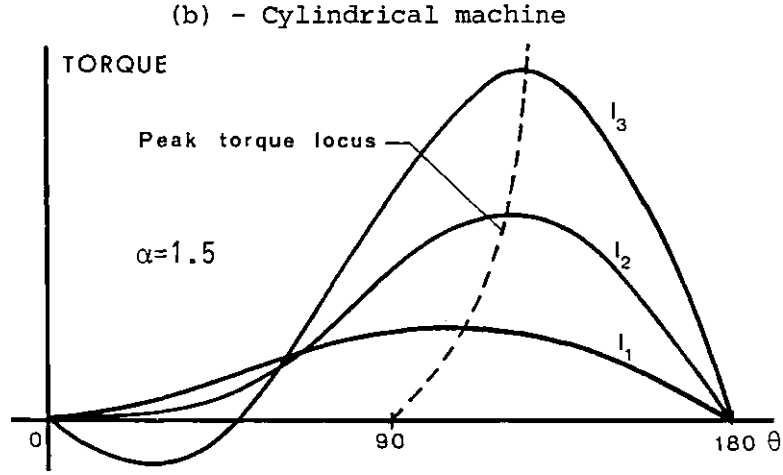

(c) - Permanent magnet excitation

Fig. 3.32 - Torque/torque angle characteristics for three different types of saliency

Fig. 3.32 shows torque/torque angle characteristics for the saliency factors $\alpha = 0.5$, $\alpha = 1.0$ and $\alpha = 1.5$ and several levels of supply current for a fixed rotor excitation. Due to the sin 2θ term introduced by the

saliency, the optimum torque angle is shifted from 90°E position as can be seen from the diagram.

The condition for maximum torque ($\frac{dT}{d\theta} = 0$) applied to Eq. (3.61) gives the optimum torque angle as:

$$\theta_{\hat{T}} = \text{acos}\left[-\frac{\sigma}{4(1-\alpha)} \cdot \frac{I_f'}{I} \pm \sqrt{\left(\frac{\sigma}{4(1-\alpha)} \cdot \frac{I_f'}{I}\right)^2 + \frac{1}{2}} \right] \qquad (3.64)$$

where the ± sign is taken for $\alpha < 1$ and $\alpha > 1$ respectively. Eq. (3.64) shows that the optimum torque angle to achieve peak torque operation depends on the ratio of current excitation to current supply (or m.m.f. ratio) and saliency, being independent of motor speed. This result is similar to that obtained in Eq. (3.47) to determine the optimum starting load angle for voltage-forced operation. Again, for a reluctance motor, the optimum torque angle is $\theta_{\hat{T}} = 45°E$.

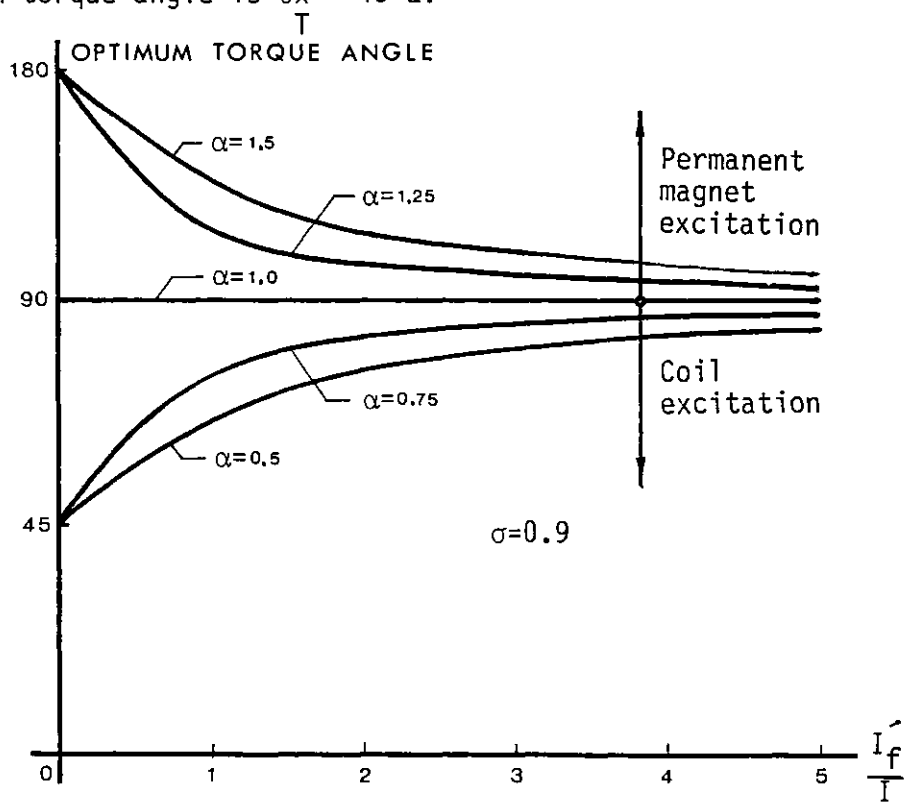

Fig. 3.33 - Optimum torque angle versus I_f'/I ratio to achieve peak torque operation

Fig. 3.33 shows plots of optimum torque angle variation versus m.m.f. ratio I_f'/I to achieve peak torque operation for several levels of saliency.

The diagram shows that for saliency $\alpha > 1$ (permanent magnet-excitation) peak torque is attainable at torque angles $\theta > 90°E$, while for $\alpha < 1$ (coil-excitation) is $\theta < 90°E$. For a cylindrical rotor machine, peak torque is achieved for $\theta = 90°E$ and it is independent of the m.m.f. ratio.

d) - Load angle variation for a fixed torque angle

Since the voltage $\bar{V}$ varies in magnitude (as already seen in fig. 3.30) and phase with speed, the load angle δ and the phase angle ϕ also varies for a fixed torque angle. From the phasor diagram, the load angle for a given speed may be obtained as:

$$\tan \delta = \frac{\omega L_q I_q - R I_d}{E + R I_q + \omega L_d I_d} \tag{3.65}$$

Hence, substitution of Eq. (3.57) and Eq. (3.58) into Eq. (3.65) and taking Eqs. (3.28) and Eq. (3.39) into account yields:

$$\delta = \text{atan} \frac{\lambda \alpha \sin \alpha - \beta_0 \cos \theta}{\lambda \sigma \frac{I_f'}{I} + \beta_0 \sin \theta + \lambda \cos \theta} \tag{3.66}$$

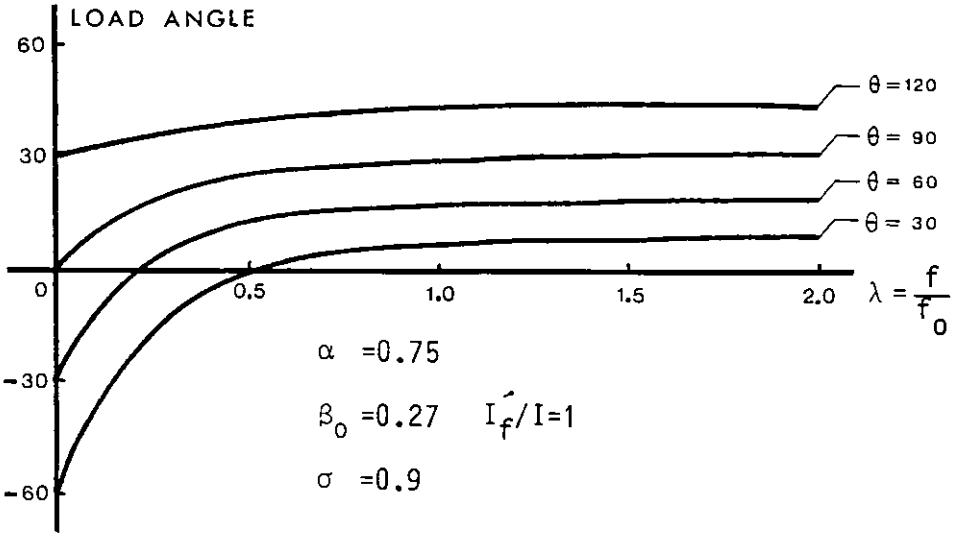

Fig. 3.34 - Load angle versus speed for several fixed torque angles

For a fixed torque angle, the load angle thus depends on the ratio I_f'/I and saliency, and varies with speed. Fig. 3.34 shows typical curves of the load angle variation versus speed for several fixed torque angles.

Again, the results show that the starting voltage is in phase with supply current, giving a unity power factor at starting.

e) - Unity power factor operation

From the phasor diagram

$$\cos \phi = \cos(90 + \delta - \theta) \tag{3.67}$$

and substitution of Eq. (3.66) into Eq. (3.67) enables computation of power factor at any rotor speed. Fig. 3.35 shows typical plots of power factor variation with speed and fixed ratio I_f'/I. At low speeds the power factor is close to unity, becoming worse as speed increases.

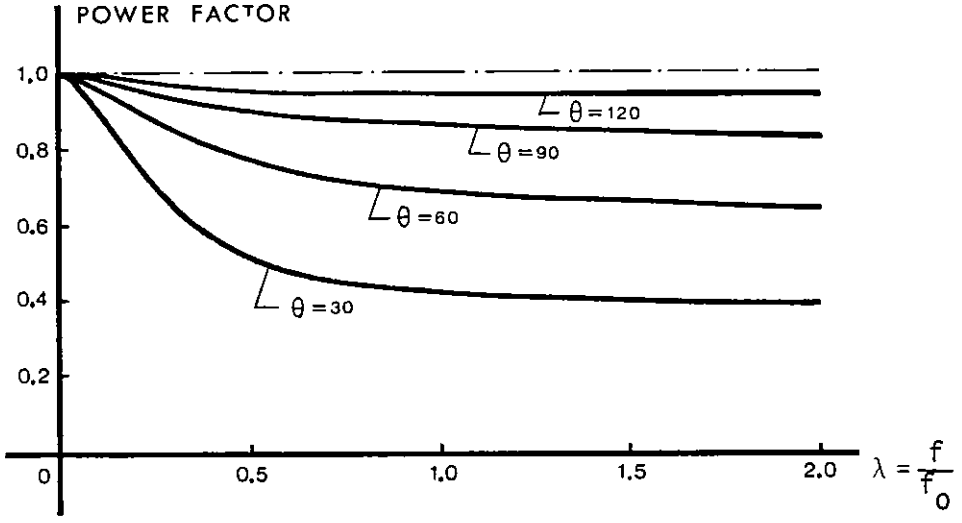

Fig. 3.35 - Power factor versus speed for several load angles and fixed I_f'/I ratio

For unity power factor operation ($\cos \phi = 1$), Eq. (3.67) gives $\theta = 90 + \delta$. Substituting $\tan \delta = \tan(\theta - 90) = -\text{cotan}\ \theta$ into Eq. (3.66) and simplifying gives the following expression:

$$\theta = \text{acos}\left[\frac{\sigma}{2(1-\alpha)}\ \frac{I_f'}{I} \pm \sqrt{\left(\frac{\sigma}{2(1-\alpha)}\ \frac{I_f'}{I}\right)^2 - \frac{\alpha}{1-\alpha}}\right] \tag{3.68}$$

where the $\pm$ sign corresponds to $\alpha < 1$ and $\alpha > 1$ respectively.

Eq. (3.68) sets the range of torque angles over which unity power factor operation is possible. The range of torque angle depends on the

ratio I_f'/I, saliency and machine leakage coefficient, and is independent of rotor speed.

Fig. 3.36 shows typical results for various types of saliency, where the torque angles to achieve unity power factor are always greater than 90°E. Comparison of fig. 3.33 and fig. 3.36 shows that peak torque and

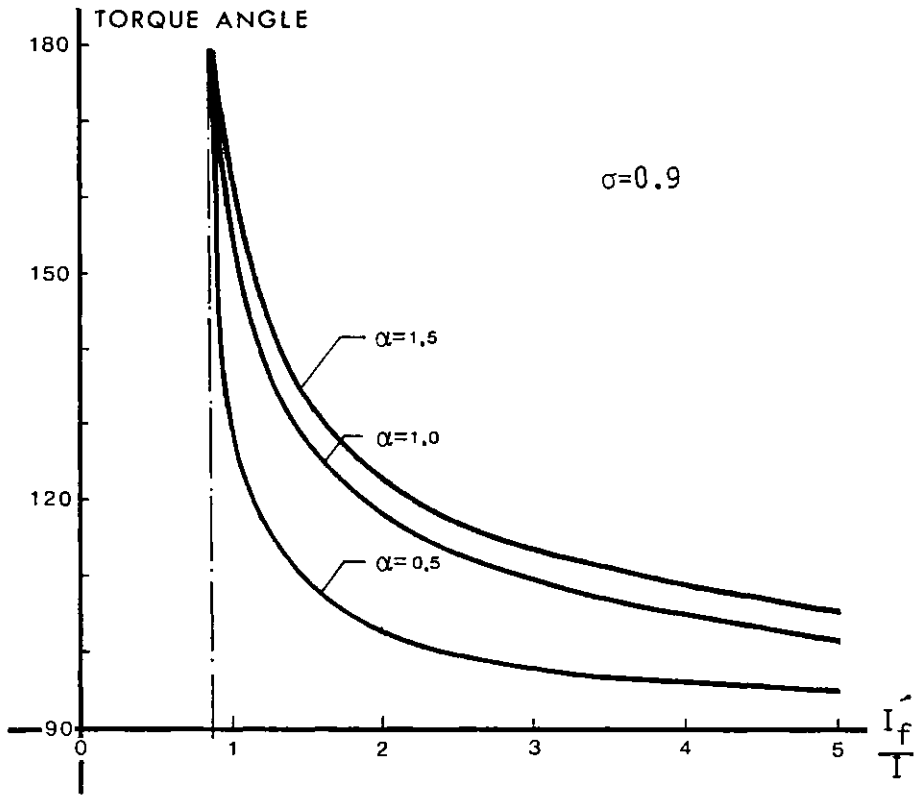

Fig. 3.36 - Torque angle versus I_f'/I ratio to achieve unity power factor

unity power factor is only possible simultaneously for permanent magnet excitation motors with saliency $\alpha > 1$. For round machines and coil-excited with saliency these two modes of operation simultaneously are then incompatible.

f) - Power factor control by stator reaction compensation

Variation of stator voltage and drop of motor power factor with speed as seen in fig. 3.30 and fig. 3.35 respectively, may be eliminated by stator reaction compensation [74, 78]. In fact, as in a conventional d.c. motor, armature or stator reaction may be cancelled by using a compensating winding in quadrature with field winding in order to produce a

voltage exactly equal and in anti-phase to the armature reaction voltage drop. Since in the synchronous motor the armature is stationary, this compensating winding must be placed on the rotor, as shown in fig. 3.37(a). Sliprings and their sliding brushes both for the exciting and compensating windings are necessary.

The shaft end of the motor is provided with a position sensor in the usual fashion and a tachogenerator. With the position sensor set at 90°E torque angle the main field flux ϕ_f is constantly in quadrature with stator m.m.f. F_a and the phasor diagram for this situation, neglecting resistance, is represented in fig. 3.37(b). By the action of F_a, armature reaction flux ϕ_a is produced and consequently a stator voltage drop

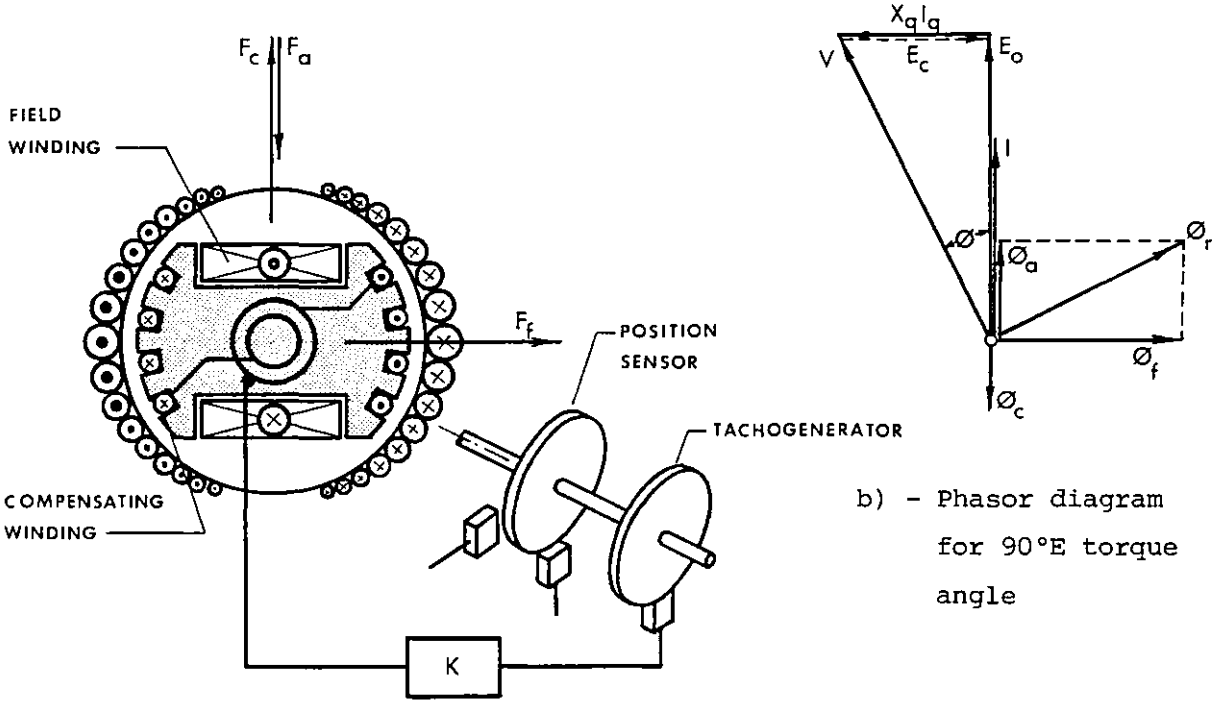

(a) - Auto-piloted motor with compensating winding

b) - Phasor diagram for 90°E torque angle

Fig. 3.37 - Stator reaction compensation with compensating winding

$X_q I$ occurs. The magnitude and direction of gap flux change from ϕ_f to ϕ_r and as a result, the stator voltage rises and a motor power factor drop takes place with operation under load.

This effect may be eliminated if the compensating winding is arranged

to produce a m.m.f. F_c with the same magnitude as F_a but in the opposite direction. The system is provided with a compensating current regulator, which receives the reference signal from the tachometer, and produces a d.c. current proportional to the armature current to be supplied to the compensating winding. Hence, an e.m.f. E_c equal to $X_q I$ is induced and terminal voltage V, irrespective of the magnitude of stator current, would constantly be equal to nominal e.m.f. E_o induced by the action of the field winding. At the same time, the power factor of the synchronous motor can be controlled near to unity.

g) - Motor efficiency

From Eq. (3.54) and neglecting iron losses and windage, the motor efficiency is given by:

$$\eta = \frac{I_d I_q (X_d - X_q) + E I_q}{VI \cos \phi} \tag{3.69}$$

Substitution of Eq. (3.57), Eq. (3.58) and Eq. (3.39) into Eq. (3.69) gives the following expression for motor efficiency as a function of torque angle as:

$$\eta = \lambda \frac{\sigma \frac{I'_f}{I} \sin \theta + \frac{1}{2}(1-\alpha) \sin 2\theta}{\frac{V}{X_{do} I} \cos \phi} \tag{3.70}$$

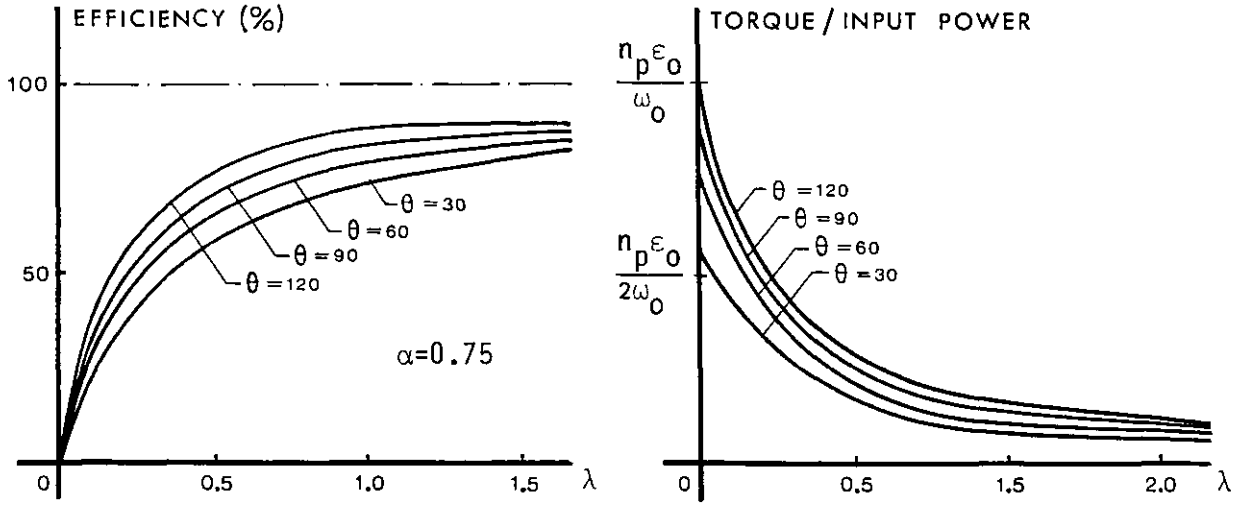

Fig. 3.38 - Efficiency and torque/input power versus normalised speed for several fixed torque angles

Since the voltage V given by Eq. (3.59) increases almost linearly with speed and cos ϕ given by Eq. (3.67) decreases with speed, Eq. (3.70) shows that motor efficiency always increases with motor speed with the current-fed mode. Fig. 3.38 shows typical efficiency and torque per input power versus normalised speed for several fixed torque angles.

3.7.3 - Operating chart for a synchronous motor at variable frequency

Under the voltage-fed or current-fed operation, the speed characteristics of an auto-piloted synchronous motor may be obtained using the previous equations developed for each case. A computer program, suitable for the calculation of all characteristics for both modes of operation under variable frequency conditions, is described in Appendix B.

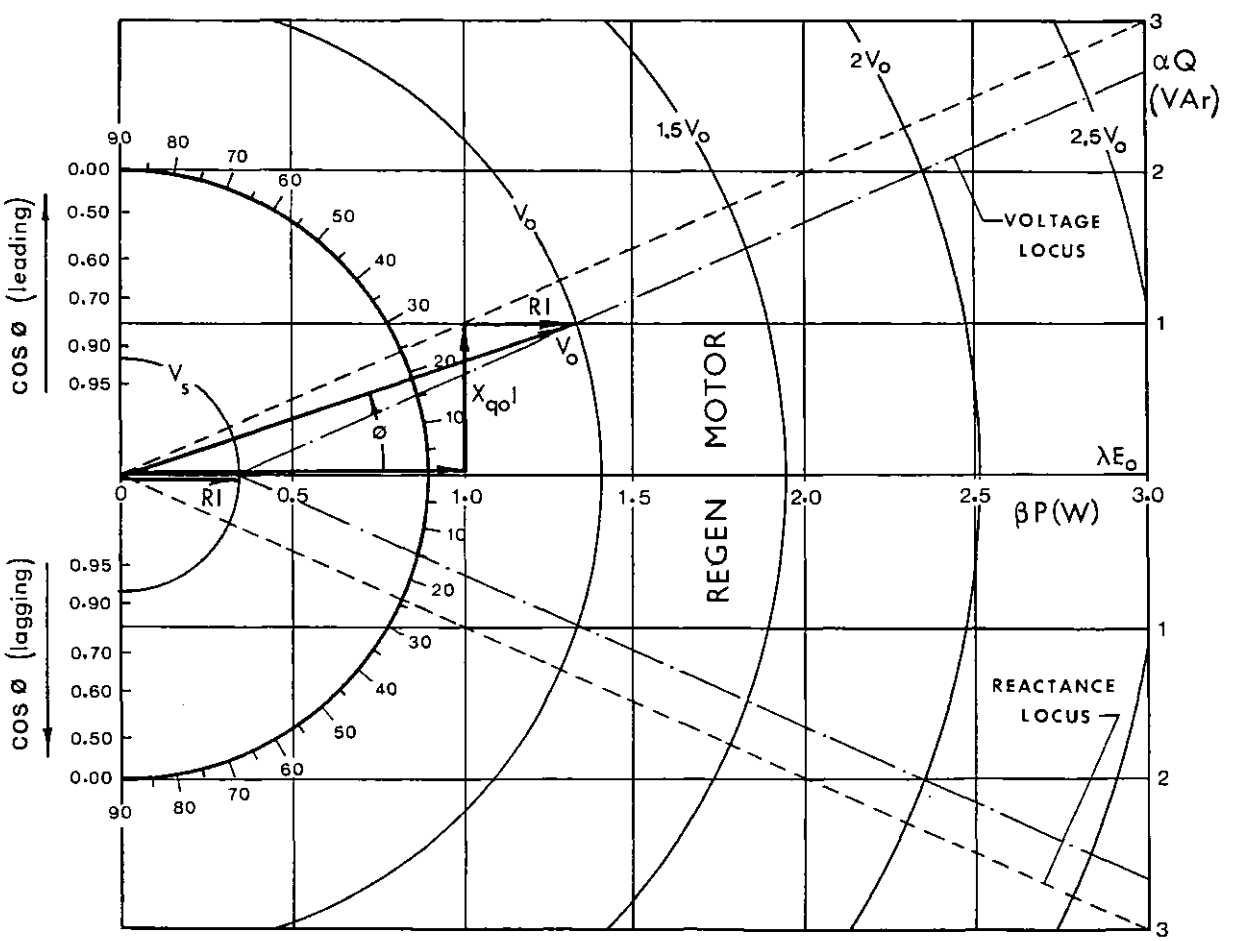

Fig. 3.39 - Operating chart for fixed excitation and $\theta = 90°E$ torque angle variable frequency synchronous machine

However, an operating chart may also be developed which enables direct readings of each particular desired characteristic. Fig. 3.39 shows a typical current-fed operating chart for 90°E torque angle and fixed rotor excitation.

3.8 - MOTOR RESPONSE TO A STEP INPUT SIGNAL

When a fixed r.m.s. input signal is suddenly applied to an auto-piloted synchronous motor, the rotor speed variation during the transient state depends on the type of the source used. The motor response is then analysed for both voltage-fed and current-fed operation.

a) - Voltage-fed response

With the position sensor set to give a load angle $\delta = 0°$, the r.m.s. two-axis supply voltage V and back e.m.f. E must be in phase. Then, for a motor with n_p-poles running with a shaft speed $\omega_r = \frac{2}{n_p}\omega$ the relevant two-axis equations for transient conditions and fixed excitation, are:

$$0 = L_q \omega i_q - \left(R i_d + L_d \frac{di_d}{dt}\right) \tag{3.71}$$

$$V = K_B \omega + R i_q + L_q \frac{di_q}{dt} + L_d \omega i_d \tag{3.72}$$

From Eq. (3.36) and Eq. (3.63) and neglecting coulomb friction, the torque equation is

$$K_T i_q + i_d i_q (L_d - L_q) = J_m \frac{d\omega_r}{dt} + D\omega_r \tag{3.73}$$

where J_m is the rotor inertia (or eventually it contains the effective load inertia) and D is the damping coefficient.

During the transient state both current components i_d and i_q vary. However the basic assumption may be made that for $\delta = 0°$ and at low speed i_d is negligible compared with i_q. Hence, when a constant r.m.s. voltage V is suddenly applied to the motor, Eq. (3.72) and Eq. (3.73) may be

written in Laplace notation as:

$$\frac{V}{s} = \frac{K_r}{2}\omega_r(s) + (R + L_q s)i_q(s) \tag{3.74}$$

$$K_T i_q(s) = (J_m s + D)\omega_r(s) \tag{3.75}$$

Eliminating $i_q(s)$ in Eq. (3.74) using Eq. (3.75) and putting $K_B' = \frac{K_r}{2}$ gives:

$$\frac{\omega_r(s)}{V} = \frac{K_r}{s[K_B' K_T + (R + L_q s)(J_m s + D)]}$$

$$= \frac{1}{sK_B'\left[1 + \frac{RD}{K_B' K_r} + s(L_q D + RJ_m)\frac{1}{K_B' K_r} + s^2 \frac{J_m L_q}{K_B' K_r}\right]} \tag{3.76}$$

If the following motor time constants are defined:

$$\tau_q = \frac{L_q}{R} \quad = \text{q-axis electrical time constant} \tag{3.77}$$

$$\tau_m = \frac{J_m}{D} \quad = \text{mechanical time constant} \tag{3.78}$$

$$\tau_{em} = \frac{RJ_m}{K_B' K_T} \quad = \text{electromechanical time constant} \tag{3.79}$$

then Eq. (3.76) may be rewritten in the form

$$\frac{\omega_r(s)}{V} = \frac{1}{sK_B'\left[1 + \frac{\tau_{em}}{\tau_m} + s(\tau_q + \tau_m)\frac{\tau_{em}}{\tau_m} + s^2 \tau_q \tau_m\right]} \tag{3.80}$$

In practice, since D is very small compared with J_m the mechanical time constant τ_m is very large compared with electromechanical and electric time constants and so Eq. (3.80) can be written approximately as

$$\frac{\omega_r(s)}{V} = \frac{1}{sK_B'[1 + \tau_{em} s + \tau_q \tau_m s^2]} \tag{3.81}$$

Additionally, in small machines $\tau_{em} \gg \tau_q$ and so $\tau_{em} \simeq \tau_{em} + \tau_q$.

Eq. (3.81) then gives:

$$\frac{\omega_r(s)}{V} = \frac{1}{sK_B'(1 + \tau_{em}s)(1 + \tau_q s)}$$

and the response in the time domain is

$$\omega_r(t) = \frac{V}{K_B'}\left[1 - \frac{\tau_{em}}{\tau_{em} - \tau_q}\left(e^{-\frac{t}{\tau_{em}}} - e^{-\frac{t}{\tau_q}}\right)\right]$$

or, neglecting τ_q compared with τ_m,

$$\omega_r(t) = \frac{2V}{K_T}\left(1 - e^{-\frac{t}{\tau_{em}}}\right) \qquad (3.82)$$

Hence, with voltage-fed conditions the response of the synchronous motor is mainly determined by the electromagnetic time constant τ_{em}.

b) - Current-fed response

When the motor is supplied from a constant current source, the response is much simplified by the fact that the motor torque is directly proportional to the input signal. For a 90°E torque angle ($i_d = 0$), when a constant r.m.s. current I is suddenly applied to the motor, the response follows directly from Eq. (3.73) as

$$K_r \frac{I}{s} = D\left(1 + \frac{J_m}{D}s\right)\omega_r(s)$$

$$\frac{\omega_r(s)}{I} = \frac{K_T}{SD(1 + \tau_m s)}$$

and the response in the time domain is:

$$\omega_r(t) = \frac{K_T I}{D}\left(1 - e^{-\frac{t}{\tau_m}}\right) \qquad (3.83)$$

Hence, with current-fed operation, the motor response is determined by the mechanical time constant.

Since $\tau_m > \tau_{em}$ it can be seen from Eq. (3.82) and Eq. (3.83) that the voltage and current-fed responses are fundamentally different. If the excitations V and I are set to give the same final rotor speed $\omega_o = 2V/K_T = K_T I/D$ or $V = K_T^2 I/2D$, then the response with voltage-feeding is considerably more rapid than with current-feeding, as shown in fig. 3.40. However, the peak current needed from the source is larger.

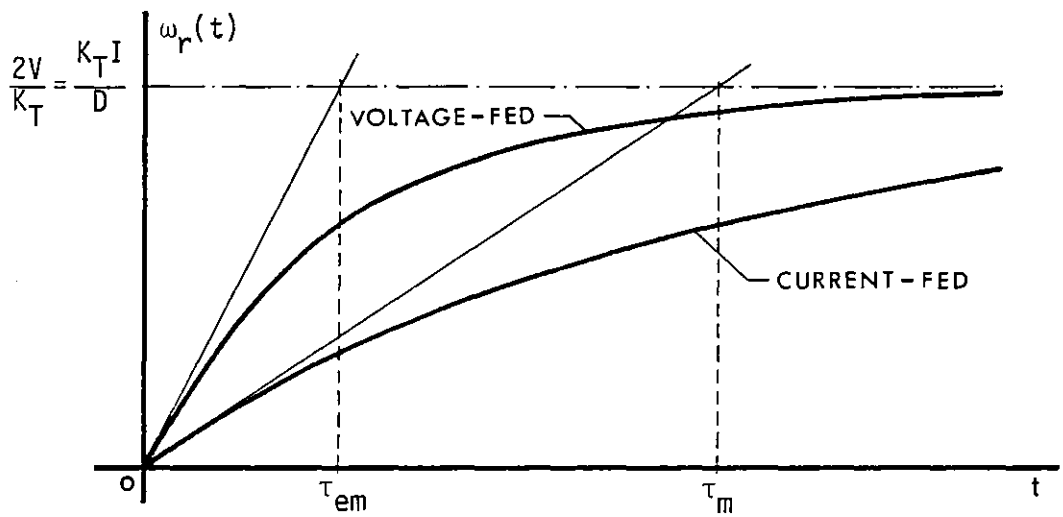

Fig. 3.40 - Voltage and current-fed response for equal conditions

Expressions for current and voltage waveforms are developed in Chapter 4, for the response analysis of the auto-piloted actuator.

☆ ☆ ☆

CHAPTER 4

LIMITED MOTION, ROTARY BRUSHLESS ACTUATOR

4.1 - GENERALITIES

In a recent project request from A.S.W.E., a 1000 lb.ft. limited motion (±20°) rotary brushless actuator was designed, built and tested at I.C. The machine was intended to be used as a direct-drive servo motor in a position control application, and an arcuate, rather than drum type configuration, was decided.

As demonstrated in section 1.11, torque per inertia, torque per volume and power rate are generally lower for an arcuate type than for a drum type machine, and this is the penalty that must be paid for the sake of mechanical simplicity. The reason for using arc type layout is that for machines with the same height, a larger torque per rotor air gap area can be developed. A further advantage for certain applications is that the drive shaft is located at the top of the actuator rather than at the geometric centre. This can be very convenient with some load configurations.

The actuator then comprises a 130° arc-shaped stator with a two-phase winding and a 90° arc-shaped rotor containing a B.P.R.E. permanent magnet field system. In this way, the use of sliprings and brush-gear is avoided and the dissipation of heat from the wound stator is relatively easy with this configuration. Also rotor losses are absent.

The machine was designed to be operated in an auto-piloted mode, and hence incorporated in a system including a position sensor (synchro-resolver) and two switch-mode current source amplifiers.

For a direct-drive servo, torques tend to be high and speeds low. A machine with a high number of poles and large diameter/length is hence desirable. The arcuate stator can be considered as part of a complete cylindrical 72-pole machine with a stator inside diameter of D_g = 945 mm and an active axial length of ℓ = 114 mm, giving a ratio of D_g/ℓ = 8.3. Consequently the actuator requires a 72-pole resolver directly coupled to the rotor shaft.

Outline design calculations and the actuator construction (winding excepted) were all completed prior to the present project. The principal tasks accomplished within the present project, and presented here, were as follows:

a) - Brief design presentation.

b) - Formulation of detailed prediction relations and field analysis of permanent magnet and air gap region.

c) - Design and construction of test rig and supply system for static tests.

d) - Flux measurements, parameter measurements and static torque tests.

e) - Correlation between predictions and measurements.

4.2 - DESIGN OF ACTUATOR STATOR

In order to minimise harmonics in the stator m.m.f. distribution, it was decided to use a number of slots per pole per phase of q = 2. Then for m = 2 phases and a pole number of n_p = 72 (for the equivalent 360° machine), the total number of stator slots would be:

$$Q = n_p m q = 288 \text{ slots}$$

with a slot pitch

$$\alpha_{mec} = \frac{360}{Q} = 1.25° \qquad (4.1)$$

For the layout shown in fig. 4.1, the stator laminations were cut to an arc length $\varepsilon + \theta$ of 131.25°, giving an actual number of slots per lamination of

$$Q' = \frac{\varepsilon+\theta}{\alpha_{mec}} = 105 \text{ slots}$$

For a rotor arc of $\varepsilon = 90°$ the maximum displacement is

$$\theta = 131.25 - \varepsilon = 41.25° \qquad (4.2)$$

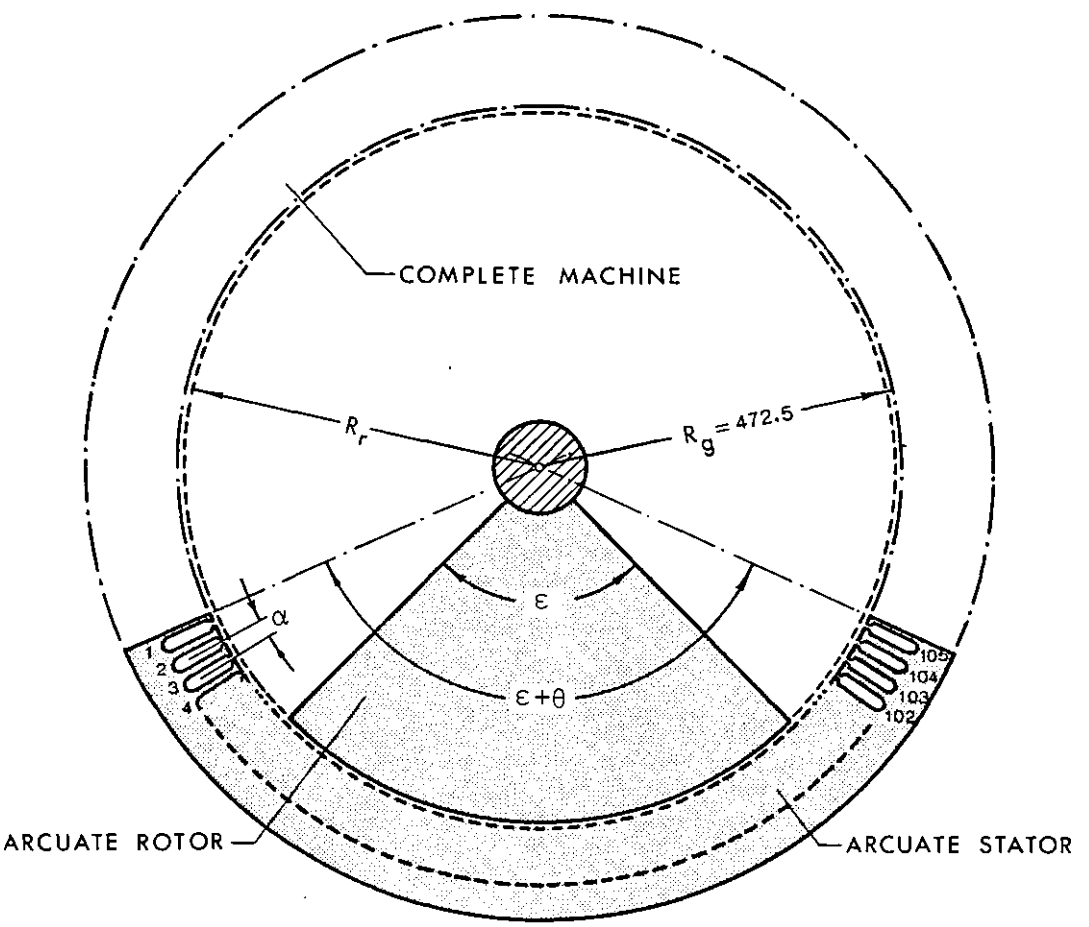

Fig. 4.1 - Actuator layout

It is essential to skew the stator in order to avoid locking torques. In some ways skewing is equivalent to distributing the winding of each slot uniformly over a stator slot pitch and this has also beneficial effect on the stator m.m.f. harmonic levels. The stator was skewed by a centre angle γ equal to one slot pitch, or, in electrical degrees

$$\gamma = \alpha = \frac{n_p}{2} \alpha_{mec} = 45°E \qquad (4.3)$$

At the assembly stage, the laminations had been stacked on a flat surface, offset to the correct skew angle, and clamped under pressure with a stack width ℓ = 114 mm, as shown in fig. 4.2. The skew angle δ is related to the centre angle by the relationship:

$$\delta = \text{atan}\left(\frac{R_g}{\ell}\,\gamma_{mec}\right) \qquad (4.4)$$

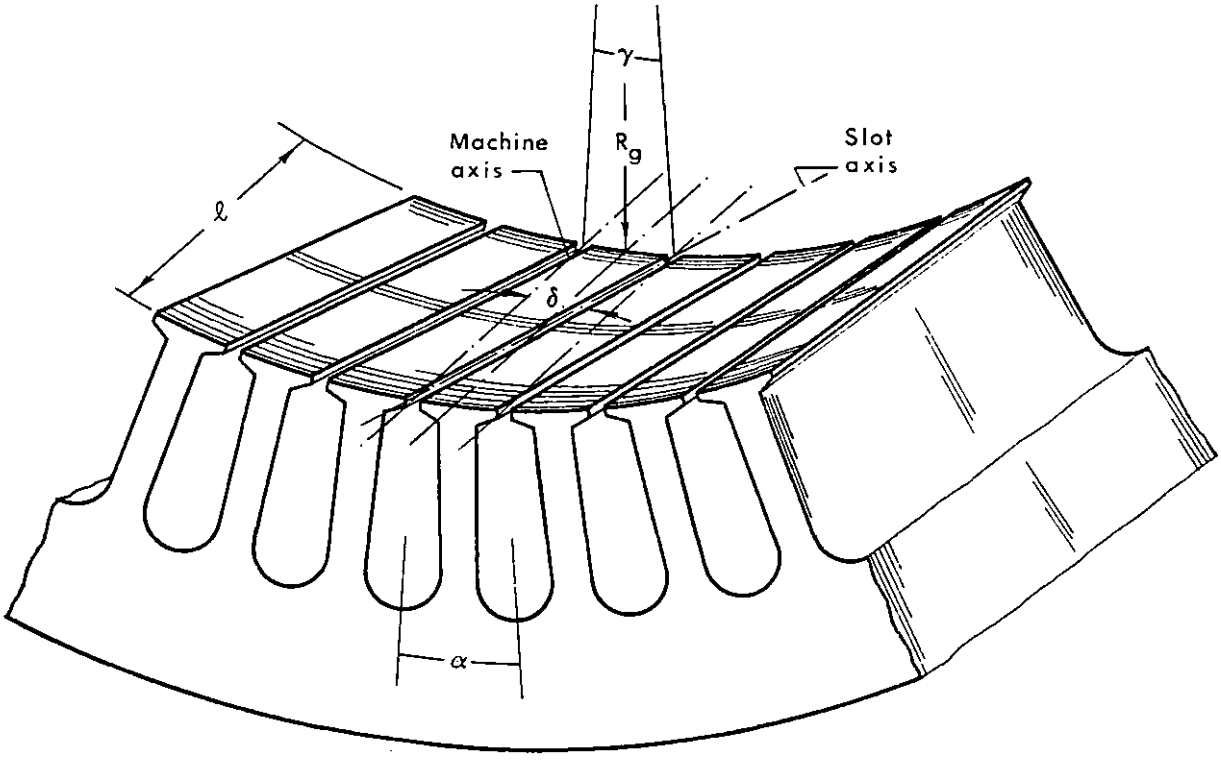

Fig. 4.2 - Skewed stator by one slot

The design of stator laminations decided upon is shown in fig. 4.3. Semi-closed slots were used to minimise slot ripple effects and slot depth was substantially increased. The slot width to tooth width ratio s/r of 1.6 was used. The lamination material was 0.35 mm thick varnite-coated "Newcor 800" with the B/H characteristic shown in fig. 4.4. It is clear that the flux density in the stator should be limited to about 1.6 T if linear torque versus current characteristics are required.

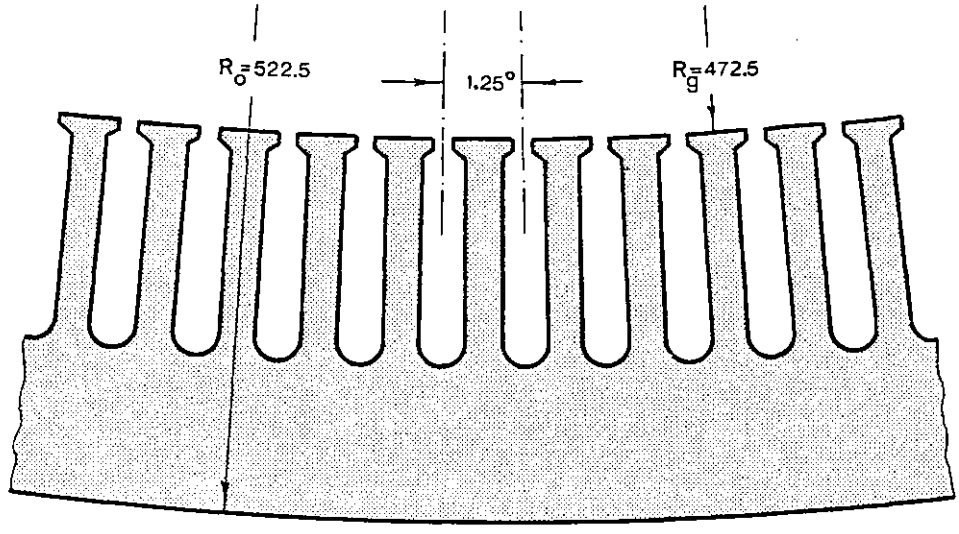

FULL SIZE VIEW OF A SECTOR LAMINATION

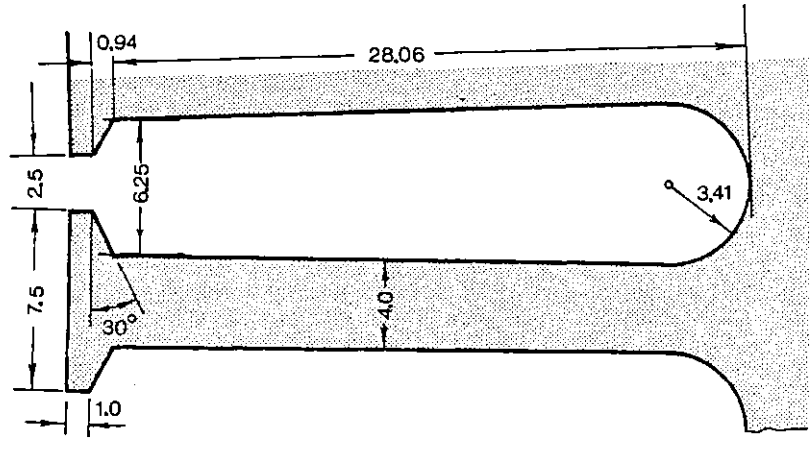

ENLARGED VIEW OF SINGLE SLOT

Slot pitch = 1.25°
Parallel teeth

Fig. 4.3 - Stator laminations design

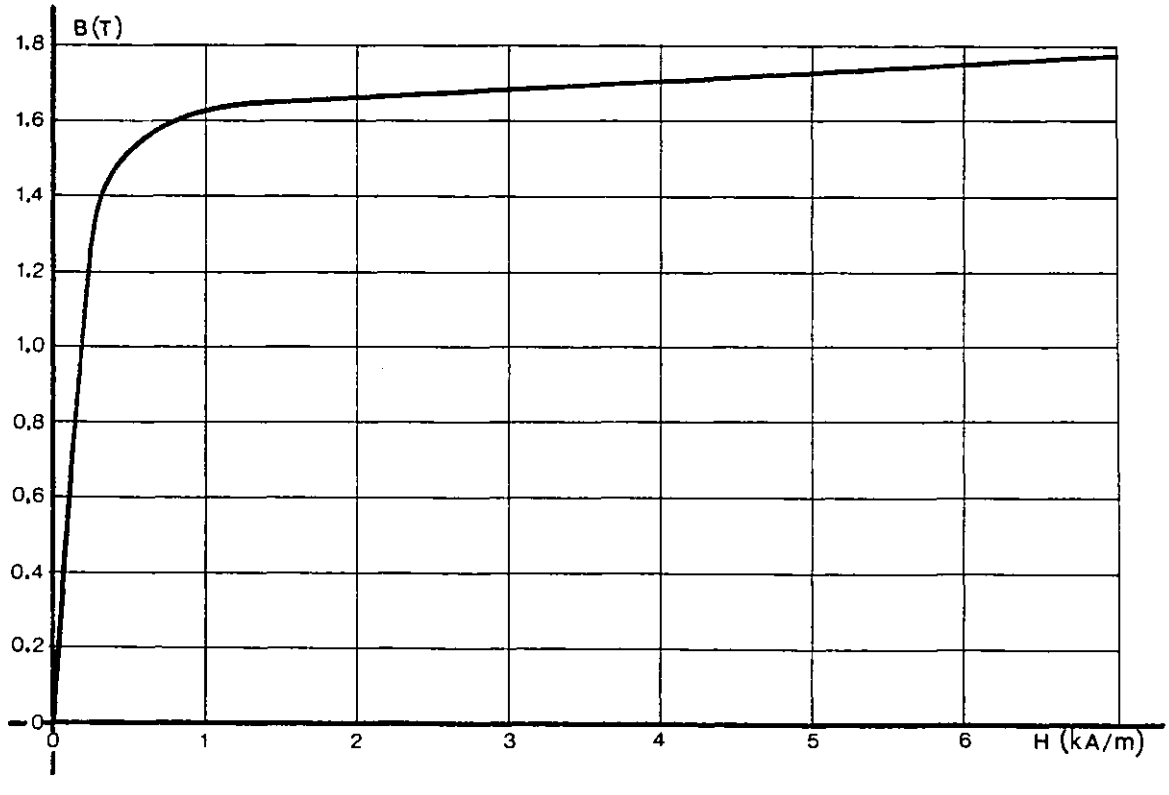

Fig. 4.4 - D.c. magnetisation characteristic for "Newcor 800"

4.3 - WINDING ARRANGEMENT

A total of the $Q' + 3 = 108$ round end coils with $n = 24$ turns each and 2 conductors in parallel were wound on a specially made former. The conductor used consisted of 1.0 mm diameter round wire (S.W.G. 19) covered with high temperature enamel to a nominal overall diameter of 1.09 mm. The coils, chorded by one slot ($\beta = 45°E$) were inserted wire by wire through the slot openings into insulated slots in order to form a double-layer basket winding as shown in fig. 4.5. This resulted in a total copper area per slot of $S_{Cu} = 75.36$ mm^2.

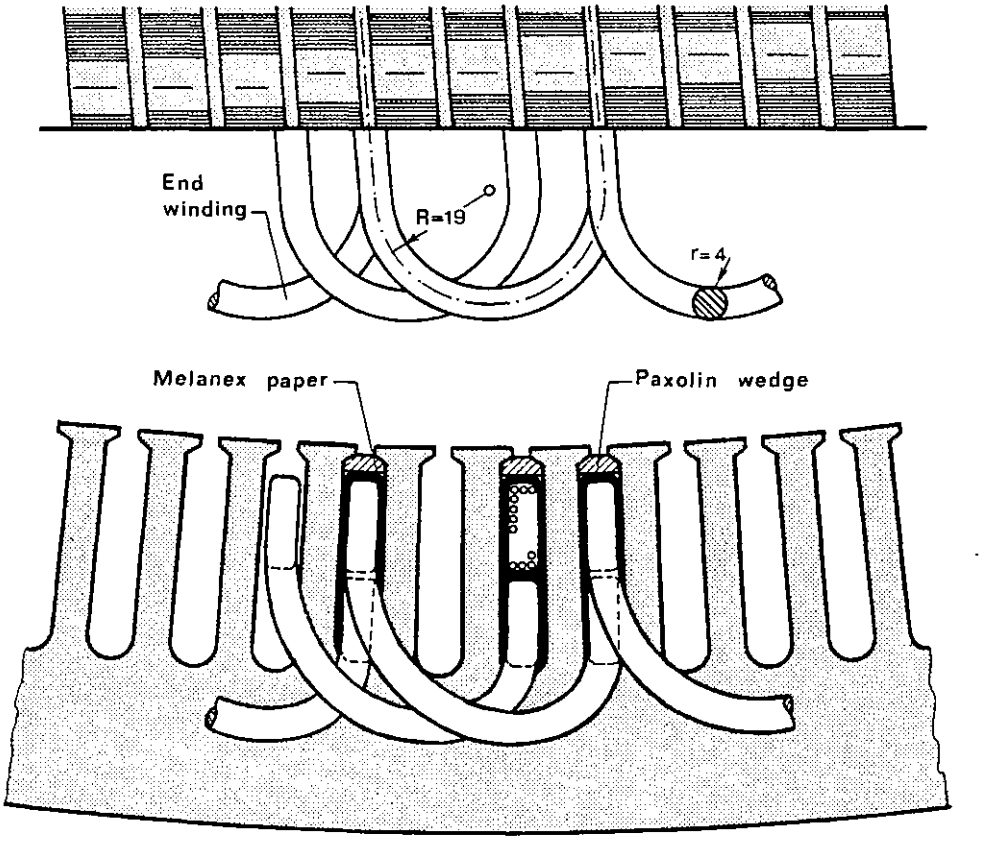

Fig. 4.5 - Double-layer basket winding arrangement

To allow the maximum possible current loading, all insulation used was to class H(180°C). Slot liners and winding layer dividers were made from 0.15 mm thick melanex paper and finally the winding blocked with a 2.5 mm thick paxolin wedge.

From fig. 4.3, the total useful slot area is $S_s = 162.46$ mm^2 which

gives a slot utilisation factor

$$f_u = \frac{S_{Cu}}{S_s} = \frac{75.36}{162.46} = 0.46$$

good enough even for an expert winder.

After all coils were inserted, interconnections were made in order to obtain a two-phase winding, and the layout is shown in fig. 4.6. Using a calculated mean turn length of L.M.T. = 390 mm, the winding series

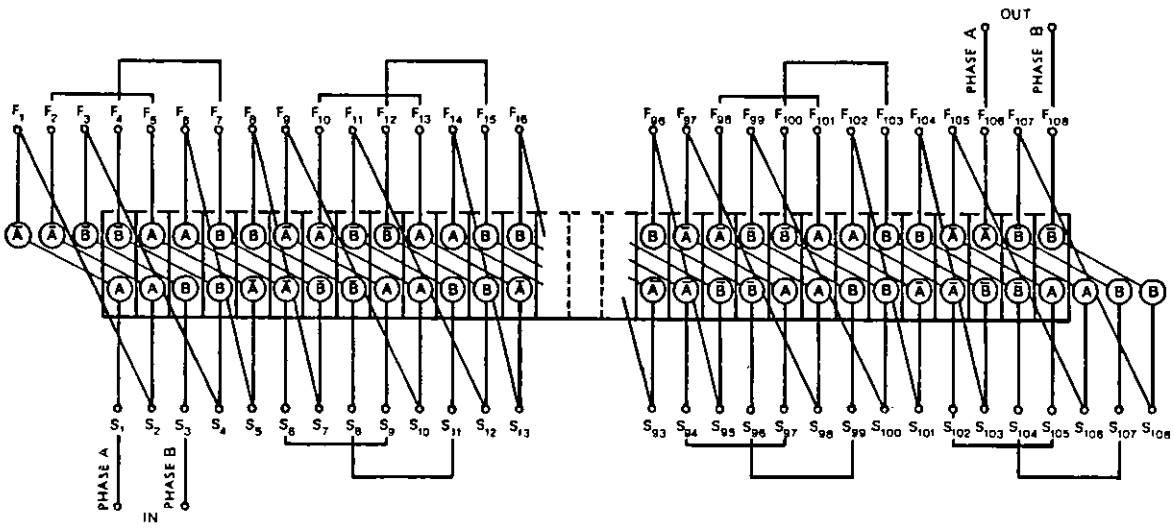

Fig. 4.6 - Winding diagram connections

resistance per phase at 20°C was calculated (allowing a factor of 1.05 for welding and connections) to be R = 6.03 Ω. The value obtained by measurement with Kelvin bridge was R´ = 6.45 Ω.

4.3.1 - Winding factor

With the following machine parameters

$$\alpha = \beta = \gamma = 45°E$$

$$q = 2 \text{ coils per pole per phase}$$

the winding factor defined by Eq. (1.35), may be evaluated for the h^{th} harmonic by using Eqs. (1.34).

Table 4.1 shows the winding factors up to the 9^{th} harmonic

Table 4.1 - Winding factors

h	K_{dh}	K_{ph}	K_{skh}	K_{wh}
1	0.294	0.924	0.975	0.832
3	0.383	0.383	0.784	0.115
5	-0.383	-0.383	0.471	0.069
7	-0.924	-0.924	0.139	0.119
9	-0.924	-0.924	-0.108	-0.092

4.4 - LEAKAGE INDUCTANCE CALCULATION

As seen in section 1.14 the leakage winding inductance is the sum of the slot leakage inductance $L_{s\ell}$ and the end-winding or overhang inductance $L_{e\ell}$. Both are now evaluated.

4.4.1 - Slot leakage inductance

In calculating the slot leakage inductance, unsaturated iron, slot fully filled with conductors and negligible distance between winding layers is assumed. The round-bottomed slot shown in fig. 4.3 is replaced by the rectangular slot of equal area shown in fig. 4.7.

With the winding arrangement described in fig. 4.6, each phase is distributed per pole as shown in fig. 4.8, i.e., slot (a) is occupied by lower layer, slot (b) is fully filled and slot (c) occupied by upper layer. Having n turns per coil and an axial slot length $\ell' = \ell/\cos\delta$ where δ is given by Eq. (4.4), then from Eq.(1.125) to Eq. (1.127) the slot leakage inductance if each slot of the group is as follows:

$$L_a = \mu_o n^2 \left(\frac{4h_1}{3s} + \frac{2h_3}{a+s} + \frac{h_4}{a} \right) \ell' \qquad (4.5)$$

$$L_b = \mu_o (2n)^2 \left(\frac{2h_1}{3s} + \frac{2h_3}{a+s} + \frac{h_4}{a} \right) \ell' \qquad (4.6)$$

$$L_c = \mu_o n^2 \left(\frac{h_1}{3s} + \frac{2h_3}{a+s} + \frac{h_4}{a} \right) \ell' \qquad (4.7)$$

In the actuator there are

$$n_p' = \frac{\varepsilon+\theta}{360}\, n_p = 26.25 \tag{4.8}$$

groups of coils as shown in fig. 4.8 embedded in slots. Then with the winding series connected, the total slot leakage inductance becomes:

$$L_{s\ell}' = n_p'(L_a + L_b + L_c) = n_p'\mu_o n^2 \left(\frac{13h_1}{3s} + \frac{12h_3}{a+s} + \frac{6h_4}{a} \right) \ell'$$

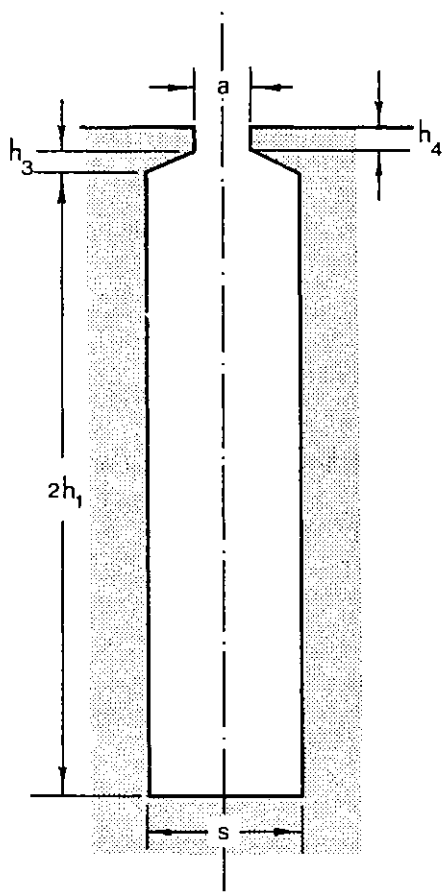

$2h_1$ = 27.44 mm
h_3 = 0.94 mm
h_4 = 1.00 mm
a = 2.50 mm
s = 6.54 mm

Fig. 4.7 - Equivalent rectangular slot

Substitution of values gives the final result as:

$$L_{s\ell}' = 27.58 \text{ mH/phase} \tag{4.9}$$

Alternatively, the slot leakage inductance may be also calculated using a numerical method. Fig. 4.8 shows the vector potential distribution for each slot individually on one pole pitch of the actuator with only one phase excited. As expected there is no flux under the upper layer in slot (c), since the flux is short-circuited by the bottom iron

slot. Details of the computer program are given in Appendix C and the analytical results given by Eq. (4.5) to Eq. (4.7) are compared with the

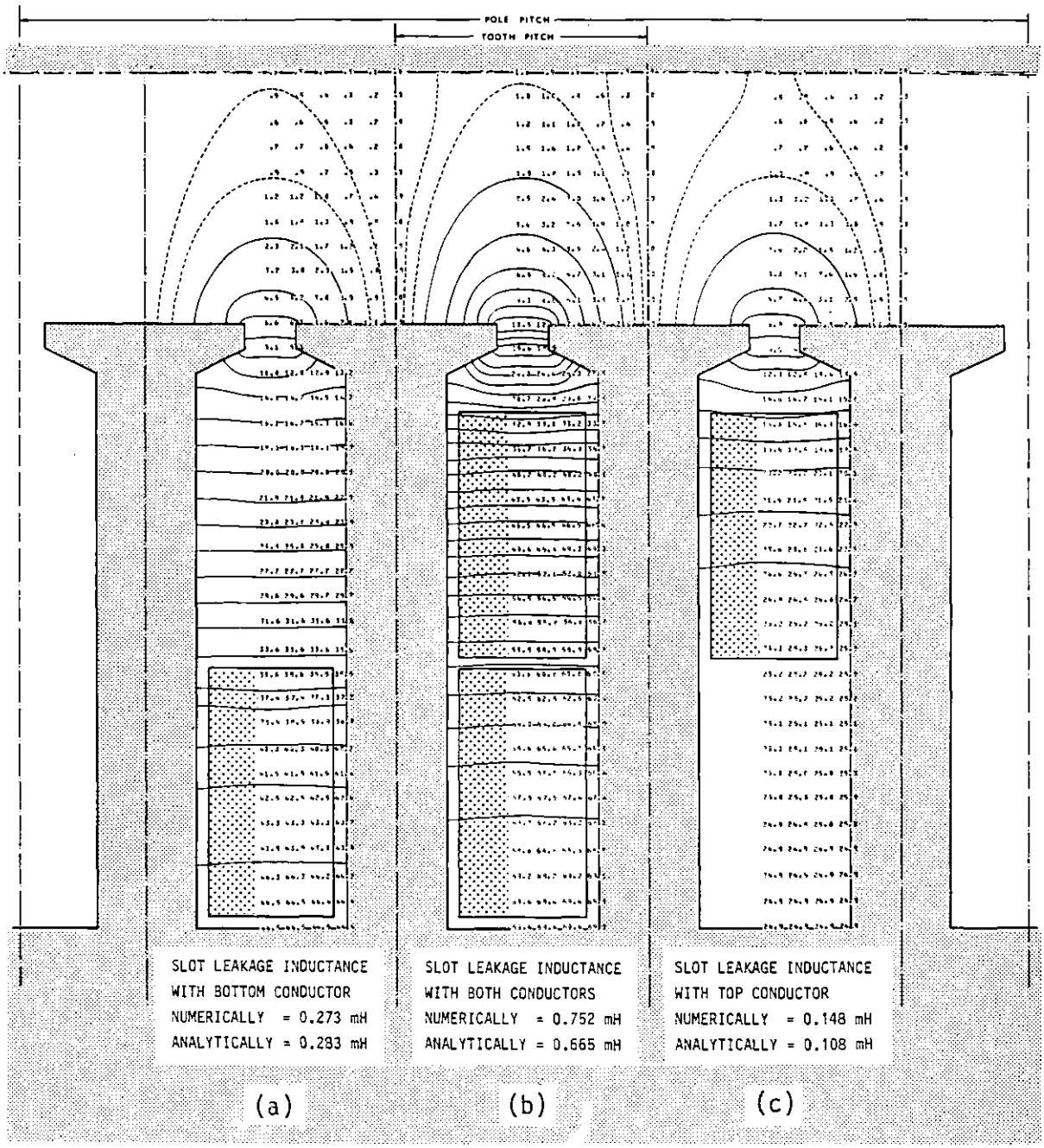

Fig. 4.8 - Vector potential distribution in one pole pitch of the slot actuator

respective numerical results under the field plotting. The total slot leakage inductance using the numerical method is

$$L''_{s\ell} = 26.25(0.273 + 0.752 + 0.148) = 30.79 \text{ mH/phase} \quad (4.10)$$

which is in good agreement with the result obtained in Eq. (4.9) by the standard method. Hence, from results (4.9) and (4.10), a mean value for slot leakage inductance may be taken as:

$$L_{s\ell} = 29.19 \text{ mH/phase} \tag{4.11}$$

4.4.2 - End-winding leakage inductance

Alger's formula given by Eq. (1.107) may be used to evaluate the end-winding leakage inductance, but the expression is only valid for the complete machine. For the actuator there are $\frac{Q'+3}{m} = 54$ coils/phase while for the complete machine there would be $\frac{Q}{m} = 144$ coils/phase. Therefore the actuator overhang inductance should be given by

$$L'_{e\ell} = \frac{Q'+3}{Q}\ 0.3\mu_o\, m\, N^2(3y_r - 1)D_g$$

Substitution of $m = 2$, $N = 2nq = 96$ conductors/pole/phase, $y_r = 1 - \beta/\pi = 0.75$ and $D_g = 0.945$ m gives:

$$L'_{e\ell} = 3.03 \text{ mH/phase} \tag{4.12}$$

The overhang inductance may be also evaluated using Eq. (1.108). From fig. 4.5, the mean radius R may be taken as 19 mm and r = 4 mm as the radius of the bundle of n = 24 conductors. Since the q = 2 coils/pole/phase are linked $n'_p = \frac{Q'+3}{qm} = 27$ times in one phase, then the end leakage inductance becomes

$$L''_{e\ell} = n'_p(qn)^2\mu_o R\left[(1+\frac{r^2}{8R^2}).\log_e\frac{8R}{r} + \frac{r^2}{24R^2} - 1.75\right]$$

Substitution of values gives

$$L''_{e\ell} = 2.86 \text{ mH/phase} \tag{4.13}$$

Taking the mean value of results (4.12) and (4.13) the end-winding leakage inductance gives:

$$L_{e\ell} = 2.97 \text{ mH/phase} \tag{4.14}$$

Consequently, from Eq. (4.11) and Eq. (4.14), the actuator leakage inductance is:

$$L_{\ell} = L_{s\ell} + L_{e\ell} = 32.16 \text{ mH/phase} \tag{4.15}$$

4.5 - DESIGN OF ACTUATOR ROTOR

The 90° arc-shaped rotor unit contains 18 poles machined from permanent magnet blocks. The rotor sectors are secured to two bosses, and the bosses secured to a shaft enlargement by a tapped dowel technique. These tapped dowels perform the dual function of torque transmission and the maintenance of precision location of the rotor components.

The main problem with the rotor construction was the accurate manufacture of the backing iron. A 5/8" mild steel sheet was rolled and then turned to size accurately on a lathe with an outside radius of 462.5 mm. Eighteen shallow grooves of 3 mm depth and 34.93 mm circumferential length were machined in order to fit the magnets. The thickness of the effective backing iron was then left with d = 7 mm. The pole pitch length at air gap level is

$$\tau = \frac{\pi D_g}{n_p} = 41.21 \text{ mm} \tag{4.16}$$

and from Eq. (1.14) the fundamental excitation flux density produces a circumferential flux density in the backing iron given by:

$$B_c = \frac{\tau}{\pi d} \hat{B}_1 = 1.88 \hat{B}_1 \tag{4.17}$$

Then, for a fundamental peak air gap flux density $\hat{B}_1 = 0.6$ T (typical for this machine as it will be seen later), results $B_c = 1.13$ T and so the rotor backing iron is unsaturated.

A radially magnetised permanent magnet arrangement was used. Each of the 18 poles were manufactured from two standard magnet "Hera" blocks of B.P.R.E. of dimensions 60 mm x 35 mm x 11 mm in the magnetised direction

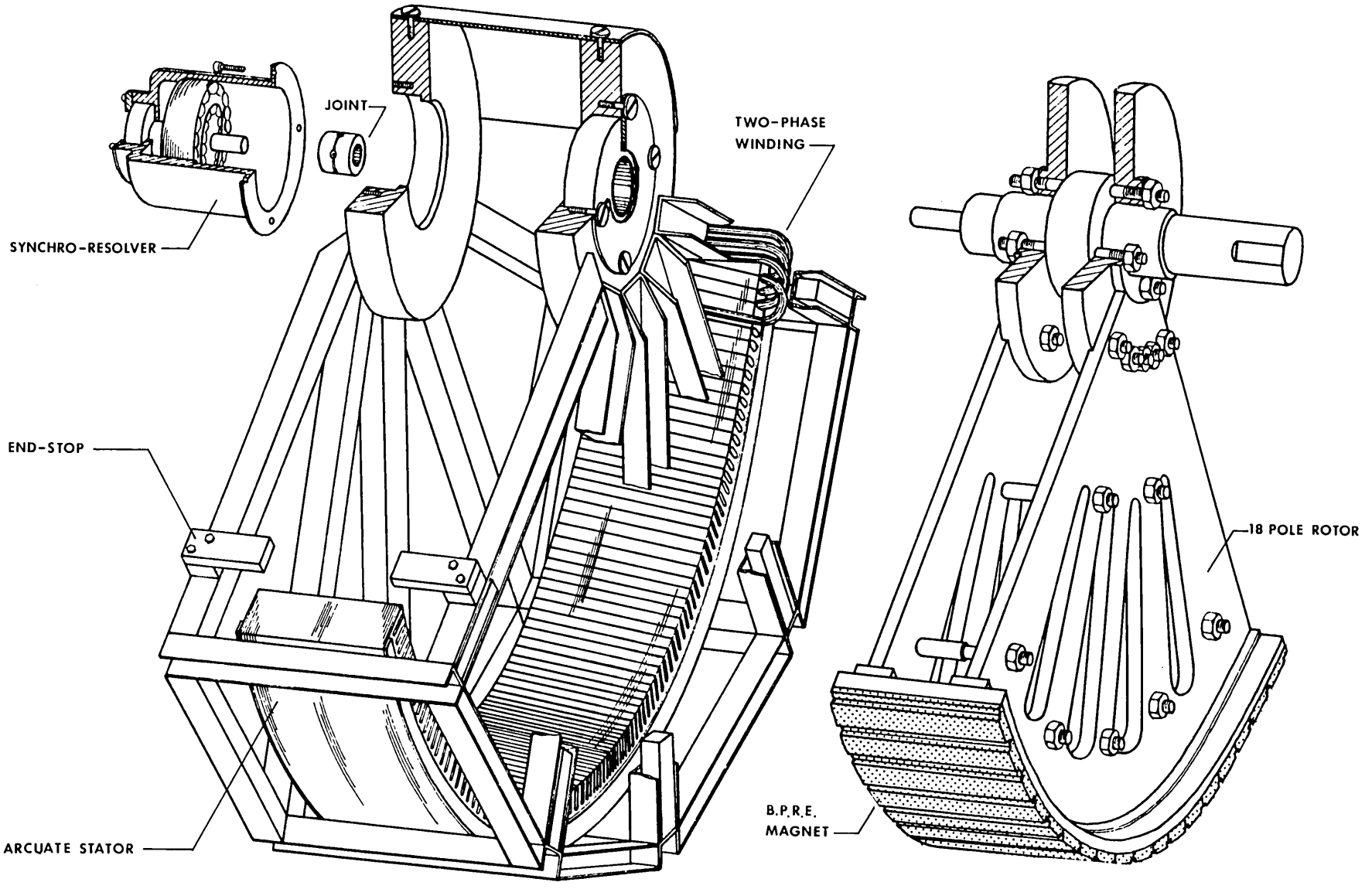

Fig. 4.9 - Exploded view of the limited motion rotary brushless actuator

and arranged in line along the rotor axis. Two aluminium strips were used to clamp each magnet.

Pure rare-earth magnets are generally difficult to machine to a desired shape and a complex profile can only be obtained accurately by using a laser beam cutting technique. The great advantages of B.P.R.E. over the basic rare-earth materials are its machineability and its relatively low cost. A suitable magnet profile can be easily obtained in order to achieve a sinusoidal air gap flux density waveform.

Fig. 4.9 shows an exploded view of the stator and rotor together with the synchro-resolver that was incorporated later. As will be shown, a very strong frame was needed to allow for the large unbalanced radial magnetic forces involved and to maintain parallelism of the air gap surfaces.

4.6 - AIR GAP FLUX DENSITY DISTRIBUTION ON NO-LOAD

As shown in section 1.6 a special profile for the pole face is needed in order to obtain a near-sinusoidal air gap flux density distribution. However, it was decided to make the magnet profile as simple as possible to minimise the machining work. The permanent magnet was then cut in just two steps, symmetrically placed about the pole centre line.

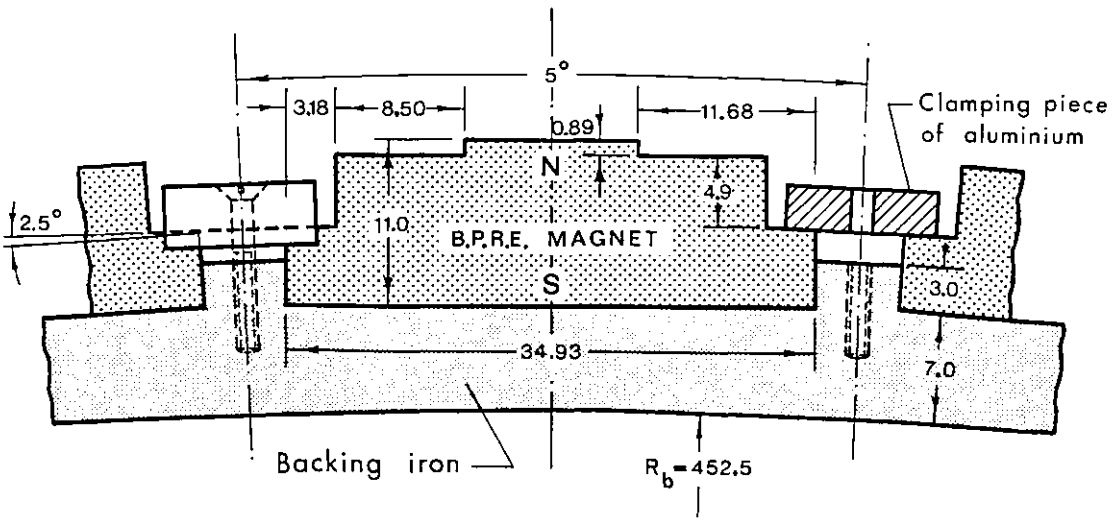

Fig. 4.10 - Pole profile for B.P.R.E. rotor

A computer program was written to calculate the resulting flux density waveform; it included the facility to vary the coordinates of the corner steps and Fourier analysis of the resulting flux density waveforms in order to determine the respective harmonic coefficients. Thus, after some attempts, the step position was optimised. Fig. 4.10 shows the geometry finally decided, although it is not optimum from magnetic point of view since the outer step has been raised 2.5° from optimum for mechanical reasons. Details of the computer program are given in Appendix D. Using the magnet manufacturer's figures of 0.55 T and 1.1 for the remanence and relative permeability, fig. 4.11 shows the computed no-load flux plot and air gap flux distribution over a pole pitch. Fourier coefficients of the resulting flux density waveform are also displayed. There is a slight shoulder on the flux density distribution waveform at about the 54°E point, which is attributed to the large second step. From the flux plot it is clear that the maximum self-demagnetising field is experienced near the inner corner of the first step, since it is in this region where the highest potential is attainable.

4.6.1 - Flux set up per tooth pitch by the B.P.R.E. magnet

In calculating the flux density distribution of the B.P.R.E. magnet rotor actuator a smooth iron stator surface was assumed. To determine the error involved, the magnetic equipotential distribution was calculated for an open and semi-closed slot assuming that the top magnet surface is a magnetic equipotential of Ω = 200 A which is valid for the centre step. The slot field plot is displayed in fig. 4.12 for both types of slot geometry. Clearly the flux penetration into an open-slot is greater than into a semi-closed one, since the iron projections act as a flux barrier.

For the open-slot the flux per curvilinear square of side h per unit machine length is

$$\Delta\phi = Bh = \mu_o Hh = \mu_o \frac{200 - 150}{h} h = 50\mu_o \quad Wb/m$$

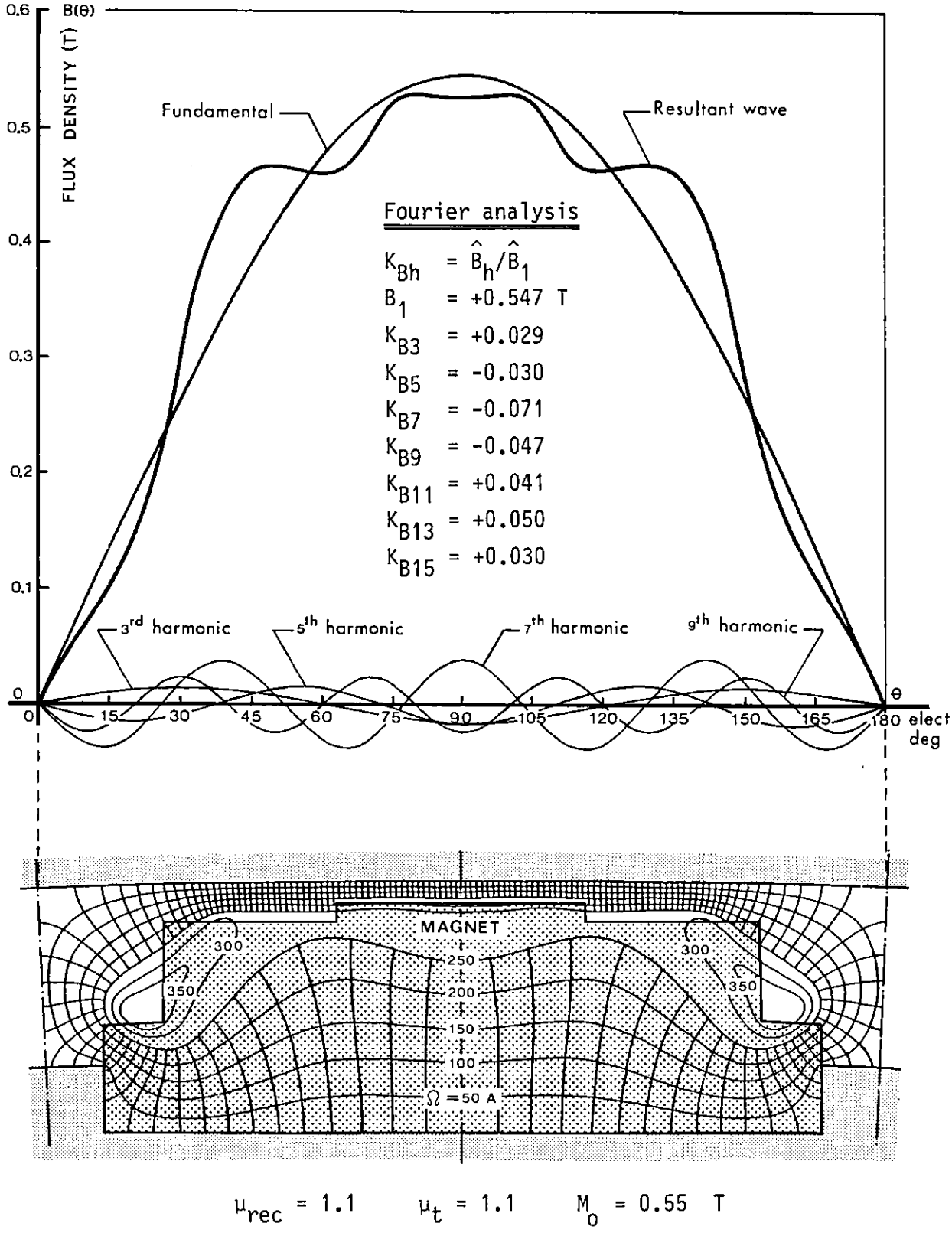

Fig. 4.11 - Air gap flux density distribution and computed no-load flux plot for B.P.R.E. magnet

There are 16 squares per tooth pitch, thus total flux per tooth pitch is

$$\phi = 16\Delta\phi = 800\mu_o \quad \text{Wb/m}$$

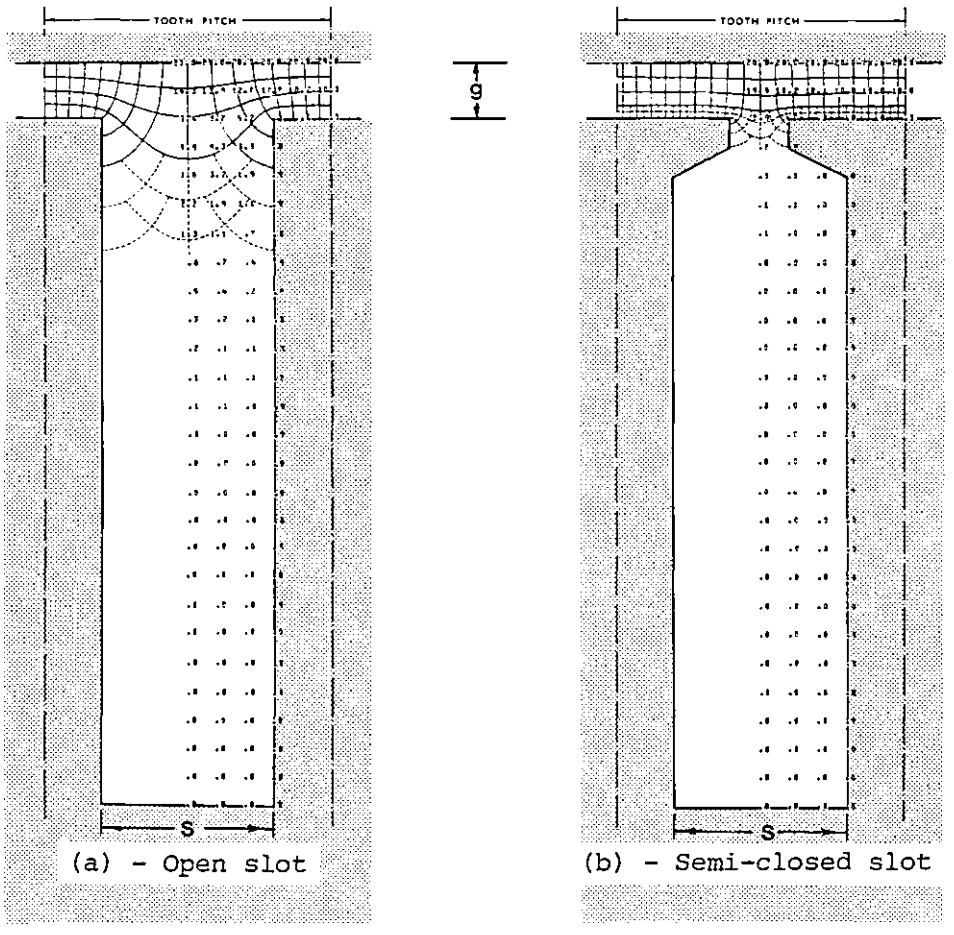

Fig. 4.12 - Slot field set up by B.P.R.E. magnet

Taking slot width s = 6.54 mm, tooth pitch w = $\tau/4$ = 10.3 mm and a gap g = 1.9 mm, the equivalent gap G of a smooth stator in order to obtain the same flux ϕ per tooth pitch with the same m.m.f. Ω = 200 A is

$$\Omega = \frac{G}{\mu_o w}\ \phi \qquad (4.18)$$

and substitution of values gives G = w/4. Since w = 5.42 g the equivalent gap for the open-slots is

$$G = 1.36\ g$$

where G/g = 1.36 is the so-called "Carter's coefficient".

For an open-slot F.W. Carter showed [81] that

$$\frac{G}{g} = \frac{w}{w - \alpha s} \tag{4.19}$$

where

$$\alpha = \frac{2}{\pi}\left[\operatorname{atan}\left(\frac{s}{2g}\right) - \frac{g}{s}\log\left(1 + \frac{s^2}{4g^2}\right)\right] \tag{4.20}$$

Since for the open-slot s/g = 3.44, Eq. (4.20) gives $\alpha = 0.41$ and from Eq. (4.19) is

$$\frac{G}{g} = 1.35$$

which is very close to the 1.36 obtained by field plotting.

For semi-closed slots, the total flux per tooth pitch with the same m.m.f. $\Omega = 200$ A is from the field plot

$$\phi' = 19 \times 50\mu_o \quad \text{Wb/m}$$

and therefore semi-closed slots increase the flux by a factor of

$$\frac{\phi'}{\phi} = \frac{19 \times 50\mu_o}{16 \times 50\mu_o} = 1.19$$

relative to open-slots. Attending to Eq. (4.18), Carter's coefficient for semi-closed slots is then

$$\frac{G'}{g} = \mu_o \frac{w}{g} \frac{\Omega}{\phi'} = 1.14$$

As expected, the smooth stator equivalent gap G' is almost the same as the actual gap g with semi-closed slots, while for open slots it is much greater. A tooth ripple of only 14% should hence be expected when assuming a smooth stator for the calculation of the air gap flux density with semi-closed slots.

4.7 - NORMAL FORCE SEEN BY THE SHAFT

Since the rotor actuator is an arc of $\varepsilon = 90°$ the radial forces due to the magnet attraction to the core are unbalanced and therefore seen by the shaft. From the mechanical point of view calculation of this force

is important for the shaft and frame design.

From Eq. (1.17) the normal force reflected on machine shaft due to one magnet is given by

$$F_n = \frac{1}{2\mu_o} \int_{\text{pole arc}} B^2 dS$$

where B is the air gap flux density. Since $dS = (1/\pi)\tau\, \ell d\theta_{elect}$ the average stress over the pole arc is

$$F_n = \frac{1}{\pi} \frac{\tau \ell}{2\mu_o} \int_0^{\pi} B^2(\theta) d\theta_{elect} \qquad (4.21)$$

and so is proportional to the dashed area represented in fig. 4.13.

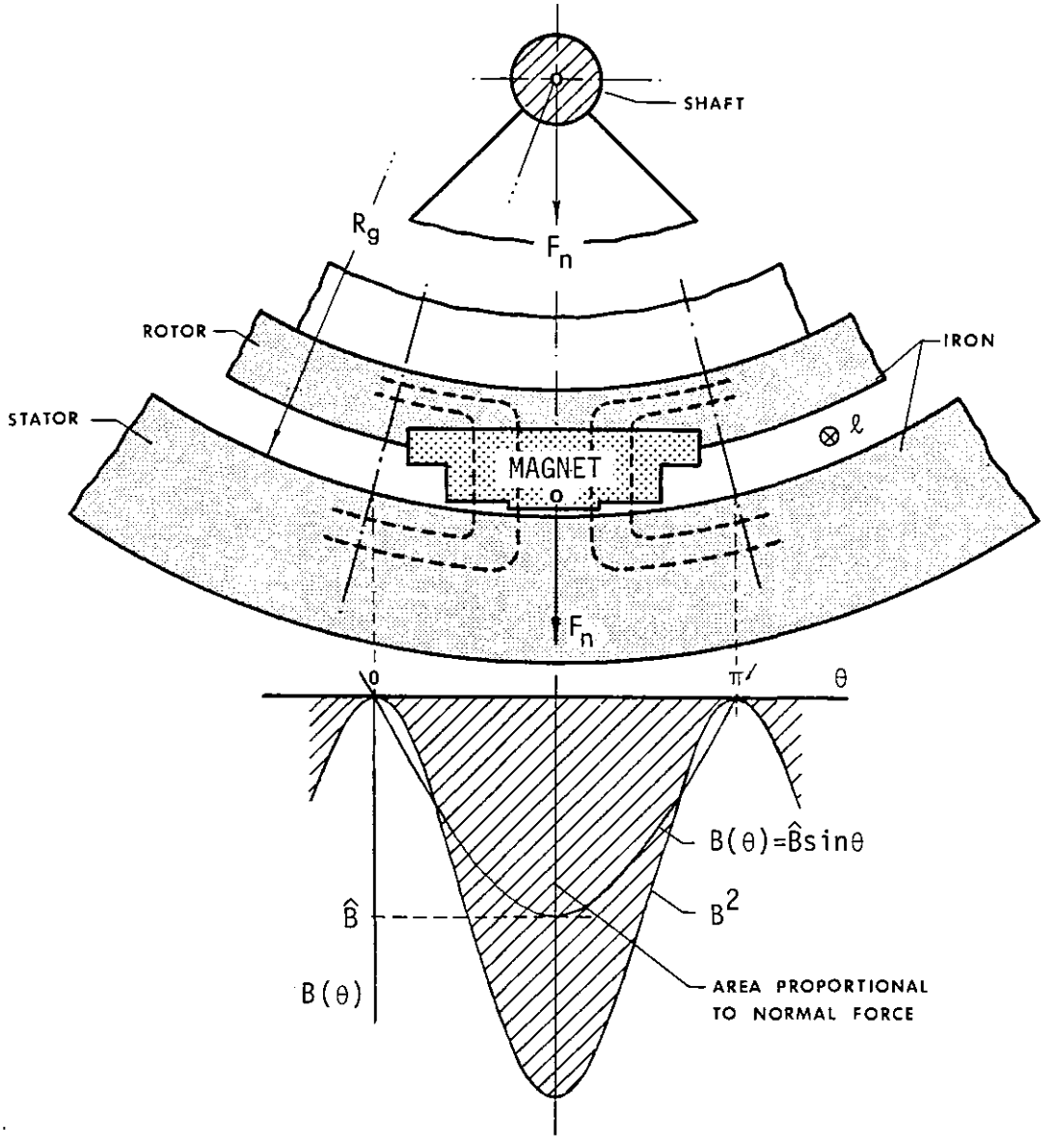

Fig. 4.13 - Normal force due to one magnet

For the fundamental sine wave flux density displayed in fig. 4.11 (of magnitude $\hat{B}_1$ = 0.547 T) and using the machine parameters τ = 41.21 mm and ℓ = 114 mm, Eq. (4.21) gives:

$$F_n = \frac{\tau \ell}{4\mu_0} \hat{B}_1^2 = 279.8 \text{ N per pole} \qquad (4.22)$$

From fig. 4.14, the total normal force on the shaft due to 18 magnets is given by:

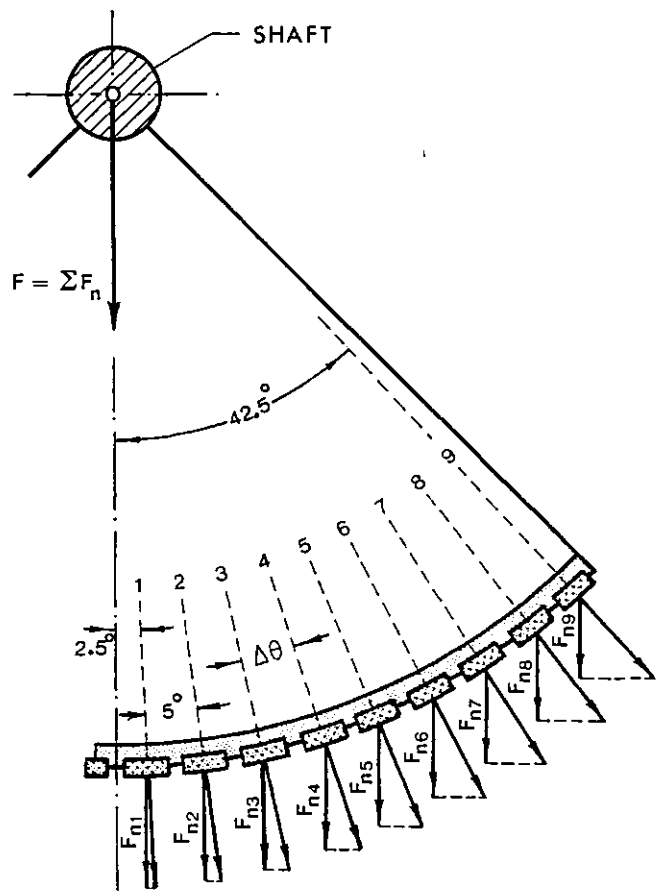

Fig. 4.14 - Total force due to rotor magnets

$$F = 2(F_{n1} + F_{n2} + F_{n3} + \ldots + F_{n9})$$

$$= 2F_n \left[\cos(\tfrac{\Delta\theta}{2}) + \cos(\Delta\theta + \tfrac{\Delta\theta}{2}) + \cos(2\Delta\theta + \tfrac{\Delta\theta}{2}) + \ldots + \cos(8\Delta\theta + \tfrac{\Delta\theta}{2})\right] \qquad (4.23)$$

and substitution of Eq. (4.22) and $\Delta\theta$ = 5° into Eq. (4.23) gives F = 462.53 Kg. To overcome this large unbalanced force a strong frame was needed and five pairs of normalised 2" steel channel spokes were used,

as shown on the photograph of the assembled actuator in fig. 4.15.

The influence of normal force produced by the magnets on the 56 mm diameter steel shaft is calculated in Appendix E and gives for maximum

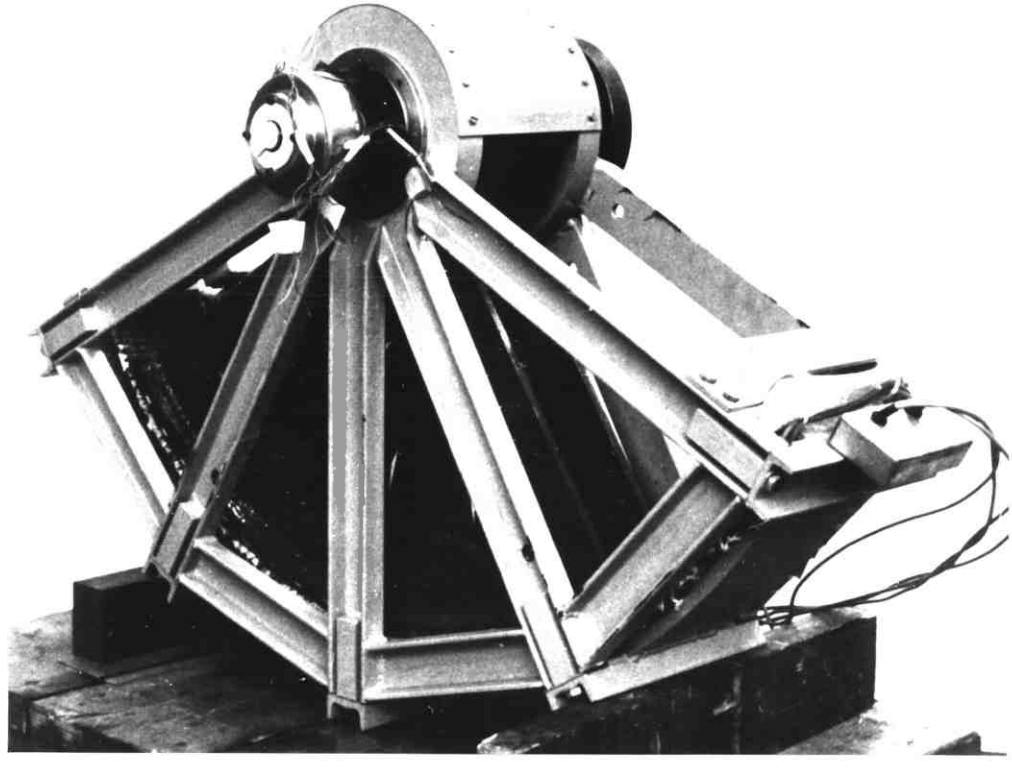

Fig. 4.15 - General view of the rotary actuator

shaft deflection $y_{max} = 0.54 \times 10^{-3}$ mm. Since the minimum gap at the centre pole axis is $g_{min} = 1.0$ mm, this result shows that the clearance is on the safe side.

4.8 - AIR GAP INDUCTANCE CALCULATION

As explained in section 1.14 the air gap inductance depends on the rotor pole profile, magnet and air region permeability, the number of stator conductors linked by self-flux and therefore on the rotor position θ. In order to calculate parameters for using in the two-axis phasor diagram shown in fig. 3.20, it is only necessary to obtain values for the direct and quadrature-axis air gap inductances. However, since the act-

uator stator is skewed 45°E, the skewed air gap inductance of those two rotor positions were taken as the average of the unskewed values over a range of ±22.5°E from each position and then values of unskewed air gap inductance over half pole pitch were calculated in steps of 3°E. Simultaneously, a plot of inductance versus rotor position may be obtained in order to see the form of its variation.

The air gap inductance was calculated using the basic method explained in section 2.7.5b. In this case, however, the actuator has 18 active poles in the rotor region and 9 inactive poles on the stator corresponding to the rotor displacement. Assuming that the inactive poles have 50% of the influence of the active poles, the air gap inductance was computed using Eq. (2.55) substituting n_p by $n_p' = 18 + 0.5 \times 9$ and $n = 24$ conductors.

The computer program written to calculate the air gap inductance is described in Appendix F and the results for unskewed air gap inductance are given in table 4.2.

Table 4.2 - Unskewed air gap inductance per phase

θ°E	d axis	3	6	9	12	15	18	21	24	27	30
L_{unsk} (mH)	24.91	24.92	24.93	24.95	24.98	25.01	25.05	25.08	25.12	25.17	25.21
θ°E	33	36	39	42	45	48	51	54	57	60	
L_{unsk} (mH)	25.25	25.27	25.36	25.50	25.71	25.90	26.08	26.10	26.13	26.17	
θ°E	63	66	69	72	75	78	81	84	87	q axis	
L_{unsk} (mH)	26.21	26.24	26.27	26.29	26.31	26.32	26.33	26.38	26.40	26.46	

The skewed air gap inductance for a given position θ_o may be now obtained by averaging the values over ±22.5°E about θ_o as shown in fig. 4.16.

Using Simpson's rule [82], the skewed air gap inductance for θ_o position is given by

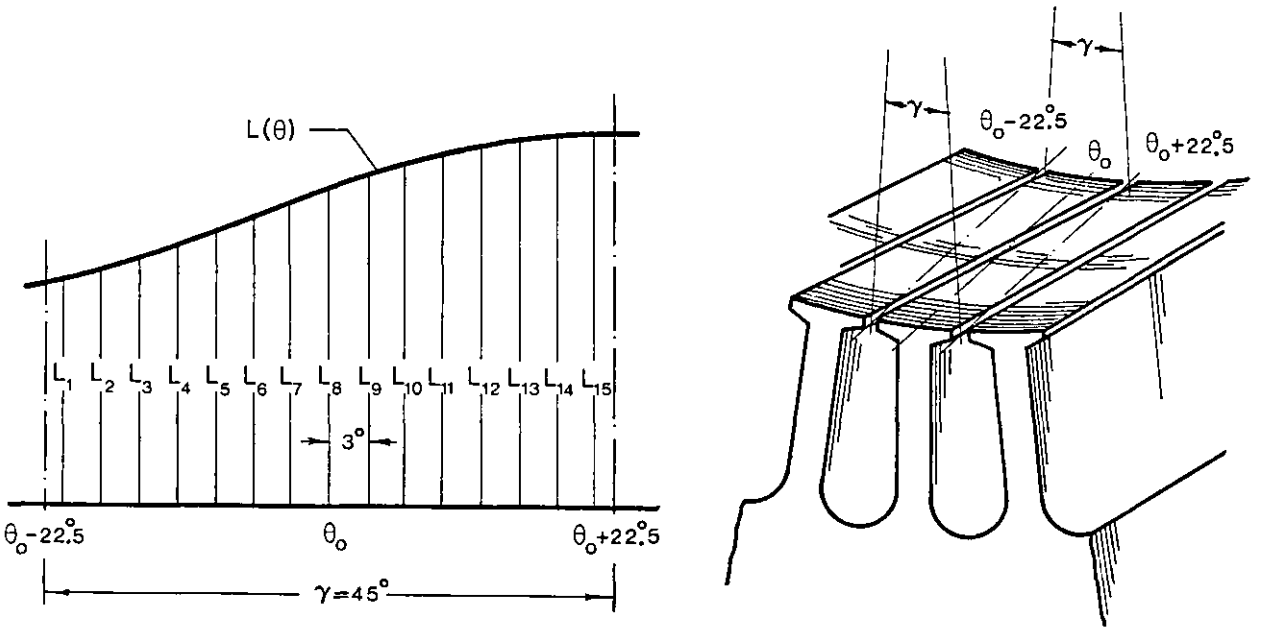

Fig. 4.16 - Average of the air gap inductance by Simpson's rule

$$L_a(\theta_o) = \frac{1}{7}\left[\frac{1}{6}(L_1+4L_2+L_3) + \frac{1}{6}(L_3+4L_4+L_5)+\ldots+\frac{1}{6}(L_{13}+L_{14}+L_{15})\right]$$

which is thus:

$$L_a(\theta_o) = \frac{1}{42}\left[L_1+4(L_2+L_4+L_6+L_8+L_{10}+L_{12}+L_{14})+2(L_3+L_5+L_7+L_9+L_{11}+L_{13})+L_{15}\right]$$

Applying this equation for each value of unskewed inductance, the full range of skewed air gap inductance is obtained, as shown in table 4.3.

Table 4.3 - Skewed air gap inductance per phase

θ°E	d axis	3	6	9	12	15	18	21	24	27	30
L_{skew} (mH)	24.98	24.98	24.99	25.00	25.02	25.04	25.07	25.10	25.15	25.21	25.29
θ°E	33	36	39	42	45	48	51	54	57	60	
L_{skew} (mH)	25.37	25.45	25.53	25.61	25.69	25.77	25.81	25.92	26.00	26.07	
θ°E	63	66	69	72	75	78	81	84	87	q axis	
L_{skew} (mH)	26.14	26.20	26.24	26.28	26.30	26.32	26.32	26.33	26.34	26.34	

From these corrected values it can be seen that there is a relatively small difference between the d and q-axis air gap inductances, being practically constant over a pole pitch. Hence, the actuator can be classified as a virtually cylindrical rotor machine. This is due to the low permeability of the permanent magnet material ($\mu_{rec} = 1.1$) therefore giving an effective long air gap between stator surface and rotor backing iron. Air gap permeances on the d and q-axis are thus very similar, although on q-axis position the permeance is a little higher due to the small projection of the backing iron, as can be seen in fig. 4.10.

4.9 - STATOR CURRENT LIMITATION

Since in the rotor actuator pole piece protection is absent, the stator current has a fixed limit set by demagnetisation of the permanent magnets. Also, if linear torque characteristics are expected, the permissible slot current should be limited by magnetic circuit saturation. In this section both values of current are now determined.

4.9.1 - Current limit for starting saturation of the magnetic circuit

Fig. 4.17 shows the layout of a pole pitch of the actuator when sinusoidally current-fed at 90°E torque angle together with the necessary parameters in order to calculate the flux density on load.

It is assumed that the stator flux path in the gap region has a mean length g_{av1} and g_{av2} under the teeth 1 and 2 respectively. Hence, taking into account the magnet permeability, the respective gap permeances are respectively:

$$P_1 = \mu_o \mu_r \frac{t\ell}{g_{av1}} \quad \text{and} \quad P_2 = \mu_o \mu_r \frac{t\ell}{g_{av2}}$$

As seen in section 1.15, the roots of teeth 1 and 2 are the parts most prone to saturation. From Eq. (1.135) to Eq. (1.138) the flux

density at the root of tooth 1 and tooth 2 at the instant of peak current in one phase is respectively:

$$B_1 = \frac{\mu_o}{r}\left[\frac{4h_1}{3s}+\frac{2h_3}{a+s}+\frac{h_4}{a}+2\mu_r\frac{t}{g_{av1}}\right] n\sqrt{2}\, i_{rms} + 0.37\,\frac{w}{r}\,\hat{B}$$

$$B_2 = \frac{\mu_o}{r}\left[\frac{2h_3}{a+s}+\frac{h_4}{a}+\mu_r\frac{t}{g_{av2}}\right] n\sqrt{2}\, i_{rms} + 0.88\,\frac{w}{r}\,\hat{B} \quad ;$$

and when equal currents are flowing in both phases:

$$B_1' = 2\,\frac{\mu_o}{r}\left[\frac{2h_1}{3s}+\frac{2h_3}{a+s}+\frac{h_4}{a}+\frac{3}{2}\mu_r\frac{t}{g_{av1}}\right] n\, i_{rms} + 0.37\,\frac{w}{r}\,\hat{B}$$

$$B_2' = \frac{\mu_o}{r}\,\mu_t\,\frac{t}{g_{av2}}\; n\, i_{rms} + 0.88\,\frac{w}{r}\,\hat{B}$$

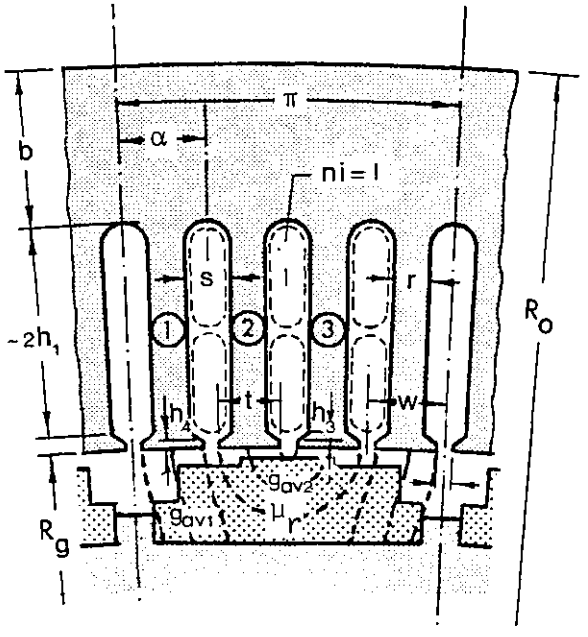

$b = R_o-(R_g+2h_1+h_3+h_4) = 20$ mm
$a = 2.5$ mm
$w = 10.3$ mm
$g_{av1} = 13.3$ mm (by measuring)
$g_{av2} = \frac{1}{4}\pi w = 8.09$ mm
$t = w - a = 7.80$ mm
$s = 6.54$ mm
$r = 4.0$ mm
$\mu_r = 1.1$
$n = 24$ turns
$2h_1 = 27.44$ mm
$h_3 = 0.94$ mm
$h_4 = 1.00$ mm

Fig. 4.17 - Physical dimensions of one pole pitch

Substituting the values shown in the diagram, and taking for excitation flux density the fundamental value $\hat{B} = 0.547$ T, the flux density in each tooth for both conditions is given in terms of conductor current i_{rms} by:

$$B_1 = 0.049\, i_{rms} + 0.520 \text{ T} \qquad (4.24)$$

$$B_2 = 0.017\, i_{rms} + 1.242 \text{ T} \qquad (4.25)$$

$$B_1' = 0.045\, i_{rms} + 0.520 \text{ T} \qquad (4.26)$$

$$B_2' = 0.007\, i_{rms} + 1.242 \text{ T} \qquad (4.27)$$

Eq. (4.24) to Eq. (4.27) are plotted versus conductor stator current r.m.s. in fig. 4.18. Clearly, it is tooth 2 which initially carries the largest value of flux density for a given stator current. Additionally, the condition of peak current in one phase is the most severe case. According to the iron magnetisation characteristic shown in fig. 4.4, the maximum flux density in the stator core without saturation being experienced is B = 1.6 T. Then, from fig. 4.18 the maximum current allowable for avoiding magnetic circuit saturation is i_{rms} = 22.0 A.

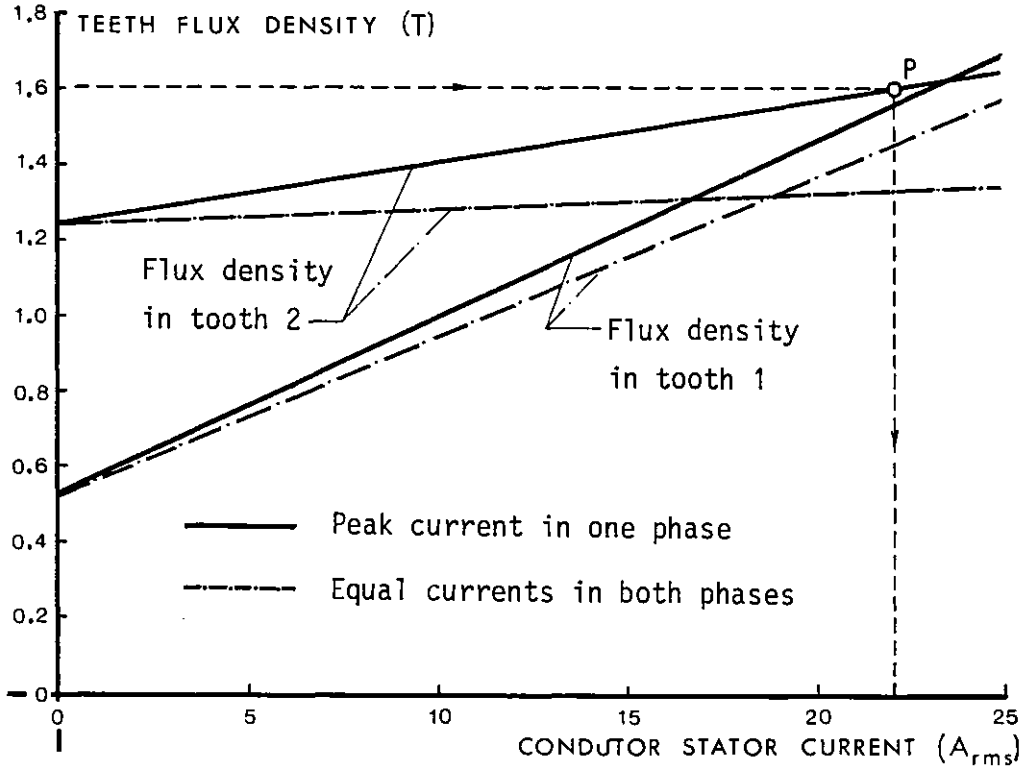

Fig. 4.18 - Flux density in teeth versus stator current for a fixed excitation flux density $\hat{B}$ = 0.547 T

From Eq. (1.39), with slot opening a = 2.5 mm and the permissible current i_{rms} = 22 A, the maximum tooth tip flux density occurring between tooth 2 and tooth 3, is

$$B_{t23} = \mu_o \frac{2n\sqrt{2}}{a} i_{rms} = 0.75 \text{ T}$$

which is far short of saturation. Also, from Eq. (1.140) the flux density in the backing iron with thickness b = 50 mm, for the fundamental excitation

flux $\hat{B}_1 = 0.547$ T, is

$$B_c = \frac{4w}{\pi b} \hat{B}_1 = 0.35 \text{ T}$$

Then, as expected, the teeth are the region of the magnetic circuit that are the first to saturate.

4.9.2 - Current limit for starting demagnetisation of the permanent magnets

As seen in the no-load field plot shown in fig. 4.11 the self-demagnetisation field in the magnet takes place in the region of the first step caused by the long effective air gap. For a 90°E torque angle the maximum stator surface potential has also its higher value in this region, as shown in fig. 4.19. It is this region where the permanent magnet is

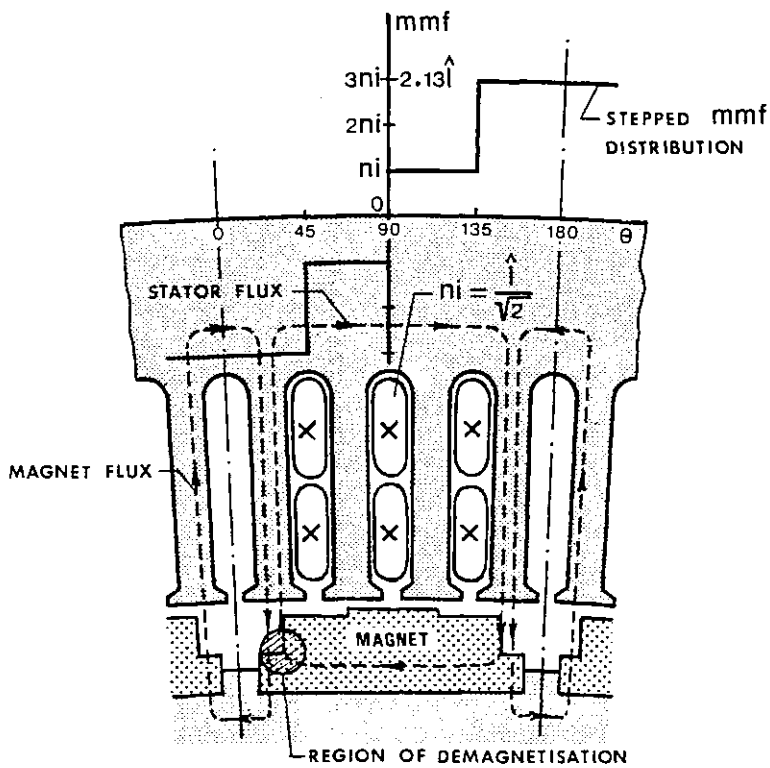

Fig. 4.19 - Region of permanent magnet demagnetisation at the instant of equal currents

hence most vulnerable to demagnetisation under the specific load conditions. Clearly, the most severe case is at the instant of equal currents in each phase, since at this condition the potential attained by the

stator is 7% higher than that at the instant of peak current in one phase. Fig. 4.20 shows a computed load equipotential plot for this condition, when a conductor current of i_o = 10 A_{rms} is flowing on the stator with the m.m.f. situated on the q-axis. From this plot it can be seen that the equipotentials are more closely spaced in the region of the first step of the magnet. As already seen in fig. 2.38, here due also to the stator m.m.f., the field is distorted, increased at one end of the pole and weakened at the other.

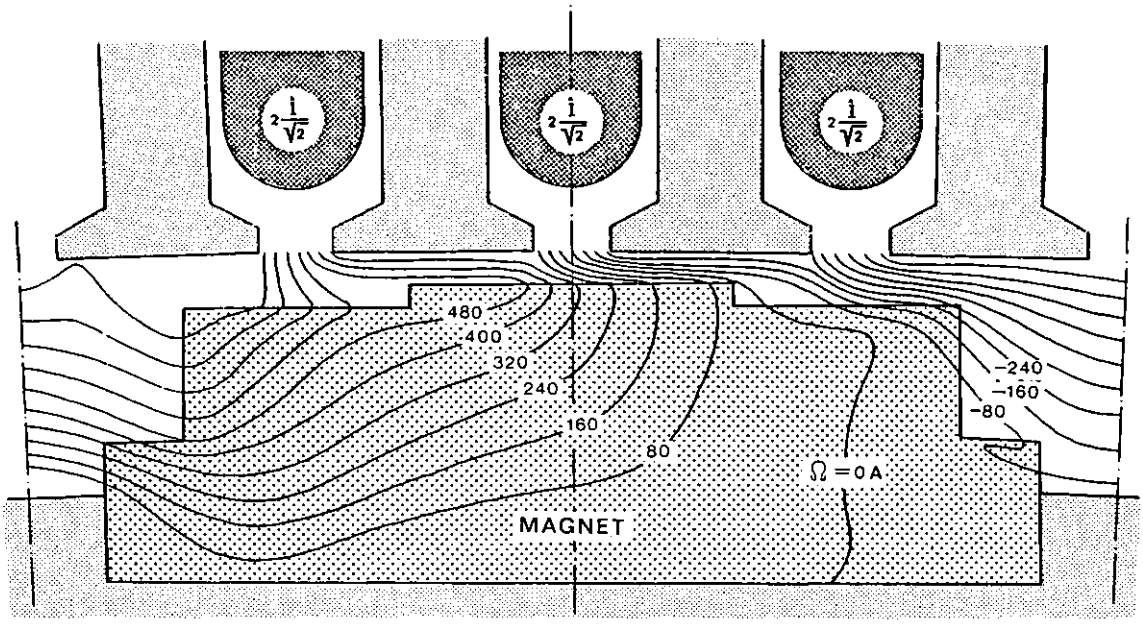

Fig. 4.20 - Computed load equipotential plot for q-axis position at instant of equal currents in each phase

The region of demagnetisation considered is situated at an m.m.f. angle of θ = 24°E between actuator radii r_{11} = 465.68 mm and r_{12} = 465.00 mm. Extracts of the computer program described in Appendix D are shown in fig. 4.21 for the relevant nodes of this specific region. In fig. 4.21(a) is displayed the no-load magnetic potential distribution and in fig. 4.21(b) the potential distribution due just to the stator m.m.f. (magnet flux generators removed).

From fig. 4.21(a) the demagnetising force H values in the permanent magnet may be obtained by taking the gradient of the scalar potential

field. The mesh distance between adjacent nodes is $r_{11} - r_{12} = 0.68$ mm, then the radial H values at points 1, 2 and 3 of the mesh are respectively:

$$H_{01} = \frac{365.3 - 332.4}{0.68 \times 10^{-3}} = 48.38 \text{ kA/m}$$

$$H_{02} = \frac{430.2 - 340.7}{0.68 \times 10^{-3}} = 131.62 \text{ kA/m}$$

$$H_{03} = \frac{391.5 - 348.6}{0.68 \times 10^{-3}} = 63.09 \text{ kA/m}$$

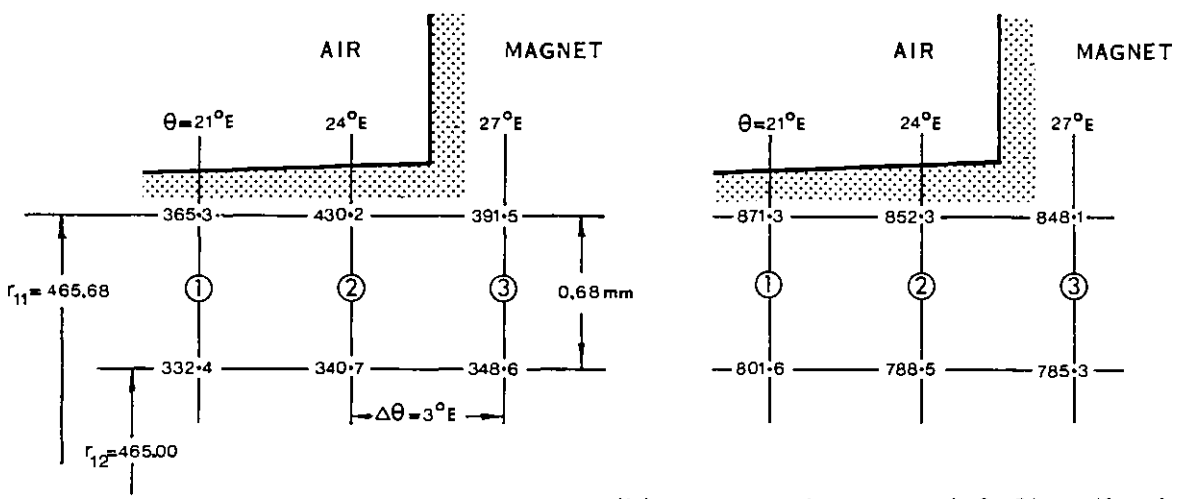

(a) - No-load magnetic potential distribution

(b) - Magnetic potential distribution for $i_o = 10\ A_{rms}$ with flux generators removed

Fig. 4.21 - Relevant parts of computed magnetic potentials under no-load and stator current conditions

For the same region and assuming linearity, the corresponding H values for a general current i_{rms} with a current $i_o = 10\ A_{rms}$ flowing are obtained from fig. 4.21(b) in a similar manner as:

$$H_{I1} = \frac{i_{rms}}{i_o} \frac{871.3 - 801.6}{0.68 \times 10^{-3}} = 10.25\, i_{rms} \text{ kA/m}$$

$$H_{I2} = \frac{i_{rms}}{i_o} \frac{852.3 - 788.5}{0.68 \times 10^{-3}} = 9.38\, i_{rms} \text{ kA/m}$$

$$H_{I3} = \frac{i_{rms}}{i_o} \frac{841.1 - 785.3}{0.68 \times 10^{-3}} = 9.23\, i_{rms} \text{ kA/m}$$

Hence, as explained in section 2.7.5.a , the resulting magnetising force H for any load condition is given by superimposing both results. For the region considered Eq. (2.53) gives:

$$H_{L1} = 48.38 + 10.25\, i_{rms} \tag{4.28}$$

$$H_{L2} = 131.62 + 9.38\, i_{rms} \tag{4.29}$$

$$H_{L3} = 92.35 + 9.23\, i_{rms} \tag{4.30}$$

From the above results, it is clear that the largest value of demagnetisation field is given by Eq. (4.29). The maximum permissible demagnetisation force is assumed to be the normal coercive force H_c and the magnet manufacturer's quote for B.P.R.E. material a coercive force of H_c = 350 kA/m. Then, replacement of H_{L2} by H_c gives for the maximum permissible stator current without magnetisation

$$i_{rms} = \frac{350 - 131.62}{9.38} = 23.28 \text{ A} \tag{4.31}$$

This result is the same order to the current limit for avoiding magnetic circuit saturation determined in the previous section. Thus, magnet demagnetisation and magnetic circuit saturation are reached at the same level of stator current!

4.10 - FUNDAMENTAL ELECTROMAGNETIC TORQUE

From Eq. (1.46), the fundamental electromagnetic torque developed by the two-phase actuator when current-fed at a 90°E torque angle is given by

$$T_1 = n_p R_g \ell N \hat{B}_1 K_{W1} \sqrt{2}\, i_{rms} = K_T i_{rms} \tag{4.32}$$

where n_p is now the number of rotor poles. Substitution of values: n_p = 18 poles, R_g = 0.4725 m, ℓ = 0.114 m, N = 2nq = 2 x 24 x 2 conductors per pole per phase, $\hat{B}_1$ = 0.547 T and K_{W1} = 0.832, gives for the torque constant:

$$K_T = \frac{T_1}{i_{rms}} = 59.73 \text{ Nm/A}_{rms} \tag{4.33}$$

As seen previously, the limitation in stator current set by magnet demagnetisation and magnet circuit may be taken as i_{rms} = 22.5 A. Then, maximum possible fundamental torque with linear operation becomes:

$$T_1 = K_T i_{rms} = 1344 \text{ Nm} \simeq 1000 \text{ lb.ft.} \tag{4.34}$$

The total actuator weight was found to be W_t = 176 kg. Hence, the maximum torque per weight is

$$\frac{T_1}{W_t} = 7.64 \text{ Nm/kg}$$

a high figure compared with the majority of commercially produced, non-conventional electric motors [83].

4.11 - PREDICTED RIPPLE TORQUE

Ripple torque is a very important machine parameter for a low speed "torquemotor". The winding factors shown in table 4.1 and the air gap flux density harmonic coefficients displayed in fig. 4.11 make it possible to predict the ripple torque of the actuator. From Eq. (1.45) the peak theoretical p.u. ripple torque for the first two ripple torque components (assuming sinusoidal currents-fed at θ = 90°E torque angle) is given by:

$$\frac{\hat{T} - T_1}{T_1} = \frac{1}{K_{W1}} \left(|K_{B5}K_{W5} - K_{B3}K_{W3}| + |K_{B9}K_{W9} - K_{B7}K_{W7}| \right)$$

Substitution of values of the winding factors and field harmonic factors previously calculated, gives:

$$\frac{\hat{T} - T_1}{T_1} = 0.021 \tag{4.35}$$

Hence, the maximum theoretical ripple torque is 4.2% peak to peak, which is acceptable for precision control applications.

4.12 - TEST RESULTS

A set of tests were performed on the actuator in order to check the accuracy of the parameters previously calculated. Torque constant, ripple torque, winding inductance, air gap flux density, temperature-rise, rotor inertia and viscous damping coefficient were measured, and the method used is explained in some detail in the following sections.

4.12.1 - Static torque tests

The test rig used to measure the shaft torque for each angular position of the rotor is shown in fig. 4.22. For good angular accuracy a scale of 0.8 m radius with 0.25° mechanical (9°E) divisions was drawn,

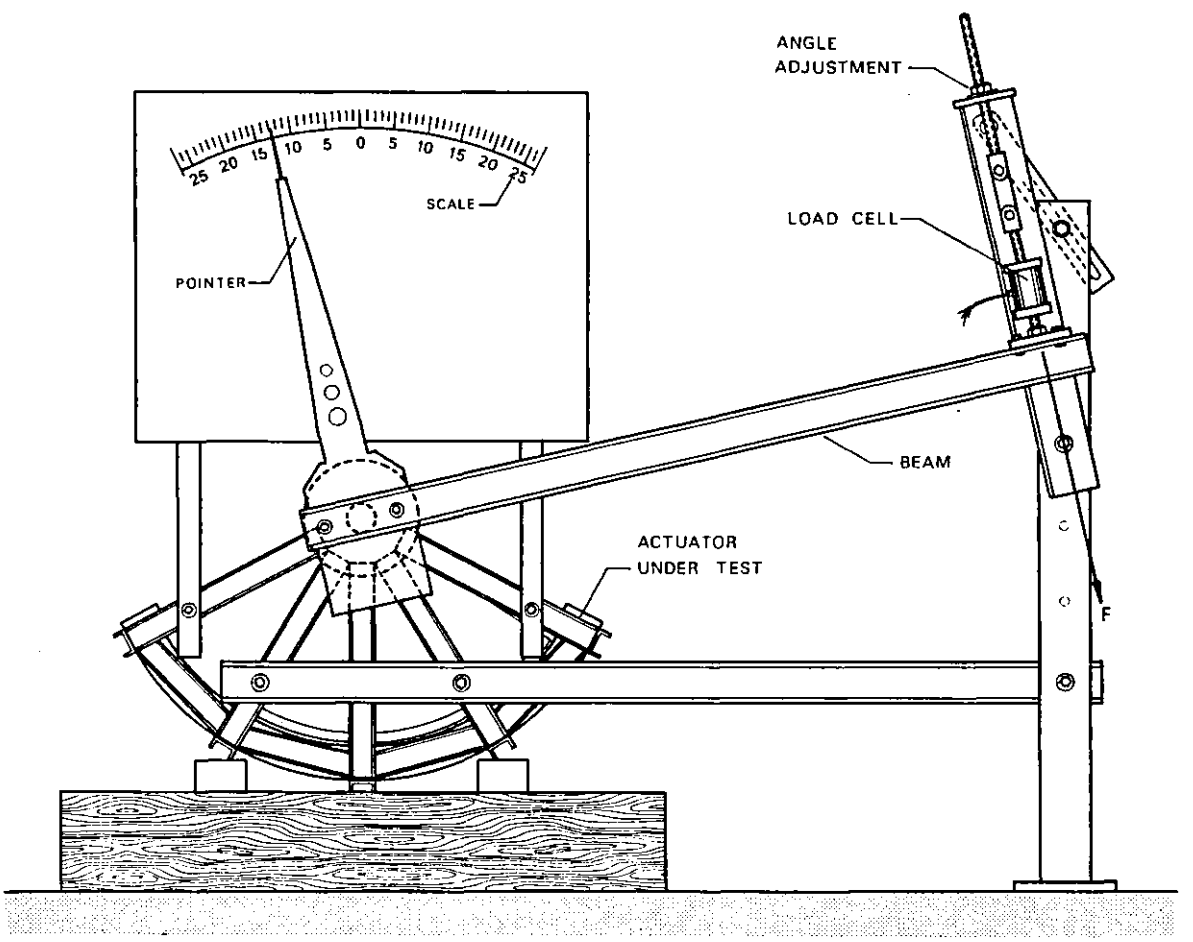

Fig. 4.22 - Mechanical layout for static torque test

fixed to the stator and centered on the shaft. The force produced was measured by means of a load cell mounted on the end of a 1.395 m steel beam, fixed to the actuator shaft. The rotor was then clamped and its

position adjusted by means of a special device that ensured that the force at the end of the beam was always in line with the load cell axis. With this device it was possible to measure the static torque over a range of ±25° mechanical about the centre position.

The circuit used to supply the two phases of the actuator is shown in fig. 4.23. Each phase was supplied by a separately excited 400 V d.c. generator, whose excitation could be varied in order to control the injected phase current. A 10 Ω, 30 A resistance was connected in series to allow

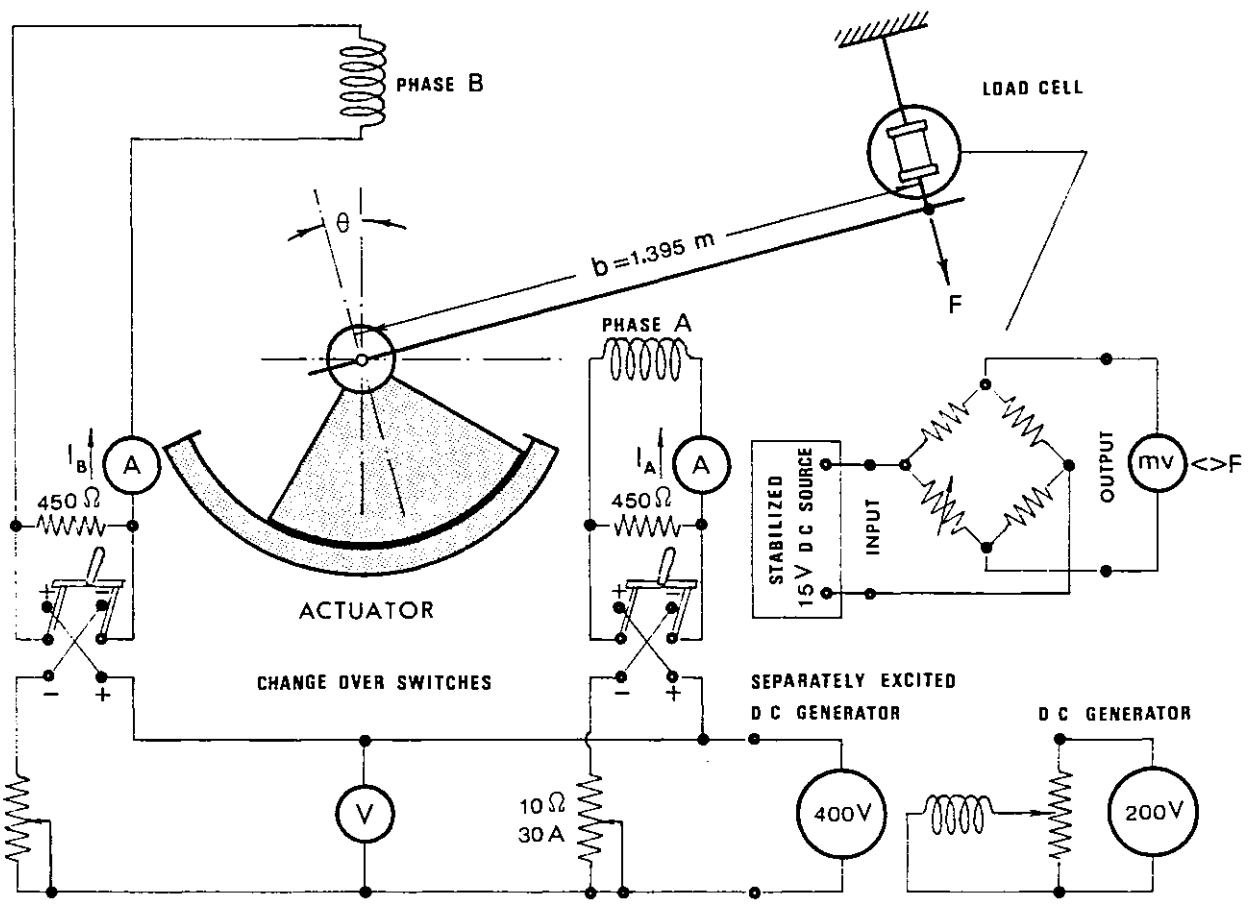

Fig. 4.23 - Circuit diagram for static torque measurement

for different phase currents if required and a 450 Ω resistance was placed in parallel with each phase to avoid large back e.m.f.'s at switch-off. Since the force varies in direction depending on the rotor position a change-over-switch was included in order to ensure that the force was always downwards.

The load cell, which was used in a Wheatstone bridge configuration,

was calibrated by using standard weights and reading the corresponding output voltage on a digital millivoltmeter. The characteristic was linear over the range of the force used. For each angular position, the unenergised reading, which takes into account the normal component of the beam weight, was recorded. This value was then subtracted from the energised reading to give the correct value of force.

a) - Torque versus torque angle characteristic for fixed excitation

In order to check if the two-phase winding was correctly connected and to examine the effects of possible saliency in the rotor, the torque versus torque angle characteristic was measured. A constant d.c current of $I_{d.c.}$ = 11 A, about half of rated current to avoid any risk of demannetisation at any rotor position, was used during this test. The resultant force F, hence torque T = Fb, was measured over a range of ±21.25° mechanical (maximum rotor displacement limited by the end-stops) in steps of 0.25° mechanical (or 9°E).

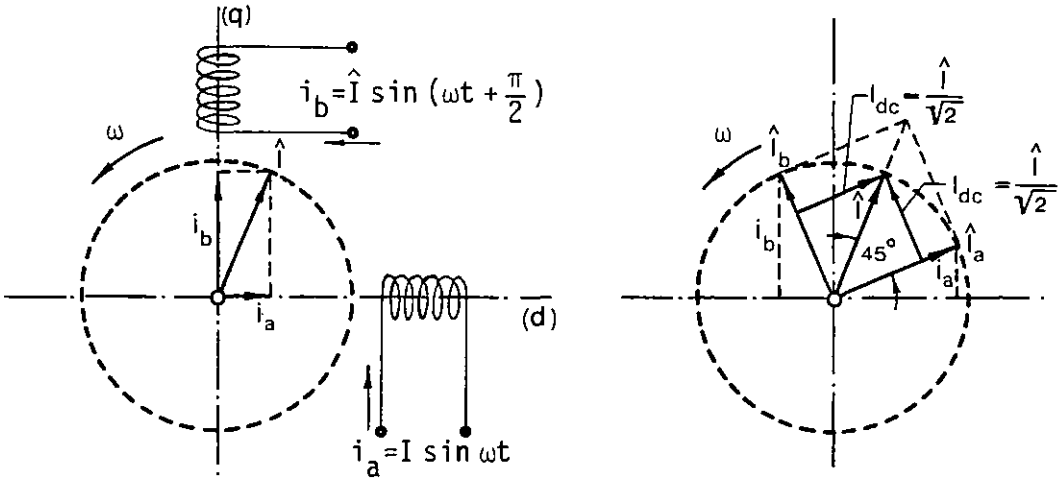

Fig. 4.24 - Total m.m.f. for a two-phase motor

Tests were made when each phase was fed alone and when both phases were fed simultaneously with equal d.c. currents. As far as torque is concerned, when both phases are supplied with equal $I_{d.c.}$ currents, conditions are equivalent to those occurring when a two-phase, position-sensor-controlled, sinusoidally varying feed is connected having a peak

current of $\hat{I} = \sqrt{2}\, I_{d.c.}$, since the two-phase currents combine to give a total m.m.f. $\hat{I}$, as shown diagrammatically in fig. 4.24.

From Eq. (3.60) the torque versus torque angle characteristic for the actuator is given by

$$T = K_T I \sin\theta + \frac{1}{2} I^2 (L_d - L_q) \sin 2\theta \qquad (4.36)$$

where I is the r.m.s. phase current and L_d and L_q are the d and q-axis air gap inductances corresponding to the n_p' poles calculated in table 4.3. Hence $L_d - L_q = -1.36$ mH, but from Eq. (4.33) is $K_T = 59.73$ Nm/A_{rms} and substitution into Eq. (4.36) and simplification gives the torque when both phases excited with $I = 11\ A_{rms}$ as:

$$T_{AB} = 657 \sin\theta - 0.08 \sin 2\theta \quad \text{Nm} \qquad (4.37)$$

When one phase only is excited, the torque for each phase becomes:

$$T_A = 466 \sin(\theta + 45°) - 0.08 \sin 2(\theta + 45°) \quad \text{Nm} \qquad (4.38)$$

$$T_B = 466 \sin(\theta - 45°) - 0.08 \sin 2(\theta - 45°) \quad \text{Nm} \qquad (4.39)$$

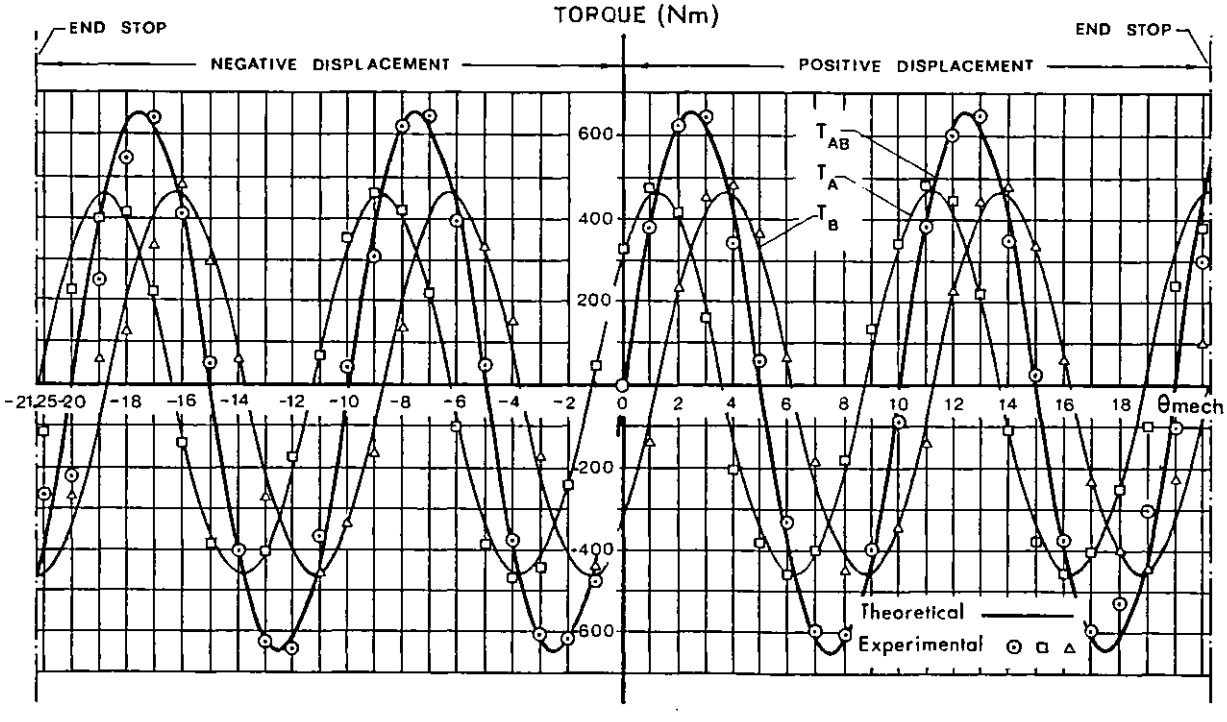

Fig. 4.25 - Torque versus rotor angle position for each phase and both phases excited with a d.c. current of 11 A

The measured torque versus rotor angular position is plotted for both cases in fig. 4.25, together with the theoretical characteristics obtained from Eq. (4.37) to Eq. (4.39).

As can be seen from the diagram, there is a close agreement between measurement and theory and the characteristics show a fairly sinusoidal variation over the entire range of rotor displacment, except at the end regions. Hence, as expected, the actuator has torque/angle characteristics identical to a round machine. Torque for each phase is shifted 90°E in space between them and the maximum torque achieved is practically the same in each cycle. This indicates that the machine is correctly balanced.

b) - Maximum torque versus stator current characteristic

In order to attempt to reach the appropriate demagnetisation or saturation torque limits, the rotor was locked at a maximum torque position and equal d.c. currents in the range 0 - 35 A were injected in each phase simultaneously. The chosen angular rotor positions were ± 2.5 and ± 7.5 mechanical degrees shown in fig. 4.25, which corresponds in a sinusoidal current-fed mode to 90°E torque angle position. The four results were then averaged and plotted in fig. 4.26 versus stator excitation.

The characteristic shows no signs of saturation up to a torque level about 1350 Nm at a current of 24.28 A_{rms}. This torque limit was deliberately exceeded, and when a current level some 30% higher was used, some levelling off of the characteristic above 1400 Nm torque level occurred as can be seen. This levelling off may be attributed to magnetic circuit saturation and possibly due to magnet demagnetisation. However an important additional factor is thought to be incorrect torque angle adjustment, since at this current level appreciable forces are involved. Nevertheless the mechanical performance of the machine under high torque conditions was satisfactory and the grooved locating technique used with the magnets seemed to be successful.

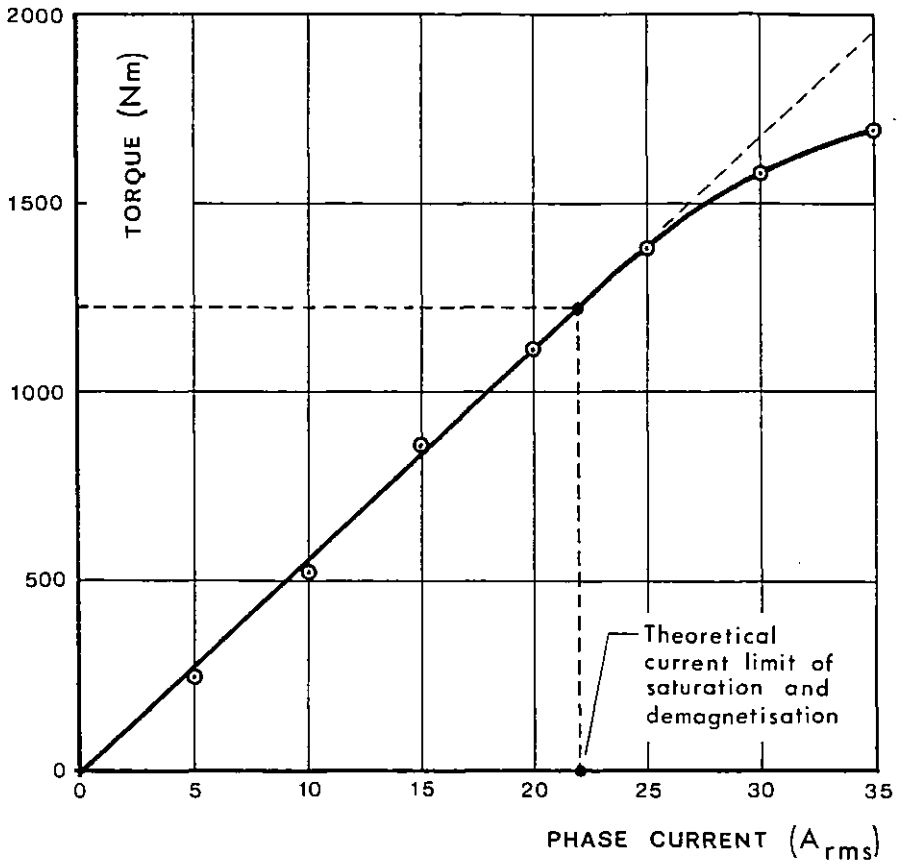

Fig. 4.26 - Measured torque versus phase current characteristic for 90°E torque angle

From fig. 4.26 the initial gradient indicates a torque constant value of K_T = 55.6 Nm/A_{rms} which is 7% below the design figure of 59.73 Nm/A_{rms} and this does not seem unreasonable.

c) - Ripple torque measurement

When the actuator is fed from a current-forced auto-piloted supply, with the position sensor set at 90°E torque angle, the torque developed, as seen in section 1.5, would be:

$$T = T_1(1 + A\cos 4\omega t + B\cos 8\omega t) \tag{4.40}$$

where

$$A = \frac{K_{B5}K_{W5}}{K_{W1}} + K_{I5} - \frac{K_{B3}K_{W3}}{K_{W1}} - K_{I3} \tag{4.41}$$

and

$$B = \frac{K_{B9}K_{W9}}{K_{W1}} + K_{I9} - \frac{K_{B7}K_{W7}}{K_{W1}} - K_{I7} \tag{4.42}$$

are the magnitudes of the parasitic torques, which are responsible for the ripple torque. As can be seen from Eq. (4.41) and Eq. (4.42) two ripple components for the torque occur. The first component, a function of stator winding factors and air gap flux distribution, is a characteristic of the machine itself. The second, depending on the time harmonic coefficients in the current waveform, is a characteristic of the electronic source used to supply the machine. In this test only the first component will be measured.

For a pure sine wave current ($K_{I3} = K_{I5} = \ldots = 0$), substitution into Eq. (4.41) and Eq. (4.42) of the winding factor values calculated in table 4.1 and the field flux density factors shown in fig. 4.11, Eq. (4.40) gives the first p.u. theoretical component as:

$$\frac{\hat{T} - T_1}{T_1} = -0.006 \cos 4\omega t - 0.015 \cos 8\omega t \qquad (4.43)$$

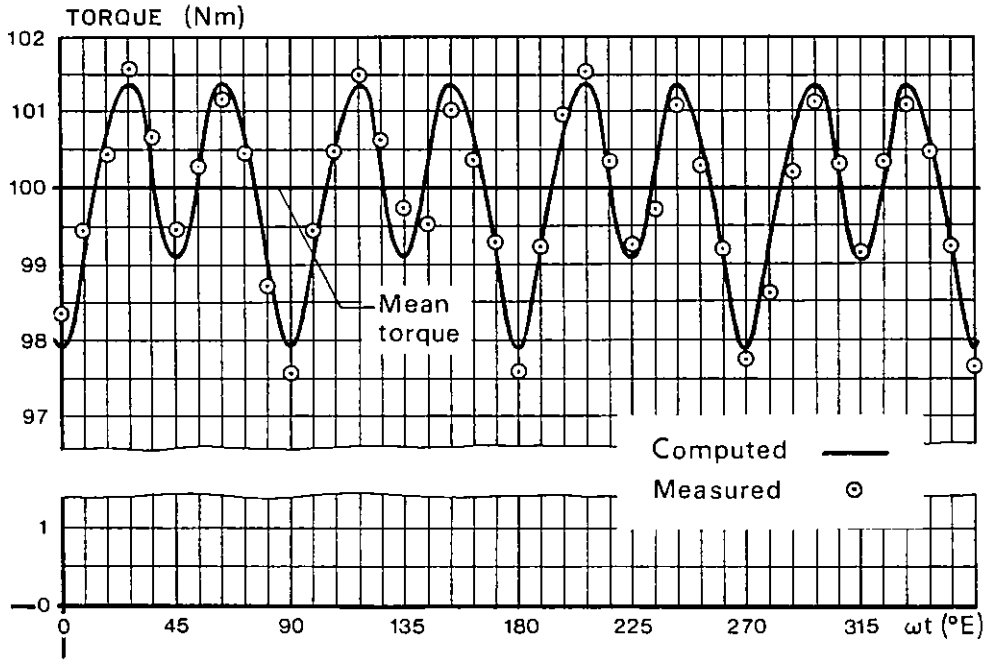

Fig. 4.27 - Measured and computed ripple torque for a sinusoidal peak current of $\hat{I}$ = 2.54 A at 90°E torque angle

The first ripple component was measured by injecting in each phase of the acutator the appropriate d.c. current in order to simulate the conditions of a two-phase sinusoidal system at various points in the a.c.

cycle, as explained in fig. 4.24. This test was carried out at intervals of 9°E for a torque at 90°E torque angle in the range of two pole pitches in the middle position of the rotor actuator. A mean fundamental torque of T_1 = 100 Nm was chosen and using the measured figure of K_T = 55.6 Nm/A_{rms} obtained in the previous test, a peak current of $\hat{I}$ = 2.54 A was taken as a basis for calculating the instantaneous phase currents to be injected at the respective rotor angular positions within the tested range. The measured torque results are plotted in fig. 4.27, together with the theoretical values obtained from Eq. (4.43).

As can be seen from the diagram, the torque waveform repeats four times as the rotor rotates through a double pole pitch (the lowest frequency harmonic occurring being the fourth), and the maximum peak to peak torque ripple is about 4.5%. This is in very good agreement with the theoretical value given by Eq. (4.35). The results of this test show the importance at design stage of the correct calculation of the permanent magnet profile and winding arrangement, if ripple torque is to be minimised. Symmetry in the entire mechanical assembly is clearly also desirable.

4.12.2 - Stator winding inductance measurement

The conventional method for measurement of the direct and quadrature-axis synchronous inductance of a synchronous machine is the so-called slip test. With the rotor unexcited a normal positive-sequence voltage is applied to the stator and the machine is driven near the synchronous speed with a low value of slip. In these conditions, oscillograms of the e.m.f. induced in the rotor winding, applied voltage and armature current are taken and from them the influence of rotor position on the stator impedance is studied. The method [14] has the advantage of direct measurement.

Obviously, this method is not applicable to the actuator for two reasons: first, the permanent magnet excitation cannot be removed and second, due to its limited motion, a continuous rotor speed near to synchronism

cannot be achieved. Hence, some other type of test must be used and two possible tests, one using a d.c. inductance bridge and one using a.c., are described below.

i) - D.c. inductance bridge

This method is described by Jones [84] and the bridge circuit used is shown in fig. 4.28(a) in which resistances R_2, R_3 and R_4 must be non-inductive. The branch R, L represents the resistance and inductance of one phase winding of the machine which has its rotor clamped in a given position θ. The instrument across the bridge is a voltage-integrator which therefore reads flux linkage with the circuit and may be either a ballistic galvanometer with a series resistor or a Grassot fluxmeter.

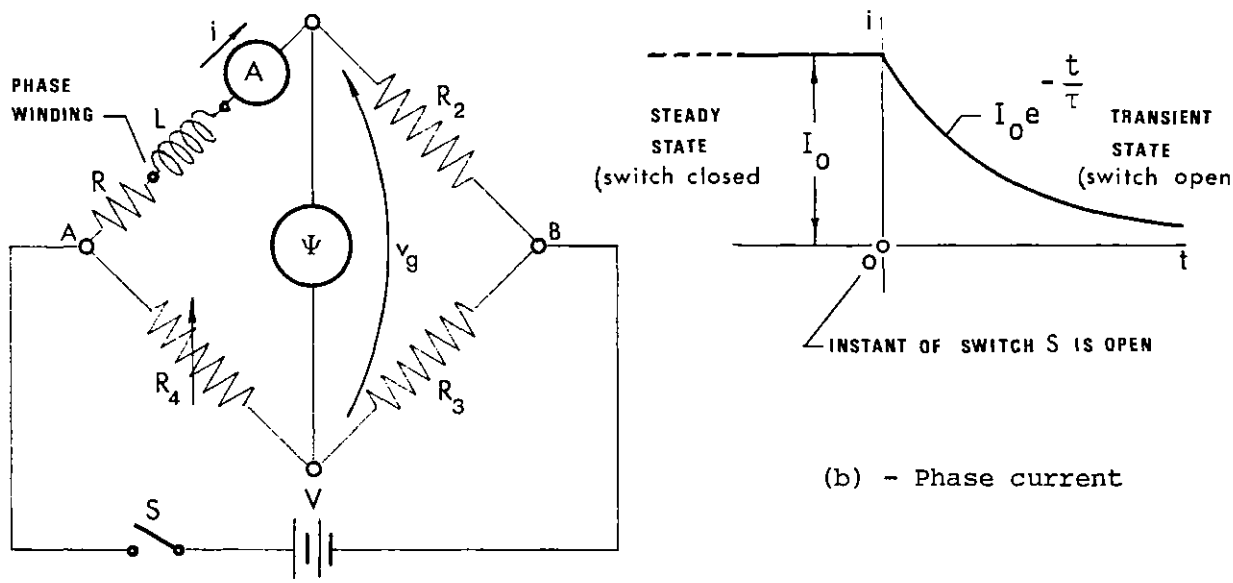

(a) - Bridge arrangement

(b) - Phase current

Fig. 4.28 - D.c. self-inductance bridge

At the beginning of the test switch S is closed, and after a sufficient time a steady-state d.c. current flows through the winding, as shown in fig. 4.28(b). At this stage the bridge is balanced by adjusting R_4 until there is no voltage across the fluxmeter, which implies $RR_3 = R_2R_4$, and current I_0 is recorded.

Since the bridge is balanced, the instantaneous voltage across R_3 will be

$$v_3 = \frac{R_3}{R_3 + R_4} v = \frac{R_2}{R + R_2} v$$

where v is the instantaneous voltage across the bridge AB during the transient period. The instantaneous voltage across R_2 will be

$$v_2 = \frac{R_2}{R + R_2} v - \frac{R_2}{R + R_2} L \frac{di}{dt}$$

Hence, the instantaneous voltage v_g across the fluxmeter becomes:

$$v_g = v_2 - v_3 = - \frac{R_2}{R + R_2} L \frac{di}{dt}$$

The deflection of the fluxmeter is proportional to the time integral ψ of this voltage, so that

$$\psi = \int_o^\infty v_g dt = - \frac{R_2}{R + R_2} L \int_o^\infty \frac{di}{dt} dt = - \frac{R_2}{R + R_2} L \int_{I_o}^o di = \frac{R_2}{R + R_2} L I_o$$

and the inductance L is therefore given by the expression

$$L = \left(1 + \frac{R}{R_2}\right) \frac{\psi}{I_o} \qquad (4.44)$$

In particular, if R_3 and R_4 are made equal and the bridge balanced by varying R_2, then Eq. (4.44) reduces to $L = 2\psi/I_o$. The influence of hysteresis can be drastically reduced by reversing the bridge supply instead of switching OFF, but in this case the above formulae for L must be divided by two.

This technique was used successfully for the inductance measurement of the disc machine (described in Chapter 5) employing a Grassot fluxmeter.

ii) - A.c. inductance test

This test consists simply of supplying the phase winding with a sinusoidal voltage and a known fixed frequency ω and measuring the respective impedance. Measuring the d.c. winding resistance R, the inductance L is then obtained.

Since inductance is by definition flux linkage/current it should be pointed out that the flux set up by the permanent magnet, although linking with the winding, does not of course affect the measurement. In fact, consider one single coil linked with the magnet excitation flux ψ_{mag}, as shown in fig. 4.29(a). When the coil is excited with a sinusoidal

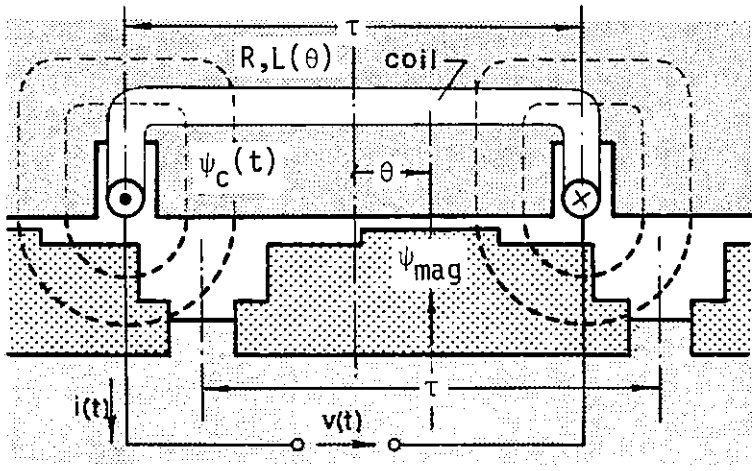

(a) - Coil and magnet arrangement

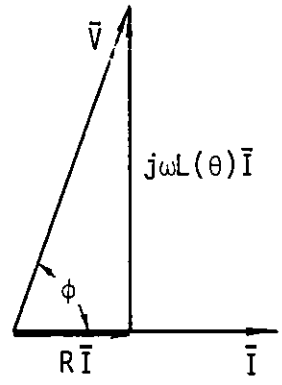

(b) - Phasor diagram

Fig. 4.29 - Flux linkage with the coil

current i(t), the total instantaneous flux linkage with the coil is given by

$$\psi(t) = \psi_c(t) \pm \psi_{mag}$$

where $\psi_c(t)$ is the flux linkage produced by i(t). Hence, the instantaneous voltage applied should satisfy the relation

$$v(t) = R\,i(t) + \frac{d\psi(t)}{dt} = R\,i(t) + \frac{d\psi_c(t)}{dt} \qquad (4.45)$$

and therefore the current is not affected by the steady flux produced by the magnet. If the magnitude of the a.c. supply is low enough to avoid magnetic circuit saturation, then $\psi_c(t) = L(\theta)i(t)$. Hence, the instantaneous equation (4.45) may be represented by the phasor diagram shown in fig. 4.29(b), whence the inductance is taken as:

$$L(\theta) = \frac{R}{\omega} \tan \phi \qquad (4.46)$$

The resistance R of the circuit seen from the supply terminals is determined by any standard method and therefore only the phase angle ϕ needs to be measured at a given rotor angle position θ. The known frequency ω must be low enough for eddy current effects to be negligible. The eddy current influence in the result may be checked by repeating the tests at different frequencies and signal levels. The influence is negligible if similar results are obtained.

a) - Inductance test results

Although the influence of eddy currents and hysteresis in the d.c. method looks to be less than in a.c. method, the latter method was chosen for simplicity. The inductance characteristic was measured over a range of half a pole pitch in steps of 9°E, and fig. 4.30 shows the arrangement and circuit diagram used.

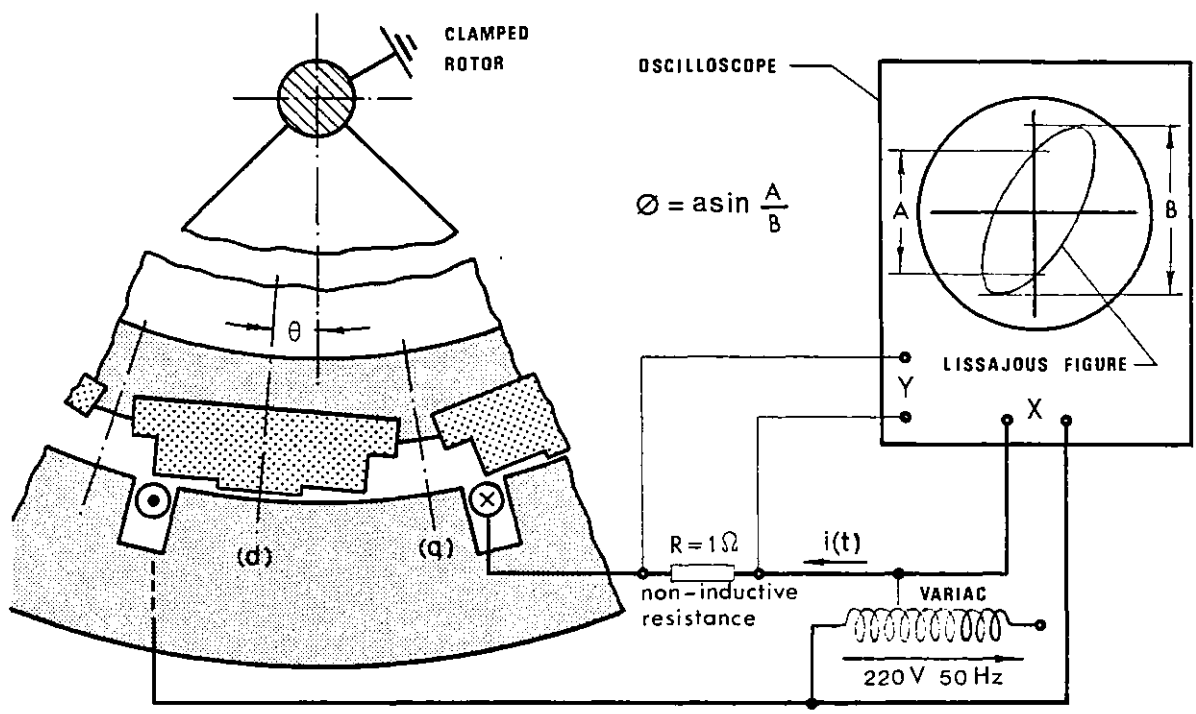

Fig. 4.30 - Layout for a.c. inductance test

It was observed during the test, that due to the sinusoidal current in the winding, the rotor experienced a sinusoidal variation in torque and moved consequently through a corresponding varying angle $\Delta\theta$ even with

the shaft rigidly clamped, except for the d-axis position. To avoid this situation the supply frequency should differ from that of the resonant frequency of the system and the current injected limited to as low a value as possible. From a variac a supply of 14.1 V peak to peak at 50 Hz was used and the phase of the current sensed using a 1.0 Ω non-inductive resistance. The total input resistance of the circuit was measured by means of the volt-amp method as 7.45 Ω and the phase angle ϕ obtained using a Lissajous figure technique on the oscilloscope [85]. Then, from Eq. (4.46) the winding inductance for a rotor position θ is given by

$$L(\theta) = \frac{7.45}{2\pi 50} \tan \phi(\theta) \quad H = 24 \tan \phi(\theta) \quad mH \qquad (4.47)$$

The values obtained for ϕ over the range were then converted into $L(\theta)$ according to Eq. (4.47). The variation is plotted in fig. 4.31, together with theoretical values for comparison. The theoretical values were obtained as the sum of the total leakage inductance of L_ℓ = 32.16 mH given by Eq. (4.15) with the skewed air gap inductances given in table 4.3.

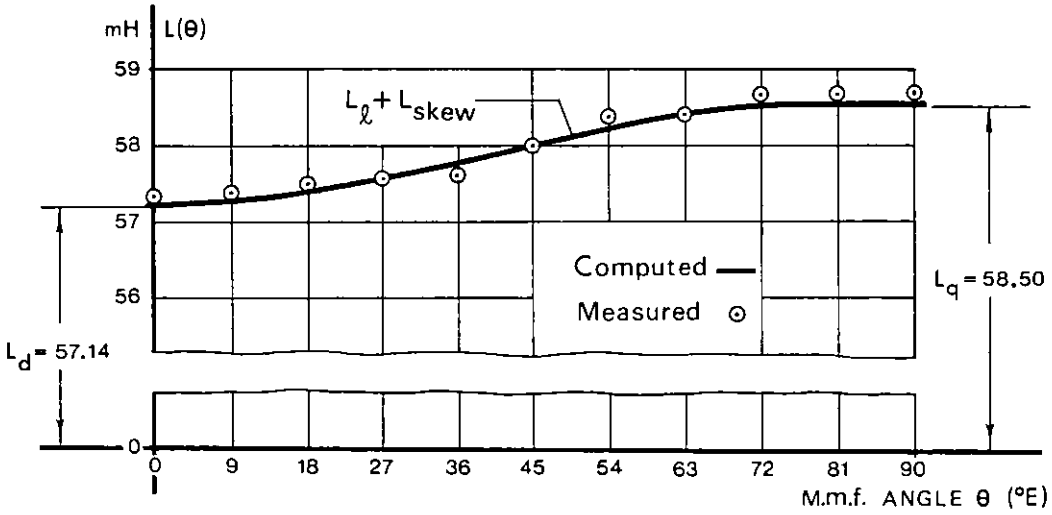

Fig. 4.31 - Computed and measured inductance characteristics

As can be seen from the diagram, all measured results show reasonably good agreement with the appropriate theoretical values.

4.12.3 - Air gap flux density measurement

The air gap flux density measurement due to the magnet excitation was carried out using a Grassot fluxmeter and readings were taken over a double-pole pitch in steps of 9°E. A tooth pitch search coil of fine gauge wire attached to the skewed stator surface was directly connected to the fluxmeter, as shown in fig. 4.32.

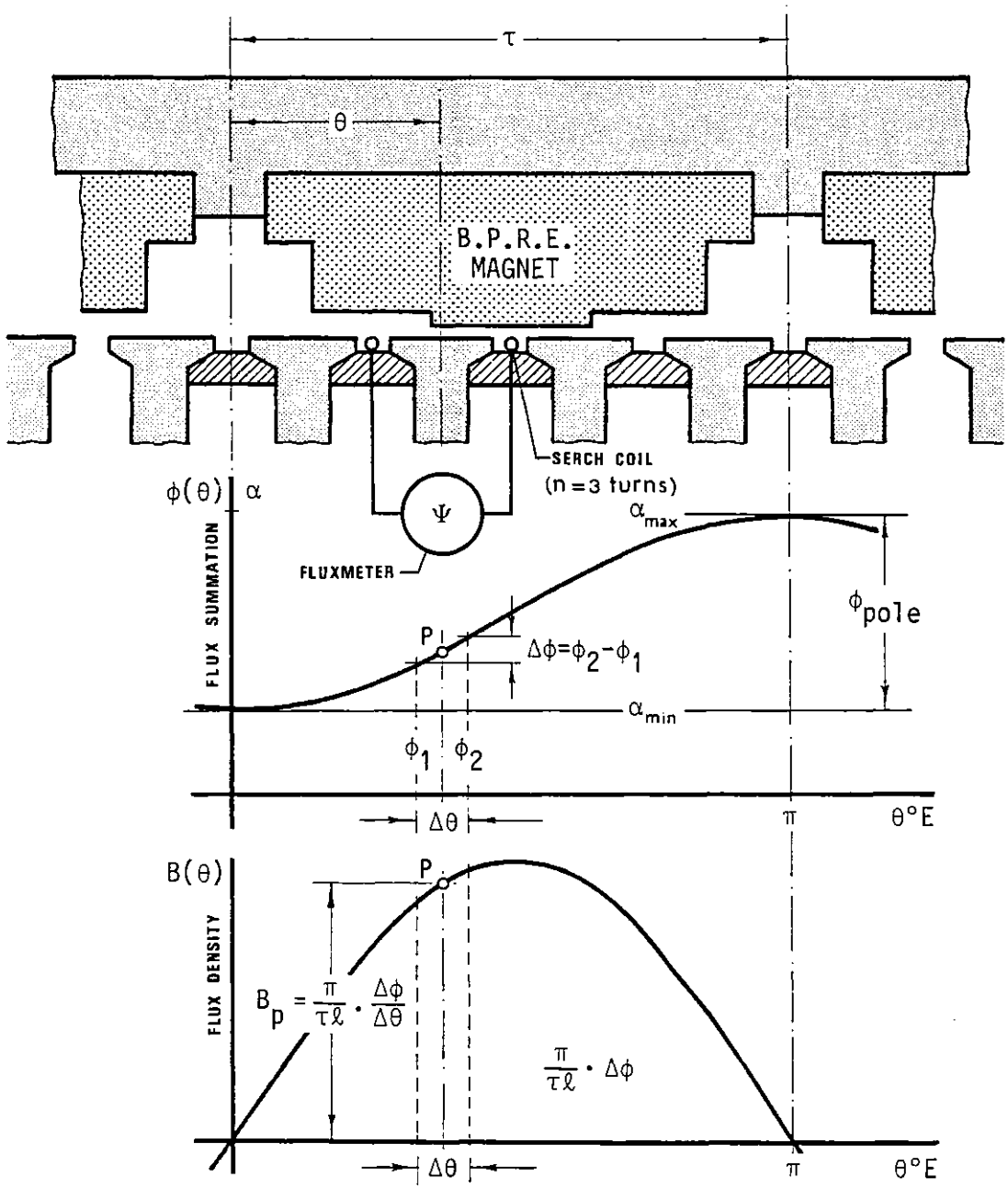

Fig. 4.32 - Basic air gap flux density test arrangement

It is well known that the fluxmeter is a moving-coil galvanometer in which the control torque has been made negligible by using very fine ligaments of annealed silver to lead the current into and out of the moving

coil. For an angular deflection $\Delta\alpha$ the fluxmeter reads a change of flux $\Delta\phi$ which according to the theory [85] is given by

$$\Delta\phi = \frac{g}{n}\,\Delta\alpha \tag{4.48}$$

where g (Wb x turn/degree) is the fluxmeter constant and n is the search coil number of turns. The instrument then measures changes of flux linking the search coil and therefore can be considered as a flux-integrator.

With the instrument used was $g = 10^{-3}$ Wb x turn/degree and n = 3 turns became the ideal number of turns on search coil as it resulted in a full scale deflection for this particular test. The values $\phi(\theta)$ given by Eq. (4.48) with g/N = 0.33 mWb/degree were then plotted over a double-pole pitch. Clearly, the difference between the maximum α_{max} and minimum fluxmeter deflection α_{min} in that range gives

$$\phi_{max} - \phi_{min} = 0.33(\alpha_{max} - \alpha_{min}) \quad \text{mWb}$$

which is the flux per pole. It was measured as $\phi_{pole} = 1.54$ mWb. From fig. 4.11 the calculated fundamental wave flux density has a peak value of $\hat{B}_1 = 0.547$ T. Hence, the theoretical approximate flux per pole should be

$$\phi_{pole} = \frac{2}{\pi}\,\hat{B}_1\,\tau\ell = 0.637 \times 0.547 \times 41.21 \times 114 \times 10^{-6} = 1.64 \quad \text{mWb}$$

which is not far from the measured value.

Knowing $\phi(\theta)$, the air gap flux density distribution $B(\theta)$ may be easily evaluated by the approximate relation

$$B(\theta) = \frac{\Delta\phi(\theta)}{\Delta S} = \frac{\pi}{\tau\ell}\,\frac{\Delta\phi(\theta)}{\Delta\theta_{elect}} \tag{4.49}$$

where $\Delta\phi(\theta) = \phi_2 - \phi_1$ is the difference of ordinates at extremes of interval $\Delta\theta$ about position θ considered, as shown digrammatically in fig. 4.32. The area enclosed by $B(\theta)$ in a pole pitch is, of course, proportional to the flux per pole, since $B(\theta)$ was found by differentiating $\phi(\theta)$ multiplied by $\pi/\tau\ell$ constant as seen in Eq. (4.49).

Fig. 4.33 shows the air gap flux density measured results obtained by the method described above, together with the computed resulting waveform shown in fig. 4.11 for comparison. The agreement between computed

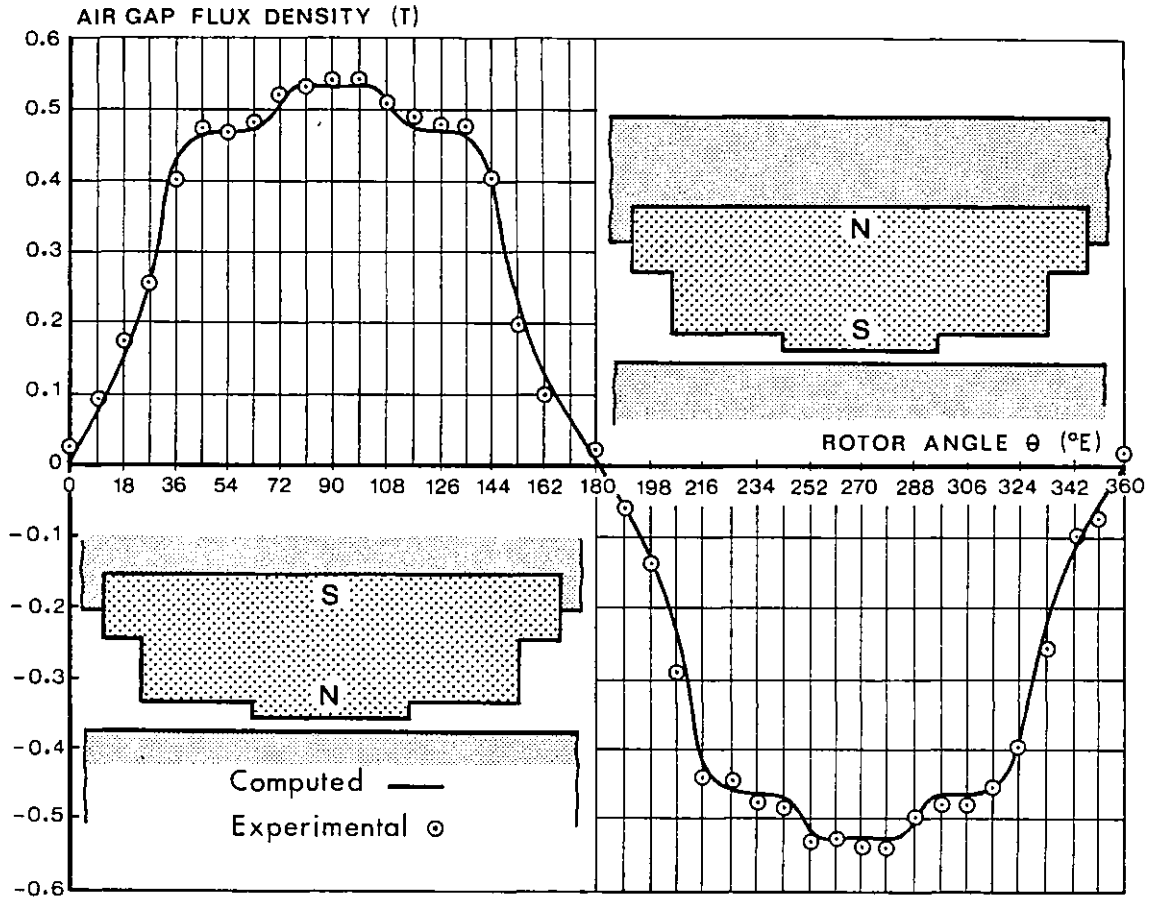

Fig. 4.33 - Computed and measured air gap flux density distribution

and measured air gap flux density distribution seems to be very reasonable, especially in view of the sharp corners associated with the magnet profile. Additionally, in two consecutive poles the corresponding magnitude values of air gap flux density are very similar.

4.12.4 - Temperature-rise test

An ideal homogenous body, internally heated and surface cooled, has a surface temperature-rise directly proportional to the rate of heat production and inversely proportional to the surface of emissivity. Under steady state conditions, the final temperature-rise is reached when the

rates of production and dissipation of heat are equal.

Let the body surface $S(m^2)$, mass G(kg) and specific heat h (J/kg°C) be at temperature θ above the ambient. If p (J/s) is the rate of heat development, in time dt the heat energy pdt is produced, a heat storage $Gh d\theta$ occurs as a result of a temperature-rise $d\theta$, and a heat quantity $\lambda S \theta dt$ is emitted from the surface where λ $(J/s.m^2.°C)$ is the specific heat dissipation. The energy balance is therefore

$$pdt = Gh d\theta + \lambda S \theta dt$$

which solves to the exponential relation

$$\theta - \theta_{amb} = (\theta_f - \theta_{amb}) (1 - e^{-\frac{t}{\tau}}) \qquad (4.50)$$

where θ_{amb} is the room temperature and

$$\theta_f = \frac{p}{\lambda S} \qquad (4.51)$$

is the final temperature-rise reached when all internal heat is dissipated from the surface and there is no further thermal dissipation and

$$\tau = \frac{Gh}{\lambda S} \qquad (4.52)$$

is the heating time constant. Good ventilation gives a small thermal time-constant, since λ is large. In electrical machines, thermal time-constants range from a few seconds to several hours, or even days, depending on the size of the machine, the cooling surface and the efficiency of heat transfer to the coolant [86].

When a hot body is cooling due to a cessation or reduction of the losses developed in it, the temperature-rise is again an exponential function

$$\theta - \theta_{amb} = (\theta_f - \theta_{amb}) e^{-\frac{t}{\tau}} \qquad (4.53)$$

from an initial θ_f. For the ideal homogeneous body postulated, the cooling and heating time-constants are equal. However, in a practical case, the cooling time-constant is greater than the heating time-constant in a

well ventilated machine.

Fig. 4.34 shows a typical exponential heating and cooling temperature rise/time curves corresponding to Eq. (4.50) and Eq. (4.53).

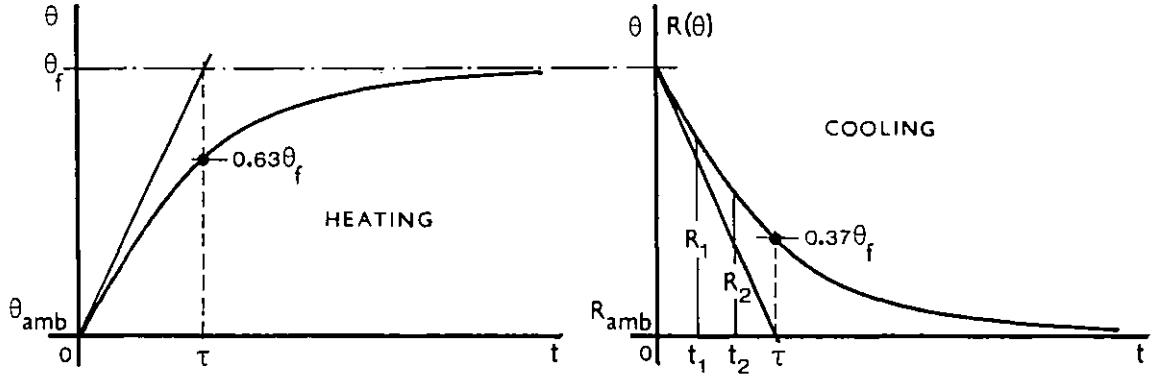

Fig. 4.34 - Exponential heating and cooling temperature-rise curves

The final temperature-rise θ_f in a machine depends on the rate of heat developed $p = R I^2$ in the winding and on the specific heat dissipation λ, which depends on the cooling conditions. In order to determine the maximum steady state winding current I permissible on the thermal grounds, it is necessary to carry out some form of temperature-rise test on the stator. The final temperature-rise θ_f for a given current I and the thermal time-constant τ can be either determined from the measured heating curve or from the cooling curve. However, using the heating curve an extrapolation must be used, since θ_f is only reached at indefinite time. On the other hand, the cooling curve is easily obtained by injecting for a sufficient short time a high current level and then adjusting it afterwards for a low level in order to reach the thermal equilibrium. In practice, thermal equilibrium is reached when the supply voltage no longer needs adjustment to maintain the current I constant. The supply is then switched off and winding temperature measured and plotted versus time from instant at switch OFF to generate a cooling curve.

The temperature may be measured by using:

i) - a thermometer applied to the surface of which the temperature is required.

ii) - a resistance-temperature detector or thermocouple embedded in various parts of the machine.

iii) - a d.c. bridge (finding the variation in winding resistance).

In fact, all three methods were used during the tests. Method i) for measuring the room temperature θ_{amb}. Method ii) for measuring the magnets' temperatures (using a nickel-aluminium wire as a thermocouple of 0.032 mV/°C). Method iii) for measuring the winding resistance by Kelvin bridge. From the relation

$$R(\theta) = R_{amb}\left[1 + \alpha(\theta - \theta_{amb})\right] \tag{4.54}$$

where $\alpha = 0.00382\ °C^{-1}$ for wound copper and R_{amb} is the winding resistance at room temperature θ_{amb}, the temperature θ was then evaluated.

Combination of Eq. (4.53) and Eq. (4.54) gives:

$$R(\theta) - R_{amb} = (R_f - R_{amb})e^{-\frac{t}{\tau}} \tag{4.55}$$

where R_f is the winding resistance at instant of switch OFF. Therefore the cooling curve may be either obtained in terms of winding temperature or winding resistance, as shown in fig. 4.34. If equispaced time intervals t_1 and $t_2 = 2t_1$, corresponding to resistances R_1 and R_2 respectively obtained from the cooling curve are considered, substitution into Eq. (4.55) gives:

$$R_1 - R_{amb} = (R_f - R_{amb})e^{-\frac{t_1}{\tau}}$$

$$R_2 - R_{amb} = (R_f - R_{amb})e^{-\frac{2t_1}{\tau}}$$

From the above equations the following relations hold:

$$R_f = \frac{(R_1 - R_{amb})^2}{R_2 - R_{amb}} + R_{amb} \tag{4.56}$$

$$\tau = \frac{t_1}{\log_e \frac{R_1 - R_{amb}}{R_2 - R_{amb}}} \tag{4.57}$$

The winding temperature at the instant of switch OFF can be obtained by combining Eq. (4.54) and Eq. (4.56):

$$\theta_f = \frac{1}{\alpha R_{amb}} \frac{(R_1 - R_{amb})^2}{R_2 - R_{amb}} + \theta_{amb} \tag{4.58}$$

Having found θ_f from a particular cooling curve produced by a steady state current I at the instant of switch OFF, the maximum steady state current I_{max} to produce the maximum temperature $\theta_{max} - \theta_{amb}$ during a heating cycle, can now be determined. Since the steady state temperature rise θ_f above θ_{amb} is proportional to the losses to be dissipated:

$$\theta_f - \theta_{amb} = \frac{\Delta R}{\lambda S} I^2 \tag{4.59}$$

Assuming ΔR constant, the maximum current I_{max} produces a maximum steady state temperature θ_{max} given by

$$\theta_{max} - \theta_{amb} = \frac{\Delta R}{\lambda S} I_{max}^2 \tag{4.60}$$

Dividing both members of Eq. (4.59) and Eq. (4.60) and re-arranging terms, gives:

$$I_{max} = I \sqrt{\frac{\theta_{max} - \theta_{amb}}{\theta_f - \theta_{amb}}} \tag{4.61}$$

The relevant British Standard Specification N°.2613:1957, gives the limiting temperature rise allowable for class H(180°C) insulation above ambient temperature up to 40°C as $\theta_{max} - \theta_{amb} = 125°C$. Hence, Eq. (4.61) becomes:

$$I_{max} = I \sqrt{\frac{125°}{\theta_f - \theta_{amb}}} \tag{4.62}$$

It should be pointed out that Eq. (4.62) errs on the optimistic side,

since the assumption of constant ΔR in Eq. (4.59) and Eq. (4.60) under constant current conditions is not strictly true, because ΔR increases with temperature-rise.

Found τ from Eq. (4.57) and I_{max} from Eq. (4.62) the winding temperature-rise θ for this current at instant t during a heating cycle can now be determined by substituting $\theta_f - \theta_{amb}$ given by Eq. (4.62) into Eq. (4.50), yields:

$$\theta - \theta_{amb} = 125 \left(\frac{I}{I_{max}}\right)^2 \cdot \left(1 - e^{-\frac{t}{\tau}}\right) \qquad (4.63)$$

Inversely, the maximum time t that any current I may be maintained from switch ON at ambient temperature up to a limit temperature $\theta - \theta_{amb} = 125°C$ is given from Eq. (4.63) by

$$t = -\tau \log_e \left[1 - \left(\frac{I_{max}}{I}\right)^2\right] \qquad (4.64)$$

where I_{max} is the current previously calculated from Eq. (4.62).

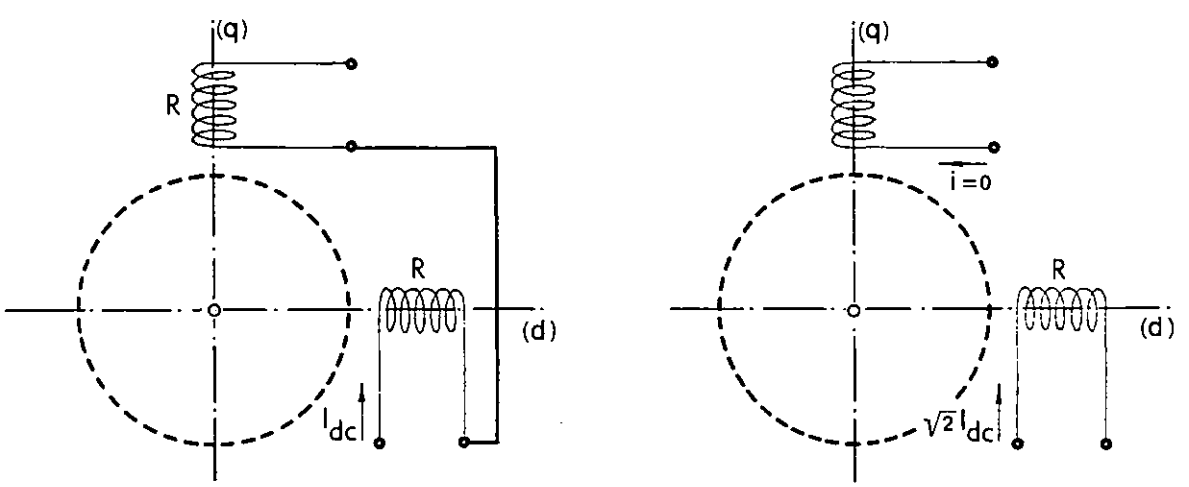

(a) - Equal r.m.s. currents condition (b) - Peak current condition

Fig. 4.35 - Conditions for winding temperature-rise test

In the two-phase actuator, which may be operated in a stalled condition, the thermal loading depends on the operating point in the a.c. cycle. Hence tests were carried out to represent the conditions of equal r.m.s. currents in each phase and peak current in one phase only. For the con-

dition of equal currents, the two-phase windings were connected in series, as shown in fig. 4.35(a). For the peak current condition only one phase was energised with $\sqrt{2}\, I_{d.c.}$, as shown in fig. 4.35(b). Obviously in either condition, assuming equal resistance for both phases, the instantaneous rate of heat developed $2R\, I_{d.c.}^2$ is the same. Test results were obtained for natural cooling and for forced cooling using two 3/4 h.p. blowers and are shown plotted in fig. 4.36 for both conditions. Note no shrouding around the winding end turns was used with the forced-cooling tests, the blower nozzles simply being traversed manually along the actuator arc.

For natural cooling and with two phases supplied with equal currents an interval of t_1 = 10 min is considered in fig. 4.36(a). The resistances R_1 and R_2 are then obtained as 12.71 Ω and 12.51 Ω respectively. With R_{amb} = 10.96 Ω and θ_{amb} = 18°C, Eq. (4.56), Eq. (4.57) and Eq. (4.58) give respectively:

$$R_f = 12.94\ \Omega$$

$$\tau = 82.4\ \text{min}$$

$$\theta_f = 65.29°C$$

From Eq. (4.62) with I = 5.4 A the maximum permissible steady state current is

$$I_{max} = 8.76\ A_{rms}$$

When a single phase is supplied a similar technique may be applied. Using again an interval of 10 min, the corresponding measured values of R_1 = 6.67 Ω and R_2 = 6.50 Ω are taken from fig. 4.36(b). The equivalent r.m.s. current is $\hat{I}/\sqrt{2}$ = 5.4 A and with R_{amb} = 5.50 Ω, θ_{amb} = 19°C the results obtained are:

$$R_f = 6.87\ \Omega$$

$$\tau = 63.69\ \text{min}$$

$$\theta_f = 84.21°C$$

$$I_{max} = 7.46\ A_{rms}$$

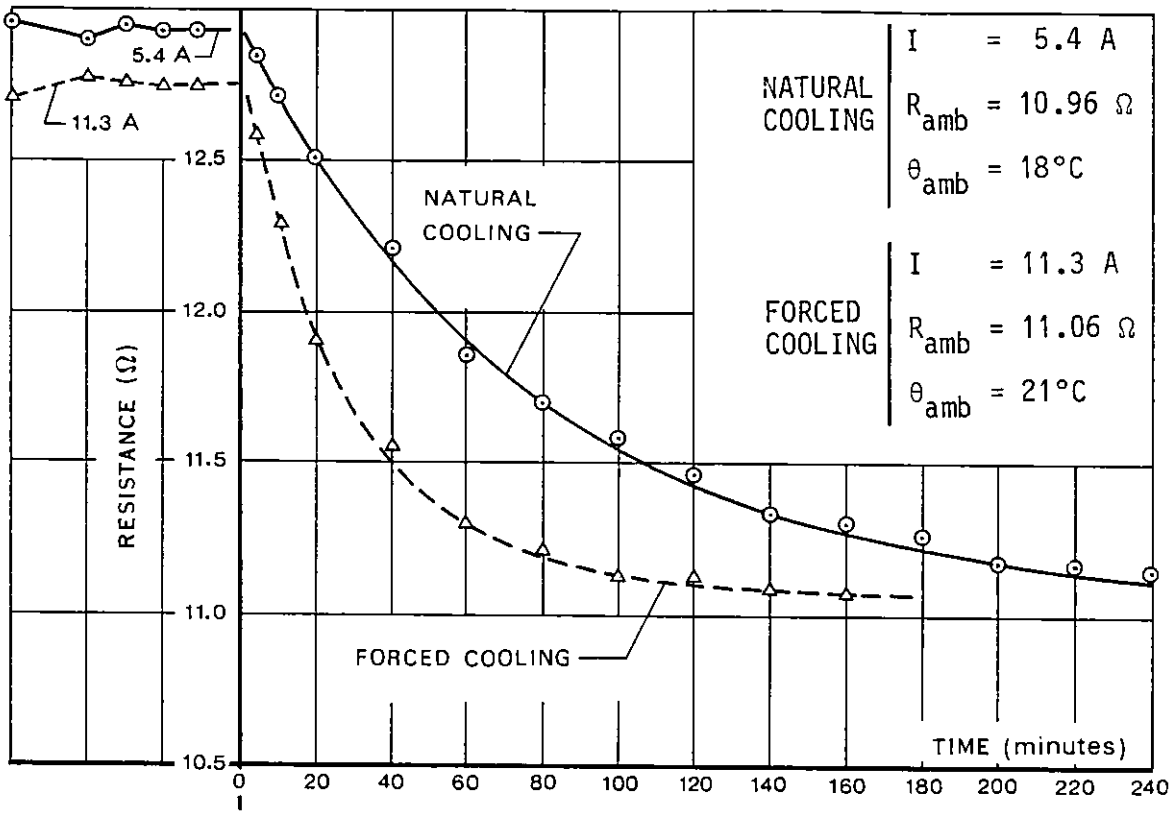

(a) - Two phases supplied in series

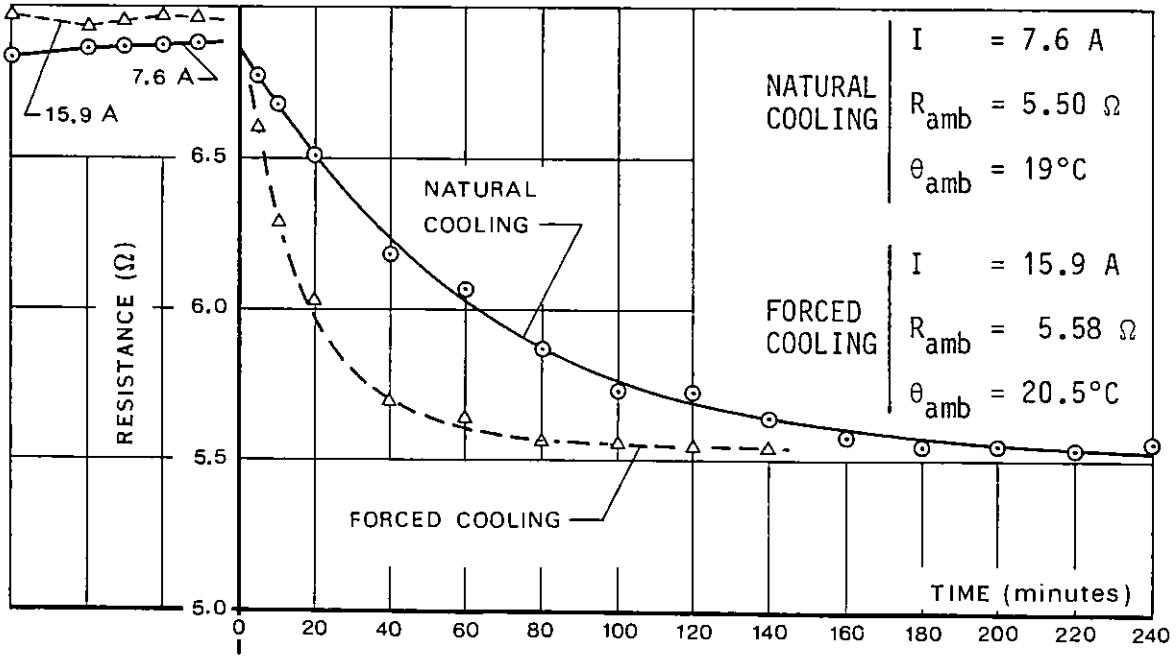

(b) - One phase only supplied

Fig. 4.36 - Natural and forced cooling curves

Clearly, the condition for one phase only supplied implies a lower permissible steady state current, a shorter thermal time-constant and a higher final temperature-rise. In fact, since the same quantity of heat must be dissipated for both cases, the condition of peak current in one phase, as compared with equal currents in each phase, should achieve the same temperature-rise in less time because only half the copper volume is directly involved. Thus, the condition of peak current in one phase is the critical case and must be taken into account for all loading calculations. The same conclusion applies for forced-cooling and from fig. 4.36(b) the following results are obtained:

$$R_f = 6.95\ \Omega$$
$$\tau = 15.65\ \text{min}$$
$$\theta_f = 84.77°C$$
$$I_{max} = 15.70\ \text{A}$$

Substitution of $\tau = 63.69$ min, $I_{max} = 7.46$ A for natural cooling and $\tau = 15.65$ min, $I_{max} = 15.70$ A for forced cooling into Eq. (4.64), a boundary condition for safe overload times when starting from ambient temperature is obtained, as shown in fig. 4.37. As an example, the maximum safe current for 10 min is about 19 A with natural cooling and 22.5 A with forced cooling used.

Similar curves may be obtained for theoretical torque based on thermal grounds, by simply multiplying the ordinates by the torque constant $K_T = 59.73\ \text{Nm/A}_{rms}$ given in Eq. (4.33). Assuming natural convection cooling, the full torque could be maintained for approximately 7 minutes. With better forced cooling, full torque could probably be maintained indefinately.

During all these tests, temperatures were taken on two magnets 30° mechanical apart. Two thermo-couples placed on the magnet surface were used and the readings averaged. The mean temperature of the magnets never

exceeded 70% of the final temperature-rise of the winding. The manufacturer's figure for the maximum operating temperature of the B.P.R.E. magnet, set by the polymer, is about 100°C above ambient temperature(*). Then, allowing the maximum permissible winding temperature of 125° the magnets are on the safe side.

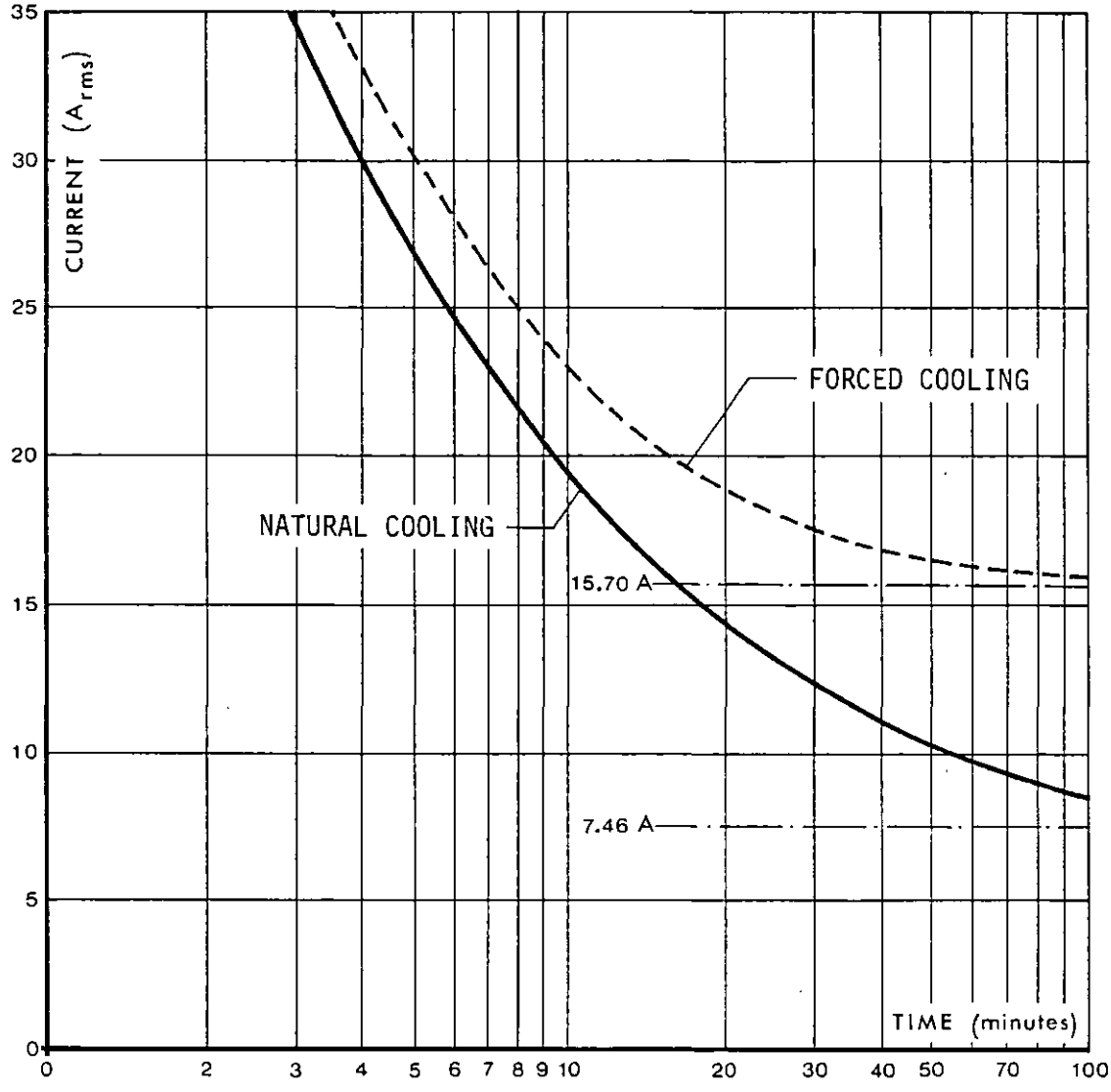

Fig. 4.37 - Safe overload time for current with switch on at ambient temperature

(*) - *Unfortunately recently revised to 60°C, a temperature which clearly necessitates a change to the actuators' cooling arrangements, or a reduction in some of the current and overload time figures discussed above.*

4.12.5 - Rotor inertia measurement

In order to attempt an analysis of the dynamic behaviour of the actuator, it is necessary to know the values of mechanical constants such as moment of inertia and viscous damping coefficient. There are various methods for measuring the moment of inertia of a rotating machine [87], but for this particular configuration it was thought best to add known weights to the end of a beam fixed to the actuator shaft. The beam is allowed to fall by gravity through a known angle from $-\theta_o$ to $+\theta_o$. The fall time is measured from X-Y plotter traces of the $\theta(t)$ curve obtained be means of a linear potentiometer mounted on the actuator shaft, as shown in fig. 4.38.

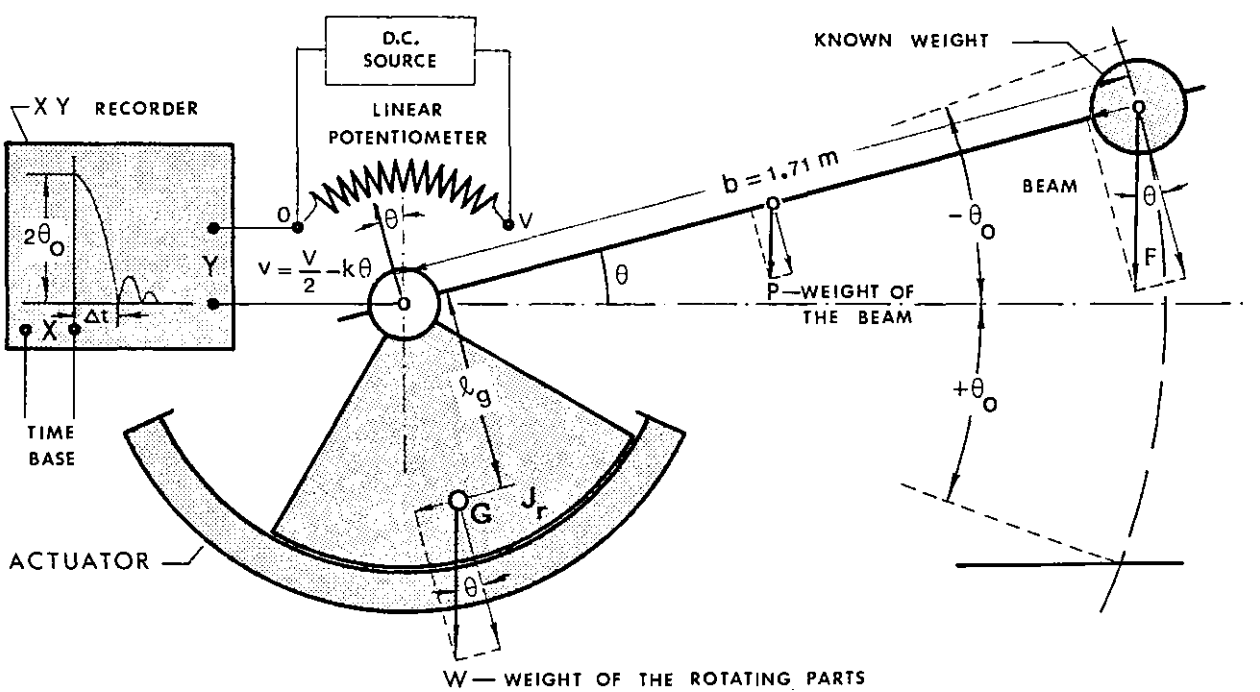

Fig. 4.38 - Layout for measuring the actuator rotor inertia

The total instantaneous torque applied to the rotor shaft is given by:

$$T = -W\ell_g \sin\theta + P\cos\theta\cdot\frac{b}{2} + F\cos\theta\cdot b \qquad (4.65)$$

The equation of motion in terms of applied torque and mechanical rotor angle is then

$$T = J\ddot{\theta} + D\dot{\theta} + W\ell_g \sin\theta \qquad (4.66)$$

where J is the moment of inertia of all rotating parts. If the applied

torque is made much greater than viscous torque $D\dot{\theta}$ and coulomb friction torque $W\ell_g \sin\theta$, then the following approximate equation holds during the fall

$$T_{ave} = J\ddot{\theta} \tag{4.67}$$

where T_{ave} is now the average torque and $\ddot{\theta}$ is the angular acceleration due to the fall by gravity during the interval Δt, which (assuming $\hat{\theta}$ small) should satisfy the equation:

$$2\theta_o = \frac{1}{2}\ddot{\theta}\ \Delta t^2 \tag{4.68}$$

From Eq. (4.65), the average torque during the fall is:

$$T_{ave} = \frac{1}{2\theta_o}\int_{-\theta_o}^{+\theta_o} T d\theta = (\frac{P}{2} + F)b\ \frac{\sin\theta_o}{\theta_o} \tag{4.69}$$

Substitution of Eq. (4.69) and Eq. (4.68) into Eq. (4.67) gives the moment of inertia of all rotating parts as:

$$J = (\frac{P}{2} + F)b\ \frac{\sin\theta_o}{4\theta_o^2}\ \Delta t^2 \tag{4.70}$$

When a mass F (kg) is placed at the end of the beam with a constant cross section and length b, then it is easily demonstrated that the total moment of inertia is given by

$$J_B = (\frac{P}{3} + F)b^2 \tag{4.71}$$

Hence, the rotor inertia is $J_r = J - J_B$ and from Eq. (4.70) and Eq. (4.71),

$$J_R = 9.81\ (\frac{P}{2} + F)b\ \frac{\sin\theta_o}{4\theta_o^2}\ \Delta t^2 - (\frac{P}{3} + F)b^2 \tag{4.72}$$

Various tests with different weights were made from an angle $\theta_o = 20°$ and the respective fall times Δt recorded. Fig. 4.39 shows a typical X-Y recording obtained corresponding to a weight F = 4.54 kg and a beam weight

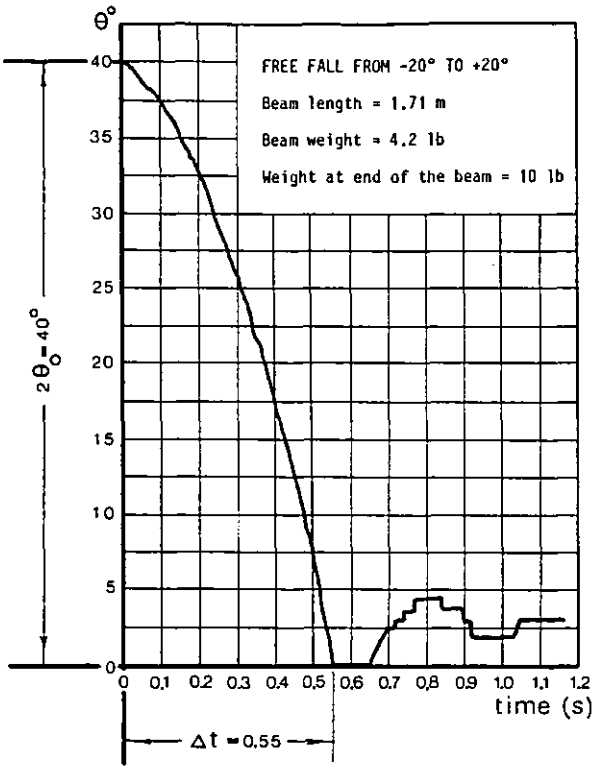

Fig. 4.39 - Free fall typical record

P = 1.90 kg. Using Eq. (4.72) the rotor inertia was then calculated and the various results averaged. The average measured value was found to be $J_R = 4.42\ kg.m^2$ which is in a good agreement with the design figure of $4.43\ kg.m^2$.

4.12.6 - Viscous damping coefficient measurement

The method used to measure the viscous damping coefficient of the actuator was to allow the rotor to oscillate freely as a pendulum and to record these oscillations $\theta(t)$ using the equipment described previously, as shown in fig. 4.40(a). From these oscillograms the damping coefficient was determined.

When the rotor is freely oscillating, the equation which governs the rotor motion is

$$J_R\ddot{\theta} + D\dot{\theta} + W\ell_g \sin\theta = 0$$

where D is the viscous damping coefficient.

For θ values up to 20°, $\sin\theta \simeq \theta$ and the above equation reduces to

$$J_R\ddot{\theta} + D\dot{\theta} + W\ell_g\theta = 0$$

The solution of this differential equation (assuming $D^2 < 4J_R W\ell_g$) is of the form

$$\theta(t) = \theta_m e^{-\alpha t}\sin(\omega_n t + \phi) \tag{4.73}$$

where

$$\alpha = \frac{D}{2J_R} \tag{4.74}$$

is the attenuation coefficient and

$$\omega_n = \sqrt{\frac{W\ell_g}{J_R} - \alpha^2} \tag{4.75}$$

is the natural angular frequency of the oscillations.

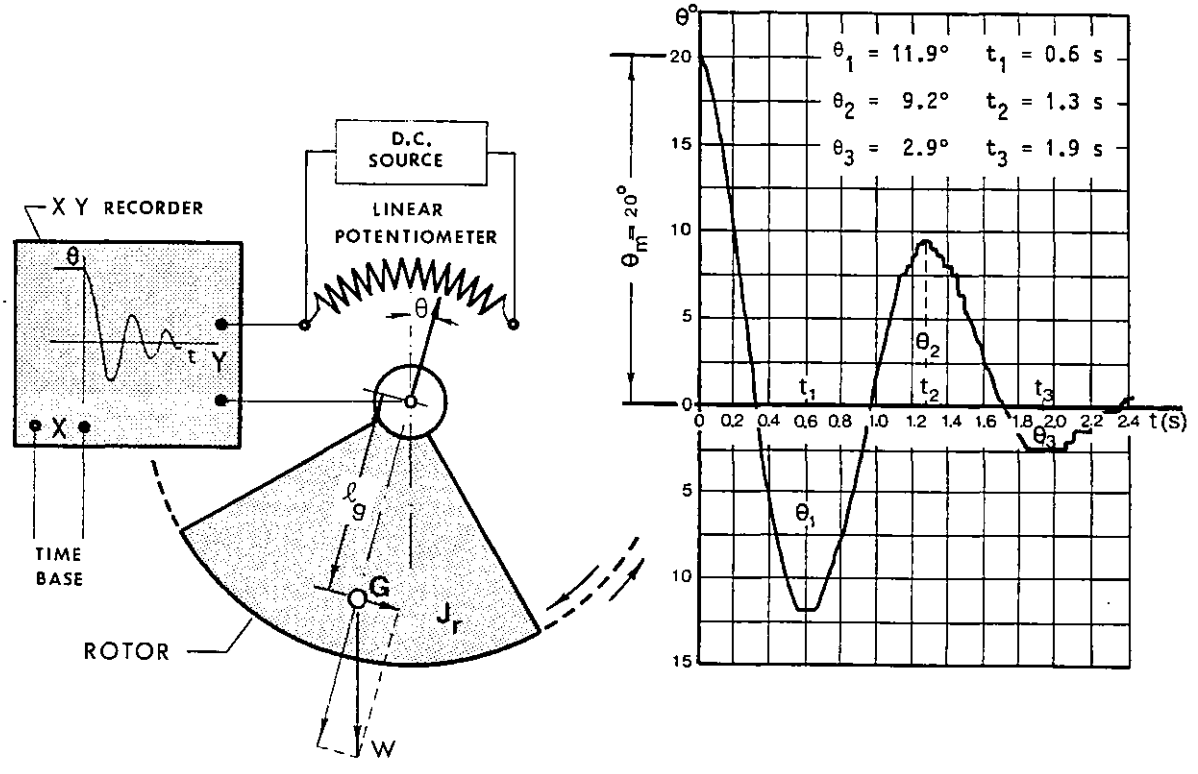

(a) - Rotor oscillating (b) - Typical oscillogram

Fig. 4.40 - Layout for measuring the viscous damping coefficient

Fig. 4.40(b) shows a typical record obtained. If two maximum rotor displacements θ_1 and θ_3 are taken at instants t_1 and t_3 respectively one period apart, then according to Eq. (4.73) the attenuation coefficient is

given by

$$\alpha = \frac{1}{t_3 - t_1} \log_e \frac{\theta_1}{\theta_3} \tag{4.76}$$

Similarly, if $\phi = 90°$,

$$\alpha = \frac{1}{t_2} \log_e \frac{\theta_m}{\theta_2} \tag{4.77}$$

From the values displayed in the diagram, the attenuation coefficent was determined by averaging the results given by Eq. (4.76) and Eq. (4.77) as $\alpha = 0.83$ rad/s. Since the rotor inertia was measured in the previous test as $J_R = 4.42$ kg.m^2, Eq. (4.74) gives for the viscous damping coefficient

$$D = 2J_R\alpha = 7.34 \text{ Nm/(rad s}^{-1}).$$

This means that when the actuator is rotating at rated speed N_r = 15 r.p.m. < > 1.57 rad/s the viscous torque produced is $D\omega_r$ = 11.52 Nm, which is about 1% of full torque.

4.13 - DESCRIPTION OF THE COMPLETE ACTUATOR SYSTEM

The overall system for the actuator in the auto-piloted mode in its most general form is shown in fig. 4.41. Some form of system giving sine/cosine rotor position signals is required and, as described previously, a synchro-resolver can fulfil this role. For the actuator, either a 72-pole synchro-resolver or a 2-pole synchro-resolver driven through a 36:1 step up system is required.

The power stage comprises one d.c. power amplifier per phase. In operation, current amplitudes proportional to torque demand are fed the stator winding and interact with the field flux to produce torque. As explained in Chapter 3 the current pattern is kept locked to the field flux by the action of sine and cosine signals from the synchro-resolver on the shaft which are fed, together with the torque demand signal, to the power amplifiers.

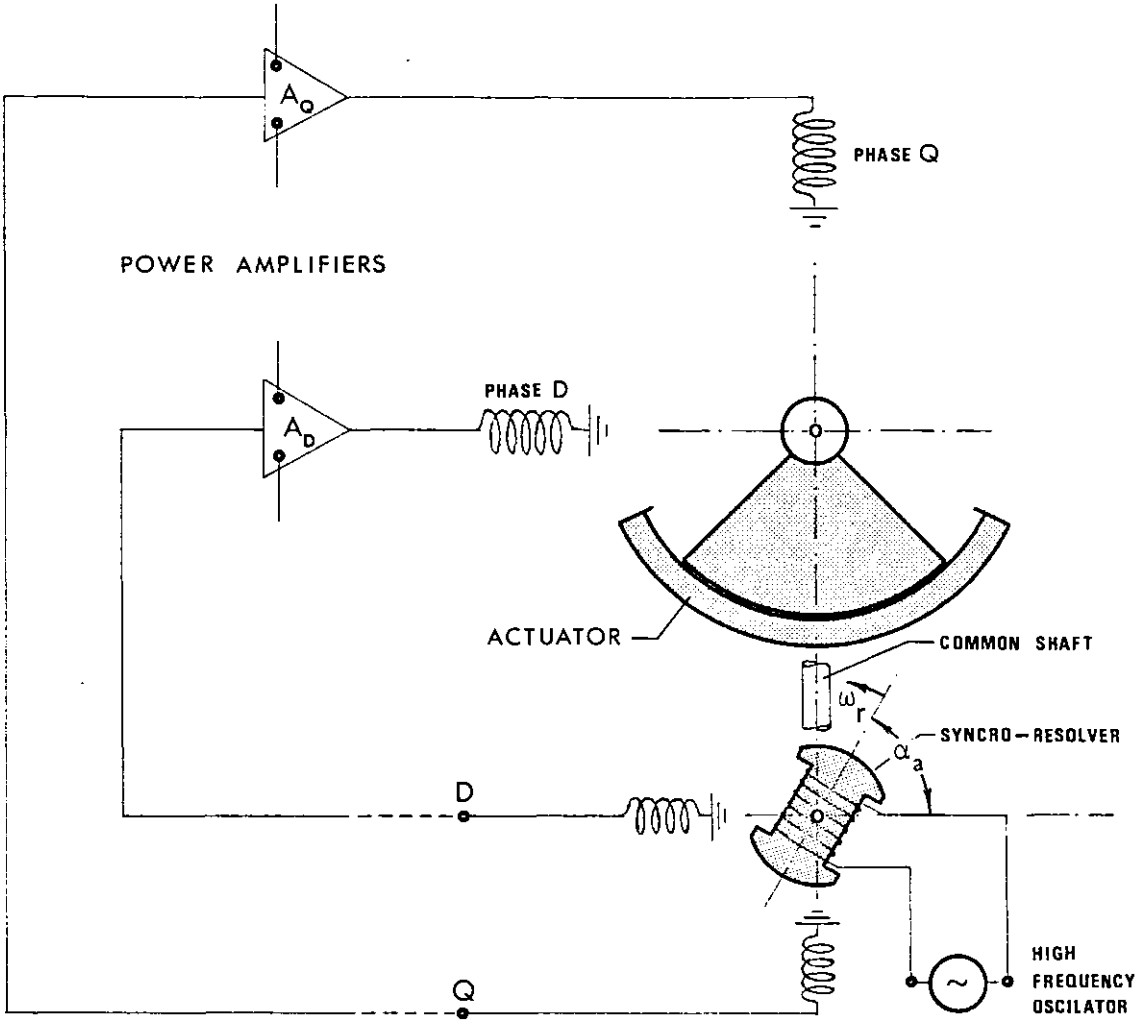

Fig. 4.41 - Basic system for the auto-piloted actuator

Fig. 4.42 shows the block diagram for one phase of such a system, which is basically the same as described in section 3.6. The circuit uses a square wave converter and an analog multiplier to clean alternatively half of the modulated synchro-resolver signal. A low pass filter then eliminates the carrier frequency of the oscillator to obtain the desired result to be inputted to the power amplifier.

Torque level control can be achieved either by synchro field variation or synchro output variation and both may be realised mechanically or electrically. Hence, four combinations are possible and fig. 4.43 shows the respective connections. The torque level control by means of an external electric signal is easily achieved using analog multipliers. The great

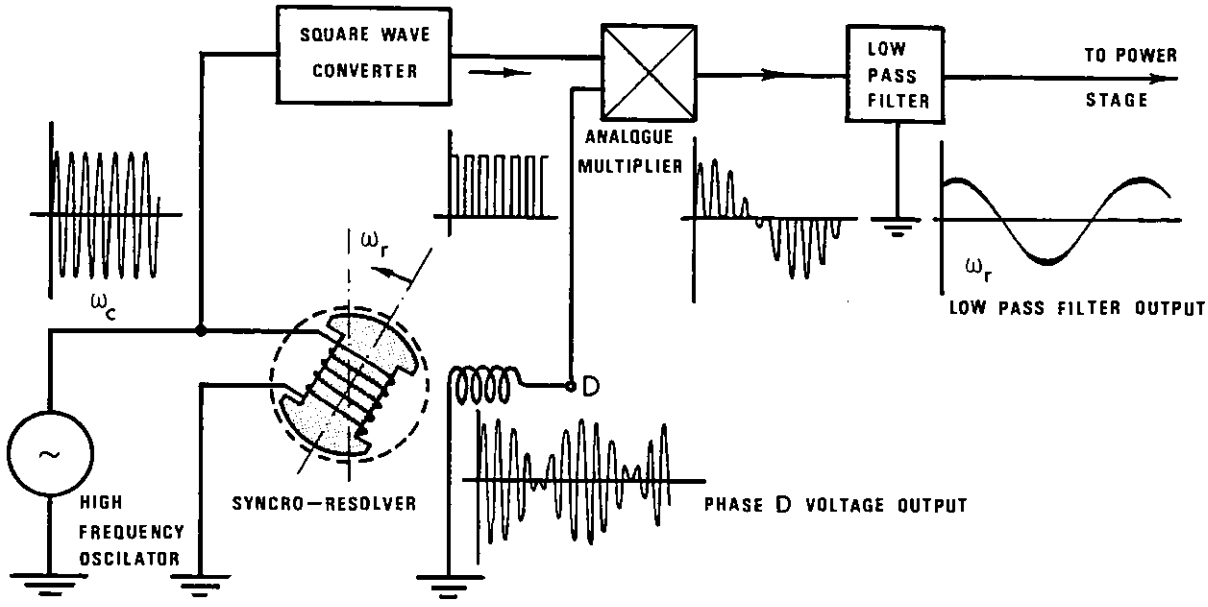

Fig. 4.42 - Block diagram of the synchro-resolver system

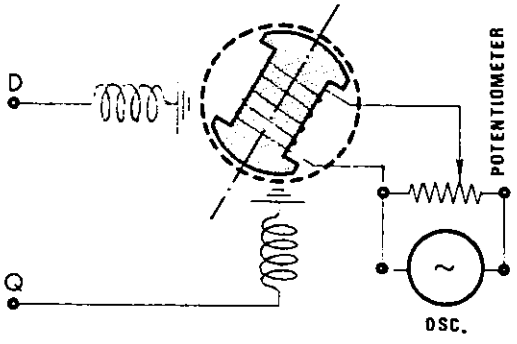

(a) - Mechanical input signal using a potentiometer

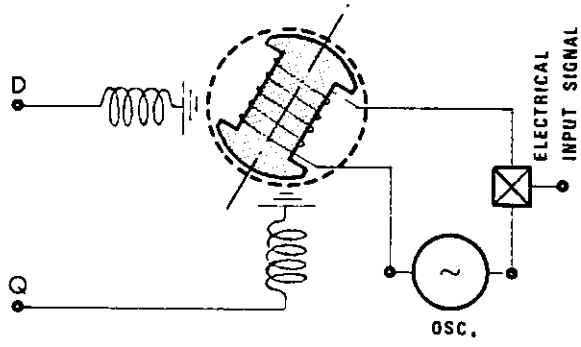

(b) - Electrical input signal using an analog multiplier

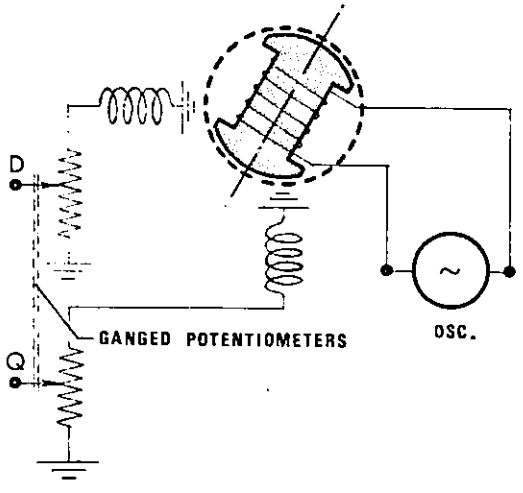

(c) - Mechanical output signal using two ganged potentiometers

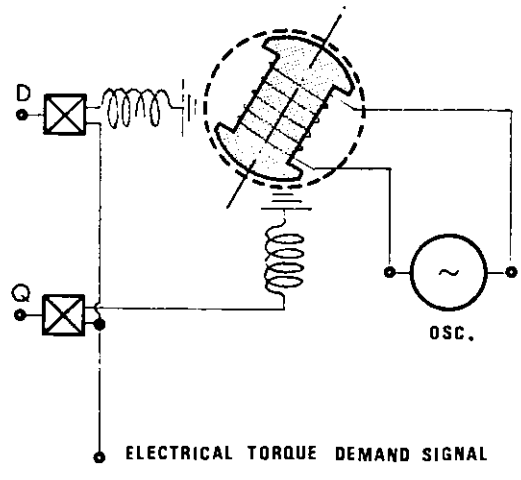

(d) - Electrical output signal using two analog multipliers

Fig. 4.43 - Possible layouts of torque level control

advantage of the electrical method, as compared with the mechanical method, is that good accuracy is achieved in setting a required torque level, the system is convenient to operate, and it is easy to incorporate the entire actuator system in a rotor position control loop.

4.13.1 - Synchro-resolver characteristics

Since the actuator has a limited motion, the synchro-resolver field may be fed by means of flying leads, avoiding in this way slipping contacts. Actually, the synchro-resolver used was a commercial three-phase brushless unit and the layout is shown in fig. 4.44.

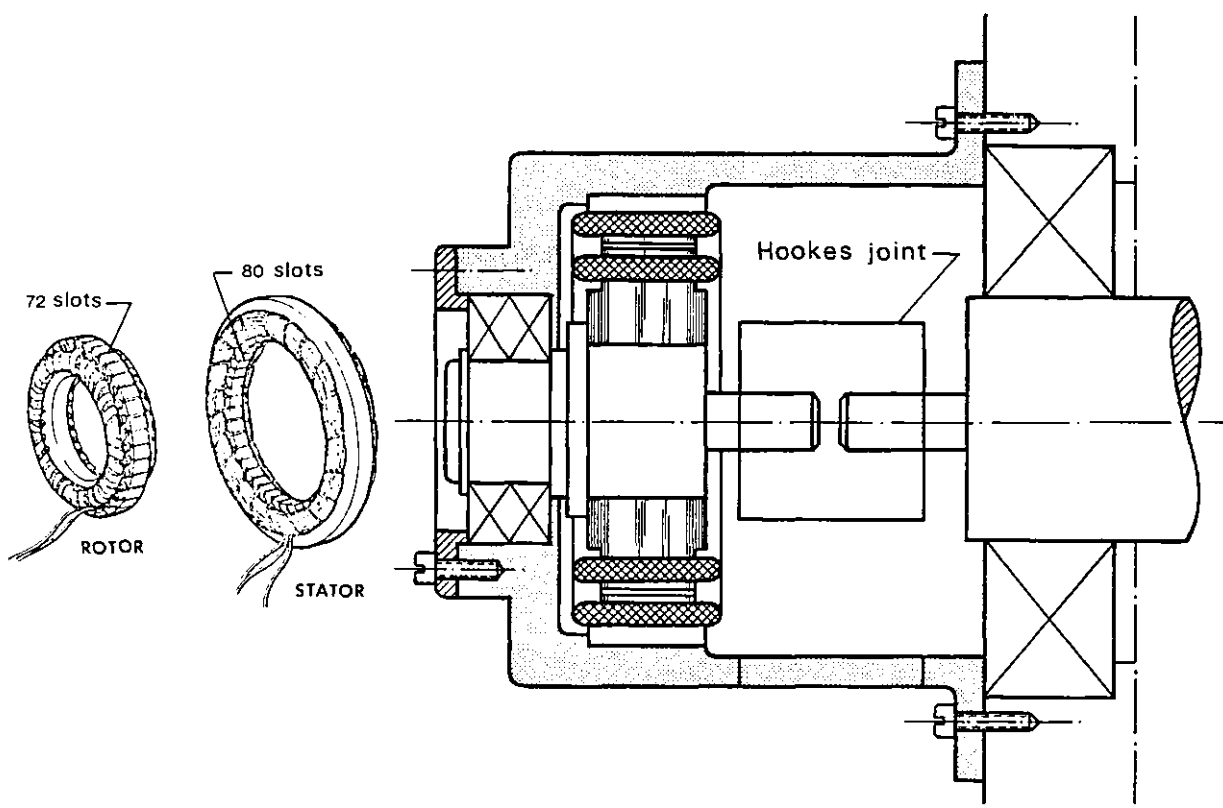

Fig. 4.44 - Synchro resolver layout

The three-phase system is converted to a two-phase system using the Scott connection [88] or simply using electronic means [89], as shown in fig. 4.45. The high input impedance differential amplifier shown in fig. 4.45(b) uses two unity gain followers on the input for buffering. With $R_4/R_1 = R_3/R_2$ and $R_1 = R_2$ the output will be $V_d = \frac{R_4}{R_1}(V_3 - V_2)$. Thus, to

obtain a two-phase system R_1/R_4 must be set to $\sqrt{3}$.

In the layout shown in fig. 4.44 there are in fact two independent machines in the one frame. On the rotor, with 72 slots, there are separate 2-pole and 72-pole single phase windings and on the stator, with 80 slots, there are separate 2-pole and 72-pole three-phase windings. The

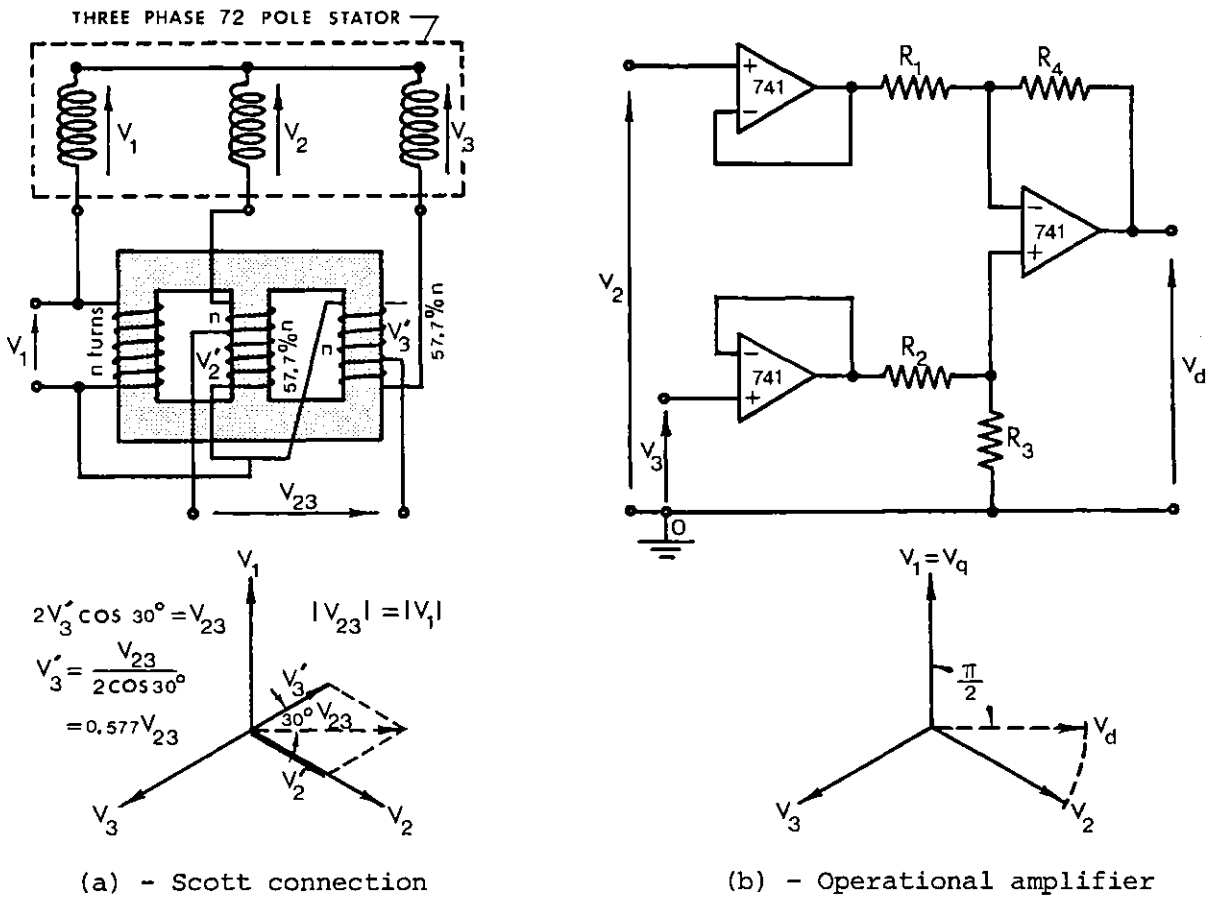

(a) - Scott connection

(b) - Operational amplifier

Fig. 4.45 - Two possible ways to convert a three-phase system into a two-phase system

2-pole machine may be used to give information of the rotor displacement in mechanical degrees and fig. 4.46 shows, as an example, how a 2-pole synchronous machine, when coupled to a radar system, can be used to give the location of an object [90]. If an a.c. signal proportional to the distance d of an object is applied to the field, in the two-phase stator winding an e.m.f. proportional to height and horizontal distance will be induced.

As described in section 4.12.1.c, to avoid the ripple torque component

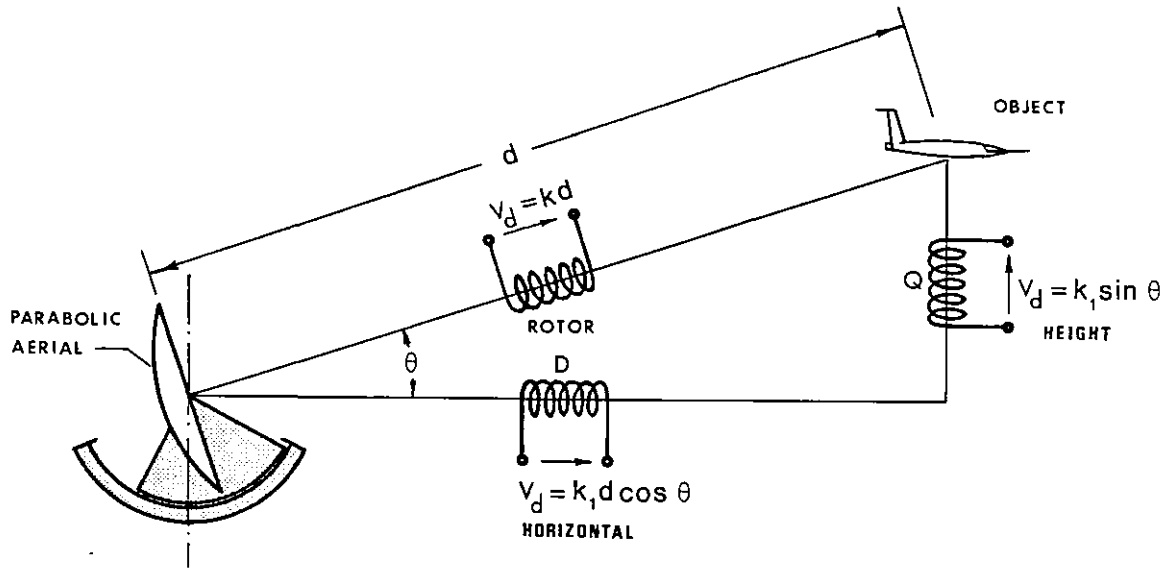

Fig. 4.46 - Location of an object using a two-pole two-phase synchro

due to the electronic source the time harmonic coefficients in the input signal waveform should be eliminated. Thus, it is desirable to obtain an output synchro-resolver waveform free of harmonics. Fig. 4.47 shows the output voltage waveform versus rotor position in a double-pole pitch range for the 72-pole synchro when a 20 V, 400 Hz sinusoidal voltage was applied to the 72-pole rotor.

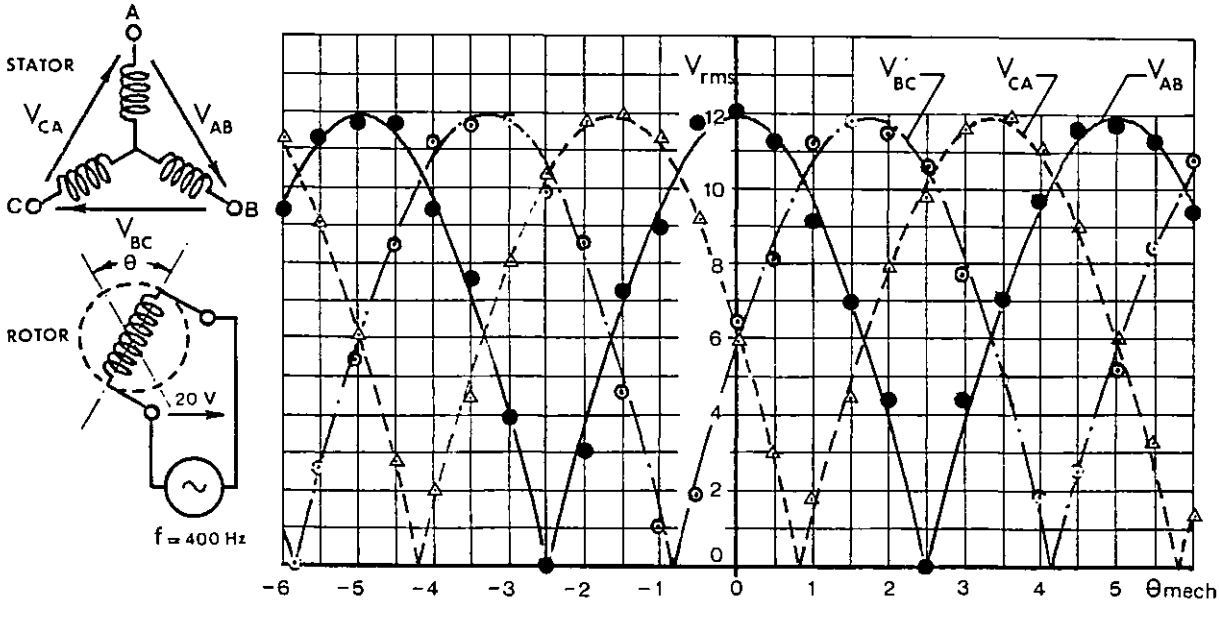

Fig. 4.47 - Synchro-resolver waveform output

The results obtained are close to a sine wave and hence ripple torque due to the position sensing system would be minimised.

4.13.2 - Machine requirements for electronic supply matching

From the knowledge of the torque constant and winding resistance, it is now possible to calculate the power required by the actuator at a given speed, and therefore the power amplifiers' characteristics for each phase may be determined.

When the rotor actuator is rotating with an angular speed $\omega_r = 2\pi N_r$ the supply angular frequency on the 72-pole complete winding is given by

$$\omega = \frac{72}{2}\,\omega_r = 3.77\ N_r \quad \text{rad/s} \tag{4.78}$$

with N_r in rev/min. For the rated rotor speed $N_r = 15$ rev/min the supply frequency becomes $f = \frac{\omega}{2\pi} = 9$ Hz.

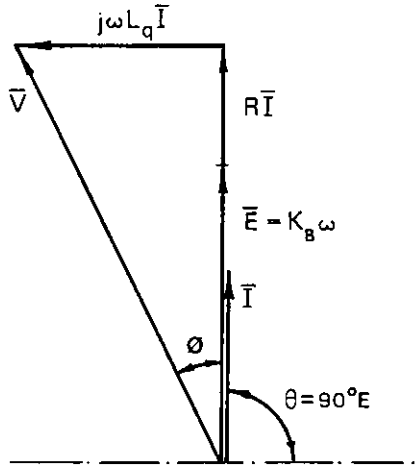

Fig. 4.48 - Phasor diagram for $\theta = 90°E$ torque angle

Neglecting friction, windage and iron losses, the input power P per phase required to produce an output torque $T = K_T I$ will be

$$P = R\,I^2 + \frac{1}{2}T\omega_r \tag{4.79}$$

where I is the r.m.s. current per phase and R the winding resistance per phase. If it is assumed that the actuator is operating with a winding temperature θ, then the winding resistance per phase, calculated as $R_{20°C} = 6.03\ \Omega$ at 20°C, is given by

$$R_\theta = R_{20°C}\left[1 + \alpha(\theta - 20°)\right] \tag{4.80}$$

Substitution of Eq. (4.78) and Eq. (4.80) into Eq. (4.79), gives:

$$P = R_{20°C}\left[1 + \alpha(\theta - 20°)\right]\left(\frac{T}{K_T}\right)^2 + 0.053\ TN_r \qquad (4.81)$$

Fig. 4.48 shows the actuator phasor diagram for current fed operation with position sensor set at 90°E torque angle, where $K_B = \frac{K_T}{72} = 0.83\ V/(rad.s^{-1})$ is the back e.m.f. constant per phase of the actuator and $L_q = L_\ell + L_{skew} = 58.50$ mH is the q-axis inductance per phase displayed in fig. 4.31. From the phasor diagram, the phase voltage at supply angular frequency ω in order to develop a shaft torque $T = K_T I$ is given by

$$V = \left[(K_B\omega + R\,I)^2 + (\omega L_q I)^2\right]^{\frac{1}{2}} \qquad (4.82)$$

Substitution of Eq. (4.78) and Eq. (4.80) into Eq. (4.82) gives

$$V = \left\{\left(3.77K_BN_r + R_{20°}\left[1 + \alpha(\theta-20°)\right]\frac{T}{K_T}\right)^2 + 3.77L_qN_r\left(\frac{T}{K_T}\right)^2\right\}^{\frac{1}{2}} \qquad (4.83)$$

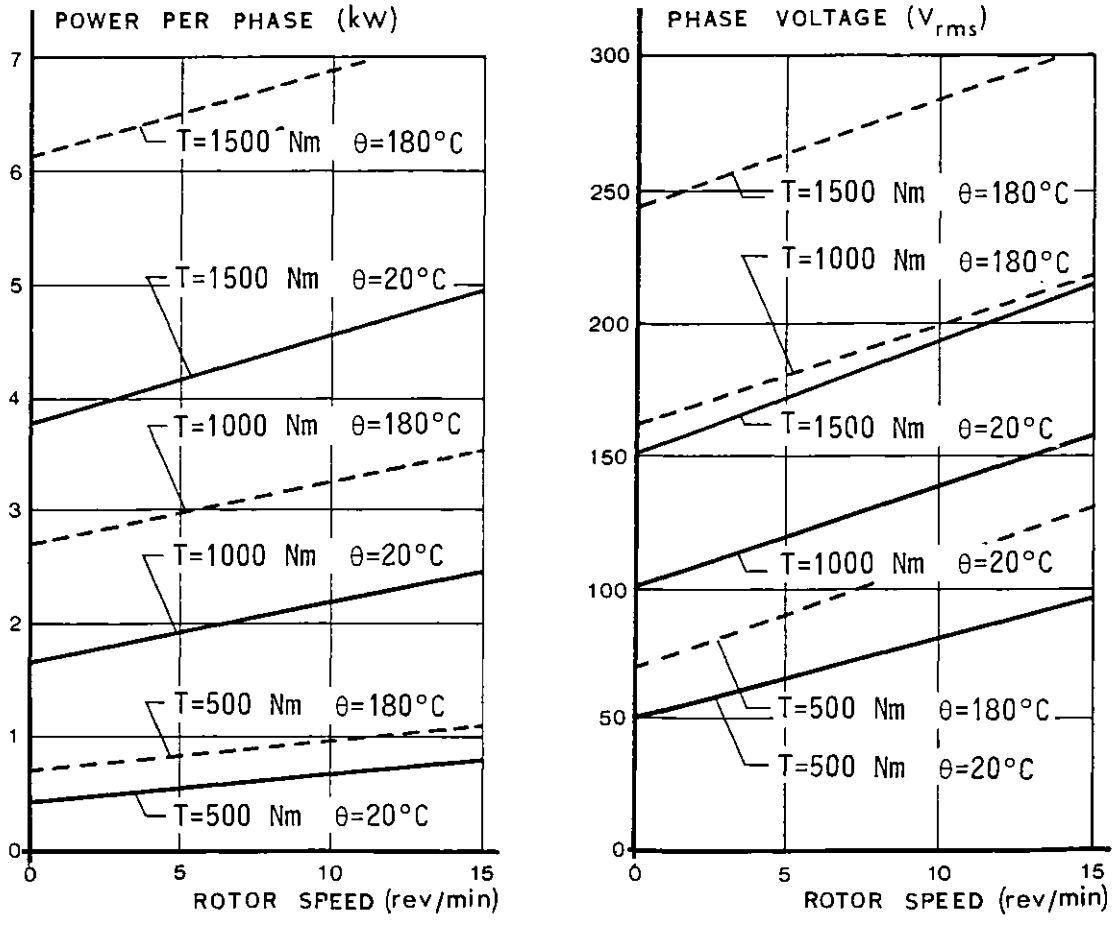

Fig. 4.49 - Power input and voltage per phase for the actuator

For winding room temperature θ = 20°C and maximum permissible temperature θ = 180°C (class H), Eq. (4.81) and Eq. (4.83) are plotted versus rotor speed N_r and three levels of output torque in fig. 4.49. If a 7 kW, 300 V linear power amplifier per channel is chosen, it is evident from these plots and fig. 4.37 that some sort of machine cooling is necessary if full torque is required for continuous operation without exceeding the maximum allowable winding temperature.

4.13.3 - Actuator dynamic behaviour

The basic system shown in fig. 4.41 can be operated with either input voltage or input current controlled in magnitude or phase. The magnitude is controlled by the torque demand input signal. If desired the phase can be controlled by adjustment of the synchro-resolver rotor position relative to the stator m.m.f. or by adjustment of the phase of the feed to the resolver primary.

If, when the actuator is at standstill a step input torque demand signal is suddenly applied, the rotor accelerates until some final condition is reached. During this transient state, since the rotor speed is instantaneously varying, the locked frequency of the stator input signal varies so as to keep the machine in synchronism. The variation of the rotor speed and hence feed frequency, depends on the mechanical and electrical constants of the machine and, of course, on the level of the demand signal.

As seen, the power stage can act as a constant voltage source or a constant current source and these two modes of operation are considered here separately. The transient state up to a fixed rotor speed N_o is studied for both cases in order for a comparison to be made.

a) - Constant voltage source

If voltage feeding is used, the load angle δ and supply voltage V is controlled. Setting the position sensor at δ = 0° load angle, the

response of the motor in the time domain for the no-load condition is given by Eq. (3.82). Thus the supply frequency becomes

$$\omega(t) = \frac{n_p}{2}\,\omega_r(t) = \frac{V}{K_B}\left(1 - e^{-\frac{t}{\tau_{em}}}\right) \tag{4.84}$$

where V is the r.m.s. supply voltage to the machine and τ_{em} is the electro-mechanical time constant. Hence, the rotor speed is

$$N_r(t) = \frac{\omega_r}{2\pi} = \frac{V}{\pi n_p K_B}\left(1 - e^{-\frac{t}{\tau_{em}}}\right) \tag{4.85}$$

For the calculated winding resistance R = 6.03 Ω, torque constant K_T = 59.76 Nm/A_{rms} and measured rotor inertia J_R = 4.42 kgm^2, the electro-mechanical time constant, given by Eq. (3.79), is:

$$\tau_{em} = \frac{2RJ_R}{K_T^2} = 0.015 \text{ s}$$

The r.m.s. voltage necessary to supply the actuator on no-load from standstill to reach a final steady state speed $N_o(\infty)$ is, from Eq. (4.85), given by

$$V = \pi n_p K_B N_o \tag{4.86}$$

Clearly, this voltage is related to the torque demand signal through the gain of the overall electronic system. From Eq. (4.84) and Eq. (4.86) the instantaneous voltage across one phase is

$$v(t) = \hat{V}\sin(\omega t + \alpha) = \sqrt{2}\,\pi n_p K_B N_o \sin\left[\pi n_p N_o\left(1 - e^{-\frac{t}{\tau_{em}}}\right)t + \alpha\right] \tag{4.87}$$

with a constant peak value and variable frequency.

The instantaneous current in the same phase is of the form

$$i(t) = \sqrt{2}\,I\sin(\omega t + \alpha - \phi) \tag{4.88}$$

where the r.m.s. current is given by

$$I = \sqrt{I_d^2 + I_q^2} \tag{4.89}$$

The current components I_d and I_q may be obtained from Eq. (3.23) and Eq. (3.24) putting $\delta = 0°$, as:

$$I_d = \frac{V - K_B\omega}{R^2 + \omega^2 L_d L_q}\,\omega L_q$$

$$I_q = \frac{V - K_B\omega}{R^2 + \omega^2 L_d L_q}\,R$$

Hence, from Eq. (4.86) and Eq. (4.89) the r.m.s. current is

$$I = \frac{K_B(\pi n_p N_o - \omega)}{R^2 + \omega^2 L_d L_q}\sqrt{R^2 + (\omega L_q)^2} \tag{4.90}$$

with a phase angle

$$\phi = \text{atan}\left(\frac{I_d}{I_q}\right) = \text{atan}\left(\frac{\omega L_q}{R}\right) \tag{4.91}$$

Substitution of Eq. (4.84), Eq. (4.90) and Eq. (4.91) into Eq. (4.88) gives an expression for the phase current at any instant. During the transient state, Eq. (4.84) and Eq. (4.90) show that the peak current is variable in time, being maximum at starting and settling to a constant value when the steady state is reached. The current is hence variable in magnitude, frequency and phase during the transient state.

b) - Constant current source

For current-fed operation with the position sensor set at 90°E torque angle, the analysis is similar, except that v(t) is replaced by i(t) and $\omega(t)$ is now given, according to Eq. (3.83), by

$$\omega(t) = \frac{n_p}{2}\,\omega_r(t) = \frac{n_p K_T I}{2D}\left(1 - e^{-\frac{t}{\tau_m}}\right) \tag{4.92}$$

where I is the r.m.s. supply current and τ_m is the mechanical time con-

stant of the machine. For the measured viscous damping coefficient D = 7.34 Nm/(rad.s^{-1}) the mechanical time constant, given by Eq. (3.78), is

$$\tau_m = \frac{J_R}{D} = 0.602 \text{ s}$$

This, as expected, is about 40 times greater than the electromechanical time constant.

The r.m.s. current I, controlled by the torque demand signal, that is needed to supply the actuator in order for it to attain a steady state speed N_o is, according to Eq. (4.92), given by

$$I = \frac{2\pi D N_o}{K_T} \tag{4.93}$$

The instantaneous phase current will be

$$i(t) = \sqrt{2}\ \frac{2\pi D}{K_T}.N_o \sin\left[\pi n_p N_o\left(1 - e^{-\frac{t}{\tau_m}}\right)t + \alpha\right] \tag{4.94}$$

with a constant peak value and variable frequency.

From the phase diagram shown in fig. 4.48 the r.m.s. voltage at any instant is given by Eq. (4.82) and the phase angle

$$\phi = \text{atan}\ \frac{\omega L_q I}{K_B\omega + R I} \tag{4.95}$$

Hence, the instantaneous voltage across the same phase will be:

$$v(t) = \sqrt{2}\left[(K_B\omega + R I)^2 + (\omega L_q I)^2\right]^{\frac{1}{2}} \sin\left[\pi n_p N_o\left(1 - e^{-\frac{t}{\tau_m}}\right)t + \alpha + \phi\right] \tag{4.96}$$

where ω is now given by Eq. (4.92) and ϕ by Eq. (4.95).

In this case, as can be seen from Eq. (4.96), the peak voltage increases during the transient state and settles at a constant value when the steady state is reached. Therefore, the voltage varies in magnitude, frequency and phase during the transient state.

Using the calculated values of d and q-axis inductance L_d = 57.14 mH

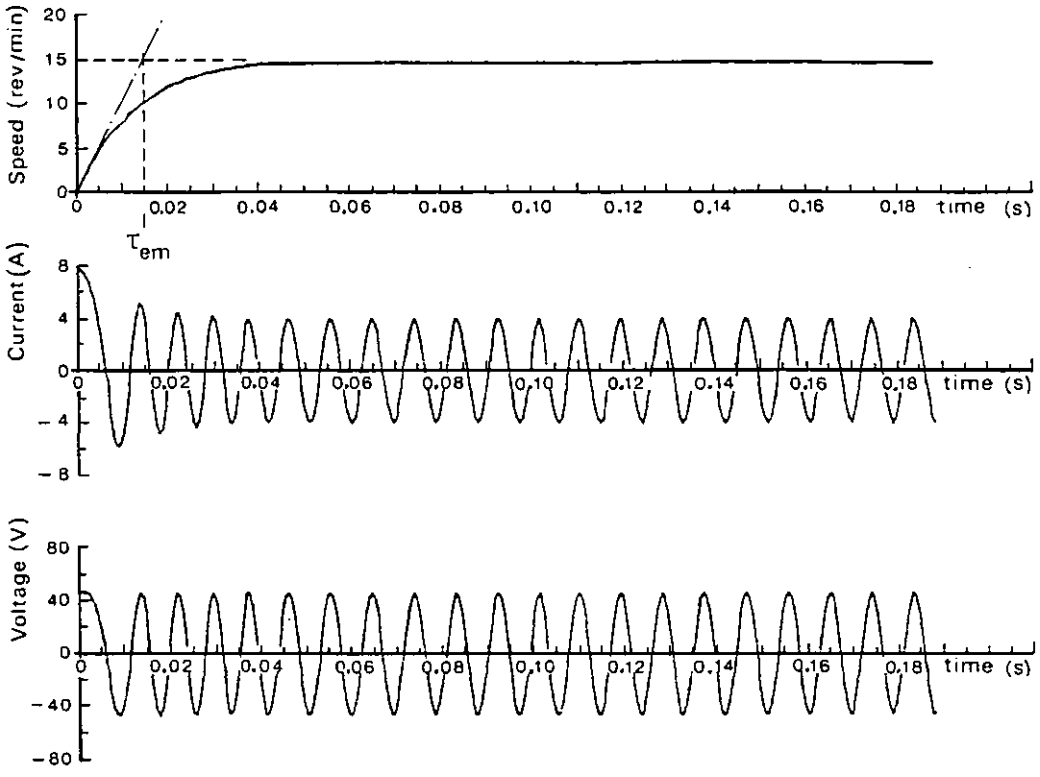

(a) - Voltage-fed response

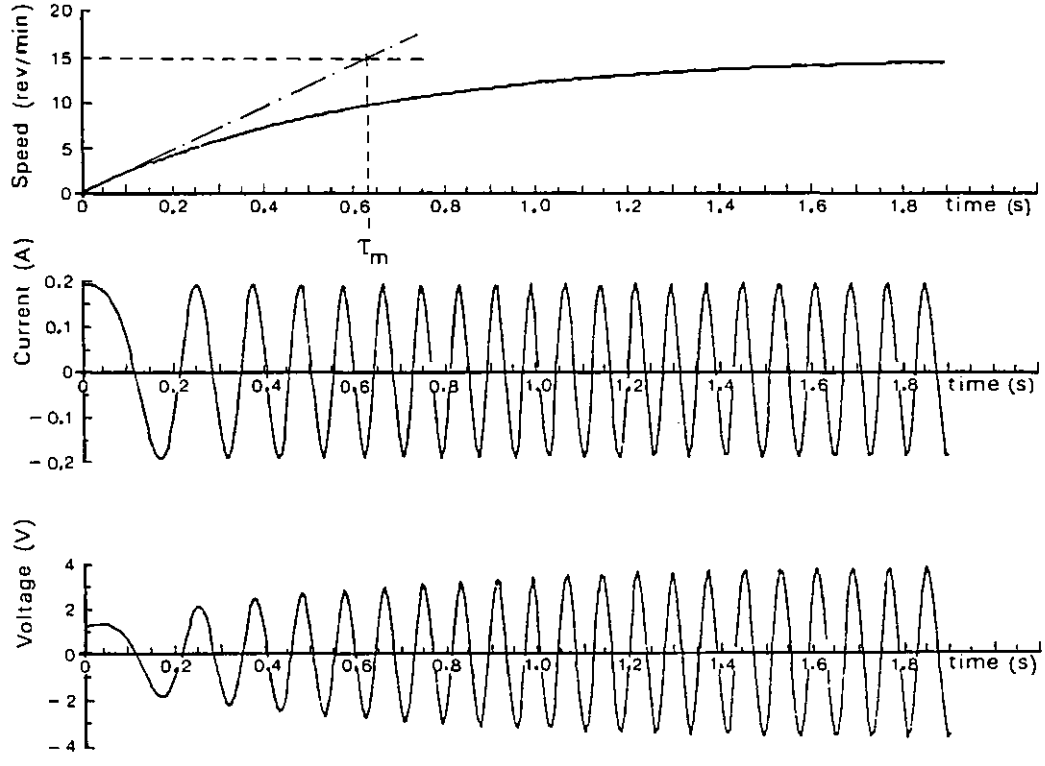

(b) - Current-fed response

Fig. 4.50 - Response of the actuator for voltage and current-fed operation due to a step input torque demand signal

and L_q = 58.50 mH, the response of the actuator on no-load for voltage-fed and current-fed operation was evaluated for a final rated speed N_o = 15 rev/min for both conditions. Fig. 4.50 shows computed plots of instantaneous rotor speed, voltage and current against time for both cases.

As can be seen from these results, voltage-fed operation gives a more rapid response than current-fed operation, because the respective time-constants involved are quite different. Clearly, in voltage-fed mode, the initial torque is improved by the initial high quadrature current component, since no back e.m.f. occurs, while in current-fed mode the r.m.s. current is set constant by the source giving a constant low torque. In practice important trade-offs involving the amplifier peak current and voltage capabilities would have to be examined at an early stage since the superior response in the voltage-fed case is of course mainly achieved in the above discussion at the expense of a higher peak current.

4.14 - POSITION CONTROLLER

For positioning duties, a typical system arrangement is shown in fig. 4.51.

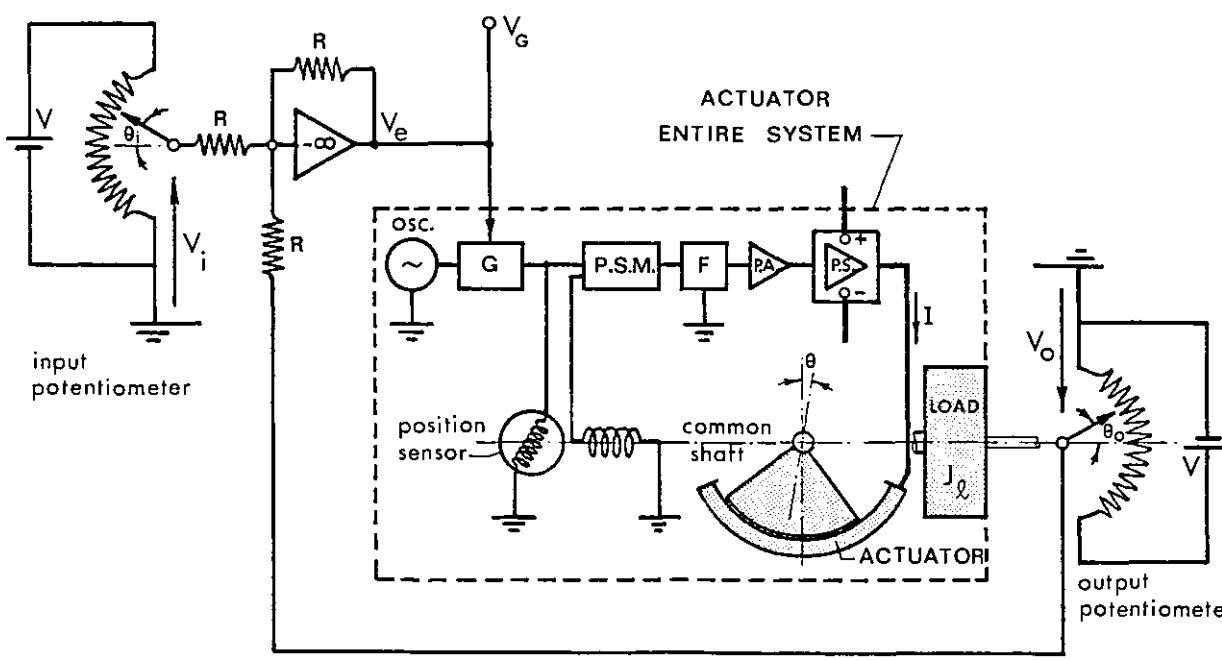

Fig. 4.51 - Remote position controller diagram

The input rotor synchro-resolver signal V_G may be related to the power amplifier output current I by $I = AV_G$ where A is the transfer function of the overall electronic system (assumed lag-free). The input and output angular positions θ_i and θ_o are directly related to the voltages on the potentiometer sliders by

$$V_i = K_p\theta_i$$
$$V_o = K_p\theta_o$$

and the error voltage V_e at the output of the unity gain operational amplifier summer is given by

$$V_e = -(V_o - V_i) \tag{4.97}$$

The actuator torque when the position sensor is set at θ torque angle and assuming $L_d = L_q$ is

$$T = K_T I \sin\theta = K_T' I$$

If the total inertia is J_ℓ (including rotor inertia) and is subjected to viscous damping D, the torque at speed ω_o (neglecting the static load torque) is

$$T = J_\ell \frac{d\omega_o}{dt} + D\omega_o$$

which may be written in Laplace notation as

$$T(s) = (J_\ell s + D).s\theta_o(s)$$

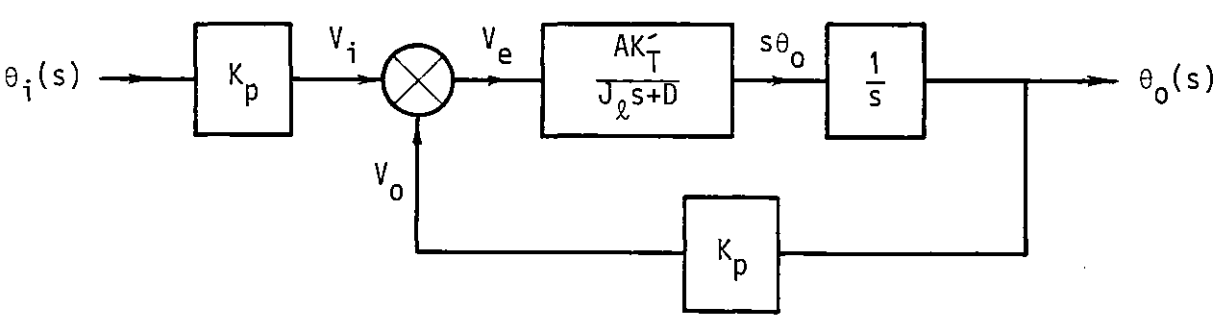

Fig. 4.52 - Position control block diagram

Hence, the block diagram of the complete system shown in fig. 4.51 is as illustrated in fig. 4.52.

Using Eq. (4.97), the transfer function for the complete system is

$$\frac{\theta_o(s)}{\theta_i(s)} = \frac{K}{s(s+a)+K} \tag{4.98}$$

where

$$K = \frac{AK_T'K_p}{J_\ell}$$

and

$$a = \frac{D}{J_\ell}$$

Eq. (4.98) may be written as

$$\theta_o(s) = \frac{\omega_n^2}{s^2 + 2\lambda\omega_n s + \omega_n^2}\theta_i(s) \tag{4.99}$$

where

$$\omega_n = \sqrt{K} = \sqrt{\frac{AK_T'K_p}{J_\ell}}$$

is the natural frequency and

$$\lambda = \frac{D}{2\sqrt{AK_T'K_pJ_\ell}} \tag{4.100}$$

is the dimensionless damping ratio.

4.14.1 - System response to a step input

If $\theta_i(t)$ suddenly changes from $\theta_i = 0$ to $\theta_i = \theta_d$ as shown in fig. 4.54(a), $\theta_i(s) = \theta_d/s$ and the response of the system is from Eq. (4.99)

$$\theta_o(s) = \theta_d \frac{\omega_n^2}{s(s^2 + 2\lambda\omega_n + \omega_n^2)}$$

Taking the inverse Laplace transform [91],

$$\theta_o(t) = \theta_d\left[1 - \frac{1}{\beta}e^{-\lambda\omega_n t}\sin(\omega_n\beta t + \phi)\right]$$

where

$$\beta = \sqrt{1-\lambda^2} \quad \text{and} \quad \phi = \text{atan}\left(\frac{\beta}{\lambda}\right)$$

The normalised transient response of this second-order system for various values of the damping ratio λ is shown in fig. 4.53(b). These results show that not only is there the usual shaft's delay between the application

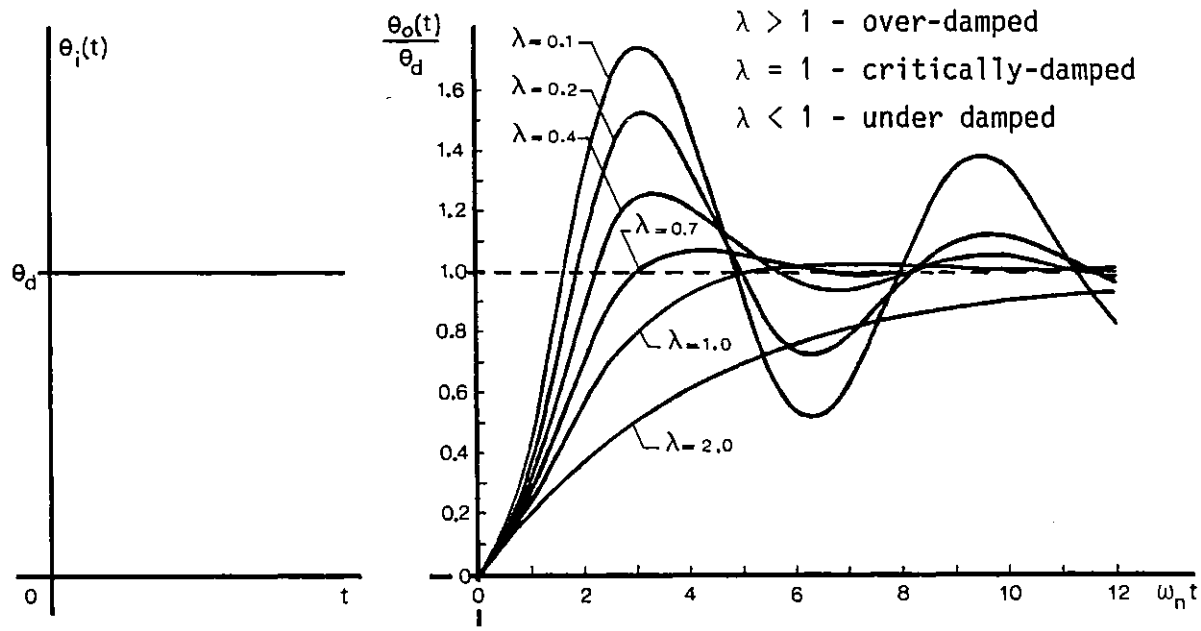

(a) - Step input (b) - Response

Fig. 4.53 - Transient response to a unit step input

of the disturbance and the reaching of its final value θ_d, but there is also the possibility of an oscillatory response the damping of which is determined by the value of λ.

4.12.2 - Effect of tachometer feedback

It is now evident that the response reaches its final value most quickly if the system is under damped ($\lambda < 1$), although it will be subject to oscillations which is normally undesirable. In practice one attempts to design a physical system having this form of response so that λ lies between about 0.60 to 0.85. One way to do this is by deliberately increasing friction, though this of course reduces the peak torque available.

The standard technique used in position control systems is to add a negative velocity feedback signal from a tachometer mounted on the actuator

shaft. This brings a kind of anticipatory action into the system. The tachometer, being a derivative device, can therefore forecast the future value of the output. A new branch with $V_o' = K_B s\theta_o(s)$, where K_B is the tachometer constant, is now incorporated in the block diagram, as shown in fig. 4.54 . The new damping ratio can be readily demonstrated to be

$$\lambda' = \frac{D + AK_T'K_B}{2\sqrt{AK_T'K_pJ_\ell}} \tag{4.101}$$

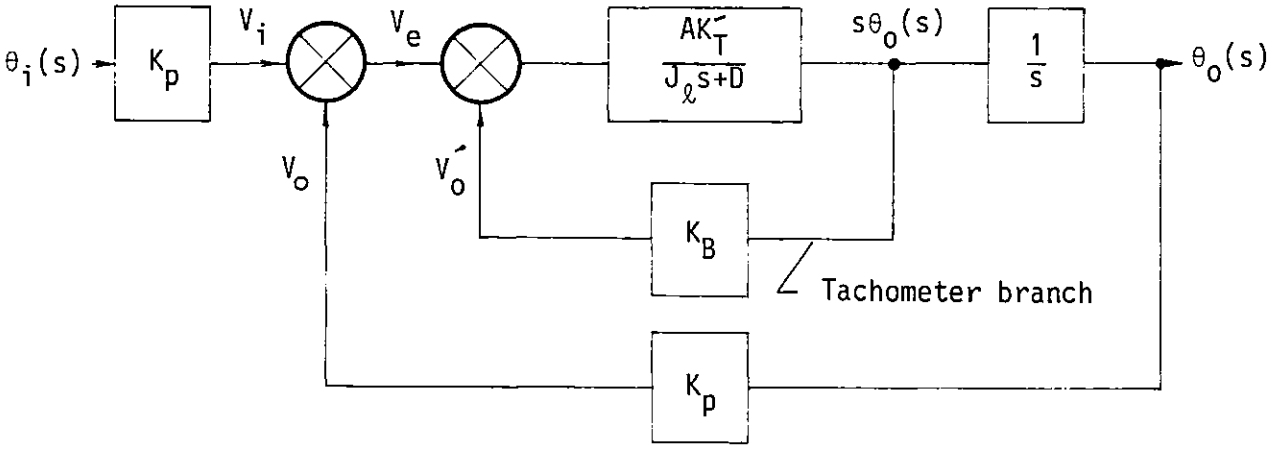

Fig. 4.54 - Block diagram with tachometer introduced

showing that the "friction" term has an additional part $AK_T'K_B$ coming exactly from the new feedback loop introduced. This way of damping the system output seems to be rather better than simply increasing mechanical friction.

4.14.3 - System response with variable input

One possible application for the actuator is as a radar aerial drive. When the aerial tracks a moving object the input signal, i.e., the predicted position of the moving object, would be continuously variable. For simplicity, the situation in which the input angular displacement is a linear function of time (a ramp function) is considered, as shown in fig. 4.55(a).

Assuming zero initial conditions is $\theta_i(s) = \frac{C}{s^2}$ and so, substitution into Eq. (4.99) gives

$$\theta_o(s) = C \frac{\omega_n^2}{s^2(s^2 + 2\lambda\omega_n s + \omega_n^2)}$$

which inverse Laplace transform [70] is

$$\theta_o(t) = C\left[-\frac{\alpha_2}{\alpha_1(\alpha - \alpha_2)} e^{\alpha_1 t} + \frac{\alpha_1}{\alpha_2(\alpha_1 - \alpha_2)} e^{\alpha_2 t} - \frac{\alpha_1 + \alpha_2}{\alpha_1\alpha_2} + t\right] \qquad (4.102)$$

where

$$\alpha_1 = \omega_n\left[-\lambda + \sqrt{\lambda^2 - 1}\right] \qquad \text{and} \qquad \alpha_2 = \omega_n\left[-\lambda - \sqrt{\lambda^2 - 1}\right]$$

and takes the form shown in fig. 4.55(b).

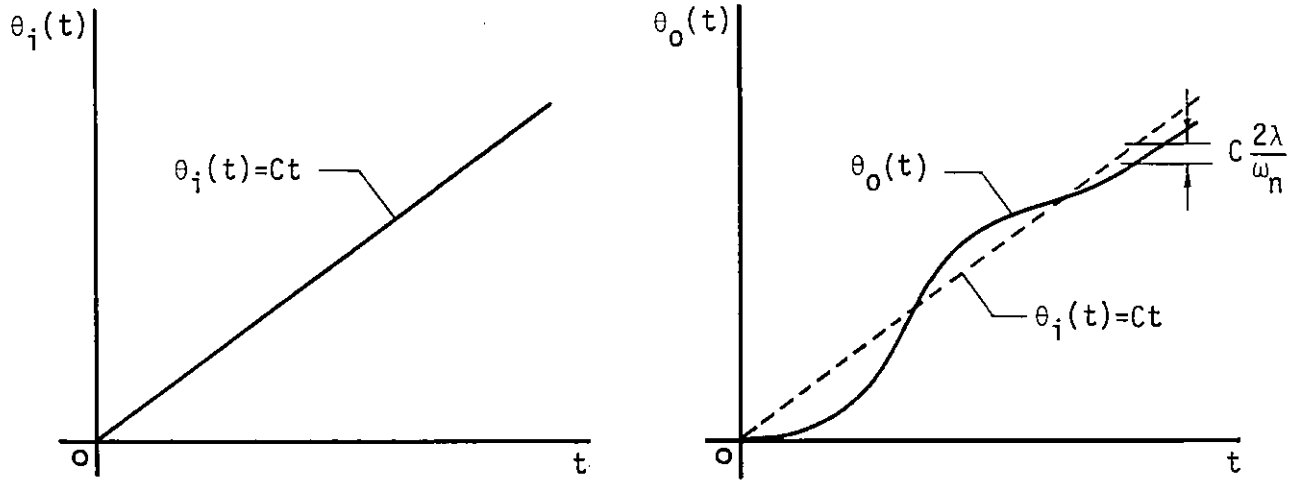

(a) - Ramp function (b) - Response

Fig. 4.55 - Transient response to a ramp function

From Eq. (4.102), after a sufficiently long period of time when the initial oscillations have died away

$$\theta_o(t) \simeq C\left[-\frac{\alpha_1 + \alpha_2}{\alpha_1\alpha_2} + t\right]$$

Thus, after a considerable time, an error always remains between the output and input, of magnitude

$$\theta_o(t) - \theta_i(t) = -C\,\frac{\alpha_1 + \alpha_2}{\alpha_1\alpha_2} = C\,\frac{2\lambda}{\omega_n}$$

This steady state error is an inevitable consequence of this type of

system and shows that when the input is changing the output cannot follow accurately, but will always lag behind. If the damping ratio is low the error to a ramp input will be small but the system will be subject to a very large transient overshoot. As before, the damping ratio λ can be controlled by the action of tachometer feedback.

4.15 - NOVEL TACHOMETER

In the block diagram shown in fig. 4.54 the speed signal may be obtained by differentiation of the position signal or using a tachometer. Ripple is a problem in any differentiation-based speed measuring scheme and conventional low speed tachometers are expensive.

Fig. 4.56 shows an exploded view of a special limited rotation tachometer that could be used to control damping of the actuator. The rotor is a wound sector enclosing a circumferential iron return path and a possible structure is shown in fig. 4.57. Permanent magnet excitation would normally be used but coil excitation would also be possible. The ring magnet is axially magnetised and a typical flux path is shown in the diagram.

As far as the flux path is concerned the device can be classified as a homopolar machine. Hence the output is d.c. and so does not require demodulation. Because teeth and slots are absent ripple levels are expected to be extremely low. The brushes and sliprings may be replaced by flexible leads, making the device inherently brushless. Therefore no contact drop, electrical noise or sparking problems occur.

The method of fabricating the moving coil could follow any number of methods developed for "moving-coil" and "printed-circuit" motors, which use an air gap winding bonded in epoxy resin. Thus the inertia of the moving element of the proposed tachometer is very low and this may be helpful in certain cases. The torque exerted by the flexible leads will be very small and will be predictable.

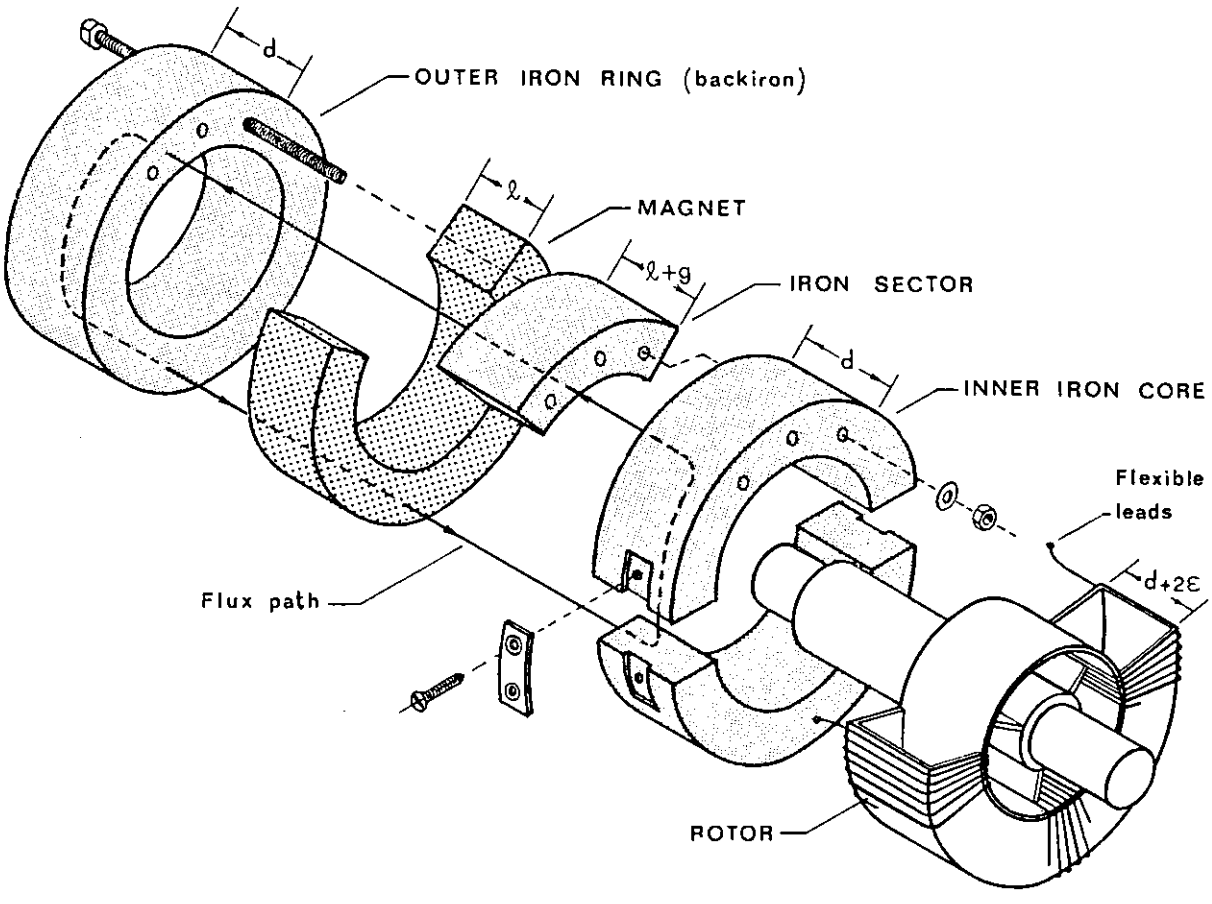

Fig. 4.56 - Exploded view of the homopolar brushless tachometer

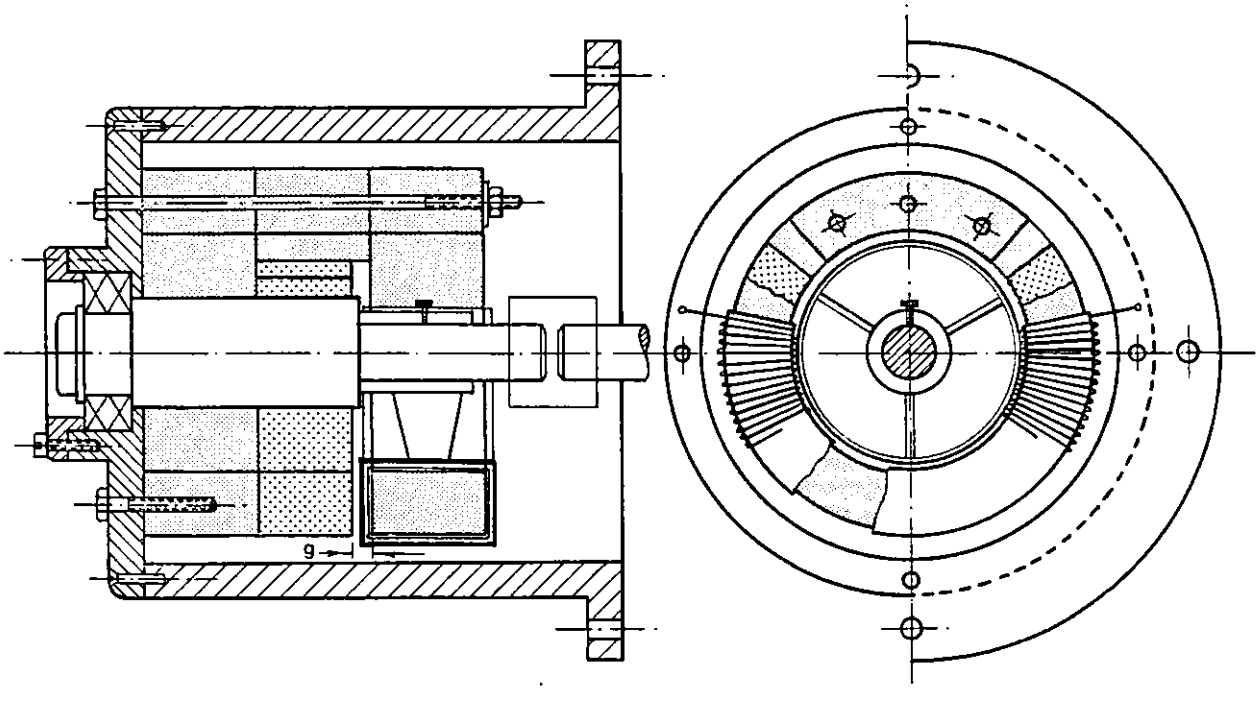

Fig. 4.57 - Structure of the limited rotary tachometer

The cost of the device should be modest because:

i) - the magnetic circuit is very simple and need not be laminated.

ii) - there is only one coil to make; the costs associated with mult-coil d.c. tachometer (coil-forming, insertion of slot insulation, insertion of coils, manufacture and assembly of commutator and brush-gear, making the connections between coils and commutator segments) are avoided.

The predicted sensitivity of the proposed tachometer is K_B = 3.46 V/(rad.s^{-1}) and a brief design is described in Appendix G.

☆ ☆ ☆

CHAPTER 5

TWO-PHASE AUTO-PILOTED DISC SYNCHRONOUS MOTOR

5.1 - GENERALITIES

The commercially-produced "disc motor" is an axial air gap machine with a multipolar, permanent magnet field system and a disc-shaped rotor. It differs from conventional machines in that the air gap flux is predominantly axial, and the active rotor conductors are radially disposed with respect to the shaft.

The first recorded instance of an electric motor was Faraday's disc invented in 1821, and an axial field was employed as shown in fig. 5.1.

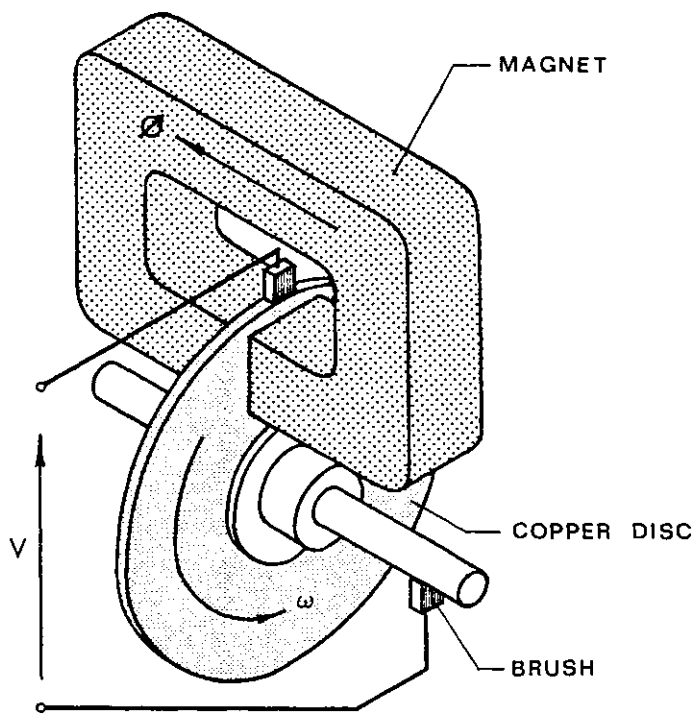

Fig. 5.1 - Faraday's disc machine

Many of the earliest machines were basically axial flux, but this feature became more a topic of historical interest than a commonly used one in the

20th century, in spite of the filing of many patents [92, 93, 94]. The fact that the disc motor configuration is generally less convenient in production than the conventional drum configuration was probably the main factor responsible for this. The strong magnetic pull in the single rotor/stator disc configuration due to the presence of iron in the rotor was another factor.

This problem, however, can be largely or entirely overcome either by using a double stator machine or by using an "ironless" rotor, and the new technology of printed circuits led Henry Baudot in the late 1950's to patent an axial air gap printed circuit armature motor [95] incorporating both features. The absence of iron in the armature gives the rotor not only a low inertia, but results in relatively small values of armature inductance. Research and development in the U.K. on d.c. ironless rotor disc motors began at the Universities of Warwick and Cambridge in 1967, and since that time several prototype motors for domestic and industrial applications have been built and evaluated [18, 96, 97, 98]. Printed circuit disc d.c. motors are now widely used, being manufactured by a number of companies under licence throughout the world. D.c. disc motors with wire-wound armatures are also produced by at least one company.

Synchronous disc motors with permanent magnet excitation and ironless armature constructions (with either rotating armature or rotating field) are worth investigating because they are able to share some of the disc d.c. motor's advantages (low armature inertia, low armature inductance, armature conductorwork can be punched out of flat copper sheet, magnets can be flat not segment-shaped) while the disadvantages of a commutator are of course eliminated. Such motors can of course be inverter-fed and operated in the auto-piloted or "brushless d.c." mode.

5.2 - MACHINE CONFIGURATION

It was decided to concentrate efforts on the rotating armature version of the motor. The motor hence possesses what is sometimes called an "inverted layout" in which the field structure is static. The ironless, disc-shaped rotor is fed via sliprings. In a fully developed design, this will enable a high torque per inertia ratio to be obtained without the use of high performance permanent magnets. Fig. 5.2 illustrates the arrangement of the prototype machine with the main dimensions shown.

The field system comprises sixteen cylindrical bars of permanent magnet material (Alcomax 3) fixed to the mild steel plates by epoxy resin adhesive in an eight-pole, double sided configuration. The entire stator assembly was in fact obtained from an existing d.c. disc motor.

Two types of rotor construction, one wire-wound and one printed circuit were investigated. The rotors' outer diameters were equal but their thicknesses differed considerably. In fact with the wire-wound rotor the magnetic air gap is relatively large and this means that armature reaction effects would be expected to be negligible, as will be shown later.

A specially constructed optical rotor position sensor assembly, coaxial with the shaft, was made and the switching circuitry attached to the motor. In integrated form, the sensor and its circuitry could be made extremely compact. The entire motor system would then possess the flat, axially-thin proportions of the standard disc d.c. motor.

5.2.1 - Wire-wound rotor construction

This rotor was wound with a number of bundle of conductors per pole per phase of $q = 2$ and a total number of coils $Q = m n_p q = 32$. The coils having $n = 20$ turns each and wound from polyester enamelled (class F) of 0.4 mm diameter, were made in a standard type of former and assembled on a flat surface, as shown in the photograph of fig. 5.3. The coils were then connected to produce a two-phase winding according to the diagram shown in fig. 5.4.

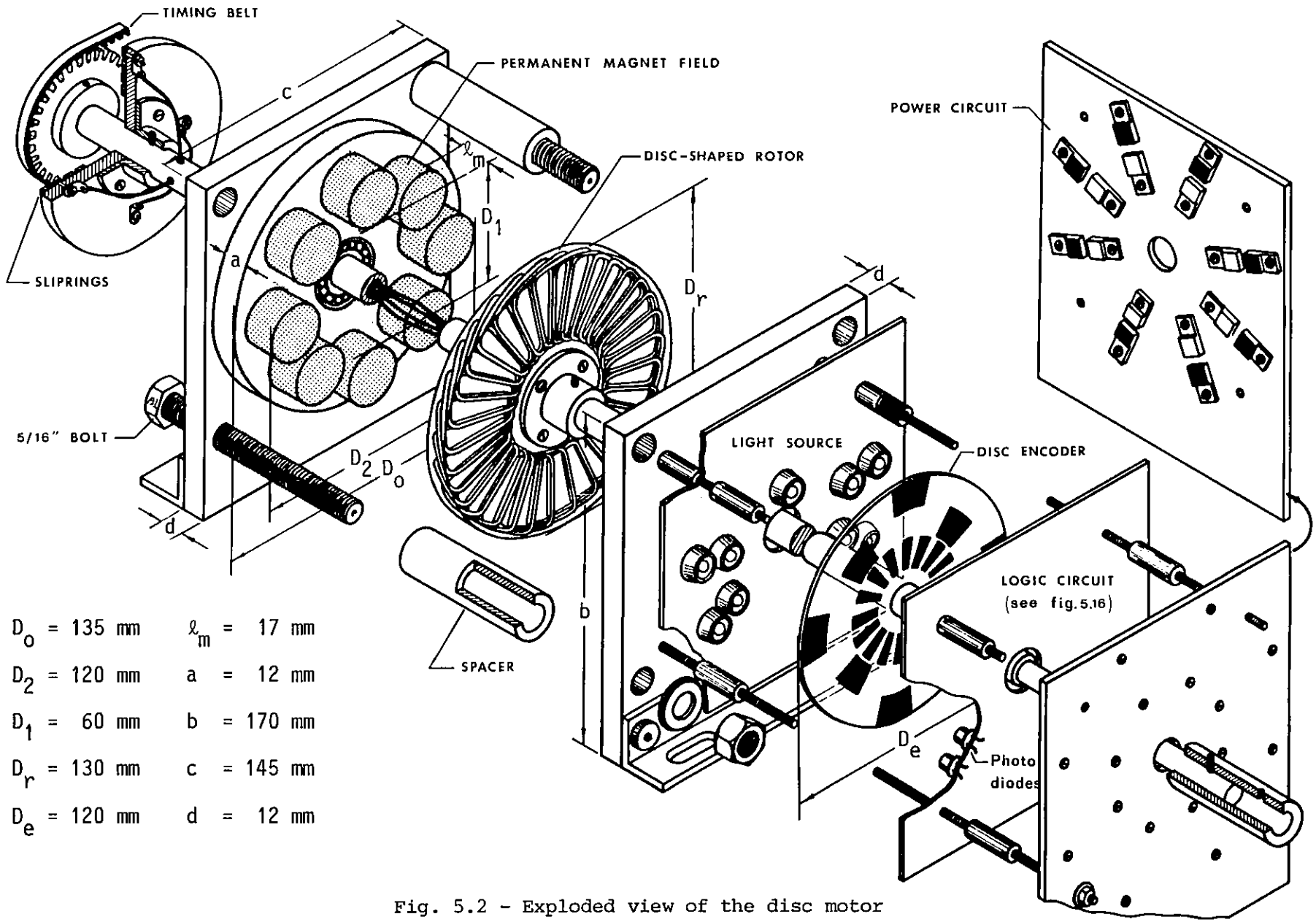

Fig. 5.2 - Exploded view of the disc motor

Fig. 5.3 - Wire-wound rotor coil assembled

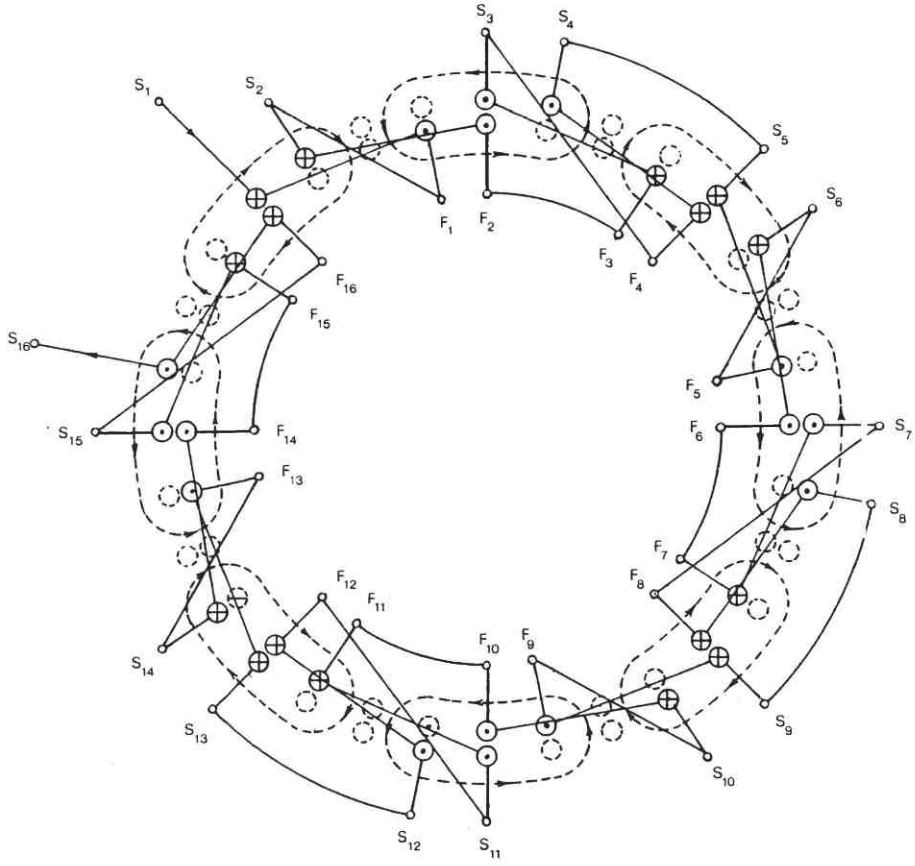

Fig. 5.4 - Rotor winding diagram connections
(only one phase shown)

The winding was then placed between two glass fibre sheets and encapsulated in a high temperature grade of epoxy-resin using a moulding technique. The whole was then machined flat. The final disc axial thickness was 6.8 mm in the active region. Fig. 5.5 shows a photograph of this rotor mounted on the non-magnetic shaft together with sliprings and disc encoder. Again, the slipring assembly was made somewhat bulkier than necessary. A much more compact unit would suffice in practice. Connections between the rotor phase winding and sliprings were made through the hollow shaft.

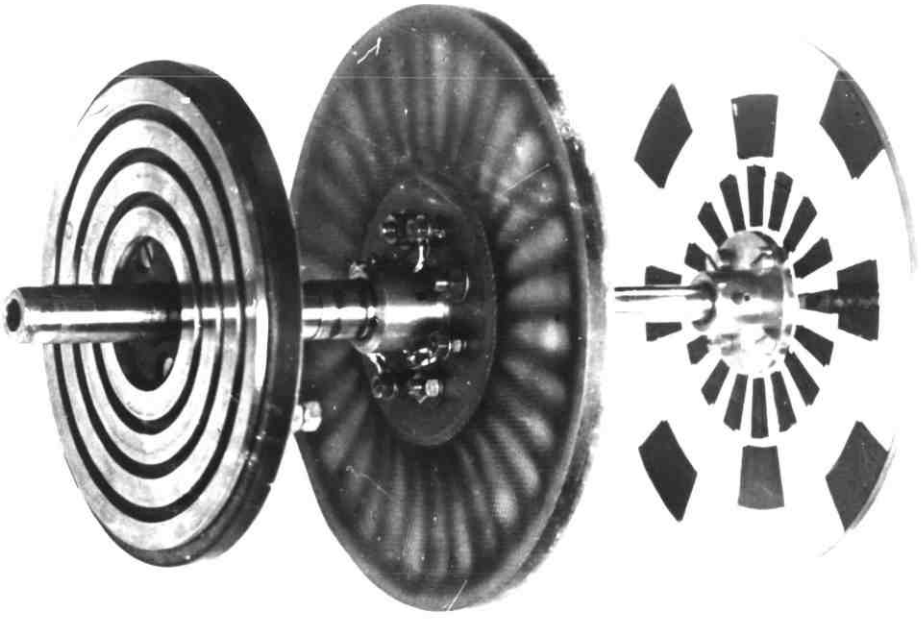

Fig. 5.5 - Wound rotor, sliprings and disc encoder

With a mean length of one turn of ℓ_{mean} = 105 mm the predicted resistance per phase was R = 4.62 Ω and the measured value obtained by using the Kelvin bridge was R_{meas} = 5.1 Ω.

In a disc configuration machine it is important to ensure that the rotor runs truly perpendicular to the shaft, so that minimum clearance

can be allowed between the disc and magnet faces. A nominal clearance on each side of the disc of 0.6 mm was achieved, giving an air gap g between the magnet faces in the prototype of 8 mm. With metallic magnets

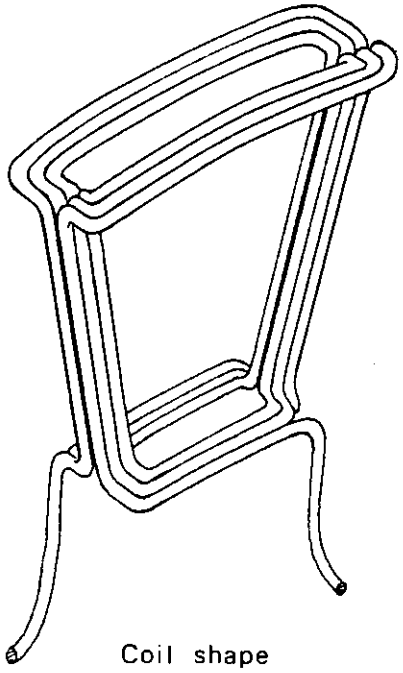

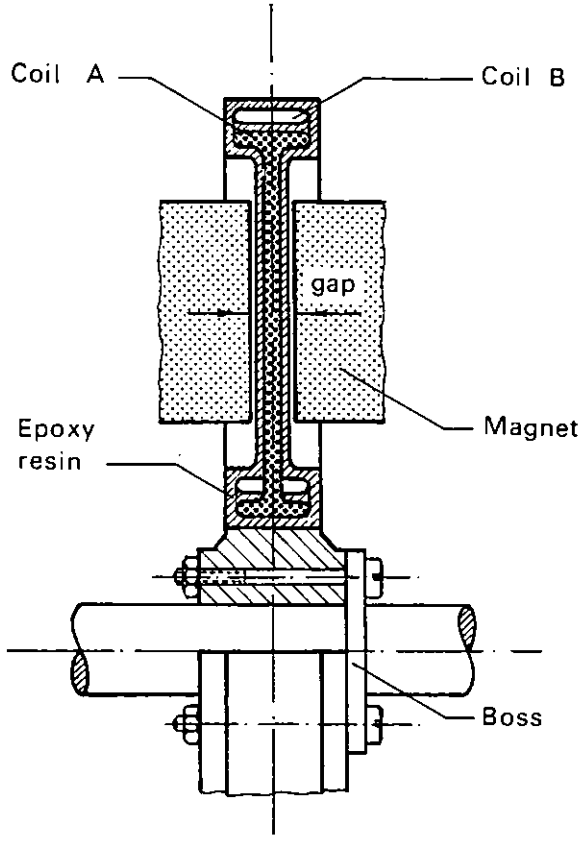

Fig. 5.6 - Improved winding arrangement

this figure is perhaps too high, but it could substantially be reduced if the end coils were extended out of the active region by arranging the winding as shown in fig. 5.6. This is a more difficult task constructionally and was not attempted.

5.2.2 - Printed rotor layout

The original rotor of the d.c. disc motor was used in modified form. Fig. 5.7 shows a photograph of the printed rotor mounted on the shaft. The rotor uses an eight-pole, wave retroprogressive winding with C = 137 coils each having a single turn, and fig. 5.8 shows the diagram connections of two turns of armature.

The radial conductors were electrodepositated on an insulated disc (the so-called "printed-circuit" technique), but punched copper or alumin-

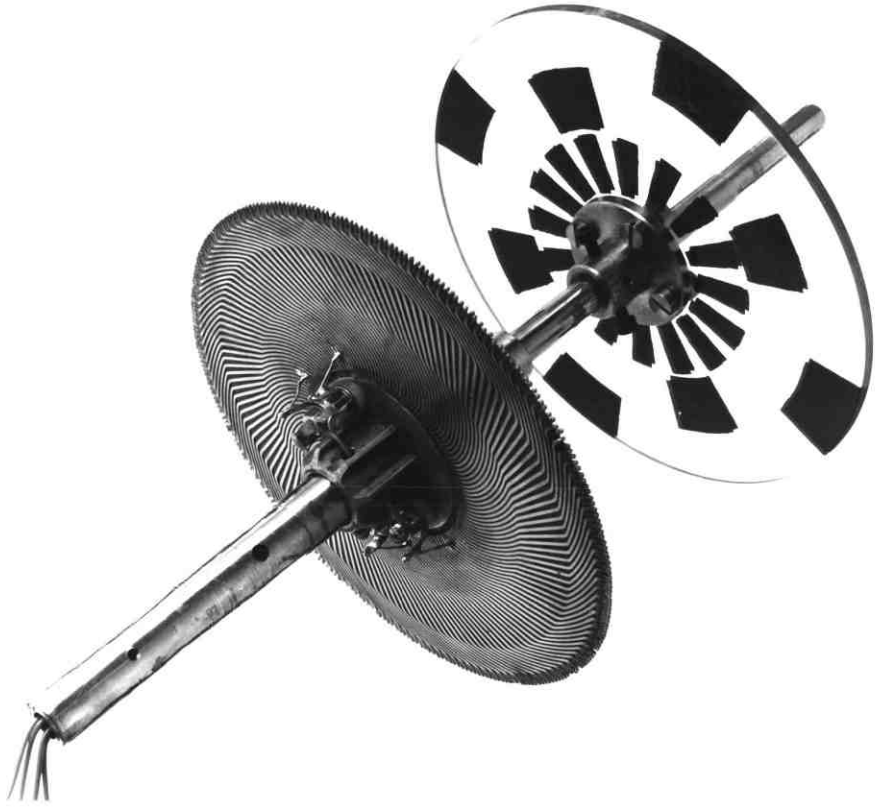

Fig. 5.7 - Printed rotor and disc encoder

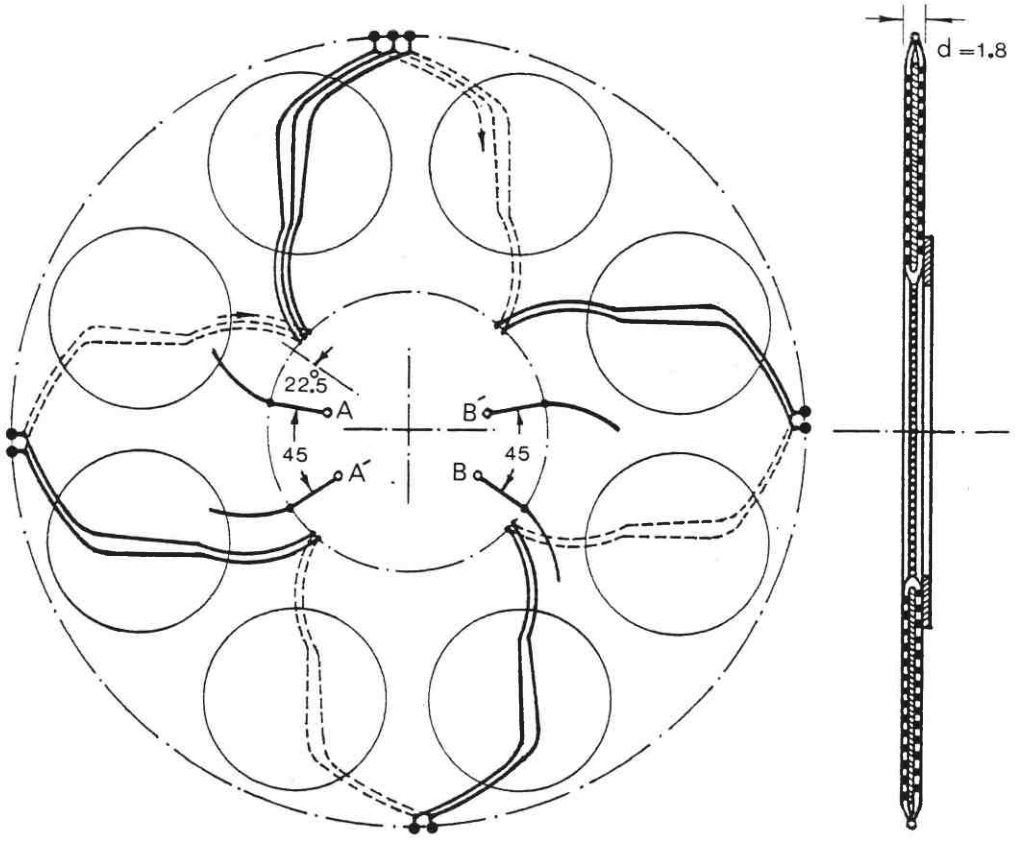

Fig. 5.8 - Printed rotor winding diagram

ium sheet may also be used. The front and back half-windings are located on the faces of an epoxy impregnated glass fibre disc, and the resin is cured under pressure. The centre hole and the sheet edges are cut away and the halves of the end connectors welded together to form the complete winding. This ironless rotor has no hysteresis or saturation, and has low inertia and inductance, although there may be a significant level of eddy-current in the copper conductors.

It is well known that for a wave winding, two brush studs, one positive and one negative suffice for any number of poles, but of course the current per brush is relatively high and there is minor asymmetry. The brushes, despite their uniform spacing around the commutator, are associated with only two regions of the winding and give a single pair of parallel circuits, regardless of the number of poles [99]. Exploiting this feature of the wave winding, it was transformed into a two-phase winding by taking two taps 90°E (22.5° mechanical) apart, as shown in fig. 5.8. The measured resistance between two taps 90°E apart was R = 2.3 Ω.

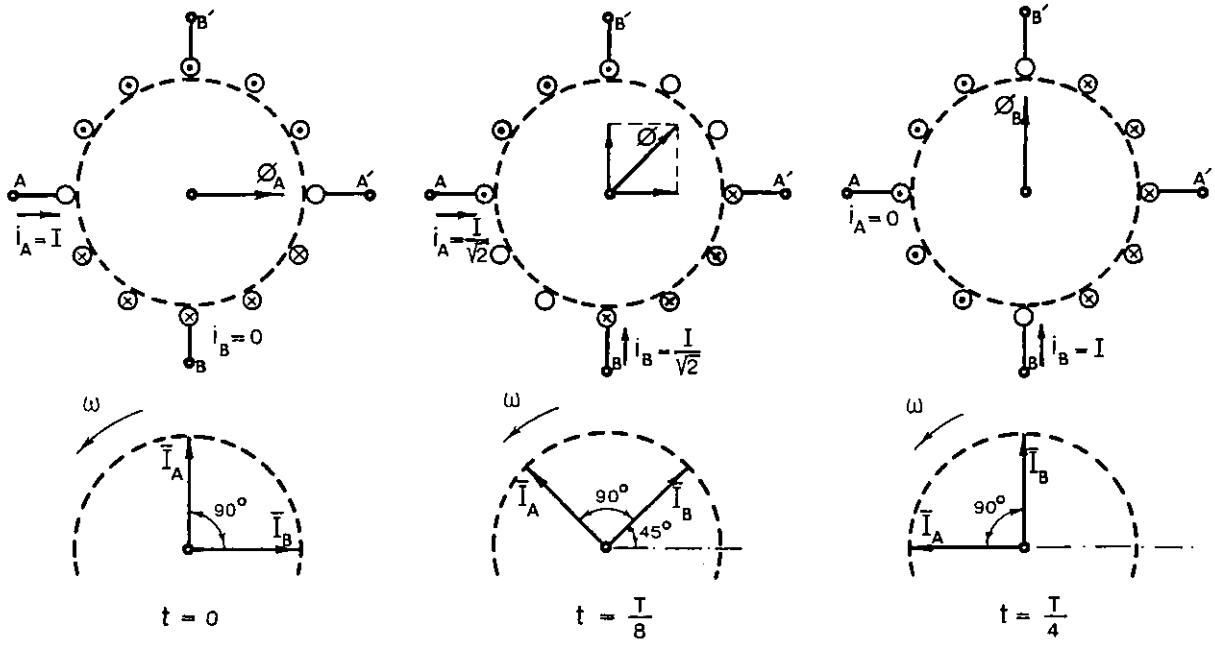

Fig. 5.9 - Generation of the rotating field

The complete closed winding is useful for each phase and this gives a better copper utilization as compared with the previous wire-wound rotor, where the two phases are distinctly separated. Fig. 5.9 illustrates how

the closed winding for a two-pole rotor generates a rotating field for a two-phase system.

The disc has an axial thickness of 1.8 mm and with the same clearance as used for the wound rotor, the magnetic air gap was g = 3 mm.

5.3 - AIR GAP FLUX DENSITY CALCULATION

The scalar potential finite-difference method described in section 2.7.7 was applied over one pole pitch of the axial field machine with its field system of cylindrical "bar" magnets. Again, the non-linear characteristic of Alcomax 3 has been represented by Eq. (2.77) and fig. 5.10(a) shows the computed no-load equipotential contours at 50 A intervals, corr-

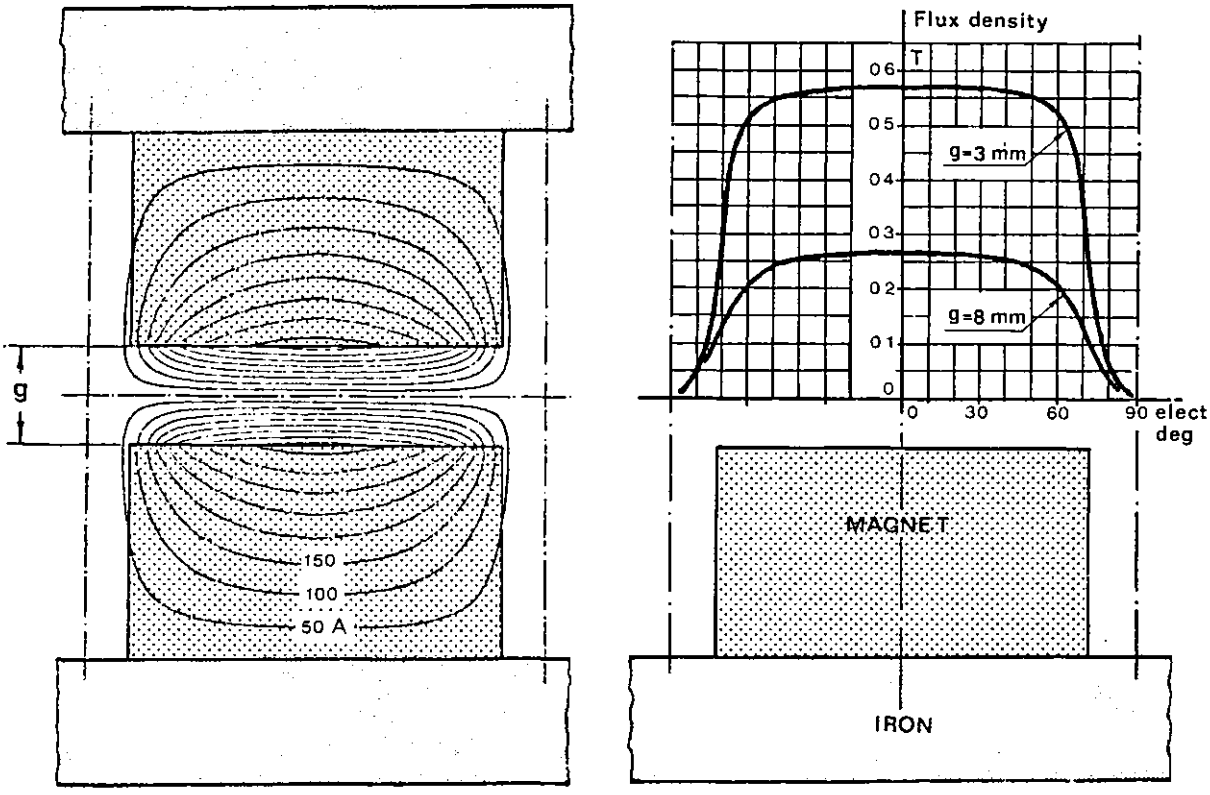

(a) - Equipotential contours (b) - Air gap flux density

Fig. 5.10 - Computed no-load air gap flux density

esponding to a gap g = 8 mm. The flux density variation versus radial position along the pole centreline for two different values of magnetic air gap: g = 3 mm and g = 8 mm (used with printed and wound rotors respectively), is illustrated in fig. 5.10(b).

As expected the flux density is practically constant in the middle region of the air gap, particularly if the gap is kept small.

5.4 - ARMATURE REACTION AND INDUCTANCE CALCULATION

As already stated, this machine has an ironless rotor. Since the relative recoil permeability used for Alcomax 3 was $\mu_{rec} = 1.91$, the magnets are seen practically as an air gap by the winding [100]. It is therefore considered adequate to evaluate the effect of armature reaction on the permanent magnet field system by superposition.

Fig. 5.11(a) shows the computed flux plot and fig. 5.11(b) illustrates the flux density variation over a pole pitch at 90°E torque angle due only to the nominal current I = 5 A.

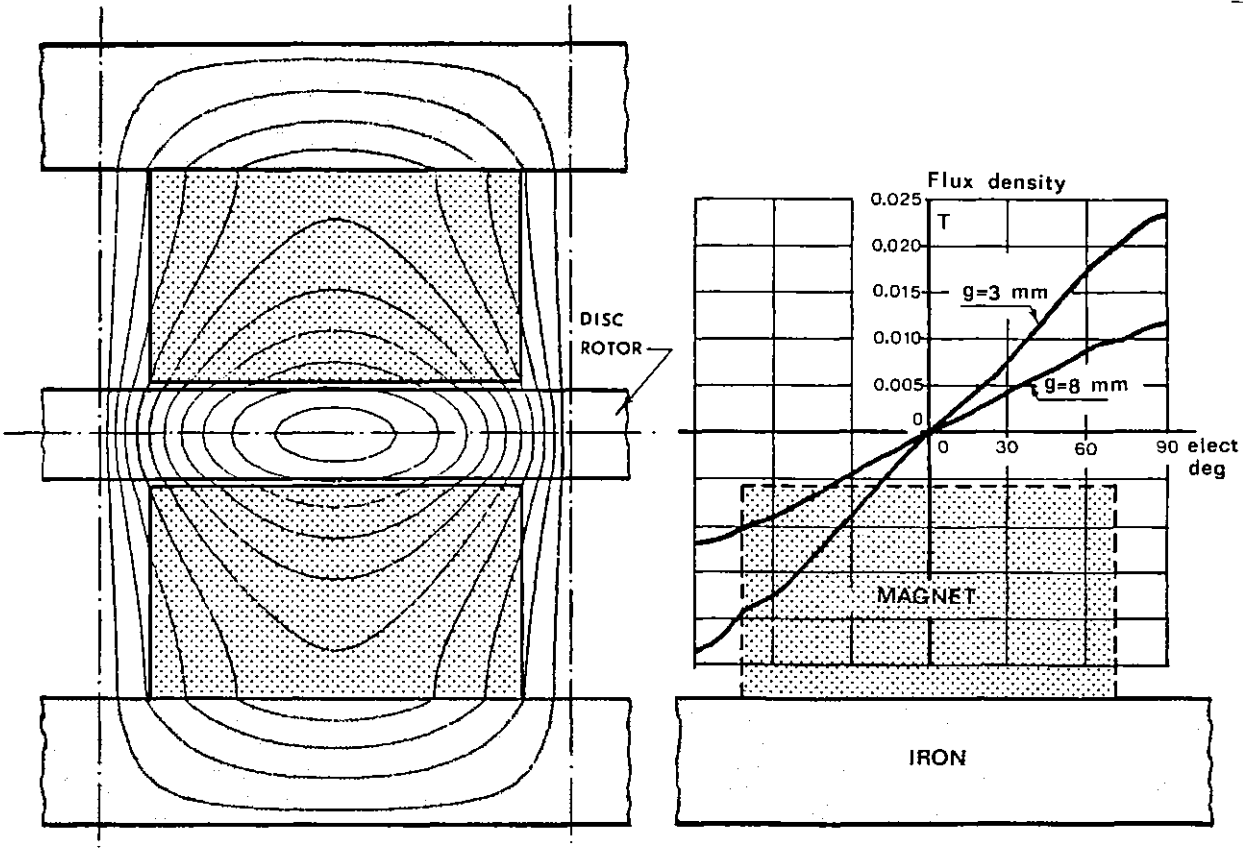

(a) - Flux lines distribution (b) - Field flux density

Fig. 5.11 - Computed armature reaction variation

These results show that the armature reaction is negligible in this motor and the maximum flux density produced by the nominal current is only

about 5% of the field flux density shown computed in fig. 5.10(b).

Assuming the radial rotor conductors to be uniformly distributed over one pole pitch, the inductance per phase was computed from the field map by calculating the stored energy in the region [51]. The inductance is then given by

$$L = r \frac{\Sigma A_k}{N n i} n^2 \qquad (5.1)$$

where r is the mean radial depth of conductors, N the total number of Poissonian field points, A_k the vector potential in each point and n the number of turns in the winding. The armature inductance computed by this method was 0.774 mH/phase for the wound rotor and 0.185 mH/phase for the printed rotor. The respective values measured during tests with the rotors assembled using the d.c. inductance bridge described in section 4.12.2.i were 0.85 mH/phase and 0.21 mH/phase, which compare reasonably with the computed values.

5.5 - BACK E.M.F. AND TORQUE CONSTANT

Although the air gap flux density is practically constant over the active conductor region, it is assumed for generality that $B(r, \theta)$ is a function of radial and angular position over a pole pitch and is normal to the rotor conductors. Then, considering the element of armature conductor dr in position (r, θ) with linear velocity $v_r = \omega_r r$ as shown in fig. 5.12, the induced electric field $E_i(r, \theta)$ becomes:

$$E_i(r, \theta) = \omega_r r B(r, \theta) \qquad (5.2)$$

Hence, the back e.m.f. per radial conductor at angular position θ is:

$$e(\theta) = -\int_{R_2}^{R_1} E_i(r, \theta) dr = \omega_r \int_{R_1}^{R_2} B(r, \theta) r \, dr \qquad (5.3)$$

It would be convenient to remove the dependence of flux density on

radius, so that the integration of Eq. (5.3) can be performed. The use of such a flux density, $B(\theta)$, would only be valid if $B(\theta)$ itself was defined as an integration of $B(r, \theta)$ over radius r. The expression for e.m.f. then becomes

$$e(\theta) = \frac{1}{2}\omega_r B(\theta)(R_2^2 - R_1^2) \tag{5.4}$$

and comparing with Eq. (5.3),

$$B(\theta) = \frac{2}{R_2^2 - R_1^2}\int_{R_1}^{R_2} B(r, \theta) r\, dr \tag{5.5}$$

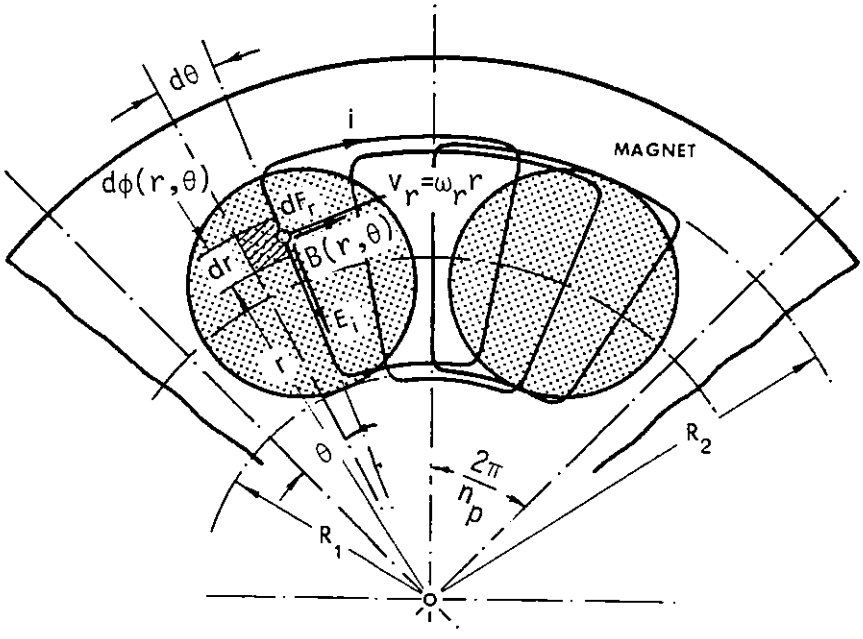

Fig. 5.12 - The induced field and elementary force on the conductor

Clearly, Eq. (5.5) does not give the mean flux density at any given angular position. In order to evaluate the e.m.f. per radial conductor it was suggested [19] that a "moment of flux density" $M(\theta)$ should be defined such that:

$$M(\theta) = \frac{1}{R_2 - R_1}\int_{R_1}^{R_2} B(r, \theta) r\, dr \tag{5.6}$$

and Eq. (5.6) gives now the mean of $B(r, \theta)$ over the active conductor radius. Substitution of Eq. (5.6) into Eq. (5.3) gives

$$e(\theta) = \omega_r M(\theta)(R_2 - R_1)$$

It is now possible to find the average conductor e.m.f. E_c for one pole pitch as

$$E_c = \frac{n_p}{2\pi} \int_0^{\frac{2\pi}{n_p}} e(\theta)d\theta = \omega_r(R_2 - R_1) \frac{n_p}{2\pi} \int_0^{\frac{2\pi}{n_p}} M(\theta)d\theta \qquad (5.7)$$

where n_p is the pole number. Using Eq. (5.6), the mean of $M(\theta)$ over a pole pitch is given by

$$M = \frac{n_p}{2\pi} \int_0^{\frac{2\pi}{n_p}} M(\theta)d\theta = \frac{n_p}{2\pi} \frac{1}{R_2 - R_1} \int_0^{\frac{2\pi}{n_p}} \int_{R_1}^{R_2} B(r, \theta)r\,dr\,d\theta \qquad (5.8)$$

which is independent of angular position. Hence, substitution of Eq. (5.8) into Eq. (5.7) gives

$$E_c = \omega_r(R_2 - R_1)M \qquad (5.9)$$

The quantity M is the mean of $B(r, \theta)\,r$ over the active area of a pole pitch. The elementary flux at position (r, θ) is

$$d\phi(r, \theta) = B(r, \theta)r\,dr\,d\theta$$

and the flux per pole

$$\phi_p = \int_0^{\frac{2\pi}{n_p}} \int_{R_1}^{R_2} B(r, \theta)r\,dr\,d\theta = M \frac{2\pi}{n_p} (R_2 - R_1) \qquad (5.10)$$

Combination of Eq. (5.9) and Eq. (5.10) will eliminate the geometry of the field system. If $B(r, \theta)$ and r are really inseparable, the average e.m.f. E_c for one pole pitch can never be defined as a function of flux density but only as a function of flux per pole such that

$$E_c = \frac{n_p}{2\pi} \omega_r \phi_p$$

However, it is most convenient to express E_c as a function of flux density, rather than as a function of flux per pole. For this purpose, the

assumption must therefore be made that $B(\theta)$, defined by Eq. (5.5), is independent of r. It is then possible to obtain the average conductor e.m.f. E_c from Eq. (5.5), Eq. (5.8) and Eq. (5.9) as

$$E_c = \frac{n_p(R_2^2 - R_1^2)\omega_r}{4\pi} \int_0^{\frac{2\pi}{n_p}} B(\theta)d\theta \qquad (5.11)$$

The specific magnetic loading B_{ave} can then be defined as the average $B(\theta)$ over one pole pitch, and Eq. (5.11) reduces to

$$E_c = \omega_r \, \ell_{ef} \, R_{ave} \, B_{ave} \qquad (5.12)$$

where $\ell_{ef} = R_2 - R_1$ is the effective conductor length and $R_{ave} = \frac{1}{2}(R_2 + R_1)$ its average radius. Having N conductors per pole per phase, the total average e.m.f. per phase is:

$$E = n_p \, N \, \ell_{ef} \, R_{ave} \, B_{ave} \, \omega_r \qquad (5.13)$$

The specific loading on the inner disc periphery is $A_i = \frac{n_p Ni}{2\pi R_1}$ and hence the rotor power becomes

$$E_i = n_p \, Ni \, \frac{1}{2} \, (R_2^2 - R_1^2) \, B_{ave} \, \omega_r = A_i \, \pi \, R_1 (R_2^2 - R_1^2) \, B_{ave} \, \omega_r$$

The maximum rotor power will therefore occur when

$$R_2 = \sqrt{3} \, R_1 \qquad (5.14)$$

which is the familiar relationship found elsewhere, and the same result could be obtained from Eq. (1.93). For the prototype wound rotor shown in fig. 5.3, R_1 = 30 mm and R_2 = 60 mm.

In fig. 5.12 the elementary torque acting on the radial conductor at distance r from the shaft is

$$dT = i \, B(r, \theta) r \, dr$$

and therefore the total torque per phase developed at 90°E torque angle becomes

$$T = n_p N i \int_{R_1}^{R_2} B(r, \theta) r \, dr \qquad (5.15)$$

Assuming again that $B(r, \theta)$ is independent of r and taking the average B_{ave} over a pole pitch, Eq. (5.15) gives:

$$T = n_p N i \, \ell_{ef} \, R_{ave} \, B_{ave} \, i \qquad (5.16)$$

Comparison of Eq. (5.13) and Eq. (5.16) gives

$$K_B = \frac{E}{\omega_r} = \frac{T}{i} = n_p N \, \ell_{ef} \, R_{ave} \, B_{ave} \qquad (5.17)$$

and, as expected, the e.m.f. constant ($V/rad.s^{-1}$) and torque constant (Nm/A) are numerically equal.

5.5.1 - Torque constant evaluation

Using Eq. (5.17) and the average value of the computed air gap flux density shown in fig. 5.10(b), the torque constant may be now evaluated for each rotor.

a) - Wound rotor

For this rotor, using the following parameters:

g = 8 mm $\quad B_{ave} = 0.24$ T

$\ell_{ef} = 27$ mm

N = 2 x 20 x 2 = 80 conductors/pole/phase

$R_{ave} = 45$ mm

the torque constant becomes

$$K_{BW} = 8 \times 80 \times 27 \times 10^{-3} \times 45 \times 10^{-3} \times 0.24 = 0.187 \text{ Nm/A}$$

b) - Printed rotor

In this case:

g = 3 mm $\quad B_{ave} = 0.55$ T

$\ell_{ef} = 24$ mm (by measuring)

$N = 2 \frac{C - 1}{n_p} = 34$ conductors/pole/phase

gives for the torque constant

$$K_{BP} = 8 \times 34 \times 24 \times 10^{-3} \times 45 \times 10^{-3} \times 0.55 = 0.162 \text{ Nm/A}$$

Although the rotors use different magnetic air gaps the torque constants differ little.

5.6 - TWO-PHASE INVERTER CIRCUITRY

A four step two-phase inverter for use with the rotor position sensor was designed and built. The ideal drive waveform is shown in fig. 5.13(a) and the simplest appropriate bridge configuration is shown in fig. 5.13(b).

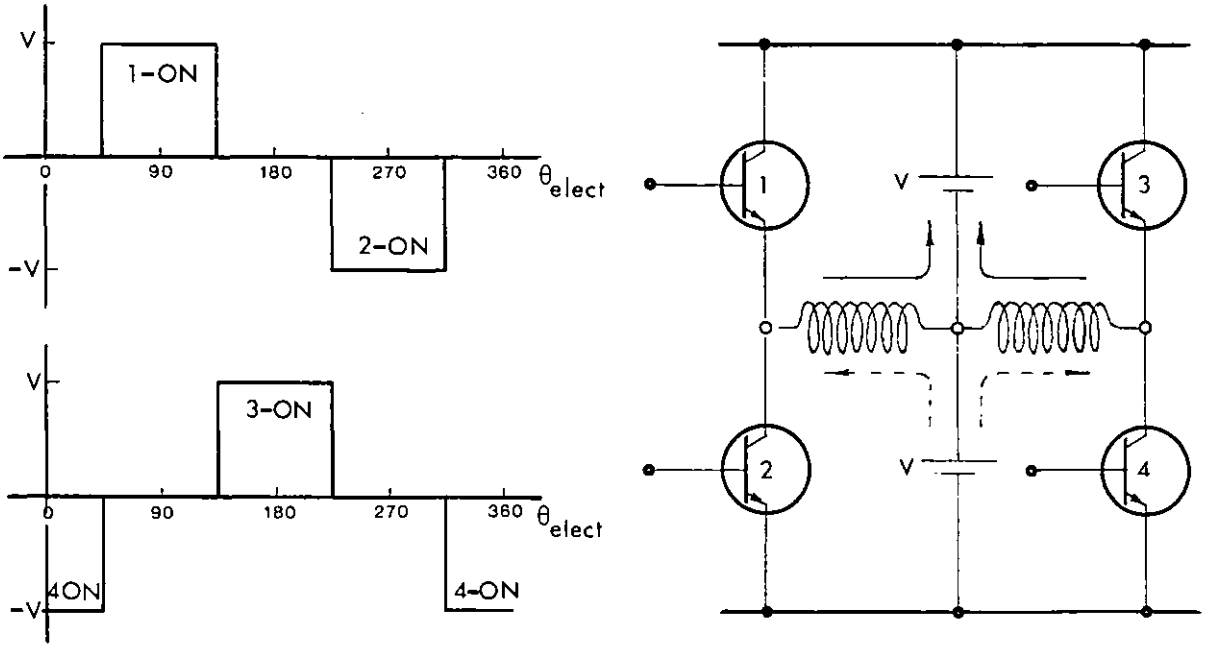

(a) - Drive waveform (b) - Transistor bridge

Fig. 5.13 - Drive waveform and transistor bridge for a two-phase synchronous motor

This bridge uses only four power transistors, but a centre-tapped d.c. source (or two d.c. sources in series) is used. If a bridge with eight power transistors is used, only one source is needed as shown in fig. 5.15. This latter arrangement was in fact used.

The position sensor disc which, here, directly controls the base

drivers, was made from a 120 mm diameter blank of perspex and the pattern (see fig. 5.14) was painted using matt black paint. The outer band controls the lower transistors NPN of the bridge and the inner band the upper transistors PNP. Sixteen slits were also painted on the disc to give a shaft speed output. (The circuit diagram for this is presented in section 5.8.1).

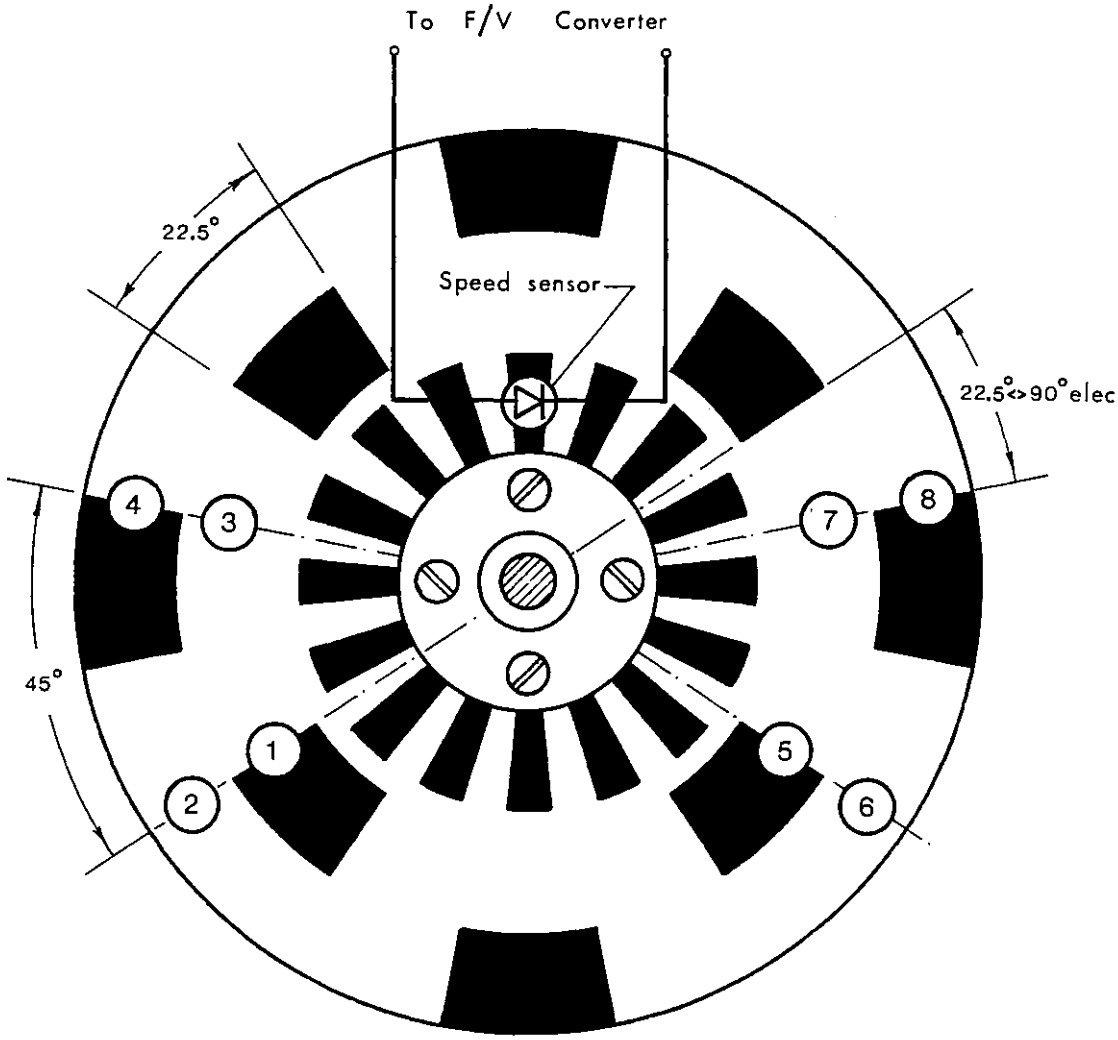

Fig. 5.14 - Disc encoder pattern

Opto-isolators were used in order to make the power circuit independent from the logic circuit. The Schmidt trigger or NAND gate used was a C-MOS integrated circuit. This ensured the logic output threshold necessary for correct switching of the photo-diode signal [101]. With the disc pattern used the respective power transistors are ON when the photo-diode is dark and inverters were placed in series with the NAND gate. (AND gates are

not available in integrated circuit form). Fig. 5.15 shows the complete circuit diagram.

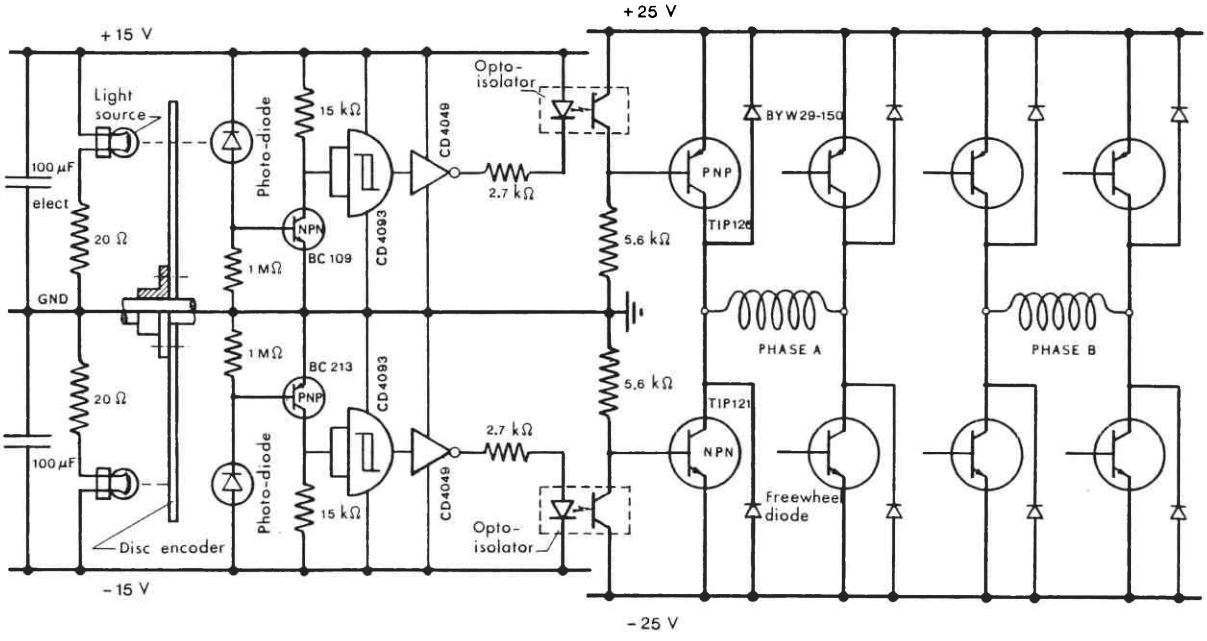

Fig. 5.15 - Logic and power circuit diagram

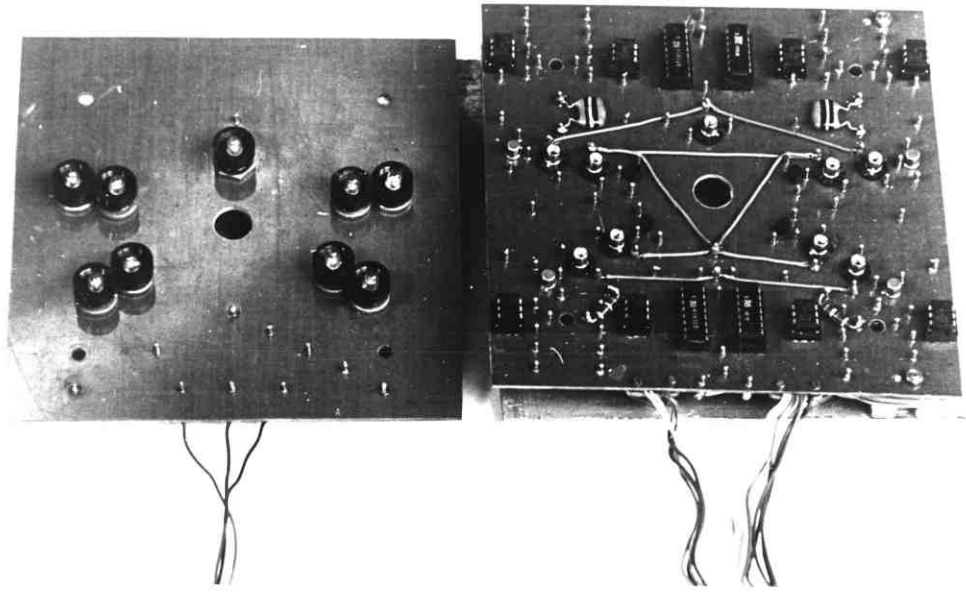

Fig. 5.16 - The inverter circuit components

Filament bulbs (14 V, 0.7 W) were used as the light sources. They were arranged on a paxolin sheet and a photograph of all electronic components is shown in fig. 5.16. The Darlington power transistors and the freewheel diodes were mounted on a 3 mm thick aluminium plate and the entire system was attached to the motor , as already shown in fig. 5.2.

5.7 - MACHINE OPERATION FROM A SINUSOIDAL SUPPLY

Ripple torque is inevitably high with the system just described. Some reduction can be obtained if the motor is sine wave-fed. Rather than employ a synchro-resolver, which if two-pole would need to be geared and whose price and level of precision would not be commensurate with those of the motor, it was decided to develop a novel sine/cosine optical sensor system based on the use of polaroid filtering.

A sinusoidal signal can of course be generated across a photo-diode possessing a linear response by sinusoidally varying the light intensity, as shown in fig. 5.17. This can be achieved with an appropriate disc whose opacity varies sinusoidally. Such opacity variation may be obtained, for example, by photographic means.

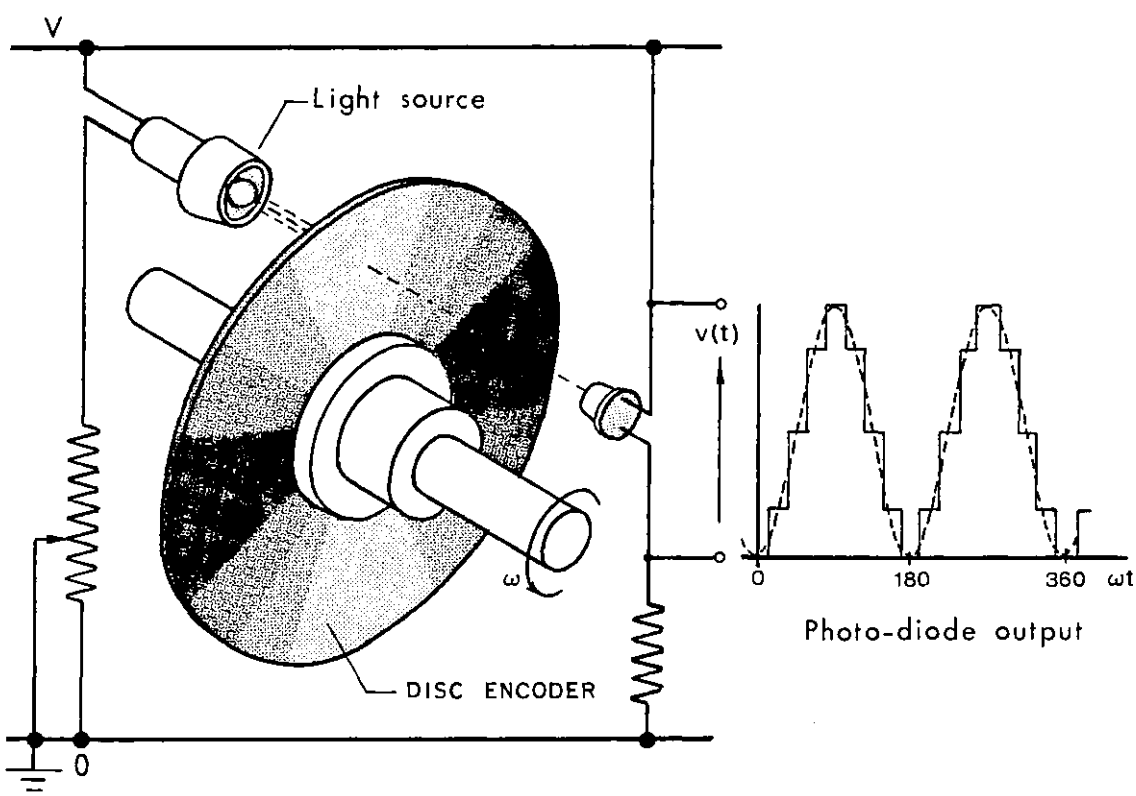

Fig. 5.17 - Principle of an optical position detector

However, opacity can also be varied very easily using two sheets of polaroid material and fig. 5.18 illustrates the principle of operation. The polaroid material polarises the light source. If the optical axes of both sheets are aligned the beam will be transmitted with maximum

intensity. If the two optical axes are at right angles, then the opacity is complete. When both axes are at an angle α_{mec} the light intensity transmitted is proportional to the cosine of this angle.

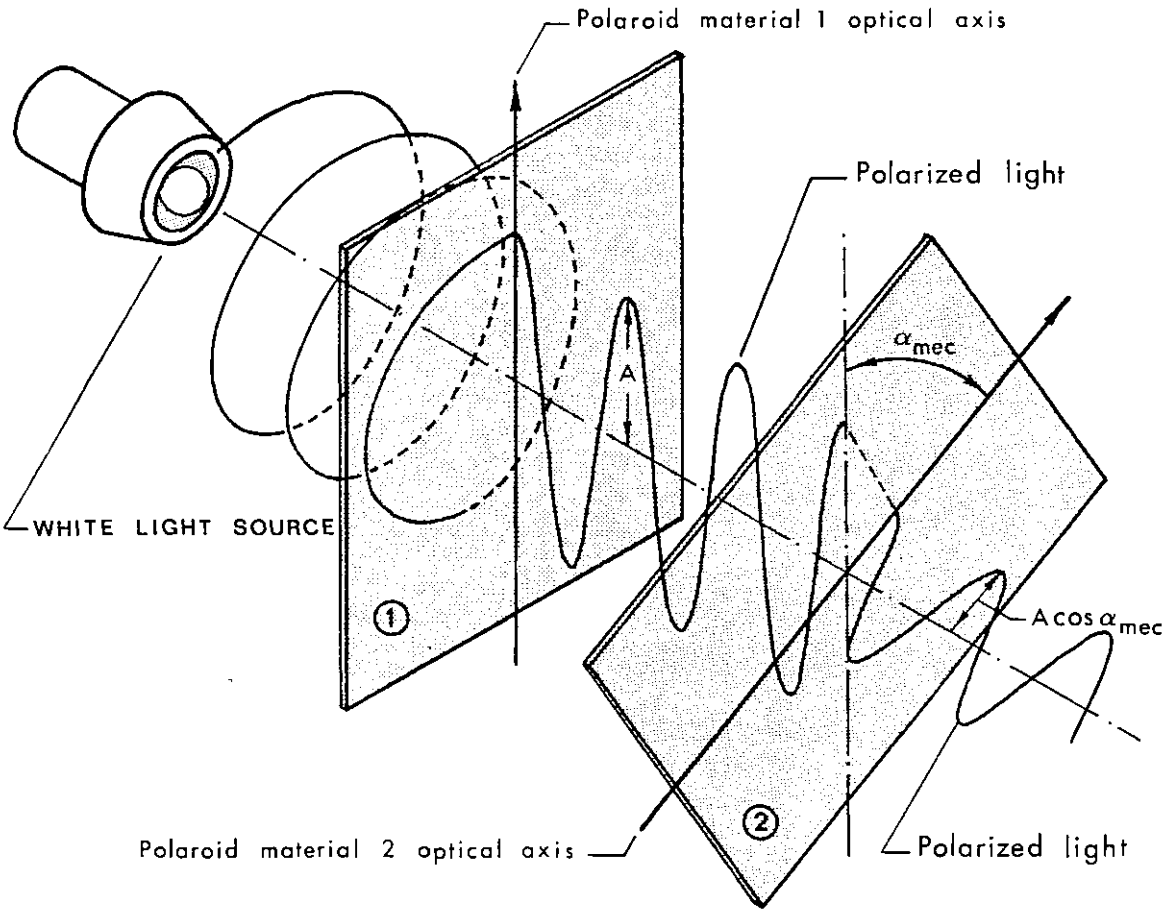

Fig. 5.18 - Principle of operation of the polaroid effect position sensor

Based on this principle an optical position sensor was built as shown in the photograph of fig. 5.19. Again, size could be substantially reduced with development. Basically it consists of a rotating disc and four fixed pieces of polaroid material intercepting each light beam. Two photo-diodes placed mutually 90° mechanical apart are used for each phase to sense the light intensity variation. The two photo-diodes elements used to produce the sine signals are hence 180° apart, and their variations in resistance are ideally of the form $R(1 + F \cos 2\alpha_{mec})$ and $R(1 - F \cos 2\alpha_{mec})$, where F is a constant dependent on the light intensity on the photo-diode.

Similarly, the variation in resistance of the sine elements shifted 45° mechanical from the first pair are of the form $R(1 + F \sin 2\alpha_{mec})$ and $R(1 - F \sin 2\alpha_{mec})$.

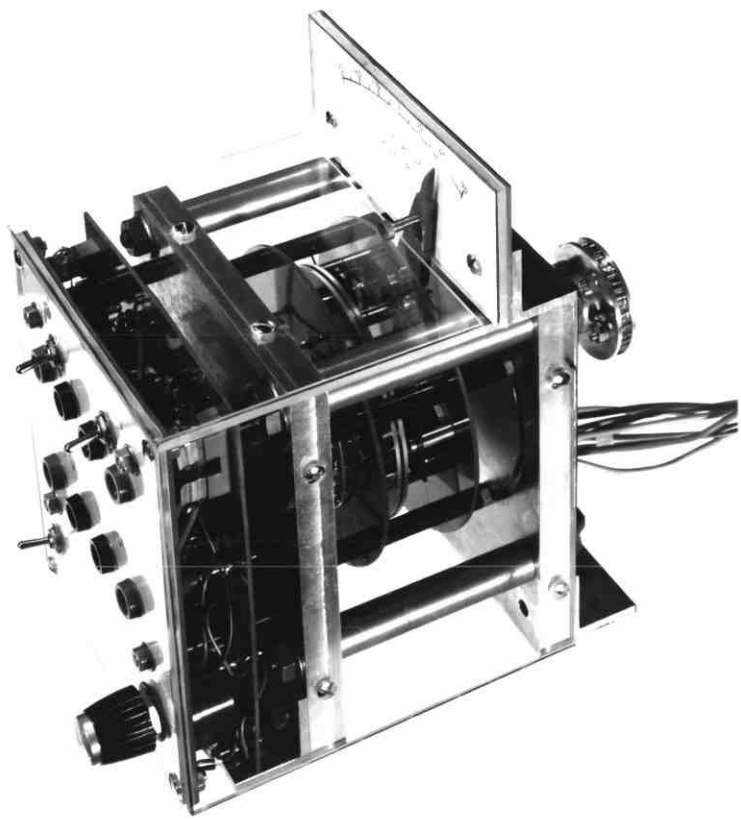

Fig. 5.19 - Polaroid effect rotor position sensor

The bridge arrangement of the optical-resistive elements and the operational amplifier circuitry used to obtain the required sine and cosine signals is shown in fig. 5.20. As compared with the synchro-resolver system, the electronic components used are substantially reduced.

The voltage at the mid point of a pair of photo-diodes is given by

$$V_{mA} = R(1 - F \sin 2\alpha_{mec}) \frac{2V - V_{mA}}{R(1 + F \sin 2\alpha_{mec})}$$

Whence:

$$V_{mA} = V(1 - F \sin 2\alpha_{mec})$$

The d.c. component is eliminated by the operational amplifier used as

a differentiator, giving an output signal

$$V_{oA} = \frac{R_f}{R_x + R_1} \; 2V - \frac{R_f}{R_2} V(1 - F \sin 2\alpha_{mec})$$

By adjusting R_x such that $R_x = 2R_2 - R_1$ the voltage output is therefore

$$V_{oA} = F V \frac{R_f}{R_2} \sin 2\alpha_{mec} \tag{5.18}$$

Similarly, for the other pair of photo-diodes

$$V_{oB} = F V \frac{R_f}{R_2} \cos 2\alpha_{mec} \tag{5.19}$$

These two signals are thus a function of the light intensity, and hence adjustment of the potentiometer P determines the output of the overall system.

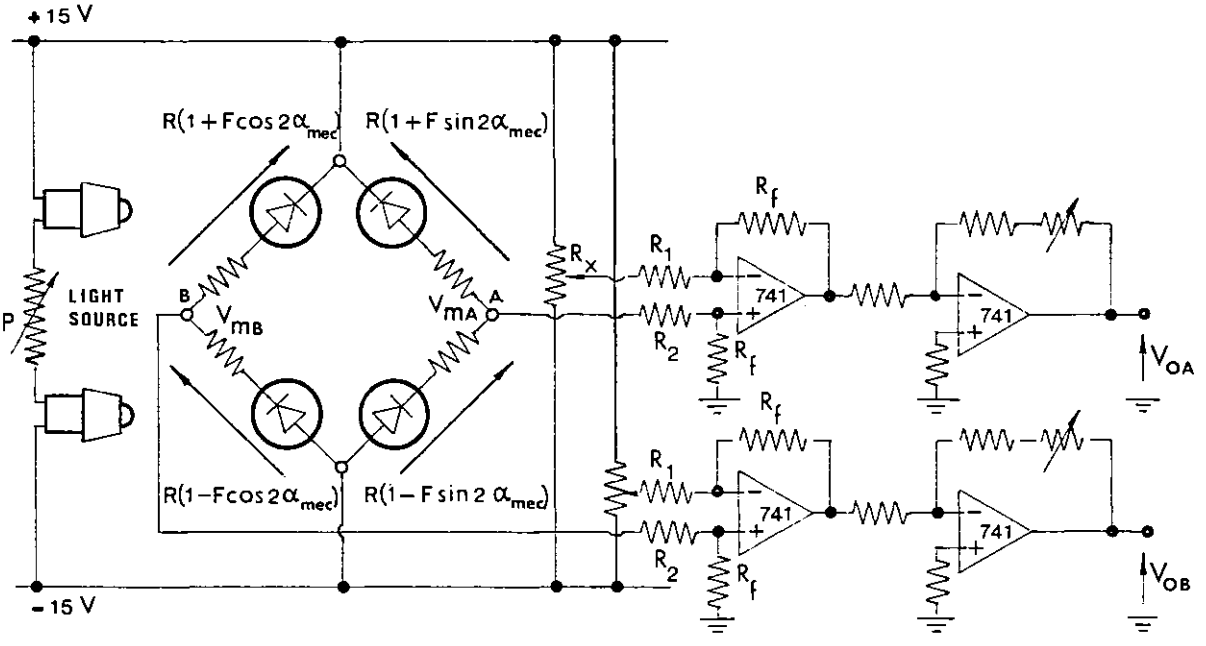

Fig. 5.20 - Optical-resistive bridge for the position sensor

Unfortunately the output corresponds to a four-pole machine and since the disc motor is an eight-pole machine, a gear 2:1 ratio has to be employed. For the project a timing-belt transmission was used. The question of

whether an arrangement using the polaroid principle existed that would output the required sin $4\alpha_{mec}$ and cos $4\alpha_{mec}$ signals was given considerable thought.

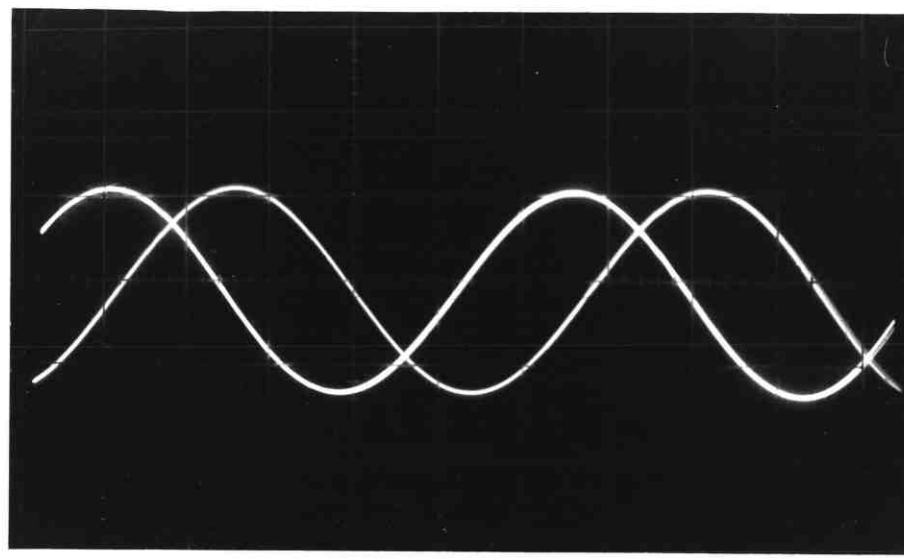

Fig. 5.21 - Polaroid effect position sensor output signal

The signal output obtained from the device can be seen in the oscillogram shown in fig. 5.21 and is thought to be acceptably good for the application (*). The signal magnitude was completely independent of motor speed including standstill, as required by the drive system. The phase of the output signal can be adjusted mechanically by means of a sliding device.

5.8 - TEST RIG FOR OBTAINING SPEED CHARACTERISTICS

In order to compare the motor performance under both square and sine wave operation, a test and display rig was built whose general layout is shown in the photograph of fig. 5.22.

(*) - *When compared with the synchronous-resolver output signal shown in fig. 3.17.d, the output signal obtained from this new position sensor presents less ripple.*

The built-in four step inverter can be by-passed if required as for instance is necessary when testing the motor with sine/cosine feeds. The

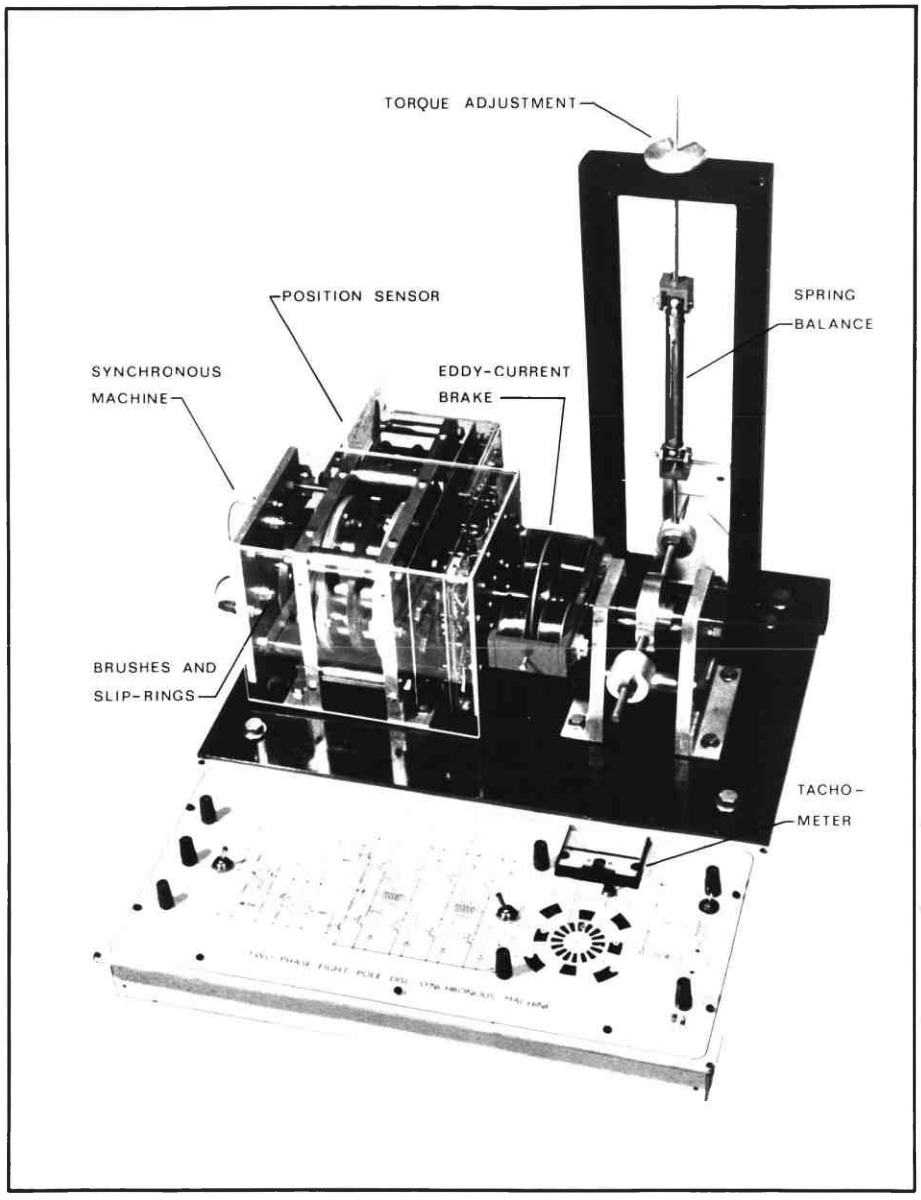

Fig. 5.22 - Axial field disc motor test rig

motor speed was measured by contactless means and the shaft torque by using an eddy-current brake. Brief descriptions of these two items are now given.

5.8.1 - The speedometer

The speed signal from the optical shaft sensor disc was to be converted to a voltage proportional to the speed, using a C-MOS frequency to voltage

(F/V) converter on a single chip [102]. The input signal to the F/V converter must cross zero in order to trip the comparator, and since the photo-diode output is a non-alternating square wave a differentiator network should be used, as shown in fig. 5.23. In order to limit the input signal to ±0.7 V a pair of back to back diodes and a series resistor R_s were

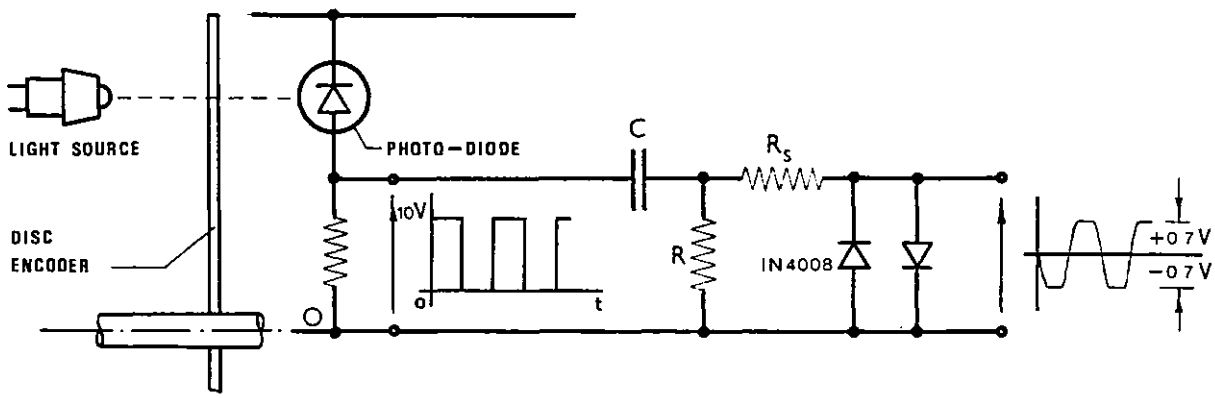

Fig. 5.23 - Frequency to voltage converter input signal

incorporated. This signal was then injected into the F/V converter and the circuit checked by applying a square wave input from an oscillator and measuring the output voltage. The output voltage, directly proportional to the motor speed, was measured in a moving-coil voltmeter calibrated in rev/min. Two full range scales of 1000 rev/min and 10,000 rev/min were available, suitable for low and high speed measurements.

5.8.2 - The eddy-current brake

There are available several methods of measuring torque, but when good accuracy is important the eddy-current brake seems the best method, since friction torque uncertainties are virtually eliminated.

The eddy-current brake consists of a 120 mm diameter copper disc mounted on the end of the motor shaft running in the air gap of a magnetic circuit excited by a d.c. field system. Four coils with a m.m.f. sufficient to develop full motor torque are used, as shown in fig. 5.24. The field system is thus mechanically independent from the motor itself and is mounted on two bearings, which allow rotation with low friction. The system is att-

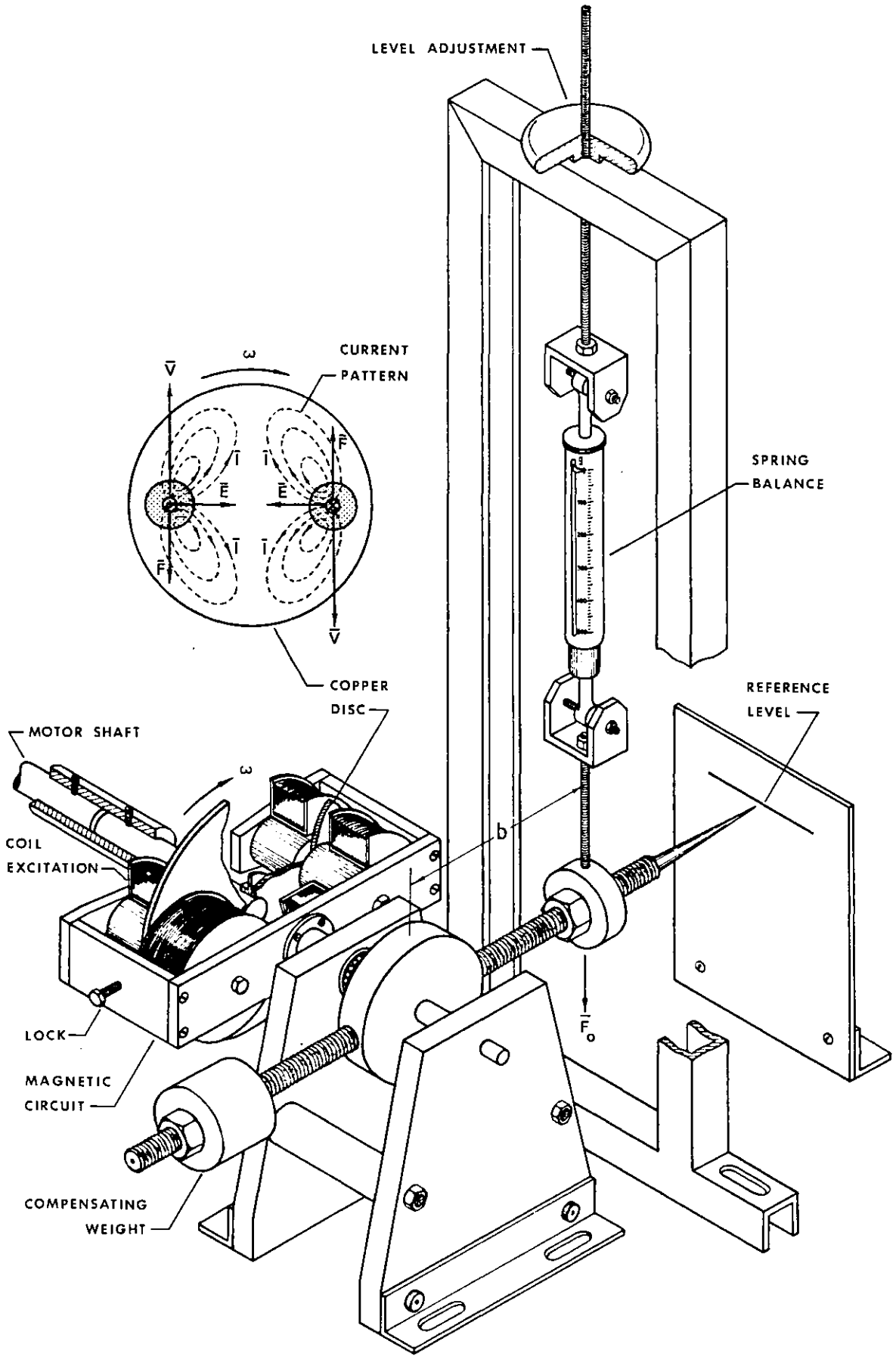

Fig. 5.24 - Eddy-current brake layout

ached to a spring balance (though a load-cell would be better) via the arm b, hence torque T = Fb may be determined.

It should be pointed out that with the double sided excitation used, axial forces on the disc are cancelled out thus minimising motor bearing friction.

Shaft motor torque is controlled by the level of the field current, but obviously the disc torque disappears at standstill. A lock was hence provided in order to take torque measurements at standstill.

5.9 - TEST RESULTS

Using the test rig described, tests were carried out on the disc motor in order to be able to compare the motor's performance with the two rotors. The results obtained are now presented.

5.9.1 - Air gap flux density measurement

Once the motor was assembled the magnets were remagnetised by discharging a capacitor through a two turn coil wound on each magnet. Air gap flux densities were then measured using a 5 mm diameter search coil and a Grassot fluxmeter, although with a Hall element probe more accurate results would be expected.

Readings of the flux density versus radial position were taken across a pole centre-line and versus circumferential position over one pole pitch, as illustrated in fig. 5.25. Plots of these two measurements are shown in fig. 5.26 for gaps g = 8 mm (wound rotor) and g = 3 mm (printed rotor).

The flux density distribution is symmetrical in a circumferential sense relative to the magnet axis and the value at magnet edge flux density is roughly equal to half of the centre reading for both gaps. For radial variation, however, the flux density has its maximum value at a radius slightly greater than the average radius. This asymmetry is due, it is thought, to decrease in leakage flux as radius increases (distance between

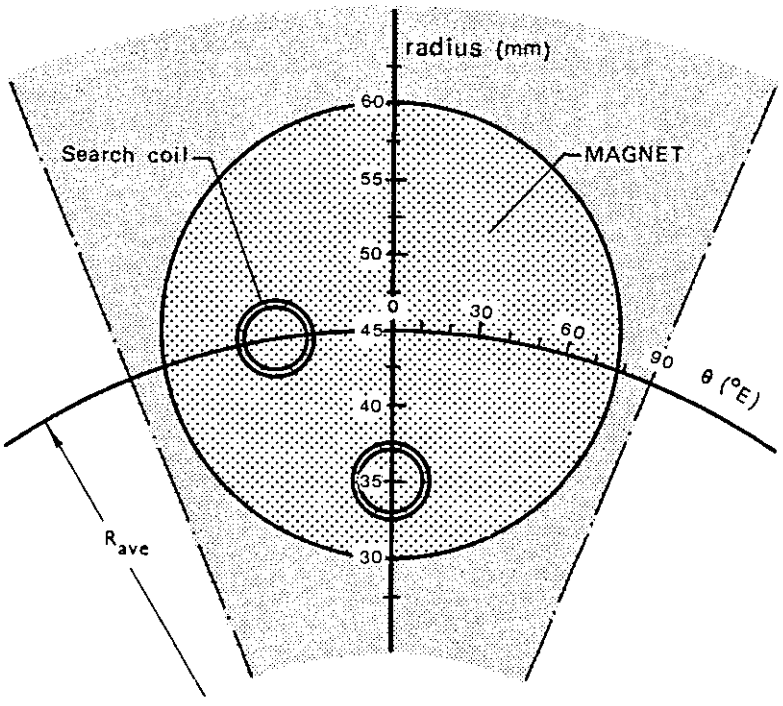

Fig. 5.25 - Search coil position

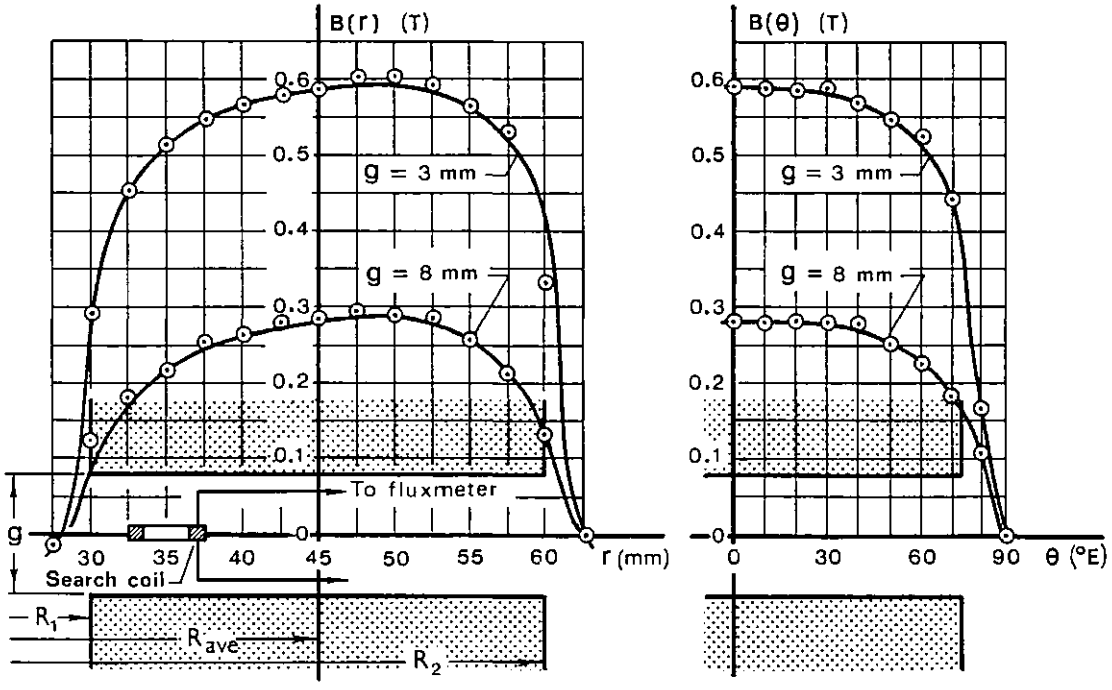

(a) - Radial (b) - Angular

Fig. 5.26 - Radial and angular flux density measurements

magnets greater for $R > R_{ave}$). The computed air gap flux density is in good agreement with the average flux density measurements as can be seen by comparing fig. 5.10(b) and fig. 5.26.

5.9.2 - Torque/current versus rotor angle measurement

When fed with a fixed value of d.c. current, the torque of the prototype would obviously be expected to alternate with rotor rotation the torque amplitude remaining unchanged whichever phase was excited, but the torque waveforms differing by 90°E. To check this, the static torque measurements were obtained by exciting the phases separately for a series of rotor positions.

Torque was measured by locking the eddy-current brake repeatedly at 2.5° mechanical (10°E) intervals over two pole pitches. Plots of these results in the form of torque per amp versus rotor angle are shown in fig. 2.27 for the wound rotor and in fig. 2.28 for the printed rotor. They show low values decay near interpolar region and high values near the pole centres as compared with the ideal sinuisoidal shape whose magnitude was predicted by Eq. (5.17). These discrepancies can be attributed to the flat-top to the flux density distribution in the centre regions of the magnets.

5.9.3 - Rotor inertia measurement

In order to determine the coulomb friction torque T_f of the motor, a knowledge of the inertia J of all rotating parts is needed. The method used was to place the rotor between two parallel straight-edges, and to cause it to make small oscillations by means of a weight of mass m, secured to the end of a light bar, as shown in fig. 5.29.

For any deflection θ, and assuming $R >> r$, the restoring torque is

$$T_R = m g R \sin \theta$$

Regarding the whole as a mass M concentrated at radius R_g (radius of gyration) the acceleration torque is

$$T_M = M R_g^2 \frac{d^2\theta}{dt^2} = J \frac{d^2\theta}{dt^2}$$

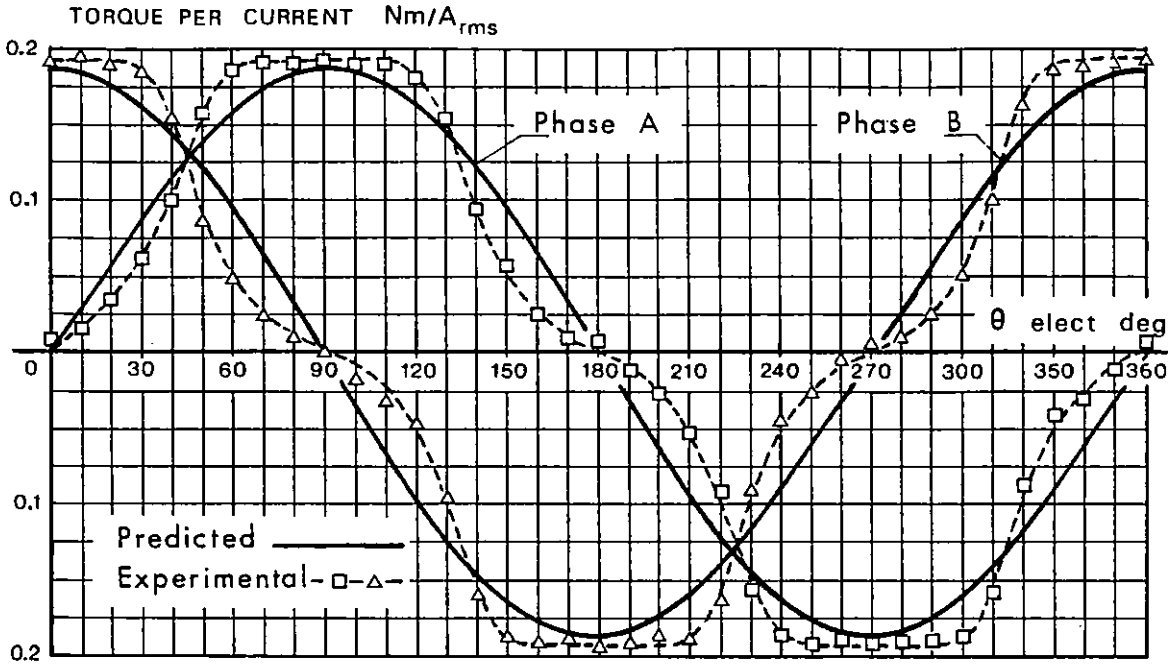

Fig. 5.27 - Torque/current versus rotor angle for wound rotor

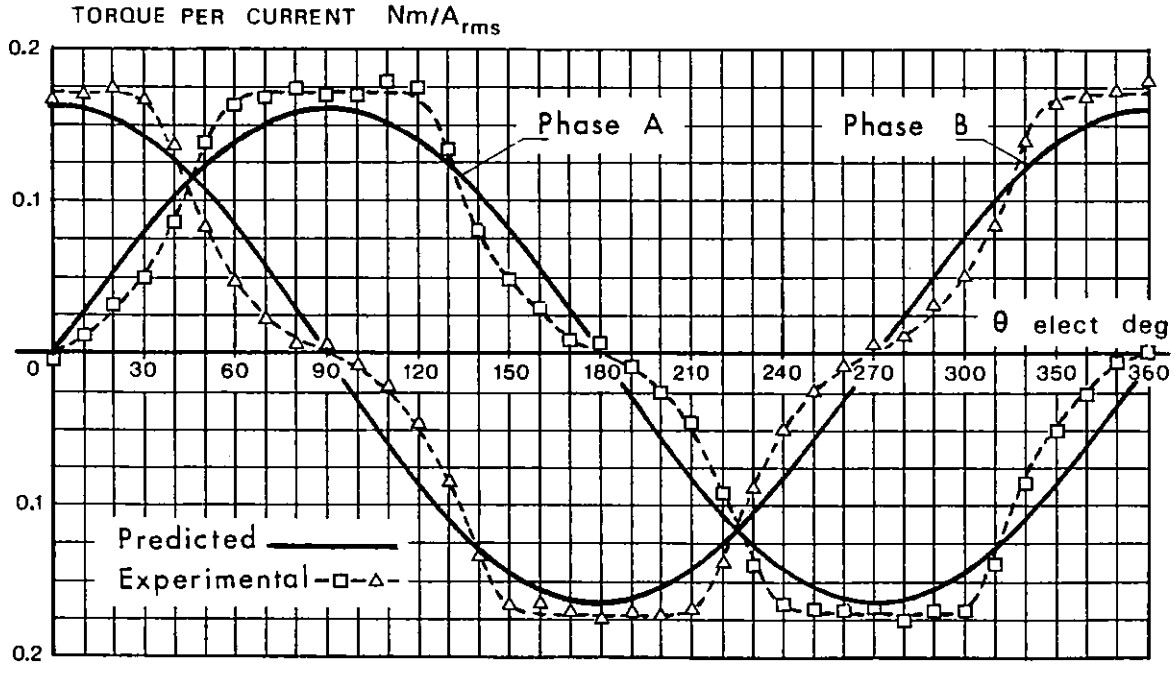

Fig. 5.28 - Torque/current versus rotor angle for printed rotor

The friction torque at the straight-edges

$$T_r = Mr^2 \frac{d^2\theta}{dt^2}$$

and the torque due to the pendulum of mass m

$$T_m = m(R - r)^2 \frac{d^2\theta}{dt^2}$$

Hence, for small oscillations ($\sin \theta \simeq \theta$), the equation of motion is

$$mgR\theta + \left[J + Mr^2 + m(R - r)^2\right] \frac{d^2\theta}{dt^2} = 0$$

or

$$g\theta + \frac{J + Mr^2 + m(R - r)^2}{mR} \frac{d^2\theta}{dt^2} = 0 \qquad (5.20)$$

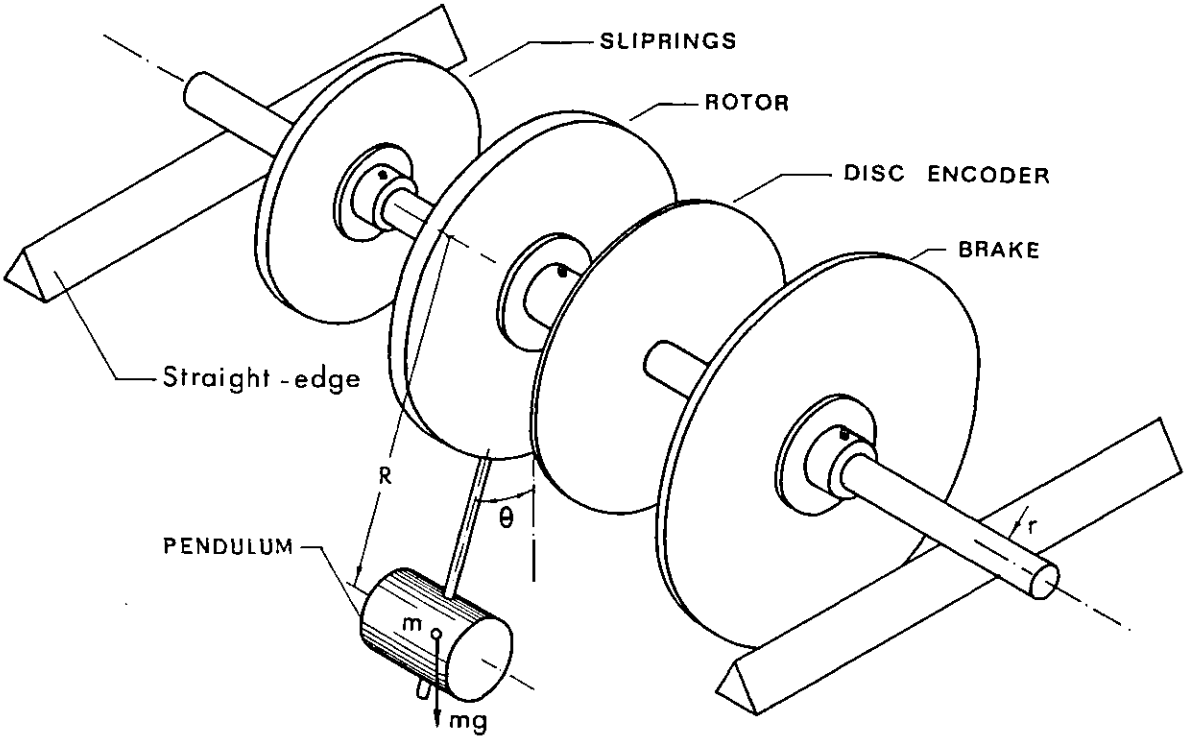

Fig. 5.29 - Inertia measurement of all rotating parts

The equation of motion of a simple pendulum of length $\ell = (\frac{\tau}{2\pi})^2 g$ oscillating with a periodic time τ, is

$$g\theta + \ell \frac{d^2\theta}{dt^2} = 0 \qquad (5.21)$$

So that, comparing Eq. (5.20) and Eq. (5.21) becomes

$$\ell = \frac{J + Mr^2 + m(R - r)^2}{mR} = \left(\frac{\tau}{2\pi}\right)^2 g$$

and the moment of inertia of all rotating parts is then given by:

$$J = mR\left(\frac{\tau}{2\pi}\right)^2 g - Mr^2 - m(R - r)^2 \qquad (5.22)$$

For the wound rotor, the method gave the following results: M = 0.75 kg, m = 0.1 kg, R = o.25 m, r = 6 x 10^{-3} m, τ = 1.1 s. From Eq. (5.22) becomes:

$$J_w = 1.54 \times 10^{-3}\ kg.m^2 \qquad (5.23)$$

Similarly, for the printed rotor with M = 0.69 kg and τ = 1.1 s:

$$J_p = 1.41 \times 10^{-3}\ kg.m^2 \qquad (5.24)$$

and both values are in a reasonably good agreement as compared with the designed figures of $1.48 \times 10^{-3} kg.m^2$ and $1.38 \times 10^{-3} kg.m^2$ respectively.

5.9.4 - Friction torque

Ignoring the effects of inductance, which is extremely small for this machine, the motor angular speed ω_r at instant t, after application suddenly the voltage V to the unloaded motor is given, according to Eq. (3.82), by

$$\omega_r(t) = \omega_m\left(1 - e^{-\frac{t}{\tau_{em}}}\right) \qquad (5.25)$$

where ω_m is the final or maximum speed and $\tau_{em} = RJ/K_B^2$ is the electro-mechanical time constant.

If the voltage is suddenly removed after the motor has reached the steady state, the following equation yields

$$J\frac{d\omega_r}{dt} = -T_f \qquad (5.26)$$

where T_f is the frictional torque due to friction on the brushes, bearings

and windage. Assuming viscous conditions $T_f = K_B \frac{K_B \omega_r}{R}$ and Eq. (5.26) becomes:

$$\tau_{em} \frac{d\omega_r}{dt} + \omega_r = 0 \tag{5.27}$$

Hence:

$$\omega_r = \omega_m \, e^{-\frac{t}{\tau_{em}}} \tag{5.28}$$

which shows that the retardation or deceleration of the motor under viscous conditions would be exponential in form.

The slope of the retardation curve is T_f/J. Since the inertia J is known, the friction torque T_f for a given speed may be then evaluated from the retardation curve.

Typical records for both rotors are shown in fig. 5.30. Both results show that the retardation speed variation is almost a straight line, which indicates that the friction torque is near constant rather than viscous over most of the speed range. This is mainly due to the relatively high friction observed on the contacts brush-sliprings as compared with friction on the bearings.

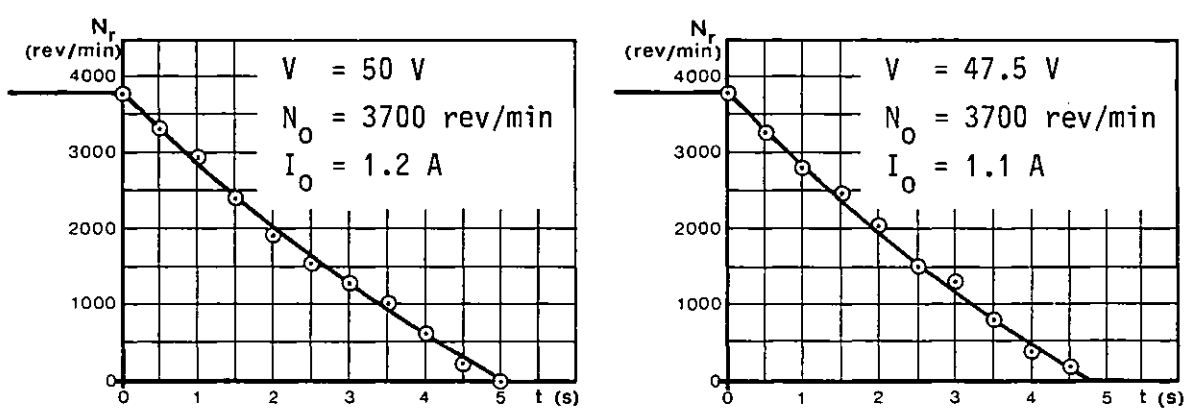

(a) - Wound rotor (b) - Printed rotor

Fig. 5.30 - Running-down records for both rotors

Hence, taking into account the results given by Eq. (5.23) and Eq. (5.24), the friction torque for wound rotor is:

$$T_{fw} = J_w \frac{\omega_m}{t_f} = 1.54 \times 10^{-3} \times \frac{2\pi \times 3700}{60 \times 5} = 0.119 \text{ Nm} \tag{5.29}$$

and similarly for printed rotor

$$T_{fp} = 0.113 \text{ Nm} \tag{5.30}$$

The friction torques are very similar for both rotors, as would be expected since the same sliprings and shaft bearings were used for each.

5.9.5 - Switching performance characteristics

With four step square wave feed conditions and the position sensor set at a switching angle $\theta_o = 45°E$, the average electromagnetic torque developed is given, according to Eq. (3.3) by

$$T_{ave} = \frac{2\sqrt{2}}{\pi} K_B I = K_B' I \tag{5.31}$$

where I is the amplitude of the phase current (assumed rectangular here).

The armature inductance of the machine is very low whichever of the ironless rotors is used and at low and normal speeds, the rectangular current assumption (which corresponds to a rectangular back e.m.f. e and $L \frac{di}{dt} \ll iR$ in the loop equation for the phase: $v = e + iR + L \frac{di}{dt}$) is not thought to involve too high a degree of approximation for practical purposes with this small motor. Note that as stated before, the interphase mutual inductance L_{12} term in the loop equation is omitted due to the negligible value of this term in a two-phase machine.

With these assumptions, the motor is predicted as behaving similarly to a d.c. motor with fixed excitation. Hence, with a fixed applied voltage V, the useful torque T_ℓ developed on the shaft is given by

$$T_\ell = T_{ave} - T_f = K_B'(I - I_o) \tag{5.32}$$

where

$$I_o = \frac{V - K_B'\omega_m}{R} \tag{5.33}$$

is the no-load current absorbed by the motor to overcome the constant friction torque $T_f = K_B' I_o$. Similarly, at an angular speed ω_r the motor

might be expected to absorb a current given approximately by:

$$I = \frac{V - K_B'\omega_r}{R} = I_s - \frac{K_B'}{R}\omega_r \tag{5.34}$$

where $I_s = V/R$ is the starting current. Substitution of Eq. (5.34) into Eq. (5.32) gives the useful or load torque at speed ω_r

$$T_\ell = K_B'(I_s - I_o) - \frac{K_B'^2}{R}\omega_r \tag{5.35}$$

and a starting load torque

$$T_s = K_B'(I_s - I_o) \tag{5.36}$$

At speed ω_r the mechanical output power developed by the motor would be given by

$$P_{mec} = \omega_r T_\ell \tag{5.37}$$

From Eq. (5.34)

$$\omega_r = \frac{R}{K_B'}(I_s - I)$$

Elimination of I_o using Eq. (5.32) and Eq. (5.36) gives

$$I_s - I = \frac{1}{K_B'}(T_s - T_\ell)$$

and so

$$\omega_r = \frac{R}{K_B'^2}(T_s - T_\ell) \tag{5.38}$$

Hence, substitution of Eq. (5.38) into Eq. (5.37) gives

$$P_{mec} = \frac{R}{K_B'^2}(T_s T_\ell - T_\ell^2) = R(I_s - I)(I - I_o) \tag{5.39}$$

and the maximum mechanical power is obtained for a load torque $T_\ell = T_s/2$ or for a current $I = (I_s + I_o)/2$. Hence, as would be the case with an ideal d.c. motor on constant excitation, the mechanical ouput power reaches

its maximum when the load torque is equal to half the starting torque or for a current which is the arithmetical mean of the starting current I_s and the no-load current I_o. This peak is then

$$P_{mec_{max}} = \frac{R}{K_B^2} \frac{T_s^2}{4} = \frac{R}{4}(I_s - I_o)^2 \tag{5.40}$$

For motors with a no-load current small compared to the starting current ($I_o \ll I_s$), Eq. (5.40) can be written

$$P_{mec_{max}} \simeq \frac{1}{4} R I_s^2 = \frac{1}{4} P_{es} \tag{5.41}$$

where $P_{es} = R I_s^2$ is the electric input power supplied to the motor at the time of starting. Hence, from Eq. (5.41) it may be deduced that the maximum mechanical output power developed by the motor is at the most, 25% of the electric power supplied to the motor at the time of starting.

Since the electric power $P_e = V I = R I_s I$, the motor efficiency becomes

$$\eta = \frac{P_{mec}}{P_e} = \frac{(I_s - I)(I - I_o)}{I_s I} = 1 + \frac{I_o}{I_s} - \frac{I_o}{I} - \frac{I}{I_s} \tag{5.42}$$

The peak efficiency is obtained as

$$\eta_{max} = \left(1 - \sqrt{\frac{I_o}{I_s}}\right)^2 \tag{5.43}$$

occuring at a current $I = \sqrt{I_o I_s}$ which is the geometric mean of the starting and the no-load currents.

The above equations for load torque, rotor speed, mechanical power and efficiency were used to draw up theoretical characteristics of both rotors at the rated terminal voltage of 50 $V_{d.c}$ between rails.

The following parameters were used:

a) Wound rotor

$R = 4.62\ \Omega$/phase

$K_B' = \frac{2\sqrt{2}}{\pi}\ 0.187 = 0.17$ Nm/A

$I_o = \frac{V - K_B'\omega_m}{R} = 1.2$ A

$I_s = \frac{V}{R} = 10.82$ A

b) Printed rotor

$R = 2.3\ \Omega$/phase

$K_B' = \frac{2\sqrt{2}}{\pi}\ 0.162 = 0.15$ Nm/A

$I_o = 1.4$ A

$I_s = 21.74$ A

With a constant d.c. voltage source V = 50V, tests were carried out for both rotors. By varying the excitation level of the eddy-current brake, load torque T_ℓ, speed ω_r, mechanical output power $\omega_r T_\ell$ and motor efficiency η were measured up to a phase current 5 A, which is the current limit of the power transistors used. A typical oscillogram of the phase current (obtained by measuring the voltage drop across a non-inductive resistor in series) when the motor was rotating at 3000 rev/min is shown in fig.5.31. It can be seen that even at this speed, except for the relatively short-lived switching transients, the current waveform is reasonably rectangular in form as assumed in the analysis.

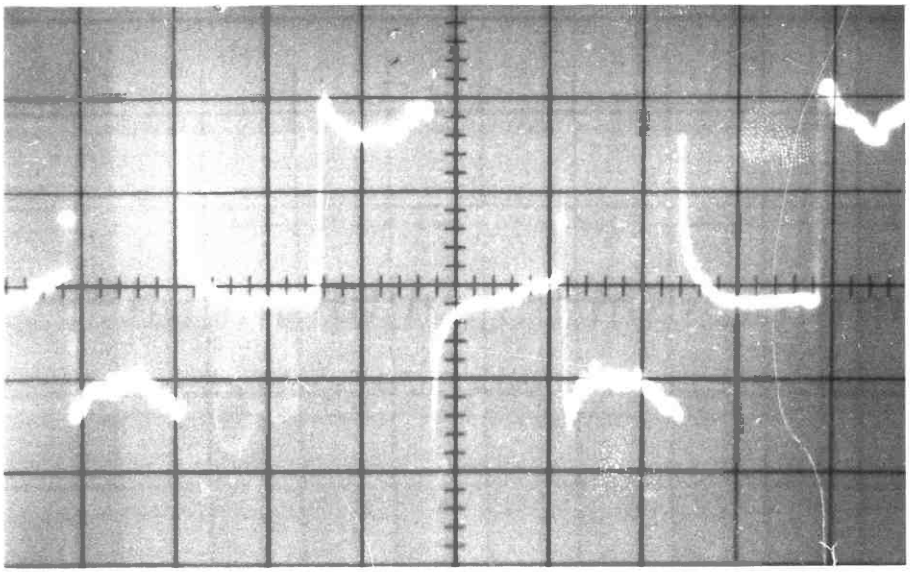

Fig. 5.31 - Current waveform when switching transistors

Comparison of the predicted and experimental results is illustrated in fig. 5.32 for the wound rotor and in fig. 5.33 for the printed rotor. Good agreement is seen between the two sets of values.

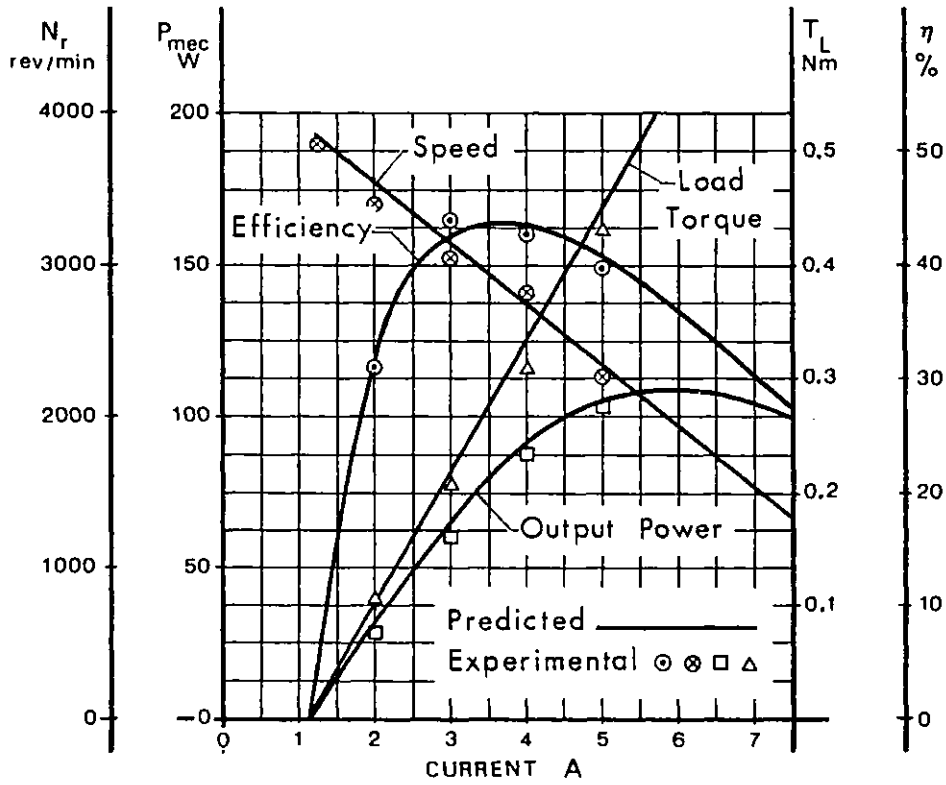

Fig. 5.32 - Performance characteristics at 50 V for wound rotor

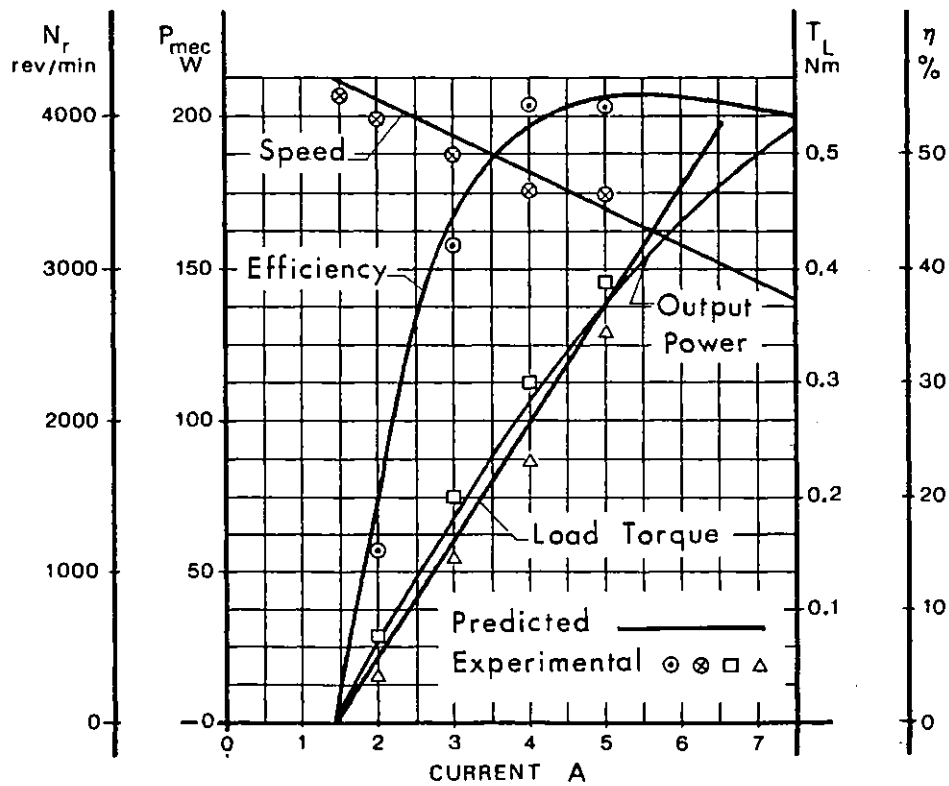

Fig. 5.33 - Performance characteristics at 50 V for printed rotor

5.9.6 - Sine wave operation characteristics

Time did not permit the building of two switched bipolar current-source feeds and none suitable were available in the laboratory. Hence, in order to be able to study the operation of the sensor and motor systems under sinusoidal conditions, a standard, two-channel d.c. transistor power amplifier was used. This is of course over-engineered for motor feeds and would be too costly and lossy for use in a practical drive scheme. The manufacturer's curve of r.m.s. output power per channel versus load impedance is shown in fig. 5.34. The tests were performed keeping the maximum power output below 250 W per channel. The units were supplied from ±62 V supply rails and the peak output current was 10 A.

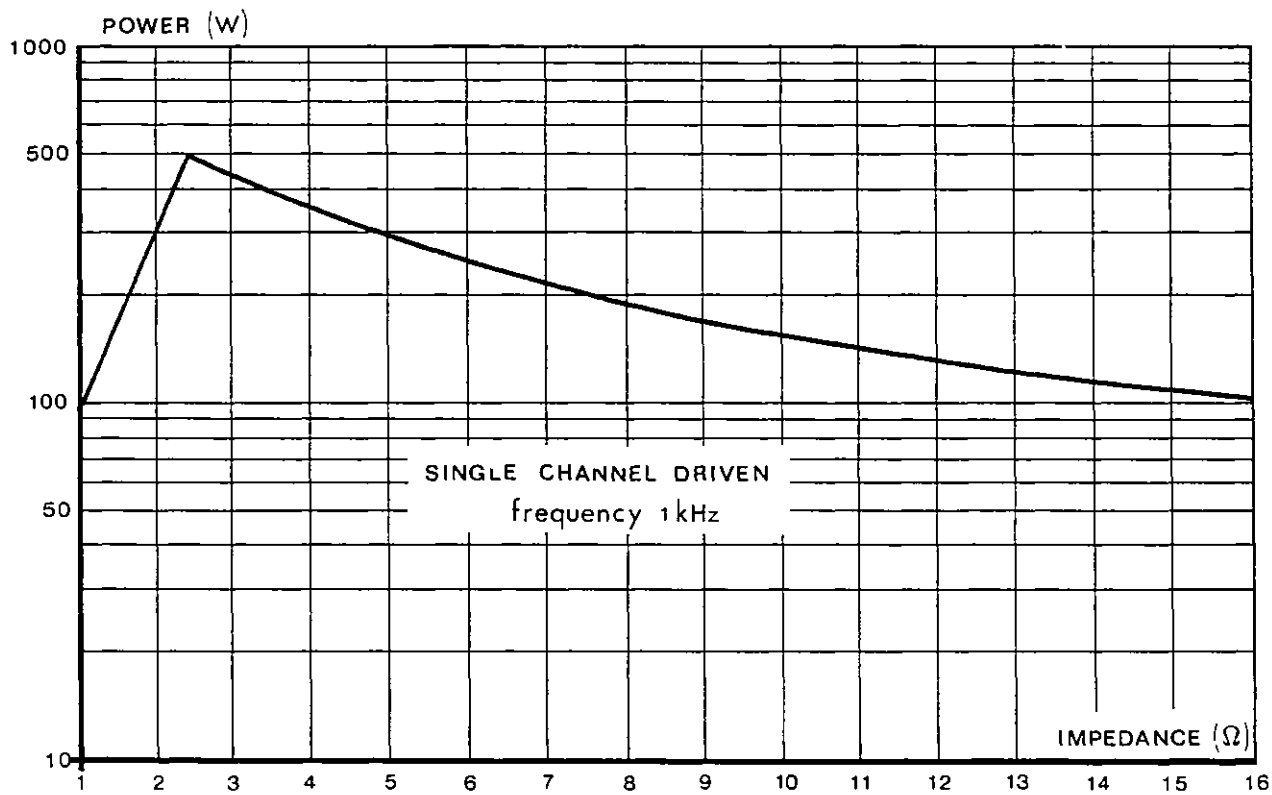

Fig. 5.34 - Amplifier output power versus load impedance

A simplified version of the circuit is shown in fig. 5.35. The output stage consists of six NPN power transistors, three in each half of the bridge connected in parallel, with one driving NPN and one PNP power transistor in each case. The Zener diode in conjunction with the resistor

R_e ensures a constant current source. The amplifier operates in class B with the pre-amplifier transferring the current generator output I_c from one half of the bridge to the other, depending on signal polarity of V_{in}. Two diodes in series are necessary to smooth the crossover point.

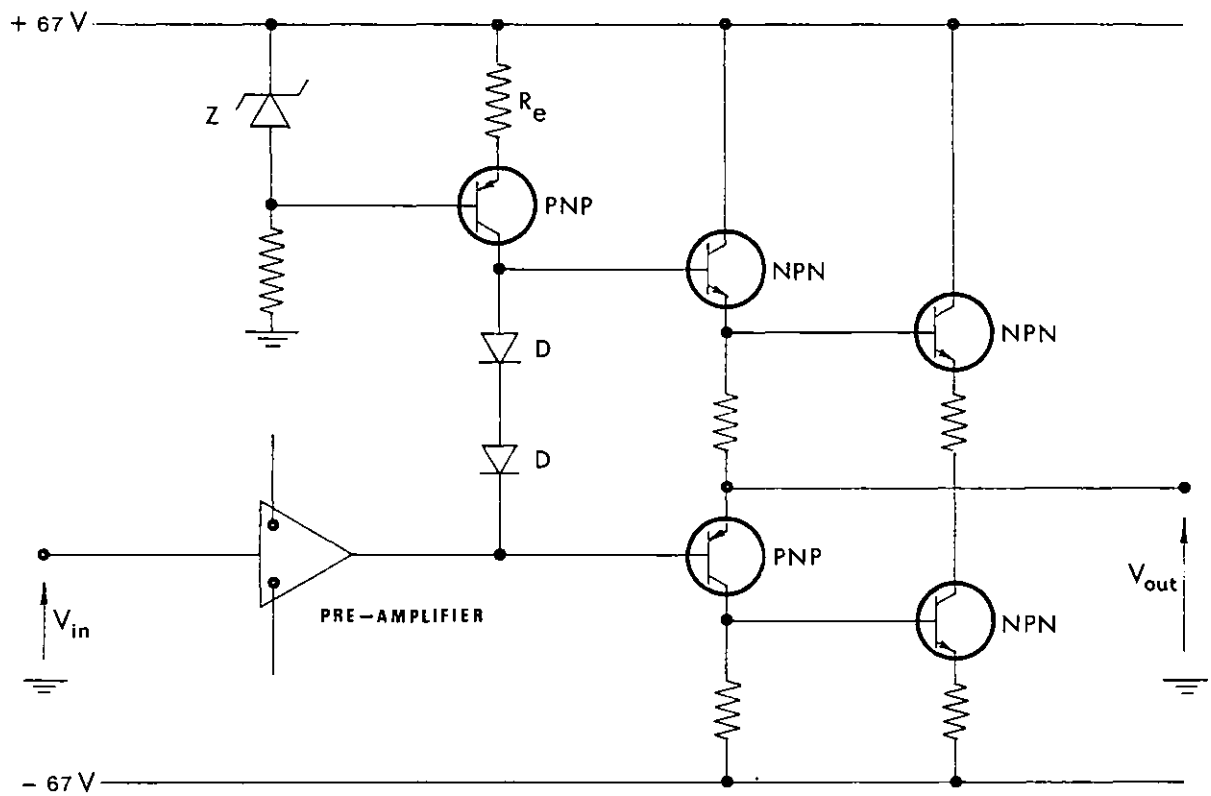

Fig. 5.35 - Basic circuit diagram of the power amplifier

The "polaroid" position sensor system was found to work very satisfactorily. As shown in fig. 5.21, the outputs were good sine waves, 90° apart in time, and with an absence of detectable lower-order harmonics at least. In order to set the relative sensor and rotor orientations, the entire system was driven by means of an auxiliary d.c. motor. The disc motor e.m.f. and the rotor position sensor output signal were then compared using a dual trace oscilloscope. The required relative orientation where the two signals are in phase was found by successive adjustments of the sensor's unit drive pulley.

Tests were performed with each rotor to determine steady-state characteristics when operated in the auto-piloted mode both with constant voltage and constant current souces.

a) - Voltage-fed speed characteristics

Fig. 5.36 shows one phase of the circuit used to achieve voltage-forced operation. Analysis of this circuit gives

$$\frac{V_{in}}{R_1} + \frac{V_1}{R_f} \simeq 0$$

and

$$\frac{V_o}{V_1} = \frac{A_2}{1 + \tau_2 s}$$

Whence:

$$V_o = - \frac{A_2}{1 + \tau_2 s} \frac{R_f}{R_1} V_{in} \qquad (5.44)$$

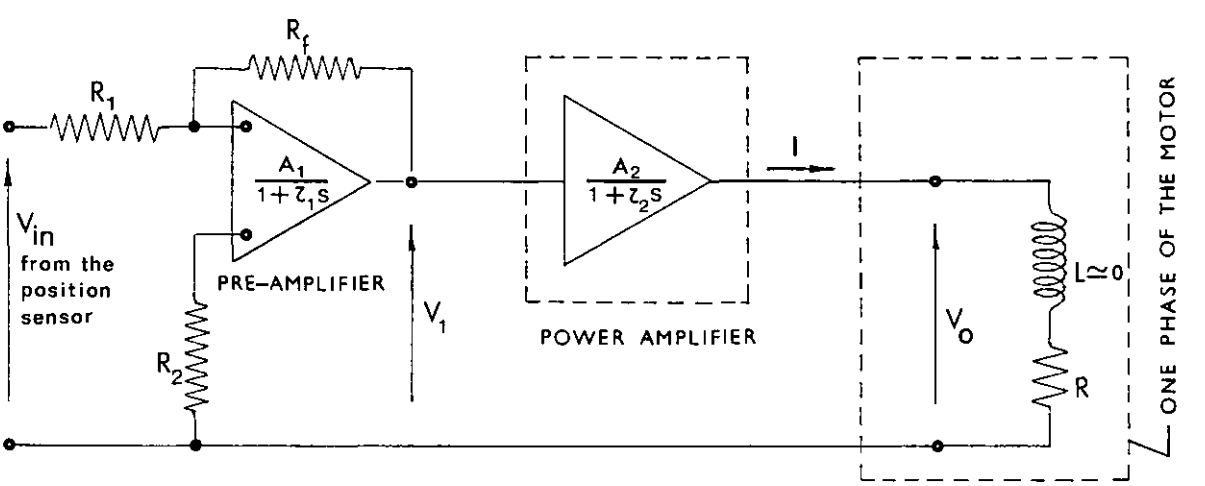

Fig. 5.36 - Voltage-fed source

The power amplifier used was linear from d.c. to 200 kHz, and so Eq. (5.44) may be written as

$$V_o = - \frac{A_2 R_f}{R_1} V_{in} \qquad (5.45)$$

where V_{in} is the rotor position sensor output signal, A_2 is the low frequency voltage gain of the d.c. linear power amplifier and V_o the voltage applied

to the motor winding. The components R_1 and R_f of the pre-amplifier were chosen in order to give V_o = 60 V for the maximum magnitude of V_{in}.

Each rotor was tested for $\delta = 0°$ and $\delta = 30°E$ load angles and four fixed values of r.m.s. voltage V_o = 20 V, 30 V, 40 V, 50 V. The respective phase diagrams, neglecting winding inductance, are shown in fig. 5.37. From them and according to the equations derived in section 3.7.1, the predicted speed characteristics were evaluated. A friction torque of 0.12 Nm was used for output torque correction for both rotors.

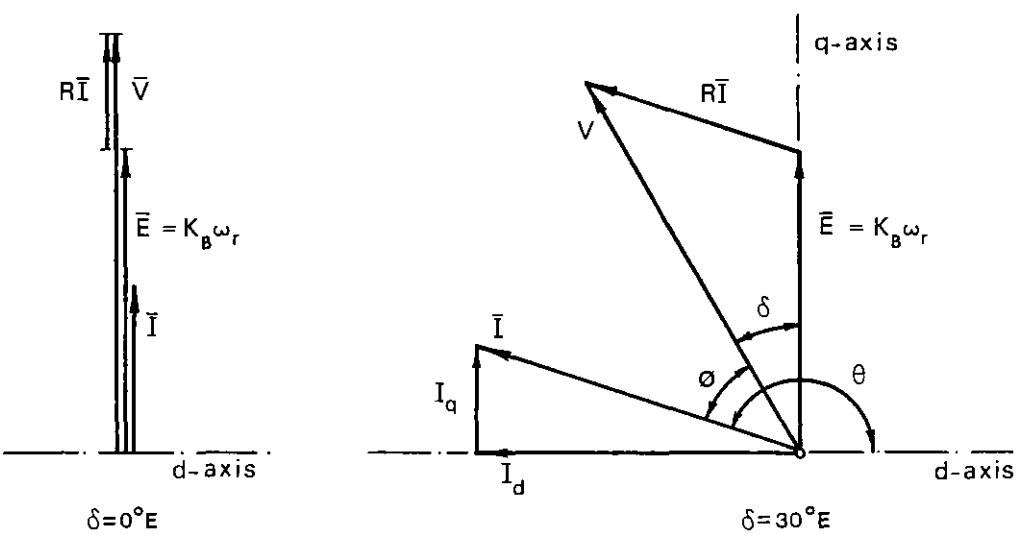

Fig. 5.37 - Phase diagrams with winding inductance neglected

Adjustment of the eddy-current brake excitation allowed variation of load torque T_ℓ and speed ω_r. Motor input voltage per phase V_o, phase current I and electric input power per phase $P_e = V I \cos \phi$ were read for each motor speed. From these readings, power factor $\cos \phi$, torque angle $\theta = 90 + \delta + \phi$ and efficiency $\omega_r T_\ell / 2P_e$ were determined. Plots of these experimental characteristics and predicted values are shown in fig. 5.38(a) and fig. 5.38(b) for the wound rotor and in fig. 5.39(a) and fig. 5.39(b) for the printed rotor.

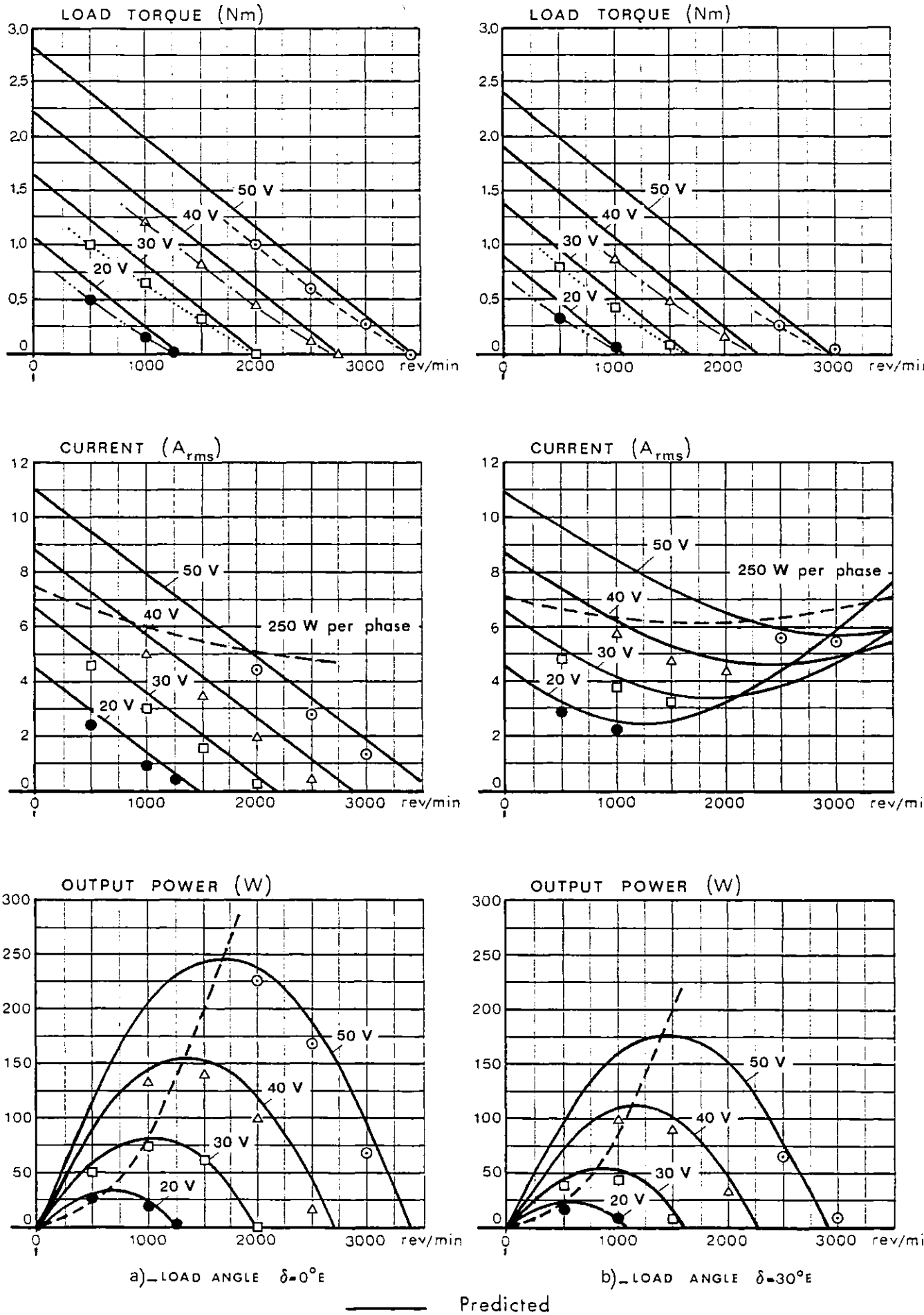

Fig. 5.38(a) - Voltage-fed speed characteristics for wound rotor

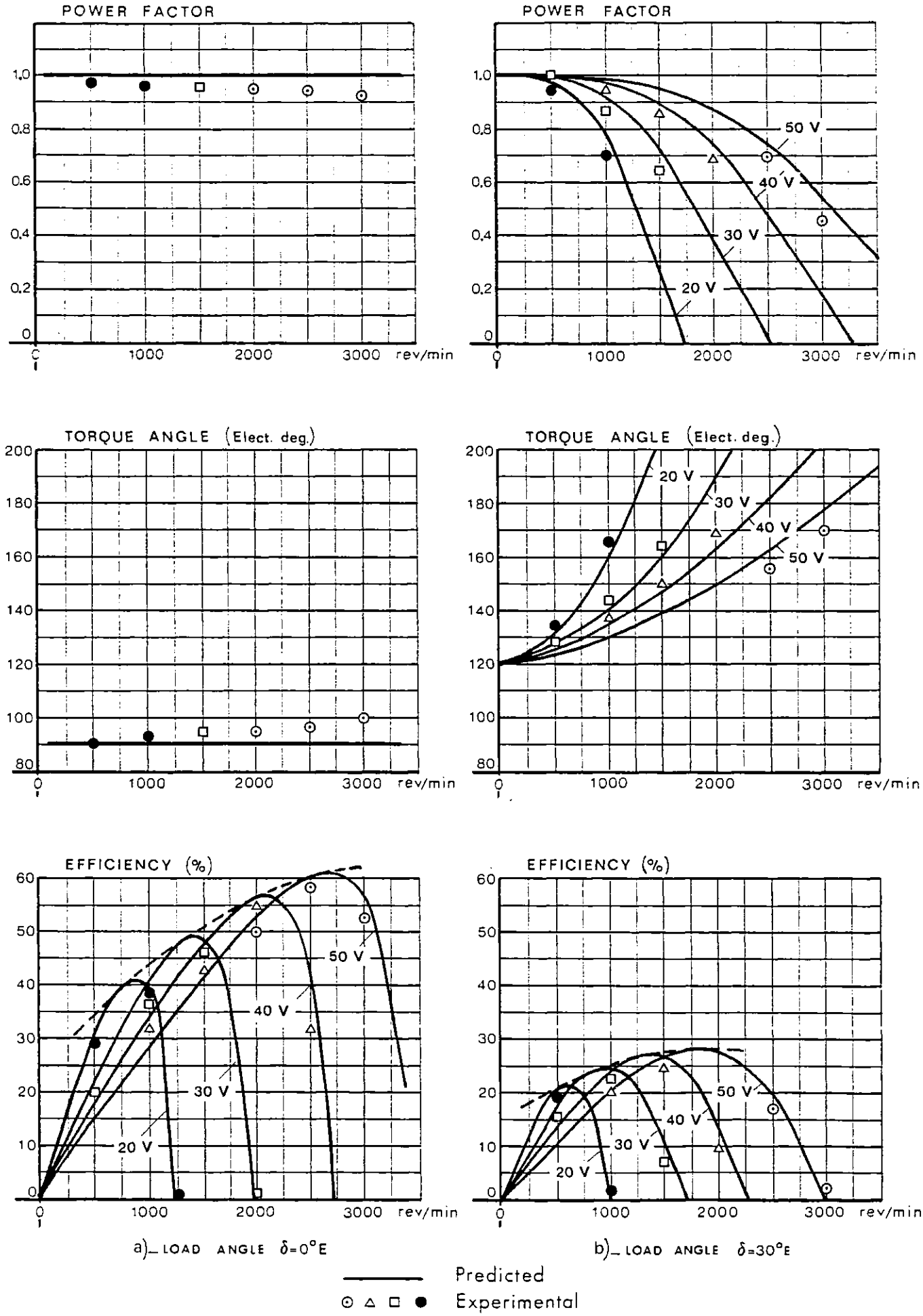

Fig. 5.38(b) - Voltage-fed speed characteristics for wound rotor

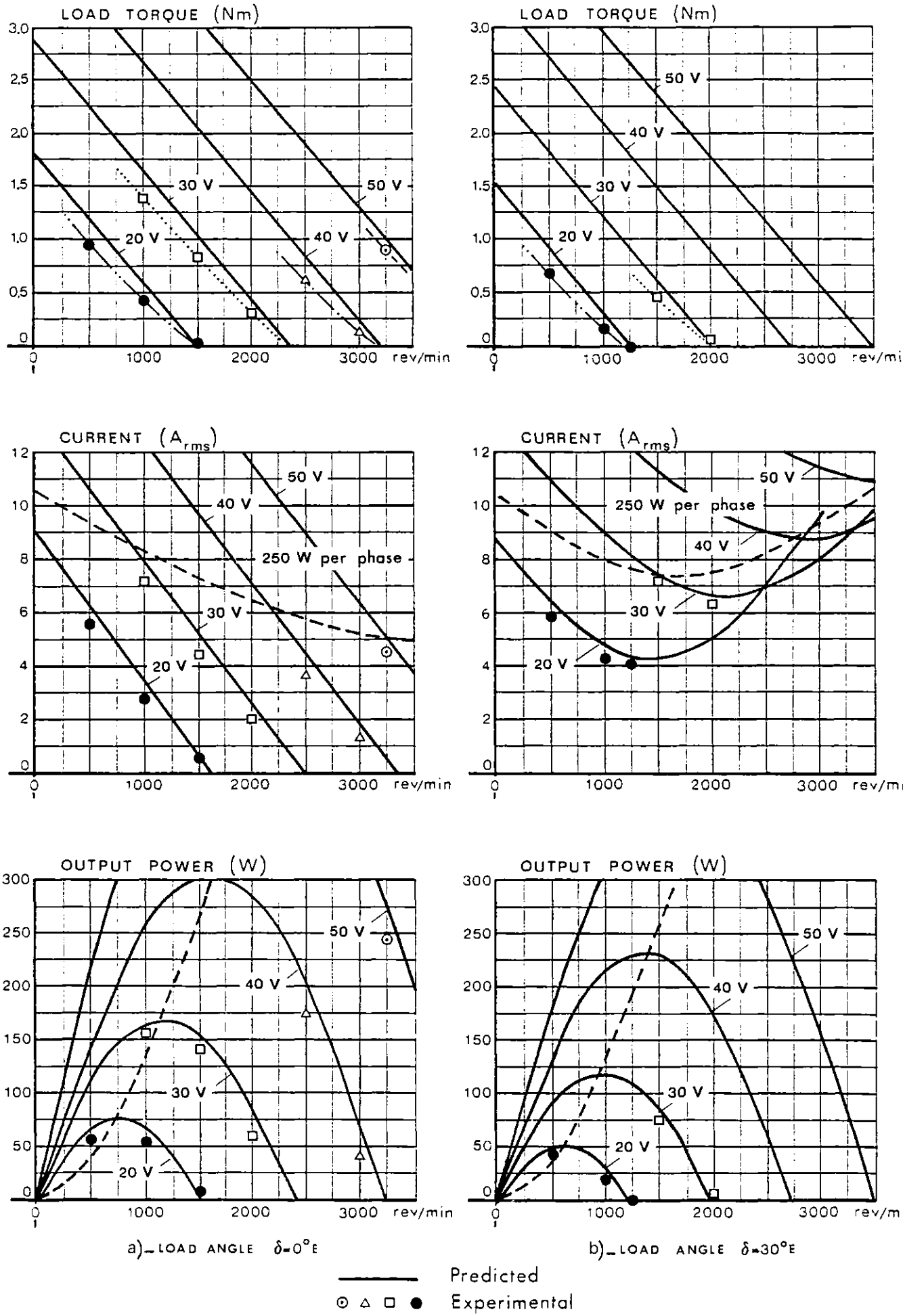

Fig. 5.39(a) - Voltage-fed speed characteristics for printed rotor

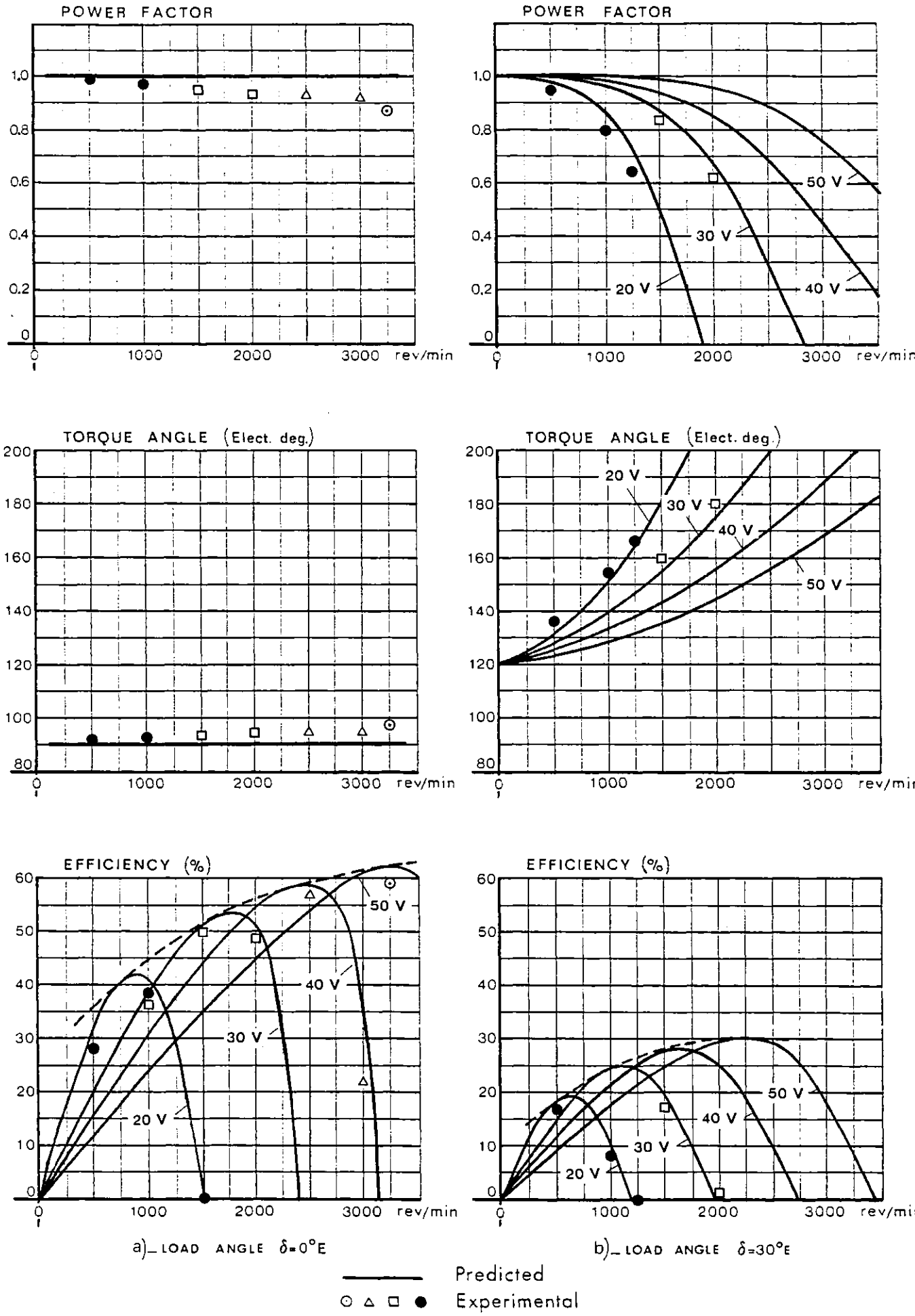

Fig. 5.39(b) - Voltage-fed speed characteristics for printed rotor

a) - Current-fed speed characteristics

The basic constant current source circuit diagram per phase is shown in fig. 5.40. The "sense" resistance R_s in series with the motor phase winding was used to produce a current feedback voltage.

Summing currents at the virtual earth gives:

$$\frac{V_{in}}{R_1} + \frac{R_s I}{R_I} = 0$$

Whence:

$$I = - \frac{R_I}{R_1 R_s} V_{in} \qquad (5.46)$$

Hence, the constant current can be controlled by varying V_{in} from the position sensor. The feedback resistances R_I and R_1 were chosen in order to have I = 5 A for the maximum magnitude of V_{in}.

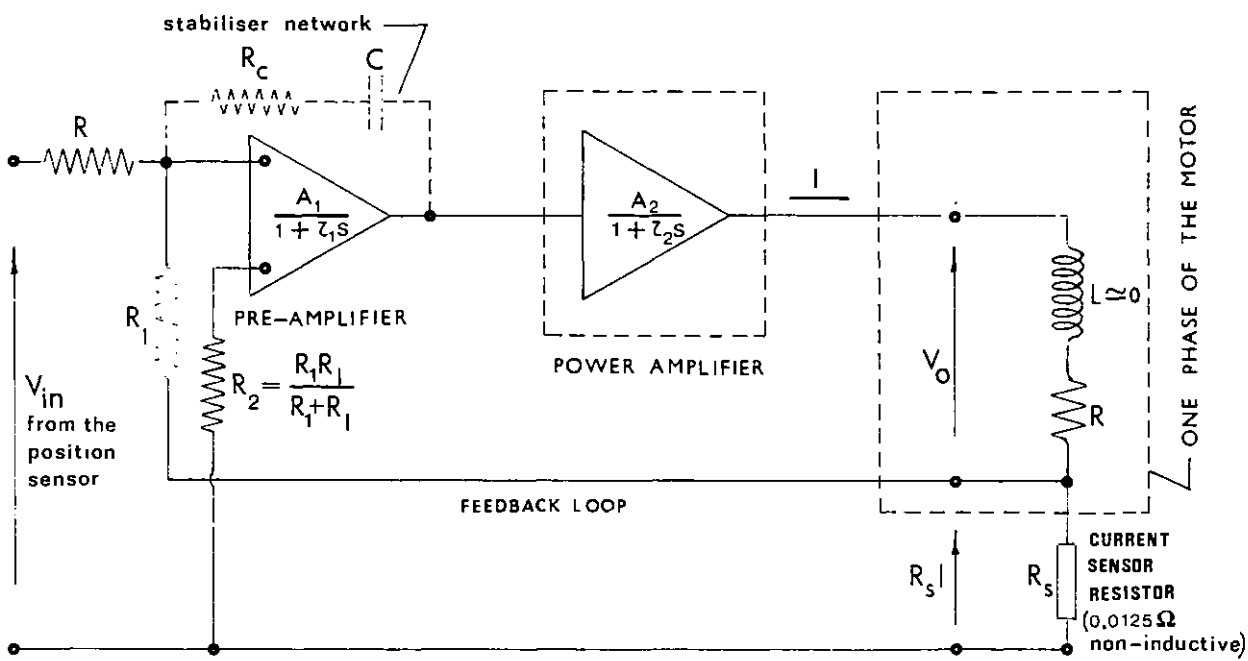

Fig. 5.40 - Constant current source

Under certain conditions this type of circuit may experience instability [103, 104], due to amplifier phase shift (expressed in terms of time constants τ_1 and τ_2) combined with the winding electrical time constant of the motor. In this situation a network $R_c C$ needs to be added to the pre-

amplifier in order to stabilise the system. For the ironless disc motor, however, the system was always stable and so no circuit compensation was required. This may be attributed to the very low electric time constant of the motor $\tau_e = L/R$ due to the negligible inductance of the winding.

With the circuit described, each rotor was tested with $\theta = 90°E$ and $\theta = 120°E$ torque angles and four fixed values of r.m.s. current I = 2 A, 3 A, 4 A, 5 A. From the equations derived in section 3.7.2, neglecting winding inductance, the predicted speed characteristics were evaluated. Plots of current-fed speed characteristics with predicted and experimental values are shown in fig. 5.41(a) and fig. 5.41(b) for the wound rotor and in fig. 5.42(a) and fig. 5.42(b) for the printed rotor.

5.9.7 - Discussion of results

The switching performance characteristics shown in fig. 5.32 and fig. 5.33 are typical of d.c. disc armature motors in which the absence of iron in the armature, and therefore freedom from saturation effects, results in a torque directly proportional to armature current. The speed falls only slightly with increasing load. For the printed rotor the efficiency is fairly constant at a high value over the normal operating range and this is due to the lower armature resistance as compared to the wound rotor.

With sine wave operation, the voltage-fed response indicates classical shunt type characteristics, as shown in fig. 5.38 and fig. 5.39. Under current-fed operation, torque is fairly constant with speed, as shown in fig. 5.41 and fig. 5.42. Clearly torque, output power, efficiency and power factor are liable to reduce sharply as load angle or torque angle diverge from the optimum settings of zero and 90°E respectively.

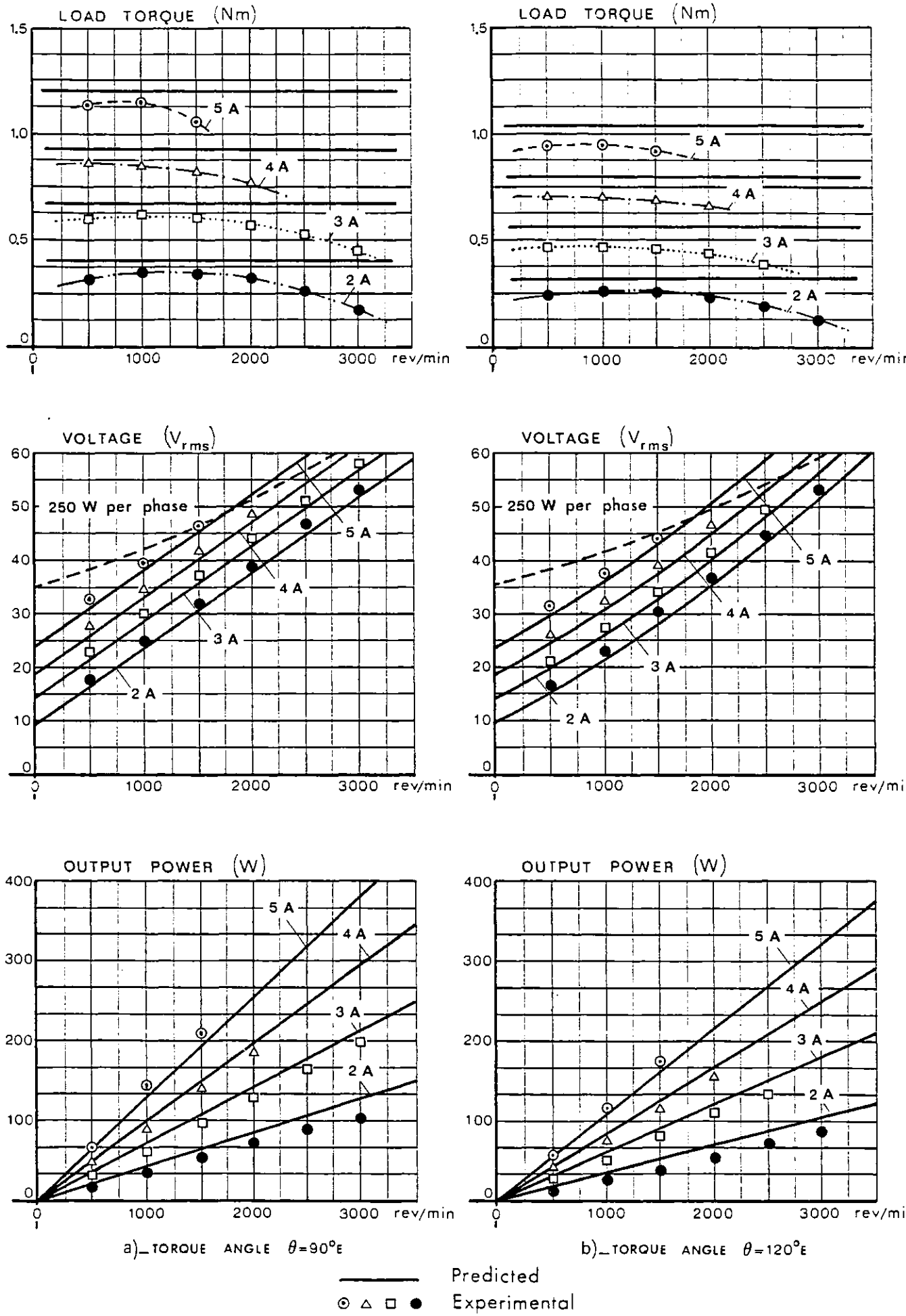

Fig. 5.41(a) - Current-fed speed characteristics for wound rotor

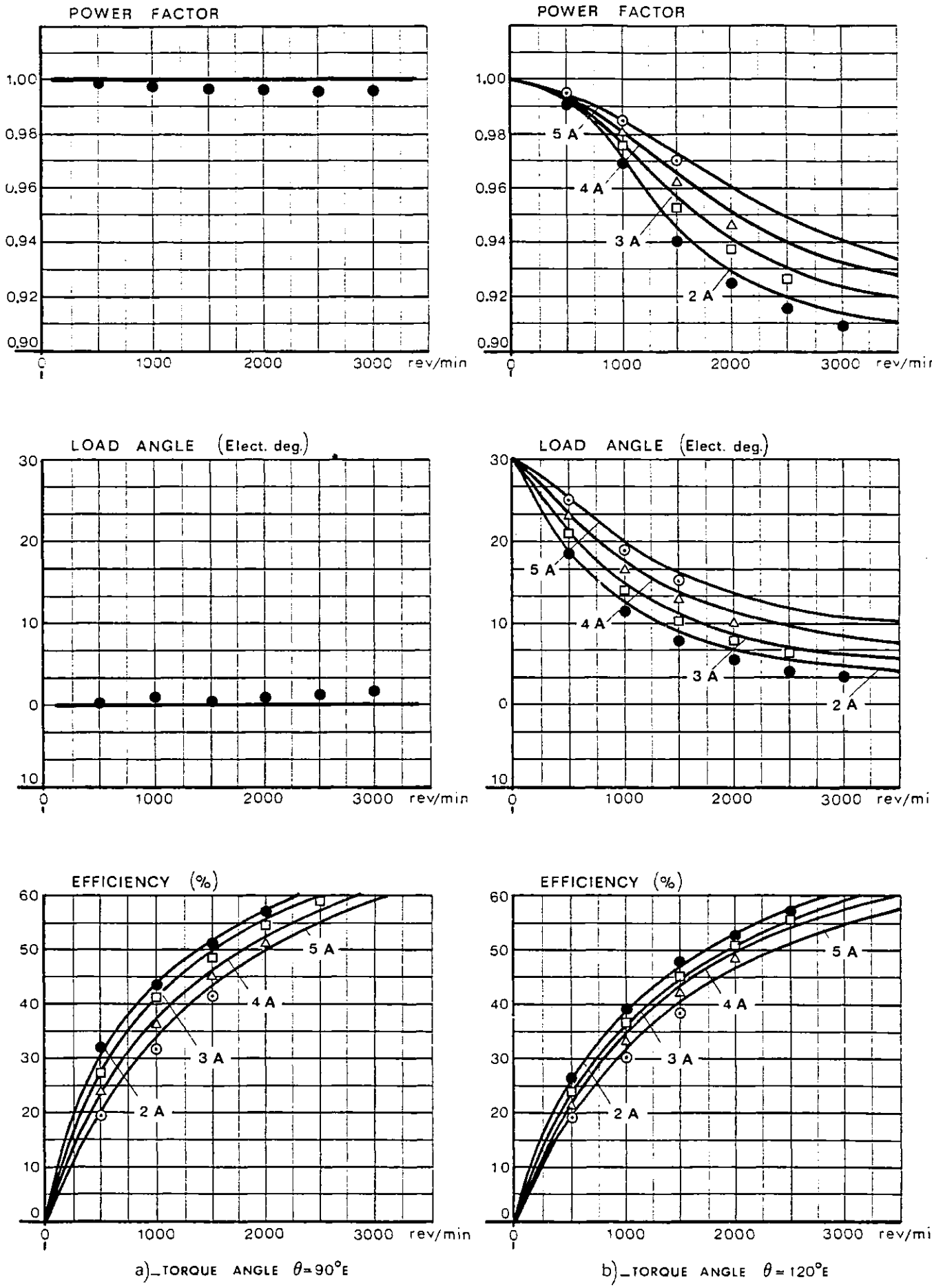

Fig. 5.41(b) - Current-fed speed characteristics for wound rotor

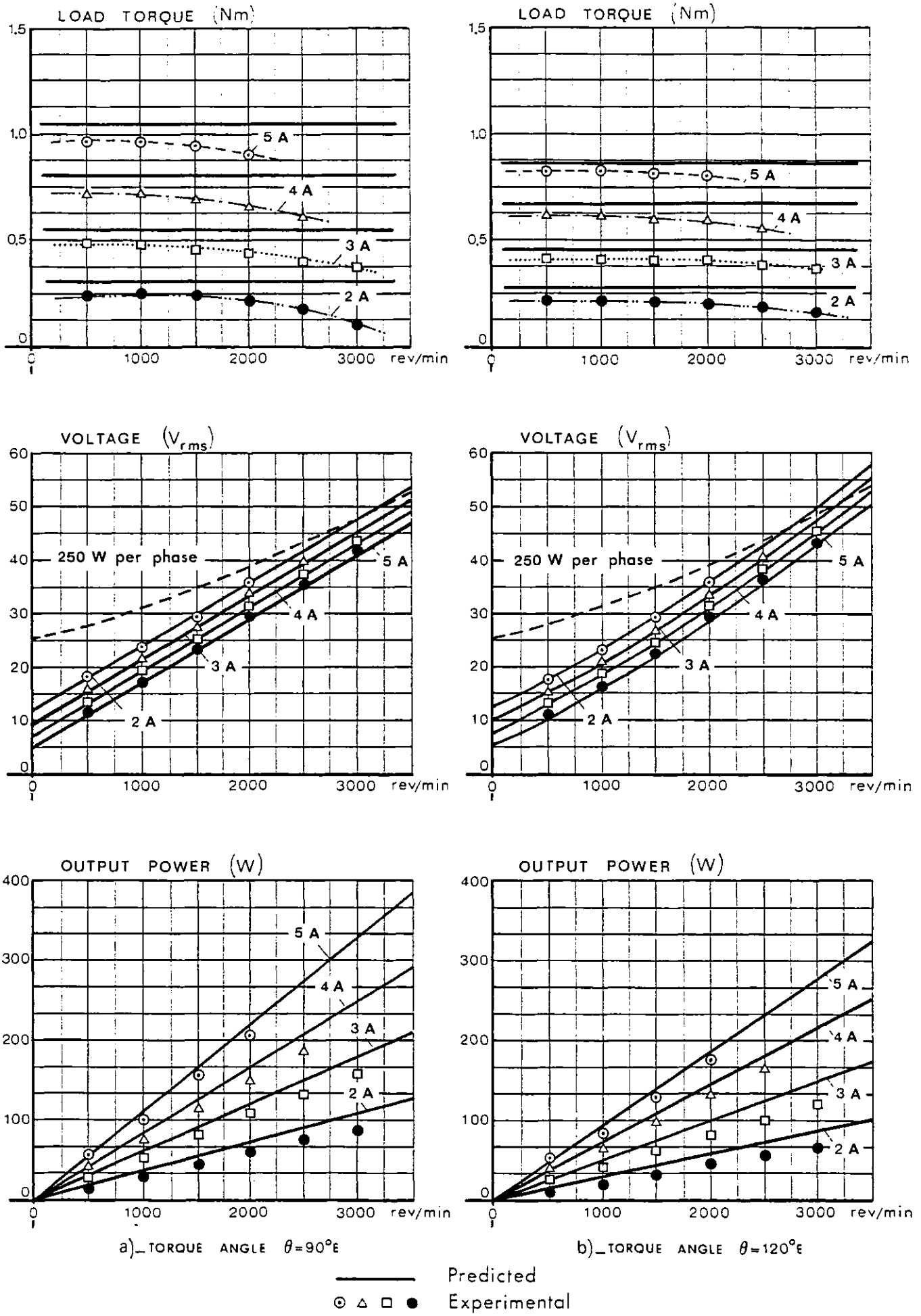

Fig. 5.42(a) - Current-fed speed characteristics for printed rotor

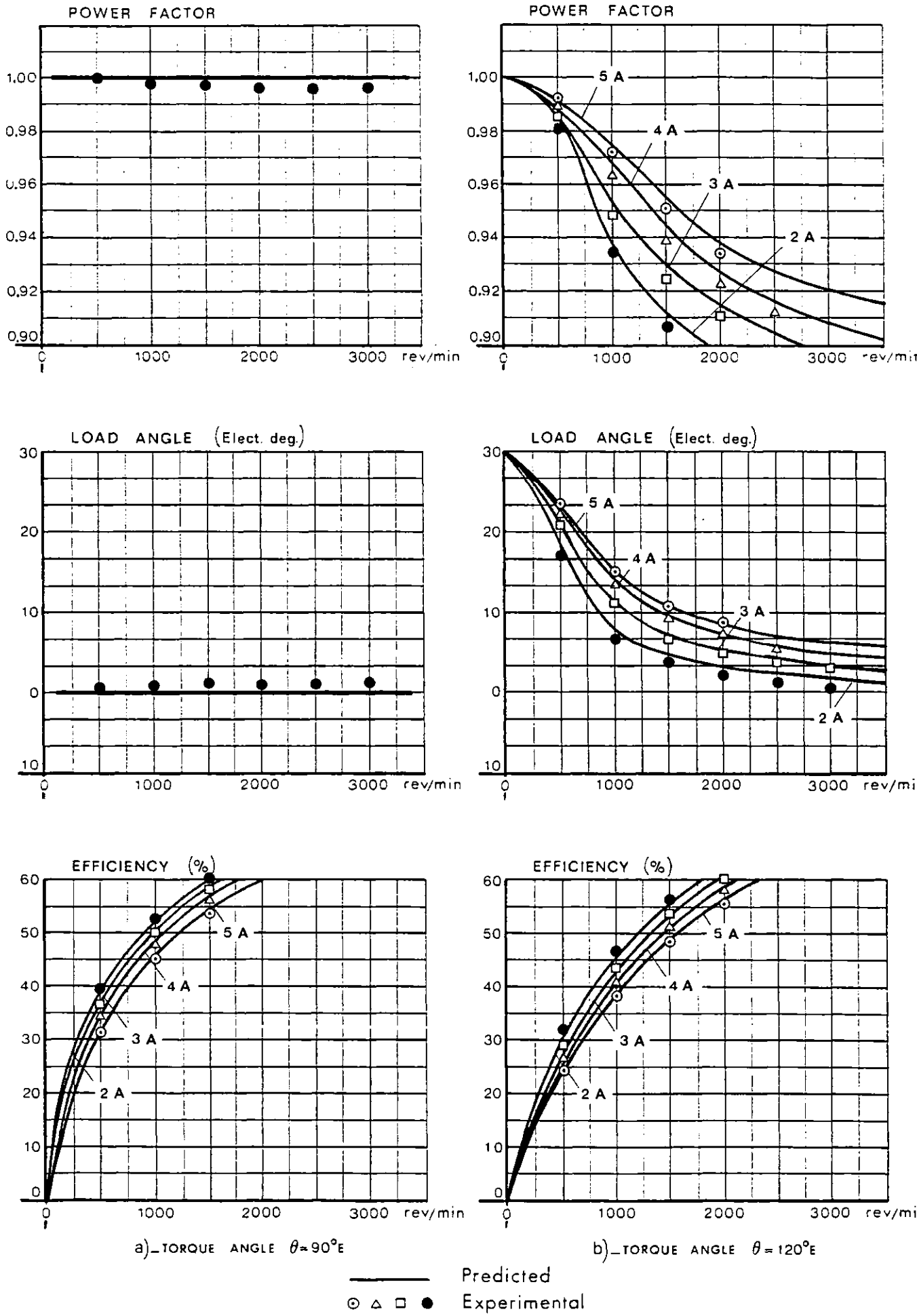

Fig. 5.42(b) - Current-fed speed characteristics for printed rotor

5.10 - COMPARISON BETWEEN SQUARE WAVE AND SINE WAVE OPERATION

With a sinusoidal flux density distribution the torque contribution by each phase when the rotor is at position θ is

$$T_a = K_B i_a \sin \theta$$

$$T_b = K_B i_b \cos \theta$$

If the current in each phase is controlled as a function of rotor angle as

$$i_a = \hat{I} \sin \theta$$

$$i_b = \hat{I} \cos \theta$$

then, as shown previously, the total output torque with sine wave operation becomes

$$T_{\sim} = T_a + T_b = K_B \hat{I}(\sin^2\theta + \cos^2\theta) = K_B \hat{I} \tag{5.47}$$

and the motor has essentially no torque ripple and has linear characteristics similar to those of a conventional d.c. motor.

If the peak supply current per phase (limited by the output transistors) is $\hat{I}$, then the maximum average output torque (with optimum switching angle) for four-step square wave operation is:

$$T_{\sqcap\!\sqcup} = \frac{2\sqrt{2}}{\pi} K_B \hat{I} \tag{5.48}$$

Comparison of Eq. (5.47) and Eq. (5.48) gives

$$T_{\sqcap\!\sqcup} = \frac{2\sqrt{2}}{\pi} T_{\sim} \tag{5.49}$$

Hence, with four-step operation the output torque is about 90% of that obtained with sine operation and in addition is not free of ripple.

The square wave motor output torque can be substantially improved, however, if a square wave flux density distribution is used. With a proper design and use of modern high coercive permanent magnets, a flux density distribution close to a square wave should be possible. For a theoretical

square wave of flux density of magnitude $\hat{B}$ and a square wave of current of magnitude $\hat{I}$ the square wave motor gives an output fundamental torque

$$T_{\sqcap\sqcup} = K \frac{4}{\pi} \hat{B} \frac{4}{\pi} \hat{I} \tag{5.50}$$

since the peak fundamental value of a square wave of magnitude A is $(4/\pi)A$. If the equivalent sine wave motor is designed to operate with sine waves of peak flux density $\hat{B}$ and current $\hat{I}$, then fundamental torque is $T_{\sim} = K\hat{B}\hat{I}$. Hence, Eq. (5.50) becomes

$$T_{\sqcap\sqcup} = \left(\frac{4}{\pi}\right)^2 T_{\sim} \tag{5.51}$$

and more torque is obtainable by using square waves of B and I than by using sine waves. Although torque ripple is likely to occur, a theoretically zero ripple torque for a square wave system is possible if each conductor within the constant flux density region carries constant current, and zero current elsewhere. This condition usually implies that a large number of phases must be used, which gives a larger number of motor leads (and sliprings with the present scheme) and the need for a large number of feed channels. On the other hand, the sinusoidal scheme gives torque free of ripple with a small number of phases, which is an economic advantage in power supply utilisation. The penalty arising from the need for switching-modulated, current-source-operated feeds is perhaps relatively small nowadays, given the availability of low cost, high-speed, Darlington transistors and the possibility of graded optical "sine" sensors using polaroid or other principles.

It should be noted that one other possibility exists for obtaining ripple-free torque without "sine" conditions. This involves the use of a motor in which either the magnet pole arc or the armature "ampere-conductor arc" is deliberately restricted. If the time waveforms of the phase currents are rectangular or nearly so, both the rotor flux density and armature surface current density distributions are rectangulars, a constant torque is produced for the range of rotor angles within which the shorter dis-

tribution moves within the longer one, as shown in fig. 5.43. The type (a) approach is used in a range of brushless d.c. motors for machine tools recently developed by the Bosch Company. Utilisation of the magnet flux or armature ampere-conductors in type (b) is of course reduced, but a low phase number can be used. Switching modulators would be required with motors of any size (and speed) to preserve rectangular current waveforms, and the two overall approaches (i.e. sine versus rectangular with restricted excitation arcs) would hence perhaps emerge neck and neck in any assessment.

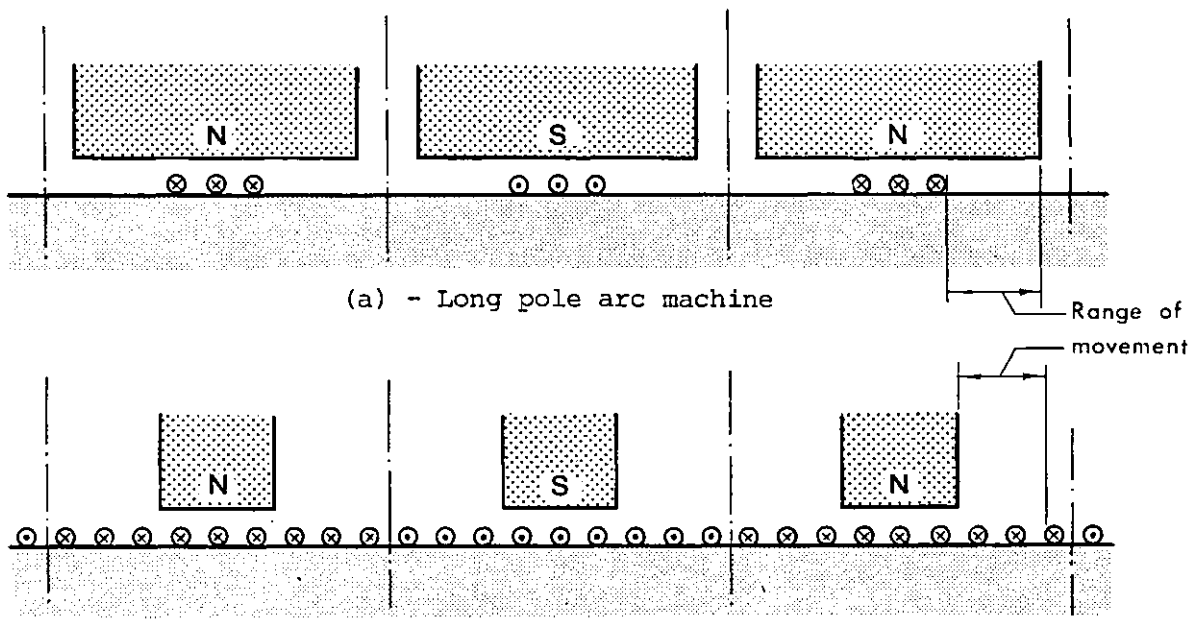

Fig. 5.43 - Design possibilities for obtaining ripple-free torque

In comparing the two schemes tested in the present project, the following conclusions arise:

a) - If torque ripple can be tolerated, then the square wave scheme is the best solution [105]. In this case the sensor and control circuit can be simple and digital in nature.

b) - In servo and other applications where ripple-free torque is required, the sine wave operation is preferable. In this case a somewhat more sophisticated rotor position sensor and feeds are needed, though the extra cost of this sophistication is nowadays not likely to be too large.

5.11 - BRIEF COMPARISON BETWEEN VOLTAGE-FED AND CURRENT-FED OPERATION

From the experimental results it may be concluded that if d.c. shunt-type torque-speed-characteristics and fast response (subject to feed current limits) are required, then voltage-fed operation is the better alternative. In addition, the constant voltage source was found to be easier to set up than the constant current source, which incorporates an inner feedback loop and has the possibility of instability in certain cases.

However, when positioning control with low torque ripple is required, in either low inertia or high inertia versions, current-fed operation is preferable. As seen, under this mode of operation, torque is directly proportional to the input signal independent of speed and rotor losses, which is an advantage when the motor is to be operated at stalled conditions.

5.12 - COMPARISON BETWEEN WOUND AND PRINTED ROTOR PERFORMANCE

A comparison between the rotors in terms of starting torque, initial angular acceleration and maximum efficiency can now be made, for both square and sine wave operation. The starting shaft torque with square wave operation is given by

$$T_s = \frac{2\sqrt{2}}{\pi} K_B (I_s - I_o)$$

and with sine waves

$$T_s = \sqrt{2}\ K_B(I_s - I_o)$$

Hence, the initial angular acceleration

$$\ddot{\theta} = \frac{T_s}{J}$$

and since K_B, I_s, I_o and J have been determined, performance figures for both rotors may be evaluated, as shown displayed in table 5.1.

Table 5.1 - Comparison of prototype rotors

Mode of operation	WOUND ROTOR			PRINTED ROTOR			$\frac{T_p}{T_w}$	$\frac{\ddot{\theta}_p}{\ddot{\theta}_w}$	$\frac{\hat{\eta}_p}{\hat{\eta}_w}$
	T_w (Nm)	$\ddot{\theta}_w$ (rad/s^2)	$\hat{\eta}_w$ (%)	T_p (Nm)	$\ddot{\theta}_p$ (rad/s^2)	η_p (%)			
Square waves V = 50 V	1.64	1065	44	3.05	2163	56	1.86	2.03	1.27
Sine waves Voltage-fed V = 50 V $\delta = 0°$	2.73	1773	60	4.86	3447	63	1.78	1.94	1.05
Sine waves Current-fed I = 5 A $\theta = 90°$E	1.20	851	52	1.04	738	55	0.87	0.87	1.06

Very briefly, it may be said that the printed rotor has the merit of cheap construction, but the wound rotor is much more robust. The printed rotor is very similar to the wound rotor tested in terms of potential torque/current capability but has the advantage of a much lower inertia. As additional benefits it has lower inductance and ease of manufacture using the printed circuit technique. From a servo point of view the printed rotor operating under voltage-fed mode has the highest starting torque resulting in an initial angular acceleration of about twice the level achieved by the wound rotor. With current-fed operation, however, the wound rotor is preferable. In terms of efficiency the printed rotor presents the highest peak values whatever mode of operation is used.

It may be concluded on the evidence of performance and manufacturing experience for the two rotors tested that the increased torque/inertia, lower inductance and the facility of dissipation I^2R losses make the printed disc motor more attractive in servo application (for example, for computer peripherals, numerical controlled machine tool drives, video and analog tape records, biomedical apparatus, automated manufacturing equipment, robots, etc).

Whether these conclusions are universally valid when comparing other wound and printed disc rotors is a matter that requires further work. One way of tackling such a comparison is perhaps to look at the following

parameters, two of them based on the idea of a reference level of armature effective ampere-turns per pole (At) at rated current:

a) - disc thickness per At.

b) - disc final temperature-rise with At.

c) - disc inertia.

Parameter a) affects the level of field flux density (and/or field system design to achieve a required flux density level), and hence the torque. Parameter b) sets the motor's continuous rating and c) its response. Each is of course closely related to the disc packing factor achieved in the air gap region and there is no doubt that this is the most crucial single factor in any small, air gap-wound motor even when rare-earth excitation systems are employed.

With the two rotors tested, the lower B_g caused by the larger thickness of the wound rotor was compensated for as far as torque per amp was concerned by a higher number of armature conductors per pole. Since the conductor cross-section was also larger in the wound rotor, there was little penalty in I^2R loss term compared with the printed rotor. The larger rotor inertia hence remained as the main penalty (apart from somewhat uncertain production and cost factors).

The extent to which the thickness in the air gap region of the wound disc tested can be reduced, for example by reshaping and thickening the end turn portion of the winding (see fig. 5.6), must remain uncertain until further work can be accomplished.

☆ ☆ ☆

CHAPTER 6

DISC AND DRUM GEOMETRY SYNCHRONOUS MOTORS

6.1 - GENERALITIES

Several forms of disc motor have been developed [106, 107, 108] and some types are used commercially nowadays. Although they do not compete with conventional drum motors for general utilisation, they have properties which are advantageous in certain specific applications. The short axial length of the machine can often be of benefit where space is limited and a compact drive is required. In addition, the high torque per inertia ratio and up-to-date designs of commercially available disc motors make them very useful in servo applications.

In this chapter some general comparisons between a number of disc and drum machines are made and a number of design aspects considered. Both coil-excitation and permanent magnet field excitation are investigated.

The choice of magnet material has a large impact on performance and cost in the case of permanent magnet-excited machines. The use of three typical permanent magnet materials is examined - Alcomax 3, Magnadur and $SmCo_5$ - and the performance levels obtained are compared.

All the machines described are intended to be operated in an auto-piloted mode with the feeds largely controlled by signals derived from a shaft position sensor. Three types of coil-excited machine are considered, two of them using an unusual category of "solid-iron" rotor construction.

6.2 - BRUSH-FED DISC MOTOR

A form of high torque per inertia, eight-pole, disc synchronous motor using two rotors of different design has been investigated in the last

chapter. The same geometry is also used here, but as part of the optimisation process, rotor thickness is now taken as a variable. The term "brush-fed" is intended to refer to the slipring and brush-fed type of rotating armature disc synchronous motor dealt with in Chapter 5, but clearly some of what follows on "brush-fed" motors is also highly relevant to the design of standard d.c. disc motors with brushes and commutators.

6.2.1 - Air gap flux density calculation

Fig. 6.1 shows the magnetic circuit of the axial field disc machine with permanent magnet field excitation. Assuming that the magnet cross

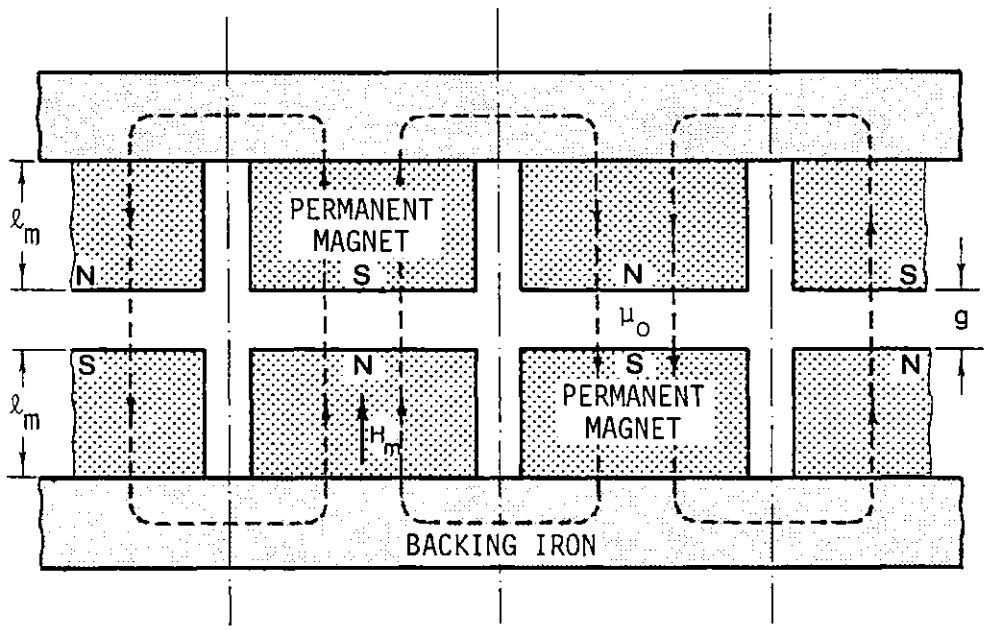

Fig. 6.1 - Basic layout of the magnetic circuit

sectional area A_m is equal to useful air gap area A_g, the unit permeance and the air gap flux density are given, according to Eq. (2.12) and Eq. (2.8), by

$$\frac{B_m}{H_m} = - \mu_o \frac{2K_1 \ell_m}{K_2 g} \tag{6.1}$$

$$B_g = \frac{B_m}{K_1} \tag{6.2}$$

where the leakage factor K_1 is a function of air gap length g.

The leakage factor will be calculated using Roters' method [43] and three leakage paths are considered as shown in fig. 6.2.

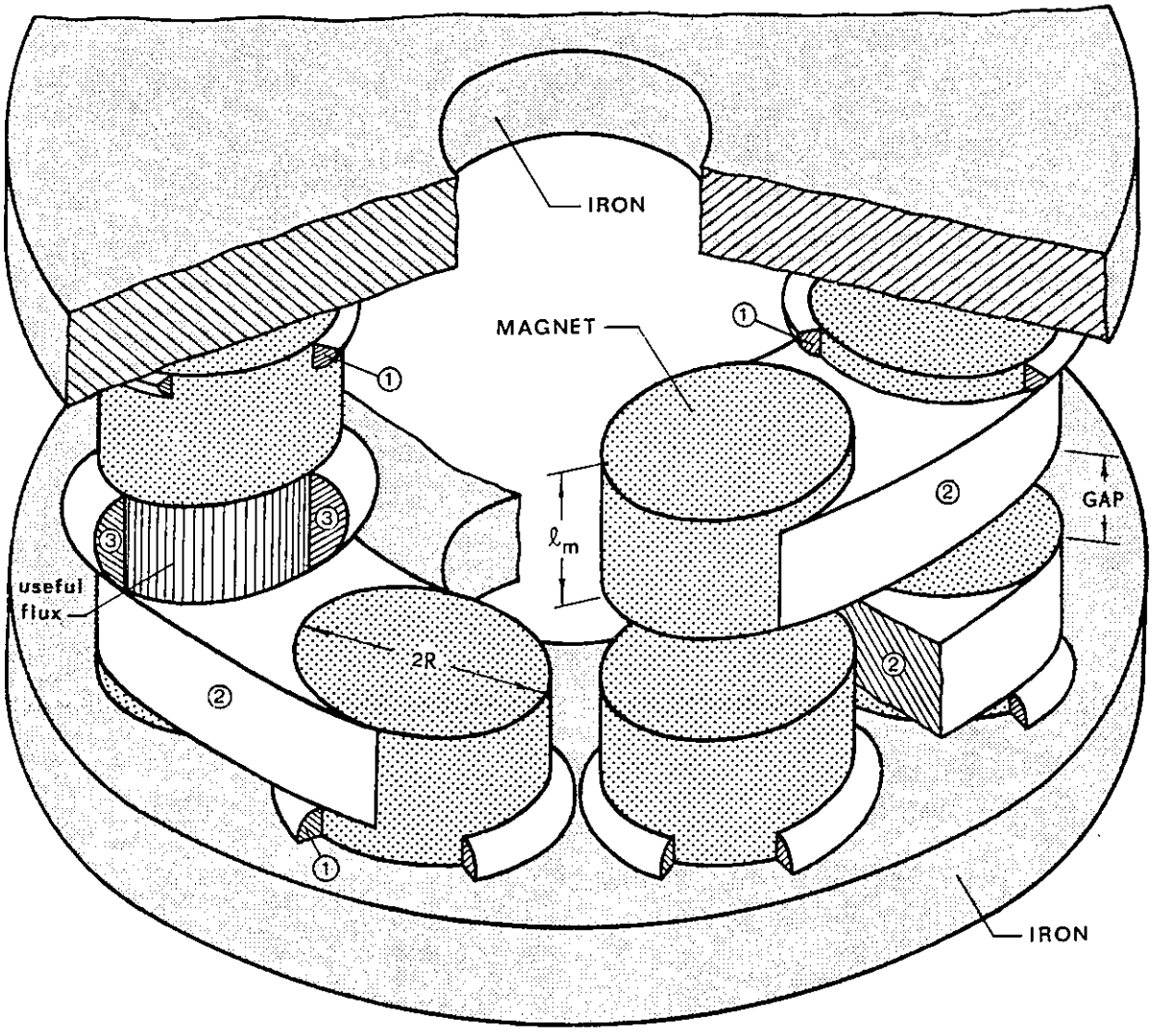

Fig. 6.2 - Main leakage paths

Path 1

This is a quadrant toroid, as shown in fig. 6.3. Assuming linearity for magnetic potential

$$\Omega_x = \Omega_h \frac{x}{h}$$

the elementary flux $d\phi_x$ emanating from the magnet to the backing iron is

$$d\phi_x = \Omega_x \, dP_x$$

where

$$dP_x = \mu_o \frac{dS}{\frac{\pi x}{2}} = \mu_o \frac{2}{\pi x} 2\pi(R + x\frac{\sqrt{2}}{2})\,dx$$

is the shell elementary permeance. Thus, the total flux emanating from

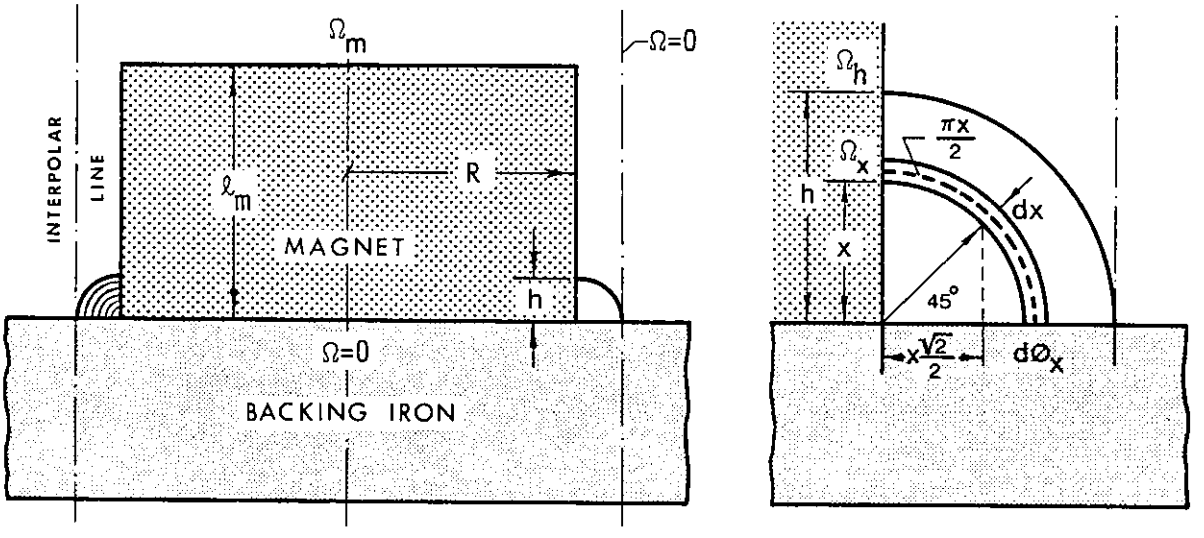

Fig. 6.3 - Quadrant toroid leakage path

the magnet per pole

$$\phi = \int_0^h d\phi_x = \frac{4\mu_o\Omega_h}{h} \int_0^h (R + x\frac{\sqrt{2}}{2})dx = 4\mu_o\Omega_h(R + \frac{\sqrt{2}}{2}h)$$

and the total leakage permeance

$$P = \frac{\phi}{\Omega_h} = 4\mu_o(R + \frac{\sqrt{2}}{4}h)$$

There are two of these permeances in parallel per pole. Hence

$$P_1 = 2P = 8\mu_o(R + \frac{\sqrt{2}}{4}h)$$

For R = 15 mm and h = 3 mm

$$P_1 = 128.46\mu_o \quad \text{mH} \tag{6.3}$$

Path 2

This is a sector between pole interfaces. For permeance calculations, the circular magnets are reduced to equivalent sector-shape magnets with the same cross sectional area, as shown in fig. 6.4.

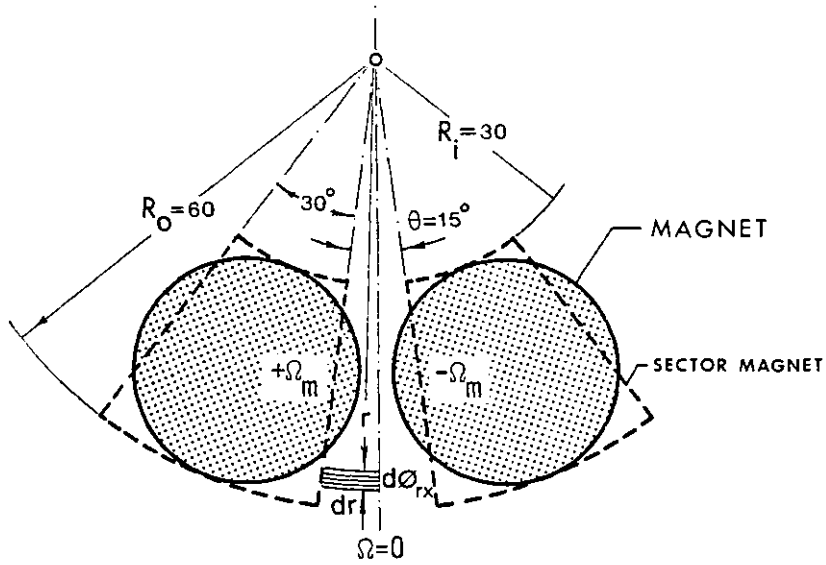

Fig. 6.4 - Circular and equivalent sector magnet

Again, assuming linearity for magnetic potential the elementary flux emanating from one side of the magnet is

$$d\phi_{rx} = \Omega_m \frac{x}{\ell_m} \frac{\mu_o dr dx}{\frac{1}{2}\theta r} = 2\Omega_m \frac{\mu_o}{\theta \ell_m} \frac{dr}{r} x dx$$

and the total flux

$$\phi = 2\mu_o \frac{\Omega_m}{\theta \ell_m} \int_{R_i}^{R_o} \frac{dr}{r} \int_{h}^{\ell_m} x dx = 2\mu_o \frac{\Omega_m}{\theta \ell_m} \log\left(\frac{R_o}{R_i}\right) \frac{\ell_m^2 - h^2}{2}$$

The total permeance of both sides of the magnet

$$P = \frac{2\phi}{\Omega_m} = \frac{2\mu_o}{\theta \ell_m} (\ell_m^2 - h^2) \log\left(\frac{R_o}{R_i}\right)$$

There are two of these permeances in series per pole. Hence

$$P_2 = \frac{P}{2} = \frac{\mu_o}{\theta \ell_m} (\ell_m^2 - h^2) \log\left(\frac{R_o}{R_i}\right)$$

Substitution of ℓ_m = 17 mm, h = 3 mm, R_o = 60 mm, R_i = 30 mm and θ = 15° = 0.26 rad gives:

$$P_2 = 87.26\mu_o \quad mH \tag{6.4}$$

Path 3

This is a hollow toroid, as shown in fig. 6.5. The mean length of the path is according to Roters' book (page 131) given by

$$\ell_{mean} = 1.22\ g$$

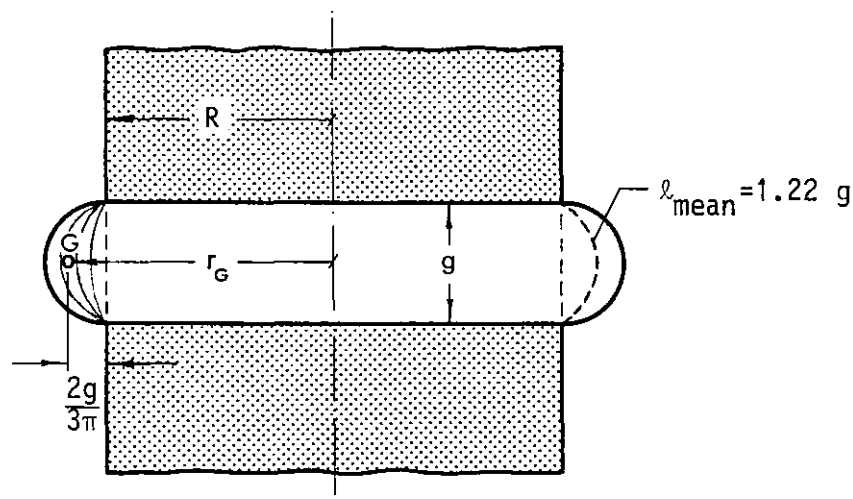

Fig. 6.5 - Hollow toroid flux path

By Pappus' theorem, the volume of this toroid is

$$V = 2\pi r_G S = 2\pi(R + \frac{2g}{3\pi})\ \frac{\pi g^2}{8}$$

and so the mean area of the flux path is

$$S_{mean} = \frac{V}{\ell_{mean}} = \frac{2\pi}{1.22}\ (R + \frac{2g}{3\pi})\ \frac{\pi g}{8}$$

Therefore, the respective permeance becomes

$$P_3 = \mu_o \frac{S_{mean}}{\ell_{mean}} = \frac{\mu_o}{4} \left(\frac{\pi}{1.22}\right)^2 (R + \frac{2g}{3\pi})$$

and since R = 15 mm

$$P_3 = 1.66(15 + 0.21g)\mu_o \quad mH \tag{6.5}$$

with g in mm.

Useful path

Assuming that the flux lines are perpendicular to the pole faces, the permeance of the air gap is

$$P_g = \mu_o \frac{\pi R^2}{g} \qquad \text{or} \qquad P_g = \frac{706.5}{g} \mu_o \ \text{mH} \qquad (6.6)$$

with g in mm.

Leakage factor

From the results (6.3) to (6.6), the leakage factor defined by Eq.(2.10) becomes

$$K_1 = 1 + \frac{P_1 + P_2 + P_3}{P_g} = 1 + \frac{172.37 + 1.66(15 + 0.21g)}{706.5} g \qquad (6.7)$$

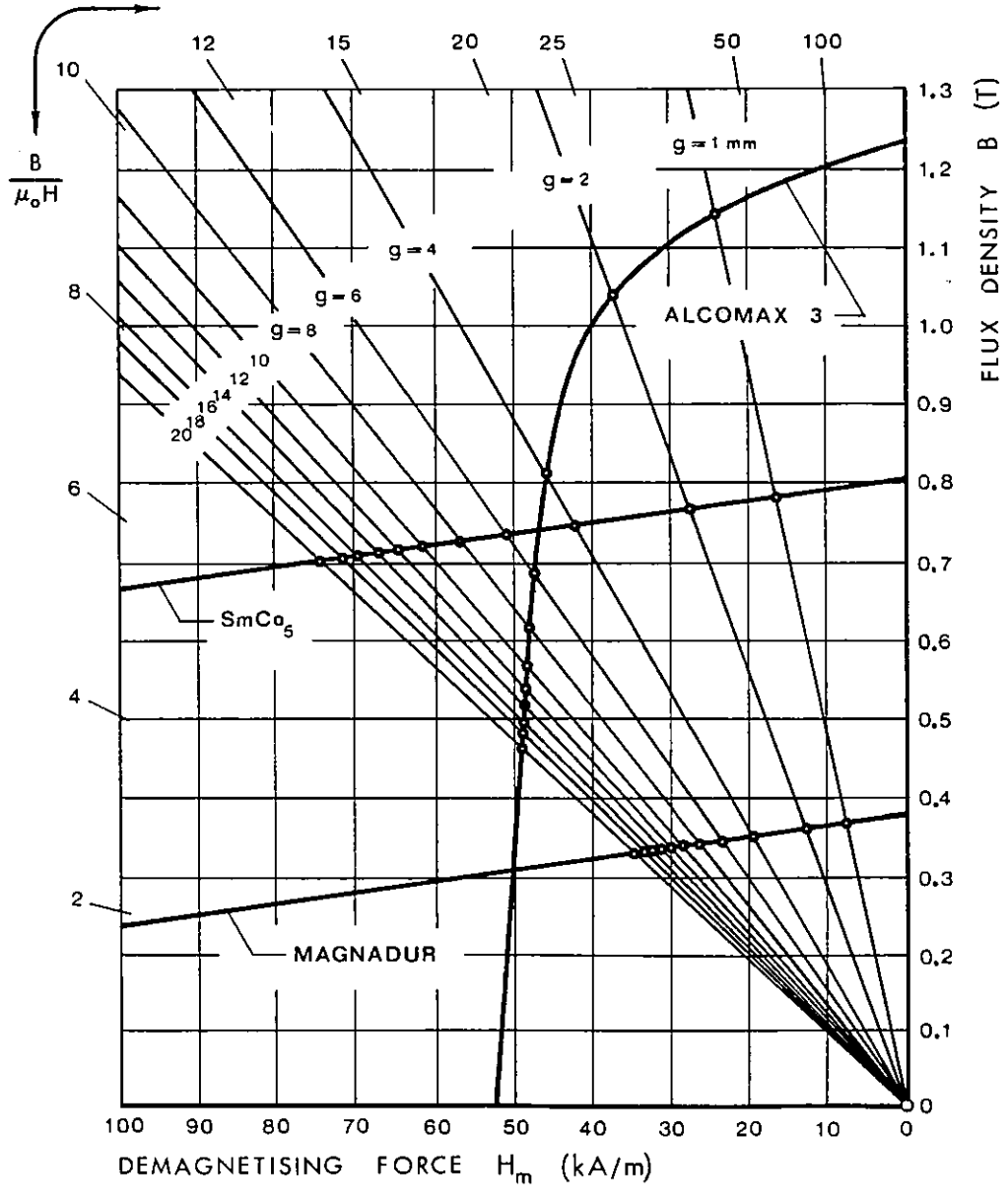

Fig. 6.6 - Second quadrant demagnetisation characteristics

Taking for the reluctance factor K_2 = 1.05, the unit permeance of the device may be now evaluated using Eq. (6.1) for a number of values of air gap. The second quadrant demagnetisation characteristics for each type of magnetic material considered earlier are also displayed in fig. 6.6. For each material and using the load-line method, the air gap flux density is then calculated from Eq. (6.2) and Eq. (6.7). The results are plotted versus gap up to 20 mm in fig. 6.7.

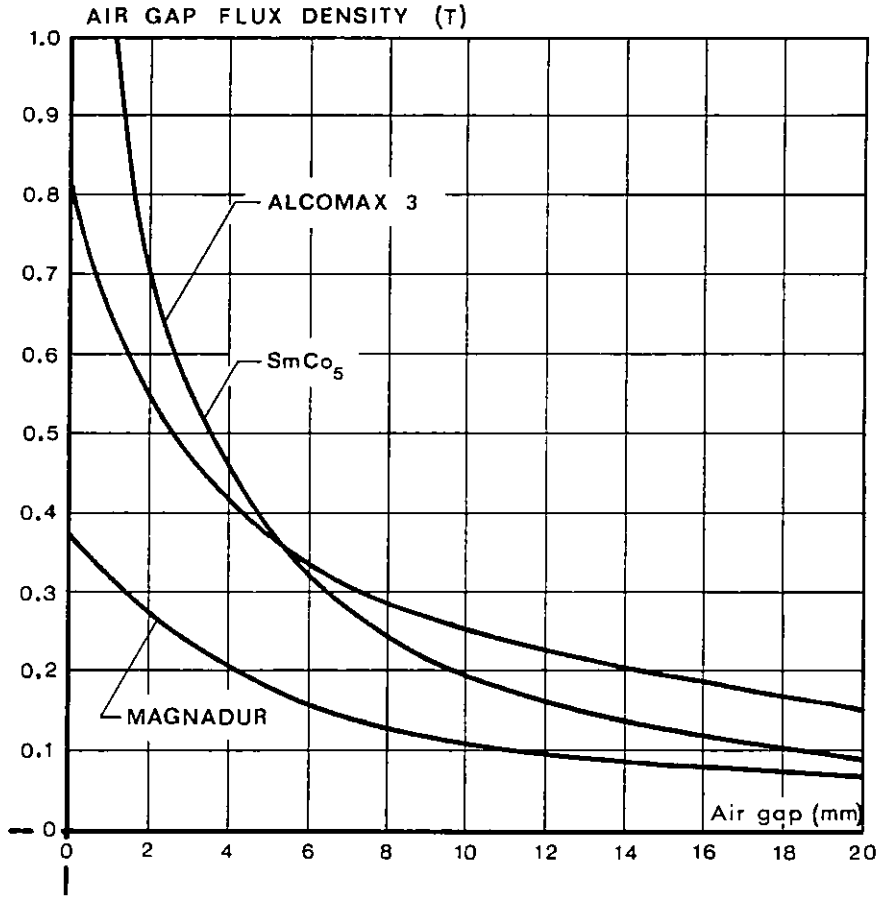

Fig. 6.7 - Air gap flux density versus gap for brush-fed disc motor

As expected, for small gaps the Alcomax 3 material gives the highest air gap flux density, but for gaps greater than 5 mm the flux density set up by the $SmCo_5$ is the best figure.

6.2.2 - Torque developed versus gap.

It is assumed that the n radial conductors are uniformly equispaced under uniform flux density B and they fill completely the inner perimeter,

as shown in fig. 6.8. According to Eq. (1.93), the total torque developed is then given by

$$T = \frac{1}{4} B n i (D_o^2 - D_i^2) \tag{6.8}$$

since $ni = A\pi D_i$, where A is the electric loading on the inner periphery.

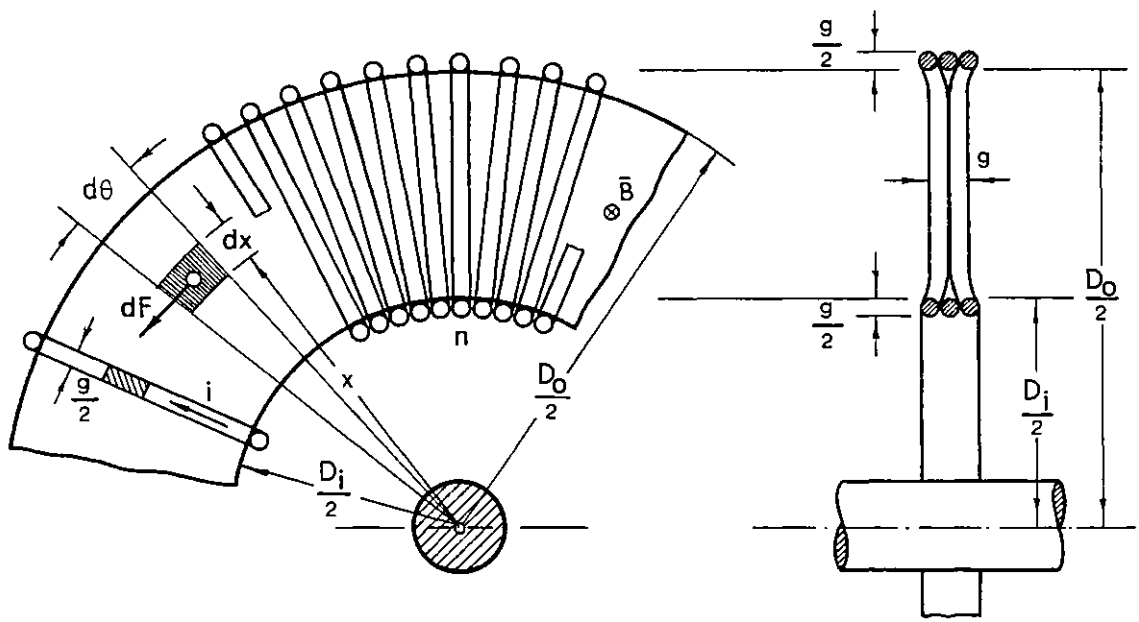

Fig. 6.8 - Basic disc rotor layout

For a fixed D_i the number of conductors n with a diameter g/2 is given approximately by the relationship

$$n \simeq \pi\left(\frac{2D_i}{g} - 1\right) \tag{6.9}$$

and the current per conductor

$$i = J_c \frac{\pi g^2}{16} \tag{6.10}$$

where J_c is the conductor current density. Clearly, it is assumed that the end-connections do not contribute for disc-shaped rotor width in the active region and only the go and return conductors of total thickness g contribute for gap width. Using Eq. (6.9) and Eq. (6.10), Eq. (6.8) may be then written in the form

$$\frac{T}{J_c} = T_u = \frac{\pi^2}{64}\left(\frac{2D_i}{g} - 1\right) g^2 B (D_o^2 - D_i^2) \tag{6.11}$$

where T_u is termed specific torque. The air gap flux density versus gap length has been calculated and displayed in fig. 6.7. Hence, substitution into Eq. (6.11) and taking D_i = 60 mm and D_o = 120 mm, enables plots of T/J_c versus gap for the three magnetic materials used, as shown in fig. 6.9.

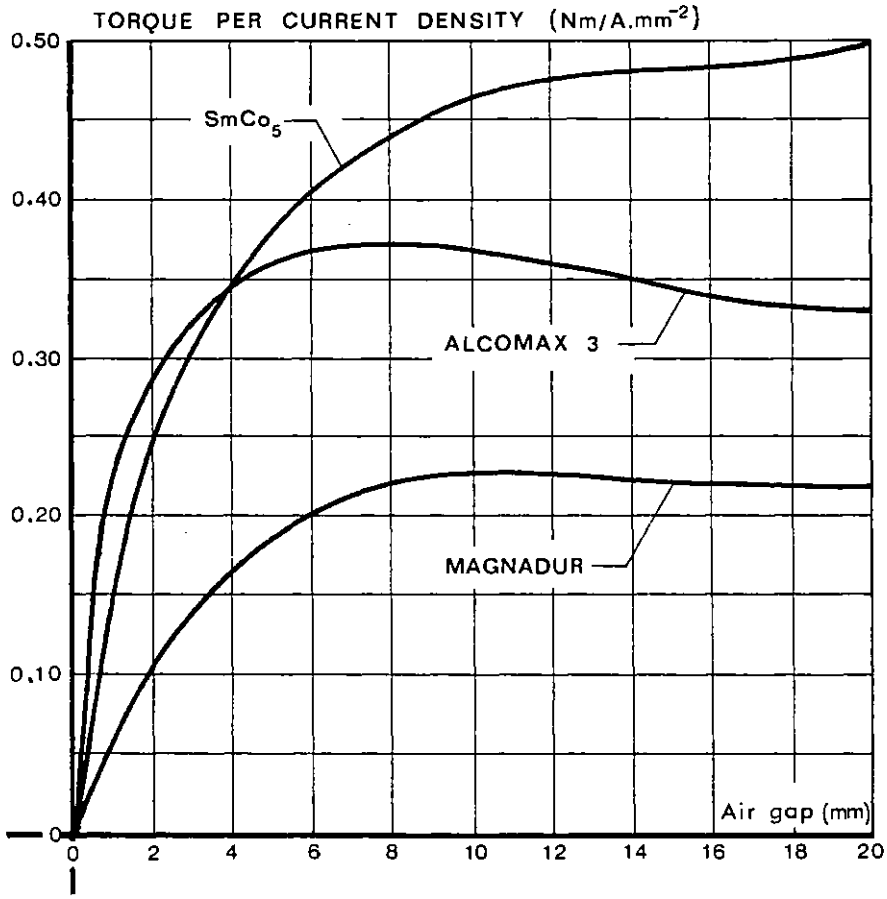

Fig. 6.9 - Specific torque versus gap for brush-fed disc motor

Again the highest torque per current density is obtainable from Alcomax 3 when gaps less than 4.0 mm are used (*). For greater gaps, however, $SmCo_5$ produces more torque.

6.3 - BRUSHLESS-FED DISC MOTOR

The previous machine could be made inherently brushless by winding the stator and using a permanent excited rotor. For this machine the rotor is

---

(*) - *Note that due to the armature m.m.f. produced, risks of demagnetisation could occur with the larger gaps within this range.*

assumed to have eight permanent magnets with the same size as each magnet used in brush-fed disc machine (same axial length ℓ_m and radius R) and, on the other hand, a double-sided stator, with air gap windings as shown in fig. 6.10.

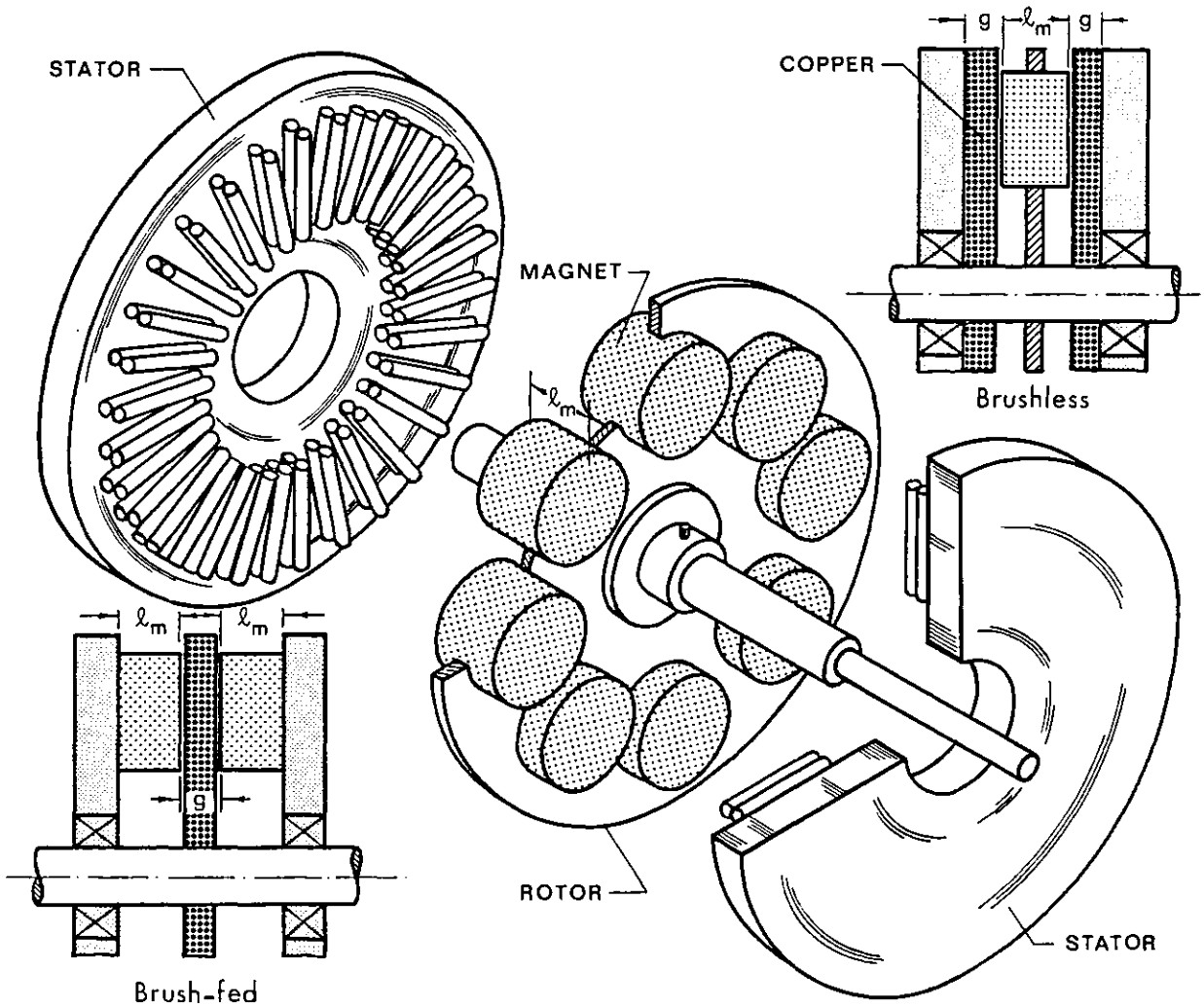

Fig. 6.10 - Brushless-fed disc motor layout

It would now unfortunately be necessary to include laminated steel in the motor (something not needed in the brush-fed, inverted form of the previous disc motor). Slotted stators with normal winding could of course be used. However to facilitate comparisons with the brush-fed disc machine and because the technical case for the air gap wound version of the rotating field machine is reckoned to be by no means negligible, attention is concentrated on this.

6.3.1 - Air gap flux density calculation

For this configuration two leakage paths are considered, as shown in fig. 6.11.

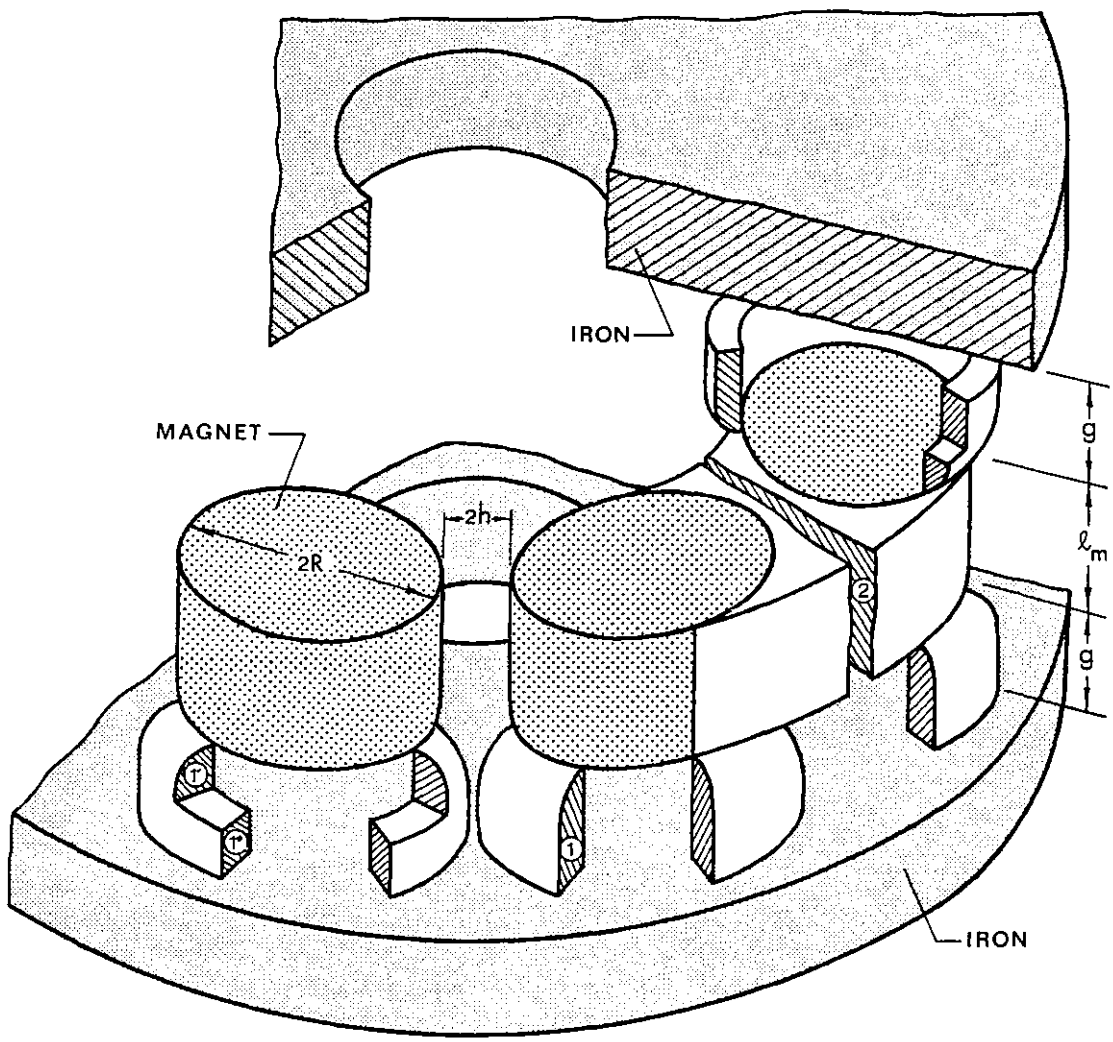

Fig. 6.11 - Leakage paths for brushless-fed disc machine

When the gap is less than half of interpolar distance h, path 1 reduces to a quarter hollow toroid and it can be easily demonstrated that the total permeance per pole of the path is given by

$$P_1 = \mu_o\, 6.62\,(R + \frac{4g}{3\pi}) \quad \text{for} \quad g < h \tag{6.12}$$

However, for gaps greater than h the permeance of path 1 becomes as a series of two permeances 1´ (quarter hollow toroid) and 1´´ (annular toroid).

Then, the total permeance of this path per pole may be expressed as

$$P_1 = \mu_o \frac{2}{\frac{1}{3.31(R+\frac{4g}{3\pi})} + \frac{g-h}{2\pi(R+\frac{h}{2})}} \quad \text{for} \quad g > h \qquad (6.13)$$

Path 2 is a sector between pole faces. By a similar method as used in brush-fed machine, the total per pole of this path was found to be

$$P_2 = \frac{1}{2} \frac{\mu_o}{\theta} \ell_m \log \left(\frac{R_o}{R_i} \right) \qquad (6.14)$$

The permeance of the useful path is readily obtainable as

$$P_g = \mu_o \frac{A_g}{2g} = \mu_o \frac{\pi R^2}{2g} \qquad (6.15)$$

Although path 1 contributes for useful flux it will be considered as leakage in order to evaluate Bg.

Hence,

$$K_1 = 1 + \frac{P_1 + P_2}{P_g} \qquad (6.16)$$

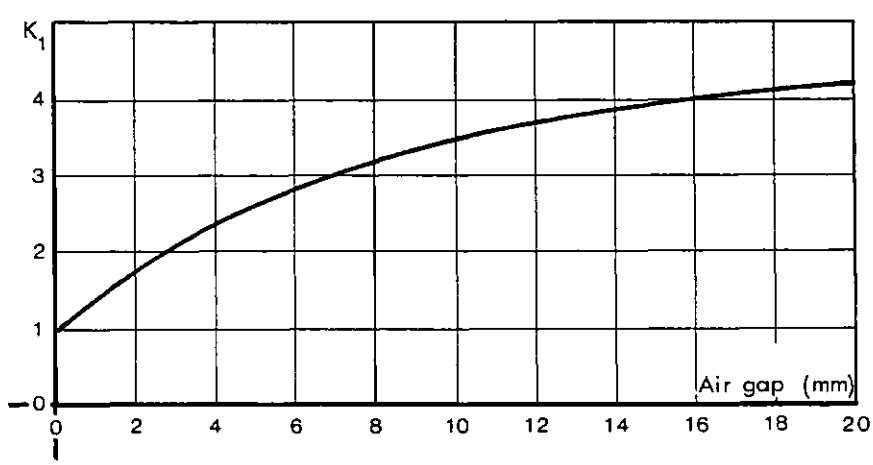

Fig. 6.12 - Variation of the leakage factor versus air gap

Substitution of R = 15 mm, ℓ_m = 17 mm, R_o = 60 mm, R_i = 30 mm and θ = 15° = 0.26 rad into Eq. (6.12) to Eq. (6.15) allows calculation of Eq. (6.16). The leakage factor was calculated for gaps up to 20 mm and it is shown plotted in fig. 6.12. From the knowledge of leakage factor and

using the demagnetisation characteristics for the three materials considered, the air gap flux density was then evaluated using the load-line method. Fig. 6.13 shows the air gap flux density variation versus gap for each magnetic material used.

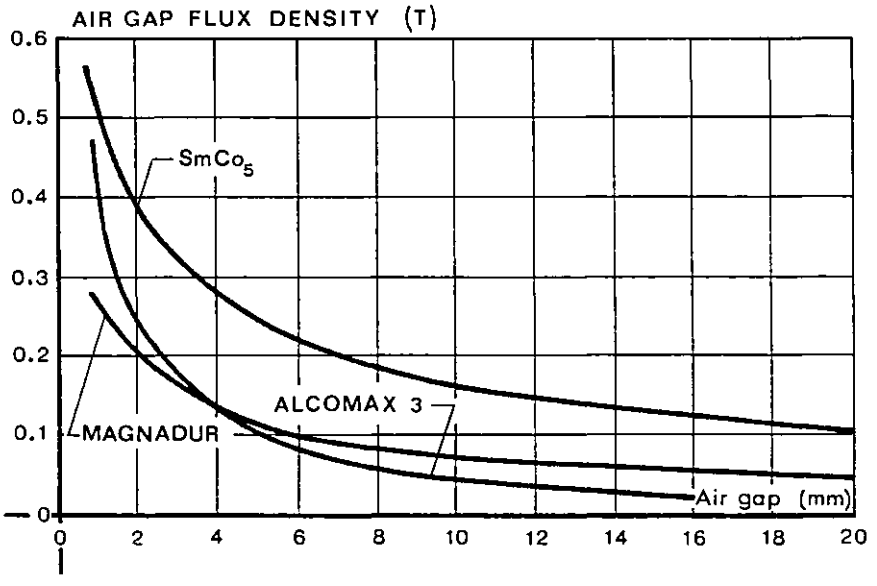

Fig. 6.13 - Air gap flux density versus gap for brushless-fed disc motor

Since the magnet length was halved and the gap length doubled compared with brush-fed disc machine, the $SmCo_5$ material consistently produces the highest flux density in this case.

6.3.2 - Torque versus gap

According to Eq. (6.11) the torque per current density for a double-stator motor is now given by

$$\frac{T}{J_c} = T_u = 2\,\frac{\pi^2}{64}\,\left(\frac{2D_i}{g} - 1\right) g^2 B\,(D_o^2 - D_i^2) \qquad (6.17)$$

Using the same outer and inner diameters as for brush-fed disc motor (D_o = 120 mm, D_i = 60 mm) and the values of air gap flux density displayed in fig. 6.13, Eq. (6.17) was evaluated for gaps up to 20 mm. The results are shown plotted in fig. 6.14 and as expected the $SmCo_5$ rotor gives the

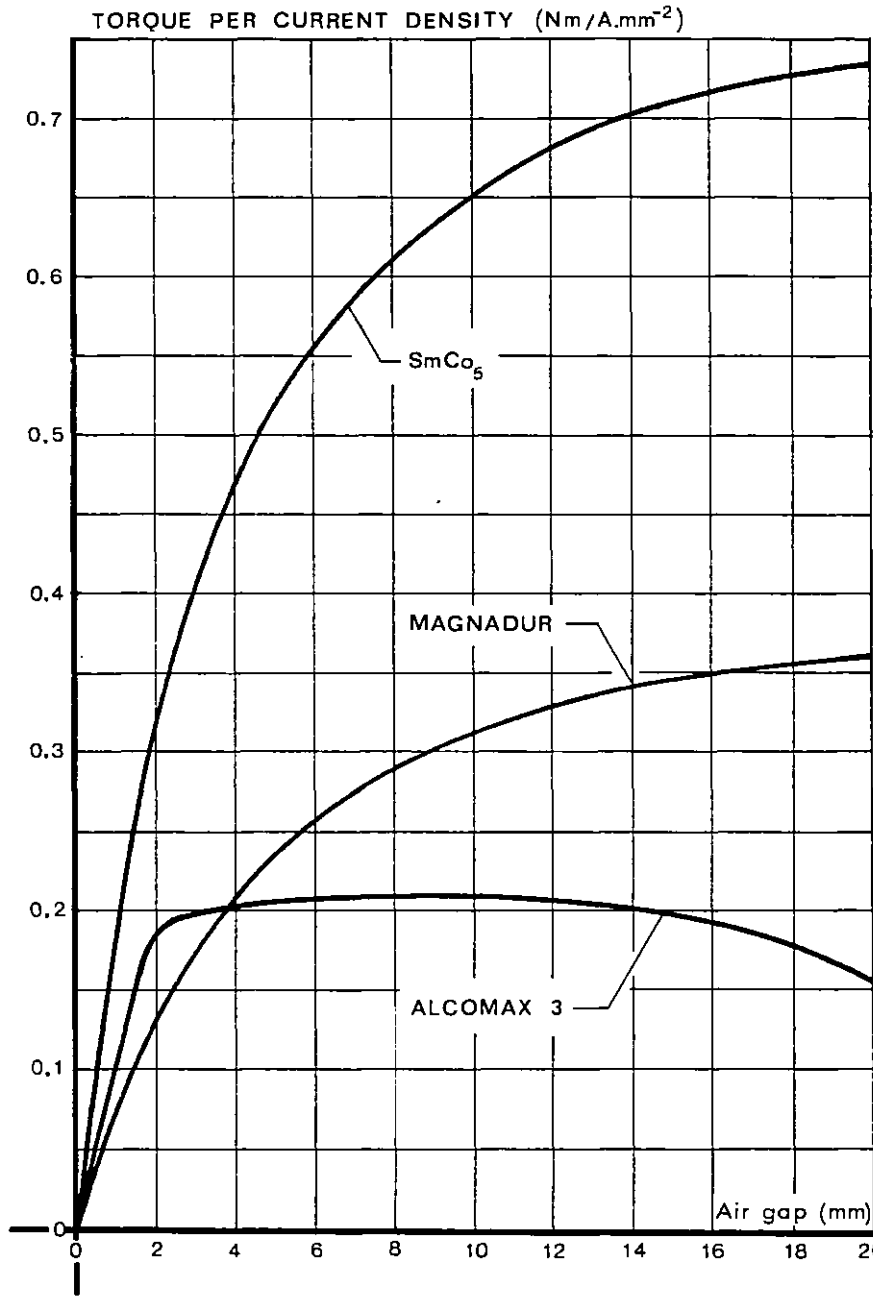

Fig. 6.14 - Torque per current density versus gap for brushless disc machine

highest performance. Due to the abrupt decay of the Alcomax 3 demagnetisation curve, the specific torque is practically constant over a large range of gap lengths.

6.4 - COMPARISON OF BRUSH AND BRUSHLESS-FED DISC MOTORS

A comparison in terms of torque per inertia of both machines previously described can now be made.

Referring to fig. 6.8, the disc rotor inertia taking account only of the n radial copper conductors of specific weight $\rho_{cu} = 8.2 \times 10^3$ kg.m^{-3} is given by

$$J = \pi\left(\frac{2D_i}{g} - 1\right)2\pi\rho_{cu}\frac{g^2}{16}\int_{(D_i-g)/2}^{(D_o+g)/2} x^2 dx = \frac{\rho_{cu}\pi^2 g}{192}\left(\frac{2D_i}{g} - 1\right)\left[(D_o+g)^3-(D_i-g)^3\right] \quad (6.18)$$

Hence, using Eq. (6.11) the specific torque per inertia for the brush fed disc machine is:

$$\frac{Tu}{J} = 3\,\frac{B(D_o^2 - D_i^2)}{\rho_{cu}\left[(D_o+g)^3-(d_i-g)^3\right]} \quad (6.19)$$

For the brushless disc machine, since the rotor size does not change with gap, the moment of inertia is contant with gap and only depends on the specific weight of the magnet material used. According to parallel axis theorem, the moment of inertia of the eight permanent magnets referred to rotor shaft is

$$J_o = 8(J_G + R_{ave}^2\, M) \quad (6.20)$$

where $R_{ave} = 45$ mm is the distance of the magnet's centre of gravity from the shaft.

Since the mass of one magnet is $M = \rho_m \pi R^2 \ell_m$ and its moment of inertia referred to its centre of gravity is $J_G = \frac{\pi}{2}\rho_m \ell_m R^4$, Eq. (6.20) becomes:

$$J_o = 8\pi\rho_m R^2 \ell_m \left(\frac{R^2}{2} + R_{ave}^2\right) \quad (6.21)$$

The manufacturers of the magnets quoted the following specific weights [109] for each material

$$\rho_{Alcomax} = 7.35 \times 10^3 \text{ kg.m}^{-3}$$
$$\rho_{SmCo_5} = 4.70 \times 10^3 \text{ kg.m}^{-3}$$
$$\rho_{Magnadur} = 5.20 \times 10^3 \text{ kg.m}^{-3}$$

Substitution of these values in Eq. (6.21) gives:

$$J_{Alcomax} = 1.51 \times 10^{-3} \text{ kg.m}^2$$
$$J_{SmCo_5} = 0.97 \times 10^{-3} \text{ kg.m}^2$$
$$J_{Magnadur} = 1.07 \times 10^{-3} \text{ kg.m}^2$$

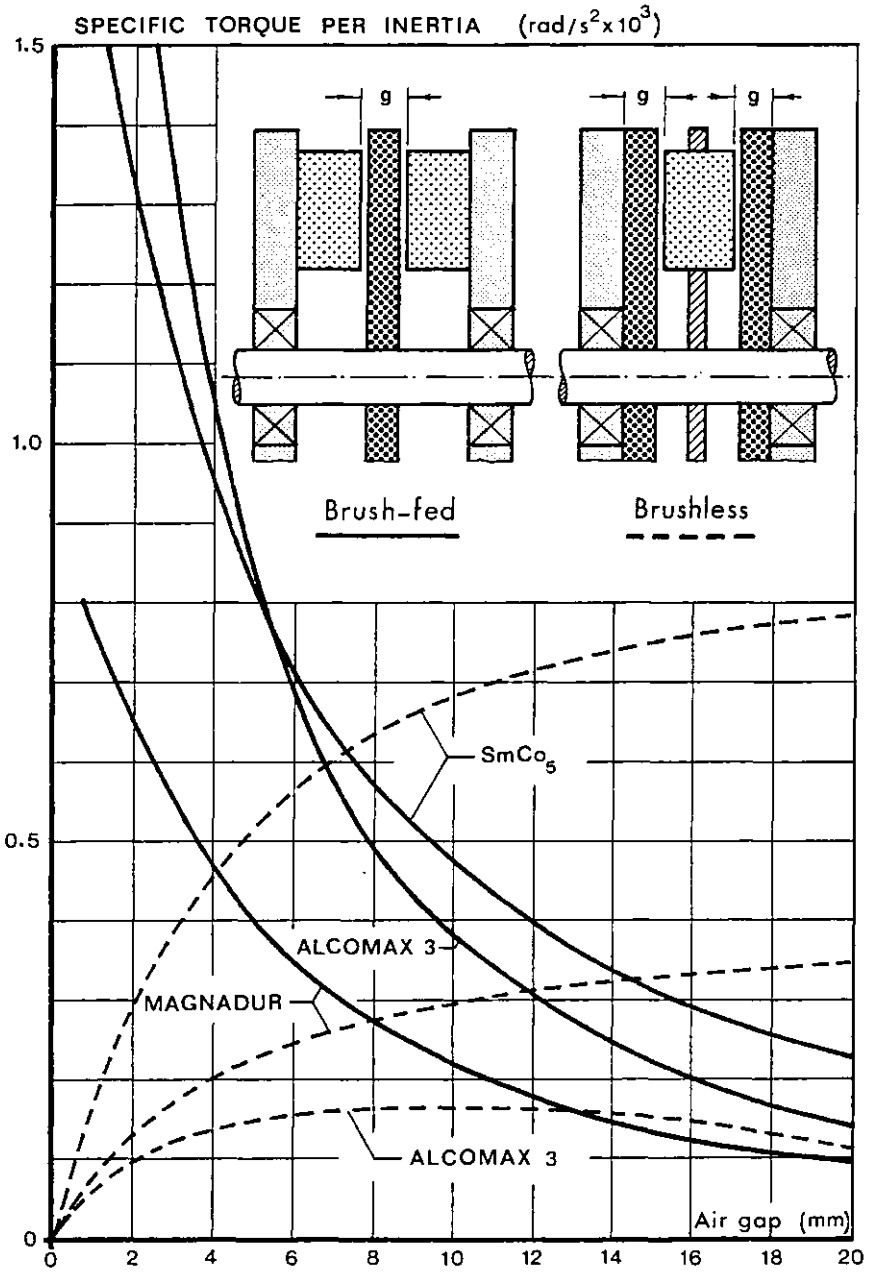

Fig. 6.15 - Comparison of torque per inertia of both disc machines

Using these figures and Eq. (6.17), the specific torque per inertia may be evaluated for each rotor. Fig. 6.15 shows plots of specific torque per inertia versus gap for this machine together with the results obtained from Eq. (6.19) for the three types of magnetic material.

From these results and on the basis laid down some interesting conclusions arise:

a) - Brush-fed disc machines have better initial angular acceleration for small gaps than equivalent brushless disc machines. This is because inertia is proportional to rotor thickness for brush-fed and constant for brushless machine.

b) - For brush-fed machines, Alcomax 3 rotors give better torque per inertia for gaps up to 5 mm. However, for greater gaps the $SmCo_5$ rotor shows that this material is ideal when long gaps are used.

c) - In the case of the rotating field, brushless machine $SmCo_5$ material is certainly preferable when gaps larger than 4.5 mm are used and may be preferable for somewhat smaller gaps also.

d) - The Alcomax 3 rotor when used in the brushless machine gives the worst performance. Therefore, this material should be used only when small gaps are involved and/or one is willing to employ a rotor (incorporating relatively long magnets) that is long in the axial direction and that possess a correspondingly high inertia.

6.5 - BRUSHLESS, COIL-EXCITED DISC MOTOR OF NOVEL CONSTRUCTION

An eight pole disc machine which is inherently brushless and which incorporates the possibility of varying field excitation is represented in fig. 6.16. The general concept of the machine is not new (the structure is represented and examined as a two-pole alternator in reference [110]) and the use of a stator-mounted field coil makes it similar in this respect with the inductor-alternator and certain other "solid-rotor" a.c. machines. A typical flux path is shown in the diagram and since the flux axial direction is invariant with rotor rotation, this machine can be classified as homopolar. Some novel and unusual features are presented, as follows:

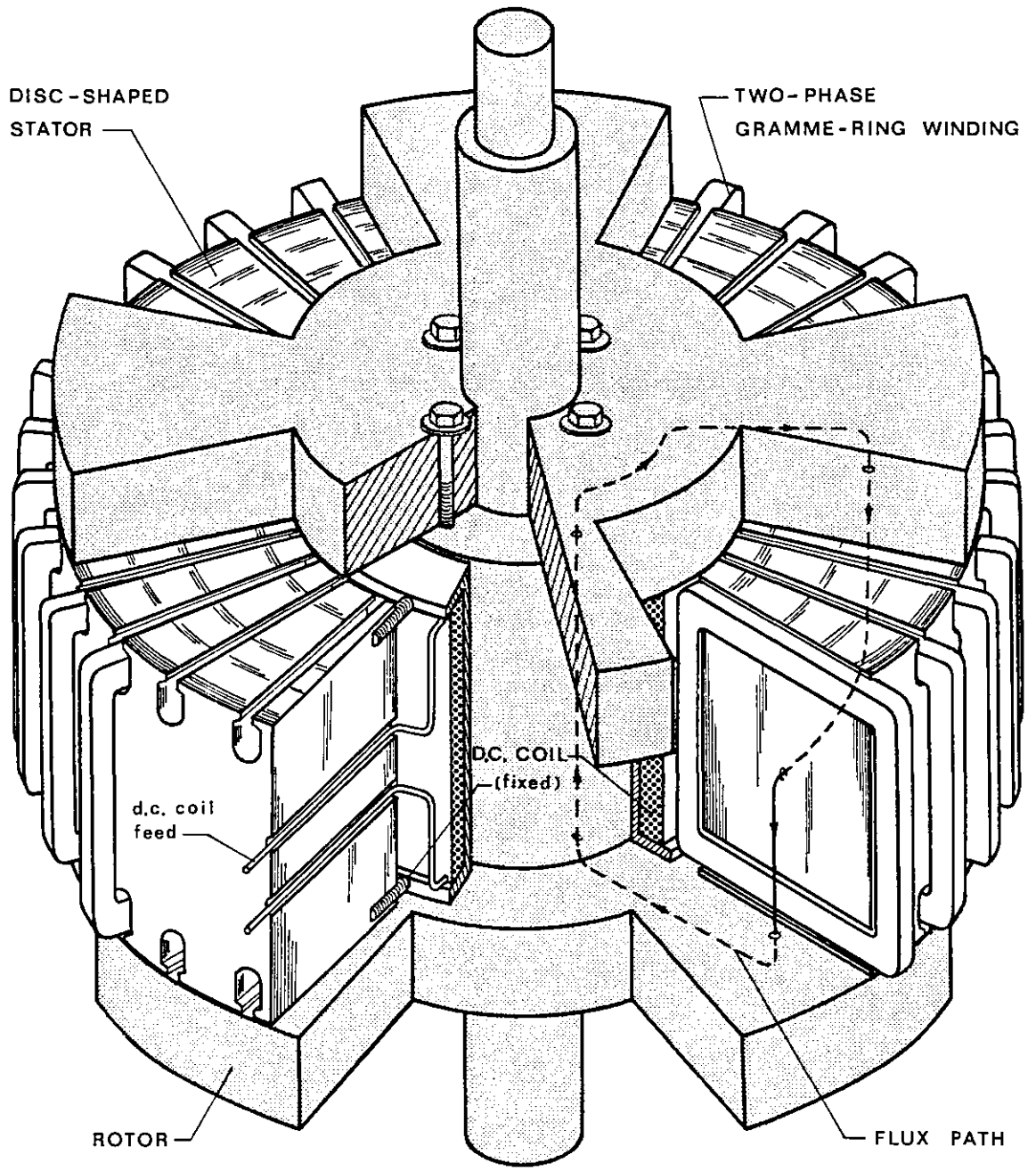

Fig. 6.16 - Brushless coil excited disc machine layout

i) - A twin disc stator construction is used which gives a high level of a.c. winding utilisation (i.e. active length per turn/total length per turn) and which minimises net axial forces on the rotor. The stator is wound with a Gramme-ring type winding connected in such a way to produce a two-phase system. The d.c. field coil is co-axial with the shaft and fixed to the stator.

ii) - The rotor is a passive steel member which has no electrical windings and requires no brushes or sliprings. Hence, if required, and as with other solid rotor machines, it can be operated at high speeds. It consists of two slotted discs with four projections (poles), shifted 90°E to respect each other. In this way the flux set up by the d.c. coil cross the upper and down radial conductors which belong to the same phase, therefore adding e.m.f.'s.

iii) - The rotor and stator are separated items. The rotor can be mounted in an existing shaft which is part of the magnetic circuit, the stator being supported separately.

6.5.1 - Machine design considerations

Some of the electromagnetic design considerations of disc machines are the same as for conventional cylindrical machines, but special features are also included in this motor. These are now described as follows:

a) - Stator design

As shown in fig. 6.16, the stator is laminated. An established method of producing a disc-motor stator is to strip-wind a core simultaneously punching the slots or to machine radial or skewed-radial slots later. Semiclosed slots normally require the former technique.

In view of a comparison to be made, the stator is assumed to have the same outer (D_o = 120 mm) and inner (D_i = 60 mm) diameters as the previous disc machines.

b) - Rotor design

Allowing a pole arc to pole pitch ratio σ = 0.8 the pole arc is $\alpha_a = \sigma 45° = 36°$. Hence, from fig. 6.17 the pole face area becomes

$$S_g = \frac{1}{2}\alpha_a (R_o^2 - R_i^2) = 847.80 \text{ mm}^2$$

By flux continuity considerations and neglecting leakage flux

$$S_c = 4 \frac{B_g}{B_c} S_g \tag{6.22}$$

where B_c is the central core flux density. Taking as typical values for air gap flux density B_g = 0.5 T and B_c = 1.6 T (iron saturation), Eq. (6.22) gives for the central core cross section S_c = 1059.75 mm^2 and a radius

$$R_c = \sqrt{\frac{S_c}{\pi}} = 18.36 \text{ mm} \tag{6.23}$$

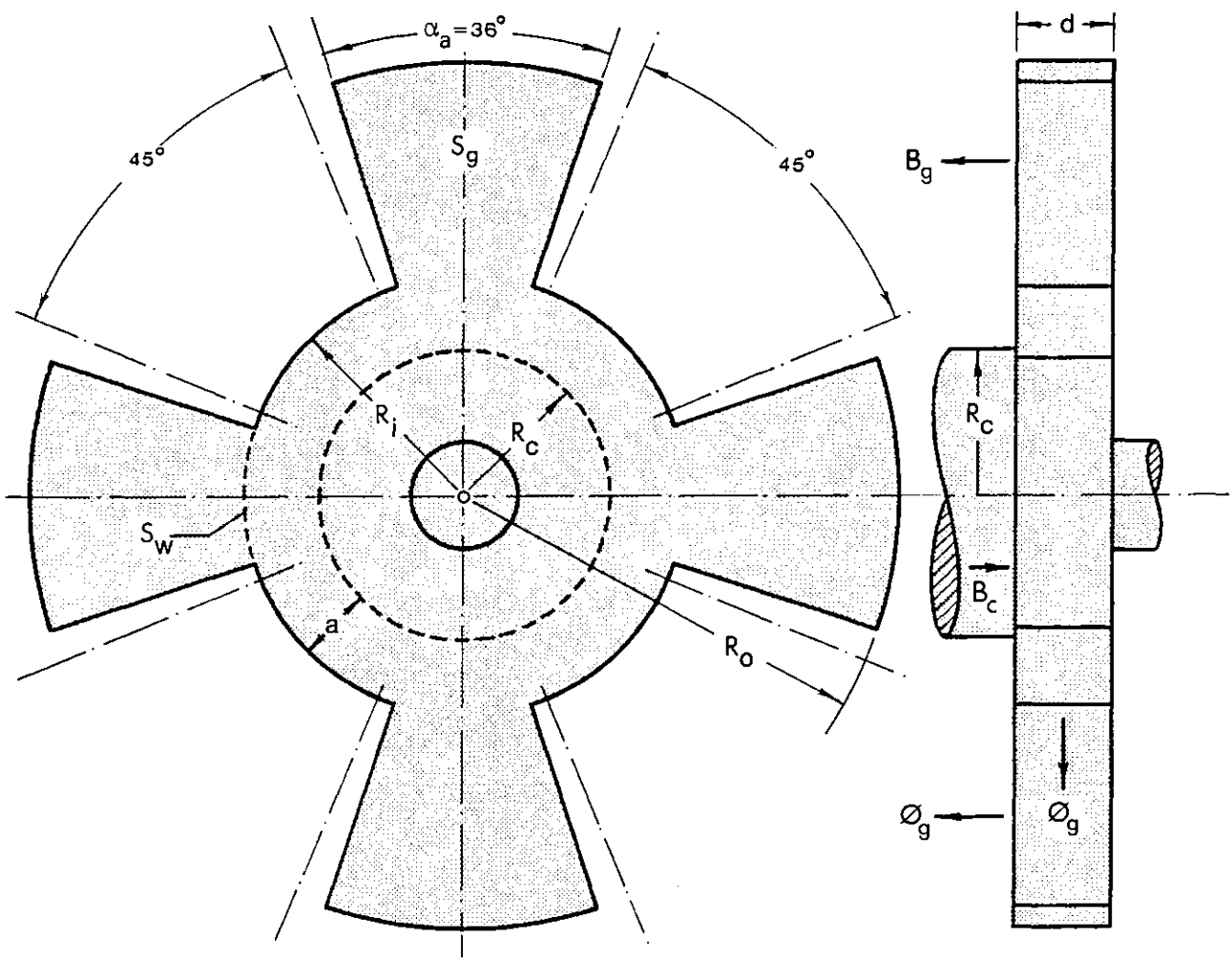

Fig. 6.17 - Slotted iron disc rotor

The smallest cross section of the slotted disc rotor is given by $S_d = \alpha_a R_i d$ where d is the disc width. Again, by flux continuity considerations

$$d = \frac{1}{\alpha_a R_i} \frac{B_g}{B_c} S_g \tag{6.24}$$

Calculating S_d to saturation, Eq. (6.24) gives for disc width d = 14.06 mm.

c) - D.c. coil excitation dimensions

As shown in fig. 6.18, the space reserved for copper between inner stator and the central core obviously is $c = R_i - R_o = 11.64$ mm. Allowing 4 mm for the stator end coil s and keeping a gap of 2.64 mm between both windings the d.c. coil width is $b = c - (s + 2.64) = 5$ mm.

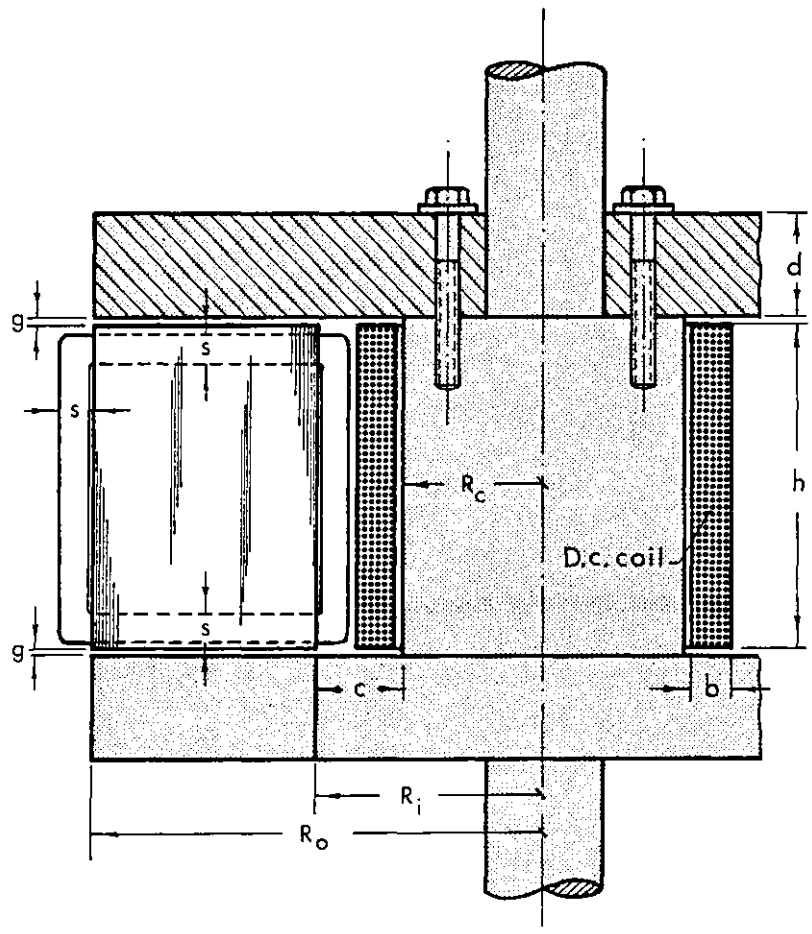

Fig. 6.18 - Brushless coil excited disc motor cross section

Neglecting m.m.f. drops in the iron, the d.c. coil m.m.f. NI necessary to produce an air gap flux density B_g is

$$NI = \frac{B_g}{\mu_o} 2g$$

If a current density J_c in the d.c. coil is assumed, its height h must satisfy the equation

$$h = \frac{2g}{bJ_c} \frac{B_g}{\mu_o} \qquad (6.25)$$

For typical values $J_c = 3$ A.mm^{-2}, $g = 0.8$ mm and $B_g = 0.5$ T, Eq. (6.25) gives for the height of the d.c. coil $h = 42.46$ mm.

d) - Stator winding

The main problem with the Gramme-ring winding is the wasted space occupied by the inner and outer end coil connections. Hence, the end stator coil must be made as short as possible. The coils are assumed to have a useful square cross section $s^2 = 9\ mm^2$. In a disc machine the radial slots are usually made with a constant width s and taking t = 2.8 mm for the inner tooth width, the inner slot pitch is then:

$$w = s + t = 5.8\ mm$$

Hence, the total number of slots will be

$$Q = \frac{2\pi R_i}{w} = 32.48 \simeq 32\ \text{slots}$$

with a slot pitch $\alpha_s = 11.25°$. This results in a total of 32 coils and for an eight-pole, two-phase winding $q = Q/m n_p = 2$ coils-pole/phase. Fig. 6.19

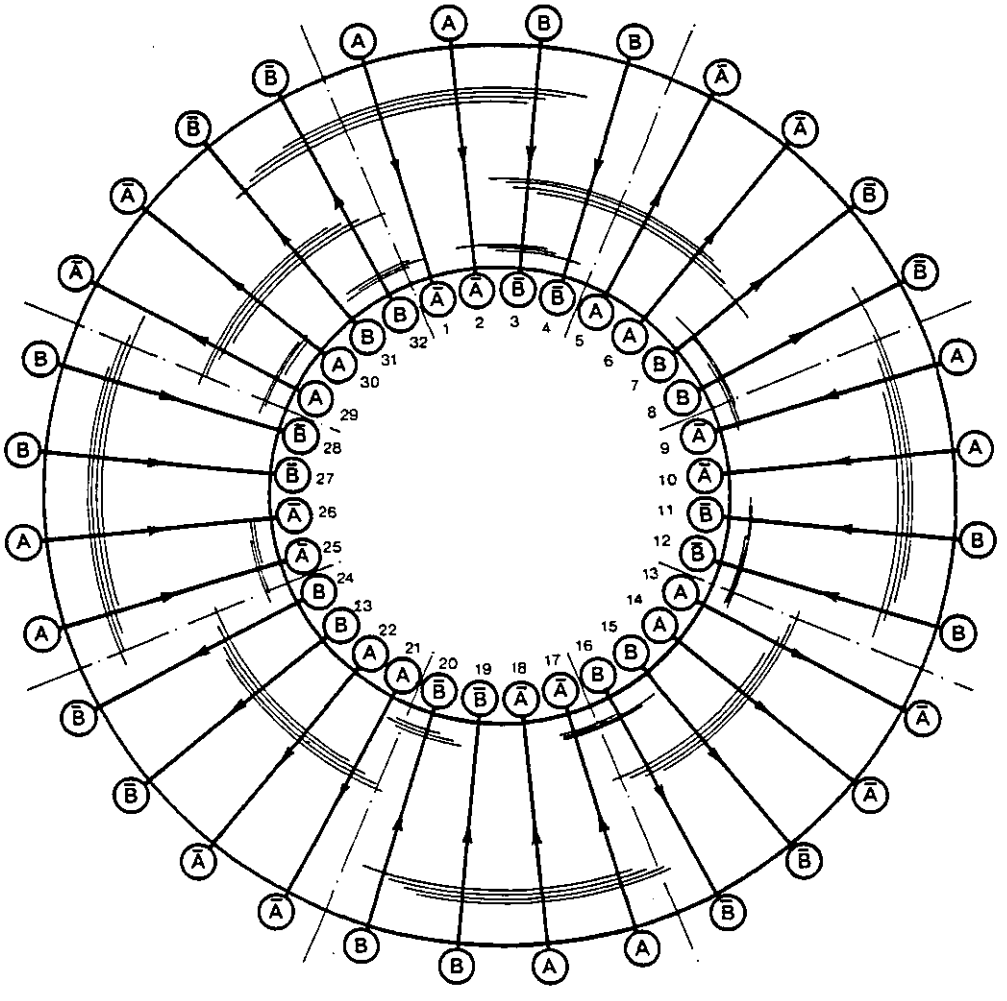

Fig. 6.19 - Winding diagram

shows one side of the winding diagram with both phases excited at the instant when the phase currents are equal.

6.5.2 - Specific torque developed

Since in this machine the gap is constant under the rotor pole face, it is then acceptable to assume that the excitation flux density distribution is a square wave, as shown in fig. 6.20. Fourier analysis of this wave

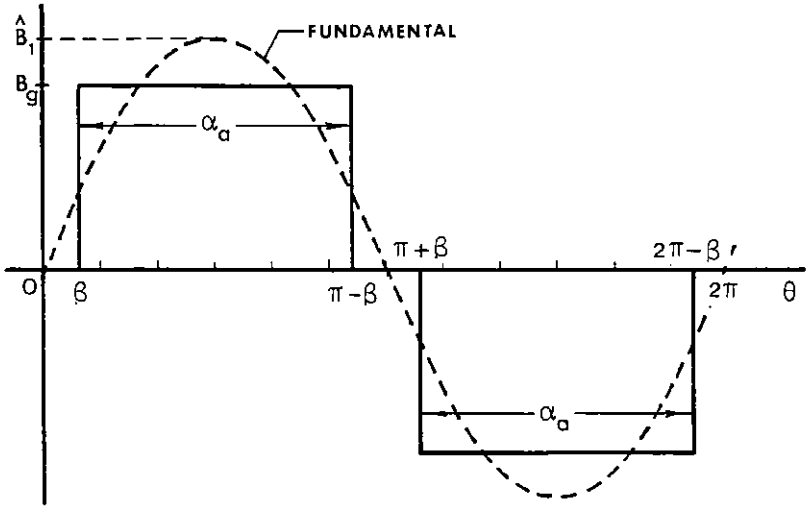

Fig. 6.20 - Air gap flux density distribution

gives the harmonic coefficients as

$$B_h = \frac{1}{\pi}\left[\int_{\beta}^{\pi-\beta} B_g \sin h\theta\, d\theta - \int_{\pi+\beta}^{2\pi-\beta} B_g \sin h\theta\, d\theta\right]$$

$$= \frac{B_g}{\pi h}\left[-\cos h(\pi-\beta)+\cos h\beta+\cos h(2\pi-\beta)-\cos h(\pi+\beta)\right] \qquad (6.26)$$

Since $\beta = \frac{1}{2}(45 - 36)4 = 18°E$, Eq. (6.26) gives the fundamental peak air gap flux density as

$$\hat{B}_1 = \frac{3.8}{\pi} B_g = 0.61\ T \qquad (6.27)$$

For 90°E torque angle operation, according to Eq. (1.46), the fundamental

torque developed is given by

$$T_1 = n_p R_{ave} \ell_{ef} N \hat{I}_1 \hat{B}_1 K_{w1} \tag{6.28}$$

There are two radial bundles of conductors per pole per phase. Assuming a stator current density $\hat{J}_s$ in a cross section s^2 the m.m.f. per pole per phase will be $N\hat{I}_1 = 2\sqrt{2}\, J_s s^2$. Substitution of n_p = 8 poles, R_{ave} = 45 mm, ℓ_{ef} = 30 mm and K_{w1} = 0.854 (unskewed slots) into Eq. (6.28) results for the specific torque developed

$$\frac{T_1}{J_s} = T_u = 0.143 \text{ Nm/A}_{rms} \text{ mm}^{-2} \tag{6.29}$$

For the brush-fed machine described in section 6.2, the equivalent conductor diameter is $g/2 = 2\ \frac{s}{\pi}$ = 3.39 mm or an equivalent gap g = 6.67 mm. With this gap fig. 6.9 shows that the Alcomax 3 field system produces a specific torque of 0.36 Nm/A mm^{-2}, which is about more than twice the specific torque developed by the machine just described. This is because some 2:1 reduction in utilisation tends to be inherent in most homopolar machines. In this one, only half the active conductors are torque producing due to the limited pole arcs of the rotor discs.

6.5.3 - Specific torque per inertia

From the rotor geometry shown in fig. 6.17 and fig. 6.18 and assuming the same specific weight $\rho = 7.8 \times 10^3$ kg.m^{-3} for all rotating parts, the moment of rotor inertia is readily obtained in the form

$$J = \rho\pi\left[R_i^4 d + 0.4(R_o^4 - R_i^4)d + 0.5\, h\, R_c^4\right]$$

Substitution of the previous design dimensions gives $J = 2.01 \times 10^{-3} \text{kg.m}^2$

Hence, from Eq. (6.29) the specific torque per inertia is

$$\frac{T_u}{J} = 0.071 \times 10^3 \text{ rad/s}^2 \tag{6.30}$$

Due to the low torque and high inertia this figure becomes much less

than those found for the equivalent permanent magnet excited disc machines, as can be seen from the results displayed in fig. 6.15. This motor is not suitable therefore for servo applications, but its robust rotor would make it suitable for very high speed use.

6.6 - ALCOMAX 3 PERMANENT EXCITED DRUM MOTOR

A basic comparison between the previously described disc motors and conventional permanent magnet excited cylindrical motor with slotted stator construction is now made. This comparison is of interest because it is this type of drum machine, rather than the direct, air gap-wound equivalent of the disc motors so far considered that is perhaps at present the main competitor in the permanent magnet-excited drives field, whether for servo or non-servo applications. Air gap-wound, rotating armature drum motors of any size seem to have defeated the attempts of manufacturers to make them sufficiently robust, though this should not be a problem with rotating field versions.

It is assumed that both disc and drum machines have the same outer diameter, the same active conductor length and the same number of poles. Since for n_p = 8 pole disc motor the outer diameter is D_o = 120 mm, from Eq. (1.61) the stator inside diameter is D_g = 90 mm, which is exactly equal to the average diameter $2R_{ave}$ used in the disc machine. This gives a machine with a D_g/ℓ ratio of 3.

6.6.1 - Rotor design

A rotor design with soft steel pole pieces is examined, since the local field gradients near the stator slot openings on load in the case of the slotted stator considered is likely to lead to demagnetisation if "base" Alcomax magnets are used.

Allowing for a minimum air gap length g_{min} = 0.5 mm the maximum centre

radius of the pole piece is

$$r_c = \frac{D_g}{2} - g_{min} = 44.5 \text{ mm}$$

For the angular position $\frac{n_p}{2}\theta_{mec} = 90°E$ at the pole piece centreline, the constant C_1 in Eq. (1.50) should satisfy the equation

$$C_1 = \frac{r_c^{\frac{n_p}{2}}}{R_g^{n_p}} - \frac{1}{r_c^{\frac{n_p}{2}}} \tag{6.31}$$

for a sinusoidal field flux distribution. Substitution of values into Eq. (6.31) gives $C_1 = -0.022 \times 10^{-6}$ mm^{-4}. Having obtained C_1, Eq. (1.50) enables one to evaluate r for varying values of θ. From values of r the radial air gap length $g = R_g - r$ at each angular position can be found. The results obtained are shown in table 6.1.

Table 6.1 - Geometry of pole piece

θ_{mech} (degrees)	1.25	2.5	5.0	7.5	10.0	12.5	15.0	17.5	20.0	22.5
θ_{elect} (degrees)	5	10	20	30	40	50	60	70	80	90
r (mm)	39.78	42.22	43.55	44.00	44.22	44.23	44.42	44.46	44.49	44.50
$g=R_g-r$ (mm)	5.22	2.78	1.45	1.00	0.78	0.77	0.58	0.54	0.51	0.50

In order to keep the interpolar flux leakage at low levels, the pole piece profile is in practice terminated at the point where the extreme flux line emanating from $\theta = 0°$ and $r = R_g$ on the stator, intersects it. For this particular flux line Eq. (1.51) gives:

$$C_2 = \frac{2}{R_g^{\frac{n_p}{2}}} = 0.488 \times 10^{-6} \text{ mm}^{-4}$$

After substitution of this constant, the simultaneous solution of Eq. (1.51) and Eq. (1.50) determines the point at which the critical flux line leaves the equipotential profile and therefore the extreme point of the pole piece. Graphical solution shows that the pole piece should start at an angle of about 14°E. The pole piece profile obtained by this method is then shown in fig. 6.21.

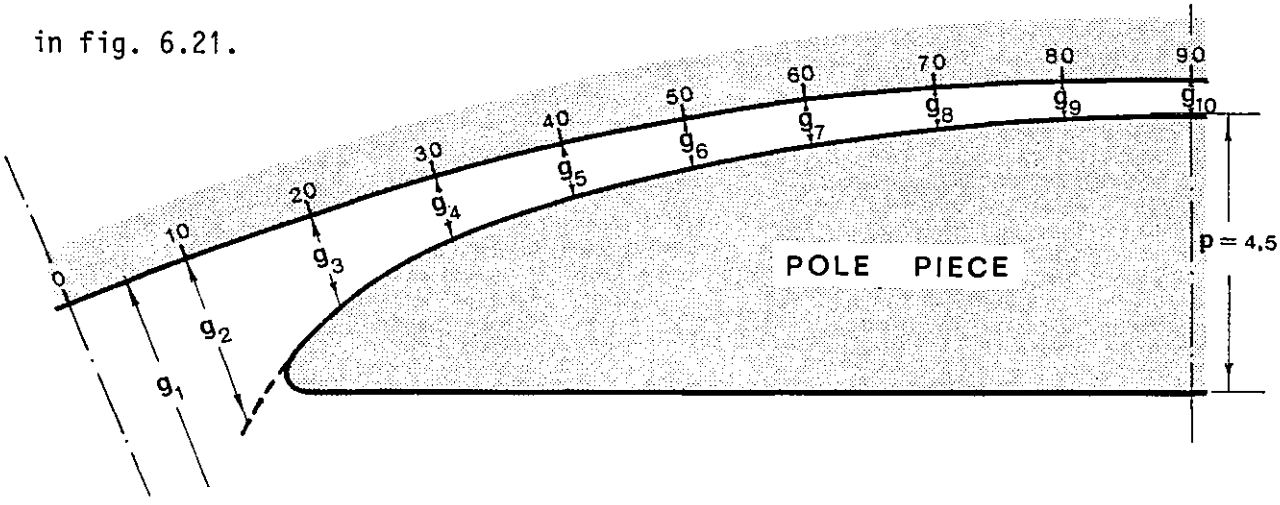

Fig. 6.21 - Pole piece profile

Blocks of Alcomax 3 magnetised in the radial direction are used with the same axial length ℓ = 30 mm of the machine, as shown in fig. 6.22. If the magnets are designed using Eq. (2.15) for the minimum volume of material,

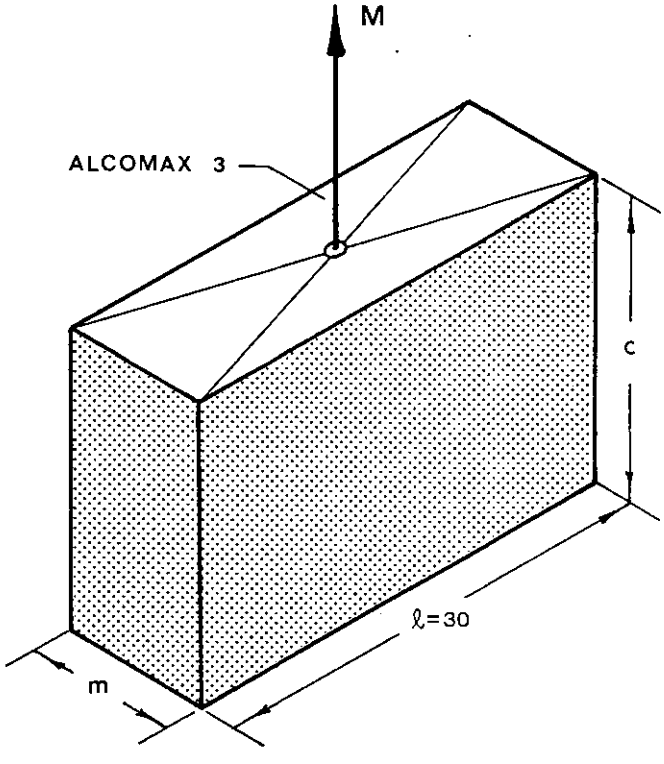

Fig. 6.22 - Dimensions of the Alcomax 3 block

the c/m ratio results of about 0.4. This gives short and fat magnets which is undesirable for metallic magnets. Magnet length c is limited by the stator inside radius R_g and pole piece thickness p. Magnet width m is limited by the pole piece arc and leakage flux between consequent poles. Then it was decided to use magnets with c = 20 mm and m = 10 mm, which gives a ratio c/m = 2 typical for this material. The final arrangement of part of the rotor is shown in fig. 6.23.

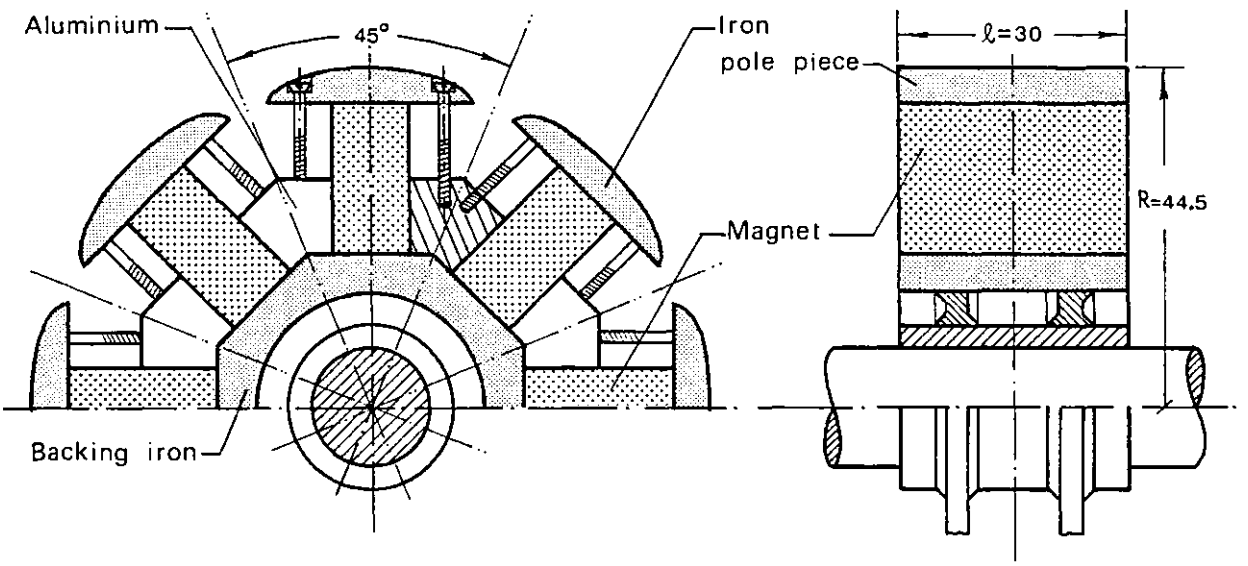

Fig. 6.23 - Eight pole Alcomax 3 rotor arrangement

Taking into account the inertia of pole pieces, magnets, aluminium slugs and backing iron, the total moment of rotor inertia, excluding shaft connections, was calculated as $J = 0.715 \times 10^{-3}$ kg.m^2.

6.6.2 - Air gap flux density

The flux $B_m A_m$ across the magnet of cross section $A_m = m\ell$ is related with the air gap flux per pole ϕ_g by the equation

$$B_m m\ell = K_1 \phi_g \qquad (6.32)$$

where K_1 is the leakage factor. The magnet m.m.f. $H_m c$ is also related to the air gap flux by the equation

$$H_m c = - K_2 \frac{\phi_g}{P_g} \tag{6.33}$$

where $K_2 = 1.05$ and P_g is the air gap permeance. Combination of Eq. (6.32) and Eq. (6.33) gives

$$\frac{B_m}{H_m} = - \frac{K_1}{K_2} P_g \frac{c}{m\ell} \tag{6.34}$$

For the pole profile used, the air gap permeance is given by Eq. (1.52), which substituted into Eq. (6.34) gives:

$$\frac{B_m}{H_m} = - 4\mu_o \frac{K_1}{K_2} \frac{c}{m} \left(\frac{r_c}{R_g}\right)^{\frac{n_p}{2}} \cdot \frac{1}{1 - \left(\frac{r_c}{R_g}\right)^{n_p}} \tag{6.35}$$

After substitution of values into Eq. (6.35):

$$\frac{B_m}{H_m} = - 80\ K_1 \mu_o \tag{6.36}$$

In order to evaluate the operating point on the permanent magnet demagnetisation characteristic, the rotor leakage factor K_1 should be calculated. Relevant calculations are described in Appendix H, resulting in a leakage factor $K_1 = 1.14$. From Eq. (6.36) the machine unit permeance is $B_m/H_m = - 91.52\,\mu_o$. In fig. 6.24 the unit permeance load-line is shown intersecting the Alcomax 3 demagnetisation characteristic at the point P of coordinates $B_m = 1.22$ T and $H_m = 11$ kA/m. Hence, from Eq. (6.32) the air gap flux becomes

$$\phi_g = \frac{B_m m\ell}{K_1} = 0.321 \times 10^{-3} \text{ Wb} \tag{6.37}$$

Since the design of the pole piece profile gives a sinusoidal flux density distribution, then the peak air gap flux density is:

$$\hat{B} = \frac{\pi}{2} \frac{\phi_g}{\tau \ell} = \frac{n_p \phi_g}{2 D_g \ell} = 0.48 \text{ T} \tag{6.38}$$

Based on these results a free-hand field map was drawn and is shown in fig. 6.25.

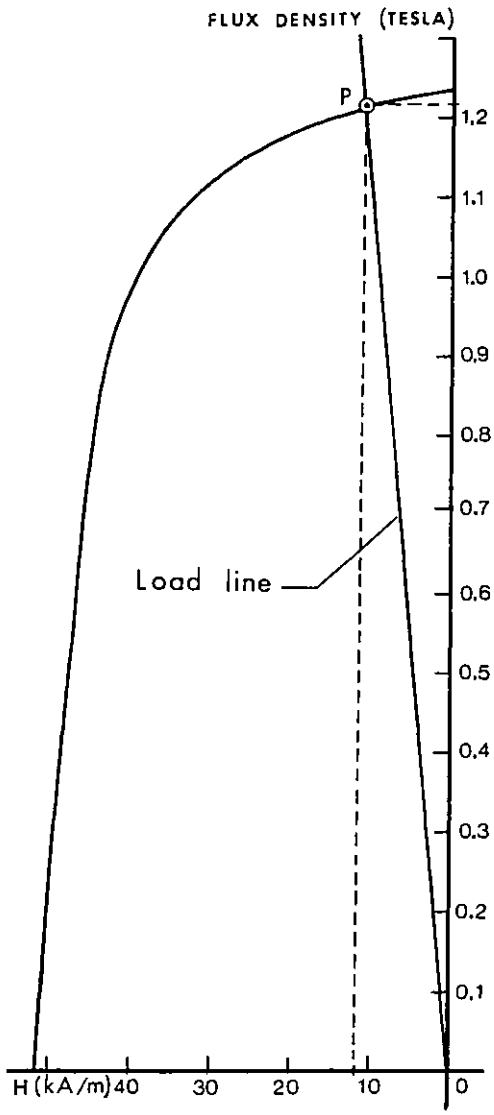

Fig. 6.24 - Working point for Alcomax 3 rotor

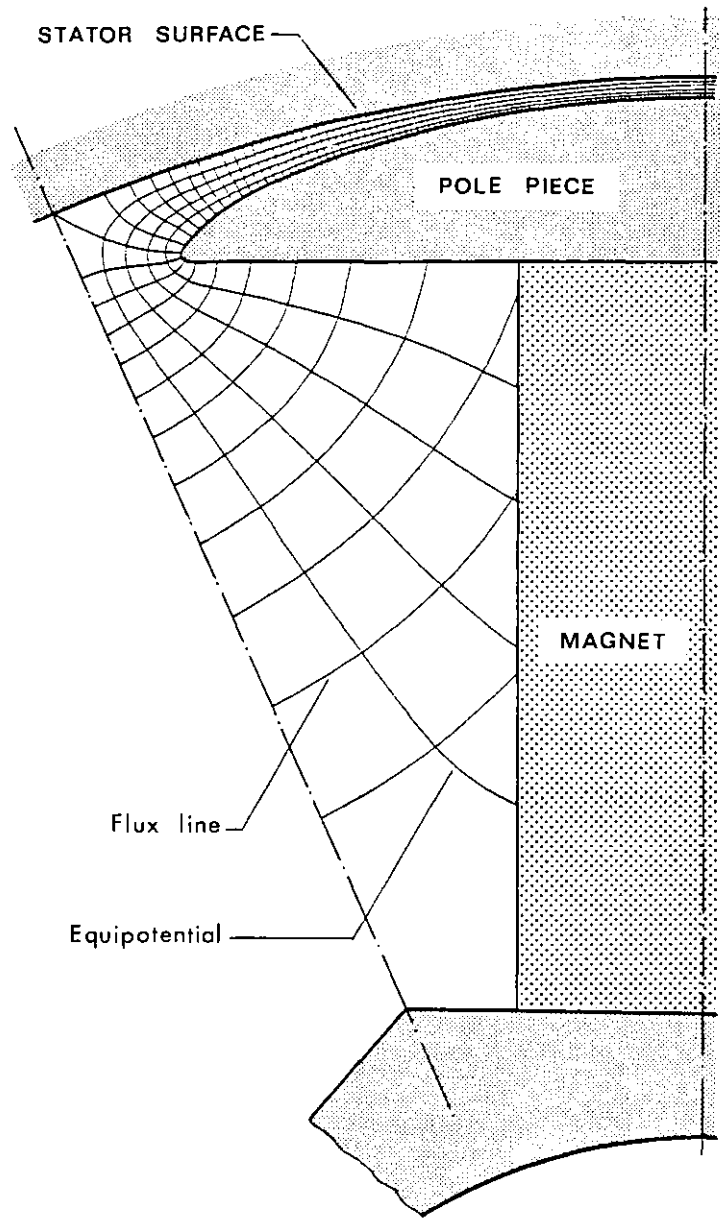

Fig. 6.25 - Alcomax 3 rotor flux plot

6.6.3 - Stator design

Considering the same total number Q of 32 slots as used in brushless coil excited disc machine, the stator winding results in $q = Q/m n_p$ = 2 coils/pole/phase. Hence, with a double-layer winding there are 4 slots/pole as shown in fig. 6.26. The outer and inner stator diameters were already fixed, and therefore the slot pitch on the stator surface is:

$$w = \frac{\pi D_g}{4 n_p} = 8.83 \text{ mm} \qquad (6.39)$$

Note that there is no need to limit the stator current unduly on account of magnet demagnetisation risks, because the presence of soft iron pieces on the rotor pole tops acts as ample protection. Hence, the stator is designed taking account of saturation limits. From Eq. (1.59), the stator backing iron width is

$$b = \frac{\pi D_g}{6n_p} = 5.89 \text{ mm} \tag{6.40}$$

and therefore the slot depth

$$h = \frac{1}{2}(D_o - D_g) - b = 9.11 \text{ mm}$$

Assuming parallel teeth, the slot dimensions may now be evaluated by calculating the tooth flux. As already shown in section 1.15, for current feeding at 90°E torque angle with peak current in one phase, tooth 2 carries the highest flux density and its value is given by Eq. (1.136).

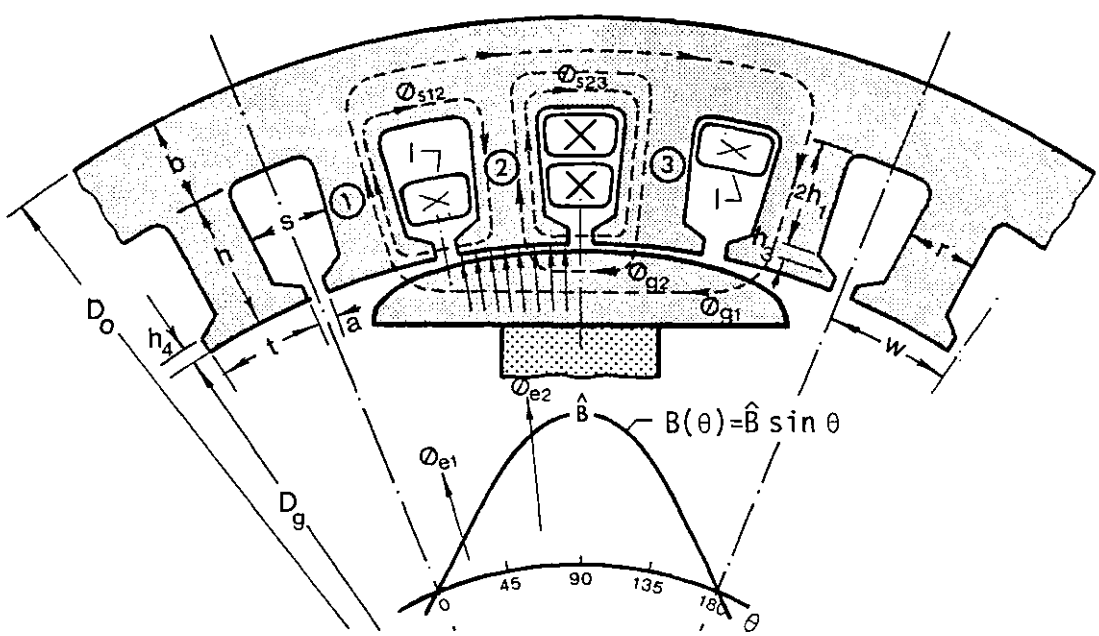

Fig. 6.26 - Alcomax 3 machine stator lamination

Assuming that the stator coil has a cross section of $h_1 s$ carrying the peak current density $\hat{J}_s$, $\hat{I} = \hat{J}_s h_1 s$. Since $s \simeq w - r$ the flux density through tooth 2 becomes:

$$B_2 = \frac{\mu_o}{r}\left[\frac{2h_3}{a+w-r} + \frac{h_4}{a} + \frac{w-a}{g_{av2}}\right]\sqrt{2}\ J_{rms} h_1 (w-r) + 0.88\,\frac{w}{r}\,\hat{B} \tag{6.41}$$

According to fig. 6.21 and table 6.1 and using Simpson's rule the average gap under tooth 2 is

$$g_{av2} = \frac{1}{2x6}\left[g_5 + 4(g_6 + g_8) + 2g_7 + g_9\right] = 0.56 \text{ mm}$$

and under tooth 1

$$g_{av1} = \frac{1}{2x6}\left[g_1 + 5(g_2 + g_3) + g_4\right] = 1.31 \text{ mm}$$

Taking as typical values $h_4 = 0.8$ mm and $h_3 = 1.31$ mm, from fig. 6.26 becomes:

$$h_1 = \frac{1}{2}\left[h - (h_3 + h_4)\right] = 3.5 \text{ mm} \qquad (6.42)$$

Assuming for maximum current density $J_{rms} = 5$ A/mm^2 (ventilated machine) the slot opening may be taken as a = 1.5 mm. Hence, for a rotor excitation flux density $\hat{B} = 0.48$ T, Eq. (6.41) may be written as a function of r (in mm) as:

$$B_2 = \frac{1}{r}\left[(4.27 - 0.41r)\frac{8.33 - r}{10.33 - r} + 3.73\right] \text{ T} \qquad (6.43)$$

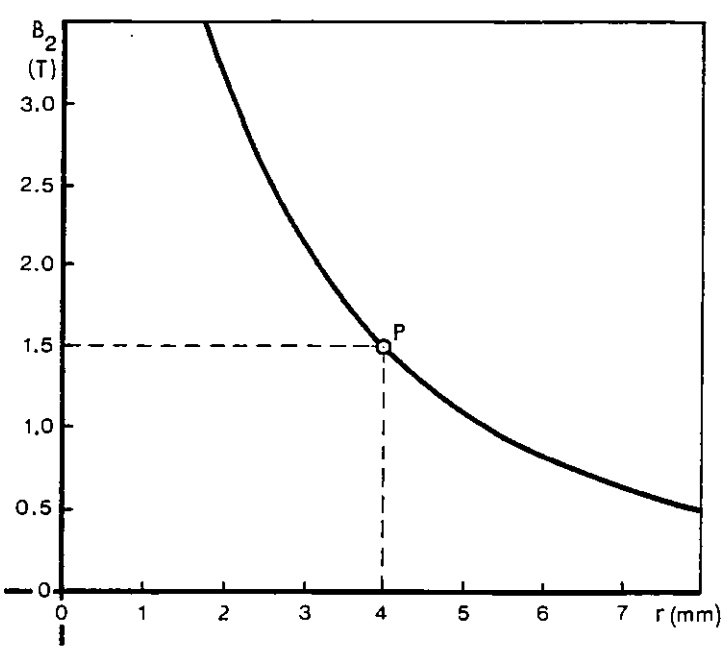

Fig. 6.27 - Flux density in tooth 2 versus root tooth width

Eq. (6.43) is plotted versus root tooth width r in fig. 6.27. From this diagram taking as saturation limit $B_2 = 1.5$ T a tooth root width r = 4 mm

results as the minimum acceptable value. Hence, for this machine a slot width to tooth width ratio becomes

$$\frac{s}{r} \simeq \frac{w - r}{r} = 1.21$$

which is typical for permanent magnet machines using metallic magnets.

6.6.4 - Specific torque per inertia

For sinusoidal operation with 90°E torque angle the stator m.m.f. per pole per phase is:

$$N \hat{I}_1 = 2q\sqrt{2}\, J_{rms}\, s\, h_1 \tag{6.44}$$

and therefore from Eq. (1.46) the specific torque becomes:

$$\frac{T_1}{J_{rms}} = T_u = 2\sqrt{2}\, n_p\, R_g\, \ell q\, s h_1 \hat{B}\, K_{w1} \tag{6.45}$$

Since the winding arrangement used is similar to that of the actuator described in Chapter 4, the fundamental winding factor may be taken as $K_{w1} = 0.832$. Hence, substitution of values into Eq. (6.45) gives:

$$T_u = 0.41\ Nm/A_{rms}\ mm^{-2} \tag{6.46}$$

Since the rotor inertia is $J = 0.715 \times 10^{-3}\ kg.m^2$, the specific torque per inertia is:

$$\frac{T_u}{J} = 0.57 \times 10^3\ rad/s^2 \tag{6.47}$$

Comparison of this figure with the results displayed in fig. 6.15 for permanent magnet excited disc machines, it may be concluded that this motor has less torque per inertia than a brush-fed disc machine of similar size when small gaps are used. However, it is better than most rotating field, brushless disc machines, though of the same order when $SmCo_5$ is used on those with thicker windings. Nevertheless, in terms of specific torque the present design offers much better performance than the equivalent Alcomax 3 disc machines as can be seen from fig. 6.9 and fig. 6.14. Hence the drum machine designed is certainly the better "torquemotor".

6.6.5 - Axis main-inductances

With the winding arrangement used, the air gap inductance per pole for a rotor position θ is given by Eq. (1.116).

Hence, for the q-axis inductance, since $\phi_{12} = \phi_{1'2'}$, the relevant equation becomes

$$L_q = \frac{n^2}{I} 2(\phi_{12} + \phi_{21'}) \tag{6.48}$$

where, according to fig. 1.35,

$$\phi_{12} = I P_2 \quad \text{and} \quad \phi_{21'} = 2 I 2 P_1 \tag{6.49}$$

Since the stator circumferential tooth length is t = w-a = 7.33 mm, the permeances between each tooth and pole piece are given by:

$$P_2 = \mu_o \frac{t\ell}{g_{av2}} = 0.39\mu_o \text{ H} \quad \text{and} \quad P_1 = \mu_o \frac{t\ell}{g_{av1}} = 0.17\mu_o \text{ H} \tag{6.50}$$

Substitution of Eqs. (6.50) and Eqs. (6.49) into Eq. (6.48) results for the q-axis inductance per pole

$$L_q = n^2 2.14\mu_o \text{ H}$$

and therefore the total q-axis air gap inductance per phase

$$L_q = n_p n^2 2.14\mu_o = n^2 17.12\mu_o \text{ H/phase} \tag{6.51}$$

For the d-axis inductance, since $\phi_{12} = \phi_{1'2'}$, Eq. (1.116) also reduces to

$$L_d = \frac{n^2}{I} 2 (\phi_{12} + \phi_{21'}) \tag{6.52}$$

but now

$$\phi_{12} = I P_1' \quad \text{and} \quad \phi_{21'} = 2 I P_t$$

where by measuring $P_1' \simeq 0.045\mu_o$ H and

$$P_t = \frac{2P_2P_{pp}}{2P_2+P_{pp}} \tag{6.53}$$

In Eq. (6.53), P_{pp} denotes the permeance below the pole piece given by the sum of rotor leakage permeance and magnet permeance as:

$$P_{pp} = P_{leak} + P_{mag} \tag{6.54}$$

The rotor leakage permeance was already calculated in Appendix H as $P_{leak} = 0.181\mu_o$ H. Using the manufacturer's figure of $\mu_r = 3.1$ for the relative recoil permeability of Alcomax 3, the permeance of the magnet may be found as

$$P_{mag} = \mu_r \mu_o \frac{m\ell}{c} = 0.046\mu_o \text{ H}$$

and so the total permeance of the region below the pole piece given by Eq. (6.54) may be taken as $P_{pp} = 0.23\mu_o$ H. Therefore, Eq. (6.53) gives $P_t = 0.18\mu_o$ H. The total d-axis air gap inductance may be then expressed as:

$$L_d = n_p n^2 2(P_1' + 2P_t) = n^2 6.48\mu_o \text{ H/phase} \tag{6.55}$$

Comparison of Eq. (6.51) and Eq. (6.55) shows that $L_q > L_d$ resulting in a saliency factor $\alpha = 2.64$. As explained in section 1.14.1.b this result is typical of permanent magnet excited machines.

6.6.6 - Torque versus torque angle characteristics

The torque expression for a m-phase n_p pole motor when current-fed at θ torque angle is, according to Eq. (3.60), given by

$$T = \frac{m n_p}{2\omega} E i \sin\theta + \frac{1}{2}\frac{m n_p}{2} i^2 (L_d - L_q)\sin 2\theta$$

where i is the current carrying conductor. For a two phase machine (m = 2), this equation reduces to

$$T = T_1 \sin\theta + \frac{1}{2} n_p i^2 (L_d - L_q)\sin 2\theta \tag{6.56}$$

where T_1 is the fundamental excitation torque given by Eq. (1.46). For this machine, from Eq. (6.46) is $T_1 = 0.41\ J_{rms}$. Substitution of Eq. (6.51)

and Eq. (6.55) into Eq. (6.56) and noting that $n^2i^2 = J_{rms}^2 (sh_1)^2$ gives:

$$T = 0.41\ J_{rms} \sin\theta - 0.015\ J_{rms}^2 \sin 2\theta \text{ Nm} \qquad (6.57)$$

where J_{rms} is the r.m.s. stator current density in A/mm^2.

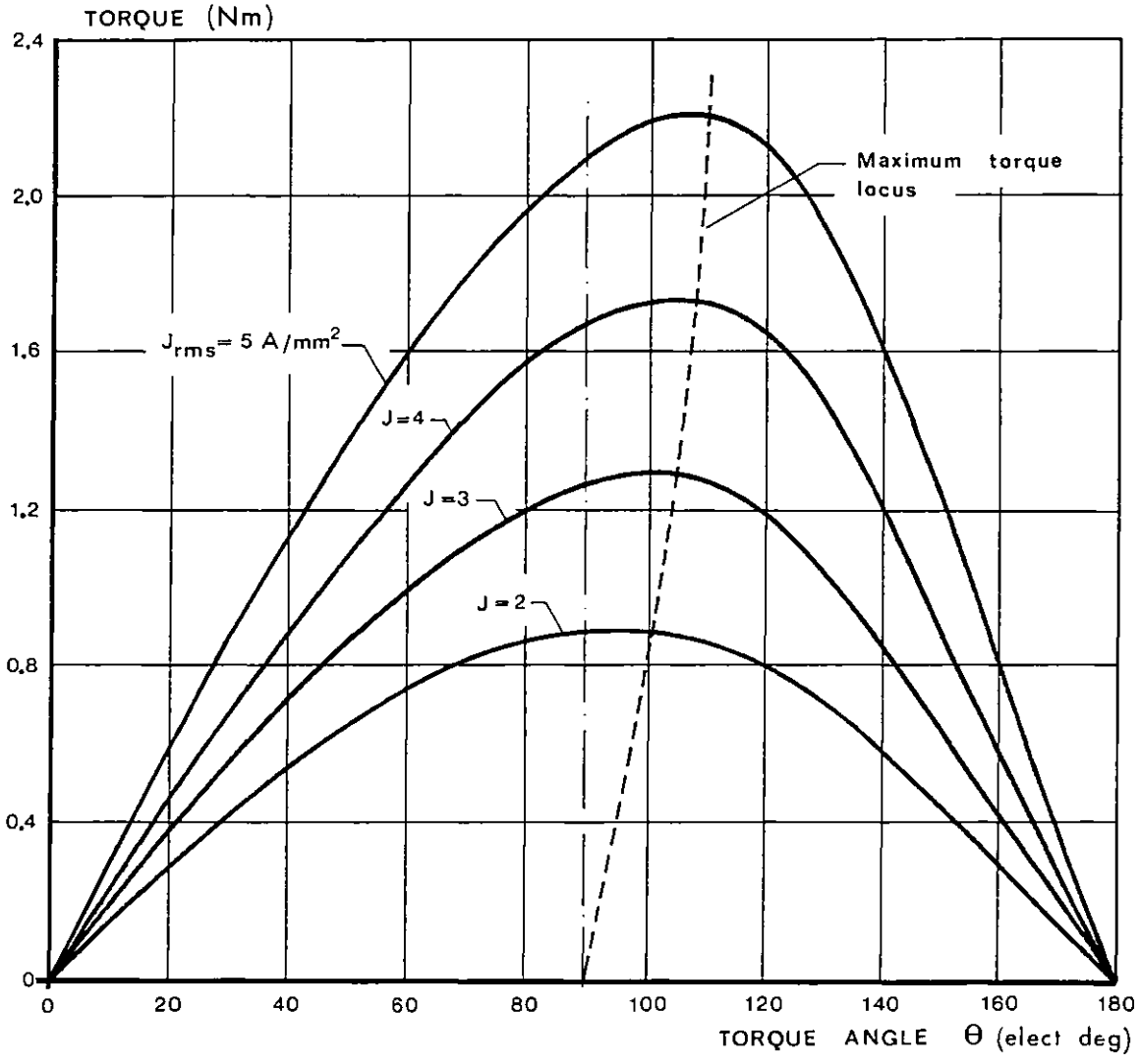

Fig. 6.28 - Torque versus torque angle characteristics for Alcomax 3 rotor

Fig. 6.28 shows plots of Eq. (6.57) versus torque angle for several levels of stator current density. Since for this machine the saliency factor is $\alpha > 1$, the characteristics show that the peak torque is attainable for a torque angle greater than 90°E.

6.7 - RARE-EARTH PERMANENT MAGNET EXCITED DRUM MOTOR

The design of a permanent magnet drum machine using the same outer and inner stator diameters as the Alcomax 3 machine is now presented. Again, the same ratio $D_g/\ell = 3$ is assumed, but to provide rotor excitation $SmCo_5$ magnets are used.

6.7.1 - Rotor design

Soft iron pole piece protection against stator m.m.f.'s are not of course required when $SmCo_5$ is used in a permanent magnet machine. This is due to the high coercive force of the material, which automatically prevents magnet demagnetisation. Also, for the same reason, this material needs small lengths in the magnetised direction when compared with metallic magnets in order to produce the same amount of flux. The volume of the permanent magnet material used in the present design is approximately 1/3 of that used in the Alcomax 3 design, and is in rough inverse proportional with the materials' $(BH)_{max}$ figures (see fig. 2.8).

Although for a sinusoidal air gap flux density distribution a magnet profile given by Eq. (1.50) must be used, as seen for the actuator and Alcomax 3 rotors, a constant air gap profile design was decided for simplicity. Allowing a pole arc α_a to pole pitch $2\pi/n_p$ ratio $\sigma = 0.75$ in order to keep the interpolar flux leakage on a reasonable level and an air gap length $g = 1.0$ mm, the inner magnet radius R_1 must satisfy the equation

$$\frac{1}{2}\,\sigma\,\frac{2\pi}{n_p}\,\ell\left[(R_g - g)^2 - R_1^2\right] = \frac{1}{3}m\ell c \tag{6.58}$$

from where $R_1 = 41.35$ mm. Hence magnet length $\ell_m = R_g - g - R_1 = 2.65$ mm.

For an average air gap flux density B_g and a rotor backing iron peak flux density $\hat{B}_c$, by flux continuity considerations the rotor backing iron thickness $R_1 - R_o$ should be:

$$R_1 - R_o = \frac{\pi D_g}{2n_p}\,\frac{B_g}{\hat{B}_c} \tag{6.59}$$

Taking as typical values B_g = 0.5 T and $\hat{B}_c$ = 1.6 T, Eq. (6.59) gives $R_1 - R_o$ = 5.52 mm or R_o = 35.83 mm.

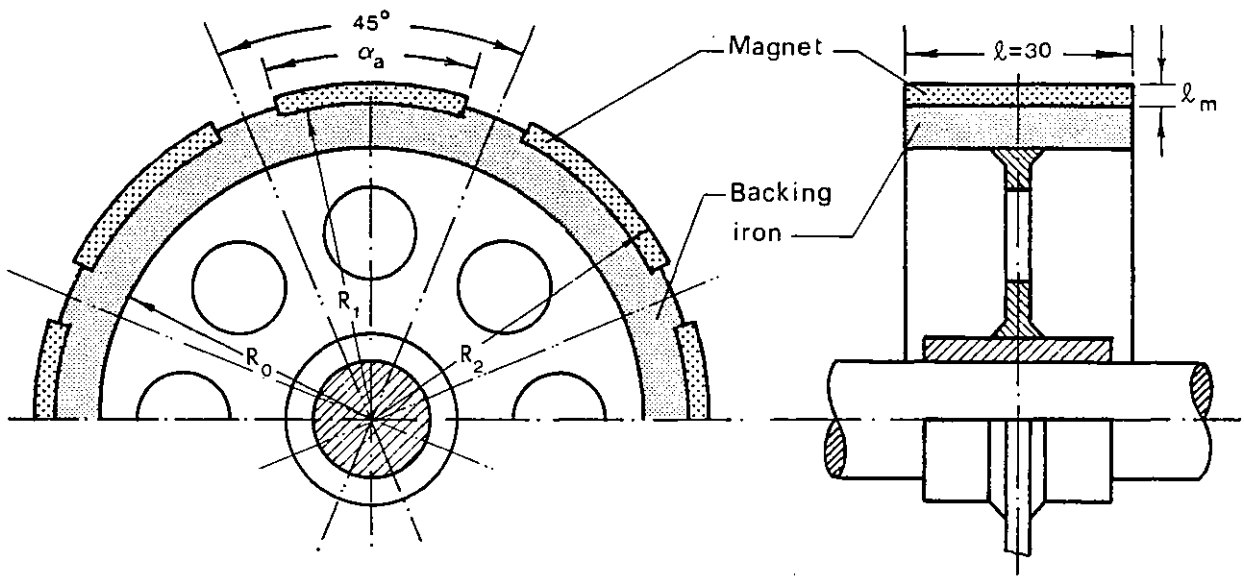

Fig. 6.29 - Eight pole $SmCo_5$ rotor arrangement

A diagram of part of the rotor is shown in fig. 6.29. With the dimensions shown and the materials used, the moment of inertia was calculated as J = 0.605 x 10^{-3} kg.m^2, which is 15% less than the Alcomax 3 rotor inertia.

6.7.2 - Air gap flux density distribution

With the rotor geometry described, six leakage flux paths and two useful paths may be considered as shown in fig. 6.30. The leakage factor K_1 was calculated using the same basic method as with the Alcomax 3 rotor described in Appendix H, but the present problem is simplified by the absence of iron pole pieces. Calculations gave a leakage factor of K_1 = 1.079 showing that the flux leakage per pole in this machine is less than 8% of the total flux set up by one magnet. Hence, the end leakage paths may be neglected compared with the main path flux.

As explained in section 2.8.2, the flux density distribution may be then found by using a simplified mesh suitable for manual solution, which takes account of the interpolar flux leakage but not the end leakage flux.

In fig. 6.31 is illustrated half of the pole pitch and the region subdivided in such a way as to obtain four nodes. The diagram shows all the necessary parameters in order to evaluate the node magnetic potentials Ω.

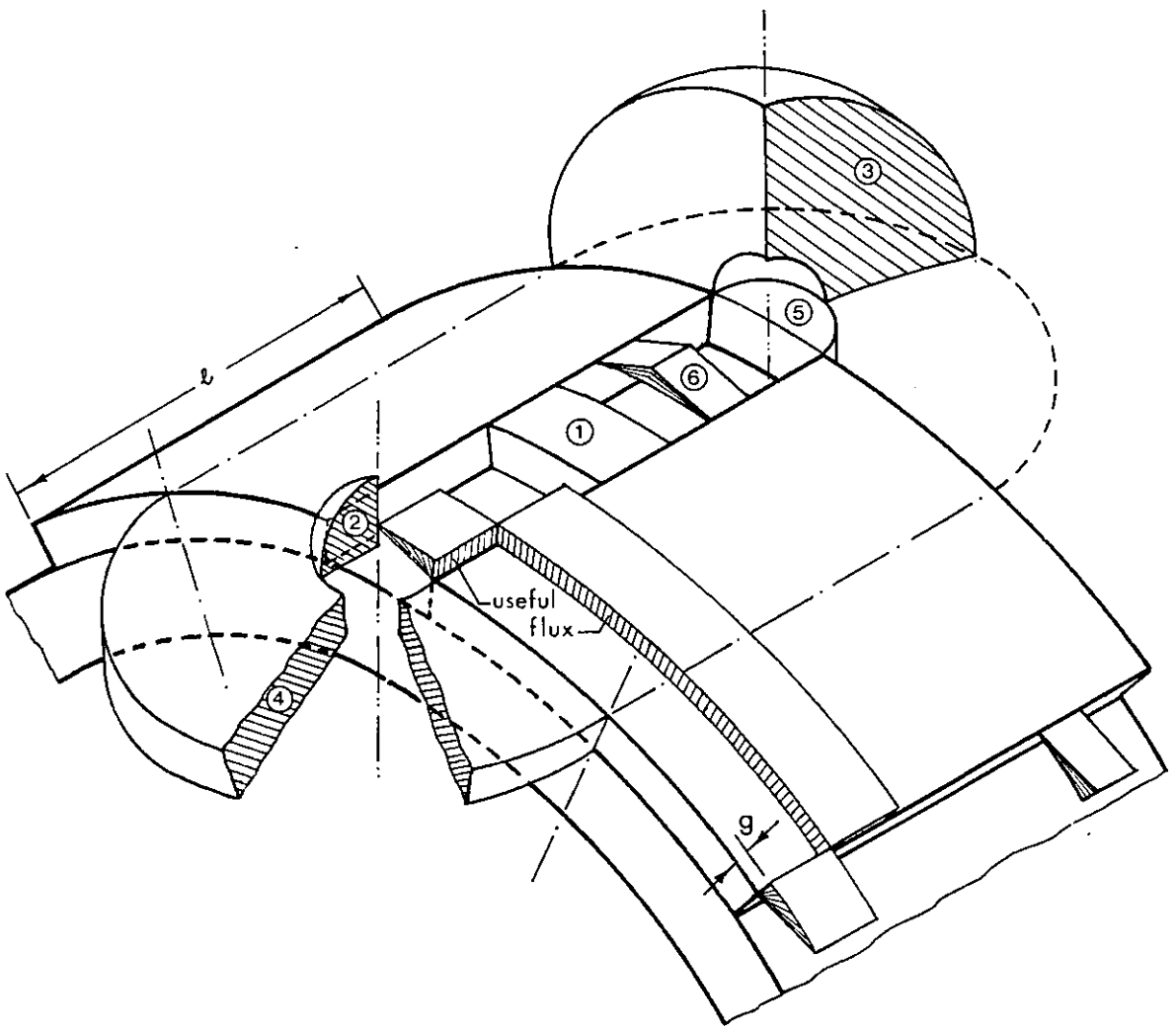

Fig. 6.30 - Leakage flux paths for $SmCo_5$ rotor

The equivalent circuit was already shown in fig. 2.53 and the corresponding matrix form for solution of Ω values is given by Eq. (2.88). Using the parameters displayed in fig. 6.31 and taking for the relative magnet permeability $\mu_r = 1.1$ and for the magnetisation M = 0.8 T, solution of Eq. (2.88) gave for the magnetic potential at each node the following results:

$$\Omega_1 = 187.21 \text{ A}, \quad \Omega_2 = 157.94 \text{ A}, \quad \Omega_3 = 412.49 \text{ A}, \quad \Omega_4 = 140.33 \text{ A}$$

The air gap flux density at nodes 1 and 3 level is therefore

$$B_1 = \mu_o H_{10} = \mu_o \frac{\Omega_1}{g} = \mu_o \frac{187.21}{1x10^{-3}} = 0.27 \text{ T} \qquad (6.60)$$

and

$$B_3 = \mu_o H_{30} = \mu_o \frac{\Omega_3}{g} = \mu_o \frac{412.49}{1x10^{-3}} = 0.51 \text{ T} \qquad (6.61)$$

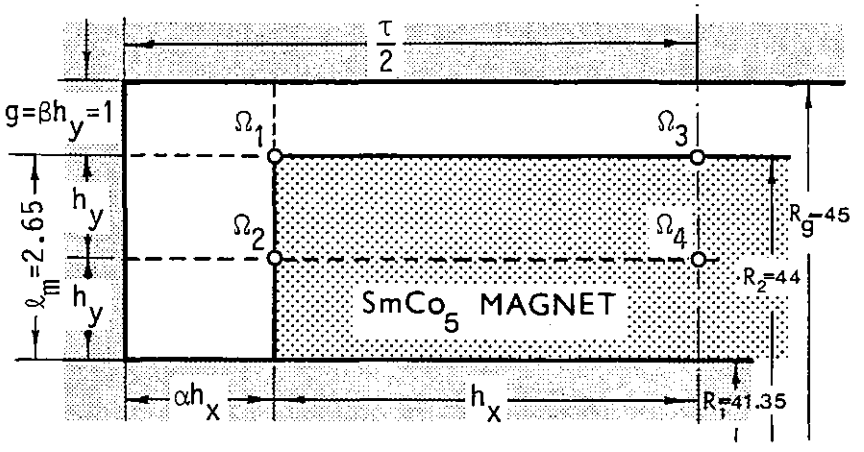

$$\alpha = \frac{1-\sigma}{\sigma} = 0.33$$

$$h_x = \sigma \frac{\pi R_2}{n_p} = 12.95 \text{ mm}$$

$$h_y = \frac{\ell_m}{2} = 1.33 \text{ mm}$$

$$\beta = \frac{g}{h_y} = 0.75$$

$$k = \frac{h_y}{h_x} = 0.10$$

Fig. 6.31 - Mesh arrangement fo $SmCo_5$ rotor

Assuming linear variation between nodes the air gap flux density distribution is shown in fig. 6.32. Fourier analysis of this curve using the

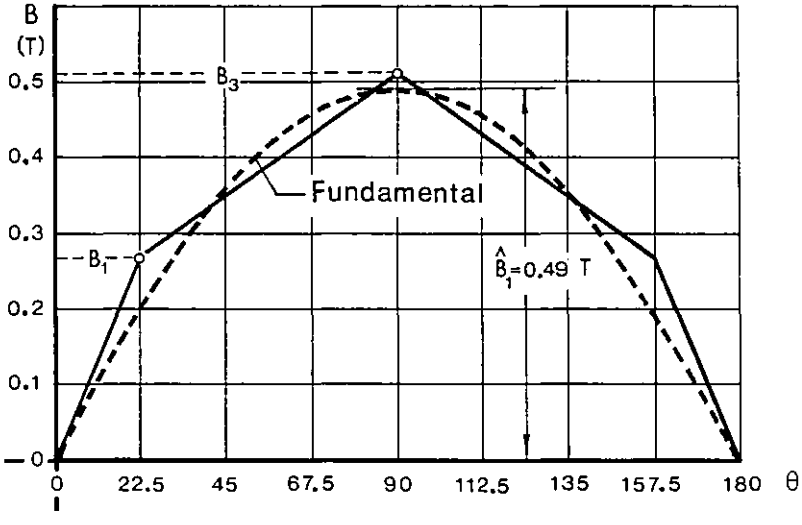

Fig. 6.32 - Air gap flux density distribution

results (6.60) and (6.61), the fundamental peak flux density was evaluated as $\hat{B}_1 = 0.49$ T, which is the same order as that found for the Alcomax 3 rotor in spite of the double gap length used in the former case.

6.7.3 - Stator design

Again the stator was designed with 4 slots per pole resulting in a slot pitch w = r + s = 8.83 mm at stator surface. However in this case due to the low permeability of the magnet the magnetic circuit is far from saturation and consequently the tooth root r can be substantially reduced, enabling wider slots and more copper to be used, as shown in fig. 6.33.

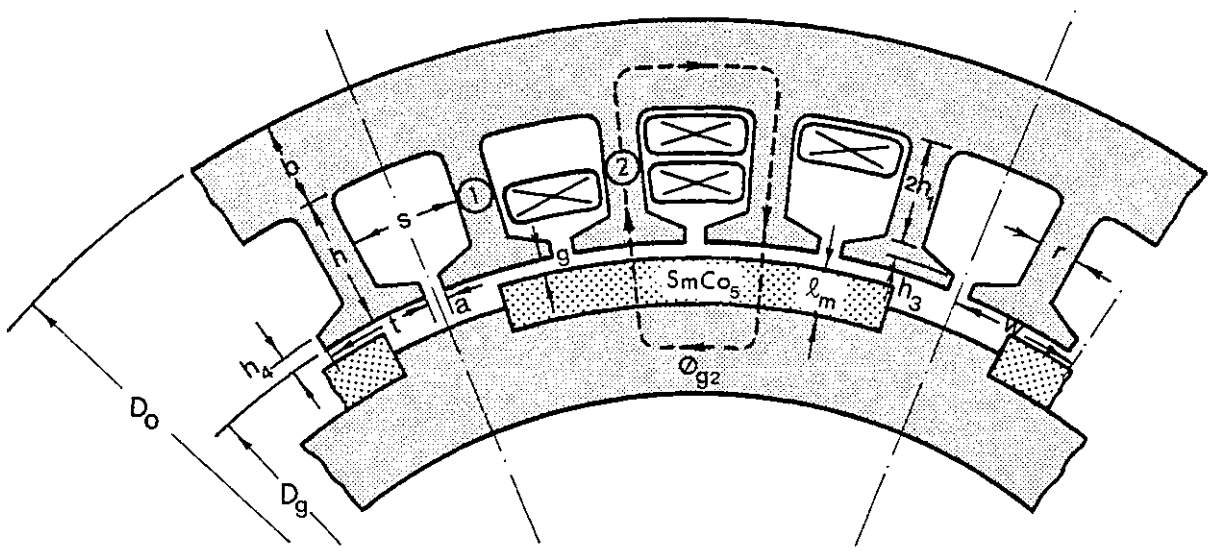

Fig. 6.33 - $SmCo_5$ machine stator lamination

For current-fed operation at 90°E torque angle with peak current in one phase, the flux density set up by the stator through tooth 2 is given by Eq. (6.41), where now $g_{av2} \simeq g + \ell_m = 3.65$ mm. Assuming the stator lamination dimensions a, b, h, h_1, h_3 and h_4 with the same values as used for Alcomax 3 machine, for an excitation peak flux density $\hat{B}_1 = 0.49$ T and stator current density $J_{rms} = 5$ A/mm^2, Eq. (6.41) becomes

$$B_2 = \frac{1}{r}\left[(0.89 - 0.08r)\,\frac{8.83 - r}{10.33 - r} + 3.81\right] \qquad (6.62)$$

where r is the tooth root in mm. Solution of Eq. (6.62) for $B_2 = 1.5$ T gives r = 2.75 mm. Hence for this machine the slot width to tooth width ratio is:

$$\frac{s}{r} \simeq \frac{w - r}{r} = 2.21$$

which is about twice that of the figure used with the Alcomax 3 rotor. The maximum peak current to avoid saturation is therefore

$$\hat{I} = \sqrt{2}\, J_{rms}\, h_1 s = 150 \text{ A}$$

It is important to check if the magnet is safe of demagnetisation for this value of stator current. Since for the magnet layout shown in fig. 6.31 is

$$\frac{m}{\ell_m} = \frac{2h_x}{\ell_m} = 9.77 \quad \text{and} \quad \frac{g}{\ell_m} = 0.38$$

from the diagram of fig. 2.58, $\frac{\hat{I}}{\ell_m} = 350$ kA/m. The maximum permissible current to avoid demagnetisation is thus

$$\hat{I} = 350\, \ell_m = 972 \text{ A}$$

which is about six times the current limit to avoid magnet circuit saturation. This shows that the slot depth could be substantially increased, increasing of course the outer stator diameter and the tooth root. This type of stator design is typically used with rare-earth magnets, as seen in Chapter 4.

6.7.4 - Specific torque per inertia

For this machine when operated at 90°E torque angle the specific fundamental torque is given by Eq. (6.45). After substitution of values,

$$\frac{T_1}{J_{rms}} = T_u = 0.53 \text{ Nm/A mm}^{-2} \qquad (6.63)$$

which is about 30% greater than the torque obtained with Alcomax 3 rotor. Hence, specific torque per inertia

$$\frac{T_u}{J} = \frac{0.53}{0.605} \times 10^3 = 0.88 \times 10^3 \text{ rad/s}^2$$

This is perhaps the best machine in terms of torque. In terms of torque

per inertia this is comparable to the brushless disc machine when $SmCo_5$ is used, as can be seen from fig. 6.15.

6.7.5 - Axis main-inductances

Due to the constant and long effective air gap, the permeances under each tooth are all equal and approximately given by:

$$P_1 = P_2 = \mu_r \mu_o \frac{t\ell}{g_{av}} = 1.1\mu_o \frac{8.83-1.5}{3.65} 30 \times 10^{-3} = 0.066\mu_o \text{ H}$$

Therefore, the total air gap inductance per phase is constant with rotor position and may be expressed as

$$L = n_p n^2 2(P_1 + 4P_2) = n_p n^2 10P_1$$

and substitution of values gives

$$L = L_d = L_q = n^2 5.28\mu_o \text{ H} \qquad (6.64)$$

which is much less than the inductance of the machine using the Alcomax 3 rotor, as expected.

6.7.6 - Torque versus torque angle characteristics

Since $L_d = L_q$ the machine is virtually a cylindrical one and therefore the reluctance torque may be ignored. Then Eq. (6.56) becomes:

$$T = T_1 \sin\theta = 0.53 J_{rms} \sin\theta \qquad (6.65)$$

Fig. 6.34 shows the torque versus torque angle characteristics for this motor for various levels of stator current density. They show that the

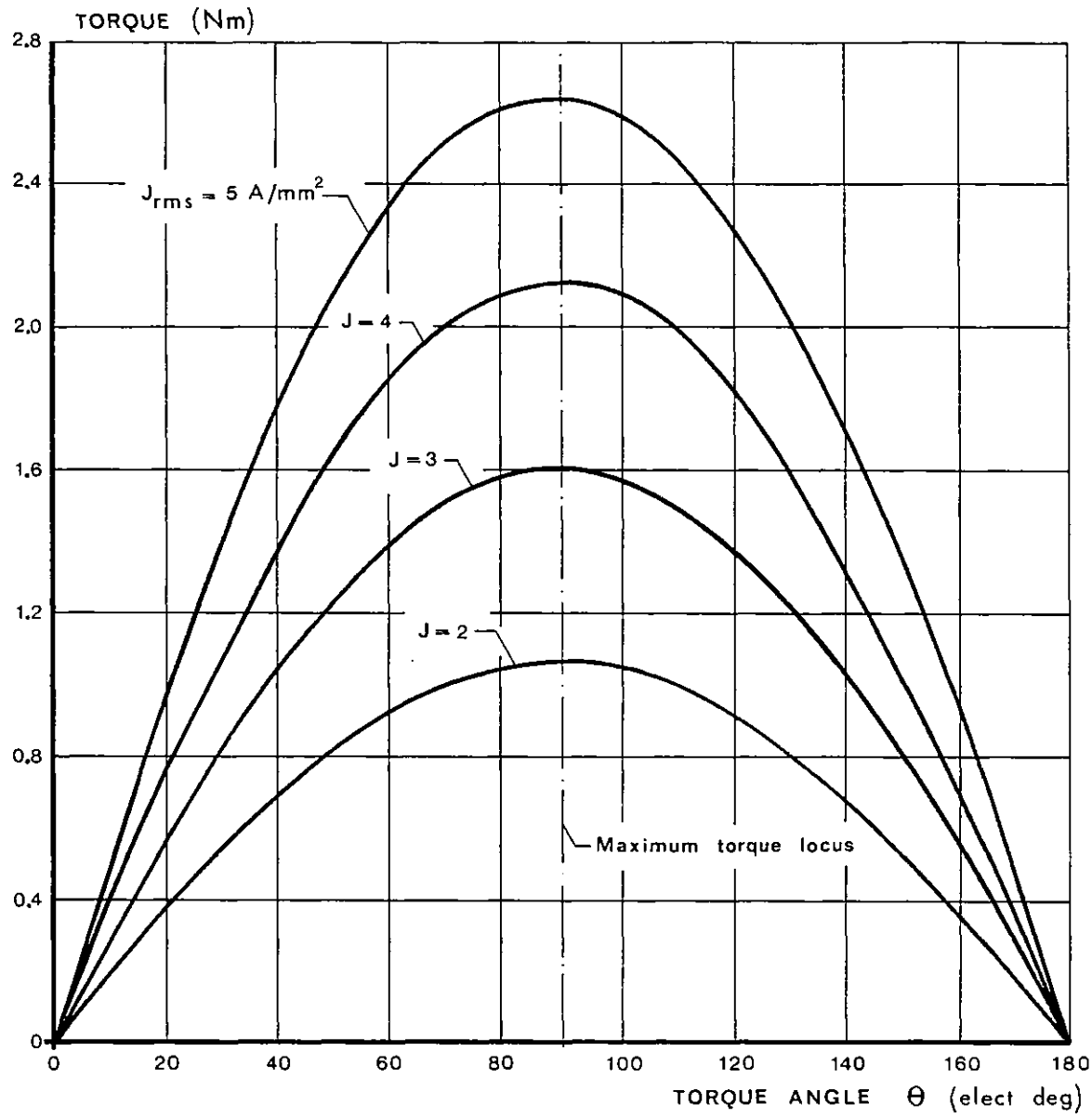

Fig. 6.34 - Torque versus torque angle characteristics for $SmCo_5$ rotor

peak torque is attainable for θ = 90°E due to the absence of reluctance torque.

6.8 - BRUSH-FED, COIL-EXCITED DRUM MOTOR

This is a conventional synchronous machine where the rotor field excitation is obtained by means of a d.c. winding fed via sliprings. The pole core is then in solid iron and in order to have a sinusoidal air gap flux density distribution the pole profile was chosen with the same design as the

Alcomax 3 rotor. Fig. 6.35 shows the pole layout with the wound coil of cross section $S_{cu} = xy$.

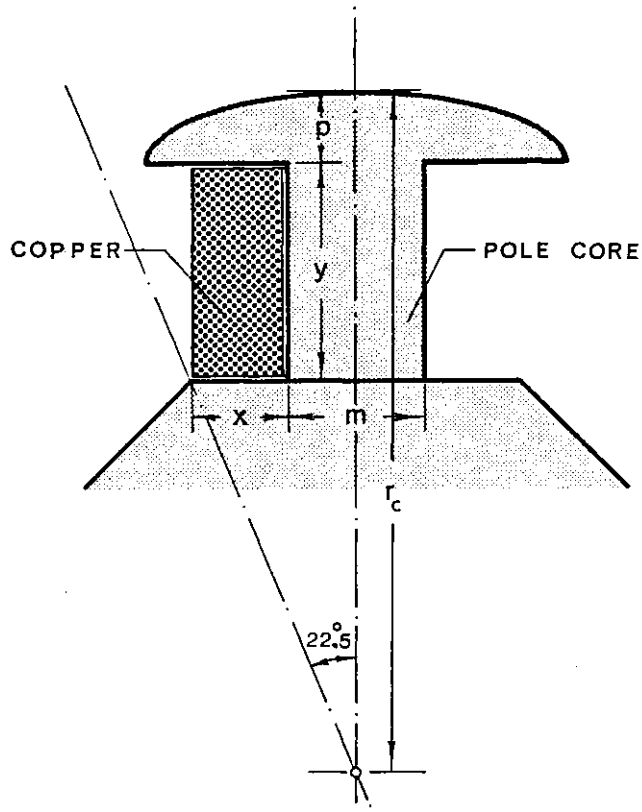

Fig. 6.35 - Pole layout

Assuming a peak air gap flux density $\hat{B}_g = 0.5$ T, by flux continuity considerations the flux density in the pole core is given by

$$B_c = K_1 \frac{2\hat{B}_g}{n_p} \frac{D_g}{m} \tag{6.66}$$

The leakage factor K_1 is a function of pole core dimensions m and y and from the diagram they are related by the equation

$$(x + \frac{m}{2}) = \left[r_c - (y + p)\right] \tan 22.5° \tag{6.67}$$

Taking m = 9 mm in Eq. (6.67) the copper cross section S_{cu} is maximised for y = 14.5 mm and x = 6.0 mm. With these dimensions, the machine leakage factor is $K_1 = 1.11$ and therefore substitution of values in Eq. (6.66) gives $B_c = 1.39$ T. Hence, the pole core is safe of saturation for the air gap

flux density level considered. In addition, the same stator laminations as Alcomax 3 machine may be used and the main dimensions are displayed in fig. 6.36.

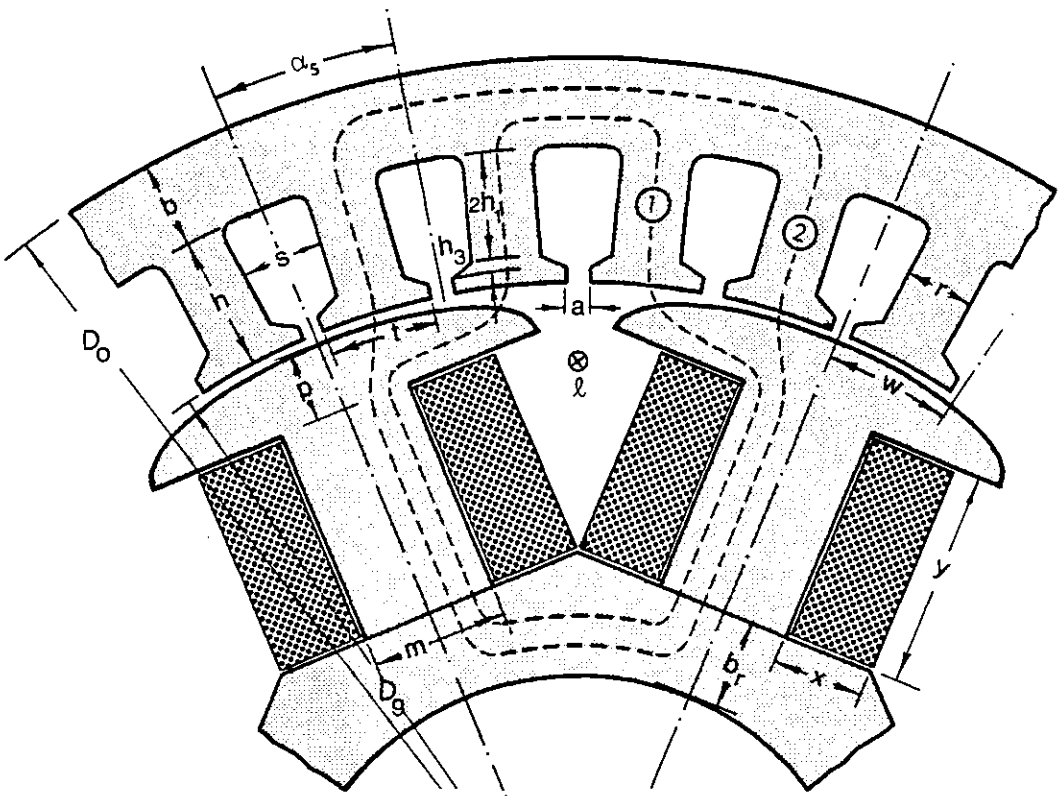

ℓ = 30.00 mm
b = 5.89 mm
h = 9.11 mm
s = 4.83 mm
r = 4.00 mm
w = 8.83 mm
a = 1.50 mm
m = 9.00 mm
x = 6.00 mm
y = 14.50 mm
b_r = 6.00 mm
p = 4.50 mm

Fig. 6.36 - Basic layout of the coil excited drum motor

Using the dimensions shown in the diagram and the specific weight of the materials used the total rotor inertia resulted in J = 0.983 x 10^{-3} kg.m^2, which is 37% greater than the Alcomax 3 rotor inertia.

6.8.1 - Magnetic characteristic

In order to evaluate the motor torque as a function of field excitation it is necessary to determine the magnetic characteristic of the machine. The method used here [111] consists of evaluating the m.m.f. drop in the various paths of the magnetic circuit and from them to find graphically the useful air gap flux ϕ_g as a function of rotor m.m.f. excitation. Three main paths - rotor, stator and leakage - are considered. If each partial characteristic is known, the total flux set up by rotor excitation ϕ_r

should satisfy the equation

$$\phi_r = \phi_s + \phi_\ell \tag{6.68}$$

where ϕ_s is the stator flux and ϕ_ℓ the total leakage flux. Using Eq. (6.68), fig. 6.37 illustrates how the useful air gap flux versus rotor m.m.f. can be obtained.

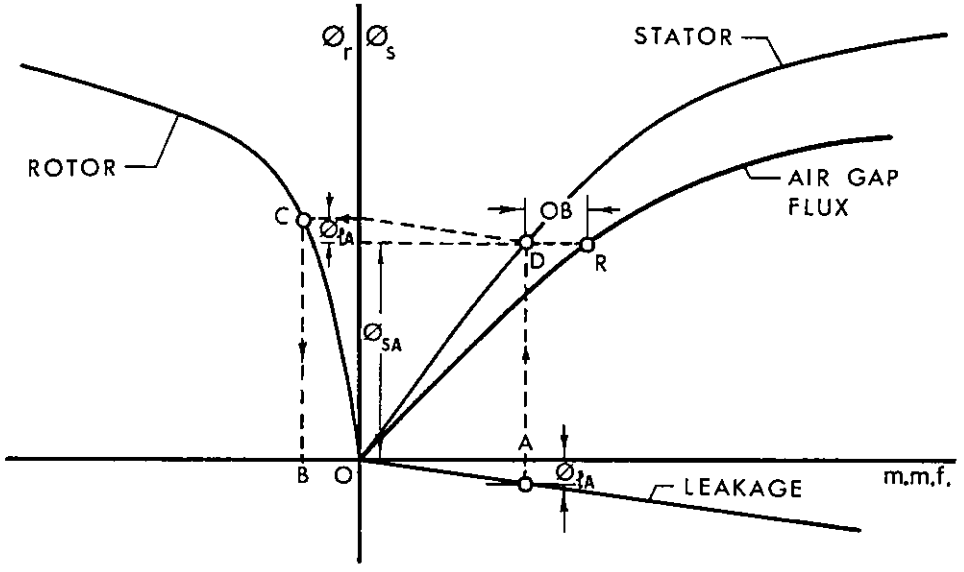

Fig. 6.37 - Graphical method for determining the air gap flux

For a given stator drop m.m.f. OA a corresponding stator flux ϕ_{sA} and a flux leakage $\phi_{\ell A}$ occurs. Adding these two fluxes, point C on the rotor characteristic is found and hence the corresponding rotor m.m.f. OB to obtain the flux CB. Adding the m.m.f. OB at D level the resulting point R on the useful characteristic is determined. Repeating the process for other points the magnetic characteristic of the machine is then evaluated.

For the sake of simplicity the iron used in the magnetic circuit of this machine is considered to have the magnetisation characteristic shown in fig. 4.4.

a) - Magnetic characteristic of the rotor

The magnetic circuit of the rotor may be considered split into three paths, as follows:

i) - Pole

Fig. 6.38 illustrates the main flux path in the pole core, and table 6.2 the magnetic characteristic $\phi = f(ni)$ for this path. Assuming uniform

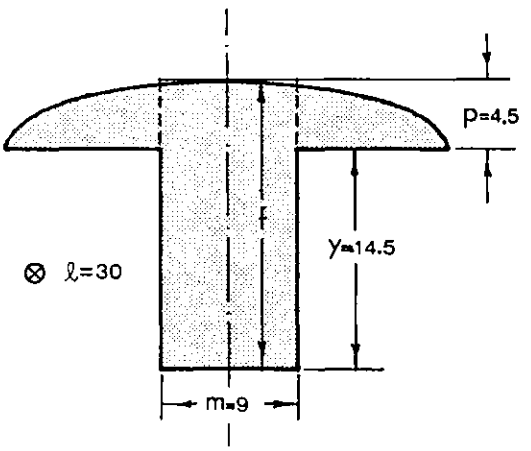

$S_p = m\ell = 270\ mm^2$

$f = y+p = 19\ mm$

Fig. 6.38 - Main flux path in the pole core

Table 6.2 - Magnetic characteristic of the pole

B (T)	H (A/m)	$\phi=BS_p$ (mWb)	ni=Hf (At)
0.2	50	0.054	0.95
0.4	75	0.108	1.43
0.6	90	0.162	1.71
0.8	100	0.216	1.90
1.0	150	0.270	2.85
1.2	180	0.324	3.42
1.4	250	0.378	4.75
1.6	1250	0.432	27.75
1.8	7650	0.486	145.35

flux density in the cross section $S_p = m\ell$ and using the magnetisation characteristic of the material, the flux ϕ and the m.m.f. drop ni = Hf were evaluated.

ii) - Joint pole-backing iron

A small gap g = 0.05 mm between the main pole and the rotor backing iron is considered, as shown in fig. 6.39.

Hence, the permeance of this air gap becomes

$$P = \mu_o \frac{m\ell}{g} = 5.4\mu_o\ H$$

Since in this path the magnetic characteristic is a straight line, the flux set up across this path is

$$\phi = 5.4\mu_o(ni) \qquad (6.69)$$

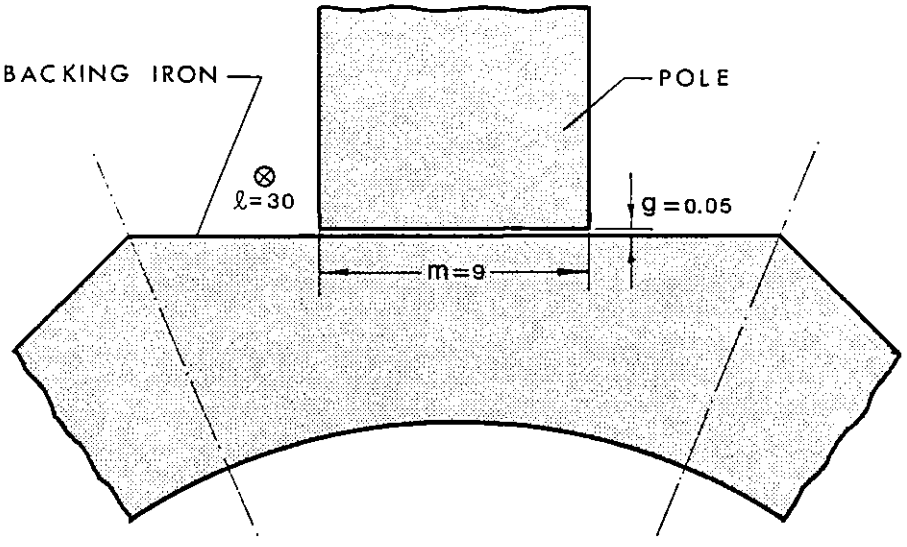

Fig. 6.39 - Joint pole-backing iron

where ni is the m.m.f. drop. For ni = 50 At, Eq. (6.69) gives ϕ = 0.34 mWb and then the magnetic characteristic of the path can be drawn.

iii) - Rotor backing iron

Fig. 6.40 shows the flux path in rotor backing iron. By measurement it may be taken ℓ_{ave} = 7 mm and S_{ave} = 150 mm^2. Using a similar process as used for pole, the magnetic characteristic of the path may be obtained.

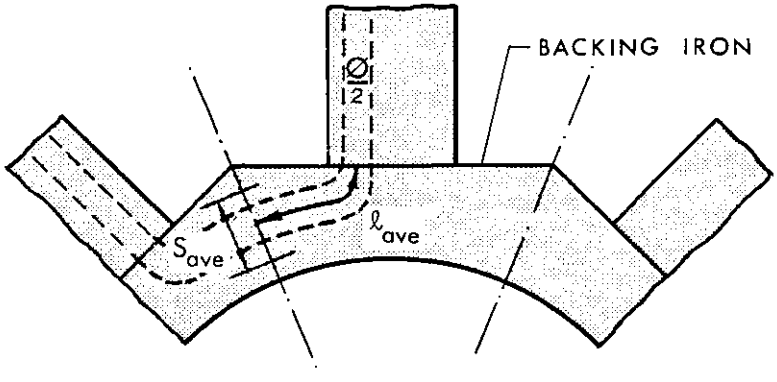

Fig. 6.40 - Flux path in rotor backing iron

In fig. 6.41 are represented the three partial magnetic characteristics

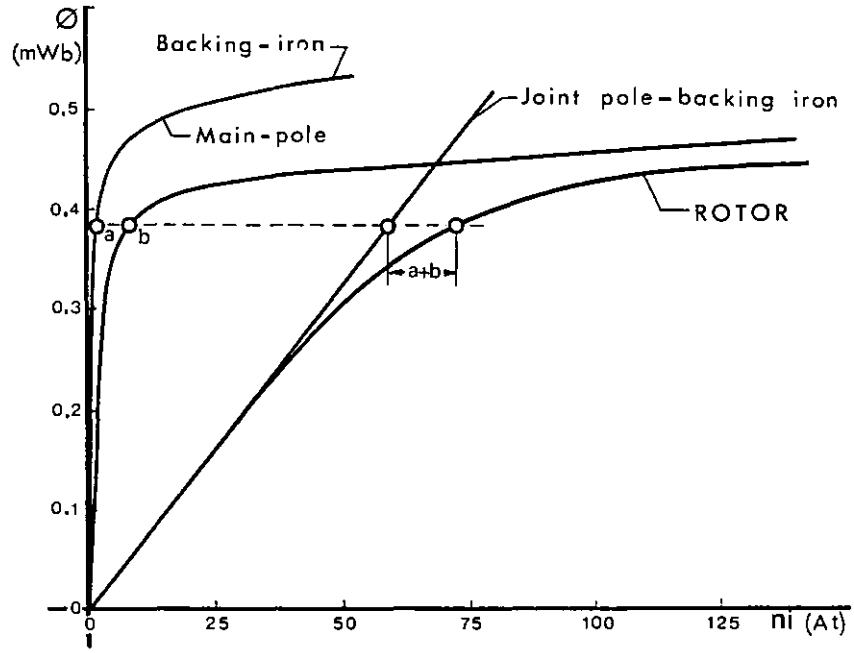

Fig. 6.41 - Partial magnetic characteristic of the rotor

determined. From them and considering flux continuity the magnetic characteristic of the rotor path is then evaluated.

b) - Magnetic characteristic of the stator

The magnetic circuit of the stator is also split into three paths.

i) - Air gap

The air gap permeance was already calculated in Appendix H for Alcomax 3 rotor, resulting in $P_g = 1.26\mu_o$ H. Again, in this path, the magnetic characteristic is a straight line

$$\phi = 1.26\mu_o(ni)$$

which gives for the particular value of ni = 100 At a flux ϕ = 0.16 mWb.

ii) - Teeth

This is the path where generally saturation first occurs. As already said tooth 2 carries the highest flux. From fig. 6.36 the excitation flux through tooth 2 for 90°E torque angle is:

$$\phi_2 = \frac{w\ell}{\alpha_s} \hat{B} \int_{45°}^{90°} \sin\theta \, d\theta = 0.71 \frac{w\ell}{\alpha_s} \hat{B} \qquad (6.70)$$

The flux per pole is:

$$\phi_p = \frac{2}{\pi} \hat{B} \, 4w\ell \qquad (6.71)$$

With a slot pitch $\alpha_s = \pi/4$, combination of Eq. (6.70) and Eq. (6.71) gives:

$$\phi_2 = 0.35\phi_p \qquad (6.72)$$

Eq. (6.72) shows that 35% of total flux per pole is driven through tooth 2 when 90°E torque angle is set up. Since the tooth root cross section is $S_r = k_f r\ell$, where $k_f = 0.95$ is the packing factor, from Eq. (6.72) the flux per pole becomes:

$$\phi_p = \frac{\phi_2}{0.35} = B \frac{k_f r\ell}{0.35} = 3.25 \times 10^{-3} \, B \quad Wb$$

The mean length of the tooth path may be taken as h = 9.0 mm and then the m.m.f. drop Hh to set up the flux ϕ_p through teeth was evaluated from the B/H curve.

iii) - Core

Half of the flux per pole crosses the stator backing iron interpolar centre-plane with a section $S_c = k_f b\ell = 157$ mm^2 and a mean length $\ell_c = \frac{\alpha_s}{2}(D_o - b) = 11.33$ mm, as shown in fig. 6.42. Hence the flux in the core

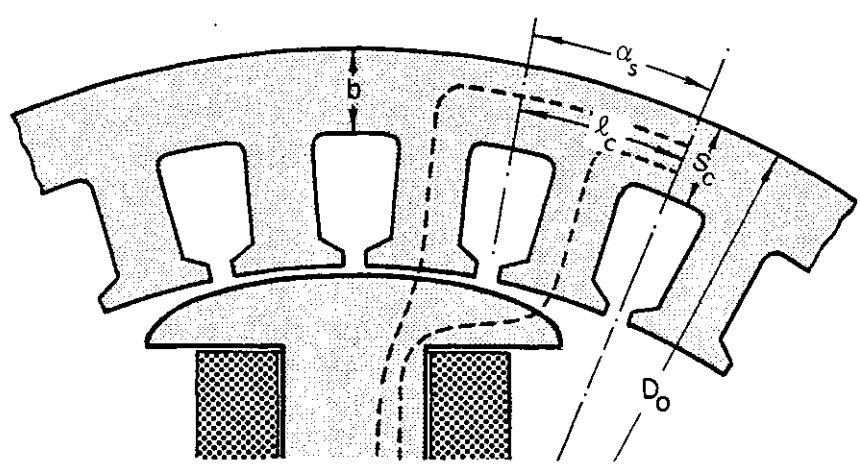

Fig. 6.42 - Stator backing iron flux path

$\phi_c = 2S_cB$ as a function of m.m.f. $H\ell_c$ was evaluated and plotted together with the other characteristics in fig. 6.43. Adding the corresponding m.m.f.'s for the same flux the magnetic characteristic of the stator path was obtained.

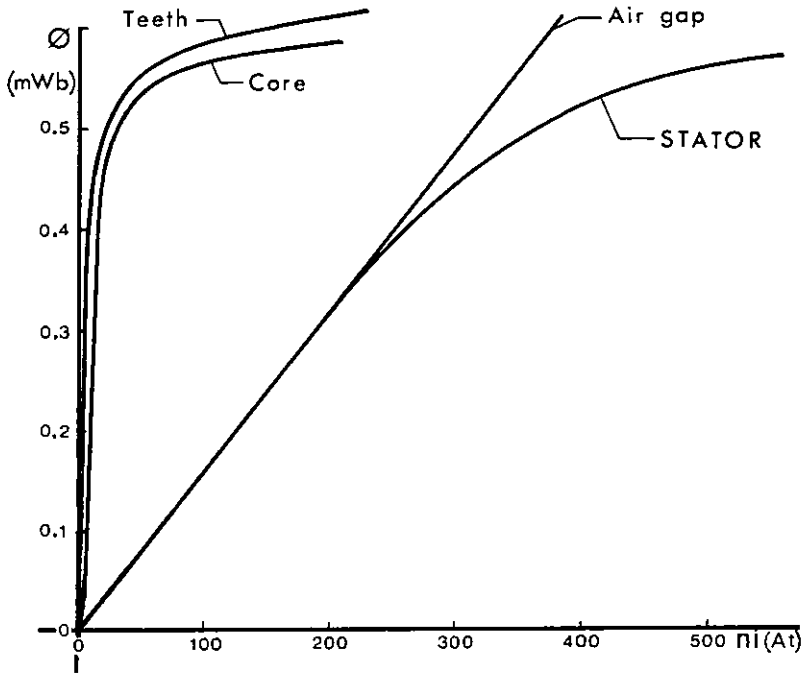

Fig. 6.43 - Partial magnetic characteristic of the stator

c) - Leakage flux characteristic

The leakage flux is given by

$$\phi_\ell = P_\ell(ni) \tag{6.73}$$

where P_ℓ is the machine leakage permeance, which can be expressed as:

$$P_\ell = (K_1 - 1)P_g \tag{6.74}$$

Substitution of Eq. (6.74) into Eq. (6.73) gives

$$\phi_\ell = (K_1 - 1)P_g\, ni \tag{6.75}$$

and since the machine leakage factor is $K_1 = 1.11$ and $P_g = 1.26\mu_o$ H, Eq. (6.75) becomes:

$$\phi_\ell = 0.143\mu_o(ni) \tag{6.76}$$

Eq. (6.76) is a straight line and for ni = 500 At results ϕ_ℓ = 0.09 mWb.

From the results of fig. 6.41, fig. 6.43 and Eq. (6.76) and using the graphical method explained in fig. 6.37 the useful air gap flux as a function of rotor m.m.f. may be obtained. Fig. 6.44 shows the magnetic

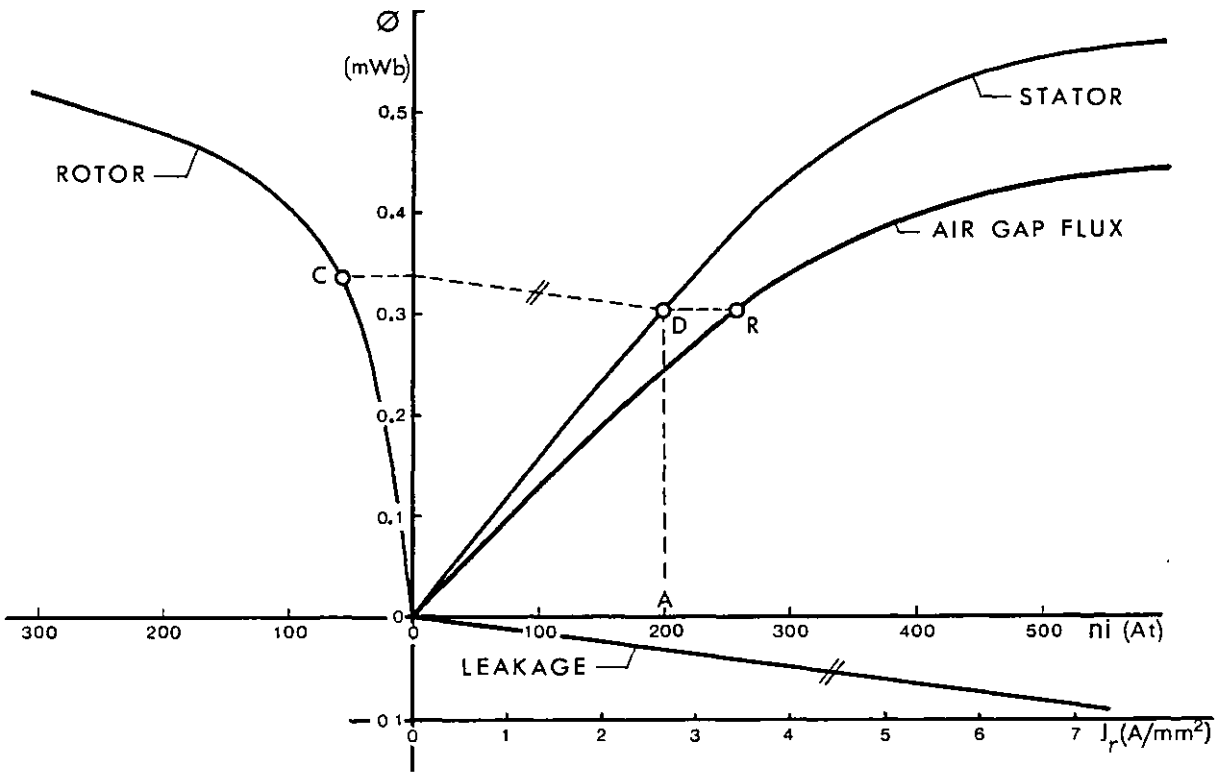

Fig. 6.44 - Useful air gap flux versus rotor excitation

characteristic of the machine obtained by the process described. Since the rotor m.m.f. is given by ni = $J_r$xy where J_r is the rotor current density excitation, a corresponding scale in A/mm^2 is also displayed.

6.8.2 - Torque versus field excitation characteristics

With a sinusoidal air gap flux density distribution with a peak value $\hat{B}$, the useful flux per pole becomes:

$$\phi_g = \frac{2}{\pi} \hat{B} \frac{2\pi R_g}{n_p} \ell \qquad (6.77)$$

Eliminating $\hat{B}$ in Eq. (6.45) by using Eq. (6.77), the fundamental torque at 90°E torque angle may be expressed as:

$$T_1 = \frac{\sqrt{2}}{2} n_p^2 \, q \, s \, h_1 \, K_{w1} \, \phi_g \, J_s \qquad (6.78)$$

where J_s is the r.m.s. stator current density. After substitution of values, Eq. (6.78) gives:

$$T_1 = 1.269\ \phi_g(J_r)\, J_s \quad \text{Nm} \tag{6.79}$$

where $\phi_g(J_r)$ is the machine magnetic characteristic in mWb as a function of rotor excitation J_r in A/mm^2 displayed in fig. 6.44.

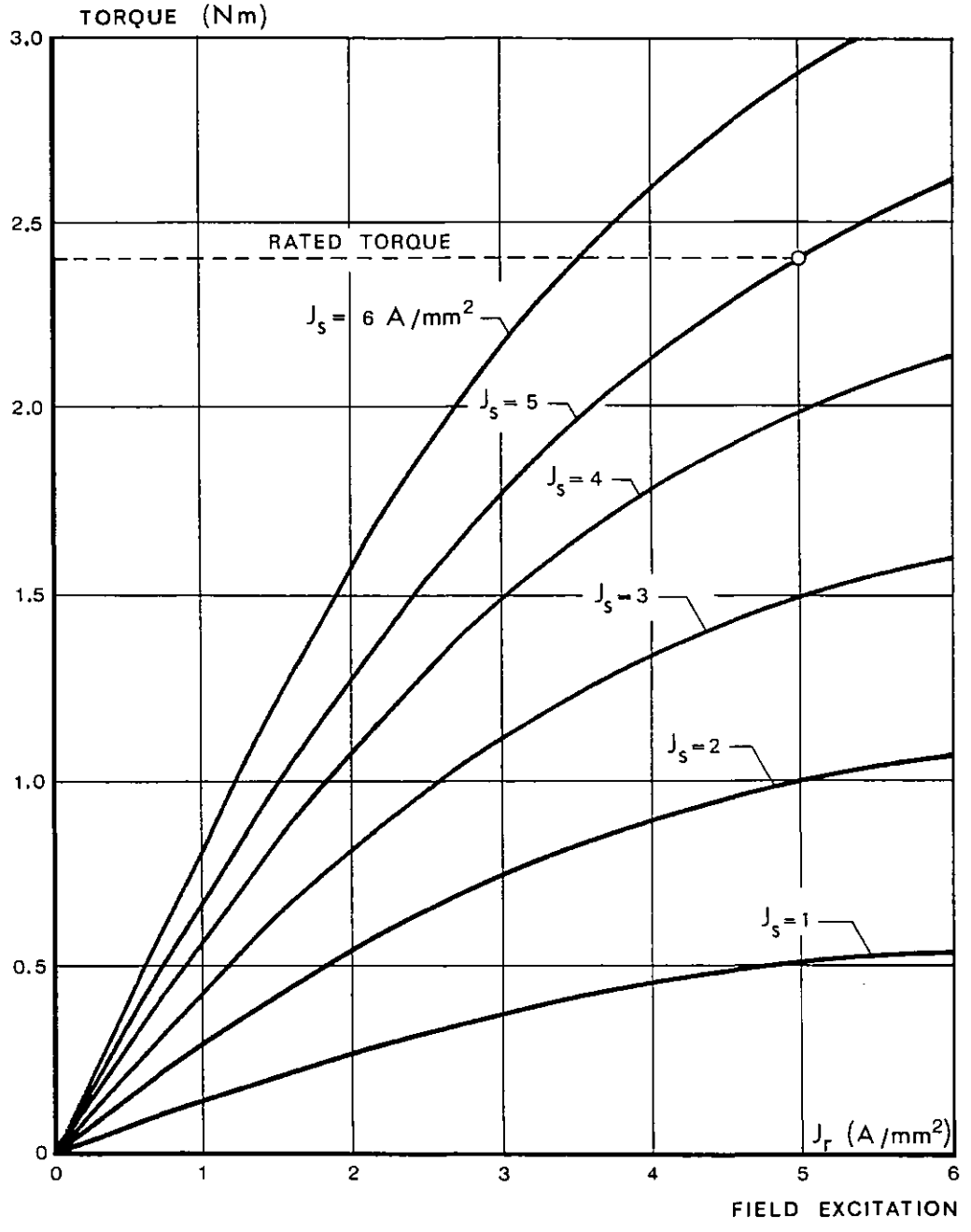

Fig. 6.45 - Torque versus rotor field excitation characteristics

Equation (6.79) was then evaluated versus rotor current density excitation for various levels of stator current density and the results are shown in fig. 6.45. The characteristics are practically linear for rotor current

density excitation up to $J_r = 3\ A/mm^2$, showing signs of saturation for higher values. The rated torque obtained was 2.46 Nm and for $J_s = 1\ A/mm^2$ the specific torque for full excitation was $T_u = 0.52\ Nm/A_{rms}\,mm^{-2}$ which is 27% greater than that obtained in Eq. (6.46) for Alcomax 3 rotor.

However, since the rotor inertia is $J = 0.983 \times 10^{-3}\ kg.m^2$ the specific torque per inertia is:

$$\frac{T_u}{J} = 0.53 \times 10^3\ rad/s^2 \qquad (6.80)$$

which is of the same order as the Alcomax 3 machine.

6.8.3 - Axis main-inductances

Fig. 1.34 shows the stator flux plot for the particular case $\theta = 0°$ (d-axis) and $\theta = 90°E$ (q-axis), when solid iron poles are used on the rotor.

For the d-axis inductance

$$\phi_{12} = I\,P_1 \quad \text{and} \quad \phi_{21'} = 2\,I\,2\,P_2$$

where the permeances, already calculated in Eq. (6.50), are

$$P_1 = \mu_o \frac{t\ell}{g_{av1}} = 0.17\mu_o\ H \quad \text{and} \quad P_2 = \mu_o \frac{t\ell}{g_{av2}} = 0.39\mu_o\ H$$

The total d-axis air gap inductance is thus:

$$L_d = n_p n^2 2(P_1 + 4P_2) = n^2\,27.68\mu_o\ H/phase \qquad (6.81)$$

For the q-axis air gap inductance

$$L_q = n_p n^2 2(P_2 + 4P_1) = n^2\,17.12\mu_o\ H/phase \qquad (6.82)$$

which is the same result as Eq. (6.51).

As expected, $L_q < L_d$ when solid iron poles are present, giving a saliency factor $\alpha = 0.62$ for the case studied.

6.8.4 - Torque versus torque angle characteristics

Substitution of Eq. (6.79), Eq. (6.81) and Eq. (6.82) into Eq. (6.56) gives the electromagnetic torque at θ torque angle

$$T = 1.269\,\phi_g(J_r)\,J_s + 0.015\,J_s^2 \sin 2\theta \text{ Nm} \qquad (6.83)$$

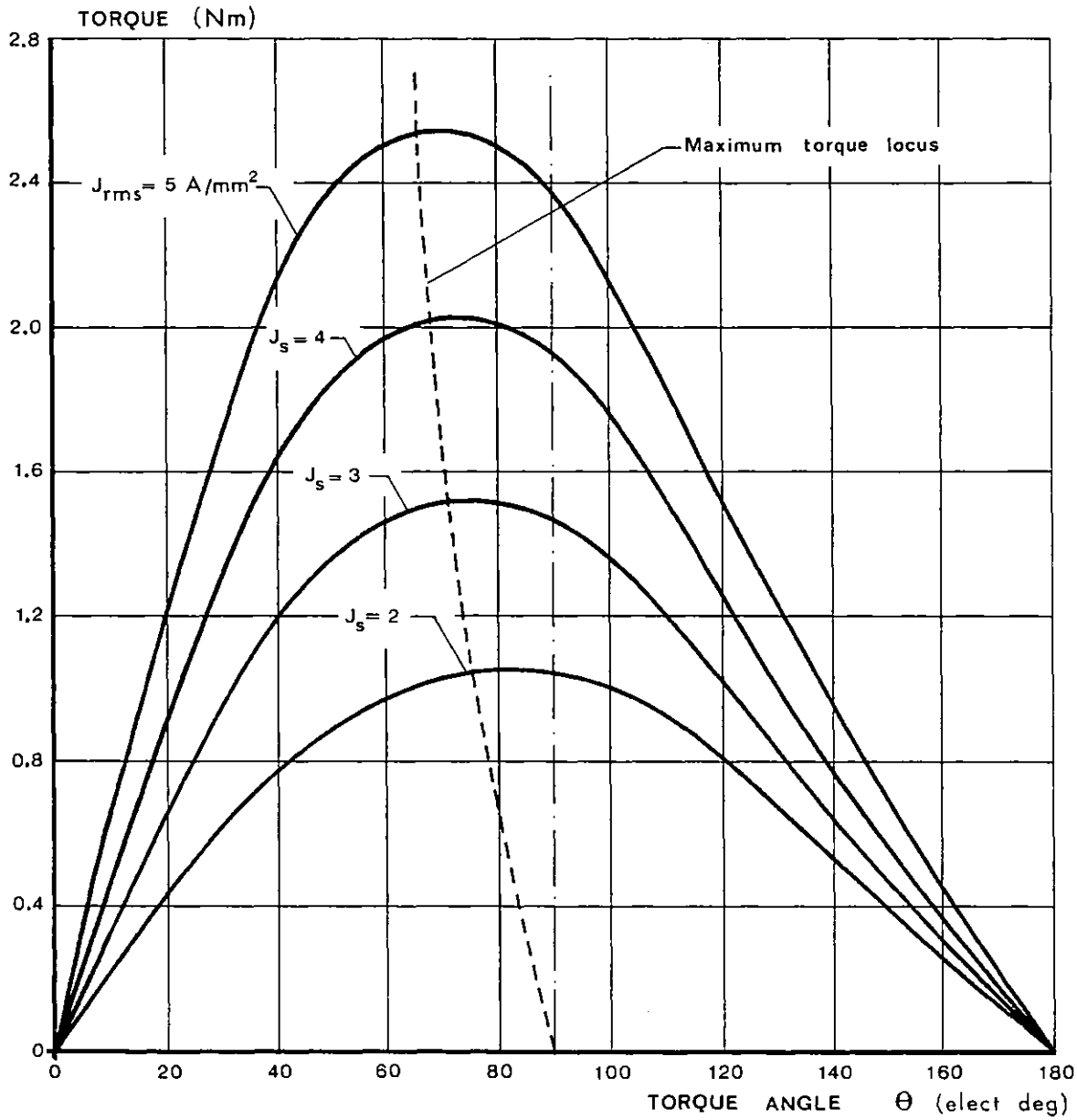

Fig. 6.46 - Torque versus torque angle characteristics for coil excited drum motor

From fig. 6.44 the useful flux per pole for full excitation (J_r = 5 A/mm^2) is ϕ_g = 0.37 mWb. Eq. (6.83) may then be plotted versus torque angle for several stator current densities and the results are shown in fig. 6.46. As expected since the saliency factor is $\alpha < 1$ the results show that the peak torque occurs for torque angles less than 90°E.

6.9 - BRUSHLESS, COIL-EXCITED DRUM MOTOR

A drum type machine corresponding to the disc, coil-excited brushless machine described in section 6.5 is now considered. The design concept is based on the Lundell type machine, frequently used in automobile and aerospace industry [62, 112].

A Lundell type eight-pole drum machine which is inherently brushless with controlled field excitation is illustrated in fig. 6.47.

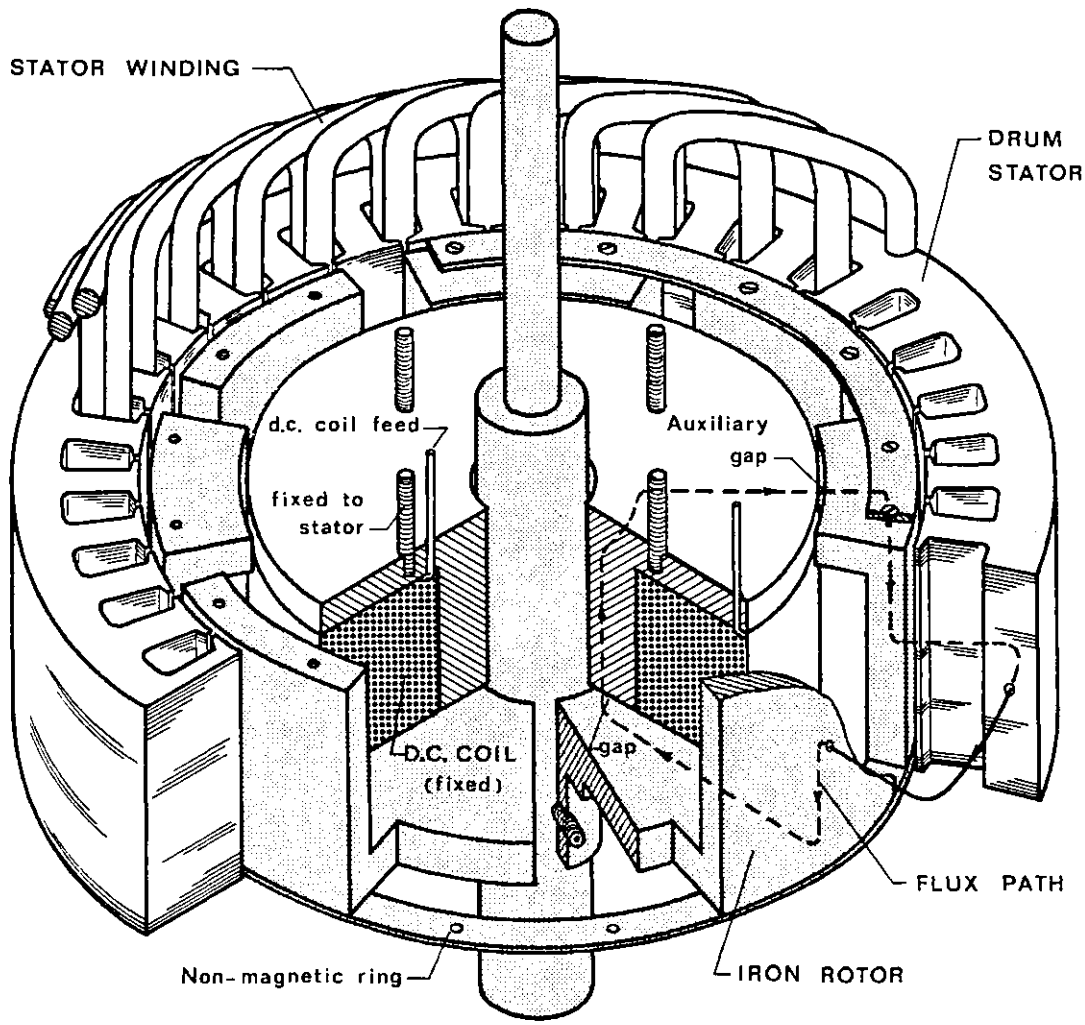

Fig. 6.47 - Eight pole brushless coil excited drum machine

The drum type stator is wound in a conventional way and the d.c. field coil assembly is co-axial and held in a cantilever fashion via fixing arrangements at one end of the stator only.

The rotor consists of eight interdigitated L-shaped iron blocks secured

by two non-magnetic rings and fixed to the shaft. The rotor can be easily inserted inside the stator from the "other" end. Two auxiliary gaps are then necessary and a typical flux path is shown in the diagram. As in the corresponding disc machine the centre flux axial direction is invariant and so this machine can also be regarded as homopolar.

6.9.1 - Design considerations

The drum type stator used in this machine is assumed to have the same laminations and axial length as the stator used in the brush-fed coil excited drum motor. Also, the winding arrangement is similar.

Hence, taking for the main and auxiliary gaps g = 0.5 mm the rotor outer radius is $R_r = R_g - g = 44.5$ mm with an axial active length $\ell = 30$ mm, as shown in the rotor layout of fig. 6.48. The other dimensions, including d.c. coil size, are now evaluated.

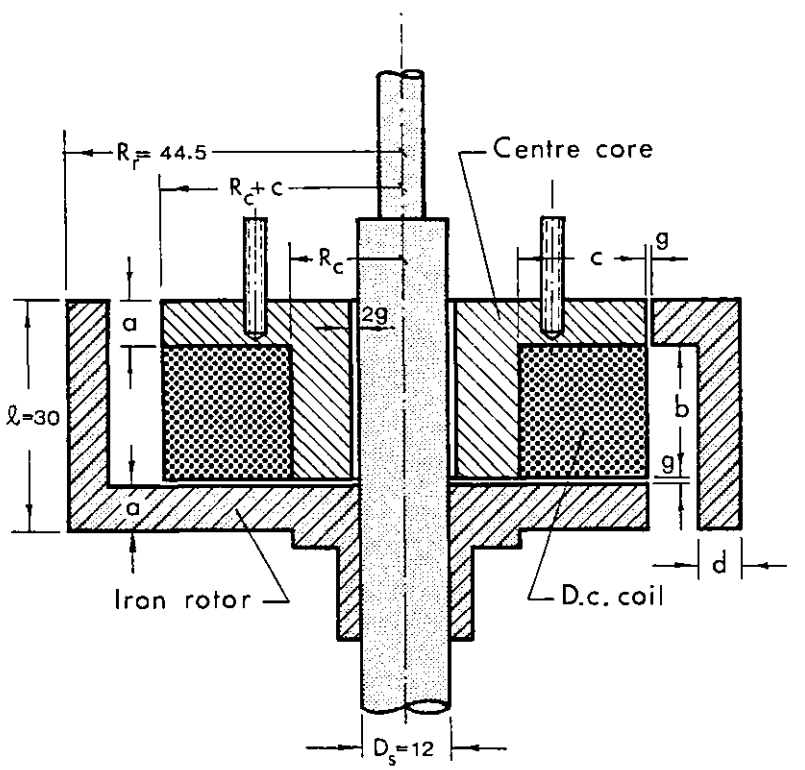

Fig. 6.48 - Brushless coil excited rotor

To keep the interpolar flux leakage at a reasonably low level the pole arc to pole pitch ratio may be taken as $\sigma = 0.8$. For an eight-pole rotor

the pole arc is $\alpha_a = \sigma \frac{2\pi}{n_p} = 0.2\pi$ rad. This gives for the pole face area $S_g = \alpha_a R_r \ell = 838.38\ mm^2$.

Neglecting flux leakage, the flux per pole $B_g S_g$ must satisfy the equation:

$$B_g S_g \simeq B_c \alpha_a R_r d \tag{6.84}$$

For an average air gap flux density $B_g = 0.25$ T and $B_c = 1.6$ T (saturation), Eq. (6.84) gives d = 5 mm. The centre core cross sectional area is

$$S_c = \pi\left[R_c^2 - \left(\frac{D_s}{2} + g\right)^2\right] \tag{6.85}$$

which may be expressed as

$$S_c = \frac{n_p}{2} \frac{B_g}{B_c} S_g \tag{6.86}$$

since the total flux $B_c S_c$ set up by the d.c. coil is entering $\frac{n_p}{2}$ poles. Hence, substitution of values in Eq. (6.86) gives $S_c = 523.4\ mm^2$ and from Eq. (6.85) results $R_c = 15$ mm.

The pole face area at radius $(R_c + c)$ is $S_g' = \alpha_a(R_c + c)a$ and the flux $B_g S_g$ must be

$$B_c \alpha_a (R_c + c)a = B_g S_g \tag{6.87}$$

For a coil current density J_c and neglecting the m.m.f. drop in the magnetic current:

$$J_c(\ell - g - 2a)c = (B_g + B_c) \frac{2g}{\mu_o} \tag{6.88}$$

Taking as typical $J_c = 5\ A/mm^2$ the simultaneous solution of Eq. (6.87) and Eq. (6.88) gives a = 6 mm and c = 17 mm. Then the coil height $b = \ell - g - 2a = 17.5$ mm. For full excitation the coil copper losses are $I^2R = \rho\pi(2R_c+c)cb\,J_c^2 = 19.6$ W.

With the design dimensions obtained and using the iron specific weight of $7.8 \times 10^3\ kg.m^{-3}$ the inertia of the rotating parts is $J = 0.615 \times 10^{-3} kg.m^2$, which is 37% less than the brush-fed, coil excited rotor.

6.9.2 - Specific torque developed

Assuming a uniform air gap flux density distribution B_g over the pole arc, the fundamental peak air gap flux density is given by Eq. (6.27). Substitution into Eq. (6.77), the flux per pole becomes;

$$\phi_g = \frac{4}{n_p} \frac{3.8}{\pi} B_g R_g \ell \qquad (6.89)$$

For full excitation (B_g = 0.25 T), Eq. (6.89) gives ϕ_g = 0.204 mWb. Hence, for 90°E torque angle operation, Eq. (6.79) gives for the fundamental specific torque:

$$\frac{T_1}{J_s} = T_u = 0.259 \text{ Nm/(A mm}^{-2}) \qquad (6.90)$$

which is 1.81 times greater than for brushless-coil excited disc machine, even using half of the air gap flux density. This is due to the fact that the drum machine torque is all produced at D_g level and better than the average disc diameter.

Finally, specific torque per inertia

$$\frac{T_u}{J} = 0.48 \times 10^3 \text{ rad/s}^2 \qquad (6.91)$$

which is 6.76 times greater than for brushless-coil excited disc machine, but it is slightly less than for the brush-fed coil-excited drum motor.

6.10 - DISCUSSION OF ALL DESIGN GEOMETRIES DESCRIBED

In this chapter, seven types of machines, all suitable for use as two-phase eight-pole synchronous motors in auto-piloted schemes have been considered. A few comments are given below about the properties of the prototype machines described. Theoretical performance figures for the four drum motors are summarised in table 6.3.

Table 6.3 - Design properties of prototype motors

PARAMETER	ALCOMAX 3	$SmCo_5$	COIL EXCITED	LUNDELL
Rotor inertia ($10^{-3}kgm^2$)	0.715	0.605	0.983	0.615
Peak flux density $\hat{B}(T)$	0.48	0.49	0.59	0.30
Specific torque (Nm/Amm^{-2})	0.41	0.53	0.52	0.26
Specific torque/inertia ($10^3 rad/s^2$)	0.57	0.88	0.53	0.48
Maximum torque (Nm)	2.05	2.65	2.46	1.30
d-axis air gap inductance (H)	$6.48\mu_0 n^2$	$5.28\mu_0 n^2$	$27.68\mu_0 n^2$	$32.64\mu_0 n^2$
q-axis air gap inductance (H)	$17.12\mu_0 n^2$	$5.28\mu_0 n^2$	$17.12\mu_0 n^2$	$32.64\mu_0 n^2$
Approximate ratio of rotor costs	2	10	6	1

The Alcomax 3 rotor has a relatively large number of parts but has the merit of utilising relatively cheap permanent magnets. The maximum torque is limited by magnetic circuit saturation even with a slot width to tooth width ratio of about unity. The relatively narrow slot gives low Amps per metre. In addition the high q-axis inductance introduces a large electrical time constant. Due to the low coercivity of the magnets, magnetisation after assembly would usually be needed but as with the other permanent magnet rotors I^2R losses and brushes are eliminated. Since the air gap flux density is sinusoidal a low torque ripple level would be expected.

The samarium cobalt rotor has the highest specific torque and specific torque per inertia. Due to the relatively low main path permeance it has a low inductance and consequently a low electrical time constant. The only problem with this rotor is the high cost of the permanent magnets and it could be argued that the five-fold increase in the overall construction cost (of $SmCo_5$ rotor over Alcomax 3 rotor) will not always be justified by 29% increase in the maximum torque obtained. However, magnetic circuit saturation is not a major problem when this rotor is used and so the stator can be designed with a larger slot size. Assuming, for example, that the $SmCo_5$ stator is designed with a 50% larger slot cross sectional area than the Alcomax 3 stator, then (for unchanged wire size) both the torque constant

and winding resistance per phase values would increase by 50%. Consequently for a given torque the copper losses are reduced by 50% and the supply requirement would be reduced to maintain the same potential output. On the other hand, the maximum torque per inertia would remain unchanged. With a good design therefore, this machine has a good mean torque per size and good peak torque per size.

The coil-excited rotor has a higher maximum torque than the Alcomax 3 rotor, but it is likely that it would have a higher manufacturing cost due to the rotor winding, sliprings and brushes. In addition a separate d.c. supply source is required, and rotor I^2R losses of course occur. The electrical time constant is of the same order as that obtained with Alcomax 3 rotor. The great advantage of this rotor is the facility for varying field excitation and therefore the possibility of controlling power factor, and of obtaining low speed flux boosting and high speed back e.m.f. reduction.

The Lundell type rotor probably would be the cheapest to make because it uses only iron and a single excitation coil. It is inherently brushless and the overall axial length can be shorter than the rotor coil-excited motor because there are no sliprings. Its main drawback is that the specific torque is the lowest of the figures obtained.

In the first three designs the saliency factors were $\alpha < 1$, $\alpha = 0$ and $\alpha > 1$ respectively. The corresponding torque versus torque angle characteristics show clearly the influence of the reluctance torque in the level of the peak torque obtainable and the torque-angle at which it occurs, as explained in section 3.7.2.c.

Finally, when comparing drum and disc machines the torque per inertia obtained with the brush-fed disc machine with small gaps ("printed" rotor) seems to be better than that produced by the drum machines considered. The Alcomax 3 excited field is preferable with the disc machine, giving the highest torque per inertia and lower cost. The air gap inductance is low resulting in a small electrical time constant. This form of motor is hence very effective in some servo applications.

☆ ☆ ☆

CHAPTER 7

CONCLUSIONS AND SUGGESTIONS FOR FUTURE WORK

This thesis has reported investigations in the field of variable speed drives based on two-phase synchronous motors with phase-locked or auto-piloted inverter supplies. The low-power prototype disc motor was used to gain a good understanding of the speed characteristics of this type of drive and to confirm the analyses of Chapter 3. The relative merits of mechanical and electronic commutation have been discussed, and arguments advanced in favour of auto-piloted drives. The similarity that exists between basic forms of auto-piloted motor and the equivalent conventional brush motor has been examined. Even though the volume of the electronic feed required for the experimental disc motor was similar to that for the motor itself and the cost of the electronics probabably about three times the cost of the motor. With the advent of improved and cheaper semi-conductor components and circuitry these figures could very probably be reduced in a rebuild, and reliably increased.

The work has also highlighted the importance of investigating new design options for given applications:

The prototype 1000.lb.ft brushless rotary actuator incorporating new design features was analysed and tested. Comparison between the measured results and those obtained by the linear scalar-potential approach described in Chapter 2 were presented. The measured air gap flux density distribution, unsaturated air gap inductance and torque ripple agreed well with theoretical values. The linear scalar-potential method has also found use in the calculation of demagnetisation limits due to armature

currents. It is felt that the machining of steps in pole faced-mounted B.P.R.E. permanent magnet blocks rotor seems a useful method of achieving an acceptable performance with a very simple manufacturing process. The design of a novel form of limited motion brushless tachometer able to give an output free of ripple, with a cheap construction, was presented.

The novel, inverted layout used with the prototype disc motor was found to work well. The disadvantage of this design, of course, is that both brushes and sliprings are required. But on the other hand it proved to have a high torque per inertia ratio without necessitating expensive permanent magnets, especially when the thinner, printed circuit rotor was used. A novel type of optical position sensor able to give a sine output without the need of demodulation, having a simple construction and circuitry, was designed and built and it proved to work satisfactorily. Again the linear scalar-potential prediction method, using cylindrical coordinates, was used for both no-load and load predictions. Comparison was made between computed and test values for a range of characteristics with exceedingly good agreement.

General comparisons were made between a number of motor configurations and in most cases, good potential performance levels were found to be possible. It is only right to point out that other configurations and indeed other auto-piloted drive schemes such as those incorporating switched reluctance motors [113] also exist. Only time will tell which of the many options will be the most successful in the future.

Perhaps the most important areas for further work are the following:

i) - Criteria for the choice of feed system design.

ii) - Further development of cheaper position sensor systems of high reliability and lifetime.

iii) - Comparison with induction start motors in the synchronous auto-piloted mode.

iv) - Optimal design of the motor itself including damper windings for control of torque fluctuations and compensating windings for power factor control; choice of magnet type and the layout of the magnets.

Doubtless improvements in permanent magnets and power and signal electronics have opened a new and exciting era in the design and usage of Electrical Machines.

§

APPENDICES

APPENDIX A

COMPUTER PROGRAM FOR SOLUTION OF THE MAGNETIC POTENTIAL DISTRIBUTION

A flow chart of the computing program for solution of the magnetic potential distribution using the standard over-relaxation technique is shown in fig. A.1.

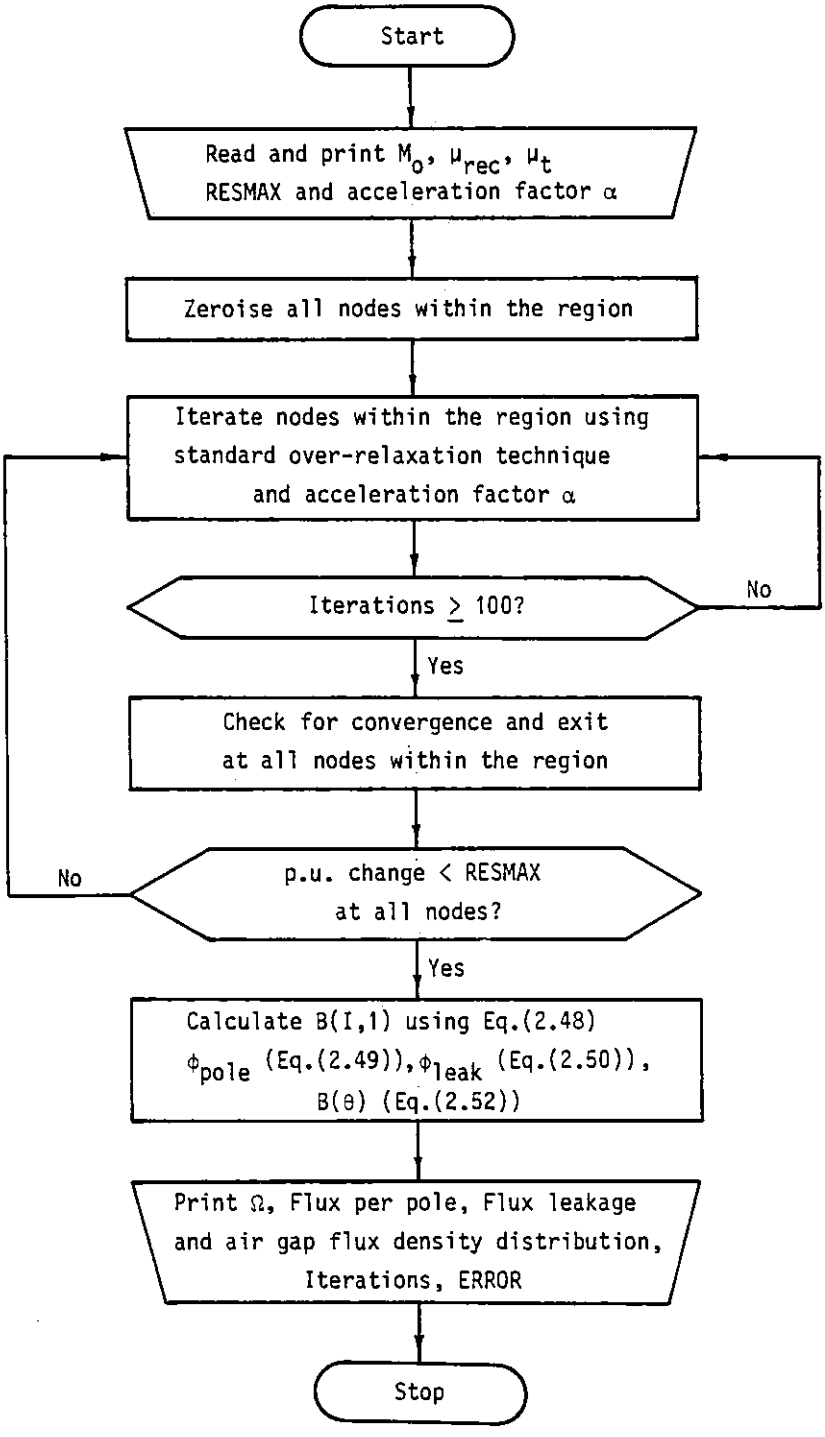

Fig. A.1 - Flow chart for program MAGNET

APPENDIX B

COMPUTER PROGRAM TO CALCULATE SPEED CHARACTERISTICS OF VOLTAGE-FED AND CURRENT-FED TWO-PHASE AUTO-PILOTED SYNCHRONOUS MOTOR

The flow chart of the computing program for calculating speed characteristics is shown in fig. B.1. For each frequency, speed characteristics for voltage-fed and current-fed operation are calculated using the equations developed in Chapter 3. The logic for both modes of operation is basically the same, with voltage and load angle replaced by current and torque angle respectively.

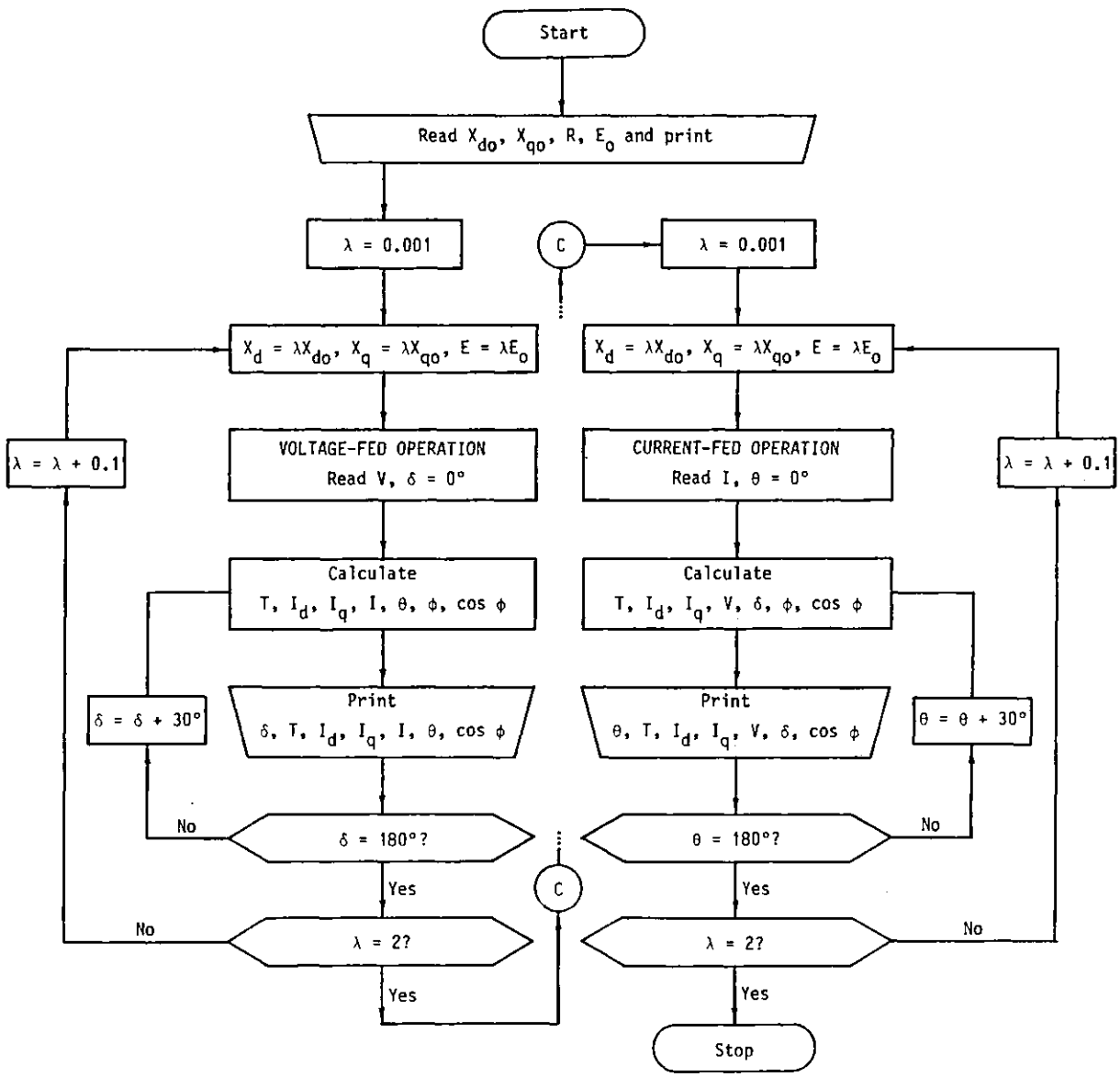

Fig. B.1 - Flow chart for program SPEEDCHAR

APPENDIX C

COMPUTER PROGRAM TO CALCULATE THE SLOT LEAKAGE INDUCTANCE OF THE ACTUATOR

A flow chart of the computer program for calculating the slot leakage inductance of the actuator is shown in fig. C.1, and the node arrangement used is illustrated in fig. C.2. The iron surfaces are assumed infinitely permeable, and account is taken of the radial air gap ab.

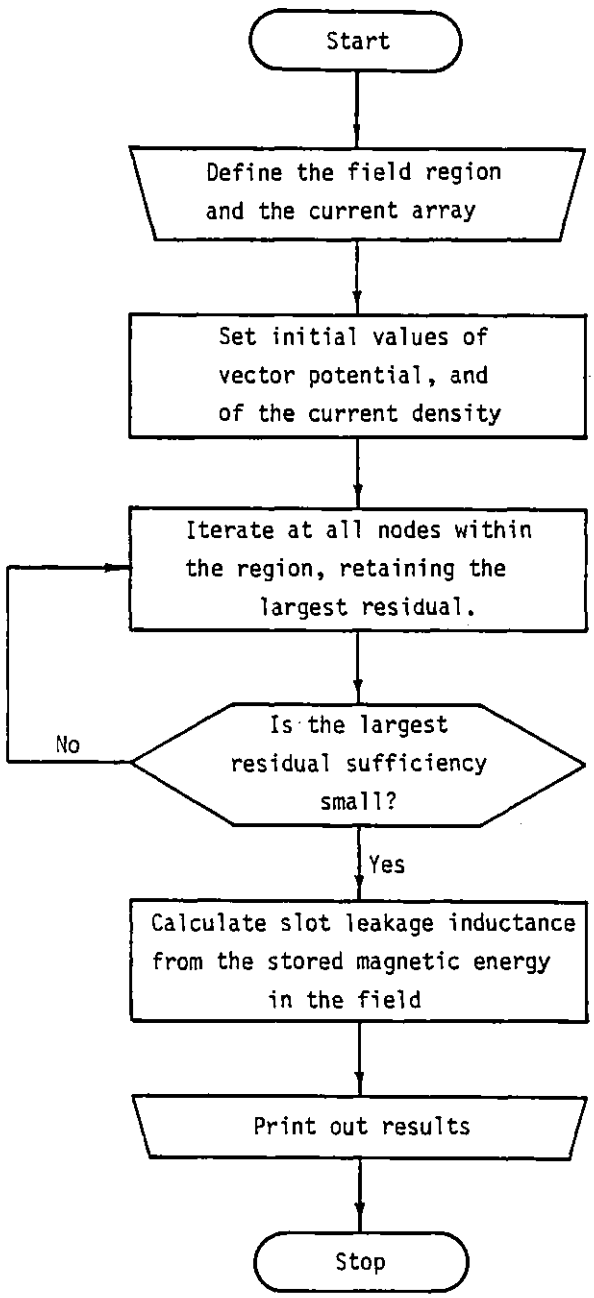

Fig. C.1 - Flow chart

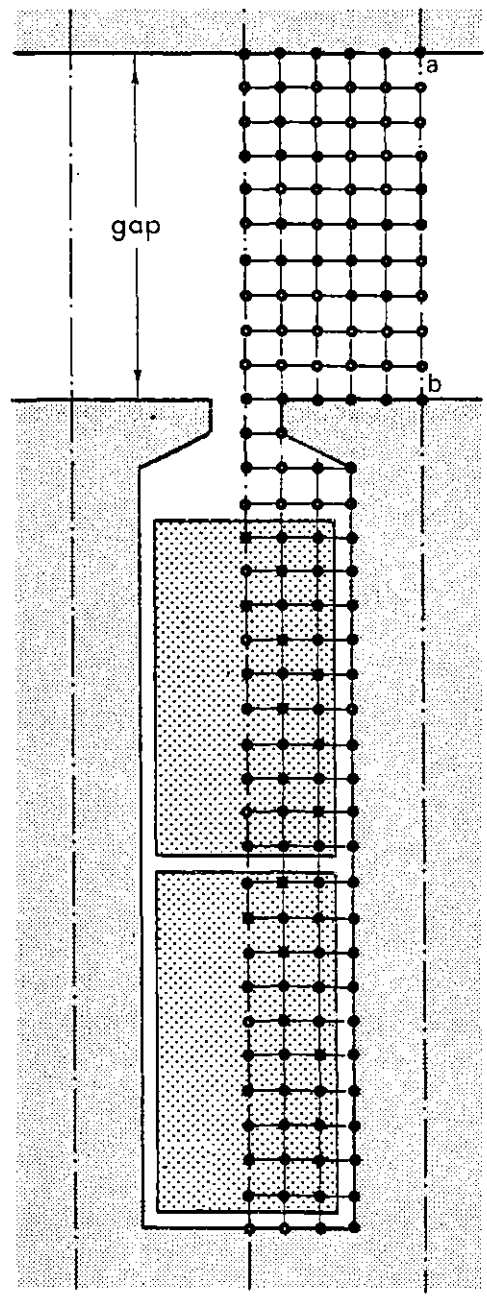

Fig. C.2 - Node arrangement

APPENDIX D

COMPUTER PROGRAM TO CALCULATE NO-LOAD FLUX DENSITY DISTRIBUTION AND THE MAGNETIC POTENTIAL DISTRIBUTION ON LOAD FOR THE B.P.R.E. MAGNET ROTOR ACTUATOR

The flow chart of the computer program for calculating the no-load flux density distribution for the stepped B.P.R.E. magnet is similar to that shown in fig. A.1, and the layout of nodes within the region is illustrated in fig. D.1. From Eq. (2.43) for $\Delta\theta$ = 3°E = 3/36°mech the ratio k = 1.0014555 was obtained to generate a logarithmic mesh.

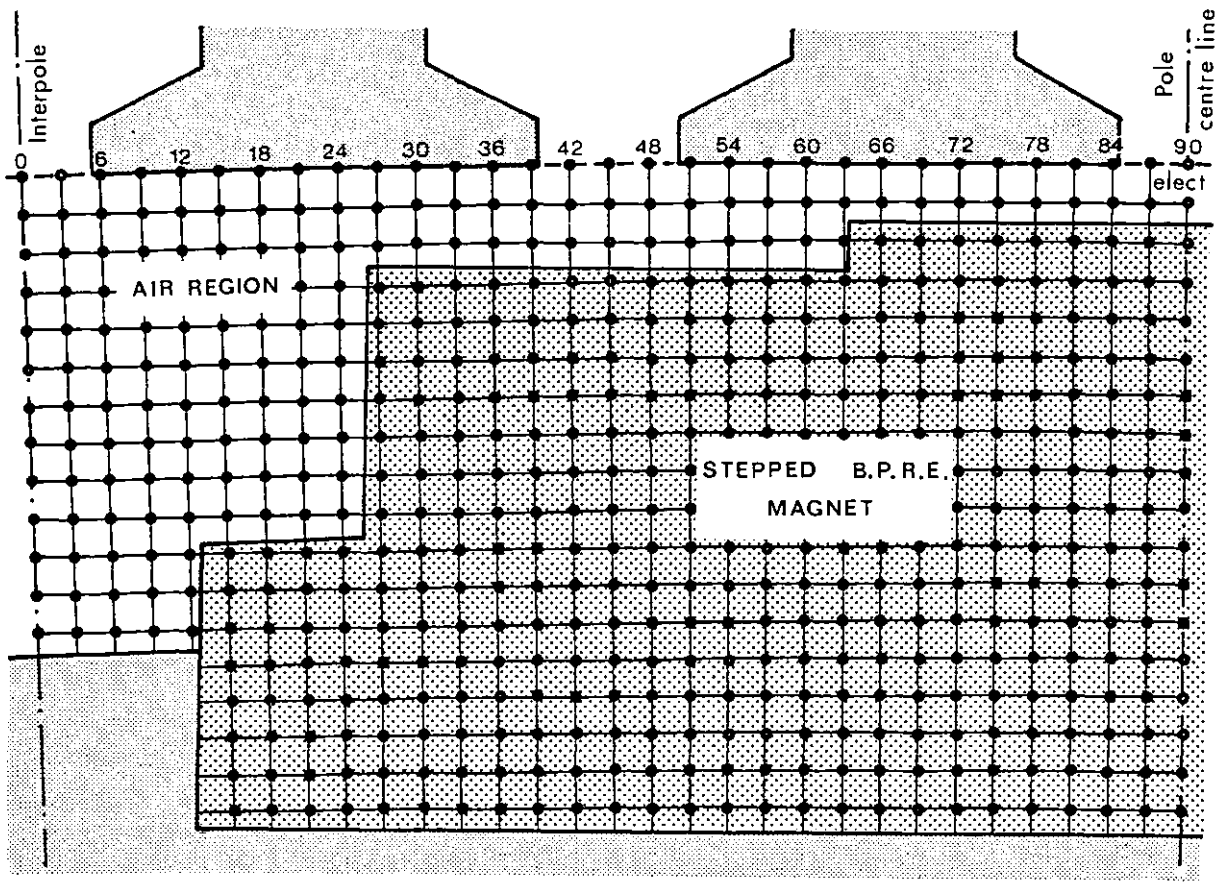

Fig. D.1 - Node arrangement used for the stepped B.P.R.E. magnet

Fourier analysis of the resulting flux density waveform was made by linearly interpolating the corresponding values at 3°E intervals, and obtaining integrals numerically using Simpson's rule.

The magnetic potential distribution on load at the instant of equal currents in each phase was obtained by assigning a stepped m.m.f. distribution on the stator with flux generators inoperative, and using the superposition principle as described in section 2.7.5.

APPENDIX E

INFLUENCE OF NORMAL FORCE ON SHAFT DEFLECTION

The shaft is considered as a simply supported beam of non-uniform cross section with the dimensions shown in fig. E.1.

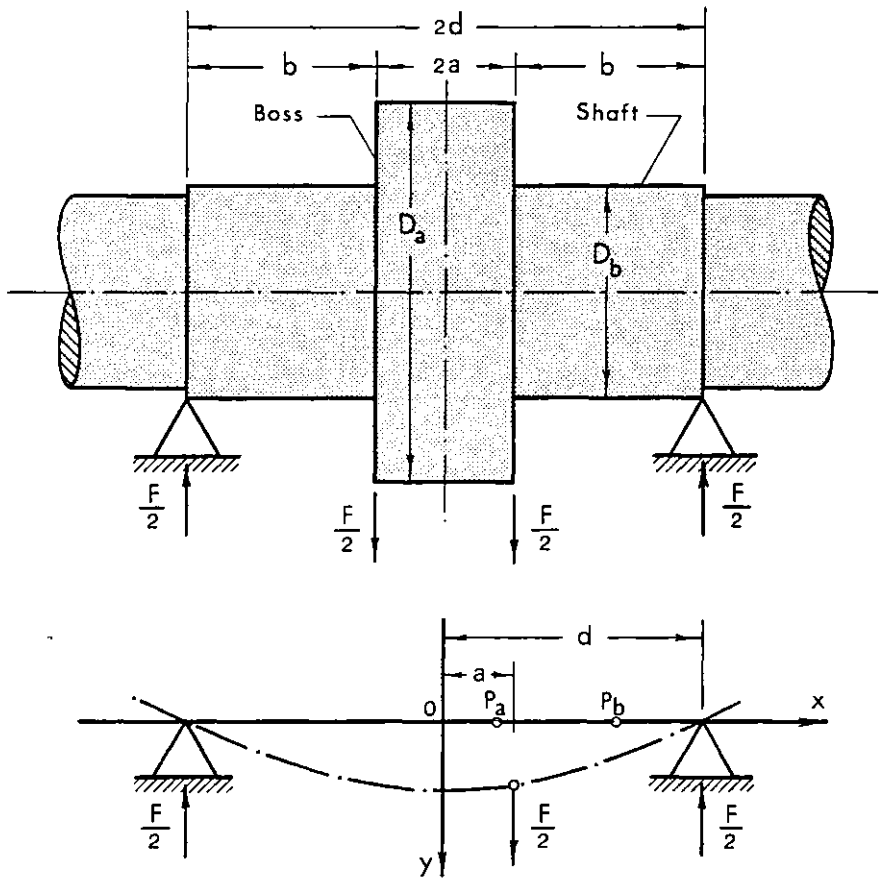

2a = 38 mm

b = 50 mm

2d = 138 mm

D_a = 100 mm

D_b = 56 mm

Fig. E.1 - Shaft deflection due to the normal force produced by the magnet

The deflection equation with uniform cross section is

$$\frac{d^2y}{dx^2} = \frac{M}{EJ} \qquad (E.1)$$

where M is the deflection moment, E is the Young's modulus and J the axis inertia ($J = \frac{\pi}{32}D^4$ for a uniform cross section of diameter D).

For a point P_a at the central thick section, the deflection moment is

$$M_a = \frac{F}{2}\left[(d - x) - (a - x)\right] = \frac{F}{2}b \quad \text{for } x < a \qquad (E.2)$$

and for a point P_b in the thinner end section

$$M_b = \frac{F}{2}(d - x) \qquad \text{for } x > a \qquad (E.3)$$

Hence, substitution of Eq. (E.2) and Eq. (E.3) into Eq. (E.1) gives:

$$E J_a \frac{d^2y}{dx^2} = \frac{F}{2}b \qquad \text{for } x < a$$

$$E J_b \frac{d^2y}{dx^2} = \frac{F}{2}(d - x) \qquad \text{for } x > a$$

Integrating,

$$E J_a y = \frac{F}{4}bx^2 + Ax + B \qquad \text{for } x < a \qquad (E.4)$$

$$E J_b y = \frac{F}{2}\left(d\,\frac{x^2}{2} - \frac{x^3}{6}\right) + Cx + D \qquad \text{for } x > a \qquad (E.5)$$

where A, B, C, D are constants.

For the central section, y and $\frac{dy}{dx}$ are zero when x = 0. Hence, A = 0 and B = 0. So, when x = a Eq. (E.4) becomes

$$E J_a y = \frac{F}{4}ba^2$$

This must give the same deflection y as Eq. (E.5) for x = a. Hence:

$$\frac{Fba^2}{4EJ_a} = \frac{1}{EJ_b}\left[\frac{F}{2}\left(d\,\frac{a^2}{2} - \frac{a^3}{2}\right) + Ca + D\right] \qquad (E.6)$$

Also, the first derivatives with respect to x must be identical at x = a. So,

$$\frac{Fba}{2EJ_a} = \frac{1}{EJ_b}\left[\frac{F}{2}\left(da - \frac{a^2}{2}\right) + C\right] \qquad (E.7)$$

Since $\frac{J_b}{J_a} = \left(\frac{D_b}{D_a}\right)^4$, Eq. (E.7) reduces to

$$C = F\left[\frac{ba}{2}\left(\frac{D_b}{D_a}\right)^4 + \frac{a^2}{4} - \frac{ad}{2}\right]$$

and from Eq. (E.6)

$$D = F\left[\frac{ba^2}{4}\left(\frac{D_b}{D_a}\right)^4 + \frac{a^3}{12} - \frac{da^3}{4}\right] - Ca$$

After substitution of values displayed in the diagram, the constants are

$$C = -518.54\ F\ kg.mm^2 \quad \text{and} \quad D = 4640.37\ F\ kg.mm^3$$

Thus, Eq. (E.5) may be written as

$$y = \frac{32}{\pi} \cdot \frac{F}{ED_b^4}\left[\frac{1}{2}\left(d\,\frac{x^2}{2} - \frac{x^3}{6}\right) - 518.54x + 4640.37\right] \qquad (E.8)$$

The normal force produced by the magnets was found to be F = 462.53 kg. Taking E = 21 x 10^3 kg/mm^2 (steel) the maximum shaft deflection at x = a + b = 69 mm is obtained from Eq. (E.8) as y_{max} = 0.54 x 10^{-3} mm.

APPENDIX F

COMPUTER PROGRAM TO CALCULATE THE UNSKEWED AIR GAP INDUCTANCE OF THE WINDING ACTUATOR

The flow chart of the computer program for calculating the unskewed air gap inductance of the winding actuator is shown in fig. F.1. A circumferential mesh spacing of 0.08° mechanical (3°E) is again used and the node arrangement is similar to that employed in Appendix D.

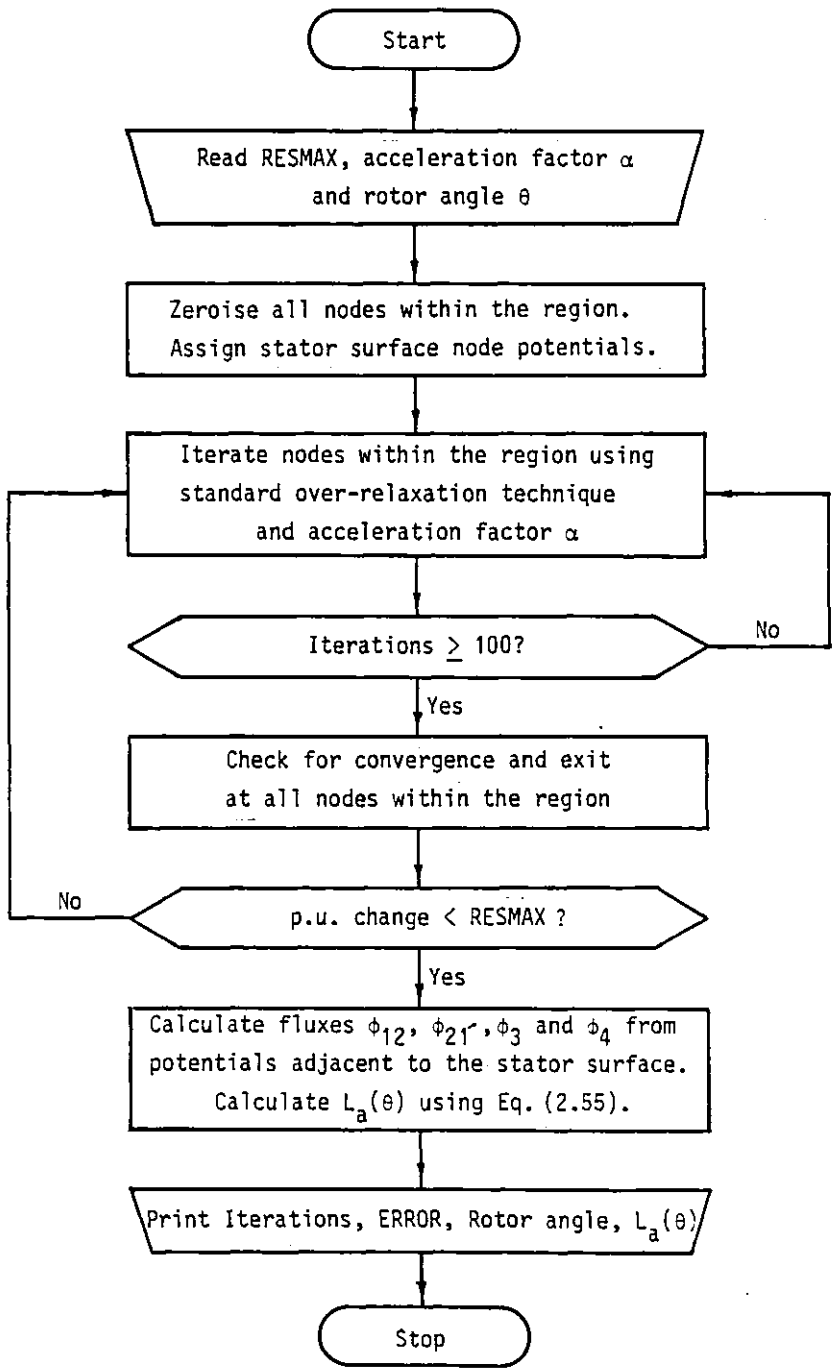

Fig. F.1 - Flow chart for program SLOTIND

APPENDIX G

LIMITED MOTION HOMOPOLAR BRUSHLESS TACHOMETER

a) - Basic construction

To obtain a high air gap flux without the need for extremely high field flux density and field m.m.f., the iron core must almost envelop the rotor as shown in fig. G.1. An outer iron ring (backing iron) and an iron sector are used for the return flux path, as shown in fig. 4.56. The field excitation could perhaps be generated by means of a metallic permanent magnet - MAGLOY - which is available in a ring-shape. Magloy magnets are exceedingly stable under normal conditions. Demagnetisation should not be a problem, since in this device coil currents are negligible.

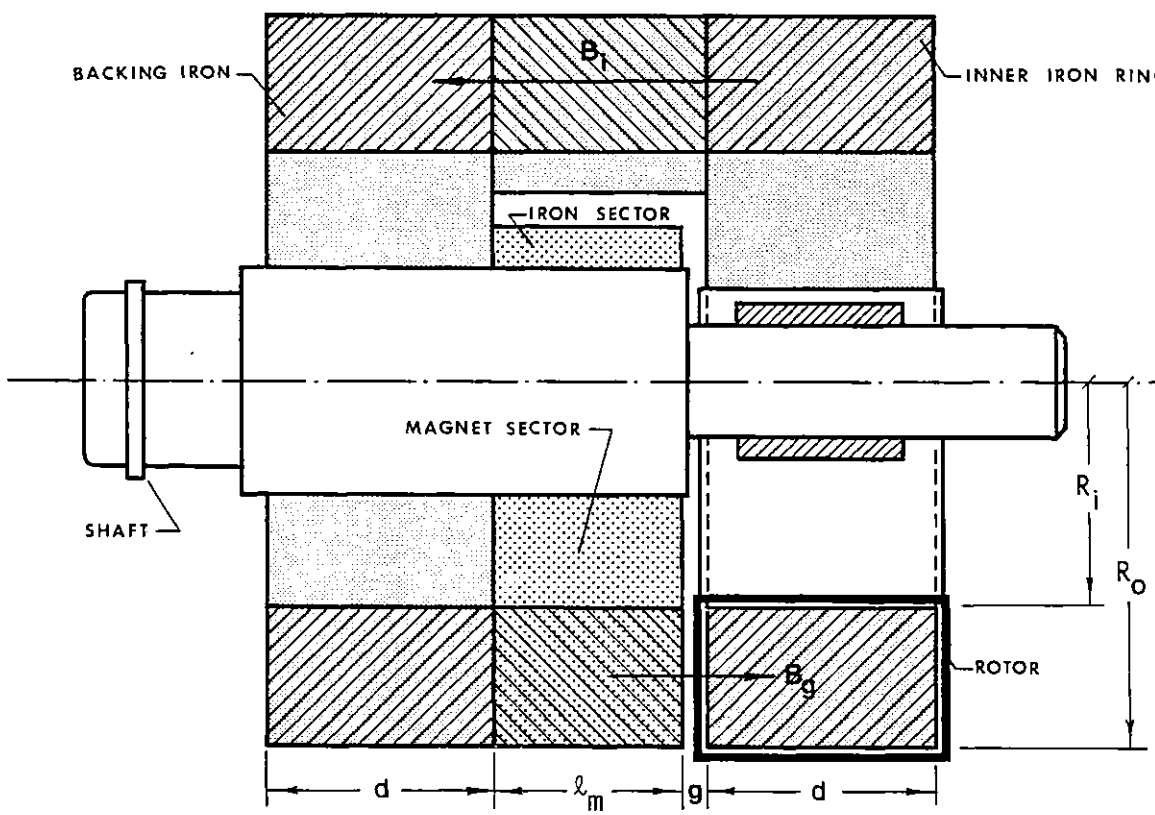

Fig. G.1 - Limited motion brushless tachometer layout

The rotor can be built with a non-magnet material, rigidly attached to the shaft by means of three or more spokes. It would be uniformly wound over a centre angle β with, for example, d = 0.1 mm diameter wire in eight layers.

Since the field is axial, only the radial conductors are useful if a double-sided stator is used. However, in order to make the machine axially as short as possible, it was decided to use a single-sided stator. This implies the use of only one bearing and hence a relatively large outside diameter (D = 1.5") is needed to keep reasonable air gap clearance, as shown in fig. 4.57.

The inner core is built up out of two half rings to allow assembly inside the rotor. These two half rings could then be linked together by means of bolts. A gap between the magnet sector and the iron sector is left in order to avoid short-circuiting the magnet end regions.

b) - E.m.f. induced in the rotor coil

Assuming that the rotor has an angular velocity ω, a single radial conductor of length $R_o - R_i$, as shown in fig. G.2, has at distance x from the centre a tangential velocity $V_x = \omega x$. Hence, at this point, there is

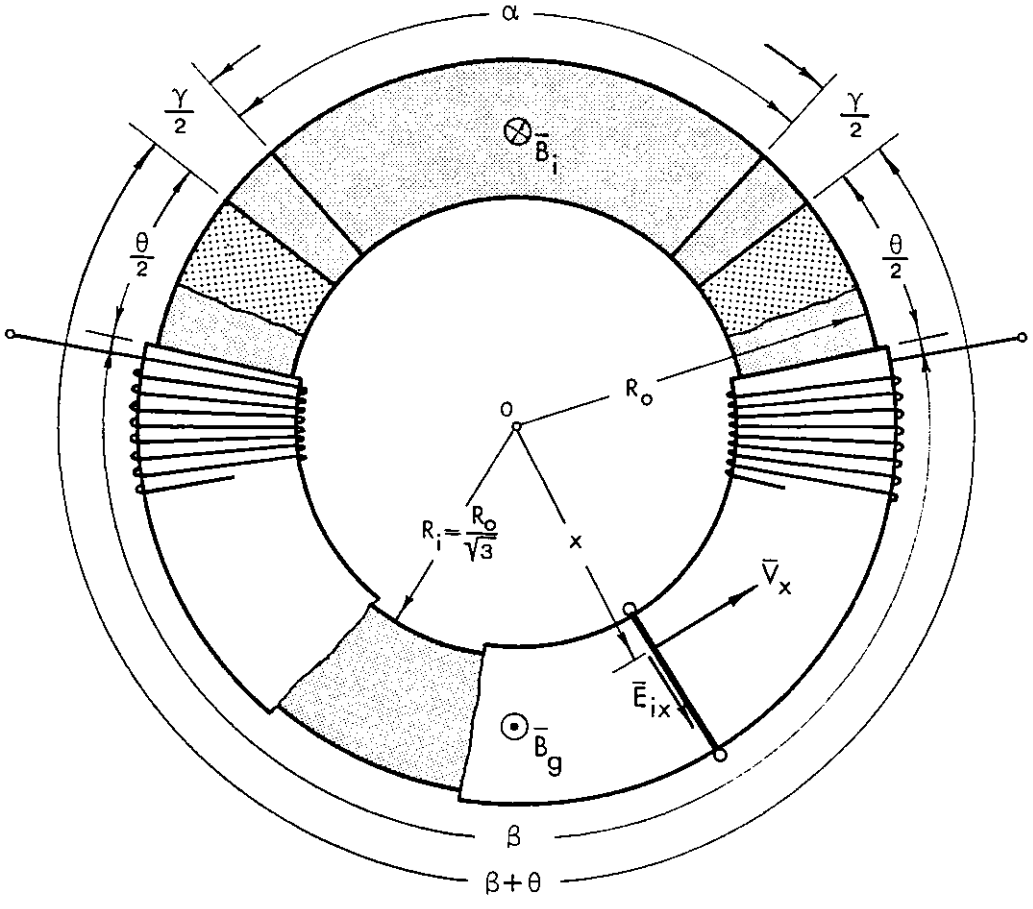

Fig. G.2 - Electric field induced on the radial conductor

an induced electric field $\bar{E}_{ix} = [\bar{V}_x \ \bar{B}_g]$. Since $\bar{B}_g$ is uniform and perpendicular to the conductor

$$E_{ix} = V_x B_g = \omega B_g x$$

Thus, the induced e.m.f. in the conductor

$$e = \int_{R_i}^{R_o} E_{ix}\, dx = \omega B_g \int_{R_i}^{R_o} x\, dx = \frac{\omega B_g}{2} (R_o^2 - R_i^2)$$

Assuming that the rotor conductors of diameter d are uniformly distributed on the rotor inner periphery, the total number of conductors in the first layer is

$$n_1 = \frac{1}{2}\beta \left(\frac{2R_i}{d} - 1 \right)$$

and for the layer f

$$n_f = \frac{1}{2}\beta \left(\frac{2R_i}{d} - 2f + 1 \right)$$

where β is the rotor centre angle. Thus, having f layers the total number of conductors is

$$N = \frac{f}{2}\beta \left(\frac{2R_i}{d} - f \right)$$

and the total e.m.f. induced

$$E = Ne = \frac{1}{4} f \beta \left(\frac{2R_i}{d} - f \right) B_g (R_o^2 - R_i^2)\omega \qquad (G.1)$$

From Eq. (G.1), if R_o is fixed, the inner radius R_i which gives the maximum rotor e.m.f. ($\frac{dE}{dR_i} = 0$), should satisfy the relation

$$R_o = \sqrt{3R_i^2 - fR_i d} \qquad (G.2)$$

c) - Calculation of the main dimensions

In the following calculations, it is assumed that the product fd is much less than inner radius R_i and therefore Eq. (G.2) reduces to

$$R_o = \sqrt{3}\, R_i \tag{G.3}$$

which gives approximately the maximum e.m.f.

The return path iron sector has an angle α and the rotor displacement is θ. From consideration of flux continuity in the axial direction (see fig. 4.56 and fig. G.2) is

$$B_g(R_o^2 - R_i^2)\,\frac{\beta+\theta}{2} = B_i(R_o^2 - R_i^2)\,\frac{\alpha}{2} \tag{G.4}$$

where B_g is the air gap flux density and B_i is the flux density in the iron. Eq. (G.4) may be rewritten in the form

$$\alpha = K(\beta + \theta) \tag{G.5}$$

where

$$K = \frac{B_g}{B_i} \tag{G.6}$$

The need for a reasonable angle of displacement θ constrains K to be small and typical values might be 0.3 to 0.5. The 1000 lb.ft. rotary actuator has a limited rotation of ±20.6° and so for the tachometer is taken to be $\theta/2 = 25°$. Fixing $B_g = 0.5$ T and $B_i = 1.5$ T (iron saturation), then from Eq. (G.6) K = 0.33. Hence, from Eq. (G.5)

$$\alpha = 0.33(\beta + \theta) = 0.33[360-(\alpha+\gamma)] \tag{G.7}$$

and leaving for the gap between the magnet and iron sector an angle $\gamma/2 = 10°$, Eq. (G.7) gives $\alpha = 85°$. Hence, $\beta = 360 - (\alpha + \gamma + \theta) = 205°$.

A standard Magloy ring magnet with $R_o = 50$ mm, $R_i = R_o/\sqrt{3} \simeq 30$ mm and $\ell_m = 25$ mm was chosen for field excitation. The magnet is then cut with a centre angle $\beta + \theta = 255°$. This gives for the minimum gap between iron sector and magnet $g_{min} = R_i\,\gamma/2 = 5.23$ mm.

The inner iron core axial length d can now be calculated. The condition that half the air gap flux, $\phi/2$, must pass circumferentially through each rectangular section at the end of the air gap gives the following equation

for the minimum volume of inner iron core:

$$\frac{1}{2} B_g (R_o^2 - R_i^2) \frac{\beta+\theta}{2} = B_{sat}(R_o - R_i)d \qquad (G.8)$$

where B_{sat} = 1.5 T is the saturation flux density of the iron. Substitution of Eq. (G.3) into Eq. (G.8) and after re-arrangement, becomes:

$$d = \frac{B_g}{B_{sat}} R_o \frac{\beta+\theta}{4} \left(1 + \frac{1}{\sqrt{3}}\right)$$

Substitution of values, gives $d \simeq 30$ mm.

Using a rotor clearance of ε = 0.35 mm its internal axial length will be $d + 2\varepsilon$ = 30.7 mm. For a coil support of 1.5 mm width and using f = 8 layers of copper with 0.1 mm diameter the total gap between the magnet and inner iron ring is g = 3 mm.

d) - Air gap flux density calculation

The air gap flux density is calculated using the load-line method described in section 2.5. Since the magnet and the inner iron ring have the same inner and outer radius, the unit permeance of the device is given, according to Eq. (2.12), by

$$\frac{B_m}{H_m} = - \mu_o \frac{K_1 \ell_m}{K_2 g} \qquad (G.9)$$

where K_1 is the leakage factor and K_2 = 1.05, is the reluctance factor. Fig. G.3 shows four possible flux leakage paths for this device and the leakage factor will now be calculated by using Roters' method.

Path 1

This is a half toroid as shown in fig. G.4.

The mean length of the flux path is approximately ℓ_{mean} = 1.22 g. By Pappus' theorem, the volume of the inner and outer half toroids is respectively

$$V_i = (\beta + \theta)(R_i - x_G) \frac{\pi g^2}{8}$$

$$V_o = (\beta + \theta)(R_o + x_G) \frac{\pi g^2}{8}$$

where $x_G = \frac{2g}{3\pi}$ is the distance of the half-circle's centre of gravity to point 0 at its diameter. Hence the mean area of the flux path will be

$$S_i = \frac{V_i}{\ell_{mean}} = (\beta + \theta)(R_i - \frac{2g}{3\pi})\, 0.32\ g$$

$$S_o = \frac{V_o}{\ell_{mean}} = (\beta + \theta)(R_o + \frac{2g}{3\pi})\, 0.32\ g$$

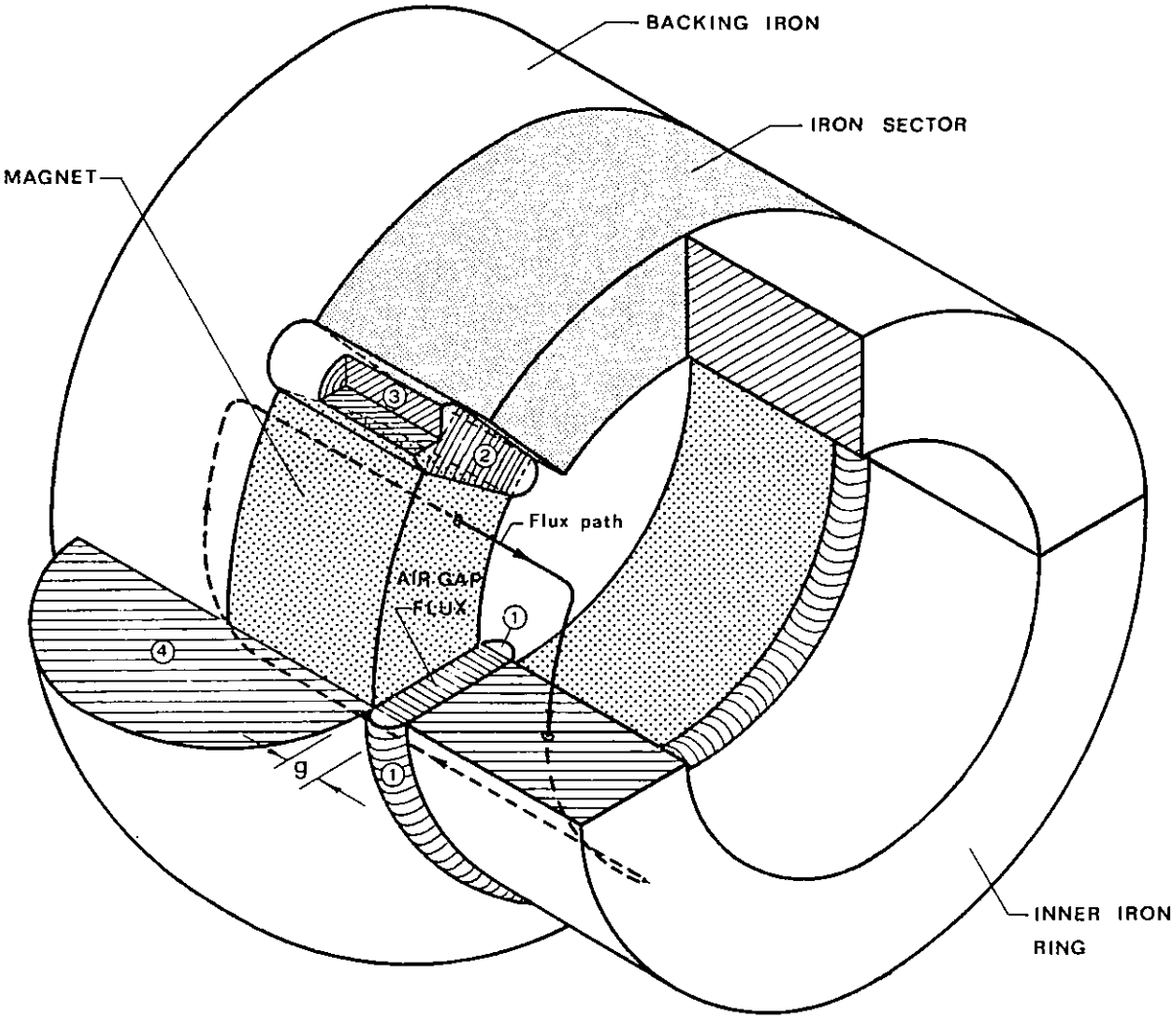

Fig. G.3 - Tachometer flux leakage paths

and the respective permeances are:

$$P_i = \mu_o \frac{S_i}{\ell_{mean}} = 0.26\mu_o(\beta + \theta)(R_i - \frac{2g}{3\pi})$$

$$P_o = \mu_o \frac{S_o}{\ell_{mean}} = 0.26\mu_o(\beta + \theta)(R_o + \frac{2g}{3\pi})$$

Since they are in parallel the permeance of path 1 will be

$$P_1 = P_i + P_o = 0.26\mu_o(\beta + \theta)(R_i + R_o)$$

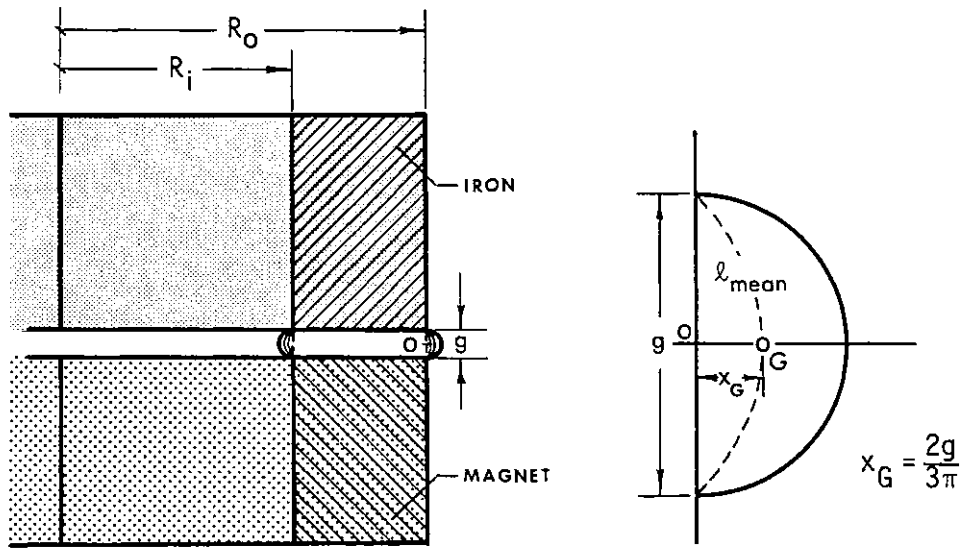

Fig. G.4 - Half toroid flux path

and substitution of values, gives:

$$P_1 = 92.53\mu_o \quad mH$$

Path 2

This is a sector of centre angle $\gamma/2 = 10°$, height $\ell_m = 25$ mm and length $R_o - R_i = 20$ mm as shown in fig. G.5.

Assuming a linear variation in magnetic potential Ω along the axial dimension of the magnet, $\Omega_x = \Omega_m \frac{x}{\ell_m}$, the elementary flux emanating from the magnet edge to the iron sector is

$$d\phi_x = \Omega_x \, dP_x = \Omega_m \frac{x}{\ell_m} \mu_o \frac{(R_o - R_i)dx}{\frac{\gamma}{2}\cdot\frac{1}{2}(R_o + R_i)}$$

The total flux is therefore

$$\phi = \int_0^{\ell_m} d\phi_x = 2\mu_o \Omega_m \frac{\ell_m}{\gamma} \frac{R_o - R_i}{R_o + R_i}$$

hence, the total permeance due to the both edges of the magnet:

$$P_2 = \frac{2\phi}{\Omega_m} = 4\mu_o \frac{\ell_m}{\gamma} \frac{R_o - R_i}{R_o + R_i}$$

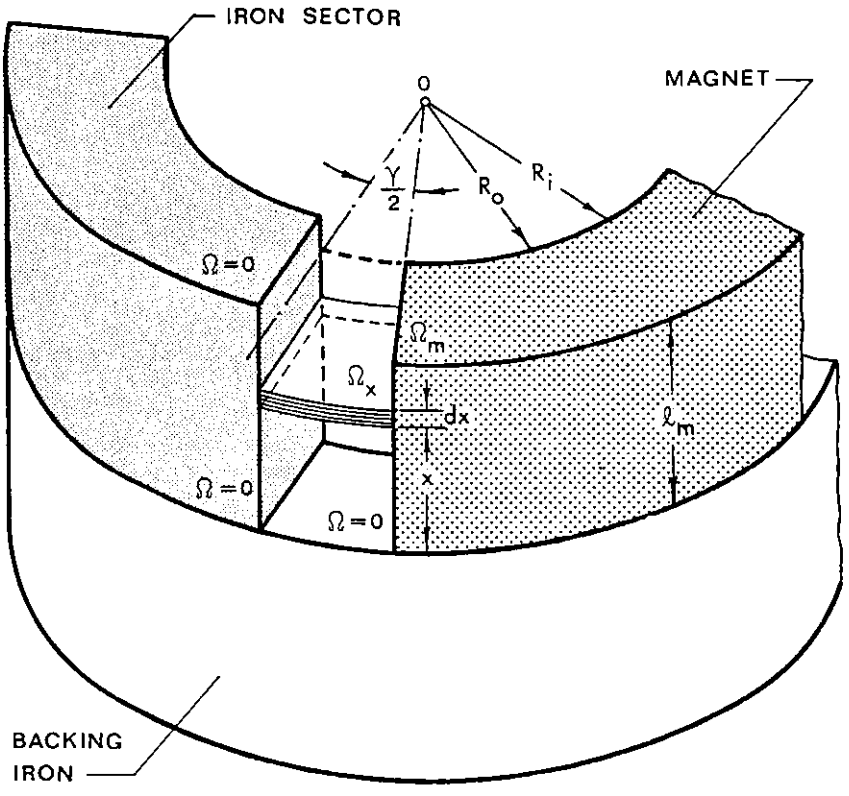

Fig. G.5 - Sector flux path

Substitution of values, gives

$$P_2 = 71.66\mu_o \text{ mH}$$

Path 3

This path consists of two half cylinders of length ℓ_m and diameters g_{min} and g_{max} respectively, as shown inf fig. G.6.

If dV is the elementary volume of the cylinder, the mean elementary area of the flux path will be

$$dS_{mean} = \frac{dV}{\ell_{mean}} = \frac{\pi g^2}{8} \frac{dx}{1.22g} = 0.322g\,dx$$

Hence, the elementary flux at level x is

$$d\phi_x = \Omega_x \, dP_x = \Omega_m \frac{x}{\ell_m} \mu_o \frac{0.322g}{1.22g} dx$$

and the total flux is

$$\phi = \int_0^{\ell_m} d\phi_x = \mu_o \Omega_m \, 0.13 \, \ell_m$$

which is independent of g. Therefore the permeance

$$P = \frac{\phi}{\Omega_m} = 0.13 \mu_o \ell_m$$

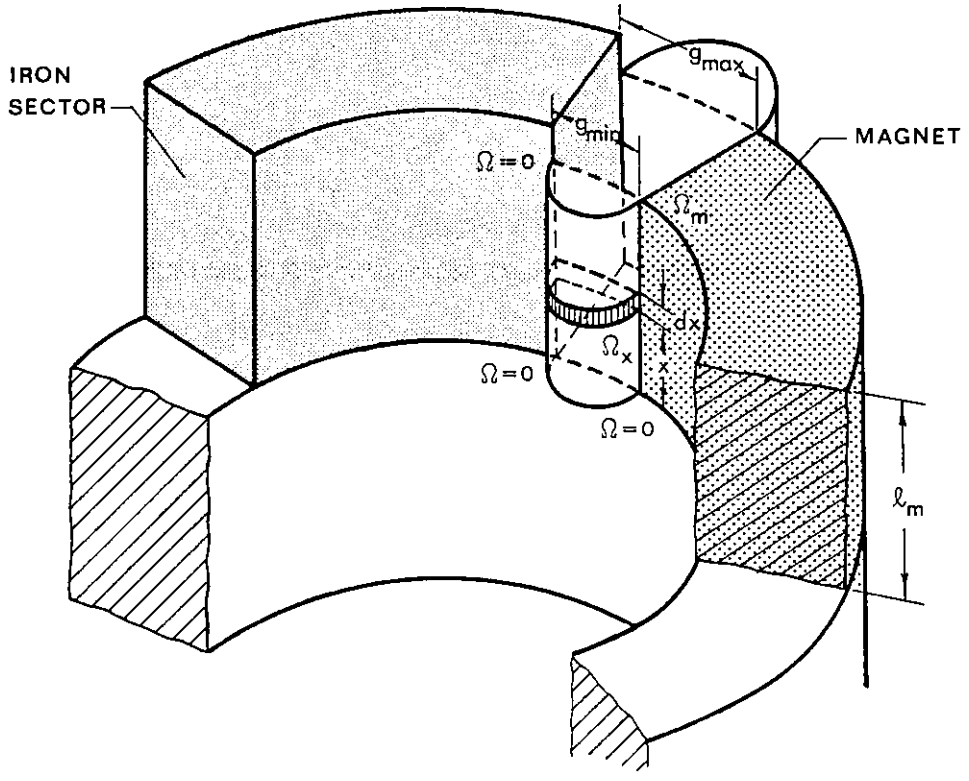

Fig. G.6 - Half cylinder flux path

There are four of these permeances in parallel for the device and so

$$P_3 = 4P = 0.52 \mu_o \ell_m$$

For ℓ_m = 25 mm gives

$$P_3 = 13.0 \mu_o \text{ mH}$$

Path 4

This is a half toroid with an arc $\beta + \theta$ and radius R_o, as shown in fig. G.7.

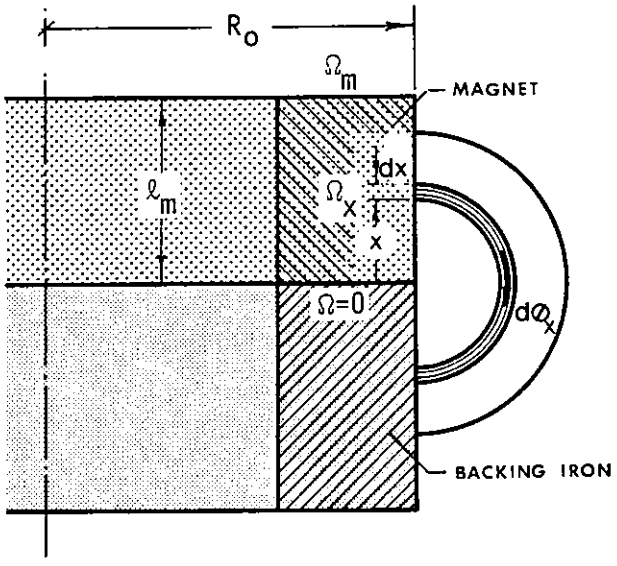

Fig. G.7 - Half toroid flux path

Assuming again linear variation in Ω_x, the elementary flux emanating at level x is

$$d\phi_x = \Omega_x \, dP_x = \Omega_m \frac{x}{\ell_m} \mu_o(\beta + \theta) \frac{R_o + x}{\pi x} dx$$

and the total flux

$$\phi = \int_0^{\ell_m} d\phi_x = \Omega_m \mu_o \frac{\beta+\theta}{\pi} \left(R_o + \frac{1}{2}\ell_m\right)$$

Thus, the permeance

$$P_4 = \frac{\phi}{\Omega_m} = \mu_o \frac{\beta+\theta}{\pi} \left(R_o + \frac{1}{2}\ell_m\right)$$

Substitution of values, gives:

$$P_4 = 88.54\mu_o \quad \text{mH}$$

Therefore, total leakage permeance

$$P_\ell = \sum_{i=1}^{4} P_i = 265.73\mu_o \quad \text{mH} \qquad (G.10)$$

Finally, useful permeance

$$P_g = \mu_o \frac{\beta+\theta}{2} \frac{R_o^2 - R_i^2}{g}$$

and substitution of values, gives:

$$P_g = 1186.22\mu_o \quad mH \tag{G.11}$$

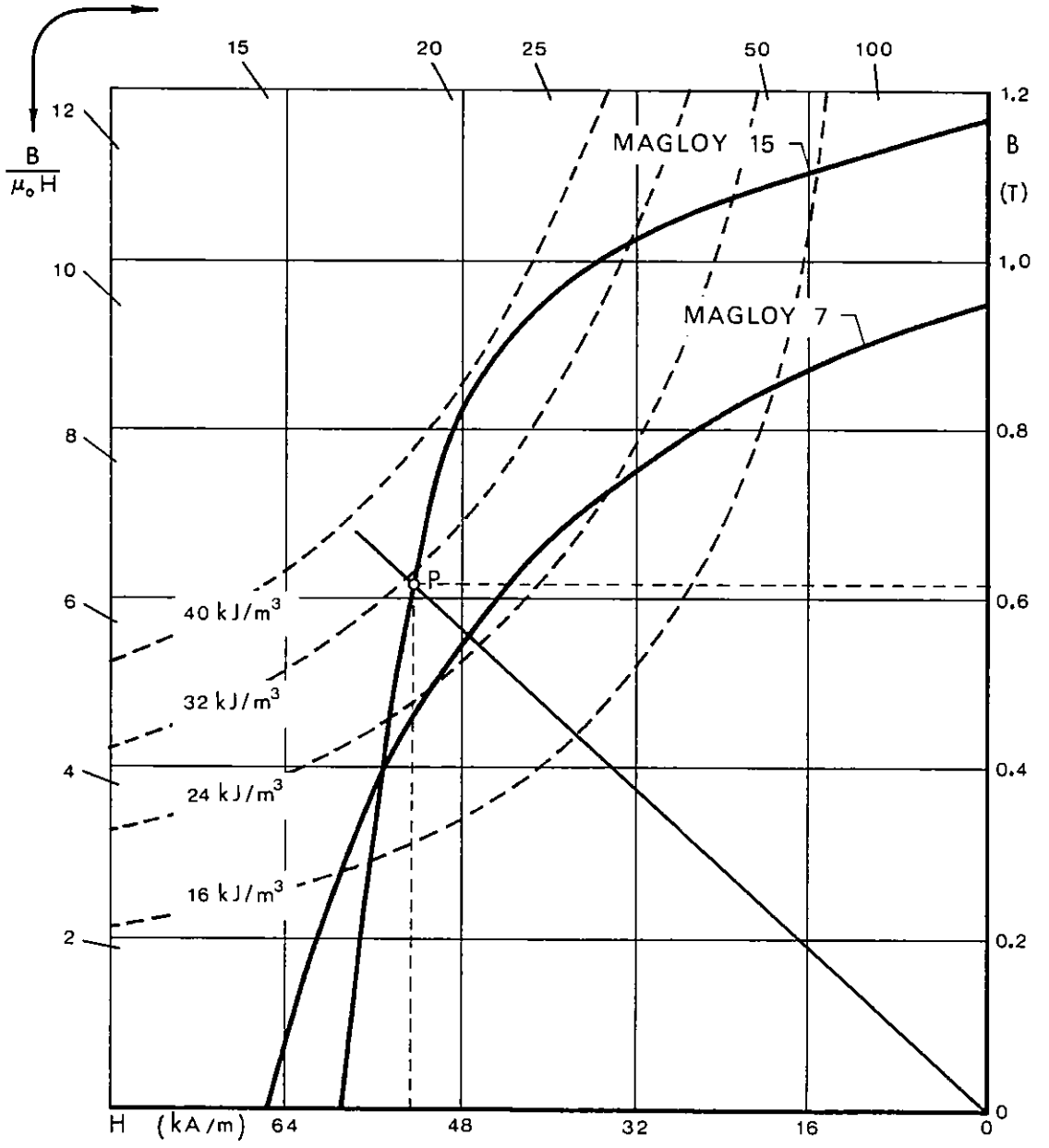

Fig. G.8 - Second quadrant demagnetisation curves for MAGLOY magnet at 25°C

From Eq. (2.10) the leakage factor is

$$K_l = 1 + \frac{P_\ell}{P_g}$$

and after substitution of results (G.10) and (G.11) gives $K_1 = 1.22$.

Thus, substitution of values in Eq. (G.9) gives for the slope of the load-line

$$\frac{B_m}{\mu_o H_m} = -9.71$$

In fig. G.8 the load-line intersects the demagnetisation curve of the MAGLOY 15 at $B_m = 0.62$ T. Hence, from Eq. (2.8) the air gap flux density is

$$B_g = \frac{B_m}{K_1} = 0.51 \text{ T}$$

From Eq. (G.1) the tachometer constant is

$$K_B = \frac{E}{\omega} = \frac{1}{4} f\beta\left(\frac{2R_i}{d} - f\right)B_g(R_o^2 - R_i^2)$$

and from the substitution of values is readily obtained as

$$K_B = 3.46 \text{ V/(rad.s}^{-1})$$

APPENDIX H

CALCULATION OF THE LEAKAGE FACTOR OF THE ALCOMAX 3 ROTOR

The analysis is carried out using Roters' method and one pole only is considered. Seven leakage paths are shown in fig. H.1.

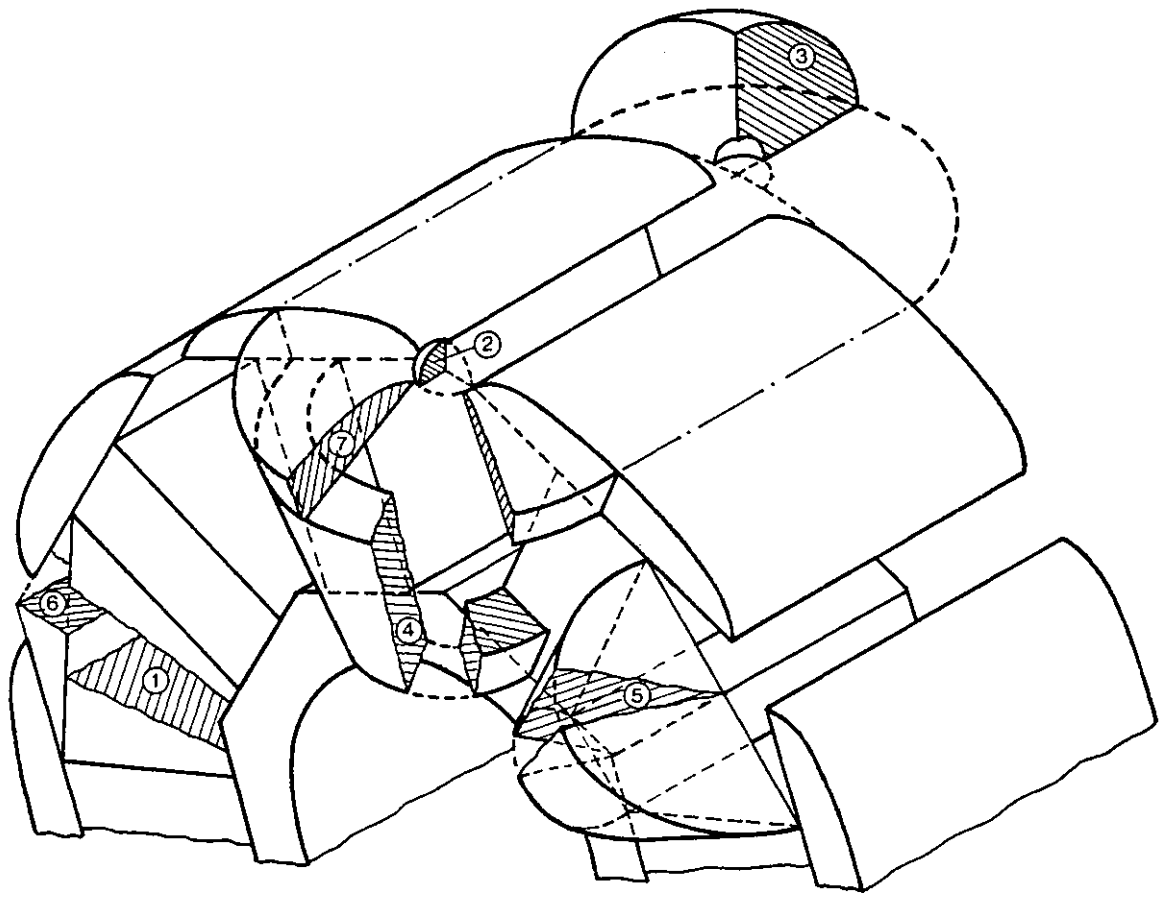

Fig. H.1 - Leakage flux paths for Alcomax 3 rotor

The permeance of each path is obtained as follows:

Path 1

In this path the flux lines have a circumferential shape between non-parallel magnet sides at variable potential, as shown in fig. H.2.

Assuming linear variation for magnetic potential

$$\Omega_r = \Omega_m \frac{r - r_1}{r_2 - r_1}$$

the elementary flux emanating from the magnet at level r is

$$d\phi_r = \Omega_r \, dP_r = \frac{2\mu_o \ell \Omega_m}{\theta(r_2 - r_1)} \frac{r - r_1}{r} dr$$

Thus the total flux emanating from one side of the magnet is

$$\phi = \frac{2\mu_o \ell \Omega_m}{\theta(r_2 - r_1)} \int_{r_1}^{r_2} (1 - \frac{r_1}{r}) dr = \frac{2\mu_o \ell \Omega_m}{\theta} (1 - \frac{r_1}{r_2 - r_1} \log \frac{r_2}{r_1})$$

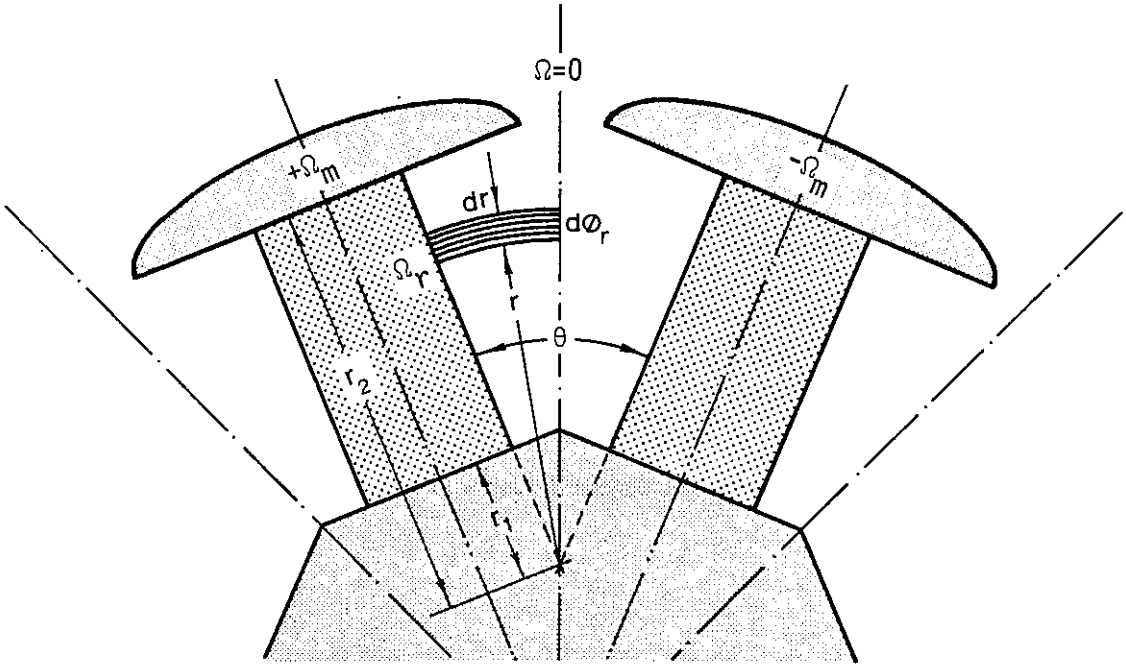

Fig. H.2 - Circumferential flux path

Hence the permeance due to both sides of the magnet per pole is

$$P_1 = \frac{2\phi}{\Omega_m} = \frac{4\mu_o \ell}{\theta} (1 - \frac{r_1}{r_2 - r_1} \log \frac{r_2}{r_1}) \qquad (H.1)$$

For $\theta = \pi/4$ rad, r_1 = 9 mm, r_2 = 29 mm, ℓ = 30 mm, Eq. (H.1) gives:

$$P_1 = 72.38\mu_o \text{ mH}$$

Path 2

This is a spherical quadrant between the pole piece corners which are a distance apart c, as shown in fig. H.3. The mean length of the path is according to Roters' book $\ell_{mean} = 1.3c$. The volume of the quadrant is

$V = (1/3)\pi(c/2)^3$. Hence the mean area of the flux path will be:

$$S_{mean} = \frac{V}{\ell_{mean}} = \frac{\frac{1}{3}\pi\left(\frac{c}{2}\right)^3}{1.3c} = 0.1c^2$$

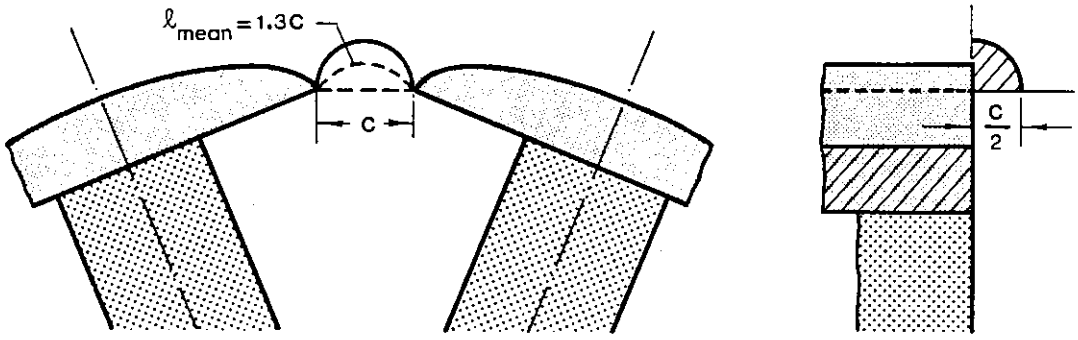

Fig. H.3 - Spherical quadrant flux path

There are four octants per pole. Thus the total permeance of the path is

$$P_2 = 4\,\frac{\mu_o S_{mean}}{\frac{\ell_{mean}}{2}} \quad 8\mu_o\,\frac{0.1c^2}{1.3c} = 8\mu_o\,0.077c \qquad (H.2)$$

In this case c = 5 mm and Eq. (H.2) gives:

$$P_2 = 3.08\mu_o \quad mH$$

Path 3

This is a quadrant of spherical shell as shown in fig. H.4. There are four octants per pole pitch. The mean length of the flux path is ℓ_{mean} =

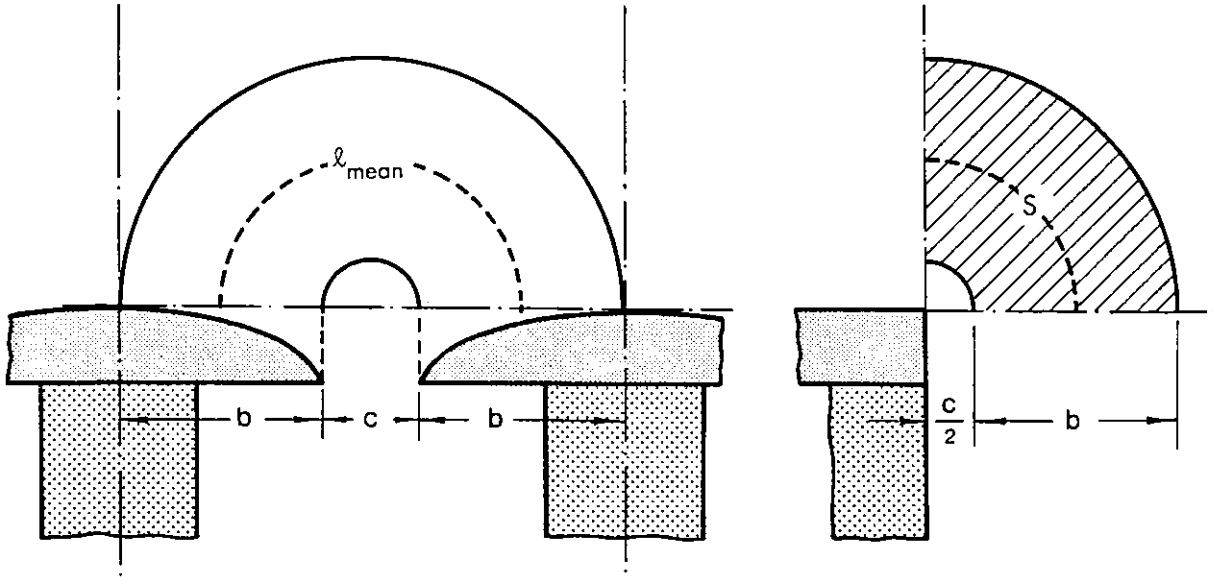

Fig. H.4 - Spherical shell flux path

$\frac{\pi}{2}(b + c)$. The maximum area of the flux path is $S = \frac{\pi}{4}b(b + c)$ and the average area of the path may be considered to be half of this value. Thus the permeance per pole pitch is

$$P_3 = 4\mu_o \frac{S_{mean}}{\frac{\ell_{mean}}{2}} = 8\mu_o \frac{\frac{\pi}{8}b(b + c)}{\frac{\pi}{2}(b + c)} = 2\mu_o b \qquad (H.3)$$

Taking b = 14 mm, the result becomes:

$$P_3 = 28\mu_o \quad mH$$

Path 4

The flux leakage fills a conic annulus of angle θ with a distributed magnetic potential, as shown in fig. H.5.

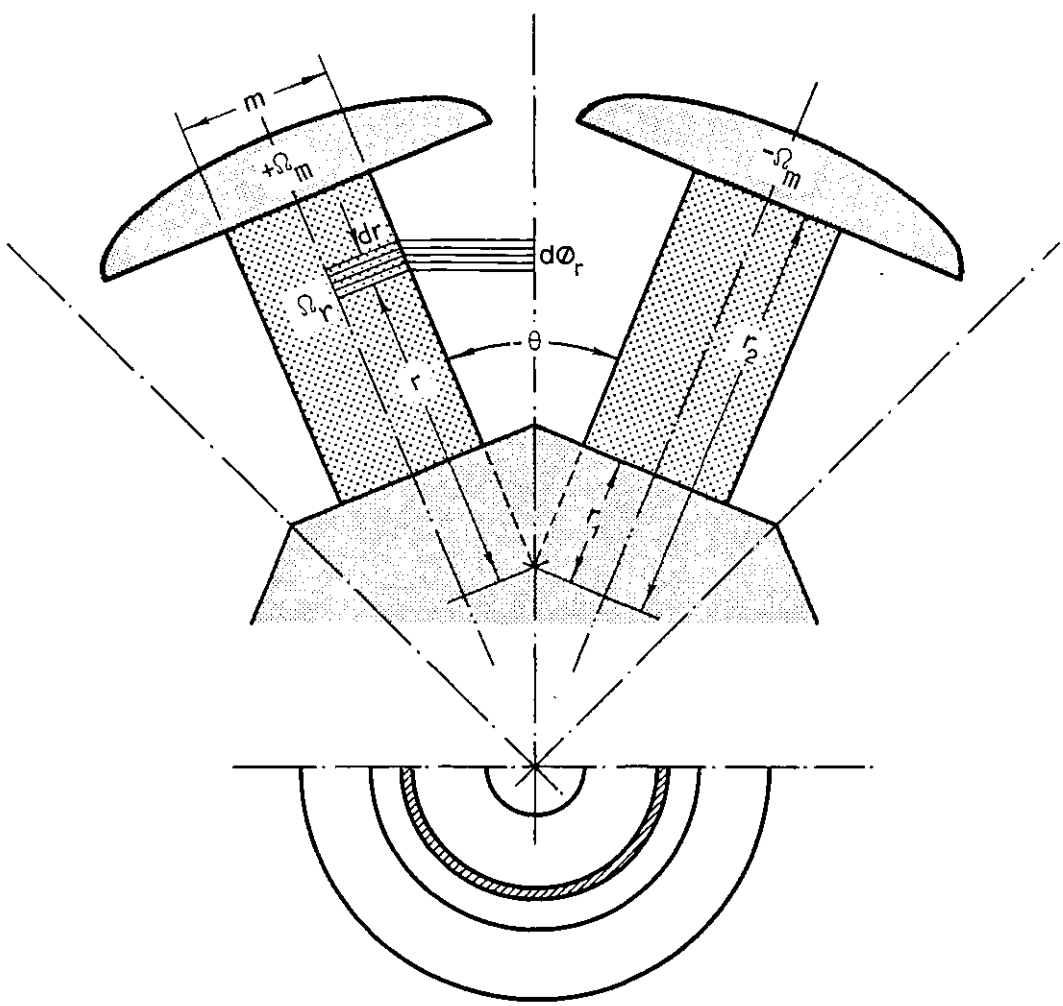

Fig. H.5 - Conic annulus flux path

The elementary flux emanating from the magnet to the interpolar plane is $d\phi_r = \Omega_r \, dP_r$ where

$$dP_r = \mu_o \frac{m}{2(r\frac{\theta}{2} + \frac{m}{4})\frac{\pi}{2}} \, dr$$

represents the elementary permeance of an area $\frac{m}{2}dr$ and mean length $\frac{\pi}{2}(r\frac{\theta}{2} + \frac{m}{4})$. Thus:

$$d\phi_r = 4\Omega_m \mu_o \frac{m}{\pi(r_2 - r_1)} \frac{r - r_1}{2\theta r + m} \, dr$$

and the total flux is therefore:

$$\phi = 4 \frac{\Omega_m \mu_o m}{\pi(r_2 - r_1)} \int_{r_1}^{r_2} \frac{r - r_1}{2\theta r + m} dr = 4 \frac{\Omega_m \mu_o m}{\pi(r_2 - r_1)} \frac{1}{4\theta^2} \left[2r\theta + m - (2r_1\theta + m) \log(2r\theta + m) \right]_{r_1}^{r_2}$$

Hence, the total permeance per pole is

$$P_4 = \frac{4\phi}{\Omega_m} = 8 \frac{\mu_o m}{\pi\theta} \left[1 - \frac{2r_1\theta + m}{2\theta(r_2 - r_1)} \log \frac{2r_2\theta + m}{2r_1\theta + m} \right] \qquad \text{(H.4)}$$

Substitution of $\theta = \frac{\pi}{4}$ rad, $m = 5$ mm, $r_1 = 9$ mm and $r_2 = 29$ mm into Eq. (H.4) gives:

$$P_4 = 6.62\mu_o \quad \text{mH}$$

Path 5

The flux leakage of this path fills half of a frustum cone generated with its diameter between the corners of the magnet, as shown in fig. H.6.

At distance r the mean length of the flux path is $\ell_{mean} = 1.22x$ and therefore the mean elementary area

$$dS_{mean} = \frac{dV}{\ell_{mean}} = \frac{\frac{\pi}{2}\left(\frac{x}{2}\right)^2}{1.22x} dr = 0.322x \, dr$$

Thus the elementary permeance of a quarter frustum cone

$$dP_r = \mu_o \frac{dS_{mean}}{\ell_{mean}} = \mu_o \frac{0.332x}{\frac{1.22x}{2}} dr = 0.52\mu_o dr$$

Again, assuming linear variation for magnetic potential the total flux becomes:

$$\phi = \int_{r_1}^{r_2} \Omega_r \, dP_r = \Omega_m \frac{0.52\mu_o}{r_2 - r_1} \int_{r_1}^{r_2} (r - r_1)dr = 0.26\mu_o\Omega_m(r_2 - r_1)$$

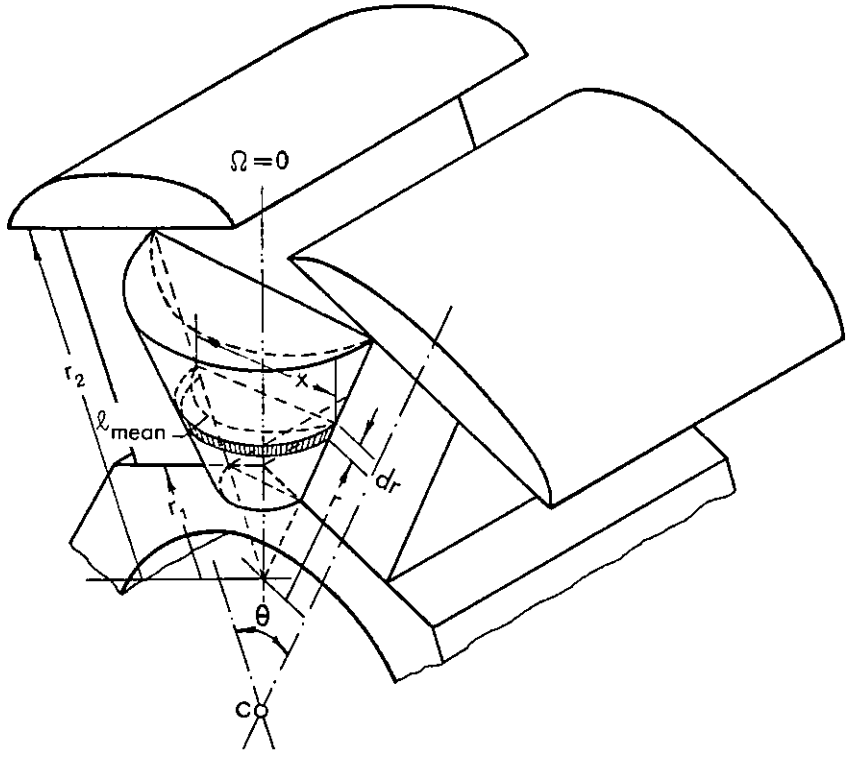

Fig. H.6 - Frustum cone flux path

The permeance per pole due to four quarters of these frustum cones is

$$P_5 = \frac{4\phi}{\Omega_m} = 1.04\mu_o(r_2 - r_1) \qquad (H.5)$$

Then, substitution of r_1 and r_2 gives:

$$P_5 = 20.8\mu_o \quad mH$$

Path 6

This is a solid trapezium joining the undersides of the pole pieces, as shown in fig. H.7.

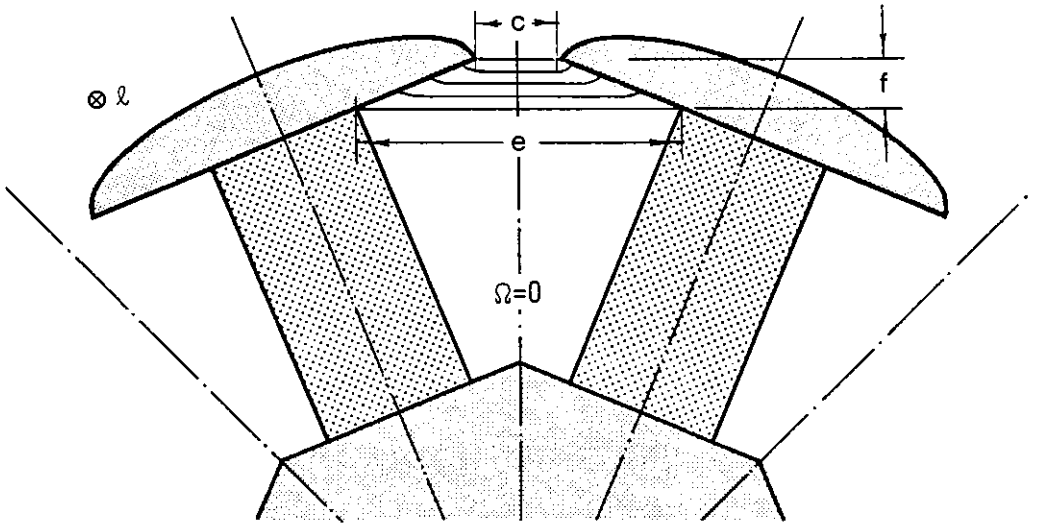

Fig. H.7 - Solid trapezium flux path

The permeance of half trapezium is

$$P = \mu_o \frac{f\ell}{\frac{1}{4}(c + e)}$$

There are two of these permeances in parallel per pole. Hence

$$P_6 = 8\mu_o \frac{f\ell}{c + e} \qquad \text{(H.6)}$$

Substitution of ℓ = 30 mm, f = 4.3 mm, c = 5 mm and e = 21 mm into Eq. (H.6) gives:

$$P_6 = 39.69\mu_o \quad \text{mH}$$

Path 7

This path is a semi-ring with a cross section S_p, as shown in fig. H.8.

The permeance of a quarter of the ring is

$$P = \mu_o \frac{S_p}{\ell_{mean}} = \mu_o \frac{S_p}{\frac{\pi}{2} R_{mean}}$$

Thus the permeance per pole

$$P_7 = 4P = 8\mu_o \frac{S_p}{R_{mean}} \qquad (H.7)$$

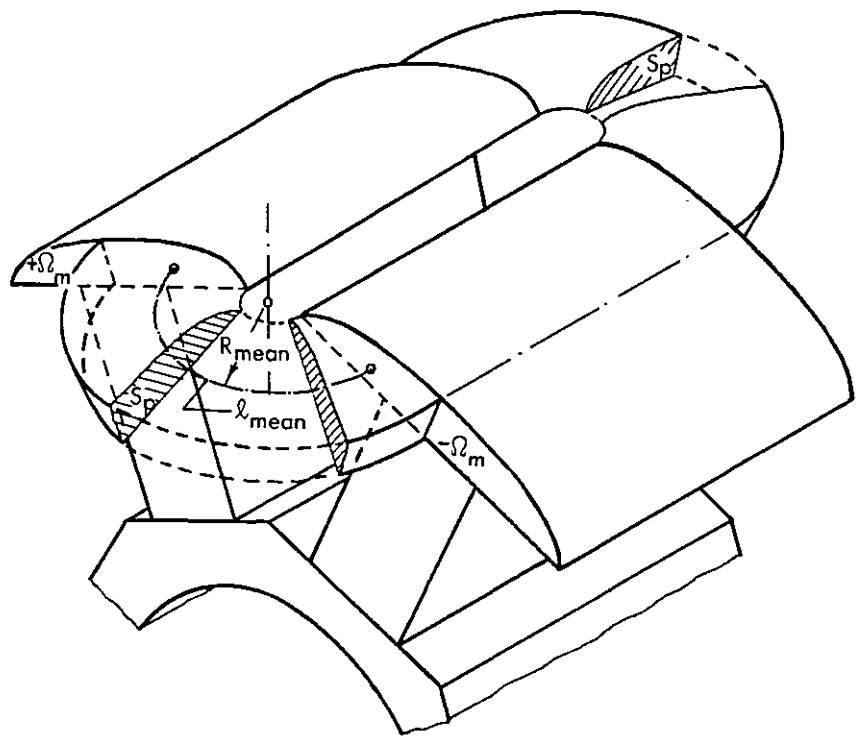

Fig. H.8 - Semi-ring flux path

By inspection of fig. 6.21 is $S_p \simeq 45$ mm^2 and $R_{mean} = 10.5$ mm. Then, substitution into Eq. (H.7), gives:

$$P_7 = 10.92\mu_o \quad \text{mH}$$

Total leakage permeance

The total leakage permeance P_ℓ is given by

$$P_\ell = \sum_{i=1}^{7} P_i = 0.181\mu_o \quad \text{H}$$

Leakage factor

The air gap permeance is given by Eq. (1.52). Substitution of $n_p = 8$, $\ell = 30$ mm, $r_c = 44.5$ mm and $R_g = 45$ mm gives $P_g = 1.26\mu_o$ H. Hence, from Eq. (2.10) the leakage factor is

$$K_1 = 1 + \frac{P_\ell}{P_g} = 1.14 \qquad (H.8)$$

REFERENCES

[1] - WILLIAMSON, A.C. and CHALMERS, B.J.: "New form of inverter-fed synchronous motor with induced excitation", 1977, Proc. I.E.E., Vol. 124, No. 3, pp. 213-217.

[2] - CHALMERS, B.J., PACEY, K. and GIBSON, J.P.: "Brushless d.c. traction drive", 1975, Proc. I.E.E., 122(7), pp. 733-738.

[3] - MACPHERSON, D.E. and SHEPHERD, J.: "Inverter-Synchronous machine parameters", 1979, I.E.E. Conference on Electrical Variable-Speed Drives, Conference Publication Number 179, pp. 54-57.

[4] - SLEMON, G.R., FORSYTHE, J.B. and DEWAN, S.B.: "Controlled-power-angle synchronous motor inverter drive system", 1973, I.E.E.E. Trans. Ind. Appl., pp. 216-219.

[5] - ASHEN, R.A.: "Some Aspects of High-Torque, Low Speed, Brushless Electric Motors", 1977, Ph.D. Thesis, Imperial College.

[6] - FANO, R.M. and ADLER, R.B.: "Electromagnetic Fields, Energy and Forces", 1066, Cambridge, Mass.: M.I.T. Press.

[7] - MATSCH, L.W.: "Electromagnetic and Electromechanical Machines", 1977, A Dun-Donnelly Publisher - New York - 2nd edition.

[8] - LAITHWAITE, E.R.: "Magnetic or Electromagnetic? - the great divide", 1973, Electronics and Power, 19(14) pp. 310-312.

[9] - BOLTON, R.H.: "The Design of Special Purpose Induction Machines", 1973, Ph.D. Thesis, Imperial College.

[10] - HUGHES,E.: "Electrical Technology", 1981, Longman, 5th edition.

[11] - KOSTENKO, M. and PIOTROVSKY, L.: "Electrical Machines", 1974, Mir Publishers, Moscow.

[12] - HAGUE, B.: "The Shape of Pole-Shoe Required to Produce a Sinusoidal Distribution of Air-Gap Flux Density", 1924, J.I.E.E., 62, pp. 921-929.

[13] - CLAYTON, A.E. and HANCOCK, N.N.: "The Performance and Design of Direct Current Machines", 1959, Pitman, 3rd edition.

[14] - SAY, M.G.: "The Performance and Design of Alternating Current Machines", 1958, 3rd edition.

[15] - BOLTON, H.R., DAWSON, C., ASHEN, R.A. and RODRIGUES, A.L.S.: "Investigation into Certain Categories of Long Travel Rotary Actuators", 1981, I.E.E. Second Conference on Small and Special Electrical Machines, Conference Publication Number 202, pp. 82-90.

[16] - "Hydraulic Motors", Machine Design, 42,(22), pp. 39-42.

[17] - "Hydraulic Actuators", ,,Machine Design, September 12, 1974.

[18] - CORBETT, A.E. and MOHAMAD, M.T.: "The disc-armature d.c. motor and its applications", 1976, I.E.E. Conference on Small Electrical Machines.

[19] - CAMPBELL, P.: "Principles of a pemanent-magnet axial-field d.c. machine", 1974, Proc. I.E.E., 121(12), pp. 1489-94.

[20] - ROTHWELL, D: "Characteristics of the Printed Circuit Servo-motor", 1966, Control, 10,(93), pp. 136-333.

[21] - FITZGERALD, A.E. and KINGSLEY, C.: "Electric Machinery", 1971, McGraw-Hill.

[22] - ELLISON, A.G.: "Electromechanical Energy Conversion", 1970, Harrap.

[23] - ALGER, P.L.: "The Calculation of the Armature Reaction of Synchronous Machines", 1928, A.I.E.E. Trans. 47,(2), pp. 493-513.

[24] - GROVER, F.W.: "Inductance Calculations, Working Formulae and Tables", 1962, Dover.

[25] - BOLTON, H.R.: "Permanent Magnets in Alternators and Special Drives", June 1980, first U.K. Conference on the Manufacture and Application of Permanent Magnets.

[26] - PARKER, R.J. and STUDDERS, R.J.: "Permanent Magnets and their Applications", 1962, John Wiley and Sons Inc., New York.

[27] - SCARBOROUGH, J.B.: "Numerical Mathematical Analysis", 1958, The Johns Hopkins Press, 4th edition, Baltimore, 1958.

[28] - BRAILSFORD, F.: "An Introduction to the Magnetic Properties of Materials", 1968, Longmans.

[29] - HECK, C.: "Magnetic Materials and their Applications", 1974, Butterworths.

[30] - CARPENTER, C.J.: "Magnetic Effects of Iron", 1972, I.C. Course on Electromagnetic Fields.

[31] - IRELAND, J.R.: "Ceramic Permanent Magnet Motors", 1968, McGraw-Hill.

[32] - GOLLHART, J.E. and BEAUDOIN, L.W.: "International Electronics", 20-23.

[33] - BURNETT, J. and OVERSHOTT, K.J.: "Analysis of the dynamic operation of permanent magnets", 1976, I.E.E. Second Conference on Advances in Magnetic Materials and their Applications.

[34] - SCHLENK, K.W.: "Magnetic Field no. 4", July 1981.

[35] - LYNCH, R,: "The Development of Samarium Cobalt Permanent Magnet D.C. Servomotors", 1976, I.E.E. Conference of Small Electrical Machines, Conference Publication Number 136, pp. 5-10.

[36] - CLEGG, A.G.: "Permanent Magnets - an Introduction", June 1980, First U.K. Conference on the Manufacture and Application of Permanent Magnets.

[37] - ARMSTRONG, M.: "Hard Ferrite Permanent Magnets", June 1980, First U.K. Conference on the Manufacture and Application of Permanent Magnets.

[38] - JOHNSON, R.E.: "The Manufacture of Sintered Samarium Cobalt Magnets", June 1980, Fist U.K. Conference on the Manufacture and Application of Permanent Magnets.

[39] - MANTEUFFEL, E.W. and HERTZENDORF, B.H.: "Brushless D.C. Torque Motor Development", 1970, G.E. Co., New York, U.S.A. Report prepared for H.Q. Space and Missile Systems Organisation, Air Force Systems Command. Report No. AD707514.

[40] - NOODLEMAN, S.: "Cobalt-Rare Earth Magnets for D.C. Machines", 1975, Goldshcmidt informiert, 4/75,(35) pp. 75-84.

[41] - BINNS, K.J. and JABBAR, M.A.: "Comparison of performance characteristics of a class of high-field permanent magnet machine for different magnet materials", September 1981, I.E.E. Second International Conference of Small and Special Electrical Machines, Conference Publication Number 202, pp. 107-110.

[42] - BINNS, K.J. and LOW, T.S.: " Multistacked permanent magnet generators - the relation between output and magnet characteristics", September 1981, I.E.E. Second International Conference on Small and Special Electrical Machines, Conference Publication Number 202, pp. 138-141.

[43] - ROTERS , H.C.: "Electromagnetic Devices", 1941, John Wiley and Sons Inc., New York.

[44] - MAYNARD, C.A.: "Analysis and Design of Permanent Magnet Assemblies", Machine Design, 29(8), pp. 122-143.

[45] - REICHERT, K.: "The calculation of magnetic curcuits with permanent magnets by digital computer", 1970, Ibid, MAG 6, pp. 283 - 288.

[46] - BINNS, K.J., JABBAR, M.A. and BARNARD, W.R.: "Computation of the magnetic field of permanent magnets in iron cores", 1975, Proc. I.E.E. 122(12), pp. 1377-1391.

[47] - SLOMCZYNSKA, J.: "Nonlinear analysis of the magnetic flux distribution in the magnet stabilsed in air", 1974, I.E.E.E. Trans., MAG 10, pp. 1109-1113.

[48] - SLOMCZYNSKA, J.: "No-load magnetic field distribution in a permanent magnet machine", 1975, Ibid, MAG 11, pp. 1720-1722.

[49] - HARROLD, W.J.: "Calculation of equipotential and flux lines in axially symmetrical permanent magnet assemblies by computer", 1972, Ibid, MAG 8, pp. 23-29.

[50] - ASHEN, R.A.: "Linear scalar-potential models for permanent magnet circuits", 1978, Proc. I.E.E., 125(12), pp. 1403-1409.

[51] - SILVESTER , P.: "Modern Electromagnetic Fields", 1968, Prentice Hall Inc., Englewood Cliffs, N.J.

[52] - REICHERT, K. and FREUNDL H.: "Computer-Aided Design of Permanent Magnets Systems", 1972, Brown Boveri Review, 59(9), pp. 469-475.

[53] - BINNS, K.J. and LAWRENSON, P.J.: "Analysis and Computation of Electric and Magnetic Field Problems", 1973, Pergamon, 2nd edition.

[54] - CARPENTER, C.J.: "A Network Approach to Fields", 1972, I.C. Easter Course on Electromagnetics of Electrical Machines.

[55] - LORRAIN, P. and CORSON, D.R.: "Electromagnetic Fields and Waves", 1970, W.H. Freeman and Co, San Francisco.

[56] - ASHEN, R.A. and BOLTON, H.R.: "Performance and design of a brushless torque motor", 1976, I.E.E. Conference on Small Electrical Machines, Conference Publication Number 136, pp. 27-30.

[57] - BEILER, A.H.: "The thyratron motor at the Logan Plant", 1938, Electrical Engineering, 57,(1), pp. 19-24.

[58] - YATES, W.W.: "Brushless D.C. Motors", 1966, Machine Design, 38,(5), pp. 136-142.

[59] - LISKA, M. and ULRICH, B.: "Magnetic Steppermotors and Brushless D.C. Motors: Principles and Applicatons in Drive Units", 1976, I.E.E. Conference on Small Electrical Machines, Conference Publication Number 136, pp. 15-18.

[60] - OHNO, E., KISHIMOTO, T. and AKAMATSU, M.: "The Thyristor Commutatorless Motor", 1967, I.E.E.E. Trans., MAG-3, (3), pp. 236-240.

[61] - SATO, N. and SEMENOV, V.V.: "Adjustable Speed Drive with a Brushless D.C. Motor", 1971, I.E.E.E., Trans., IGA-7, No.4, pp. 539-543.

[62] - JANONIS, V.F.: "High Voltage D.C. Brushless Torpedo Propulsion Motor", 1973, Lear Siegler, Inc. Power Equipment Division, Cleveland, Ohio, pp. 57-62.

[63] - RADZIWILL, W.: "A Highly Efficient Small Brushless D.C. Motor", 1969, Philips Technical Review, volume 30.

[64] - WATANABE, T., INAGAKI, J., TAKADUMA, S. AND TANAKA, S.: "Transistor Motor, a Brushless D.C. Motor", 1970, Toshiba Review, pp. 50-54.

[65] - WERNINCK, E.H.: "Electric Motor Handbook", 1978, McGraw-Hill.

[66] - BOSH, G. and JANSSEN, J.H.H.: "Integrated Circuit with Hall Device for Brushless D.C. Motors", 1970, Philips Technical Review, volume 34, pp. 366-368.

[67] - R.S. COMPONENTS LIMITED: "Magnetic Pick-Ups", March-June 1982.

[68] - R.S. COMPONENTS LIMITED: "Waveform Generators", Data Sheet R/2141, July 1979.

[69] - TAYLOR, P.L.: "Servomechanisms", 1965, Longmans.

[70] - KING, R.: "Electronic Circuits and Systems", 1978, Nelson.

[71] - HILBURN, J.L. and JOHNSON, D.E.: "Manual of Active Filter Design", 1973, McGraw-Hill.

[72] - ADKINS, B.: "The General Theory of Electrical Machines", 1964, Chapman and Hall Ltd.

[73] - INAGAKI, J., KUNIYOSHI, M. and TAKADUMA, S.: "Commutators get the brushoff", 1973, I.E.E.E. Spectrum, 10,(6), pp. 52-58.

[74] - OKUYAMA, T., KONISHI, T., SHIBATA, T., MORINO, N., IWATA, K. and SUKEGAWA, T.: "Cycloconverter-fed Synchronous Motor Drive for Steel Rolling Mill", 1978, Toshiba Review, pp. 820-823.

[75] - MOKRYTZKI, B.: "Pulse Width Modulation Inverters for A.C. Motor Drives", 1967, I.E.E.E. Trans., IGA-3, No. 6, pp. 493-503.

[76] - BURGER, P.: "Analysis of a Class of Pulse Modulated D.C. to D.C. Converters", 1973, I.E.E.E. Trans., I.E.C.I.-22, No. 2, pp. 104-116.

[77] - SLEMON, G.R., DEWAN, S.B. and WILSON, W.A.: "Synchronous Motor Drive with Current-Source Inverter", 1974, I.E.E.E. Trans., IA-10, No. 3, pp.412-416.

[78] - HAYSHI, K., TAKABAYASHI, H. and SATO, N.: "A Study of Forced Commutation Methods of Constant-Current Inverters for Commutatorless Motors", 1976, Electrical Engineering in Japan, Vol. 96, No. 2, pp. 14-22.

[79] - BOWLER, P.: " A wide bandwidth servo amplifier", 1974, I.E.E. Conference on Power Electronics - Power Semiconductors and their Applications, pp. 112-126.

[80] - PACEY, K.: "Variable-speed characteristics of synchronous motor drives with rotor position control", 1974, Ph.D. Thesis, University of Manchester.

[81] - CARTER, F.W.: "Air Gap Induction", 1901, Electrical World and Engineer, pp. 884-888.

[82] - KREYSZIG, E.: "Advanced Engineering Mathematics", 1979, 4th edition.

[83] - "Development and manufacture of a linear induction motor propulsion system for the tracked air cushion research vehicle", Airesearch Manufacturing Co., (Garret Corp.), Calif., U.S.A.

[84] - JONES, C.V.: The Unified Theory of Electrical Machines", 1971, Butterworths.

[85] - BUCKINGHAM, H: "Principles of Electrical Measurements", 1959, The English Universities Press Limited, London.

[86] - SAY, M.G. and TAYLOR, E.O.: "Direct Current Machines", 1980, Pitman.

[87] - COTTON, H.: "Advanced Electrical Technology", 1967, Pitman.

[88] - HINDMARSH, J.: "Electrical Machines and their Applications", 1977, Pergamon, 3rd edition.

[89] - "Application for Operational Amplifiers and Comparators", R.S. Data Sheet R/202, July 1976.

[90] - UPSON, A.R.: "Synchro Engineering Handbook", 1965, Muirhead and Co. Ltd.

[91] - DORFF, R.C.: "Modern Control Systems", 1970, Addison-Wesley.

[92] - JEHL, F.: "Dynamo-Electric Machine", U.S. Patent 376307, January, 1888.

[93] - NELSON, L.W.: "Dynamo-Electric Machine", U.S. Patent 1038494, September, 1912.

[94] - SOCIETE D'ELECTRONIC ET D'AUTOMATISURE: "A flat air gap electrical rotating machine", British Patent 874394, August 1961.

[95] - HENRY-BAUDOT, J.: "Rotating Electrical Machines with Printed-Circuit Windings", U.S. Patent 3144574, October 1957.

[96] - CORBETT, A.E.: "A disc-armature d.c. motor", 1970, EM70 Conference Publication, University of Dundee, 42.

[97] - CAMPBELL, P.: "A new wheel motor for electric commuter cars", 1972, Elect. Rev. 190, 10, pp. 323-333.

[98] - CAMPBELL, P. and CORBETT, A.E.: "The pancake motor", 1974, Automotive Des. Eng., 13, July/August 1974, pp. 34-35.

[99] - LIWSCHITZ-GARIK, M.: "Direct-Current Machines", 1956, D. Van Nostrand Co. Inc.

[100] - D'ANGELO, M.V.K. and CAMPBELL, P.: "Three-Dimensional Finite Element Solution for a Permanent Magnet Axial-Field Machine", 1982, I.E.E.E. Trans.

[101] - R.S. COMPONENTS LIMITED: "C-MOS", 4000B series Data Sheet.

[102] - R.S. COMPONENTS LIMITED: "Voltage to Frequency Converter", Data Sheet 307-070.

[103] - SPALLA, L.J.: "Current Feedback Drives for D.C. Torque Motors", 1971, Instruments and Control Systems, 44, (5), pp. 105-108.

[104] - COWAN, P.: "Current Loop Drive for D.C. Motors", Inland Motors Application Notes issued 24th July, 1974.

[105] - ELECTRO-CRAFT CORPORATION: "D.C. Motors, speed controls, servo systems", 1977, Pergamon Press.

[106] - CORBETT, A.E.: "Disc-armature motors for low-power traction drives", 1981, I.E.E. Conference on Small and Special Electrical Machines, Conference Publication Number 202, pp.162-165.

[107] - CAPALDI, B.: "The theory and performance of a.c. axial flux machines", 1973, Ph.D. thesis, University of Warwick.

[108] - EVANS, P.D.: "Disc geometry reluctance motors", 1977, Ph.D. thesis, Imperial College.

[109] - JAMES NEILL: "Permanent magnets catalog", 1981, Napier Street.

[110] - EVANS, P.D. and EASTHAM, J.F.: "Disc-geometry homopolar synchronous machine", 1980, Proc. I.E.E., Vol. 127, pp. 299-307.

[111] - LANGSDORF: "Principles of D.C. Machines", 1955, MacGraw-Hill.

[112] - WHARTON, E.: "Unusual machine configurations", 1976, I.E.E. Conference on Small Electrical Machines, Conference Publication Number 136.

[113] - CHATRATANA, S.: "Single-phase induction generators and switched reluctance motors", 1982, Ph.D. thesis, Imperial College.

☆ ☆ ☆